

AD 739577

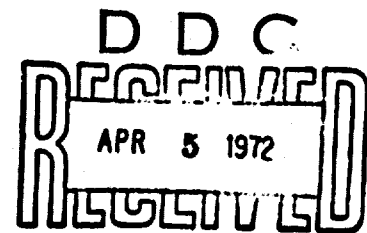
Y
Bulletin 42
(Part 4 of 5 Parts)

**THE
SHOCK AND VIBRATION
BULLETIN**

**Part 4
Isolation, Damping, Prediction Experimental Techniques**

JANUARY 1972

**A Publication of
THE SHOCK AND VIBRATION
INFORMATION CENTER
Naval Research Laboratory, Washington, D.C.**



AD 739577
**Office of
The Director of Defense
Research and Engineering**

**Reproduced by
NATIONAL TECHNICAL
INFORMATION SERVICE
Springfield, Va 22151**

264
This document has been approved for public release and sale; its distribution is unlimited.

SYMPOSIUM MANAGEMENT

THE SHOCK AND VIBRATION INFORMATION CENTER

William W. Mutch, Director
Henry C. Pusey, Coordinator
Rudolph H. Volin, Coordinator
Edward H. Schell, Coordinator

Bulletin Production

Graphic Arts Branch, Technical Information Division,
Naval Research Laboratory

ACCESSION for	
CPSTI	WHITE SECTION <input checked="" type="checkbox"/>
DB	BUFF SECTION <input type="checkbox"/>
ANNOUNCED	<input type="checkbox"/>
STIFICATION	
Y <i>Volin</i>	
DISTRIBUTION/AVAILABILITY CODES	
DIST.	AVAIL. AND IN SPECIAL
<i>A</i>	<i>21</i>

Bulletin 42
(Part 4 of 5 Parts)

THE SHOCK AND VIBRATION BULLETIN

JANUARY 1972

**A Publication of
THE SHOCK AND VIBRATION
INFORMATION CENTER
Naval Research Laboratory, Washington, D.C.**

The 42nd Symposium on Shock and Vibration was held at the U.S. Naval Station, Key West, Florida, on 2-4 November 1971. The U.S. Navy was host.

Details of illustrations in
this document may be better
studied on microfiche

**Office of
The Director of Defense
Research and Engineering**

Details of illustrations in
this document may be better
studied on microfiche

CONTENTS

PAPERS APPEARING IN PART 4

Isolation and Damping

TRANSIENT RESPONSE OF REAL DISSIPATIVE STRUCTURES,	1
R. Plunkett, University of Minnesota, Minneapolis, Minnesota	
DYNAMIC RESPONSE OF A RING SPRING	7
R. L. Eshleman, IIT Research Institute, Chicago, Illinois	
SHOCK MOUNTING SYSTEM FOR ELECTRONIC CABINETS,	15
W. D. Delany, Admiralty Surface Weapons Establishment, Portsmouth, U.K.	
METHODS OF ATTENUATING PYROTECHNIC SHOCK,	21
S. Barrett and W. J. Kacena, Martin Marietta Corporation, Denver, Colorado	
ENERGY ABSORPTION CAPACITY OF A SANDWICH PLATE WITH CRUSHABLE CORE	33
D. Krajcinovic, Argonne National Laboratory, Argonne, Illinois	
ON THE DAMPING OF TRANSVERSE MOTION OF FREE-FREE BEAMS IN DENSE, STAGNANT FLUIDS,	41
W. K. Blake, Naval Ship Research and Development Center, Bethesda, Maryland	
OPTIMUM DAMPING DISTRIBUTION FOR STRUCTURAL VIBRATION	57
R. Plunkett, University of Minnesota, Minneapolis, Minnesota	
A LAYERED VISCOELASTIC EPOXY RIGID FOAM MATERIAL FOR VIBRATION CONTROL,	65
C. V. Stahle and Dr. A. T. Tweedie, General Electric Company, Space Division, Valley Forge, Pa.	
OPTIMIZATION OF A COMBINED RUZICKA AND SNOWDON VIBRATION ISOLATION SYSTEM,	77
D. E. Zeldler, Medtronic, Inc., Minneapolis, Minnesota, and D. A. Frohrib, University of Minnesota, Minneapolis, Minnesota	
TRANSIENT RESPONSE OF PASSIVE PNEUMATIC ISOLATORS	85
G. L. Fox, and E. Steiner, Barry Division of Barry Wright Corporation, Burbank, California	
EXPERIMENTAL DETERMINATION OF STRUCTURAL AND STILL WATER DAMPING AND VIRTUAL MASS OF CONTROL SURFACES.	93
R. C. Leibowitz and A. Kilcullen, Naval Ship Research and Development Center, Washington, D.C.	
DAMPING OF A CIRCULAR RING SEGMENT BY A CONSTRAINED VISCOELASTIC LAYER	121
Cpt. C. R. Almy, U.S. Army Electronics Command, Ft. Monmouth, New Jersey, and F. C. Nelson, Department of Mechanical Engineering, Tufts University, Medford, Medford, Mass.	

DYNAMIC ANALYSIS OF THE RUNAWAY ESCAPEMENT MECHANISM	125
G. W. Hemp, Department of Engineering, Science and Mechanics, University of Florida, Gainesville, Florida	

Prediction and Experimental Techniques

A METHOD FOR PREDICTING BLAST LOADS DURING THE DIFFRACTION PHASE	135
W. J. Taylor, Ballistic Research Laboratories, Aberdeen Proving Ground, Maryland	
DRAG MEASUREMENTS ON CYLINDERS IN EVENT DIAL PACK	157
S. B. Mellsen, Defence Research Establishment Suffield, Ralston, Alberta, Canada	
DIAL PACK BLAST DIRECTING EXPERIMENT,	175
L. E. Fugelso, S. F. Fields, and W. J. Byrne, General American Research Division, Niles, Illinois	
BLAST FIELDS ABOUT ROCKETS AND RECOILLESS RIFLES.	185
W. E. Baker, P. S. Westine, and R. L. Bessey, Southwest Research Institute, San Antonio, Texas	
TRANSONIC ROCKET-SLED STUDY OF FLUCTUATING SURFACE-PRESSURES AND PANEL RESPONSES,	201
E. E. Ungar, Bolt Beranek and Newman Inc., Cambridge, Massachusetts, and H. J. Bandgren, Jr. and R. Erwin, National Aeronautics and Space Administration, George C. Marshall Space Flight Center Huntsville, Alabama	
SUPPRESSION OF FLOW-INDUCED VIBRATIONS BY MEANS OF BODY SURFACE MODIFICATIONS.	215
D. W. Sallet and J. Beresow, Naval Ordnance Laboratory, Silver Spring, Maryland	
AN EXPERIMENTAL TECHNIQUE FOR DETERMINING VIBRATION MODES OF STRUCTURES WITH A QUASI-STATIONARY RANDOM FORCING FUNCTION.	229
R. G. Christiansen and W. W. Parmenter, Naval Weapons Center, China Lake, California	
RESPONSE OF AIR FILTERS TO BLAST	253
E. F. Witt, C. J. Arroyo, and W. N. Butler, Bell Laboratories, Whippany, N.J.	

PAPERS APPEARING IN PART 1

Invited Papers

SMALL SHIPS-HIGH PERFORMANCE

Rear Admiral H. C. Mason, Commander, Naval Ship Engineering Center, Washington, D.C.

Specifications

SURVEY OF VIBRATION TEST PROCEDURES IN USE BY THE AIR FORCE

W. B. Yarcho, Air Force Flight Dynamics Laboratory, Wright-Patterson Air Force
Base, Ohio

SPECIFICATIONS - A PANEL SESSION

**SOME ADMINISTRATIVE FACTORS WHICH INFLUENCE TECHNICAL APPROACHES
TO SHIP SHOCK HARDENING**

D. M. Lund, Naval Ship Engineering Center, Hyattsville, Maryland

Measurement and Application of Mechanical Impedance

**FORCE TRANSDUCER CALIBRATIONS RELATED TO MECHANICAL IMPEDANCE
MEASUREMENTS**

E. F. Ludwig, Assistant Project Engineer, and N.D. Taylor, Senior Engineer, Pratt & Whitney Aircraft, Florida Research & Development Center, West Palm Beach, Florida

**THE MEASUREMENT OF MECHANICAL IMPEDANCE AND ITS USE IN
VIBRATION TESTING**

N. F. Hunter, Jr., and J. V. Otts, Sandia Corporation, Albuquerque, New Mexico

**TRANSIENT TEST TECHNIQUES FOR MECHANICAL IMPEDANCE AND MODAL
SURVEY TESTING**

J. D. Favour, M. C. Mitchell, N. L. Olson, The Boeing Company, Seattle, Washington

**PREDICTION OF FORCE SPECTRA BY MECHANICAL IMPEDANCE AND ACOUSTIC
MOBILITY MEASUREMENT TECHNIQUES**

R. W. Schock, NASA/Marshall Space Flight Center, Huntsville, Alabama and G. C. Kao, Wyle Laboratories, Huntsville, Alabama

DYNAMIC DESIGN ANALYSIS VIA THE BUILDING BLOCK APPROACH

A. L. Klosterman, Ph.D. and J. R. Lemon, Ph.D., Structural Dynamics Research Corporation Cincinnati, Ohio

**MOBILITY MEASUREMENTS FOR THE VIBRATION ANALYSIS OF CONNECTED
STRUCTURES**

D. J. Ewins and M. G. Sainsbury, Imperial College of Science and Technology, London, England

LIQUID-STRUCTURE COUPLING IN CURVED PIPES -- II

L. C. Davidson and D. R. Samsury, Machinery Dynamics Division, Naval Ship Research and Development Center, Annapolis, Maryland

Transportation and Packaging

A SURVEY OF THE TRANSPORTATION SHOCK AND VIBRATION INPUT TO CARGO

F. E. Ostrem, General American Research Division, General American Transportation Corporation, Niles, Illinois

THE DYNAMIC ENVIRONMENT OF SELECTED MILITARY HELICOPTERS

M. B. Gens, Sandia Laboratories, Albuquerque, New Mexico

HIGHWAY SHOCK INDEX

R. Kennedy, U. S. Army Transportation Engineering Agency, Military Traffic Management and Terminal Service, Newport News, Virginia

**DEVELOPMENT OF A ROUGH ROAD SIMULATOR AND SPECIFICATION FOR TESTING
OF EQUIPMENT TRANSPORTED IN WHEELED VEHICLES**

H. M. Forkols and E. W. Clements, Naval Research Laboratory, Washington, D.C.

LABORATORY CONTROL OF DYNAMIC VEHICLE TESTING

J. W. Grant, U. S. Army Tank-Automotive Command, Warren, Michigan

IMPACT VULNERABILITY OF TANK CAR HEADS

J. C. Sheng and J. E. Everett, General American Research Division,
General American Transportation Corporation, Niles, Illinois

A STUDY OF IMPACT TEST EFFECTS UPON FOAMED PLASTIC CONTAINERS

D. McDaniel, Ground Equipment and Materials Directorate, Directorate for Research,
Development, Engineering and Missile Systems Laboratory, U. S. Army Missile Command
Redstone Arsenal, Alabama, and R. M. Wyskida, Industrial and Systems Engineering
Department, The University of Alabama in Huntsville, Huntsville, Alabama

DEVELOPMENT OF A PRODUCT PROTECTION SYSTEM

D. E. Yound, IBM General Systems Division, Rochester, Minnesota, and
S. R. Pierce, Michigan State University, East Lansing, Michigan

**MOTION OF FREELY SUSPENDED LOADS DUE TO HORIZONTAL SHIP MOTION IN
RANDOM HEAD SEAS**

H. S. Zwibel, Naval Civil Engineering Laboratory, Port Hueneme, California

PAPERS APPEARING IN PART 2

Ground Motion

SINE BEAT VIBRATION TESTING RELATED TO EARTHQUAKE RESPONSE SPECTRA

E. G. Fischer, Westinghouse Research Laboratories, Pittsburgh, Pennsylvania

SEISMIC EVALUATION OF ELECTRICAL EQUIPMENT FOR NUCLEAR POWER STATIONS

R. H. Prause and D. R. Ahlbeck, BATTELLE, Columbus Laboratories, Columbus, Ohio

**SHOCK INPUT FOR EARTHQUAKE STUDIES USING GROUND MOTION FROM UNDERGROUND
NUCLEAR EXPLOSIONS**

D. L. Bernreuter, D. M. Norris, Jr., and F. J. Tokarz, Lawrence Livermore Laboratory,
University of California, Livermore, California

**ROCKING OF A RIGID, UNDERWATER BOTTOM-FOUNDED STRUCTURE SUBJECTED TO
SEISMIC SEAFLOOR EXCITATION**

J. G. Hammer and H. S. Zwibel, Naval Civil Engineering Laboratory, Port Hueneme,
California

**DEVELOPMENT OF A WAVEFORM SYNTHESIS TECHNIQUE-A SUPPLEMENT TO RESPONSE
SPECTRUM AS A DEFINITION OF SHOCK ENVIRONMENT**

R. C. Yang and H. R. Saffell, The Ralph M. Parsons Company, Los Angeles, California

**THE RESPONSE OF AN ISOLATED FLOOR SLAB-RESULTS OF AN EXPERIMENT IN
EVENT DIAL PACK**

J. M. Ferritto, Naval Civil Engineering Laboratory, Port Hueneme, California

A SHOCK-ISOLATION SYSTEM FOR 22 FEET OF VERTICAL GROUND MOTION

E. C. Jackson, A. B. Miller and D. L. Bernreuter, Lawrence Livermore Laboratory,
University of California, Livermore, California

**THE COMPARISON OF THE RESPONSE OF A HIGHWAY BRIDGE TO UNIFORM GROUND
SHOCK AND MOVING GROUND EXCITATION**

N. E. Johnson and R. D. Galletly, Mechanics Research, Inc., Los Angeles, California

DEFORMATION AND FRACTURE OF TANK BOTTOM HULL PLATES SUBJECTED TO MINE BLAST

D. F. Haskell, Vulnerability Laboratory, U.S. Army Ballistic Research Laboratories, Aberdeen Proving Ground, Md.

THE IMPULSE IMPARTED TO TARGETS BY THE DETONATION OF LAND MINES

P. S. Westline, Southwest Research Institute, San Antonio, Texas

CIRCULAR CANTILEVER BEAM ELASTIC RESPONSE TO AN EXPLOSION

Y. S. Kim and P. R. Ukrainetz, Department of Mechanical Engineering, University of Saskatchewan, Saskatoon, Canada

MEASUREMENT OF IMPULSE FROM SCALED BURIED EXPLOSIVES

B. L. Morris, U.S. Army Mobility Equipment Research and Development Center, Fort Belvoir, Virginia

Dynamic Analysis

THE EFFECTS OF MOMENTUM WHEELS ON THE FREQUENCY RESPONSE CHARACTERISTICS OF LARGE FLEXIBLE STRUCTURES

F. D. Day III and S. R. Tomer, Martin Marietta Corporation, Denver, Colorado

INTEGRATED DYNAMIC ANALYSIS OF A SPACE STATION WITH CONTROLLABLE SOLAR ARRAYS.

J. A. Heinrichs and A. L. Weinberger, Fairchild Industries, Inc., Germantown, Maryland, and M. D. Rhodes, NASA Langley Research Center, Hampton, Virginia

PARAMETRICALLY EXCITED COLUMN WITH HYSTERETIC MATERIAL PROPERTIES

D. T. Mozer, IBM Corporation, East Fishkill, New York, and R. M. Evan-Iwanowski, Professor, Syracuse University, Syracuse, New York

DYNAMIC INTERACTION BETWEEN VIBRATING CONVEYORS AND SUPPORTING STRUCTURE

M. Paz, Professor, Civil Engineering Department, University of Louisville, Louisville, Kentucky, and O. Mathis, Design Engineer, Rex Chainbelt Inc., Louisville, Kentucky

RESPONSE OF A SIMPLY SUPPORTED CIRCULAR PLATE EXPOSED TO THERMAL AND PRESSURE LOADING

J. E. Koch, North Eastern Research Associates, Upper Montclair, N.J., and M. L. Cohen, North Eastern Research Associates, Upper Montclair, N.J., and Stevens Institute of Technology, Hoboken, N.J.

WHIRL FLUTTER ANALYSIS OF PROPELLER-NACELLE-PYLON SYSTEM ON LARGE SURFACE EFFECT VEHICLES

Yuan-Ning Liu, Naval Ship Research and Development Center, Washington, D.C.

THE DYNAMIC RESPONSE OF STRUCTURES SUBJECTED TO TIME-DEPENDENT BOUNDARY CONDITIONS USING THE FINITE ELEMENT METHOD

G. H. Workman, Battelle, Columbus Laboratories, Columbus, Ohio

VIBRATION ANALYSIS AND TEST OF THE EARTH RESOURCES TECHNOLOGY SATELLITE

T. J. Cokonis and G. Sardella, General Electric Company, Space Division, Philadelphia, Pennsylvania

FINITE AMPLITUDE SHOCK WAVES IN INTERVERTEBRAL DISCS

W. F. Hartman, The Johns Hopkins University, Baltimore, Maryland

ACCELERATION RESPONSE OF A BLAST-LOADED PLATE

L. W. Fagel, Bell Telephone Laboratories, Inc., Whippany, New Jersey

**EFFECT OF CORRELATION IN HIGH-INTENSITY NOISE TESTING AS INDICATED
BY THE RESPONSE OF AN INFINITE STRIP**

C. T. Morrow, Advanced Technology Center, Inc., Dallas, Texas

PAPERS APPEARING IN PART 3

Test Control

ON THE PERFORMANCE OF TDM AVERAGERS IN RANDOM VIBRATION TESTS

A. J. Curtis, Hughes Aircraft Company, Culver City, California

**A MULTIPLE DRIVER ADMITTANCE TECHNIQUE FOR VIBRATION TESTING OF
COMPLEX STRUCTURES**

S. Smith, Lockheed Missiles & Space Company, Palo Alto Research Laboratory,
Palo Alto, California, and A. A. Woods, Jr., Lockheed Missiles & Space Company,
Sunnyvale, California

EQUIPMENT CONSIDERATIONS FOR ULTRA LOW FREQUENCY MODAL TESTS

R. G. Shoulberg and R. H. Tuft, General Electric Company, Valley Forge,
Pennsylvania

COMBINED-AXIS VIBRATION TESTING OF THE SRAM MISSILE

W. D. Trotter and D. V. Muth, The Boeing Company, Aerospace Group,
Seattle, Washington

SHOCK TESTING UTILIZING A TIME SHARING DIGITAL COMPUTER

R. W. Canon, Naval Missile Center, Point Mugu, California

**A TECHNIQUE FOR CLOSED-LOOP COMPUTER-CONTROLLED REVERSED-
BENDING FATIGUE TESTS OF ACOUSTIC TREATMENT MATERIAL**

C. E. Rucker and R. E. Grandle, NASA Langley Research Center,
Hampton, Virginia

**PROGRAMMING AND CONTROL OF LARGE VIBRATION TABLES IN UNIAXIAL
AND BIAXIAL MOTIONS**

R. L. Larson, MTS Systems Corporation, Minneapolis, Minnesota

A DATA AMPLIFIER GAIN-CODE RECORDING SYSTEM

J. R. Olbert and T. H. Hammond, Hughes Aircraft Company, Culver
City, California

**STABILITY OF AN AUTOMATIC NOTCH CONTROL SYSTEM IN SPACECRAFT
TESTING**

B. N. Agrawal, COMSAT Laboratories, Clarksburg, Maryland

Test Facilities and Techniques

SINUSOIDAL VIBRATION OF POSEIDON SOLID PROPELLANT MOTORS

L. R. Pendleton, Research Specialist, Lockheed Missiles & Space Company,
Sunnyvale, California

CONFIDENCE IN PRODUCTION UNITS BASED ON QUALIFICATION VIBRATION
R. E. Deltrick, Hughes Aircraft Company, Space and Communications Group,
El Segundo, California

SIMULATION TECHNIQUES IN DEVELOPMENT TESTING
A. Hammer, Weapons Laboratory, U. S. Army Weapons Command, Rock
Island, Illinois

A ROTATIONAL SHOCK AND VIBRATION FACILITY
R. T. Fandrich, Jr., Radiation Incorporated, Melbourne, Florida

THE EFFECTS OF VARIOUS PARAMETERS ON SPACECRAFT SEPARATION SHOCK
W. B. Keegan and W. F. Bangs, NASA, Goddard Space Flight Center, Greenbelt,
Maryland

**NON-DESTRUCTIVE TESTING OF WEAPONS EFFECTS ON COMBAT AND
LOGISTICAL VEHICLES**
R. L. Johnson, J. H. Leete, and J. D. O'Keefe, TRW Systems Group, Redondo
Beach, California, and A. N. Tedesco, Advanced Research Projects Agency,
Department of Defense, Washington, D.C.

**THE EFFECT OF THE FIN-OPENING SHOCK ENVIRONMENT ON GUIDED MODULAR
DISPENSER WEAPONS**
K. D. Denton and K. A. Herzing, Honeywell Inc., Government and Aeronautical
Products Division Hopkins, Minnesota

DEVELOPMENT OF A FLUIDIC HIGH-INTENSITY SOUND GENERATOR
H. F. Wolfe, Air Force Flight Dynamics Laboratory, Wright-Patterson
Air Force Base, Ohio

DEVELOPMENT OF A LIGHTWEIGHT, LINEAR MECHANICAL SPRING ELEMENT
R. E. Keefe, Kaman Sciences Corporation, Colorado Springs, Colorado

**TECHNIQUES FOR IMPULSE AND SHOCK TUBE TESTING OF SIMULATED
REENTRY VEHICLES**
N. K. Jamison, McDonnell Douglas Astronautics Company, Huntington
Beach, California

**VIBRATION FIXTURING -- NEW CELLULAR DESIGN, SATURN AND ORBITAL
WORKSHOP PROGRAMS**
R. L. Stafford, McDonnell Douglas Astronautics Company, Huntington Beach,
California

WALL FLOW NOISE IN A SUBSONIC DIFFUSER
E. F. Timpke, California State College, Long Beach, California, and R. C. Binder
University of Southern California, Los Angeles, California

PAPERS APPEARING IN PART 5

Shock and Vibration Analysis

BANDWIDTH-TIME CONSIDERATIONS IN AUTOMATIC EQUALIZATION
C. T. Morrow, Advanced Technology Center, Inc., Dallas, Texas

**A REGRESSION STUDY OF THE VIBRATION RESPONSE OF AN
EXTERNAL STORE**
C. A. Golueke, Air Force Flight Dynamics Laboratory, Wright-Patterson
Air Force Base, Ohio

FACTOR ANALYSIS OF VIBRATION SPECTRAL DATA FROM MULTI-LOCATION MEASUREMENT

R. G. Merkle, Air Force Flight Dynamics Laboratory, Wright-Patterson Air Force Base, Ohio

RESPONSES OF A MULTI-LAYER PLATE TO RANDOM EXCITATION

H. Saunders, General Electric Company, Aircraft Engine Group, Cincinnati, Ohio

RESPONSE OF HELICOPTER ROTOR BLADES TO RANDOM LOADS NEAR HOVER

C. Lakshminathan and C. V. Joga Rao, Army Materials and Mechanics Research Center, Watertown, Massachusetts

INSTRUMENTATION TECHNIQUES AND THE APPLICATION OF SPECTRAL ANALYSIS AND LABORATORY SIMULATION TO GUN SHOCK PROBLEMS

D. W. Culbertson, Naval Weapons Laboratory, Dahlgren, Virginia, and V. F. DeVost, Naval Ordnance Laboratory, White Oak, Silver Spring, Maryland

THE EFFECT OF "Q" VARIATIONS IN SHOCK SPECTRUM ANALYSIS

M. B. McGrath, Martin Marietta Corporation, Denver, Colorado, and W. F. Bangs, National Aeronautics and Space Administration, Goddard Space Flight Center, Maryland

RAPID FREQUENCY AND CORRELATION ANALYSIS USING AN ANALOG COMPUTER

J. G. Parks, Research, Development and Engineering Directorate, U.S. Army Tank-Automotive Command, Warren, Michigan

INVESTIGATION OF LAUNCH TOWER MOTION DURING AEROBEE 350 LAUNCH

R. L. Kinsley and W. R. Case, NASA, Goddard Space Flight Center, Greenbelt, Maryland

ON THE USE OF FOURIER TRANSFORMS OF MECHANICAL SHOCK DATA

H. A. Gaberson and D. Pal, Naval Civil Engineering Laboratory, Port Hueneme, California

WAVE ANALYSIS OF SHOCK EFFECTS IN COMPOSITE ARMOR

G. L. Filbey, Jr., USAARDC Ballistic Research Laboratories, Aberdeen Proving Ground, Maryland

STATISTICAL LOADS ANALYSIS TECHNIQUE FOR SHOCK AND HIGH-FREQUENCY EXCITED ELASTODYNAMIC CONFIGURATIONS

K. J. Szczański and K. C. Park, Clarkson College of Technology, Potsdam, New York

Structural Analysis

NASTRAN OVERVIEW : DEVELOPMENT, DYNAMICS APPLICATION, MAINTENANCE, ACCEPTANCE

J. P. Ramey, Head, NASTRAN Systems Management Office and D. J. Weidman, Aerospace Engineer, NASA Langley Research Center, Hampton, Virginia

EXPERIENCE WITH NASTRAN AT THE NAVAL SHIP R&D CENTER AND OTHER NAVY LABORATORIES

P. Matula, Naval Ship Research & Development Center, Bethesda, Maryland

RESULTS OF COMPARATIVE STUDIES ON REDUCTION OF SIZE PROBLEM

R. M. Mains, Department of Civil and Environmental Engineering, Washington University, St. Louis, Missouri

STRUCTURAL DYNAMICS OF FLEXIBLE RIB DEPLOYABLE SPACECRAFT ANTENNAS

B. G. Wrenn, W. B. Halle, Jr. and J. F. Hedges, Lockheed Missiles and Space Company, Sunnyvale, California

INFLUENCE OF ASCENT HEATING ON THE SEPARATION DYNAMICS OF A SPACECRAFT FAIRING

C. W. Coale, T. J. Kertesz, Lockheed Missiles & Space Company, Inc., Sunnyvale, California

DYNAMIC WAVE PROPAGATION IN TRANSVERSE LAYERED COMPOSITES

C. A. Ross, J. E. Cunningham, and R. L. Sierakowski, Aerospace Engineering Department University of Florida, Gainesville, Florida

R-W PLANE ANALYSIS FOR VULNERABILITY OF TARGETS TO AIR BLAST

P. S. Westine, Southwest Research Institute, San Antonio, Texas

PERFORM: A COMPUTER PROGRAM TO DETERMINE THE LIMITING PERFORMANCE OF PHYSICAL SYSTEMS SUBJECT TO TRANSIENT INPUTS

W. D. Pilkey and Bo Ping Wang, Department of Aerospace Engineering and Engineering Physics, University of Virginia, Charlottesville, Virginia

STRUCTURAL DYNAMIC ANALYSIS AND TESTING OF A SPACECRAFT DUAL TRACKING ANTENNA

D. D. Walters, R. F. Heidenreich, A. A. Woods and B. G. Wrenn, Lockheed Missiles and Space Company, Sunnyvale, California

Ship's Problems

DETERMINATION OF FIXED-BASE NATURAL FREQUENCIES OF A COMPOSITE STRUCTURE OR SUBSTRUCTURES

C. Ni, R. Skop, and J. P. Layher, Naval Research Laboratory, Washington, D.C.

EQUIVALENT SPRING-MASS SYSTEM: A PHYSICAL INTERPRETATION

B. K. Wada, R. Bamford, and J. A. Garba, Jet Propulsion Laboratory, Pasadena, California

LONGITUDINAL VIBRATION OF COMPOSITE BODIES OF VARYING AREA

D. J. Guzy, J.C.S. Yang, and W. H. Walston, Jr., Mechanical Engineering Department, University of Maryland, College Park, Maryland

SIMPLIFIED METHOD FOR THE EVALUATION OF STRUCTUREBORNE VIBRATION TRANSMISSION THROUGH COMPLEX SHIP STRUCTURES

M. Cherniawski and C. Arcidiacono, Gibbs & Cox, Inc., New York, New York

ISOLATION AND DAMPING

TRANSIENT RESPONSE OF REAL DISSIPATIVE STRUCTURES

R. Plunkett
University of Minnesota
Minneapolis, Minnesota

Almost all the information we have on damping has been gained from measurements on structures vibrating at a single frequency at constant or almost constant amplitude. In calculating system response to transient, random or fluctuating excitation, it is customary to use spectral decomposition, modal analysis or some other procedure involving linear superposition. In most cases of transient excitation this will give conservative results since most real damping increases non-linearly with amplitude; this may result in a greatly overdesigned structure and prejudice the designer against the use of frangible stress relief devices. In a few cases involving coulomb friction where the damping decreases with increasing amplitude, it may lead to underdesign or instability.

INTRODUCTION

Classical analysis has shown that the maximum response of a single degree of freedom system to simple shock inputs is remarkably independent of damping [1]. On the other hand, damping may be a very important factor when the load time history has a spectrum which is rich with discrete frequencies [2]. Typical problems of this second type include seismic excitation, automobile crashes and light components on relatively massive structures. In an attempt to make the analysis of these problems tractable, they have often been attacked by linear or quasi linear techniques [3]; this leads naturally to superposition and transform methods and our attention has been diverted to a consideration of appropriate bounds for maximum response [4]. If one accepts linear analysis and spectral decomposition, it is obvious that the sum of the absolute values of the Fourier components or the integral of the absolute value of the integrand will furnish an upper bound using one of the many variants of Schwarz' inequality. Since we are dealing with a maximum and since we are often concerned with a displacement type of failure, this upper bound may be high by a factor of two or three which can impose a severe design penalty. Much effort has been given to a reasonable lowering of this upper bound by various mathematical and numerical studies.

It has been realized for some time

that there are certain mathematical difficulties associated with the assumption of frequency dependent linear damping but these appear not to have much practical effect [5]. Little attention has been paid to the physics of the problem as controlled by the definition of dissipative systems.

As can be seen from figure 1, the maximum response spectrum of a single degree of freedom system due to simple excitation depends only slightly upon damping until the damping becomes very large. Figure 2, on the other hand, shows that this same response spectrum is very sensitive to damping when the excitation is highly oscillatory as in an earthquake. In spite of this, there is little difficulty dealing with either case if we can treat the physical structure as a single degree of freedom system. Unless the shock response spectrum has a very wide frequency band, there is also little problem with multi-degree of freedom systems unless the frequencies are close together. Typical building frequencies are in the ratio 1, 3, 5, etc.; typical missile bending frequencies or submarine bending frequencies are in the ratio 1, 6, 18, etc.; either of these sequences furnish adequate separation. Massive machinery in buildings, however, can split these sequences to make them much denser; an elevator shaft, a building with two connected towers, a power plant or nuclear reactor can make a simple single degree of freedom analysis unrealistic.

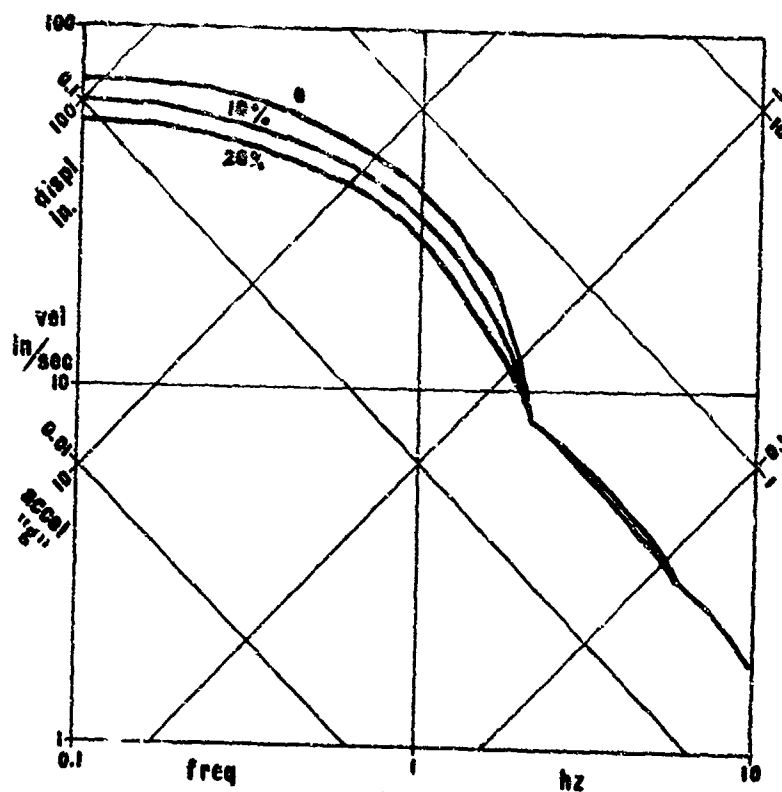


Fig. 1 Shock response spectrum. Half sine wave acceleration pulse, 0.3g max, 1 second long, damping parameter, Ref 1.

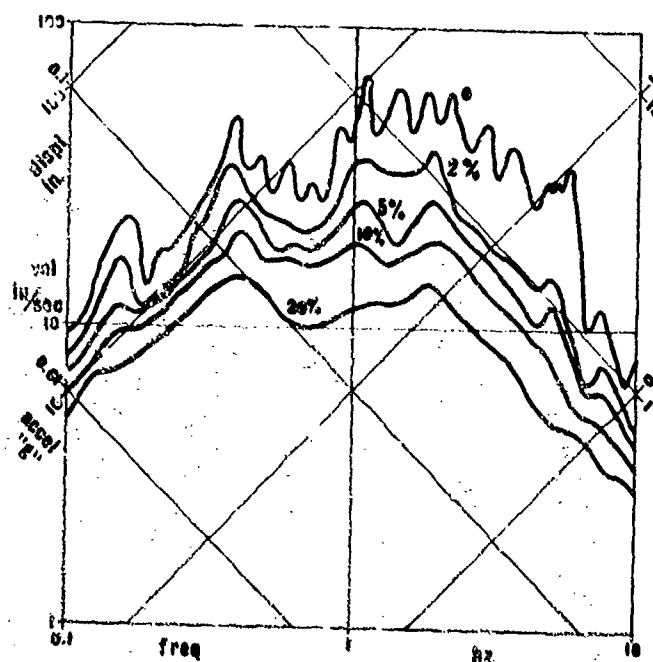


Fig. 2 Shock response spectrum. El Centro earthquake, 1940, damping parameter, Ref 2.

The accepted design procedure is to use a dynamic response analysis with reasonable damping factors to approximate the response [6]. For a relatively simple excitation spectrum such as a depth charge, a nuclear explosion or a head-on crash into a fixed barrier, this gives good results. For seismic excitation or a more realistic crash we simply do not have enough information about damping effects in complex time histories to find the response.

DAMPING MECHANISMS

Before we get too deeply into the physics of shock response, it is helpful to consider the various types of damping mechanisms. The simplest is energy radiation which is a linear mechanism resulting when elastic energy is radiated away from the structure of interest. It may be the major mechanism for damping turbine bucket vibration where the disk support at Christmas trees scatters the elastic energy to all parts of the rotor in such a way as to return in a completely incoherent fashion, if at all. It is probably also an important factor in large buildings supported on bed rock or in flexible bridges. Radiation damping can be very efficient from shell structures to water; the impedance mismatch is greater but the area contact is larger than in turbine buckets or buildings. Acoustic radiation from submarines to the ocean causes large damping at intermediate frequencies. For very large flat panels, acoustic radiation to air is sometimes important. By its very nature, radiation damping is elastic and linear; therefore, even though it is frequency dependent, superposition works.

Material damping is a very general name for a large collection of phenomena. It is the kind of energy dissipation which takes place in the volume of solid materials which are cyclically stressed and is independent of any energy loss at the boundaries [7,8]. The physical mechanisms responsible for this type of damping are basically non-linear with the possible exception of polymeric or visco-elastic organic compounds [9]. The behavior at high strain levels associated with shock conditions is strongly non-linear so that superposition is completely unwarranted.

For most complex structures in shock or vibration at amplitudes below that necessary for permanent deformation, there has been a growing realization over the past decade that most of the energy dissipation is caused by

relative motion between the parts. This relative motion, in turn, causes rubbing friction, impact, elastic energy release, gas pumping or turbulent fluid behavior around relatively sharp edges. All of these mechanisms are highly non-linear.

ANALYSIS

Even though the physical mechanism involved in material damping is non-linear, it is customary to use a quasi-linear analysis for steady state vibration problems in which experience guides us toward the proper damping value for the problem at hand. As far as we know, we have not gotten in serious trouble in this area, probably because damping increases very rapidly before the fatigue limit of most materials is reached. We are also aided by the resonant nature of vibration problems; whether we are dealing with flutter, critical speeds, wheel shimmy or building sway, one mode of vibration dominates and the time history is sinusoidal. Even in randomly excited forced vibration, the response of lightly damped systems is quasi-sinusoidal.

The shock response of large structures loaded below the point of permanent deformation has not been examined in great detail. It has been difficult enough to get even meager information about the frequencies, mode shapes and damping of buildings with sinusoidal loadings in non-destructive tests, without worrying about more complex situations [10]. We have only recently had sufficient strong motion instrumentation to get any information at all about the motion of large buildings in destructive earthquakes [11]. The preliminary results seem to indicate that destructive, non-linear deformation of redundant, non-support elements reduces the shock loading to the rest of the structure somewhat in the same fashion that crushable supports do in packaging. Thus, the destruction of interior shear panels can give important frequency shifts and energy dissipation for tall buildings in earthquakes and offer some protection to the main skeleton. Limber and weak first story flexible shear supports, on the other hand, may protect against weak shocks but be disastrous in strong ones.

CURRENT PROBLEMS

This gives rise to many unanswered questions if we are to arrive at economical, safe and sturdy designs for complex structures subject to explosions, earthquakes and crashes. The relatively simple, single-degree of

freedom methods which have been so successfully used for package cushioning will not work for these problems. This raises serious questions for the rational design of military structures to withstand nuclear and conventional explosions, of buildings and power stations to withstand earthquakes, and of automobiles to withstand moderate crashes and protect the occupants against severe ones.

The kind of problem which may exist is most easily seen by considering the details of energy dissipation due to friction in built-up structures. Experience over the years has led us to use overall structural damping which is relatively independent of amplitude for single mode vibratory motion in the analysis of such systems. The damping coefficient (ratio of imaginary to real part of effective complex modulus) is usually taken to be about 0.02 for aircraft, has been measured at 0.04 for tall structures [10] and has been deduced to be as high as 0.10 for large ships. The difficulty with most of these figures is that they were necessarily determined at very low amplitudes, well below that permissible for severe earth quakes or other non-recurring transients. In addition they are only valid for sinusoidal or quasi-sinusoidal motion in a single mode of vibration at a time.

It is not difficult to construct a plausible argument which says that the interactive effects of two or more frequencies are such as to reduce the damping for that motion which has the smaller amplitude; this necessarily leads to the conclusion that the two frequency decay spectrum is almost independent of the spectral content of the excitation for quite a wide range in the ratio of the two components. This result comes from the fact that the direction of friction force depends on the direction of slip and that no slip takes place until the force reaches a limiting value. As a result, there will be essentially no energy dissipation for the frequency corresponding to that mode of motion in which there is no velocity reversal. This means that if the maximum relative velocity corresponding to one frequency of a two frequency motion is less than the instantaneous velocity in the other, there will be little or no energy dissipation in it even though there is damping in the corresponding motion by itself.

In the other direction, we have the experimental fact that damping in most materials and structures rises abruptly at the level of permanent deformation or

fatigue change [7]. Since we expect this behavior to be associated with peak strain or displacement, it has a very important influence on the maximum force in a structure. The maximum of a complex time history cannot be found from spectral decomposition, it can only be bounded and that not accurately. For instance, consider a spring mounted mass in which the base is subjected to an earthquake input; let the spring have an elastic perfectly plastic characteristic, and let the input be such as to cause significant plastic deformation at some time in the response. Under these circumstances which correspond to moderately severe earthquakes or crashes, the time history of the excitation prior to maximum displacement is irrelevant and the residual response after maximum displacement is often a simple sinusoidal decay. Such behavior is often not very destructive to components housed in the main structure. A typical example is the protection offered to automobile passengers by collapsible bumper supports or by destruction of front grill work; in most cars, there is no such protection available from side impacts. In any case, this makes a flexible and frangible first story support structure for buildings look attractive. If it is to be effective, some provision must be made for final support of the building itself and the frangible links must be easily replaced.

There are two major areas of research that appear to me to cry out for solution. The first is analysis; what are the appropriate analytical techniques and design criteria for complex structures subject to transient inputs which do not have a simple time history? We can be certain that the simple linear superposition implicit in spectral decomposition methods are inappropriate here. While they will probably overestimate the response for most reasonable assumptions, they will probably impose unreasonable requirements for fail safe design in many cases. In addition, they will automatically discourage the use of frangible or yielding redundant links to mitigate the damage to building contents. At the moment, the two most suitable techniques appear to be a quasi-elastic deformation analysis and the use of digital, analogue or hybrid computers to make time history predictions. For either of these methods to be useful, we need much better sets of input ensembles. We also need a large library of trial solutions and a reasonable number of destructive tests for comparison.

The other important area of research is a little closer to my academic heart. We have absolutely no information on the interactive effects of modal damping when a material or structure is vibrating simultaneously in two or more frequencies. Whether it be material or structural damping, we do not know if the interaction between strain or motion at two or more different frequencies increases or decreases the damping of either component.

A great deal of attention has been paid, in this country and abroad, to the problems associated with analytical and computer solutions for structures subjected to random, complex, steady state and transient excitation. These techniques and solutions have all been based upon descriptions of the system behavior which have been chosen for their mathematical tractability rather than their relationship to physical fact. If we are to have any real ability to predict vibration and shock response for these important problems, we had better learn more about the physical behavior of real materials and systems.

REFERENCES

- [1] Mindlin, R. D., F. W. Stubner and H. L. Cooper "Response of Damped Elastic Systems to Transient Disturbances" Proc. Soc. Exptl. Stress Anal. 5:2, 69-87 (1948).
- [2] Housner, G. W. "Behavior of Structures During Earthquakes", Proc. ASCE, Vol. 85, No. EM4, 1959, pp. 109-129.
- [3] Pisarenko, G. S. "Vibrations of Elastic Systems Taking Account of Energy Dissipation in the Material" Translation WADD TR 60-582, Feb. 1962, Air Force Systems Command, Wright-Patterson AF Base, Ohio e.g., Section 1-6.
- [4] Hansen, R. J., Ed. "Seismic Design for Nuclear Power Plants" MIT Press Cambridge, Mass., Introduction pp. 1-68.
- [5] Crandall, S. H. "The Role of Damping in Vibration Theory" Journ. Soun Vib. (1970) 11(1) pp. 3-18.
- [6] Barton, M. V., ed. "Shock and Structural Response" ASME, New York 1960.
- [7] Lazan, B. J. "Damping of Materials and Members in Structural Mechanics" Pergamon Press, 1968.
- [8] Plunkett, R. "Vibration Damping" in Applied Mechanics Surveys, Abramson, Liebowitz, Crowley and Juhasz, Spartan Books, Washington, D. C. 1966, pp. 691-702.
- [9] Ferry, J. D. "Viscoelastic Properties of Polymers" Wiley, New York 2nd Ed. 1970.
- [10] "Full Scale Testing of New York World's Fair Structures-III Chimes Tower", Nat. Acad. Sci. Publ. 1722, Wash. 1969.
- [11] Hudson, D. E. "Dynamic Properties of Full-Scale Structures Determined from Natural Excitations" in Symposium on Dynamic Response of Structures, G. Herrmann, Stanford, 1971.

DYNAMIC RESPONSE OF A RING SPRING

by

Ronald L. Eshleman
IIT Research Institute
Chicago, Illinois

The dynamic response of a ring spring to high rate loading was studied analytically and experimentally with special emphasis on high frequency effects. Explicit analytical expressions for ring spring force-deflection curves with separate stiffness and damping terms were formed. The mathematical model which represents the spring mass elasticity and damping is a form of the classical wave equation. This model was used in conjunction with a massive rigid body to study its shock isolation characteristics analytically and experimentally. Tests were conducted on one and one-half inch diameter springs in an MTS closed loop electrohydraulic shock isolation test machine.

INTRODUCTION

The dynamic response of the ring spring to high rate input loadings was studied analytically and experimentally. Special emphasis was placed on the understanding of high frequency effects. When high rate input loadings are applied to a ring spring, surging of the isolator can occur at one or a combination of its natural frequencies if its inherent damping is not effective. High rate loading results from weapon effects, machinery excitation or transportation environments. A distributed parameter model was used to calculate the local response of the isolator and the higher order effects on the isolated mass. Finite difference equations programmed on the digital computer were utilized in the local response calculation.

MODELING

The analytical and experimental studies on the response of the ring spring to high rate input loading were conducted on simple isolator-mass models. The analytical model consisted of a ring spring and its associated isolated mass, as shown in Figure 1. The isolators were modeled as massless, flexible, damped elements so that gross response of the isolated mass to programmed high rate input motion could be obtained. In addition, the ring spring was modeled as having continuously distributed mass and elasticity for local response. This

model is capable of predicting surging of the ring spring and high frequency response of the isolated mass.

The high rate input motion, pulse, shown in Figure 2, had a 2.71 in. peak-to-peak displacement. The maximum input velocity was 150 in./sec, 90g and higher accelerations were obtained depending on the exact shape of the pulse.

The experimental models consisted of parallel ring spring-mass systems (Figure 3). The experimental model of the ring spring isolation elements was selected to meet the physical constraints of the test fixture. The MTS closed loop electrohydraulic test machine was used to induce the controlled pulse to the shock isolation system's base.

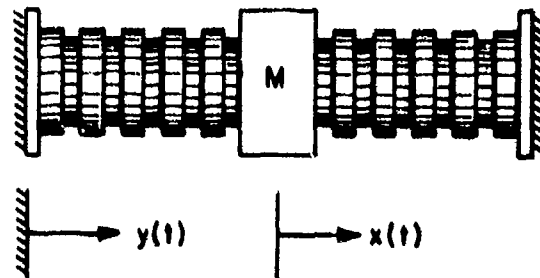


Fig. 1 Shock Isolation System Model, Analytical

Preceding page blank

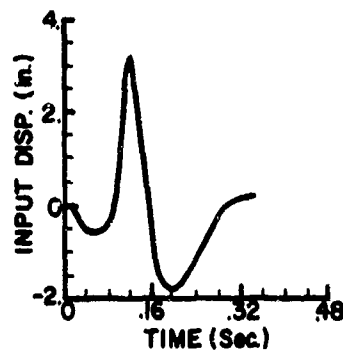


Fig. 2 High Rate Input Motion

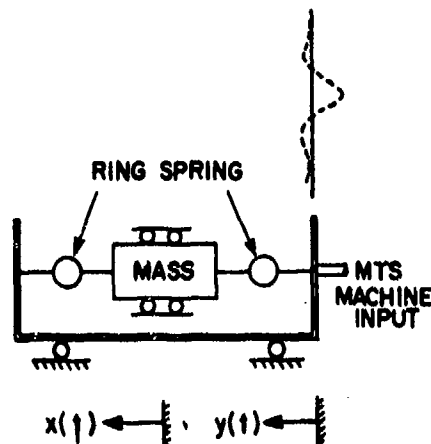


Fig. 3 Shock Isolation System Model, Experimental

PHENOMENOLOGY

The ring spring, shown in Figure 4, is used where space is limited and a large amount of energy must be absorbed. Energy is absorbed by the coulomb friction forces at the interfaces of the adjoining sections. The spring deflection in the axial direction is obtained from circumferential compression of the inner rings and stretching of the outer rings. The damping force between the conical surfaces of the adjacent rings is proportional to axial displacement. Figure 5 shows a typical ring spring load deflection curve with its hysteresis loop. For increasing loads, the friction forces and elastic forces act in the same direction to absorb a large amount of energy. Upon release, the friction force reverses and some of the elastic energy stored in the rings is used to overcome the opposed friction force. This results in a load release curve of smaller slope. The area inside these curves represents the energy dissipated by the spring per use cycle.

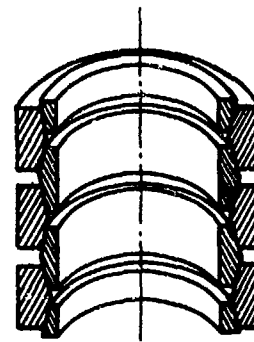


Fig. 4 Diametral Section through Ring Spring

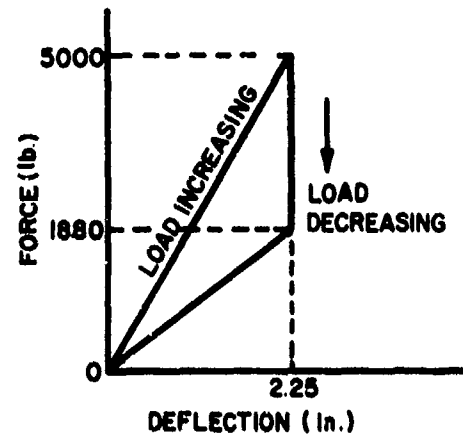


Fig. 5 Ring Spring Load Deflection Curve

The analytical expressions (reference 1) for the ring spring force-deflection curves in compression and return are given respectively as

$$P_c = \left[\frac{\pi E A_1}{r_m n \left(1 + \frac{A_1}{A_0}\right)} \frac{\tan \alpha (\mu + \tan \alpha)}{1 - \mu \tan \alpha} \right] \delta \quad (1)$$

$$P_R = \left[\frac{\pi E A_1}{r_m n \left(1 + \frac{A_1}{A_0}\right)} \frac{\tan \alpha (\tan \alpha - \mu)}{1 + \mu \tan \alpha} \right] \delta \quad (2)$$

where:

- P = Force
- δ = Deflection
- E = Modulus of Elasticity
- α = Angle of taper, conical surface
- r_m = Mean radius of rings
- n = Number of rings
- A_1 = Cross-sectional area of inner ring

A_o = Cross-sectional area of outer ring
 μ = Coulomb friction coefficient

Let

$$\beta = \frac{\pi E A_1 \tan \alpha}{r_m n \left(1 + \frac{A_1}{A_o}\right)} \quad (3)$$

Then

$$P_c = \beta \delta \frac{(\mu + \tan \alpha)}{1 - \mu \tan \alpha} \quad (4)$$

$$P_R = \beta \delta \frac{\tan \alpha - \mu}{1 + \mu \tan \alpha} \quad (5)$$

Expanding equations (4) and (5) for small values of $\mu \tan \alpha$ and dropping higher order terms, the force-deflection curves in compression and return become

$$P_c = \delta \beta (\mu + \tan \alpha + \mu^2 \tan \alpha + \mu \tan^2 \alpha + \dots) \quad (6)$$

$$P_R = \delta \beta (\tan \alpha - \mu - \mu \tan^2 \alpha + \mu^2 \tan \alpha + \dots) \quad (7)$$

The spring and damping terms for the ring spring can be obtained by separating equations (6) and (7). The spring constant is

$$K = \beta \tan \alpha. \quad (8)$$

The damping constants are

$$C_c = \beta \mu (\sec^2 \alpha + \mu \tan \alpha) \quad (9)$$

$$C_R = -\beta \mu (\sec^2 \alpha - \mu \tan \alpha) \quad (10)$$

Equations (6) and (7) show that the damping force due to Coulomb friction is a function of ring spring deflection. This phenomenon results from the fact that the normal force between the friction surfaces is regulated by the elasticity of the spring. Equations (8) shows that the ring spring stiffness is a function of the spring geometry and its modulus of elasticity. These relationships were used in the analysis of the spring's shock isolation qualities. The data on ring spring used in the tests is listed below.

$$\beta = 6350 \text{ lb/in.}$$

$$\mu = 0.105$$

$$k = 1530 \text{ lb/in.}$$

$$C_c = 721 \text{ lb/in.}$$

$$C_R = -688 \text{ lb/in.}$$

ANALYSIS

The ring spring isolation system was analyzed for its natural frequencies, gross response and local response. The analytical studies were conducted with the aid of the previously described models. The eigenvalue problem for determination of the natural frequencies was solved graphically utilizing analogous solutions existing in the literature. The dynamic response of the ring spring to high rate input loading was programmed in FORTRAN IV and calculated on an IBM 7094 digital computer.

The model distributed mass and elasticity isolator system shown in Figure 6 was used for the calculation of the system's natural frequencies and response to high rate input loading. The equation of motion, Equation (11), and boundary conditions, Equations (12) and (13), were used to analyze the response of the isolation systems.

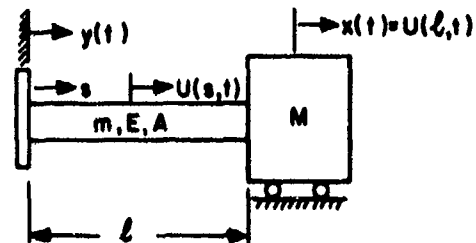


Fig. 6 Distributed Parameter Isolation System Model

$$\frac{\pi E A_1 \tan \alpha (\tan \alpha + \mu)}{r_m n (1 - \mu \tan \alpha) \left(1 + \frac{A_1}{A_o}\right)} \frac{\partial^2 u}{\partial s^2} = \pi \rho \frac{n}{l^2} A_1 r_1 \left(\frac{r_o A_o}{r_1 A_1} + 1\right) \frac{\partial^2 u}{\partial t^2} \quad (11)$$

where

$u(s, t)$ = local displacement of ring spring
 s = space
 t = time
 l = length.

At $s = 0$,

$$\begin{cases} 0 & \text{for natural frequency calculation} \\ y(t) & \text{for response calculation.} \end{cases} \quad (12)$$

$$M \frac{\partial^2 u}{\partial t^2} (l, t) = - \frac{\pi E A_1 \tan \alpha (\tan \alpha \pm \mu) l}{r_m n (1 \mp \mu \tan \alpha) \left(1 + \frac{A_1}{A_0}\right)} \frac{\partial u}{\partial s} (l, t) \quad (13)$$

These equations show the linear elastic characteristics of the spring and the directional characteristics of the damping force. The undamped natural frequencies of the system were obtained using equation (11). From the analogy to a bar in longitudinal motion, the wave equation yields the following frequency equation.

$$\delta \tan \delta = \epsilon \quad (14)$$

where

- $\epsilon = m/M$
- m = mass of the ring spring
- M = isolated mass
- $\delta_1 = l \Omega_1 / a$, roots of equation (14)
- l = length of isolator
- Ω_1 = natural frequency
- $a = l \sqrt{k/m}$ wave velocity
- k = equivalent stiffness (equation (8)).

For the small values of mass ratio, ϵ , obtained in these configurations, the solutions to the frequency equation are given in Equation (15).

$$\delta^2 \approx \epsilon \text{ first mode} \quad (15a)$$

$$\delta_1 \approx i\pi \text{ second and higher modes} \quad (15b)$$

Equation (15a) given the first mode natural frequencies of the systems directly and is

$$\Omega = \sqrt{k/M} \quad (16)$$

merely the rigid mass, M , massless isolator, k , natural frequency that is obtained from simple vibration analysis. This occurs because the isolated mass is so much larger than the mass of the isolation element. In addition, for the higher modes of vibration (surging), the isolator appears to have fixed end conditions.

$$\Omega_1 = i\pi \frac{f}{l} \quad (17)$$

The following numbered values were obtained for the natural frequencies of the ring spring isolation system tested.

- $k = 1530 \text{ lb/in.}$
- $m = 0.0079 \text{ lb-sec}^2/\text{in.}$
- $M = 2.50 \text{ lb sec}^2/\text{in.}$
- $\epsilon = 0.0032$
- $a = 6000 \text{ in./sec}$
- $l = 14.9 \text{ in.}$
- $\Omega_1 = 3.95 \text{ Hz}$
- $\Omega_1 = 2201 \text{ Hz.}$

The local response of the shock isolation system to high input loading was numerically calculated on the digital computer. The wave equation (Equation (11)) which describes the motion of the system is basically a force equation. Motion inputs are constraints on the system and are therefore time dependent boundary conditions. If the motion input occurs within the physical boundary of the continuous element rather than at the boundary, then it is termed a specified internal boundary condition at an internal boundary. Input motions must be given relative to an inertial reference.

Since the input motion of the isolator cannot be characterized in a functional form it is advantageous to use its digital description as an input to a finite difference description of the system. The present ISOLATOR program contains a digital description of the input wave form. The subroutine that calculates the local response of the ring spring uses central difference equations. This analysis is described in detail in reference 2.

The results of the local dynamic response calculations are shown in Figure 7. It shows the acceleration response in g's of the 960 lb mass isolated from the input wave form (Figure 2) by a ring spring.

EXPERIMENTATION

The dynamic response of the ring spring to high rate input loading was studied experimentally using a closed loop electrohydraulic test machine. The shock wave form shown in Figure 2 was applied to the isolator-mass system.

The electrohydraulic test system is comprised of five basic elements: the pump, the servovalve-actuator system, the load frame, the transducer-feedback system and the control console. These units provide primary hydraulic power, electrohydraulic control, specimen or component containment and control. The machine has the following capabilities:

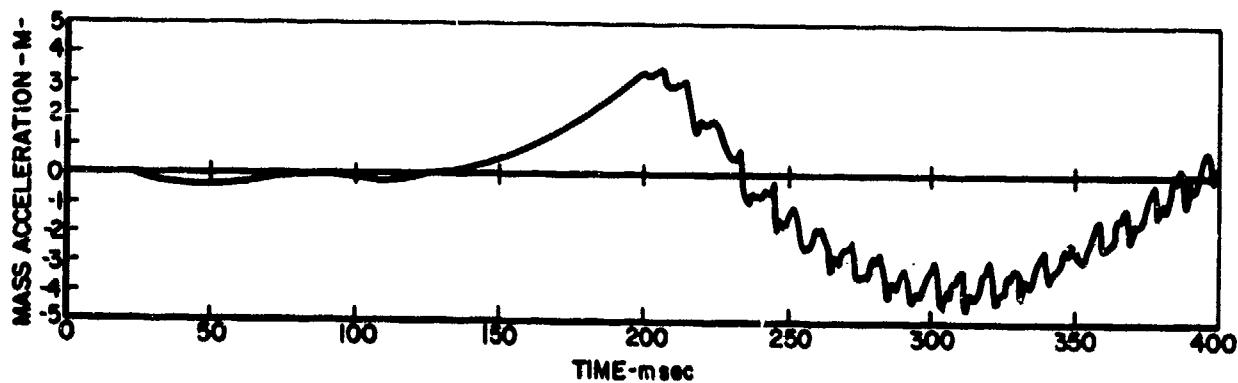


Fig. 7 Local Response of the Isolated Mass Subject to 1MT Input Pulse - Ring Spring

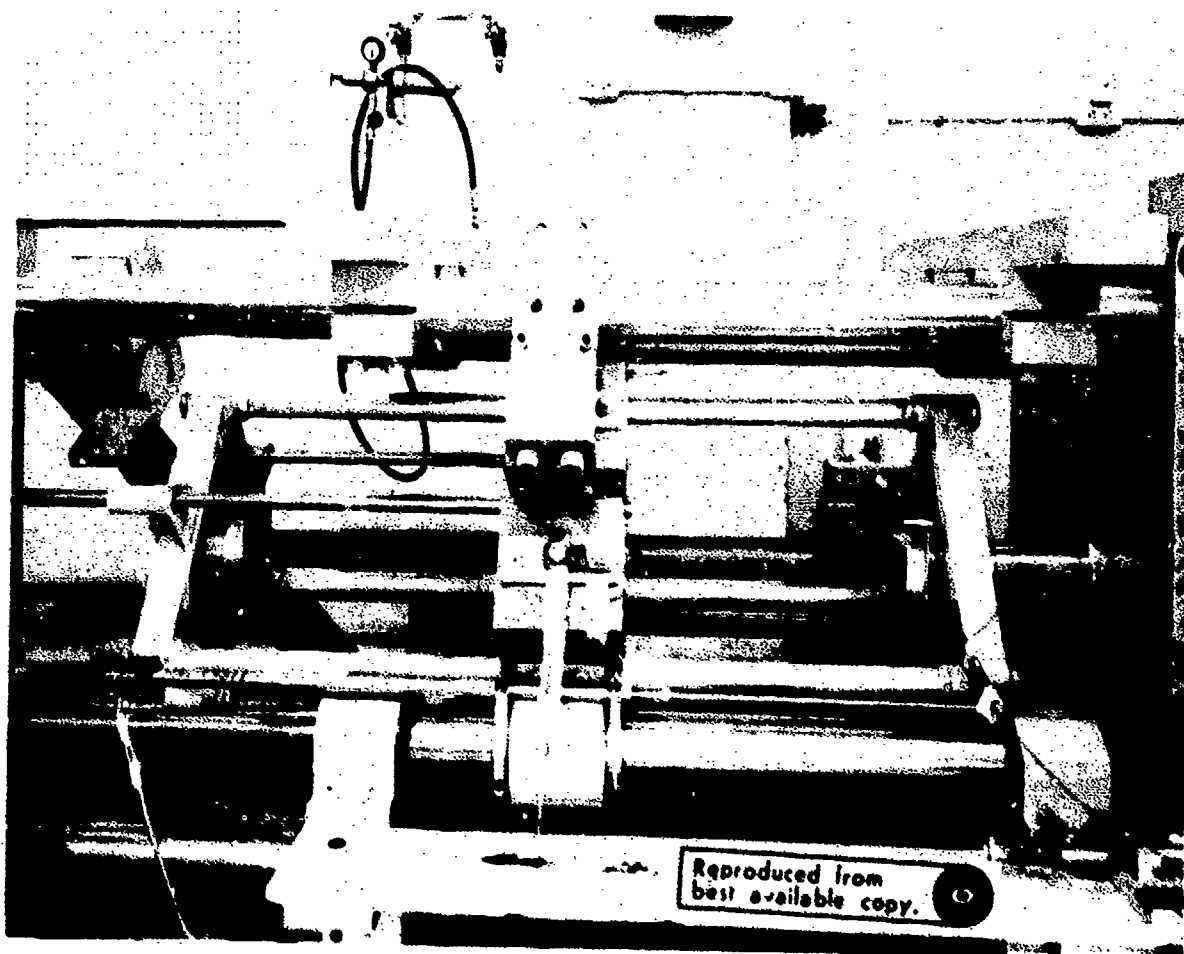


Fig. 8 Ring Spring Shock Test Equipment

the stroke range is ± 5 in.; maximum stroke rate is 12,000 in./min; maximum acceleration is 160 g. Its characteristics, capabilities and operation are further described in reference 3.

The guided loading fixture, with the ring spring, Figure 8, provides the base loading of the isolator, and a 960 lb lead weight simulates the isolated equipment. Both items are free to move on the test machine loading and reaction frame. The loading ram applies the machine generated to the shock isolator under test. The loading fixture was designed to have a minimum weight and a high natural frequency. Individual support fixtures are designed and built for each shock isolation system tested. The details of the test equipment, instrumentation and testing are recorded in reference 3.

The ring spring consisted of two columns of 62 rings on each side of the mass. A wave form with a 2.71 in. peak-to-peak displacement was used because the stroke of the ring spring was short. The elements were not precompressed. The rings were held in their proper relative

position by internal and external sleeves. Figure 9 shows the results of these tests.

DISCUSSION

The analytical-experimental results of this investigation are summarized in table 1.

The experimentally determined response of the mass isolated with a ring spring shows good isolation characteristics as compared to a helical spring (reference 2) where local surging is observed. The ram acceleration of 116g reduced to a mass response of 1.61g gave 98 percent isolation. The local response results are in fair agreement with the experimental results. In the experimental record no surging was observed, but the natural frequency of the ring spring isolator was found analytically to be 220 Hz. The local response study showed a peak response acceleration amplitude of the mass of 0.8g at 230 Hz.

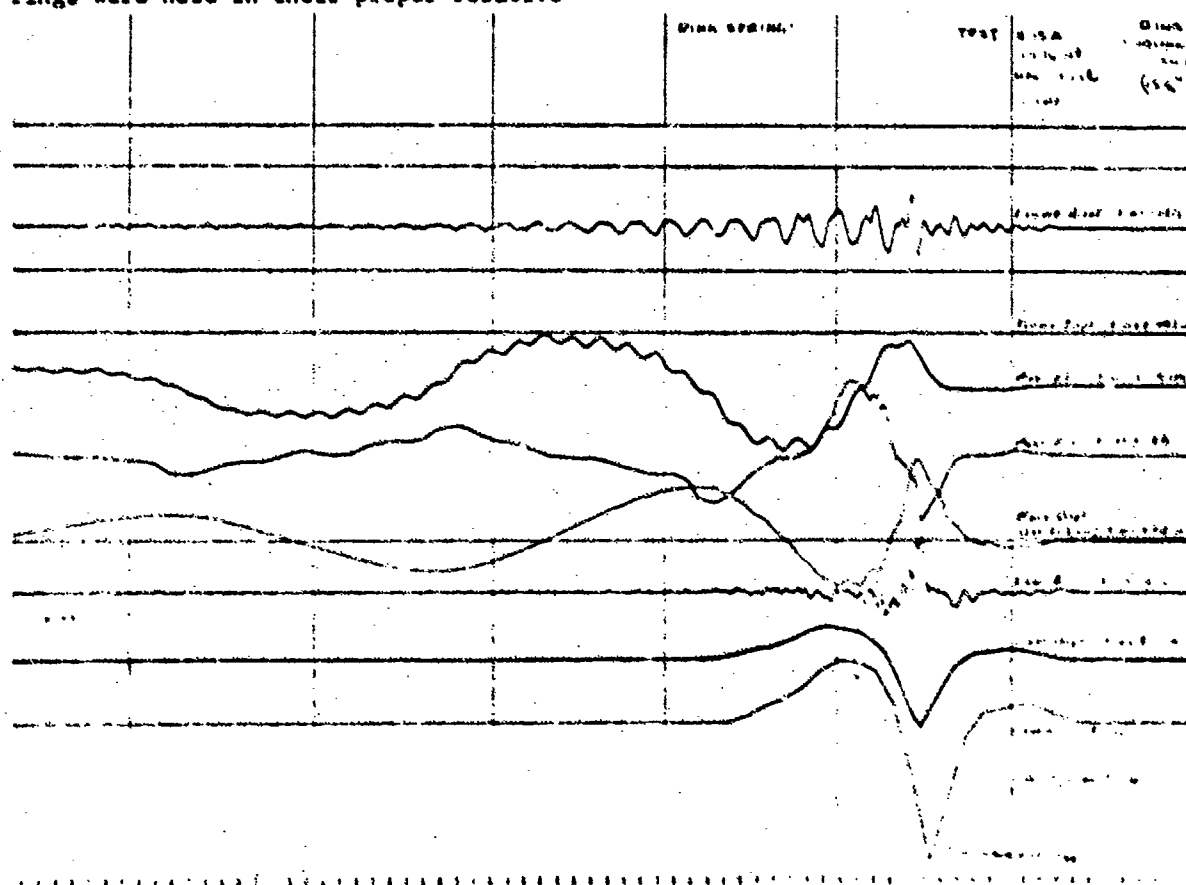


Fig. 9 Response of a 960 lb Mass Isolated by Two Ring Springs Subject to a High Rate Input Loading

Table 1

**A SUMMARY OF THE EXPERIMENTAL-ANALYTICAL RESULTS OF THE RESPONSE
OF A RING SPRING-MASS SYSTEM TO HIGH RATE INPUT LOADING**

Time (ms)	Ram Disp. (in.)	Ram Accel. (g)	Relative Mass Displacement (in.)		Mass Acceleration (g)		Mass Velocity (in./sec)		Secondary Effects		Fundamental Natural Frequency First Mode Damping
			Exp. #15A	Anal. #21	Exp. #15A	Anal. #21	Exp. #15A	Anal. #21	Exp. #15A	Anal. #21	
08	0	---	---	---	---	---	---	---	No surging observed	Surge frequency = 220 cps Microresponse amplitude = 1.6g peak to peak frequency = 230 cps	First mode damping constant = 1.41 lb sec/in. First natural frequency = 2.9 cps Experimental First natural frequency = 3.9 cps Analytical
0.006	0	---	---	---	---	---	---	---			
0.03	-0.259	---	---	---	---	---	---	---			
0.043	-0.238	-23.0	-0.22	-0.24	---	---	-1.04	---			
0.06	-0.151	---	---	---	---	---	---	-4.68			
0.066	0	---	---	---	---	---	---	---			
0.07	0.194	---	---	---	---	---	---	---			
0.091	1.858	116.0	2.42	+1.91	1.41	3.04	1.05	---			
0.095	1.728	---	---	---	---	---	---	---			
0.110	0	-37.0	---	---	---	---	---	23.4			
0.112	-0.087	---	---	---	---	---	---	---			
0.120	-0.475	---	---	---	---	---	---	---			
0.128	-0.755	---	-1.37	-1.64	---	---	---	---			
0.146	-0.994	---	---	---	-1.61	-2.61	---	---			
0.157	-0.865	---	---	---	---	---	---	---			
0.169	-0.583	---	---	---	---	---	---	---			
0.183	-0.346	---	---	---	---	---	-1.50	-30.0			
0.220	0	---	---	---	---	---	---	---			
0.30	0	---	---	---	---	---	---	45.0			

CONCLUSIONS

It can be concluded from this study that the ring spring is an excellent shock isolator for attenuation of high rate loading phenomena. High frequency vibration of the isolated mass due to spring surging is not obtained because the local Coulomb damping forces in the spring control this phenomena. From this result, it can be concluded also that externally generated high frequency phenomena would be attenuated by the ring spring.

The major disadvantage of the ring is the rattlespace required for its use. Its ratio of free height to solid height is large due to the small deflections obtained per ring. In order to use the ring spring in practical situations, many rings must be stacked in series.

REFERENCES

1. A.M.Wahl, "Mechanical Springs", Penton Publishing Co., Cleveland, Ohio 1944.

2. R.L. Eshleman and P.N. Rao, "The Response of Mechanical Shock Isolation Elements to High Rate Input Loading," The Shock and Vibration Bulletin, No. 40, pt 3, pp 217-234, Dec. 1969.
3. P.N. Rao and K.E. Hofer, "Design and Development of a Shock Isolation Evaluation System for High Rate Input Loading," The Shock and Vibration Bulletin, No. 40, pt 3, pp 245-260, Dec. 1969.

ACKNOWLEDGEMENT

The work reported in this paper was performed at the IIT Research Institute, Chicago, Illinois under the Department of the Air Force, Space and Missiles Systems Organization, Contract No. F04694-67-C-0076. The author takes this opportunity to acknowledge the helpful assistance, support and criticism of Mr. N. Kfoury of Aerospace Corporation and the assistance of Mr. P. Eakins and P. Rao of IIT Research Institute in conducting the experiments.

DISCUSSION

Mr. Clevenston (Langley Research Center): You showed the compressive characteristics of your spring. Can we assume that the tensile characteristics are similar?

Mr. Eshleman: It can not take tension. It must be used in a situation where it is compressed and then released. There are no tension characteristics.

Mr. Schell (Naval Research Laboratory): How would they be stacked mechanically?

Mr. Eshleman: We put a post on the outside and a post on the inside, like a telescoping device with the spring in between.

Mr. Plunkett (University of Minnesota): I am concerned, in this kind of device, with respect to damping that unless you reverse the motion you in fact get no dissipation at all. Wouldn't you think it would be possible to get a high frequency vibration on top of a relatively long-travelled low frequency vibration that would see no damping?

Mr. Eshleman: I think if you used a single spring, this is possible. We used a double spring, one on each side, so one of them was always in compression. It is difficult to use one because it does not take any tension. Yes,

you could get the high frequency transmitted if you used it that way, but if you use it always with one side in compression, then I think you get the damping.

Mr. Gertel (Kinetic Systems): You made the observation that there would be high frequency attenuation. Judging from the hysteresis or the force deflection curve, with the friction bowtie loop on it, I would suspect that near the end of the stroke of the spring where the friction hysteresis force would be rather significant, you would be essentially locked out friction-wise and any high frequency vibrations within that friction band, interpreted in terms of g relative to the load, on the spring, would be locked out and transmitted directly through with the usual disadvantage of a friction damped system.

Mr. Eshleman: You must remember that during the use of the spring, and during the motion each spring is in a different part of the hysteresis curve. That curve is a static curve, but really it is a massive dynamic system. That means that while at one end of the spring you may be on one part of the hysteresis curve, on the other end you may be on a different part. There may be occasions when what you say is true.

SHOCK MOUNTING SYSTEM FOR ELECTRONIC CABINETS

W. D. Delany
Admiralty Surface Weapons Establishment
Portsmouth, U.K.

(U) Shock and vibration isolation of electronic equipment on naval ships can be adequately provided by a viscous damped spring system which has a vertical natural frequency of 6 Hz, damping 0.15 critical, and a relative displacement of $2\frac{1}{2}$ inches. The major difficulty in the design of shock mounts for general use is meeting these requirements when an additional constraint is applied of limiting the space which the system may occupy, such as for a tall cabinet in the usual environment in a ship's compartment. A useful shock mount should not fail on repeated deflection due to either shock or vibration, nor should its performance vary unduly with temperature. An experimental shock mounting system has been designed to meet these requirements. Results are given of some shock, vibration and endurance tests.

INTRODUCTION

A commonly used electronic cabinet in RN ships has the dimensions: 5-6 ft. height by 2ft x 2ft plan, and weight: 400-600 lb. Such cabinets may be banked closely together in rows, and are usually mounted on a plinth against a bulkhead, but are sometimes free standing. There is often only very limited headroom above the cabinet due to the presence of cable trays, and ventilation ducting.

The experimental shock mounting system described was designed specifically for this application. The main objective in its development was to isolate such a cabinet from any number of shocks of any degree that would be lethal to a ship, without increasing the prescribed space necessary to achieve this.

SPECIFICATION OF MOUNTING SYSTEM

Assuming a viscous damped spring system, it was considered that the vertical natural frequency should be as low as possible, subject to the amplitude being acceptable for resonance at the subharmonics of ship whipping. The damping must take account of this and also be sufficient to minimise the effects of fatigue on components in the electronic cabinets.

Experience based on these assumptions has shown the following specification to be a reasonable

compromise for these requirements:

Natural frequency	6 Hz
Damping	0.15 critical
Deflection	$\pm 2\frac{1}{2}$ inches

This allows an acceleration on the load of 9g at maximum deflection.

It must be recognised that to some extent the specification and the design of any shock mounting system are dependent on each other. If the main criterion were minimum deflection the use of a non-linear spring, or non-linear damping might be required. In the design described however the above specification is adequate, and is generally accepted as such.

The additional constraints implied in the requirement of the design were that the isolating system should occupy the minimum space, particularly above the cabinet, and between base and deck. It should also withstand all likely ship transmitted shock.

DESCRIPTION

Fig. 1 is a photograph of a test frame carrying an electronic cabinet on the mounting system.



Fig. 1. Side view of mounting system.

The spring suspension is at the base and consists of four glass reinforced plastic (G. R. P.) leaf springs.

Fig. 2. is a photograph of one of these springs which is a hot press moulding of epoxy resin and continuous glass filaments laid longitudinally. The outer surface of the moulding is glass cloth, which binds the filaments together and prevents

Reproduced from
best available copy.

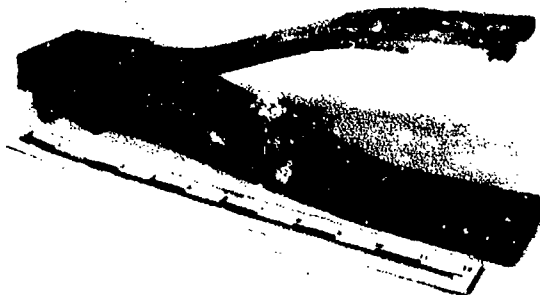


Fig. 2. G. R. P. leaf spring.

splitting. The middle region of each of the spring leaves is reduced in thickness, in order to obtain low stiffness, at the same time keeping the stresses low in the region of the fixing bolts. Countersunk washers are beaded to the mouldings to spread the clamping force, and do not encroach on the space available for deflection.

Fig. 3. is a photograph of the combined back fixing, lateral spring, and damping mechanism. It consists of two foam butyl rubber pads bonded to a metal plate attached to the cabinet, which passes between two rollers in a frame attached to the ship's bulkhead.



Fig. 3. Damping mechanism.

ASSEMBLY OF CABINET AND SHOCK MOUNTING SYSTEM

This would be carried out on board ship as follows. The roller frame would be attached to the bulkhead by bolts, or welding, an operation for which there need be little precision. The springs are bolted to the plinth, or directly to the deck if suitable, and would have to be located by a jig. The cabinet to which a suitable back bracket had previously been fixed would then be brought to position on the springs and bolted. The sandwich plate would be pushed between the rollers and bolted to the back bracket on the cabinet.

In some cases it may be more convenient for the foam rubber plate to be arranged in one of the alternative ways illustrated in Fig. 4.

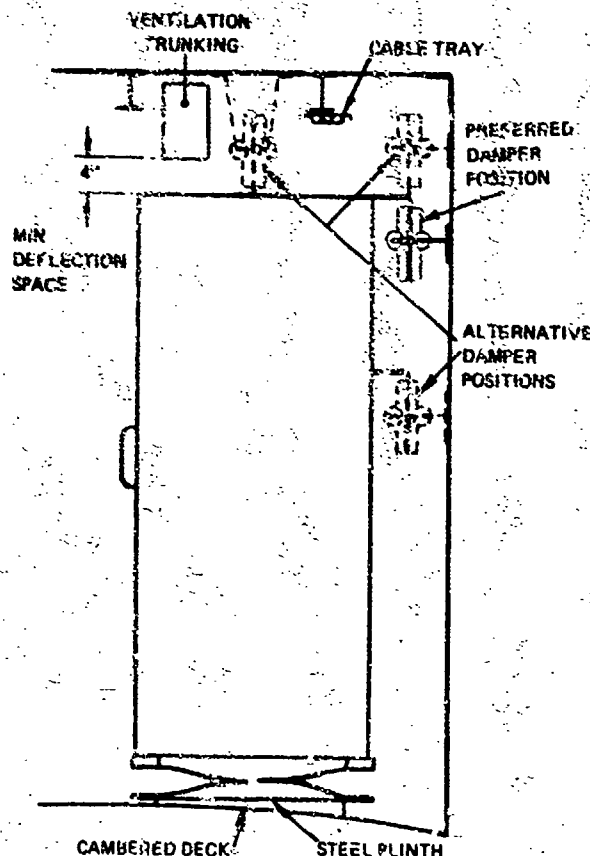


Fig. 4. Side view of alternative installations.

Free standing console which must not be attached to the deckhead will require a false bulkhead to be fixed to the deck to provide a rigid fixing for the damping mechanism. This may be behind the console, or alternatively smaller ones could be placed either side if more convenient.

When the cabinet is mounted in position, electrical cables, water hoses, flexible air ducting, etc. may be connected, due allowance being made for full deflection of the mounting.

ADVANTAGES OF SYSTEM

These are:-

1. Shock isolation up to ship lethality.
2. Minimum space requirement above and below cabinet.
3. Easy installation, not requiring high precision.
4. No maintenance required.

5. Reliable - can easily be inspected.
6. Not subject to fatigue - long life expectancy.
7. Wide temperature operating range.
8. Resistant to chemical and oil attack.
9. Overhead cable entry to the cabinet is facilitated.
10. Wide manufacturing tolerances are acceptable.
11. Lateral shock isolation is provided, with independently adjustable stiffness.
12. Damping material utilised in displacement due to shock is not statically loaded, and not subject to creep.
13. Damping material is loaded only by compression during shock motion.
14. Non magnetic - could be non-metallic if required.
15. Low cost.
16. No backlash in damping mechanism.

DESIGN DATA

G. R. P. Spring

Material: Epoxy resin with anhydride hardener/glass filament, press moulded at 100°C for 4 hours. Glass/resin ratio 80% midway along spring gradually reducing towards ends to 60/40%.

Nominal load per spring	100 lb.
Vertical height unloaded	4.1 inches.
Vertical height loaded	3.5 inches.
Width	3.0 inches.
Overall length	14 inches.
Available deflection-compression	2.7 inches.
Available deflection-extension	3.0 inches.

Calculated maximum stress at 100 lb load = 8,700lb/sq. inch.

Fatigue tests:

10⁸ cycles at amplitude 0.064 inch peak to peak at 18 Hz.
30 minutes continuous at amplitude 2.5 inches peak to peak at 6 Hz.

No deterioration was observed on conclusion of these tests.

Fig. 5. shows typical load/deflection characteristics for one spring for a range of temperatures. The springs were tested in pairs.

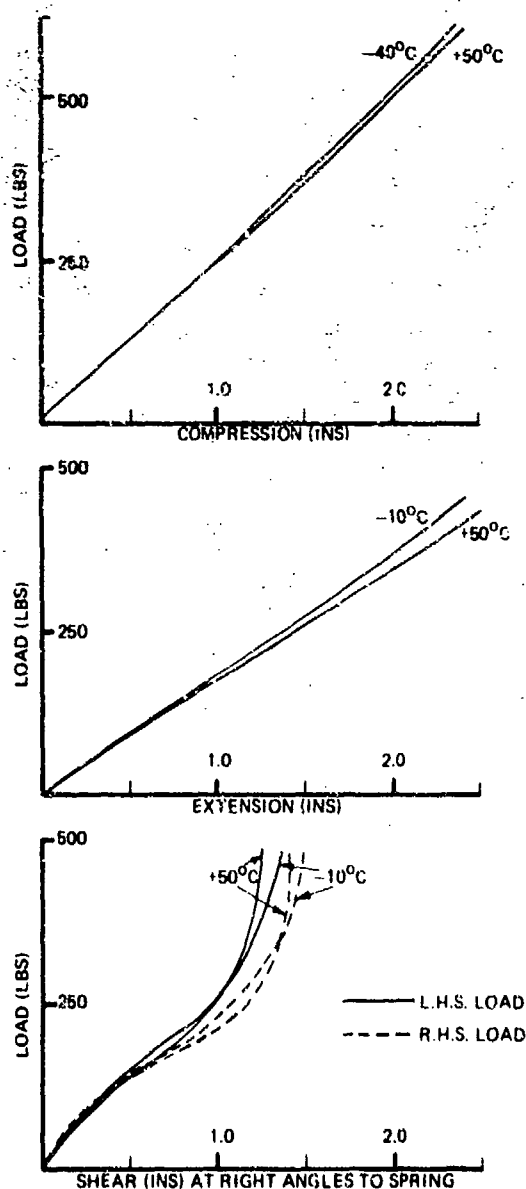


Fig. 5 Load/deflection curves of G. R. P. spring

Damping mechanism

Material: Foam butyl rubber - commercial grade used in the building industry.

Density	36 lb/cub. ft.
Width	8 inches
Thickness	1 inch
Compression	0.7 inch
Roller dia.	2 inches
Roller length	18 inches

LABORATORY TESTS

The cabinet shown in Fig. 1. was the mounting system tested. The cabinet weight was 400 lb, dimensions 5ft height by 2ft x 2ft plan, and the height of the C.G. was 32 inches above base level. Four springs were used for the mounting, and one damping mechanism was used for back fixing.

Vibration tests were carried out at A. S. W. E. and the results are given in Table 1. The decrease in amplification at the lower amplitude in the Vertical direction should be noted, which is probably due to a coulomb friction effect in the plain roller bearings.

TABLE 1. Vibration tests.

Direction	Natural Frequency (Hz)	Input amplitude (Inch) Peak to Peak	Amplification
Vertical	5.5	0.010	2
		0.020	4
Horizontal (parallel with roller axis)	4.2	0.02	10
Horizontal (rt. angles to roller axis)	5.6	0.02	12

Shock tests were carried out at Admiralty Engineering Laboratory, West Drayton, Middlesex on the Admiralty 2 ton shock test machine. This machine consists of a horizontal table which is struck from below by a projectile driven up a vertical tube by compressed air released from a storage chamber.

TABLE 2, Shock Tests

MEASURED RESONANT FREQUENCY OF SYSTEM VERTICAL AND HORIZONTAL 5.5 Hz.			DECK (Input)			CABINET (Load)			DEFLECTION (In Direction Of Shock)	
Test No.	Direction	Applied acceleration (g)	Velocity (ft/sec)	Deceleration (g)	Acceleration (g)	Velocity (ft/sec)	Deceleration (g)	Compression (inches)	Extension (inches)	
1	Vertical	74.5	15.6	51.0	2.46	1.75	2.71	1.9	2.97	
2	Vertical	250.0	26.2	125.5	1.74	1.12	1.58	1.78	1.8	
3	Vertical	480.0 Limit Of Test Machine's Capabilities	34.8	197.0	1.83	1.12	1.68	1.3	1.5	
4	Horizontal	28.4	5.5	24.4	1.45	1.14	1.33	At Top Of 60 inches High Cabinet		
5	(along	49.6	8.0	40.0	1.98	1.18	2.44	1.27	1.08	
6	roller axis)	69.8	11.25	60.7	3.62	1.75	3.11	1.24	1.89	

These results were obtained at a temperature of 20°C approx.
The same four springs and damping mechanism were used throughout the tests.

CONCLUSION

The experimental shock mounting system for electronic cabinets described in this paper has a number of practical advantages. The results of laboratory tests have shown that the protection given against any transmitted shock up to lethal severity in the naval ship environment should be adequate.

The system has not yet been subjected to test on board ships however. Trials on an RN destroyer are taking place in October 1971 to evaluate installation, ship machinery vibration, shock due to mortar explosions and sway in heavy seas. The system will be further tested in 1972 on a target ship of destroyer size which will be subjected to shock of lethal severity.

DISCUSSION

Mr. Pakstys (General Dynamics Corporation):
I noticed in the vertical shock test the second set of values were less than the first set of values even though the input was larger. Is there a good explanation for that?

Mr. Delany: I do not have an explanation other than that the first set of values may be nearer the natural frequency of the system. There must be some sort of interaction between the testing machine and the system under test. But this is quite right, there was actually less deflection for the larger shocks.

Mr. Koen (Bell Telephone Laboratories):
What were the time intervals of each of your shock tests?

Mr. Delany: Is it of any help if I give you the velocity in feet per second in addition to the applied accelerations? It would be something corresponding to sine input.

Mr. Tinn (Admiralty Engineering Laboratory, West Drayton, Middlesex): The shock machine is a long tube and there is a collapsible bullet which is fired with compressed air. When

it strikes the anvil this puts the input shock into the system and the shape is controlled by the collapsing head on the slug. The deceleration phase is controlled by the damper settings on the table. This is the Admiralty Standard 2 Ton machine which takes items up to 2 tons total weight.

Mr. Koen: What was the shock pulse shape?

Mr. Delany: The shape is controllable to a certain extent in that they usually try to obtain something approximating a damped sine wave in the velocity.

METHODS OF ATTENUATING PYROTECHNIC SHOCK

S. Barrett and W. J. Kacena
Martin Marietta Corporation
Denver, Colorado

A series of tests has been performed to evaluate the shock reduction effects of using various materials as shock isolators both at component mounting locations and at mechanically fastened structural joints. This paper describes these tests, presents the results, and compares the effects of the various shock isolation configurations on a shock response spectrum basis.

INTRODUCTION

Mechanical pyrotechnic devices are widely used on space vehicles to perform many vital mission functions. Unfortunately, a high-intensity pyrotechnic shock environment usually results as an undesirable side-effect of their operation. The severity of this environment varies with the kind of device and its location relative to sensitive components. In the past, most vehicles used relatively few pyrotechnic devices and good design practice had the more sensitive components mounted as far as possible from the devices to minimize the shock. However, the trend on more recent vehicles is to use increasing quantities of pyrodevices (50 or more), making it impossible to rely on distance alone to attenuate the pyrotechnic shock environment reaching sensitive equipment.

Failures during shock qualification tests and actual flights [1,2] have shown that pyrotechnic shock can be a critical environment for certain types of electronic components. A need to develop techniques for attenuating pyrotechnic shock clearly exists and the purpose of this study was to identify and evaluate such techniques. The study was sponsored by the National Aeronautics and Space Administration, Langley Research Center, Hampton, Virginia, under Contract NAS1-9000.

Four basic approaches are apparent:

- 1) Reduce the shock produced by the pyrotechnic source;
- 2) Isolate the shock source from its supporting structure;
- 3) Increase the attenuation occurring in mechanical joints in the shock path between the source and components;
- 4) Shock-mount components.

These approaches are listed in their order of desirability; obviously, if 1) could be achieved effectively, then the problem would be solved. However, it may not be possible to modify and requalify a piece of flight hardware in the time available on a particular program; in addition, such a solution would probably be different for each kind of device. The second approach is also greatly dependent on the individual application. Separation nuts, for example, frequently connect major structural elements and are required to transmit large forces, so there are obvious restrictions on the kind of isolation materials that can be added to the system. Thus, the last two approaches listed are probably the most universal in their application. The study described in this paper was directed toward obtaining test data on these methods.

When the shock pulse caused by a pyrodevice travels across a mechanical interface, some attenuation of the pulse occurs due to the reflections of the wave transmitting the energy. This attenuation can be increased if two different materials make up the interface. In this context, the materials are required to have different mechanical impedances. This phenomenon is discussed in detail in Appendix A.

Shock mounting of sensitive components can be achieved in several ways. These include hard mounts where the impedance mismatch of dissimilar materials provides shock reduction, mounting brackets where the impedance effects of bracket geometry are important, and soft mounts where relative motion is the significant parameter. Of these the greatest shock reduction is generally achieved with the soft mount. The primary effect of the soft mount is to create a low-frequency single-degree-of-freedom system which changes the shock waveform as though it had been treated by a low-pass me-

chanical filter. The low-pass mechanical filter concept is described in detail in Appendix B.

TEST PROGRAM

Joint Attenuation Tests

A number of tests were run on a model incorporating a simple mechanical interface, in which different materials could be inserted. A shock pulse was applied on one side of the joint and the shock level was measured on both sides. The test setup, including accelerometer locations and the joint details, is shown in Fig. 1 and 2.

Three families of materials were investigated. These were metals, hard nonmetals, and soft nonmetals. The actual materials and configurations tested are listed in Table 1. The joint was first tested with no insert, to provide a basis for comparison with subsequent joint configurations. A total of 35 joint configurations was tested. In every case, the effectiveness of the configuration was judged, in terms of the resulting shock spectra on the side of the interface furthest from the input, by comparison with the result from the untreated joint.

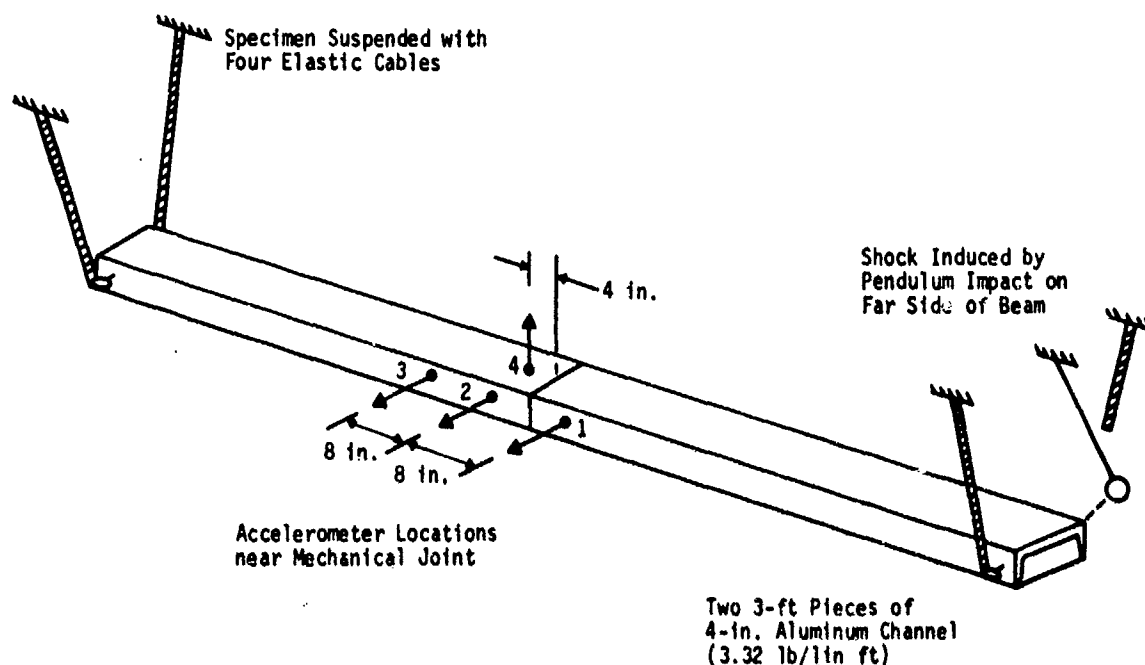


Fig. 1 Beam Specimen Test Setup

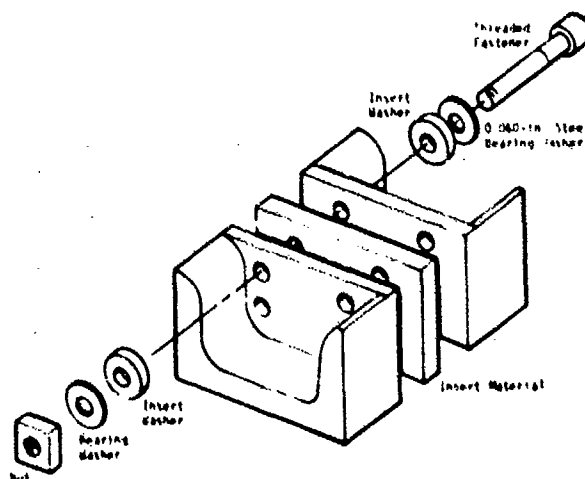


Fig. 2 Joint Details

TABLE 1
Joint Configurations (See Fig. 2)

Joint Configuration Number	Insert Materials	Insert Washers Used	Insert Thickness (in.)	Durometer (Shore A)
1*	None	No	--	--
2	Steel (S)	No	0.060	--
3	Magnesium (M)	Yes	0.125	--
4	Teflon (T)	Yes	0.125	--
5	Phenolic	Yes	0.100	--
6	Fiberglass	Yes	0.125	--
7	Asbestos	Yes	0.125	--
8	S-S	No	+	--
9	T-M-S-T	No	+	--
10	M-S	No	+	--
11	M-S-M-S	No	+	--
12	S-M-S	No	+	--
13	M-S-M	No	+	--
14	M-S-S-M	No	+	--
15	1 Steel Washer (W)	No	0.060	--
16	2W	No	+	--
17	4W	No	+	--
18 ¹	4W	No	+	--
19	6W	No	+	--
20 ¹	6W	No	+	--
21 ¹	M-S-S-M	No	+	--
22*	None	No	--	--
23 ¹	Neoprene	Yes	0.063	50
24 ¹	Neoprene	Yes	0.063	60
25 ¹	Silicon Rubber	Yes	0.063	50
26 ¹	Viton A	Yes	0.063	75
27 ¹	Adiprene	Yes	0.060	87
28 ¹	Viton A	Yes	0.125	75
29 ¹	Neoprene	Yes	0.250	80
30 ¹	Viton A	Yes	0.094	75
31 ¹	Neoprene	Yes	0.125	50
32 ¹	Neoprene	Yes	0.250	50
33 ¹	Aluminum	Yes	0.250	--
34 ¹	Aluminum	No	0.250	--
35 ¹	Lead	Yes	0.100	--

*Hard joint (baseline) configurations.

¹Thickness of multiple inserts is the sum of individual thicknesses previously listed.

²Loose joint.

³Rubber sleeves around bolts.

The results are summarized in Table 2, with typical comparative shock spectra shown in Fig. 3 through 8.

Component Isolation Tests

Shaker tests were performed on 13 different component configurations. Fourteen of these involved the 1.58-lb component depicted in Fig. 9. The input shock shown in Fig. 10 was synthesized using Ling Shock Synthesis/Analysis equipment. Testing proceeded first with a hard mounted configuration, followed by 13 soft mounted configurations. The soft mounted configurations utilized a pair of soft washers to simulate commercially available grommet-type mounts. Table 3 presents the relevant configuration data.

Table 4 shows these test results in the form of percent of reduction in shock level at the spectrum peak, and Fig. 11 and 12 illustrate typical shock response spectra at accelerometer location 2 for the hard mount and other configurations.

TABLE 2
Observed Shock Reductions from Joint Isolation Tests

Joint Configuration Number	Shock Reduction (Relative to Hard Mount) at Spectrum Peaks (%)		
	Location 2	Location 3	Location 4
2	16		22
3	20		14
4	40		25
5	4		11
6	12		14
7	16		14
8	32		31
9	20		20
10	36		51
11	40		34
12	34		40
13	40		17
14	32		40
15	24		34
16	0		6
17	0		14
18	46		48
19	16		20
20	56		62
21	40		40
23	0	21	
24	0	0	
25	47	42	
26	14	15	
27	23	42	
28	35	50	
29	23	47	
30	42	42	
31	44	52	
32	41	40	
33	17	15	
34	17	0	
35	35	40	

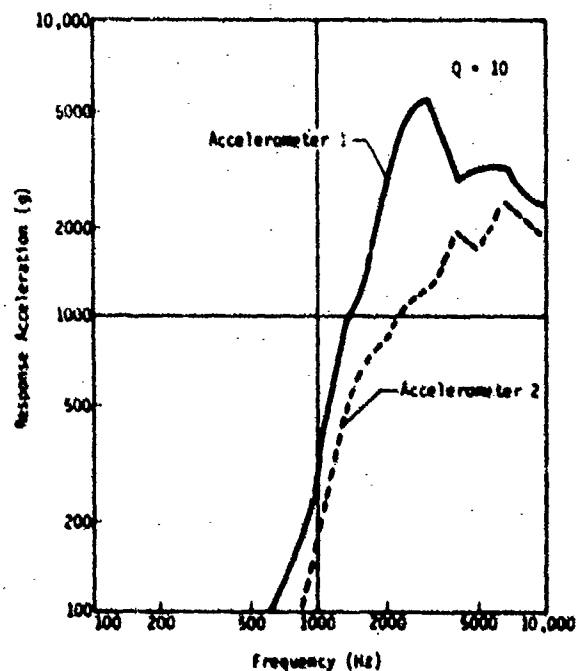


Fig. 3 Shock reduction across untreated joint, Configuration 1

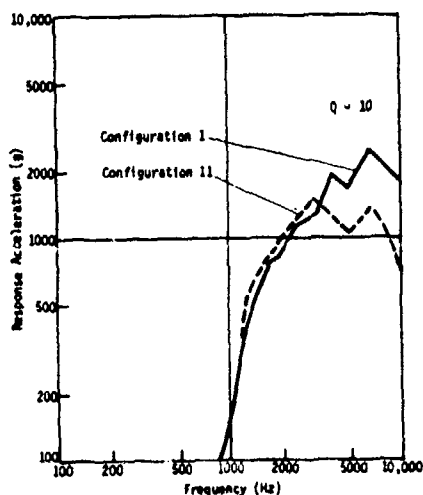


Fig. 4 Shock spectrum for metal inserts, Accelerometer 2

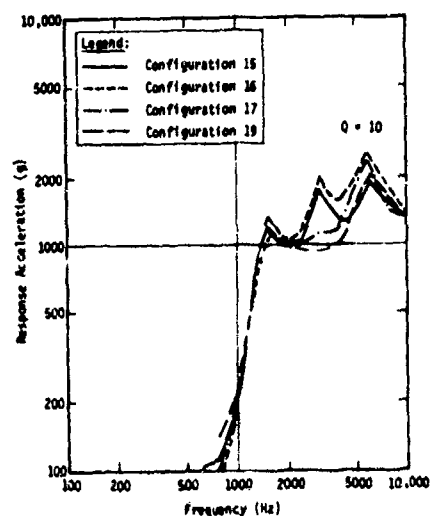


Fig. 7 Shock spectrum comparison, single and multiple inserts, Accelerometer 2

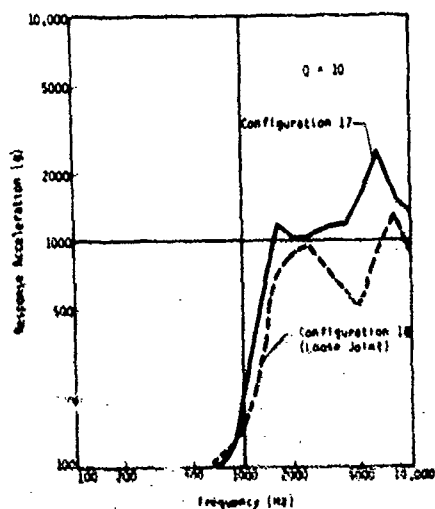


Fig. 5 Shock spectrum comparison, tight and loose joints, Accelerometer 2

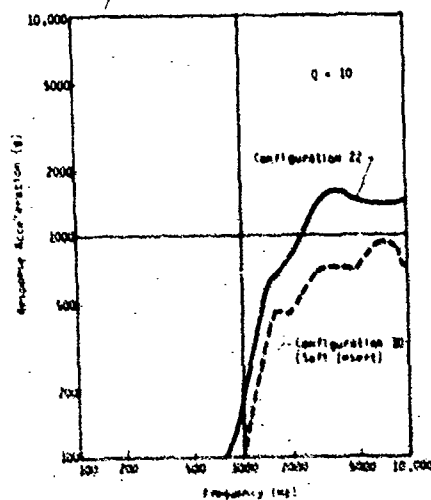


Fig. 8 Shock spectrum for soft insert material, Accelerometer 2

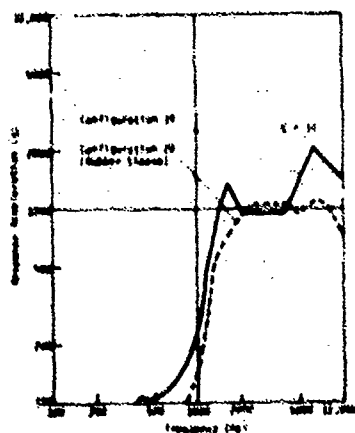


Fig. 6 Shock spectrum comparison, with and without rubber sleeve, Accelerometer 2

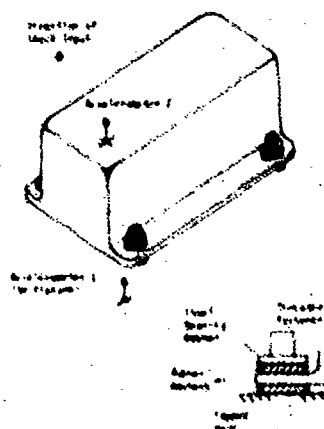


Fig. 9 Component shock test setup and mount details

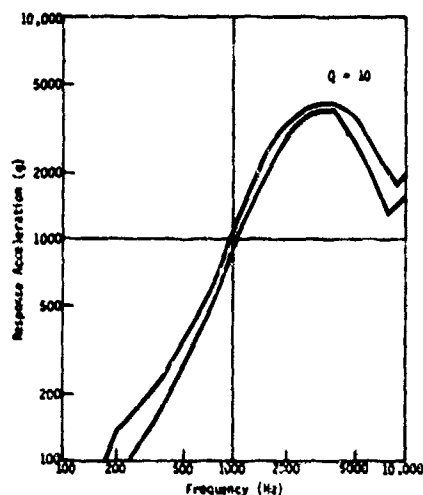


Fig. 10 Input shock spectrum range for component tests, Accelerometer 1

TABLE 3
Component Isolation Configurations

Component Isolation Number	Isolation Method	Approximate Natural Frequency (Hz)	Shock Reduction Relative to Hard Mount (%)
1	None	700	0
2	Isolator A	700	25
3	Isolator B	600	33
4	Isolator C	600	33
5	Isolator D	375	88
6	Isolator E	450	84
7	Isolator F	450	71
8	Isolator G	600	41
9	Isolator H	550	50
10	Isolator I	320	75
11	Isolator J	225	84
12	Isolator K	300	90
13	Isolator L	360	88
14	Isolator M	100	94

TABLE 4
Observed Shock Reductions from Component Isolation Tests

Component Configuration Number	Approximate Mounted Natural Frequency (Hz)	Shock Reduction Relative to Hard Mount (%)
2	700	25
3	600	33
4	600	33
5	375	88
6	450	84
7	450	71
8	600	41
9	550	50
10	320	75
11	225	84
12	300	90
13	360	88
14	100	94

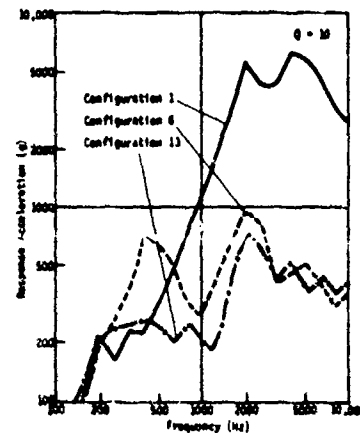


Fig. 11 Typical component shock spectra, Accelerometer 2

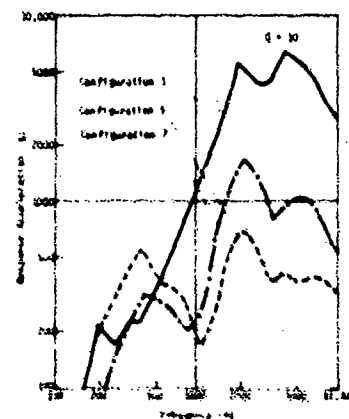


Fig. 12 Typical component shock spectra, Accelerometer 2

The final configuration was a 21-lb relay package mounted on four Lord H11-10 center-bounded mounts to produce a mounted natural frequency of approximately 30 Hz. The shock spectrum data for two accelerometers on the fixture and two on the package are presented in Fig. 13.

DISCUSSION OF RESULTS

Joint Attenuation

The results of the joint attenuation tests lead to the following observations.

A. GENERAL

1. The mechanical joints with no insert provided approximately 50% reduction in shock spectrum level at all frequencies (Fig. 3).

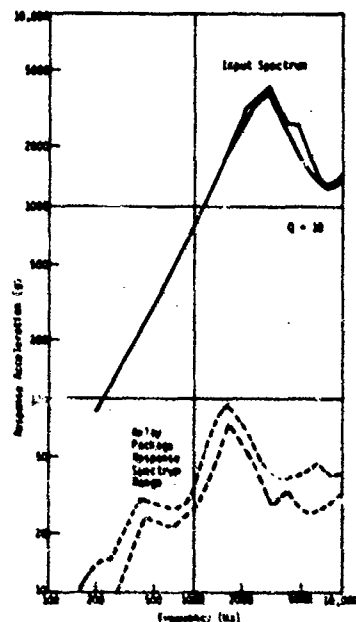


Fig. 13 Relay package shock spectra

2. A heat-shrink rubber sleeve around the bolts fastening the joint introduced significant shock reduction (Fig. 6).

3. Assembling the joint to be loose caused additional shock reduction across the joint (Fig. 5).

B. METAL INSERTS

1. Lead was the only material to produce significant shock reduction when used alone.

2. Multiple inserts of steel or steel washers were no more effective than a single steel insert, giving only a slight reduction (Fig. 7).

3. Alternate layers of steel and magnesium as inserts provided the best reductions, up to 30 or 40% (Fig. 7).

4. Any reduction achieved through the use of metal inserts only applied to the upper frequency range; there was effectively no reduction below about 1500 Hz (Fig. 4).

C. HARD NONMETALS

1. No significant attenuation was achieved using single inserts of hard nonmetals.

D. SOFT NONMETALS

1. The thicker and softer materials showed more than 40% shock reduction at higher frequencies, with about 30% reduction at lower frequencies (Fig. 8).

As a result of the theoretical developments in Appendix A and attempts to correlate these developments with the joint test data, it was found that the attenuation effects of the untreated joint and of the isolated joint could not be predicted analytically. Although several joint configurations did exhibit shock reduction characteristics, the best estimate of attenuation for other configurations will have to be based on empirical results such as those presented in this paper.

Of the joint configurations tested in this study, a loose joint exhibited the greatest attenuation. However, the use of loose joints is not particularly good design practice and is likely to create more problems than it solves. Furthermore, when the insert materials used are elastomers or lead, which are subject to cold flowing under load, the time between assembly and flight may degrade the efficiency of these materials, thus precluding their use. Finally, many design engineers frown on the use of a rubber sleeve around the fasteners at major structural joints. Their rationale is that it is bad design practice to rely on friction to carry shear loads in a joint that is not supposed to displace.

Based on the results of this study and the objections stated above, the most practical joint isolation insert material would involve multiple layers of two or more metals. The exact configuration, of course, would depend on the available space and the structural materials on each side of the joint. If the primary structure is aluminum, and if inserts of steel and magnesium are available, as they were in this study, the recommended insert would be four alternate layers of magnesium-steel-magnesium-steel in order from the shock side to the response side of the joint. This is an area where more test data needs to be accumulated in order to identify the importance of the many parameters involved. Other types and thicknesses of material should be tried, as well as different forms of shock input. Further testing in this area is scheduled to be performed by the authors, using a test model more characteristic of a real spacecraft and actual pyrotechnic devices. The results of these tests will be available in the early part of 1972.

Component Isolation

Data from the component isolation tests, summarized in Table 4, indicate that the shock attenuation tends to increase as the mounted natural frequency decreases. This trend is consistent with the mechanical filter concept, and is illustrated in Fig. 14.

A second characteristic of a mechanical filter is a slight amplification of the shock spectrum up to the mounted natural frequency but with reduced levels at higher frequencies.

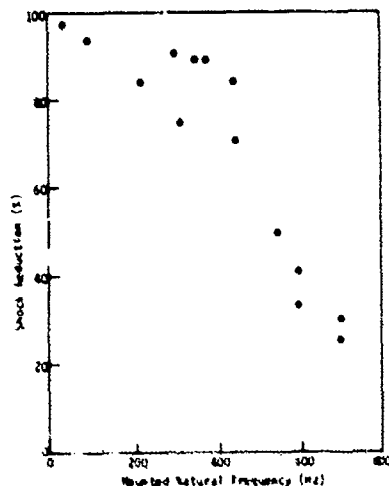


Fig. 14 Shock reduction versus mount frequency

This characteristic is also quite evident in the data presented in Fig. 11 and 12. On the relay package tests, the existence of low frequency amplification could not be verified because of a relatively high noise level in the low-frequency data.

The analytical discussion of a shock-mounted component, which is presented in Appendix B, concludes with a technique for predicting the shock reduction. This prediction technique requires a shock spectrum of the motion input to the component and knowledge of the mounted natural frequency. It assumes that motion input is impulsive in nature and that the component moves in a single degree-of-freedom with a known value of damping in the mount.

This technique was applied using the input shock spectrum envelope from these component tests and assuming 10% damping in the mount. In Fig. 15, the solid line represents the predicted shock attenuation; the dashed line also represents the predicted attenuation, but here the prediction has been reduced by an arbitrary factor of two.

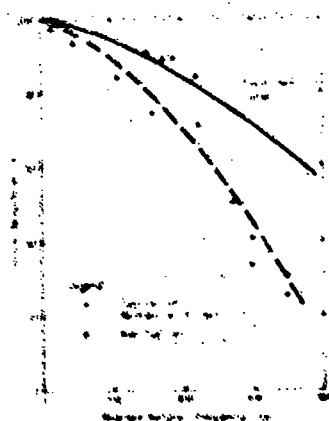


Fig. 15 Comparison between test data and predictions

Although the dashed curve is a more conservative prediction, it also appears to be more descriptive of the test data, particularly for the higher frequency mounts.

This noticeable lack of correlation between test and prediction is not necessarily attributed to deficiency in the prediction technique. In Fig. 15, the data points represented by "e" came from shock spectra having shapes characteristic of the mechanical filter concept, but the data points represented by "o" came from shock spectra having an initial peak at the mount frequency and a higher peak at approximately 2000 Hz. The existence of this second peak (Fig. 12) indicates that the component, at least where the response accelerometer was mounted, did not operate in a single degree of freedom. Furthermore, a 2000-Hz natural frequency of the component's structure could be driven by a rather lightly damped sinusoid at approximately one-third the frequency, say 550 to 700 Hz.

The discussion immediately preceding may sound like rationalization to justify the prediction technique, for it is the opinion of the authors that the shock response of a soft mounted component is relatively predictable even on a shock spectrum basis. The primary concern of an equipment designer, of course, is usually for the effects of shock on the parts inside his component. This problem is not very amenable to analysis because of the complexity of the model that would be required; however, it is considered that the approach discussed here can be used to derive an estimate of the overall shock environment for an isolated component.

CONCLUSIONS

The study shows that an effective and practical method of reducing the transmission of high frequency shock across a load-carrying structural joint is to use multiple inserts of two or more metals. On an aluminum structure the best results were obtained with layers of magnesium-steel-magnesium on steel, starting at the input side of the joint. Up to 70% total reduction was achieved with this configuration. This reduction applies only to the high-frequency portion of the shock spectrum, above 1500 Hz or so. Attempts to derive an analytical prediction method for this phenomenon were not successful.

A technique was developed for predicting the degree of protechnic shock isolation achieved on a shock-mounted component, as a function of its mounted frequency and the input shock spectrum. Reductions as great as 95% of the input spectrum peak were obtained during test, using elastomeric grommet-type mounts.

APPENDIX A - IMPEDANCE CONSIDERATIONS

References [3] and [4] present some analytical developments that are repeated here to clarify what is meant by impedance effects on shock wave transmission. The symbols used are:

f	force magnitude
T	period of time
λ	wavelength
Δ	deflection
A	cross-section area
E	modulus of elasticity
ρ	density
σ	stress
u	particle displacement
$v, \frac{du}{dt}$	particle velocity
$\epsilon, \frac{\Delta u}{\Delta x}$	strain
c	wave velocity
g	solution function
Z	impedance

Consider the generation of the plane compression wave of Fig. A-1. The wave is introduced by the application of a uniform force, f , applied longitudinally to the end of the bar for a short period of time, T , resulting in a wavelength, λ , and deflecting the bar a length, Δ .

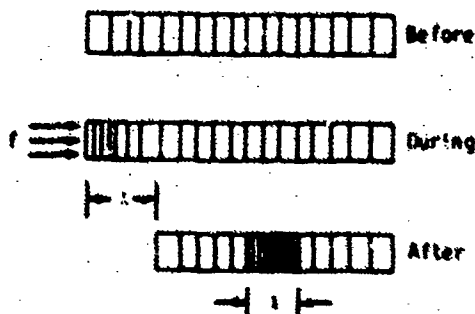


Fig. A-1 Wave generation

The energy relationship is developed as follows:

$$\Delta = \frac{fT}{AE}$$

$$\text{Internal work} = U = \frac{f^2 T^2}{2AE}$$

$$\text{Potential energy} = \frac{f^2 \lambda}{2AE}$$

$$\text{Kinetic energy} = \frac{1}{2} \rho A \lambda v^2$$

$$\frac{f^2 \lambda}{2AE} = \frac{f^2 \lambda}{2AE} + \frac{1}{2} \rho A \lambda v^2 \quad (A-1)$$

Notice in the Eq (A-1) for conservation of energy that half the energy is kinetic and half is potential. Solving (A-1) for particle velocity yields

$$v = \frac{f}{A \sqrt{DE}} \quad (A-2)$$

The momentum change due to the applied impulse is

$$\text{Momentum change} = \rho A \lambda (v - 0)$$

and the impulse is

$$\text{Applied impulse} = fT$$

The impulse/momentum relationship is then

$$\rho A \lambda v = fT \quad (A-3)$$

Since the wave front propagates a distance, λ , during the time, T , the wave propagation velocity is:

$$c = \frac{\lambda}{T} = \frac{f}{\rho A v} \quad (A-4)$$

Substitution of (A-2) for v in equation (A-4) gives

$$c = \sqrt{E/\rho} \quad (A-5)$$

Dynamic equilibrium of the differential element in Fig. A-2 results in the one-dimensional wave equation:

$$-\frac{\partial f}{\partial x} = \rho A \frac{\partial^2 u}{\partial t^2} \quad (A-6)$$

Since the differential element represents compressive forces, compressive stresses will be considered positive. However, due to the sign conventions on u and x , compressive strain $\left[\frac{\partial u}{\partial x} \right]$ is negative. Hence,

$$-\frac{\partial f}{\partial x} = -A \frac{\partial \sigma}{\partial x} = AE \frac{\partial^2 u}{\partial x^2} \quad (A-7)$$

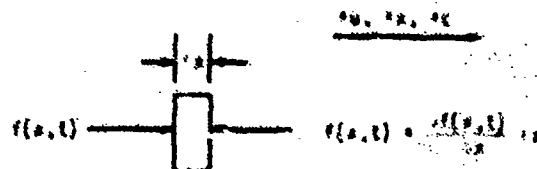


Fig. A-2 Differential element

When (A-7) and (A-5) are substituted into (A-6), the wave equation (A-8) results:

$$\frac{\partial^2 u}{\partial x^2} = \frac{1}{C^2} \frac{\partial^2 u}{\partial t^2} \quad (A-8)$$

The form of the solution to the wave equation can be used to derive a relationship between stress and particle velocity.

$$\text{Solution} = u(x, t) = g(x - ct)$$

$$\frac{\partial u}{\partial x} = g' = \epsilon \quad (A-9)$$

$$\frac{\partial u}{\partial t} = -cg' = -c\epsilon = \frac{C\sigma}{E} = v \quad (A-10)$$

From (A-4), $E = c^2 \rho$ and (A-10) becomes

$$\sigma = \rho cv \quad (A-11)$$

Equation (A-11) has some important physical significance: compressive stresses result ($\sigma > 0$) when the particle velocity and the wave velocity are in the same direction ($cv > 0$), and for tensile stresses the particle and wave velocities are in opposite directions.

Using the developments presented above, equilibrium and compatibility at the joint in Fig. A-1 can be used to demonstrate mechanical impedance effects. At the joint three plane waves exist: an incident wave, a reflected wave and a transmitted wave. All waves are assumed to be compressive, and the length of the joint is so small that inertia of the joint is a higher order effect and can be neglected. The equilibrium equation becomes

$$F_i + F_r = F_t \quad (A-12)$$

where the subscripts i, r, and t refer to the incident, reflected, and transmitted waves, respectively.

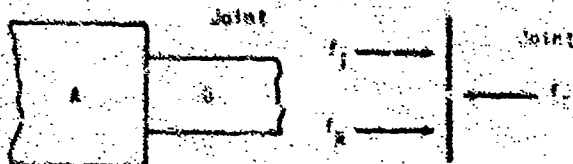


Fig. A-1 Joint analysis

A compatibility relationship is that the instantaneous particle velocity on the A-side of the (infinitesimal) joint is equal to that on the B-side. Remembering the significance of Eq. (A-11), it is clear that the particle velocity of the compressive reflected wave is opposite that of the compressive incident wave, and the velocity compatibility is written as

$$v_i - v_r = v_t \quad (A-13)$$

Substitution of (A-2) into (A-13) yields

$$\frac{F_i - F_r}{A_A \sqrt{\rho_A E_A}} = \frac{F_t}{A_B \sqrt{\rho_B E_B}} \quad (A-14)$$

Denoting $A \sqrt{\rho E}$ as the mechanical impedance Z , and solving Eq. (A-12) and (A-14) simultaneously for the ratios F_r/F_i and F_t/F_i gives:

$$\frac{F_r}{F_i} = \frac{1 - Z}{1 + Z} \quad (A-15)$$

$$\frac{F_t}{F_i} = \frac{2Z}{1 + Z} \quad (A-16)$$

where Z is the impedance ratio

$$Z = \frac{Z_A}{Z_B} = \frac{A_A \sqrt{\rho_A E_A}}{A_B \sqrt{\rho_B E_B}} \quad (A-17)$$

Equations (A-15) through (A-17) indicate that reflections are tensile and transmissions are small when a plane, longitudinal shock wave transmits from a stiff, dense material of large area into a soft, light material with small cross-sectional area. For this situation the reflected wave is tensile, and in the limiting case ($Z \rightarrow \infty$) the behavior is that of a free end.

The most practical aerospace application of mechanical impedance mismatching is the insertion of a dissimilar material in a structural joint where both sides are the same material. When only one insert material is used, two transmissions must exist and, for the second transmission becomes 1/0, thus, the transmission equation becomes

$$\frac{F_t}{F_i} = \frac{2Z}{(1 + Z)^2} \quad (A-18)$$

Fig. A-2 is a plot of this equation. Note it is no longer clear whether Z should be greater than or less than 1.0 to still be consistent with a practical range of insert materials. It is obvious, however, that Z must either be considerably greater than 1.0 or considerably less than 1.0 to achieve a large shock reduction.

Unfortunately, the wavelength of most shock waves is long compared with the thickness of the insert material. Hence, the wave reflected at the second interface has the opportunity to re-reflect at the first interface and constructively combine a short time later with the incident wave at the second interface. This means that attenuation effect of "aged"

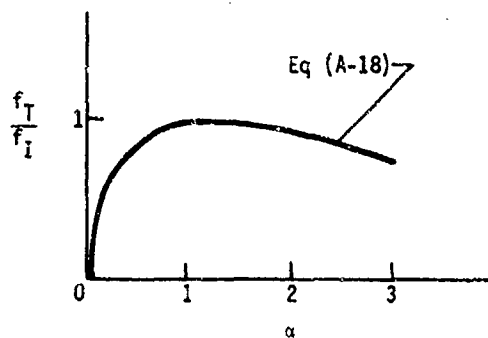


Fig. A-4 Plot of transmission equation

ance is probably not as great as that predicted by Eq (A-18).

Even neglecting re-reflection and constructive and destructive combinations of waves, predictions based on Equations (A-15) through (A-18) are not very accurate, especially for mechanically fastened joints. The primary problem is that mechanical joints are not perfect. Figure A-5 illustrates that one mechanical joint on the microscopic scale is really three joints, and the cross-section areas of sections B and C cannot be determined analytically. These unknown section areas preclude a reasonable determination of α at all three of the joints.

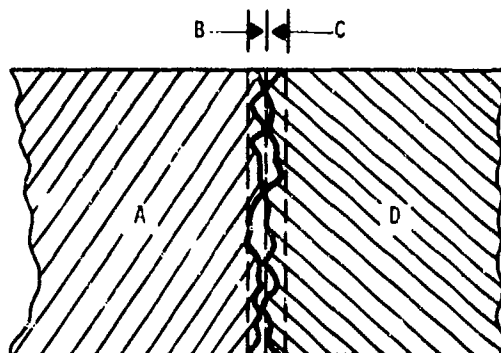


Fig. A-5 One joint, or three? or more?

This appendix has derived some of the equations governing the motion of plane longitudinal waves and has illustrated what is meant by the effect of mechanical impedance at structural discontinuities. Furthermore, two of the failures in using impedance characteristics for prediction purposes have been pointed out. Finally, a wave analysis becomes vastly more complicated when waves are no longer considered planar and when shear and flexural waves are included.

APPENDIX B - MECHANICAL FILTER

Analysis of the mechanics of structural motion can be achieved by a wave approach, as in Appendix A, or by a modal approach. It is more convenient to pursue a modal analysis when the structure tends to move with only one degree-of-freedom. Hence, the analysis that follows treats the motion of a shock mounted component as a single-degree-of-freedom system forced by a motion input at the base.

When the hard-mounted system shown in Fig. B-1 is forced with the base motion δ , the shock sensitive element inside the component will also be forced with the base motion δ . Generally, in shock analysis the potentially damaging input to the sensitive element is greatly simplified from δ to the shock response spectrum of δ . For the components tested during this study, the shock spectrum at the base was in the range depicted in Fig. B-2.

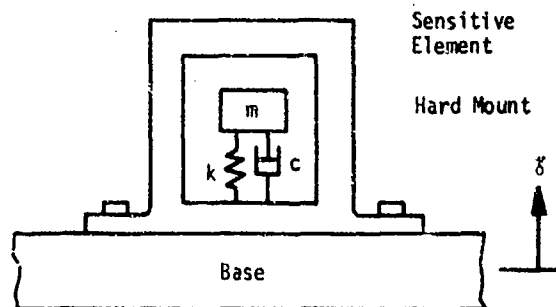


Fig. B-1 Hard mounted component

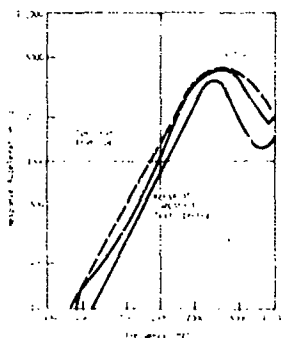


Fig. B-2 Envelope of component test data

For the shock mounted component operating in a single degree of freedom, the idealized system pictured in Fig. B-3 results. The equations of motion for this two-degree-of-freedom system are:

$$\left. \begin{aligned} M \ddot{X} + C (\dot{X} - \dot{X}_1) + K (X - X_1) &= 0 \\ M_1 \ddot{X}_1 + C_1 (\dot{X}_1 - \dot{\delta}) - C (\dot{X} - \dot{X}_1) &+ K_1 (X_1 - \delta) - K (X - X_1) = 0 \end{aligned} \right\} \quad (B-1)$$

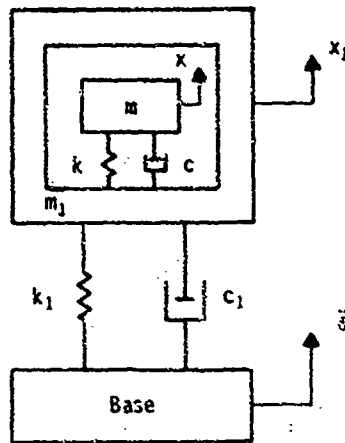


Fig B-3 Shock mounted component

If the mass ratio M/M_1 is so small that the motion of M does not influence the motion of M_1 , the equations of motion become uncoupled:

$$M \ddot{X} + C (\dot{X} - \dot{X}_1) + K (X - X_1) = 0 \quad (B-2)$$

$$M_1 \ddot{X}_1 + C_1 (\dot{X}_1 - \dot{\delta}) + K (X_1 - \delta) = 0 \quad (B-3)$$

It now becomes a simple matter when δ is known, to solve Eq (B-3) for \ddot{X}_1 , which is base motion input to the sensitive element M . Hence, the system in Fig. B-3 reduces to the system pictured in Fig. B-1 where the motion input is now \ddot{X}_1 instead of δ .

For shock evaluation of the soft mount, the shock spectrum of \ddot{X}_1 is the important parameter, and not the shock spectrum of δ . Within the limitations of some additional assumptions, the shock spectrum of \ddot{X}_1 can be estimated based on the shock spectrum of δ . It must first be assumed that δ is impulsive in nature and not a sustained transient. This means that the magnitude of the shock spectrum of δ at the mounted natural frequency, f_1 ($f_1 = \frac{1}{2\pi} \sqrt{K_1/M_1}$), is almost independent of the value of damping assumed in the spectrum analysis of δ . It is also assumed that the response motion of the component is a damped sinusoid of the form

$$\ddot{X}_1 = A e^{-\zeta 2\pi f_1 t} \sin 2\pi f_1 \sqrt{1-\zeta^2} t \quad (B-4)$$

where ζ is the damping ratio.

The maximum value of \ddot{X}_1 in Eq (B-4) occurs at approximately

$$\left. \begin{aligned} \tau &= \frac{1}{4 f_1 \sqrt{1-\zeta^2}} \\ \ddot{X}_{1\max} &\approx A e^{-\frac{\pi \zeta}{2 \sqrt{1-\zeta^2}}} \end{aligned} \right\} \quad (B-5)$$

Assuming $\zeta = 0.10$ for the shock mounted component, the maximum value becomes

$$\ddot{X}_{1\max} \approx 0.854A \quad (B-6)$$

Since $\ddot{X}_{1\max}$ is known from the shock spectrum of δ , Eq (B-4) becomes

$$\ddot{X}_1 = 1.17 \ddot{X}_{1\max} e^{-0.2\pi f_1 t} \sin 2\pi f_1 t \quad (B-7)$$

The term $\sqrt{1-\zeta^2}$ does not appear in Eq (B-7) as its value is very nearly 1.0.

The shock spectrum of the expression in Eq (B-7) is plotted in Fig. B-4. This shock spectrum is the effect of a low-pass mechanical filter (the shock mount) on the original input shock spectrum.

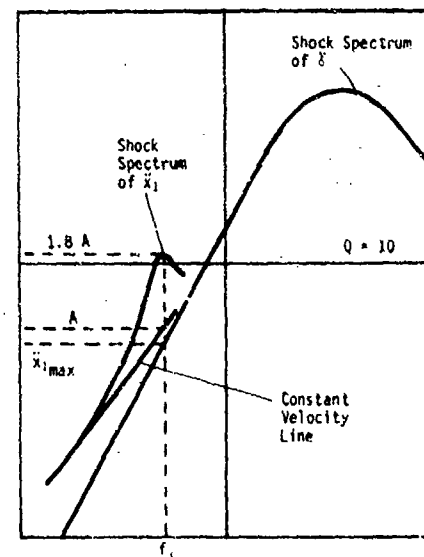


Fig. B-4 Shock spectrum of damped sinusoid with 10% damping

The new spectrum peak occurs at approximately the natural frequency, f_1 , and the shock level is slightly amplified at all frequencies below f_1 , but reductions occur at higher frequencies in the flat region of the spectrum.

The magnitude at the peak is 1.8 times the modulus of the damped sinusoid, which is 1.17 times the value of the original spectrum at the frequency, f_1 . This yields a total ampli-

fication factor of 2.1 over the original spectrum value at f_1 .

In the low frequencies, the shock spectrum of X_1 is asymptotic to a line of constant velocity (a slope of 1 on logarithmic paper). This constant velocity line intercepts the frequency, f_1 , at an acceleration level a factor of 1.17 above the original spectrum.

If the curve in Fig. B-4 really does represent the shock spectrum of X_1 , the shock reduction due to soft mounting can be predicted as follows.

- 1) Determine the natural frequency of the shock mounted component.
- 2) Read the acceleration magnitude off the original input shock spectrum curve at the natural frequency.
- 3) Multiply this acceleration value by 2.1 (1.17 x 1.8 for $\zeta = 0.1$).
- 4) Calculate the percent of shock reduction by comparing this value with the peak of the input spectrum.

REFERENCES

1. W. J. Kacena, III, Dr. M. B. McGrath, and W. P. Rader, "Aerospace Systems Pyrotechnic Shock Data (Ground Test and Flight)," MCR-69-611, Martin Marietta Corporation, Denver, Colorado, March 7, 1970.
2. F. A. Smith and R. W. Burrows, "Analysis of Shock Failure Data and Estimate of Viking Program Impact," VER-117, Martin Marietta Corporation, Denver, Colorado, January, 1971.
3. L. H. Donnell, "Longitudinal Wave Transmission and Impact," Presented at ASME Semiannual Meeting, Detroit, Michigan, June 9-12, 1930.
4. H. Kolsky, Stress Waves in Solids, Dover Publications, Inc., New York, 1963.

DISCUSSION

Mr. Deltrick (Hughes Aircraft Co.): When you are using these soft shock mounts on components are you concerned with thermal control? Our thermal control people do not like isolated things like this for spacecraft, hence we have been rather unsuccessful at soft isolation.

Mr. Kacena: We do not like to either unless there is a good reason for it. We have some relay packages that might not survive the types of environment that we have predicted, so we have soft mounted them and we have looked at the potential problems. Suppose something fails the qualification test and we do not have time to redesign it. We take the component as it is to find out what it is good for by qualifying a couple of other units, and if we find one that is reasonable and it finally passes, then we will try to shock mount it. But if there are thermal problems, such as a transmitter that radiates a lot of heat, then there is not much that can be done except to put it as far away from every-

thing as possible. We are aware of this problem but we hope our transmitters do not fail.

Mr. Thomas (Honeywell Incorporated): What type of components are sensitive to this type of shock?

Mr. Kacena: Relays are notoriously sensitive to pyrotechnic shock. Other components have to be looked at subjectively. For example if you have an oscillator that has a fine tuning screw and if that tuning screw does not have a positive lock of some kind it may turn. That is not a catastrophic failure such as when structure goes flying all over the place. However you may get some pretty garbled data back, and generally pyrotechnic shock failures are of this nature. Our reliability people have found that the most significant structural failures from pyrotechnic shock, are in the realm of shocking something to its qualification level eighteen times. Eighteen is the magic number and things start to fail, although that may be a bit unrealistic.

ENERGY ABSORPTION CAPACITY OF A SANDWICH PLATE
WITH CRUSHABLE CORE

D. Krajcinovic
Argonne National Laboratory
Argonne, Illinois

Presented is a simple, approximate dynamic analysis of a sandwich type pressure vessel head plate with a significant energy absorbing potential. The analysis is based on the propagation of a compression (shock) front through the core made of crushable material.

1. INTRODUCTION, BACKGROUND AND OBJECTIVE

Basic structural requirement of a nuclear reactor pressure vessel design is the absorption of the energy associated with a hypothetical (design basis) accident. Since the vessel itself is located in a cavity, the collapse of the cylindrical part is not considered nearly as serious as the rupture of the head cover plate. The reason is obviously that the rupture of the head plate is followed by a substantial leakage of irradiated substances (such as plutonium aerosol and liquid sodium in case of a Fast Breeder Reactor) from the vessel into the area in which people work. It is, therefore, considered imperative to design out the possibility of a head plate failure by providing for the absorption of the energy directed upwards.

To this end two alternatives were considered during the recent design of the FFTF (Fast Flux Test Facility) pressure vessel. According to the first alternative, in addition to the strain energy dissipated in the plastic deformation of the head plate itself, the main part of the energy is entrusted to an external energy absorbing mechanism such as a system of stretch bolts and/or dashpots. Obviously, a substantial motion of the head plate is necessary to trigger this external energy absorbing system. This, however results in loss of plate-vessel integrity and opening of substantial potential leakage paths.

According to the alternate idea, the energy absorber is located within the vessel as an integral part of the head plate. This design consists of an upper head plate, providing the bending stiffness, rigidly attached to supports and the cylindrical part of the vessel, a layer of crushable material having high energy

absorbing potential, and a driver plate not attached to the plate with main purpose to distribute the load across the cross section and to spread it over a longer time period. Two major benefits of the latter design are the fact that the upper plate is fixed, enabling better sealing during and after the accident, and (as it will be seen later) the possibility of the choice of the maximum pressure intensity to be transmitted to the upper plate. A negative feature is increase in vessel length by choosing a layer of honeycomb of excessive thickness. In order to avoid this problem it is possible to couple two designs and choose the upper limit of the pressure over which the head plate will leave supports and activate the external energy absorbers. In this case only for most severe, low probability accidents one will be faced with the leakage problem.

From the computational point of view, the second sandwich type alternative is a more complicated one. It is our objective to formulate a simple dynamic model which will, in early stages of the design, provide information leading to the choice of optimal geometrical and material parameters of the entire three layer model. To this end, a series of assumptions and simplifications will be introduced in full awareness of a need of eventual development of a more complete computational model. The purpose of the presented computation is to provide some information on the intensity and the pressure time history for the upper plate and on the energy absorbed in the process of crushing. In addition to this, the model should provide for a first estimate of the influence of various design parameters on the absorbency and finally survivability of the entire structure for a given accident.

2. COMPUTATIONAL MODEL

An "exact" analytical description of the model, even for the axisymmetrical case, would

* Work done under the auspices of the U.S. Atomic Energy Commission.

involve a set of nonlinear (both physically and geometrically) partial differential equations (a mixed nonlinear initial value and boundary value problem). Corresponding solution is apparently attainable, if at all, only through application of large computer codes being utterly inefficient in early design stages. As it is usually done in structural problems in order to simplify the analysis, we will approximate the real structure with a one-dimensional model. As far as the upper plate (bent by the pressure) is concerned, no special problem is anticipated. The approximation of dynamically loaded circular plates (deformed elastically in its first or fundamental mode) by a one-dimensional mass-spring oscillator is a routine engineering approach. In the case of plastic deformation, the procedure is not any more straightforward, but a method presented in [1] or [2] may possibly be extended to cover the case when the load (and not only ideal impulse) is acting upon the plate.

The crushable layer is approximated by a rigid-perfectly plastic-rigidly locking model (Fig. 1). In this way we neglect elastic

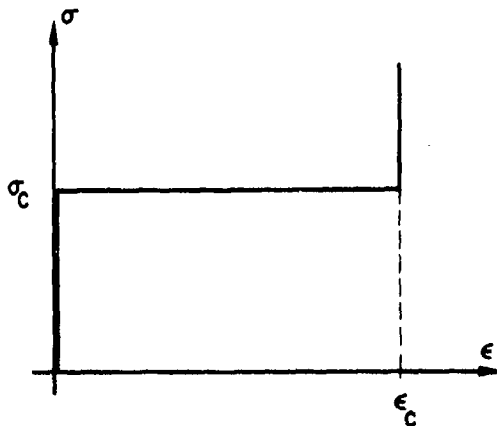


Fig. 1. Stress-strain law for the crushable material

deformation and consider material as being perfectly rigid up to some crushing pressure p_c at which the skeleton collapses and without further load increment compresses to a certain density ρ_c (defining also some ultimate strain ϵ_c). Once crushed (compressed to ρ_c) the material acts as incompressible. Although extremely simple, this type of behavior is in a very good accord with the experimental data reported in the literature (see for example Refs. 3-5). We should probably mention that for high crushing velocities (higher than what is expected in the case considered) some rather high peaks may take place in σ - ϵ diagram [3,5]. This problem may be alleviated by dimpling the layer on both surfaces. The main source of uncertainty is the definition of the effective crushable area in the transition to a one-dimensional model. This depends not only on the bending of both plates, but also on the

slug radius and finally on the designed distribution of the crushable layer across the plate (penetrated by all types of openings).

As a result of our choice of the material model for the crushable layer, the propagation of elastic stresses is instantaneous throughout the model. Changes in relative positions of various points (strains) will commence only after the applied pressure $p(t) \geq p_c$ exceeds or equals the crush strength of the material. Due to the fact that the part of the stress-strain curve $0 \leq \epsilon \leq \epsilon_c$ is horizontal, no plastic waves will propagate either. However, as a result of strong concavity of the stress-strain curve in the vicinity of $\epsilon = \epsilon_c$, a sharp compaction (shock) front will be generated. This type of behavior probably deems some explanation.

We recognize the fact that the behavior of a representative crushable material such as, for instance, honeycomb is dictated primarily by its geometrical configuration (and much less by actual characteristics of the material itself). This explains the fact that both steel (i.e., ductile) and phenolic-glass (i.e., brittle) honeycombs perform much in the same way, although the process on the local level is completely different (buckling vs. actual crushing). Gross behavior exhibits significant plasticity (functional in nature) although as a result of the absence of strain hardening no plastic waves will propagate. The predominant process is obviously that of compaction, i.e., propagation of a compaction (shock) front through the crushable layer.

Since the entire process is dictated by the geometry and not material characteristics of constituent materials, no significant unloading waves will propagate and the entire process is strongly irreversible. In other words, once crushed and compacted to the density ρ_c (corresponding to the locking strain ϵ_c), the honeycomb will be assumed to behave as a rigid material.

The lower, driver plate is assumed to be rigid and no credit is given to its energy absorption (strain energy, etc.). The plate is modeled by a concentrated mass m_1 and is assumed to provide only for a more uniform distribution of crushing.

The analytical model described above is presented in Fig. 2. We note that the model accounts only for mechanical means (strain energy and crushing) of energy absorption. At this stage the energy dissipation mechanisms such as pneumatic [6] and thermal [7] damping, having to do with mass and heat transport within gas filled porous materials, are not considered. A potentially significant subject directly related to the energy degradation is also the dissipation mechanism resulting from viscous effects in two phase (say liquid sodium mixed with gas) fluids. This effect is not considered to be within the scope of this paper. All of those neglected effects, being

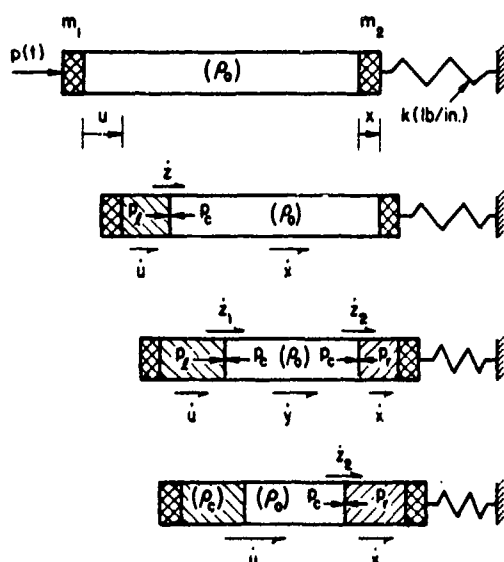


Fig. 2. Adopted computational model: a) initial state, b) one front propagating from the loaded side, c) two fronts propagating, d) one front propagating from the spring side

dissipative mechanisms, are expected to diminish the pressures we are calculating with herein. In that respect results to be presented are on the conservative side.

3. GOVERNING EQUATIONS

We consider the mechanism presented in Fig. 2a, subjected to a pressure $p(t)$ with a known load-time history. The pressures less than p_c will instantaneously propagate through the sandwich followed by the ensuing deformation of the elastic spring. Increase of pressure in excess of p_c will generate a discontinuity (compaction, shock) front which will start propagating through the crushable layer. We notice that the generation of the front is not the function of the suddenness of the impact but the direct result of the adopted stress-strain law. The front itself is a traveling discontinuity surface for the stress, strain, and density. As such it may be considered as a strong discontinuity wave or simply a shock wave (see for instance [8]). We will employ the so-called elementary theory of shock waves (see for instance Refs. 8, 9) considering the process to be adiabatic and disregarding the variation of the internal energy as a result of the impact (so-called, weak shock waves). This simplified theory is to a certain degree justified by rather small impact speeds of the coolant slug, although the jump in pressure intensity may cause variations in internal energy and temperature worth considering at some later stage.

The following notation is used. Densities (initial and terminal) are denoted by ρ_0 and ρ_c , $\epsilon_0 = 0$ and ϵ_c are corresponding strains in virgin and compacted zone. Pressures behind and in front of the compaction front are denoted by p_- and p_+ . Masses (lumped) of the lower (driver) and upper (head) plate are denoted by m_1 and m_2 , mass of the crushable layer (per unit of length) is m . Thickness of the crushable layer is L , while k is the spring constant of the head plate computed either from the static deflection for unit load or from the first natural frequency.

a) One Compaction Front

We introduce an Eulerian coordinate system and denote by $u_1(t)$ the displacement of the lumped mass m_1 (driver plate) and by $u_2(t)$ the displacement of the mass m_2 (upper plate) and consequently spring as well. Two corresponding velocities are denoted by $\dot{u}_1(t)$ and $\dot{u}_2(t)$. Consider first the case of one compaction front (Fig. 2b), generated at the unloaded end (on the interface with the driver plate), propagating through the crushable layer towards the spring (upper plate). Denote the velocity of the compaction front by $\dot{z}(t)$. As a result of our choice of the stress-strain law both uncompacted and compacted zones move as rigid bodies with velocities \dot{u}_2 and \dot{u}_1 . In order for the front to propagate, the following inequality has to be satisfied

$$\dot{z} > \dot{u}_1 > \dot{u}_2 \quad (1)$$

The violation of the first inequality stops the front propagation, while the second inequality prevents the generation of the unloading (tensile rarefaction) wave which is ruled out a priori.

From the conservation of mass

$$\rho_- \dot{u}_- = \rho_+ \dot{u}_+ \quad (2)$$

and conservation of momentum

$$p_- + m\dot{u}_- = p_+ + m\dot{u}_+ \quad (3)$$

equations, we write two Hugoniot equations relating discontinuities in pressure p , density ρ and velocity \dot{u} , ahead (sign "+") and behind (sign "-") the compaction front,

$$[\rho(\dot{u} - \dot{z})]_-^+ = 0 \quad (4)$$

$$[\rho\dot{u}(\dot{u} - \dot{z}) + p]_-^+ = 0 \quad (5)$$

Further details are available in Refs. 8 and 9 (the case considered herein is, to repeat, adiabatic and with constant internal energy). After simple algebraic manipulations, we rewrite (4) and (5) in a slightly different way

$$\rho_0(\dot{u}_2 - \dot{z})(\dot{u}_2 - \dot{u}_1) - p_- + p_+ = 0 \quad (6)$$

and

$$\dot{z} - \dot{u}_2 = \frac{\rho_c}{\rho_c - \rho_0} (\dot{u}_1 - \dot{u}_2) \quad (7)$$

Since the motion starts from rest (i.e., $z \equiv u_1 \equiv u_2 \equiv 0$ at $t = 0$) integration of (7) leads to

$$z - u_2 = \frac{\rho_c}{\rho_c - \rho_0} (u_1 - u_2) \quad (8)$$

It is interesting to note that in [10], where a similar, although less general, problem is solved (with a single front and without the spring, i.e., with forces known at both ends), equation (8) is derived as some kind of a constitutive equation establishing the relation for the compacted strain in terms of two densities.

Finally we write two dynamic (equilibrium) equations. For the already compacted zone (behind the compaction front) from the free-body diagram it follows

$$[m_1 + \rho_c(z - u_1)]\ddot{u}_1 = p(t) - p_- \quad (9)$$

where the second term in brackets is the mass of the already compacted zone. For the uncompacted front in the same way it follows

$$\rho_0(L - z + u_2)\ddot{u}_2 = p_+ - q \quad (10)$$

where q is the reaction from the spring.

Finally, we write the equation of the motion for the spring

$$m_2\ddot{u}_2 + ku_2 = q \quad (11)$$

Altogether we have five independent equations (6,8,9,10,11) in five unknowns, u_1 , u_2 , z , p_- and q . Note that $p_+ = p_c$, i.e., the pressure just in front of the compaction front is the known crush pressure being the property of the material used. Eliminating z , p_- and q it follows

$$[m_1 + \rho_c(u_1 - u_2)]\ddot{u}_1 = p(t) - p_c - \rho_c(\dot{u}_2 - \dot{u}_1)^2 \quad (12)$$

$$(m_2 + m_c - \rho_c(u_1 - u_2))\ddot{u}_2 + ku_2 = p_c \quad (13)$$

where $m_c = \rho_0 L$ is the mass of the crushable layer and $\rho_c = \rho_0 \rho_c / (\rho_c - \rho_0)$.

If the structure was initially at rest the associated initial conditions are

$$u_1(0) = \dot{u}_1(0) = \dot{u}_2(0) = u_2(0) = 0 \quad (14)$$

b) Two Compaction Fronts

At some point of the previous phase, the pressure on the interface between the head plate and the crushable layer may exceed the crush strength p_c of the crushable layer. At that instant a new compaction front will be generated and will start propagating in the direction of the lower (driver) plate. As in Fig. 2c, we denote the velocities of three zones by \dot{u}_1 (compacted zone on the load side), \dot{u}_3 (uncompacted zone in the middle) and \dot{u}_2 (compacted zone on the spring side). Corresponding displacements are u_1 , u_3 and u_2 . Velocities of two compaction fronts are \dot{z}_1 (generated from the load side) and \dot{z}_2 (generated from the spring side).

As for the previous case we write equations of the mass and momentum conservation (4,5) across both discontinuity fronts. After some algebraic manipulations, for the first compaction front they read

$$\rho_0(\dot{u}_3 - \dot{z}_1)(\dot{u}_3 - \dot{u}_1) - p_- + p_c = 0 \quad (15)$$

$$z_1 - u_3 = \frac{\rho_c}{\rho_c - \rho_0} (u_1 - u_3) \quad (16)$$

Across the second compaction front, one has

$$\rho_0(\dot{u}_3 - \dot{z}_2)(\dot{u}_2 - \dot{u}_3) - p_c + p_- = 0 \quad (17)$$

$$u_3 - z_2 = \frac{\rho_c}{\rho_c - \rho_0} (u_3 - u_2) \quad (18)$$

In addition, we write three dynamic (equilibrium) equations. For the compacted zone on the load side

$$[m_1 + \rho_c L_1 + \rho_c(z_1 - u_1)]\ddot{u}_1 = p(t) - p_- \quad (19)$$

For the uncompacted zone in the middle

$$\rho_0(L_{c1} - z_1 + z_2)\ddot{u}_3 = p_c - p_c \quad (20)$$

and finally for the compacted zone on the spring side

$$\rho_c(z_2 - u_2)\ddot{u}_2 = p_- - q \quad (21)$$

The last equation of motion is written for the mass-spring system

$$m_2\ddot{u}_2 + ku_2 = q \quad (22)$$

The length L_1 is the length of the uncompacted material at the initiation of this phase (or termination of the previous phase), while L_{c1} is the length already compacted during the previous phase.

Finally, we have a system of eight independent equations (15-22) in eight unknowns,

$u_1, u_2, u_3, z_1, z_2, p_-, \bar{p}_-,$ and q . We again eliminate all of the unknowns except the first three, such that

$$[m_1 + \rho_c L_1 + \rho_e (u_1 - u_3)] \ddot{u}_1 = p(t) - p_c - \rho_e (\dot{u}_1 - \dot{u}_3)^2 \quad (23)$$

$$[m_2 + \rho_e (u_3 - u_2)] \ddot{u}_2 + k u_2 = p_c + \rho_e (\dot{u}_3 - \dot{u}_2)^2 \quad (24)$$

$$\ddot{u}_3 = 0 \quad (25)$$

Associated initial values are determined from terminal values of the preceding phase

$$\begin{aligned} \dot{u}_1(t^*) &= \dot{u}_1^* & u_1(t^*) &= u_1^* \\ \dot{u}_2(t^*) &= \dot{u}_2^* & u_2(t^*) &= u_2^* \\ \dot{u}_3(t^*) &= \dot{u}_2^* & u_3(t^*) &= u_2^* \end{aligned} \quad (26)$$

(with asterisk denoting terminal value of the preceding phase). From (25) and (26) it follows that

$$u_3 = u_2^* + \dot{u}_2^* \tau \quad (27)$$

where $\tau = t - t^*$ is measured from the beginning of the two fronts phase. Hence, one finally has from (23, 24) and (27) two equations governing the motion in this phase

$$[m_1^* + \rho_e (u_1 - \dot{u}_2^* \tau)] \ddot{u}_1 = p(t) - p_c - \rho_e (\dot{u}_1 - \dot{u}_2^*)^2 \quad (28)$$

$$[m_2^* + \rho_e (\dot{u}_2^* \tau - u_2)] \ddot{u}_2 + k u_2 = p_c + \rho_e (\dot{u}_2^* - \dot{u}_2)^2 \quad (29)$$

where

$$m_1^* = m_1 + \rho_c L_1 - \rho_e u_2^*$$

$$m_2^* = m_2 + \rho_e u_2^*$$

The requirement for the propagation of the front generated on the load side is

$$\dot{u}_1 > \dot{u}_1^* > \dot{u}_3 \quad (30)$$

For the spring side front the propagation requirement is

$$\dot{u}_3 > \dot{u}_2 > \dot{u}_2^* \quad (31)$$

If one of the inequalities is violated, the corresponding front stops propagating. It is also possible for two fronts to collide in which case the entire layer is crushed and the subsequent motion is that of a lumped mass attached to a spring.

c) Single Front from the Spring Side

Finally we examine the remaining case when the front from the load side stops propagating (inequality (30) violated) while the front from the spring side still keeps progressing. Without further elaboration we just write down the final equations of motion

$$[m_1'' - \rho_e (u_1 - u_2)] \ddot{u}_1 = p(t) - p_c \quad (32)$$

$$[m_2 + \rho_e (u_1 - u_2)] \ddot{u}_2 + k u_2 = p_c + \rho_e (\dot{u}_1 - \dot{u}_2)^2 \quad (33)$$

where masses m_1'' and m_2'' include masses of already compacted zones adjacent to lower and upper plate, respectively.

The requirement for the front propagation is

$$\dot{u}_1 > \dot{u}_2 > \dot{u}_2^*$$

4. SOLUTION OF GOVERNING EQUATIONS

In each of three cases analyzed in the preceding section, the motion of the system is governed by two coupled nonlinear differential equations of second order with given initial values. In nuclear reactor applications the nonlinear terms turn out to be small compared with others. This is especially true for the nonlinear term on the left-hand side being the mass of the compacted crushable layer which is in most cases negligible when compared with the mass of two plates. This, of course, means that equations may be conveniently solved using the perturbation method [11, 12]^{*}. In linear approximation for the first phase considered it follows from Eqs. 12 and 13 that

$$\ddot{u}_1 \approx \frac{p(t) - p_c}{m_1} \quad (34)$$

$$\ddot{u}_2 + \omega^2 u_2 \approx \frac{p_c}{m_2} \quad (35)$$

where $\omega^2 = k/m_2$. The solution of the first equation obviously depends on the load-time history, while in first approximation $u_2(t)$ is given by

^{*}We note that the design with a very thin driver plate $m_1 \rightarrow 0$ leads to a singular problem warranting the use of so-called singular perturbation methods (see for example Ref. 13).

$$u_2 \approx \frac{p_c}{k} (1 - \cos \omega t) \quad (36)$$

From where the pressure on the upper plate is finally computed to be

$$q_{\max} = k u_{2\max} \approx 2p_c \quad (37)$$

In other words the maximum pressure on the head plate depends mainly on the crush pressure p_c of the crushable material. Moreover, having an approximate analytic expression for the pressure-time history for the upper plate it becomes much easier to incorporate its dynamic plastic behavior (instead of purely elastic as considered herein).

Apart from first approximations listed above it becomes questionable whether one should continue with a perturbation technique in quest of a more accurate analytical solution or simply resort to numerical integration using standard computer routines. Since the sub-routines for the solution of a set of nonlinear differential equations (initial value problem) are today in ample supply, the only programming one has to do is to write a simple driver routine enabling transitions between various phases of crushing. It is apparent that in this case the nonlinear terms need not be small when compared with linear. It is also well known that the initial value problems are especially suitable for computer applications. The computing time in most cases totals a few seconds.

5. NUMERICAL EXAMPLES

As a numerical example we analyze a few different designs of a sandwich head plate subjected to two different loadings (corresponding to two coolant levels). The calculations leading to the determination of the pressure-time history were of the simple "sodium" hammer type, but were later verified by results obtained through application of a big finite-difference computer code (REXCO). The two loading cases, one consisting of only one and another of two shocks, are diagrammed in Fig. 3.

The total weight of the sandwich plate (and attached accessories) is estimated at 0.9×10^6 lbs. In order to estimate the influence of the mass distribution, two designs are considered: for the first, the mass of the head plate was twice as big as that of the driver plate $m_2 = 2m_1$, while for the second, two masses were taken as equal $m_2 = m_1$. Also, two different 17-7 PH stainless steel honeycombs are considered for the crushable layer. For the first one $\sigma_c = 300$ psi and $\sigma_0 = 2.85$ lb/ft², for the second $\sigma_c = 1150$ psi and $\sigma_0 = 7.74$ lb/ft². The layer was assumed to be $L = 18.5$ inches thick with an effective cross-sectional area of 200 ft². In both cases, the compacted density $\rho_c = 3.33 \rho_0$.

LOAD CASES $p(t)$

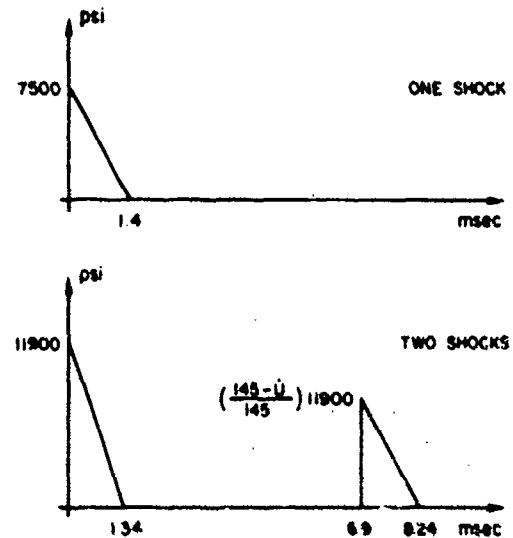


Fig. 3. Two cases of loading considered

The results of computations are presented in Figs. 4, 5 and 6^a. The displacement of the lower (driver) plate $u_1(t)$ is shown in Fig. 4. For load consisting of only one pulse (and $m_2 = 2m_1$), the entire layer does not crush, which means that its absorbing capacity is not fully utilized. For the case of two loads, one

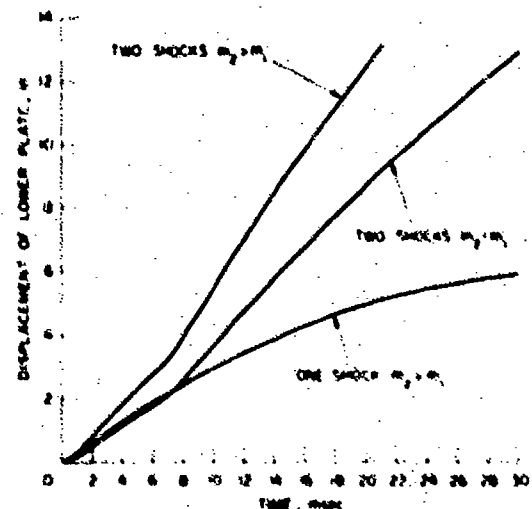


Fig. 4. Displacement of the lower (driver) plate vs. time

^a It is noteworthy that the results computed from the first approximation formulas (36,37) were not more than a few percent off. This is quite visible from diagrams in Figs. 4, 5, 6, i.e., $u_1(t)$ is almost linear and $q(t)$ almost sinusoidal.

notices the kink in $u(t)$ associated with the second pulse. It is important to note that the increase of the mass m_1 (driver plate) increases the duration of the crushing process which may be of vital significance in case of multiple shocks.

Pressure on the head plate (i.e., displacement u_2) is plotted vs. time in Figs. 5 and 6. As Fig. 6 shows, the distribution of masses affects only the period of the pressure pulse but not the maximum intensity (as pre-

dicted by approximate formulas from the linearized analysis). Moreover, the intensity of the slug pressure $p(t)$ has also almost no effect on the pressure of the head (upper) plate. In Fig. 6 open circles denote transitions from one phase to another while crossed solid dots denote the instant at which the entire layer is crushed.

The effect of the choice of p_c (or σ_c) on the pressure of the upper (head) plate is demonstrated by Fig. 5. Moreover, in the case

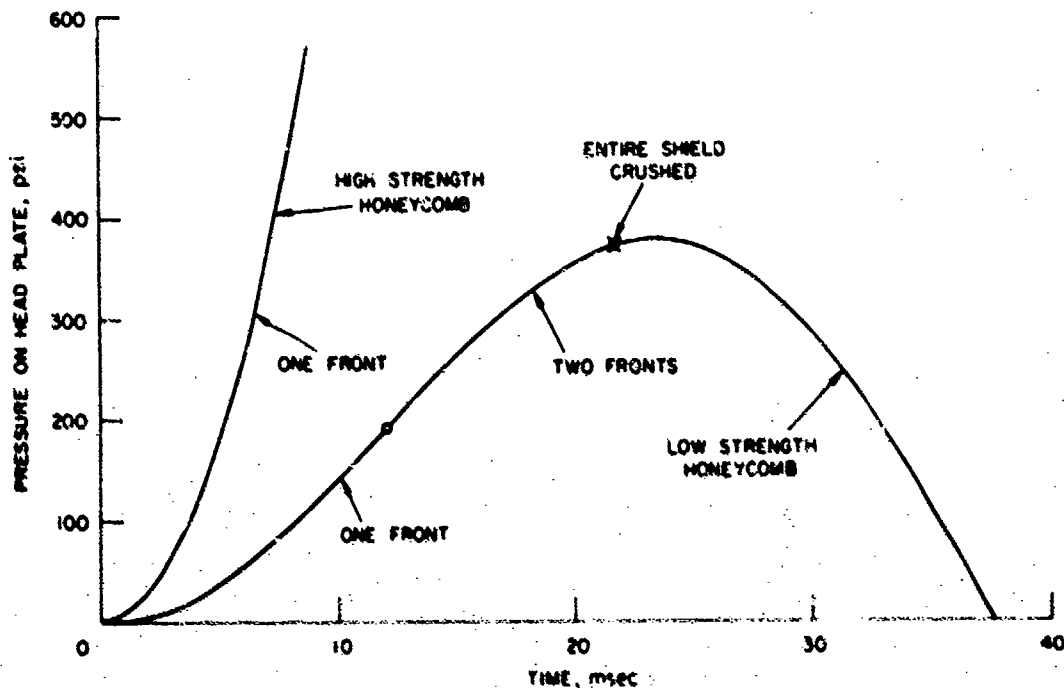


Fig. 5. Pressure on the head plate vs. time for various honeycomb strengths

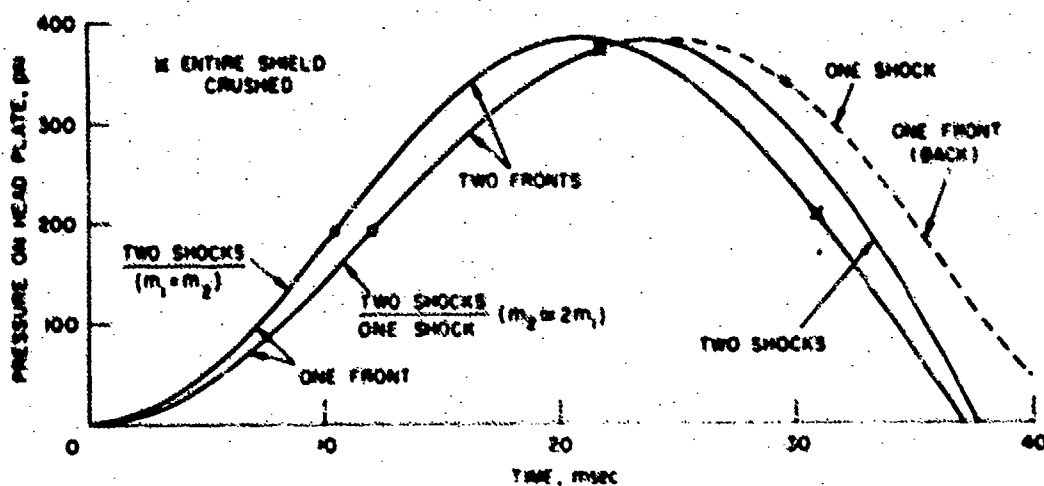


Fig. 6. Pressure on the head plate vs. time for various mass distributions and loadings

of the high strength honeycomb only a few inches were crushed so that the otherwise significant energy absorption potential was not utilized in the best way.

6. SUMMARY AND CONCLUSIONS

Presented is an approximate, one-dimensional model for the dynamic analysis of a sandwich head plate of a pressure vessel. The equations of motion, derived for the model, lend themselves well to computation and a series of interesting conclusions are arrived at.

- The pressure on the load-bearing upper head plate depends primarily on the crush strength of the crushable layer.
- The distribution of mass between lower and upper plate affects only the crushing period. Increase in mass of the lower (driver) plate, lengthens the crushing period which may be important if repeated pressure pulses are expected.
- Although the high strength crushable material possesses high specific energy absorption capability, it may be utilized only partially, since it will transmit loads of high intensity to the upper (head) plate without significant crushing.

In conclusion, the presented analysis appears to be simple enough to enable some kind of an optimal design in the early stages of analysis. The subsequent refinement of the analysis will undoubtedly introduce computational difficulties preventing random search at a more sophisticated level. However, such a refined model appears to be necessary to confirm and support results obtained from the presented model.

REFERENCES:

1. Martin, J. B., Symonds, P. S., "Mode Approximations for Impulsively-Loaded Rigid-Plastic Structures," *J. of the Eng. Mech. Div., ASCE*, Vol. 92, EM3, 1966, pp. 43-66.
2. Kalishky, S., "Approximate Solutions for Impulsively Loaded Elastic Structures and Continua," (in: *J. Non-Linear Mechanics*, Vol. 5, 1970, pp. 143-150).
3. Mott, G. I., "Theory and Practice of Cushion Design," *The Shock and Vibr. Inf. Center, U.S. Dept. of Def., Washington, D.C.*, 1968.
4. Weaver, R. W., Rivenes, A. S., "Expandable Metal Honeycomb for High-Temperature, Load-Bearing Structures," *ASME Publication* 67-DE-14.
5. Coppa, A. P., "New Ways to Soften Shock," *Machine Design*, Vol. 40, March 1968, pp. 130-140.
6. Maidanik, G., "Energy Dissipation Associated with Gas-Pumping in Structural Joints," *J. of the Acoustical Soc. of America*, Vol. 40, 1966, pp. 1064-1072.
7. Otis, D. B., "Thermal Damping in Gas-Filled Composite Materials During Impact Loading," *J. of Appl. Mech.*, Vol. 37, 1970, pp. 38-43.
8. Cristescu, N., "Dynamic Plasticity," North-Holland Publ. Co., Amsterdam, 1967.
9. von Mises, R., "Mathematical Theory of Compressible Fluid Flow," Academic Press, Inc., New York, 1958.
10. Salmon, M. A., Constantino, C. J., "Analysis of the Response of Containment Vessels," Task I in "Studies of Reactor Containment Structures" Summary Report by Well, N. A. et al., IITRI-578P22-9.
11. Mitropol'skii, Yu. A., "Problems of the Asymptotic Theory of Nonstationary Vibrations," Israel Program for Sci. Transl., Jerusalem, 1965.
12. Grundmann, H., "Eine Ergaenzung zur Methode von Krylow und Bogoljubow," *ZAMM*, Vol. 50, No. 8, 1970, pp. 501-502.
13. Cole, J. D., "Perturbation Methods in Applied Mathematics," Blaisdell Publ. Co., Waltham, 1968.

DISCUSSION

Mr. Witt (Bell Telephone Laboratories): How did you determine when the second front in your crushable material formed?

Mr. Krajcinovic: A pressure wave (sodium slug) generated by a hypothetical excursion propagates upward, hits our sandwich plate (first pulse), reflects downward, hits the bottom of the vessel, reflects upwards and hits again the sandwich plate (second pulse). Throughout the process some of the energy is dissipated radially so that every subsequent pulse grows weaker. The analysis performed was of a simple sodium-hammer type which was later on to a certain extent confirmed by a more sophisticated analysis (REXCO computer code). However, we are not sure whether the load is really well represented by either one of the two loads considered, due to circumstances beyond our control. Luckily, the determination of the load itself is not central to the analysis presented.

ON THE DAMPING OF TRANSVERSE MOTION OF
FREE-FREE BEAMS IN DENSE, STAGNANT FLUIDS

William K. Blake
Naval Ship Research and Development Center
Bethesda, Maryland

The damping of free-free beams vibrating in dense, still fluids has been studied experimentally. The decay of transverse vibration following an impulsive load on the beams was dominated by viscous damping at low frequencies and by radiation damping at high frequencies.

Viscous dissipation was examined in mixtures of glycerine and water using a series of beams with different geometries, thus the independent effects of varying fluid viscosity, ν , beam thickness, h , and frequency of vibration, ω , were established. Damping was determined by measuring 60 dB decay times at resonant frequencies following an impact. Loss factors, η , based on the dry beam mass were found to depend as $\eta = 4.4\rho_0\sqrt{\nu}/\rho h$ at low frequencies; ρ_0 and ρ are the densities of the fluid and beam respectively. The loss factors are independent of the length and width of the beams and of the sharpness of the beam edges.

In a parallel series of experiments, acoustic radiated power was measured in a water-filled reverberant chamber. Both the densities and the geometries of the beams were varied in order to establish the effects of dense fluid loading. Results are reported as ratios of radiated power to mean-square beam velocity and these ratios are compared with theoretical estimates. The radiation, modeled as a finite line of dipoles, is seen to be determined by the motion of the beam near the tips.

The results raise considerable question concerning the validity of measuring the damping characteristics of material samples in water. It appears that the shapes of material samples on which damping measurements are to be made must be designed to minimize spurious fluid-damping effects, otherwise the results may be more particular to the experiment configuration than to the material itself.

INTRODUCTION

Dissipative losses in vibrating structures immersed in a stagnant fluid can be internal, occurring in the material fibers and joints of the structure; viscous, caused by dissipation in the flow of surrounding fluid around the structure; and acoustic, caused by sound radiation away from the structure. In air-borne structures damping is often dominated by frictional losses at joints and supports. Coulomb and viscous friction at built-in supports can depend on the structure vibration mode and on the support geometry. Internal dissipation within the structure material can provide the second most important source of damping in air-borne structures. This type of damping, which has been given considerable empirical investigation (see e.g., Lazan [1]), can depend on the stress levels within the structure. Lazan has empirically related the

low frequency specific damping energy of materials to local applied stress level. Acoustic radiation is the third major energy-loss mechanism for air-borne structures; it is most important at high frequencies when the acoustic wavelength becomes less than or equal to a structural wavelength. A fairly extensive investigation of the damping of supported beams in different gases has been done by Kneser [2]. His investigation determined the relative importances of support, material, viscous, and radiation damping. Lyon and Maidanik [3], both analytically and experimentally, determined the air-borne acoustic radiation from a beam set in a rigid baffle.

In the case of water-borne structures, damping is caused by all of the losses discussed above, but the relative magnitudes of the constituent dissipations are, perhaps, somewhat altered. Viscous dissipation in the surrounding

¹References are on page 15.

fluid, which is apparently unimportant in air, could be an important damper in water. Internal mechanical dissipation is probably only slightly affected, but acoustic radiation could be increased by orders of magnitude when a vibrating structure is immersed in water.

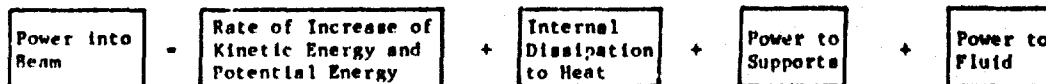
In this paper the energy balance of a vibrating beam immersed within a heavy fluid will first be examined. Although there is certainly nothing new in this energy balance presentation, it does serve as a useful review of some interesting fundamentals and it enables us to view the current experimental results in their proper perspectives. The results of an experimental examination of the vibration of un baffled free-free beams in different fluids are then discussed to define the dominant paths of dissipation of vibration energy. Measured total loss factors are compared to radiation loss factors measured recently and reported elsewhere [4]. The beam, fluid, and fluid basin are considered as a single system and the decay of the vibration level of an impulsively loaded beam is discussed as a measure of the energy dissipation in that system. The investigation is similar in extent to that of Kneser [2] which was done in different gases.

ENERGY BALANCE FOR AN ENCLOSED FLUID - BEAM SYSTEM

We consider the fluid-beam system constrained by an enclosure of arbitrary geometry and construction. If the immersing fluid is unbounded, the only fluid energy carried away from the immediate vicinity of the beam by a non-dissipative process, is acoustic. If the fluid is bounded by a containing structure, as it is in some of the experiments described in the following sections, some fluid energy is lost through tank walls. Figure 1 is a simplified power-flow diagram of the fluid-beam-tank system driven by an outside power source. (The structure has been specialized, but our arguments can apply to any immersed structure). In a typical experiment the applied force and resultant acceleration (magnitudes and phases) measured somewhere on the beam (frequently both at the drive-point) are the only rate variables measured for the entire system. The extent to which a single sub-system rate variable can be used to describe the instantaneous energy content within the total system will be shown.

Steady-state power balances are written below for the beam and for the fluid in terms of the rate variables that are shown in Figure 1.

ENERGY BALANCE FOR THE BEAM



The instantaneous power into the beam is $\dot{Q}_{in} = F_0 v_0^*$, where F_0 is the input force and v_0 is the velocity of the beam at the drive point. The asterisk denotes complex conjugate. The kinetic energy for a beam in transverse vibration, neglecting rotatory inertia, is (Rayleigh [5])

$$T_0 = \frac{1}{2} \int_0^L A \left(\frac{\partial \xi}{\partial t} \right)^2 dx \quad (1)$$

where ρ_p is the volume density of the beam material, A is the local cross-section area of the beam, ξ is the transverse beam displacement, and x is the coordinate measured along the beam axis. The bending potential energy of the beam is

$$U_0 = \frac{1}{2} \int_0^L x^2 EA \left(\frac{\partial^2 \xi}{\partial x^2} \right)^2 dx \quad (2)$$

where x is the radius of gyration of the beam section and E is Young's modulus for the beam material.

The mechanical dissipation in the beam is, for low stress levels and for our purposes, conveniently represented as

$$\dot{D}_m = \frac{1}{2} \int_0^L EA x^2 \left(\frac{\partial^2 \xi}{\partial x^2} \right)^2 dx \quad (3)$$

which neglects the shear strain contribution to dissipation. The dynamic modulus, which in general is complex, can be determined from the cyclic extensional deformation of material samples. Our discussions are primarily concerned with fluid damping mechanisms so it will suffice to make the fairly common assumption that $F_0 = \eta_m E$ where E is Young's modulus and η_m is the (so-called) mechanical loss factor.

The power into the supports carries energy away from the beam and is thus considered dissipative. It can be written

$$\dot{W}_s = F_s v_s^* \quad (4)$$

where v_s is the velocity of the beam at the support and F_s is the force exerted by the beam on the support.

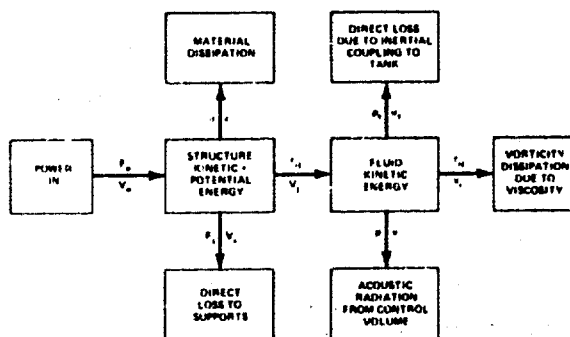
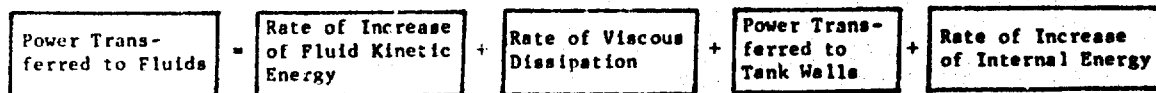


Figure 1 Power Flow Diagram for a Structure in a Dense, Viscous Fluid

ENERGY BALANCE FOR THE FLUID



The power transferral into the fluid, \dot{W}_f , is accomplished by the fluid stresses, τ_{ij} , on the surface of the beam which are out of phase with the beam surface velocity, v_j . Thus we have

$$\dot{W}_f = \text{Re} \left\{ \int (\tau_{ij} v_j^*) ds \right\} \quad (5)$$

where S is the surface area of the beam and τ_{ij} includes both viscous, τ'_{ij} , and normal, p , stresses, i.e.,

$$\tau_{ij} = \tau'_{ij} + p \delta_{ij}$$

The kinetic energy of the fluid is

$$T_f = \frac{1}{2} \iiint_V \rho u^2 dV \quad (6)$$

where ρ_0 is the fluid density and u is the local fluid velocity; integration is over the whole fluid volume. The viscous dissipation rate is (see, for example, Bird, Stewart, and Lightfoot [6])

$$\dot{D}_v = \iiint_V \tau'_{ij} \frac{\partial u_i}{\partial x_j} dV \quad (7)$$

where summation over both indices i, j is understood. The local viscous shear stress in the fluid is proportional to viscosity; it is

$$\tau'_{ij} = -\mu \left[\frac{\partial u_i}{\partial x_j} + \frac{\partial u_j}{\partial x_i} \right] + \frac{2}{3} \mu \nabla \cdot \mathbf{u} \delta_{ij}$$

Power transferred to tank walls gives a dissipation rate

$$\dot{D}_r = \iint_{\Sigma} p u_n dS \quad (8)$$

where p and u_n are the pressure and normal velocity of the fluid at the walls; integration is over the entire surface area of the tank. In a free-field experiment, one in which the fluid is virtually unbounded, Equation (8) represents the power transferred through a closed control volume of surface Σ . The rate of change of fluid internal energy is

$$\dot{E} = \iiint_V \rho \nabla \cdot \mathbf{u} dV$$

which is the reversible energy stored in dilatational waves associated with the acoustic field generation within compressible fluids. Now, the condensation, s , is defined by $\rho = \rho_0(1 + s)$ where ρ is the fluctuating fluid density and ρ_0 is the mean, undisturbed fluid density. The continuity equation for the fluid is

$$\frac{\partial \rho}{\partial t} = -\nabla \cdot (\rho \mathbf{u})$$

which, using the definition of condensation, and neglecting the fluid convection, $u \cdot \nabla p$, gives $\dot{s} \approx \nabla \cdot u$. Employing the acoustic approximation for adiabatic acoustic waves [8], we have

$$p \approx \left(\frac{\partial p}{\partial \rho} \right) (\rho - \rho_0) = \rho_0 s c$$

where the derivative is taken at constant entropy. We obtain the internal energy in terms of s

$$E \approx \frac{1}{2} \iiint_V \rho_0 c^2 (s)^2 dV. \quad (9)$$

ENERGY BALANCE FOR THE COMBINED FLUID - BEAM SYSTEM

Combination of Equations (1) through (9) gives

$$\begin{aligned} \dot{E}_V &= \frac{\partial}{\partial t} \left\{ \frac{1}{2} \iiint_V \rho_0 \left(\frac{\partial \xi}{\partial t} \right)^2 + \dots \right. \\ &+ \frac{1}{2} (1 + \gamma_m) \left[\int_0^L EA \left(\frac{\partial^2 \xi}{\partial x^2} \right)^2 dx + \frac{1}{2} \iiint_V \rho u^2 dV + \dots \right. \\ &+ \frac{1}{2} \iiint_V \rho_0 c^2 s^2 dV \left. \right] + \mu \iiint_V \xi dV + \dots \\ &+ \sum \int \rho u_i dS + \dot{W}_s \end{aligned} \quad (10)$$

which is the complete energy balance for the beam-fluid system. We have re-expressed Equation (7) in terms of the fluid dissipation function Φ , where Φ is [5]

$$\Phi = \frac{1}{2} \sum_j \left[\left(\frac{\partial u_j}{\partial x_j} \right)^2 + \left(\frac{\partial u_j}{\partial x_j} \right)^2 - \frac{2}{3} (\nabla \cdot u) \delta_{ij} \right]$$

The kinetic and potential energy terms in Equation (10) in general display apparent quadratic dependence on velocity or amplitude, v_0 . The total kinetic and potential energies in the beam are thus proportional to v_0^2 ; the material dissipation in the beam is also proportional to v_0^2 to the extent that $\gamma_m E$ is independent of strain. If fluid gradients are linearly dependent on v_0 we can expect the fluid velocity u_i to be similarly dependent. When this condition is fulfilled fluid kinetic energy is

proportional to v_0^2 . The cases of fluid dissipation and acoustic radiation will be considered separately. Losses to the supports and to the container walls can be legitimately argued as depending quadratically on beam velocity. Thus within the limitations of the assumptions described in the preceding sections we see that v_0^2 can be used as a descriptor of the total energy state of the beam-fluid system. We note that if temporal behavior of the decay of v_0^2 following an impact is not perfectly exponential, one or more of the dissipation rates described above must be somehow dependent on the transverse beam velocity and the relative magnitudes of the terms in the energy balance, as we have outlined them, cannot be preserved during vibration decay.

The total loss factor, η_T is defined (Crandall [8]) as the ratio of the energy lost per radian to the peak potential energy stored in the cycle, U' , i.e. at constant frequency ω

$$\eta_T = \frac{\dot{D}_T / \omega}{U'}$$

where \dot{D}_T is the total dissipation rate for the beam. Using the energy balance, Equation (10), anticipating that $\eta_T \ll 1$, and using the fact that at resonance the peak kinetic and potential energies that occur in a cycle are equal we can write

$$\begin{aligned} \eta_T &= \eta_m + \dots \\ &+ \frac{(\dot{W}_s / v_0^2) + (\dot{D}_v / v_0^2) + (\dot{D}_r / v_0^2)}{\omega (M_0 + m_0)} \end{aligned} \quad (11)$$

where m_0 and M_0 are the entrained fluid mass and beam mass per unit length respectively. This we can write as

$$\eta_T = \eta_m + \eta_s + \eta_v + \eta_r \quad (12)$$

using separate terms for the mechanical (m), support (s), viscous (v), and radiation (r) loss factors respectively. Note also that we have used $\dot{D}_m = \eta_m \dot{U}_B$ from Equation (3).

Crandall [8] has discussed the limitations of a mathematical model of damping which characterizes the dissipation as due to the action of a linear dashpot which produces a force in

opposition to the local beam velocity so the dissipation rate occurring in the dashpot is quadratically dependent on velocity. This requires the dissipation to occur principally as we have already idealized it, and furthermore it gives rise to a friction force which is directly proportional to and in opposite phase with the beam velocity. Thus we write

$$\dot{Q}_r = R_r \dot{\xi} \dot{\xi}^* \quad (13)$$

where $R_r = \eta \pi \omega (m_0 + M_B)$ is a frequency-dependent and velocity-independent, resistance to motion. Thus if we assume cyclic motion of the beam, integrate by parts, and use the free-free boundary condition on the beam, we obtain from Equation (10)

$$\begin{aligned} & x^2 E A \frac{\partial^2 \xi}{\partial x^2} + \rho A \omega^2 \xi = \\ & - m_0 \omega^2 \xi - i \omega \xi \dot{\xi} + \frac{E}{L} \int (x - x_0) \end{aligned} \quad (14)$$

which is the equation of motion for the point-driven beam. Here, the linear dashpot model has been used to apply a distributed dissipating force per unit length idealized as $r_T \dot{\xi}$ along the beam.

In the case of negligible dissipation relative to the peak beam potential energy in a cycle of beam vibration, the natural frequencies of the fluid-beam system are given from Equation (10) by

$$\omega_m^2 = \frac{\int E A x^2 \left(\frac{\partial^2 \xi_m}{\partial x^2} \right)^2 dx + \iiint_V \rho c^2 (\nabla \cdot \xi_m)^2 dV}{\int \rho A (\xi_m)^2 dx + \iiint_V \rho (\xi_m)^2 dV} \quad (15)$$

where ξ and δ are the instantaneous beam and local fluid displacements and ξ_0 is the beam displacement amplitude. There are as many natural frequencies as there are characteristic modes of vibration, $(\xi/\xi_0)_m$. The denominator of Equation (15) is the sum of the beam mass (for

uniform beams), $M_B L$, and the entrained fluid mass, $m_0 L$; the numerator is the sum of the potential energy of the beam plus the total internal energy of the fluid. We see that the low frequency effect of the fluid is to reduce the natural frequencies by a factor $[M_B/(M_B + m_0)]^{1/2}$. At higher frequencies the fluid internal energy increases because the fluid motion involves dilatation as well as local inertial entrainment. Just as at low frequencies the structure and fluid kinetic energies can be comparable resulting in a reduction of the resonant frequencies of the structure, at high frequencies the acoustic effects which are related to the energy stored in dilatation can further affect the beam motion. For free-free beams in vacuum, or at low frequencies in real fluids if $m_0 \ll M_B$, we have the natural frequency

$$\omega_n = \frac{\pi^2 c_0 x}{4 L^2} (2n+1)^2 \quad (16)$$

(See Kinsler and Frey [7]) where C_B/E and the integer, n , refers to mode order.

Assuming for convenience, that the beam motion is expandable as a Fourier series of characteristic functions, $\xi_m(x)$, the velocity at any point on the beam is found to be

$$v(x) = \sum_n \frac{E \xi_m(x) \dot{\xi}_m(x)}{(m_0 + M_B) \omega \{1 - (k_n/k_r)^2 + i \eta_n\}} \quad (17)$$

where

$$k_r = \frac{M_B + m_0}{x^2 E A} \quad (18)$$

and

$$k_n = \frac{(2n+1)\pi}{2L} \quad (19)$$

In practice the $\xi_m(x)$ for fluid-loaded beams are not the same as the invacuo mode shapes because the fluid couples the invacuo modes as well as reduces the natural frequencies. The problem as evidenced by the terms in Equation (10) is to couple the motion over a finite surface with the fluid potential in a fluid volume. Furthermore, to fully account for the spatial distribution of fluid motion and dilatation would require intricate coupling of fluid and structure, which would necessarily couple invacuo modes. To

account for the modal coupling would require (a) abandonment of the linear dashpot model, (b) considerable generalization of our simplification of the entrained mass and (c) maintenance of the internal energy term in Equation (15). Equation (17) gives the point impedance $Z_p/v(x_0)$ which is controlled by the loss factor at and near resonance. Near resonance, $\omega \approx \omega_m$, if $\eta_T \ll 1$ the summation, Equation (17), is dominated by the $n = m$ term and the vibration pattern is $v_m(x)$. The total loss factor for the mode at resonance is $\eta_T = R_T / \omega(m_0 + M_B)$.

ACOUSTIC RADIATION FROM VIBRATING BEAMS

Theoretical and experimental analyses of the acoustic radiation from vibrating beams have already been given. Lyon and Maidanik [3] have examined the radiation from baffled simply supported beams in air. Baffled beams are those for which there is no fluid motion across a plane parallel to and coincident with the neutral surface of the beam. In this configuration there is no fluid motion between the top and bottom surfaces of the beam. Unbaffled beams are those for which this motion is permitted. Blake [4] has provided a similar analysis of radiation from unbaffled free-free beams in water. In this section the beam radiation will be considered on physical grounds.

The baffled beam has been considered by Maidanik [9] as a strip radiator modeled with a finite line of monopoles. The configuration is shown schematically in Figure 2a for an even mode (mode $n = 6$). The strip is of width w and length L ; the volume velocity of a monopole element of length dx is

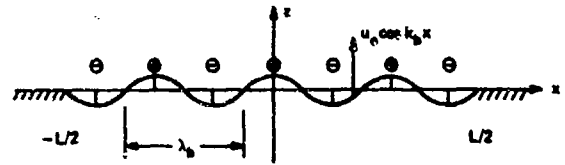
$$dQ = u_0 w \cos k_n x \, dx \quad (20)$$

where k_n is $(2n+1)\pi/L$ for $n \geq 0$. We will consider narrow beams for which $\lambda_0 \gg w$. Each composite monopole source radiates a pressure at a distance R and angle θ from the x axis,

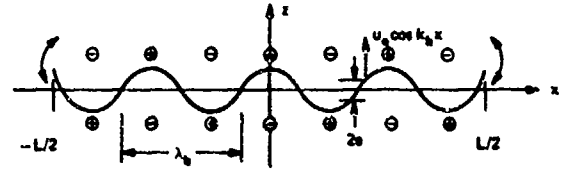
$$dp = \frac{i\omega_0 dQ}{4\pi R} e^{ikR}$$

The total radiated pressure from the array of these sources for distances $R \gg L$ is approximately

$$p(R, \theta) = \frac{i\omega_0}{4\pi R} w u_0 \frac{e^{ikR}}{R} \int_{-L/2}^{L/2} \cos k_n x e^{ikx \cos \theta} dx \quad (21)$$



(a) Baffled Beam, Simply Supported



(b) Unbaffled Beam, Free-Free Supported

Figure 2 - Schematics of Beam Mode Shapes

Maidanik has argued that for the case of the beam wavelength, λ_b , less than an acoustic wavelength, λ_0 and $\lambda_0 \ll L$, the radiation is equivalent to contributions from decoupled monopoles situated at the ends of the beam, $x = \pm L/2$. This is because adjacent regions of alternate phase along the beam interfere leaving remaining monopoles of length $\lambda_b/4$ at each end of the beam. In this circumstance the acoustic power radiated into the region $z > 0$ above the beams has been shown to be

$$P_M = \frac{\rho_0 c_0}{\pi} w^2 \left(\frac{k_0}{k_n}\right)^2 \frac{u_0^2}{4}$$

where the subscript, M , denotes monopole power.

For the unbaffled beam, shown schematically for the even ($n = 7$) mode in Figure 2b, the radiation can be modeled as that due to an array of dipoles. As before the beam is depicted as a strip radiator composed of $2L/\lambda_b$ half wavelengths of opposite phase. Each composite dipole, which in turn is composed of monopoles in opposite phase and separated a distance $2e$ apart, radiates a far-field acoustic pressure (see Junger and Feit [10])

$$dp(r, \theta) = \frac{i\omega_0}{2\pi r} dQ \sin(k_e \cos \theta) \frac{e^{ikr}}{r}$$

where θ is measured in the plane normal to the x axis. The elemental volume velocity is given by Equation (20) but in this case k_n is given by Equation (19). The adjacent dipoles of length $\lambda_b/4$ interfere as do monopoles in the

baffled beam leaving resultant dipoles situated near $z = \pm L/2$. The tip motions of the baffled and unbaffled beams, however, differ considerably. In the former case displacement is zero at $z = \pm L/2$ while in the latter the beam amplitude is maximum there. This motion would be expected to substantially reduce the net strength of the tip dipole. At low wave numbers, however, it can be argued that fluid motion around the tips (denoted by curved arrows in Figure 2b) reduces the influence of the tips. If this motion were not permitted, as for example by placing the beam in a strip baffle, the dipole strengths would be reduced. Thus, instead, the free-free unbaffled beam behaves as a simply supported strip segment of length $L - \lambda_b/4$ set in a long rigid strip. Since $\lambda_b/4$ is considerably less than unity we can express the resultant acoustic pressure far from the beam, $R \gg L$, as

$$p(R, \theta, \phi) = \frac{i\omega\rho}{2\pi} W U_b (\sin(k_b L \cos\theta)) x \dots \quad (22)$$

$$\dots \frac{e^{ikR}}{R} \int_{-L/2}^{L/2} \cos k_n x e^{ik_n x \cos\phi} dx.$$

The acoustic dipole power radiated to the upper half-space is

$$P_b = \int_0^\pi d\phi \int_{\pi/2}^\pi d\theta \frac{p^2(R, \theta, \phi)}{2\rho c_0} R^2 \sin\theta.$$

Comparison of Equations (21) and (22) show that the dominant distinction between the baffled and unbaffled strips is in the k_0 dependence. For small values of k_0 we can determine the ratio of unbaffled (dipole line) to baffled (monopole line) power as

$$\frac{P_b}{P_n} = \frac{(k_0 L)^2}{2}.$$

A more detailed analysis [4] gives the ratio of radiated powers as a function of beam width, specifically

$$\frac{P_b}{P_n} \sim \frac{(k_0 W)^2}{19.6}.$$

Thus the characteristic dipole length, e , appears to be approximately one-third the beam width. The ratio of radiated power to mean-square beam velocity is the radiation resistance, R_r . This is for the baffled beam

$$R_r = \frac{\rho c_0 A_b}{\pi} \left(\frac{k_0}{k_n}\right)^2 \left(\frac{W}{L}\right), \quad (23)$$

and for the unbaffled beam

$$R_r = \frac{\rho c_0 A_b}{\pi} \left(\frac{k_0}{k_n}\right)^2 \frac{(k_0 W)^2}{19.6} \left(\frac{W}{L}\right). \quad (24)$$

Equation (23) has been experimentally verified by Lyon and Maidanik [3] and Equation (24) by Blake [4]. The latter investigation was directed at determining fluid loading effects on the radiation from point-driven beams. Samples were driven at their centers; the space-time averaged mean-square beam velocity was measured at beam resonance frequencies. The radiated power was simultaneously obtained by measuring the acoustic pressure in the large reverberant tank within which the beams were driven. Measurements were made in air and in water. Figure 3 is an example of a measurement performed in air; Equation (24) is shown with Lyon and Maidanik's relation for the baffled beam. Equation (24) which applies for low k_0/k_n is shown in Figure 4 with a similar comparison for aluminum and steel beams in water. The measured radiation resistance in water is lower on the aluminum beam. The steel beam result agrees with Equation (24) down to mode 7; the R_r for mode 5 is lower than that given by Equation (24) because of the fluid loading. These results and those for a 3-inch width beam show that the measured radiation resistance is reduced by a factor $4\rho c_0/\rho_b h\omega$ from the theoretically determined radiation resistance. The measured ratio of radiated power to mean-square velocity is reduced from that given by Equation (24) because the fluid coupling altered the assumed source distribution, Equation (20). Since the low wave number radiation is determined by tip motion, the alteration in source distribution may have been most dominant there.

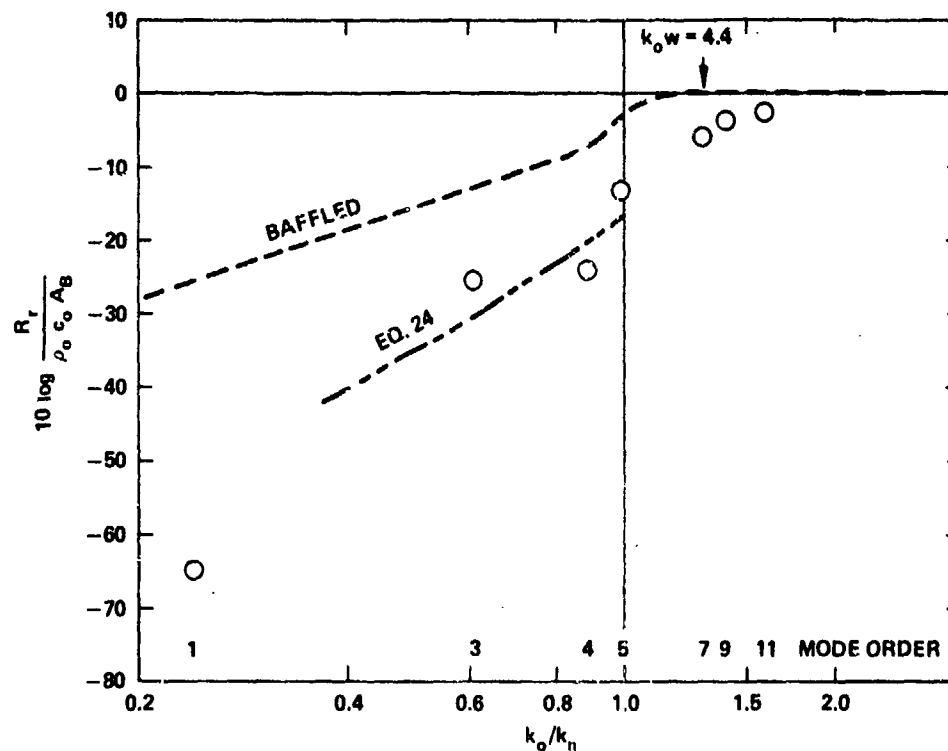


Figure 3 - Radiation Resistance of (1.5 in. x 0.125 in. x 9.6 in.) Aluminum Beam in Air

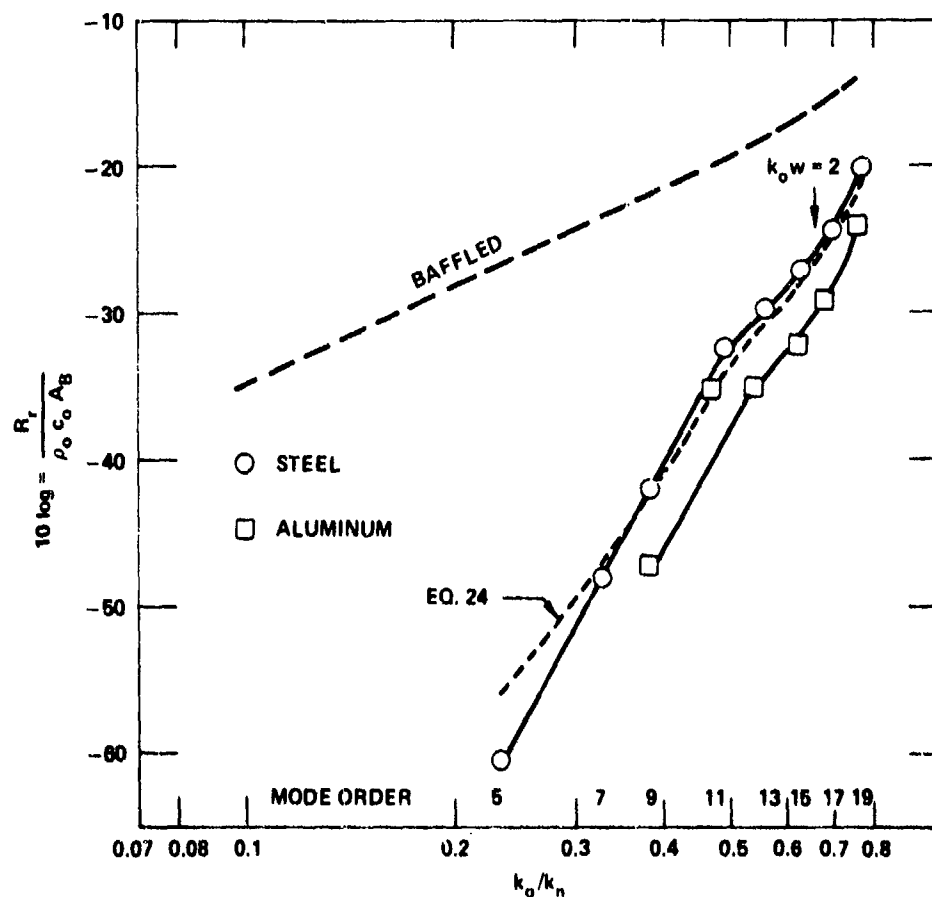


Figure 4 - Radiation Resistances of (1.0 in. x 0.375 in. x 17 in.) Beams in Water

VISCOUS DISSIPATION AND BEAM VIBRATION

The local dissipation rate per unit volume of fluid, $\mu \dot{\epsilon}$, can be expressed in terms of fluid gradients, i.e.,

$$\mu \dot{\epsilon} \sim \mu \frac{\partial u_i}{\partial x_j} \frac{\partial u_j}{\partial x_i}$$

If we assume that the length scale, l , is sufficient to define the fluid velocity gradient, then we can consider

$$\mu \dot{\epsilon} \sim \mu \frac{u^2}{l^2}$$

which dimensionally describes the dissipation function. The total dissipation rate \dot{D}_V in the fluid can be described as $\mu \frac{u^2}{l^2} V_D$ where V_D is a measure of the volume of fluid within which dissipation rates are high. We note here that l can be dependent on the velocity. The total fluid kinetic energy is

$$\frac{1}{2} \rho u^2 V_I$$

where V_I is a measure of the volume of fluid around the beam where u is perceptibly different from zero. Now if the ratio of local kinetic to local dissipated energy in the high dissipation region near the beam is small (A condition which cannot be extant everywhere in the fluid, especially far from the beam.) i.e., if the local Reynolds number,

$$\frac{\rho u l}{\mu} \ll 1,$$

then flow around the beam is viscosity-dominated and much of the work done on the fluid is dissipated by viscosity near the beam. Under these conditions the ratio of the rate of total fluid kinetic energy loss to the total dissipation rate can be assumed as

$$\frac{\frac{1}{2} \rho u^2 V_I}{\mu \frac{u^2}{l^2} V_D} \sim \text{constant, independent of } u$$

where T is the period of vibration $\frac{2\pi}{\omega}$. Thus we can write

$$\frac{1}{2} \frac{\omega}{l^2} = \text{constant, independent of } u$$

and the characteristic dissipation length, l , appears to depend largely on $\omega^{-\frac{1}{2}}$ and $\nu^{\frac{1}{2}}$. If the beam dissipation is dominated by viscous losses in the fluid then the instantaneous energy balance, Equation (11), leads to the simple result that the peak kinetic energy in a cycle behaves as

$$\frac{\partial}{\partial t} [(m_o + M_o) L \dot{x}^2] =$$

$$- K \mu \frac{V_o^2}{l^2} \cdot 2 \omega L l$$

where K is a constant. We have written $V_D = 2\omega L l$ for the volume of high fluid dissipation. If V_o decays as $e^{-\eta t}$ then we have

$$\eta = \frac{K \rho \omega}{m_o + M_o} \sqrt{\frac{2\nu}{\omega}}$$

where η is the loss factor of the beam. If η is based on the dry mass of the beam, $M_o = \rho_o h w$, we have

$$\eta_{\text{DRY}} = \frac{M_o + m_o}{M_o} \eta$$

so that

$$\eta_{\text{DRY}} = K' \frac{\rho_o}{\rho_o h} \sqrt{\frac{2\nu}{\omega}} \quad (25)$$

which we will hereafter call η'_V for the viscous loss factor. Loss factors based on the dry beam mass will be denoted by a prime superscript. The validity of this expression was

examined by a parametric study of vibrating beam decay rates that will be described in the next section. Use of this definition of loss factor facilitates comparison of results without the complication of considering added mass. Direct comparisons of beam resistance are thus possible using this definition.

DESCRIPTION OF THE MEASUREMENTS AND APPARATUS

Measurements of natural frequencies and total loss factors were made on various beams in fluids. The small size and light weight of the beams made accurate measurements of damping difficult. Losses at the supports and dissipation at the contact point of the beam with the impedance head were difficult to minimize and, after considerable experiment, the assembly described below was used. The beam was suspended from 25 pound brass weights using piano wire (0.01 inch diameter and 1 to 2 feet long) loosely looped through a small hole at the edge of the beam at the center of the beam span. The brass weights were suspended from the ceiling using bungee cord. The beam was mounted in this manner to minimize vibration loss through its support; when the weights were removed, so that the piano wire was connected directly to the bungee cord, the beam damping increased perceptibly.

Natural frequencies of the beam above 100 Hz were determined by point impedance measurements. The impedance head was mounted to the center of the beam using a set screw or "Eastman 910" adhesive. The force and acceleration signals were both filtered and the shaker input was servo-regulated to maintain a frequency-independent force. Natural frequencies below 100 Hz were determined by tuning a 3 Hz filter to give maximum output with an input acceleration signal which was generated by tapping on the beam. For this measurement a small accelerometer was mounted on the tip of the beam and the shaker-impedance head assembly was removed. Some natural frequencies above 100 Hz were also obtained from impact response as well as from the point impedance measurement. The fundamental frequencies measured in air were generally within a few Hz of those calculated using Equation (16).

Quality factor measurements at resonant frequencies as determined from the bandwidths of the resonant peaks gave higher damping than the impulse measurements probably because of losses sustained at the impedance head mounting point. Measurements of decay times following impulse excitation of the beam instrumented with a single accelerometer were the most successful. This measurement was performed by monitoring the decay of 1/3 to 1/10-octave filtered tip acceleration signals on a Bruel and Kjaer graphic level recorder or on the Spencer-Kennedy Laboratory (SKL) decay rate meter. In either case, 60 dB reverberation times were used to obtain loss factors. The use of filters to obtain the decay rates of

separate beam modes in this manner is possible when the bandwidth of the filter is larger than that of the beam resonance. Measurements were generally repeatable to within 30%. The vibration levels were found to decay exponentially in air and in water.

Beam specimens were selected to vary width, thickness, length, edge condition (sharp, round, etc.), beam material density, and material damping. Beams of steel and of aluminum had widths that ranged from 1 inch to 3 inches, thickness from 3/16 inch to 1/2 inch, and lengths from 17 inches to 36 inches. A beam with high material damping was constructed with two 3 inch by 17 inches by 1/8 inch thick steel plates sandwiched around a sheet of self adhering, cold-pipe insulation tape sold under the trade name "Prestite." This is a cork-tar composition that readily adhered to the metal plates which were held together with flat-head screws tightened until the overall thickness of the composite beam was 5/16 inch. The beam had a dry mass of 0.12 slug.

Fluids, in addition to air, were glycerine-water mixtures which provided kinematic viscosities ranging nominally from 1 to 400 centistokes. Glycerine was selected because of its complete miscibility with water, its high viscosity, and the comparability of its ρ_0 and c_0 with those of water.

The accelerometer used in the impulse measurement was waterproofed with "Digel" wax. The impedance head-shaker assembly was waterproofed with "PRC" compound.

EXPERIMENTAL RESULTS

ENTRAINED MASS

The entrained mass was determined from the ratio of resonance frequencies of a mode determined in air and water. The relationship,

$$\frac{M_0}{M_0 + m_e} = \left(\frac{\omega_2}{\omega_1} \right)^2$$

where subscripts 1 and 2 refer to the natural frequencies of a given mode in air and in water, was used. The added mass per unit length of a long elliptical cylinder in steady motion has been given by Lamb [11] as

$$m_e' = \frac{\pi}{4} \rho w^2$$

where w is the width of the strip measured normal to the flow direction. If we adopt this as the $w \rightarrow 0$ limit for the beam Blake [4] has found

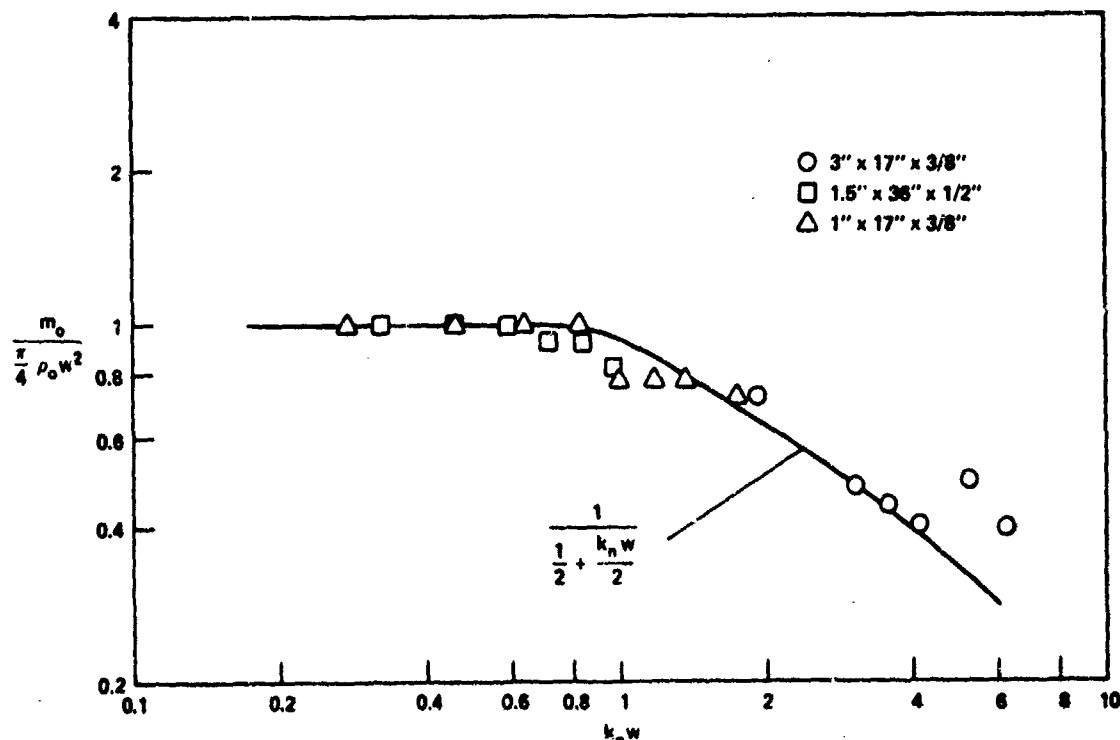


Figure 5 Entrained Mass of Vibrating Beams in Water

$$\frac{m_0}{\frac{\pi}{4} \rho_w w^2} = \frac{2}{1 + k_n w} \quad , \text{ for } k_n w > 1$$

which is shown with experimental results in Figure 5 for three of the beams. The static beam mass has been safely assumed equal to the modal mass since the beams are of uniform cross section. For high $k_n w$ the added mass per unit length is $\frac{\pi}{2} \rho_w w / k_n$ which is just $\pi/2$ larger than the result obtained by Davies [12] for a finite plate in a baffle.

DAMPING OF VIBRATING BEAMS IN AIR

Loss factors measured in air are shown for the steel beams in Figure 6, width and thickness are varied independently. The highest loss factors were measured on the lightest beam (1.5" X 3/16" X 36") and the lowest on the heaviest beam (1.5" X 1/2" X 36"). The figure includes the 3-inch beam radiation loss factor derived from Reference 4. The loss factors in air are not dominated by acoustic radiation for $f < 10$ kHz so that the measurements give, for consideration in Equation (12), only the structural and support losses. Kimball's [13]

review of the literature quotes some results that give η_m for steel between 10^{-4} and 10^{-3} which are comparable to the measurements in Figure 6. Losses at the supports and dissipation associated with motion of the accelerometer cable are both apt to contribute to damping in air. Support losses are possibly due to Coulomb friction at the juncture of the piano wire with the beam as well as to traveling waves sent up the support wires and induced in the instrument cables which are unlikely to depend strongly on beam mass. Important contribution from these external causes would explain why the thick and thin 1.5" width steel beams have loss factors in the approximate ratio 2.6 which is also the ratio of the beam masses. This leads

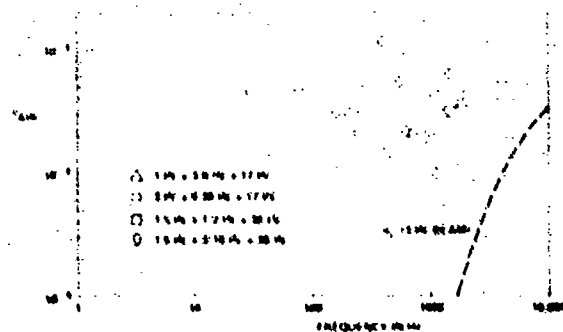


Figure 6 Loss Factors for Beams in Air

to the consideration that the R_{air} does not depend on which specimen is used to determine it, thus the above results provide strong evidence that the air-borne dissipation is not dominated by internal losses.

DAMPING OF BEAM VIBRATION IN GLYCERINE - WATER MIXTURES

The loss factors based on the dry beam mass, for various beams in water are shown by the open points in Figure 7. Measurements for the 3" X 0.36" X 17" steel beam were made in the Naval Ship Research and Development Center (NSRDC) test pond, a large, effectively unbounded, volume of water. The values of loss factors for this beam fall between rather narrow limits. Near 10 kHz the total loss factor is dominated by acoustic radiation; the result for the radiation loss factor, η_r , has been taken from Blake [4]. In the frequency range of 1 to 10 kHz the loss factor is nearly constant at 0.0025. Two 3-inch beams, one with rounded edges the other with knife edges had the same loss factors in water, thus in-water damping did not substantially depend on the beam edge condition. Loss factors for a (1" X 0.36" X 17") beam were the same as those for the 3" beam, thus showing independence of

beam width. Loss factors for the (1.5" X 0.188" X 36") beam are included; the results show clearly an increase in loss factor with a decrease in thickness. The 0.188" thick beam shows a $f^{-1/2}$ (Note the line 4 in Figure 7) dependence which covers a larger frequency range than shown by the other beams. Furthermore, the loss factors do not appear to depend on beam length. The slightly higher η_r for the 3" X 0.36" X 17" beam than for the (1.5" X .5" X 36") beam can be accounted for by the thickness difference. Finally, mode order does not appear to be a dominant effect, i.e., there appear to be no separate dependencies for even or odd-numbered modes.

The dependence of the loss factor on viscosity was determined by measuring the damping of the (3" X 0.36" X 17") beam in an aquarium using glycerine-water mixtures. U.S.P. -grade glycerine, $\nu = 390$ centistokes, and 85% by weight glycerine-water mixture $\nu = 44$ centistokes, were used in a 20 gallon aquarium. The viscosities were measured using the rates of laminar flow discharge through long tubes [6]. A measurement in water, $\nu = 1$ centistokes, showed that for frequencies less than 100 Hz the loss factors measured in the aquarium were comparable to those measured

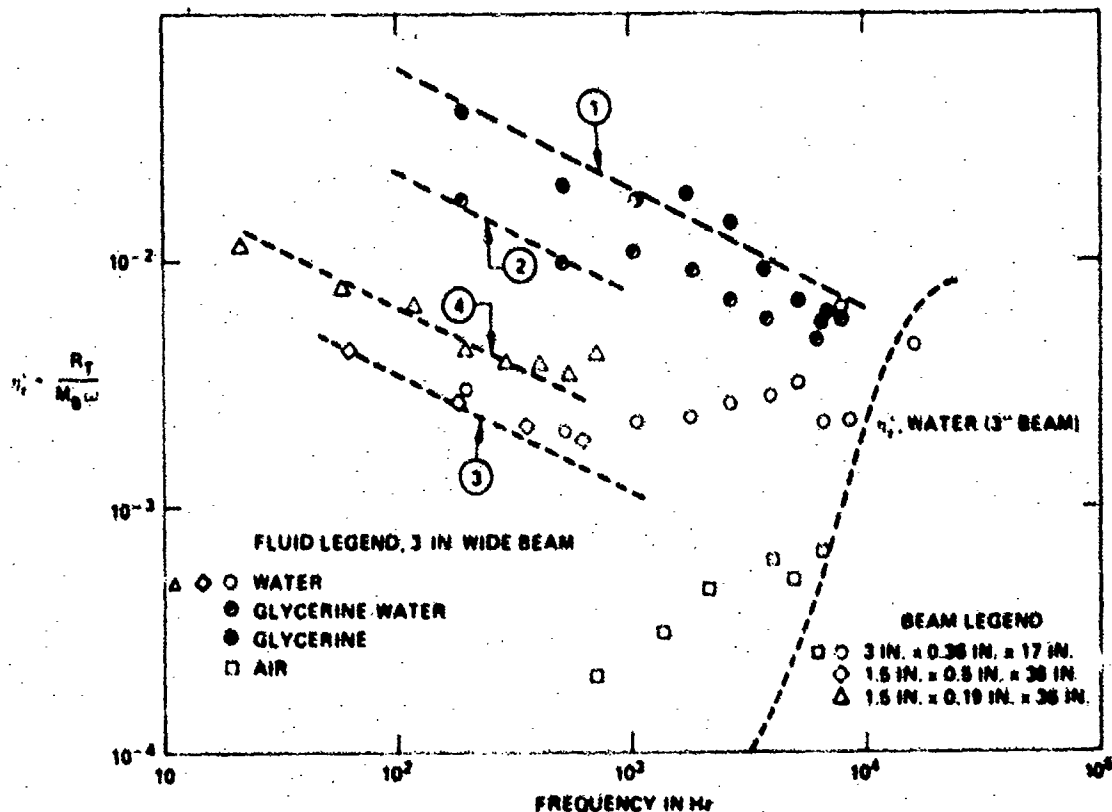


Figure 7 Loss Factors for Beams in Fluids of Varying Viscosity

in a free field. Above 100 Hz the loss factors were only slightly higher than those in the free field, and the higher loss factors indicated some energy loss to the tank through inertial coupling of the beam with the tank walls.

The results of measurements in glycerine solutions show clearly an increase in loss factor with viscosity. Furthermore, the frequency range of near-dependency on $f^{-1/2}$ for the 3"-wide beam was extended to nearly 10 kHz and line 1 in Figure 7 is considered to be representative of that dependence in glycerine. Lines 2, and 3, are calculated from line 1, assuming that $\eta \sim \nu^2$, they are in approximate (30% to 40%) agreement with the measurements. In calculating line 4 we go one step further by assuming $\eta \propto \nu h^{-1}$ and scale line 1 for the condition of the beam (1.5" X 0.19" X 36") in water. It is well to point out that since the densities and speeds of sound are similar for glycerine and water the radiation loss factor shown in Figure 7 is assumed to apply to all liquids.

We can summarize the results of the previous paragraphs: the loss factors in viscous liquids at low frequencies are nearly inversely proportional to the thickness of the beam, to the square root of frequency, and to the beam density; they appear to be directly proportional to the square root of kinematic viscosity. Thus at low frequencies, at least, we can write

$$\eta'_v = k \frac{\rho}{\rho} \frac{\sqrt{\nu \omega}}{h}$$

which is the result Equation (25). The results give $k \approx 5$. Finally, at low frequencies the condition of the beam edges does not appear to be an important variable in determining the overall loss factor. It is possible that local viscous stresses near the beam edges especially at the tips could have contributed to the phenomenon of fluid loading shown in Figure 4. Although these viscous stresses did not appear to dominate the total damping they could have altered the vibration patterns near the tips.

The water loss factors in the frequency range 1 kHz to 10 kHz could be, in part, caused by support and cable motion induced by the beam. If the air measurements are interpreted to give

$$\eta'_a = \eta'_m + \eta'_2$$

and the water measurements to give (see Equation (12))

$$\eta'_w = \eta'_m + \eta'_2 + \eta'_v$$

then

$$\eta'_w - \eta'_a \approx \eta'_v$$

if η'_v is unaffected by the water. Reduction of the loss factors in Figure 7 by an amount equal to η'_{sa} reduces the observed water loss factors from 0.0025 to 0.002. If both η'_{rv} and η'_{sa} are deleted from the loss factors near 7 kHz, we obtain $\eta'_v \approx 0.001$. However, there is little assurance that the support losses are the same in all media. It is more likely that support losses are somewhat increased by the viscosity of the fluid, since those losses would have to do with transverse motions.

DAMPING IN THE COMPOSITE BEAM IN AIR AND WATER

Our discussions of beam damping are completed by considering the measured loss factors of the composite beam in air and in water. The results serve to illustrate that the contribution of fluid damping to the total loss factor can be considerable even though the test sample is mechanically damped. Figure 8 shows the results for the 3rd through 11th modes as measured by the quality factors of the resonance bandwidths [7]. The air measurement shows a maximum loss factor of 0.0074 at 2.3 kHz, the loss factor decreases at higher and lower frequencies. The loss factors of 3-layer composite structures have been theoretically derived by Ross, et.al. [14]. Their relations for the maximum loss factor of the composite and for the frequency of that maximum loss factor can be used to obtain the effective shear loss factor and Young's modulus of the Prestite. The computations give the shear loss factor 0.1 and an effective Young's modulus 2.7×10^9 psi for the layer. These estimates in no way account for the constraining effect of the screws that hold the plates together, this effect would possibly be to increase the effective modulus. The calculated loss factor and storage modulus are also consistent with the approximate frequency dependence sketched in Figure 8.

The loss factors in water are about 0.0019 or about 25% higher than those measured in air. This difference is apparently due to the water damping discussed in the last subsection

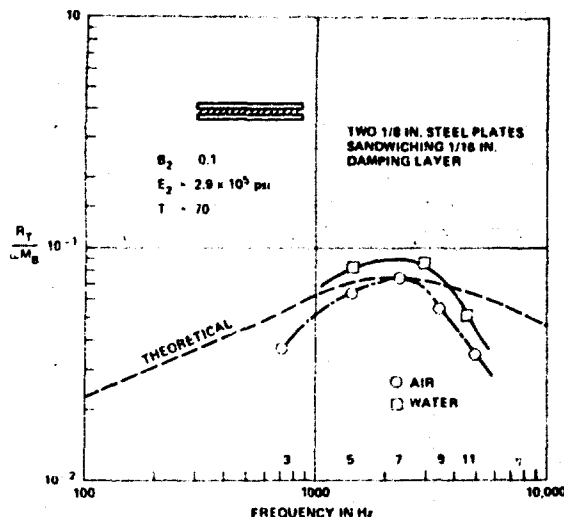


Figure 8 Loss Factors for the Composite Beam in Air and in Water (70F)

assuming that the material damping was the same in both measurements.

DISCUSSION

We have examined the dissipation of free-free beams in various fluids in order to distinguish the relative importance of internal, radiation, and viscous damping. For the simple geometry investigated, low frequency dissipation was apparently dominated by support losses in air, and by viscous dissipation in heavy fluids. High frequency damping on the other hand, was controlled by acoustic radiation. The results are applicable for unbaffled structures whose dimensions are small relative to an acoustic wavelength. In this case acoustic radiation accounts for very little damping so that the other, perhaps, less obvious losses are dominant.

Although the mechanism of the viscous dissipation cannot yet be clearly defined, we can propose arguments that at least postulate its connection with low Reynolds number flow around the beam. Low Reynolds number viscous oscillatory drag due to flow around bodies depends on the first power of the instantaneous speed, U , of the body. Lamb [11] gives, for example, the drag force on a sphere oscillating in transverse motion with frequency as

$$F_s = -6\pi\mu a U [1 + \sqrt{\frac{2}{3}} \frac{a}{\lambda}]$$

where μ is fluid viscosity and a is the sphere radius. The quantity $6\pi\mu a U$ is the steady motion drag of a sphere. Batchelor [15] gives a similar result. We assume, heuristically, that the oscillatory Stokes drag can be approximated by an equation similar to the above as

$$F = F_0 [1 + \frac{d_1}{\sqrt{2} \lambda}]$$

where F_0 is the steady flow drag and d_1 is some major proportion of the half-width of the body measured normal to the direction of motion. For a long elliptic cylinder Lamb quotes the steady drag per unit length as

$$\frac{dF_s}{dL} = 2\pi c \mu U$$

where c is a Reynolds number-dependent factor which, for our arguments, we can take as unity. Thus we can write the resistance per unit length see Equations (13) and (14), as

$$T_1 = 2\pi \rho \omega [1 + \alpha \frac{w}{2} \sqrt{\frac{\omega}{2\nu}}] \quad (26)$$

for a vibrating strip. Batchelor's [15] result for a circular cylinder is analogous. We have written $d_1 \propto \frac{w}{2}$. If the frequency-dependent term in a bracket far-exceeds unity we have

$$\eta_v' = \frac{\pi \alpha \rho}{12} \frac{1}{h} \sqrt{\frac{\omega}{2\nu}}$$

which is identical to Equation (25). Experimental results give the low frequency value of α as 2.2 suggesting that $d_1 = w$ would have been a better selection than $w/2$.

At frequencies above 1 kHz, dissipation associated with fluid motion parallel to the surface of the beam could account for additional fluid damping. This dissipation would exist because the fluid motion at the surface and in the plane of the surface must vanish because of the "non-slip" condition on the beam. Thus at structural node lines the motion near the wall must increase rapidly from zero; the resultant gradients could account for substantial dissipation. Of course, this is in the realm of some speculation because support losses in the current experiments have not been discounted from importance.

We point out again that the experimentally-determined curves of log-amplitude vs time during

a vibration decay was linear thus the energy balance was not noticeably vibration-amplitude dependent. Unfortunately, the impact measurements could not be controlled to yield specified vibration amplitudes, but the peak vibration levels were low enough that in water the Reynolds number, $\frac{u'w}{\nu}$, where u' is the peak transverse beam velocity amplitude, was always less than 10. This places the near-field flow around the beam in the viscous flow region where Equation (26) is most apt to be valid.

The results show also that fluid damping can contribute materially to the total loss factor measured for a structure immersed in the fluid and could conceivably dominate small to modest differences in measured loss factors. Since fluid effects, both acoustic and viscous, are geometry-dependent and since material specimens for testing are geometrically dissimilar to their eventual application, the need for in-water damping measurements is questioned. It would be more advantageous to make careful in-air measurements to at least establish the material loss and thereafter estimate analytically the fluid losses involved with the specific application in a structure. In general fluid-loading will be a nearly indeterminate variant, but for low values of $\rho_0 c_0 / \rho_b h$ those effects may be safely neglected. When fluid-loading effects are important, erroneous neglect of those effects will lead to an overestimate of the fluid radiation damping.

ACKNOWLEDGEMENTS

The assistance of Mr. J. Hicks in performing the measurements and discussions on experimental technique with Mr. G. Remmers is acknowledged. Support for this investigation was provided by Naval Ship Systems Command.

REFERENCES

1. Iazan, B.J., "Energy Dissipation Mechanisms in Structures with Particular Reference to Material Damping," paper in "Structural Damping," ASME Colloquium on Structural Damping, J.E. Ruzicka, Ed. (1959)
2. Kneser, J.O., "Über die Dämpfung Schwingender Zylindrischer Stäbe durch das umgebende Medium," Zeitschrift für angewandte Physik, Vol. 3, page 113 (1951)
3. Lyon, R.H. and Maidanik, G., "Power Flow Between Linearly Coupled Oscillators," J. Acoust. Soc. Am., Vol. 34, page 623, (1962)
4. Blake, W.K., "Radiation from Free-Free Beams Under Influences of Light and of Heavy Fluid Loading," NSRDC Report 3716 in preparation, (1971)
5. Rayleigh, J.W.S., "The Theory of Sound," Dover Publication, New York, (1945)
6. Bird, R.B., Stewart, W.E., and Lightfoot, E.N., "Transport Phenomena," John Wiley and Sons, New York, (1960)
7. Kinsler, L.E., and Frey, A.R., "Fundamentals of Acoustics," John Wiley and Sons, New York, (1962)
8. Crandall, S.H., "The Role of Damping in Vibration Theory," J. of Sound Vibration, Vol. 11, page 3, (1970)
9. Maidanik, G., "Response of Ribbed Panels to Reverberant Acoustic Fields," J. of Acoust. Soc. Am., Vol. 34, page 809, (1962)
10. Junger, M.C. and Feit, D., "Sound, Structures and Their Interaction," MIT Press (to be published)
11. Lamb, H., "Hydrodynamics," Dover Publications, New York, (1945)
12. Davies, H.G., "Acoustic Radiation from Fluid Loaded Rectangular Plates," MIT Acoustics and Vibration Laboratory, Rep. 71476-1 (Dec 1969)
13. Kimball, A.L., "Vibration Problems," J. Appl. Mechanics, Vol. 8, page 135, (1941)
14. Ross, D., Ungar, E.E., Kerwin, E.M., Jr., "Damping of Plate Flexural Vibrations by Means of Viscoelastic Laminates," paper in "Structural Damping," ASME Colloquium on Structural Damping, J. E. Ruzicka, Ed., (1959)
15. Batchelor, G.K., "An Introduction to Fluid Dynamics," Cambridge University Press, (1967)

DISCUSSION

Mr. Briggs (General Electric Co.): If you used your viscous damping approximation, and at higher frequencies if you assume turbulent flow around the beam and use turbulent fluid flow damping, how does that compare with the dissipation factors that you obtained from the acoustical observations, or did you do that?

Mr. Blake: The peak Reynolds number, which was determined after the first impact, was less than 10 and this was based on the width of the beam. The flow was not turbulent, and it is pertinent that these are edge effects. Beams with rounded edges and beams with knife edges gave the same loss factors. So it has to do with pressure difference associated with the entrained inertia between the upper and lower surfaces of the beam and the flow around it.

Mr. Baker (Southwest Research Institute): In the past we have done quite a few damping experiments on thin beams vibrating transversely in air. The same effect that you call a viscous effect for the beams vibrating in water is also present. It could be that the air damping will predominate for low frequencies for slender cantilevers or free-free beams, vibrating in air. I would suggest that you not only determine the material damping out of water but out of air also. Secondly the Reynolds number by itself is not important. This non-zero viscosity and the actual physical mechanism, although it is only affected slightly by the shape of the beam, is one of vortex shedding and it correlates well with some old work that Killigan and Carpenter have done at NBS on moving waves past little barriers.

Mr. Blake: Actually there has been a study of the air damping by Kanesser in Germany maybe 15 years ago. He stuck a beam in a bell jar and evacuated it and then put carbon dioxide in and he performed the same kind of experiment.

Mr. Mains (Washington University): The relationship you used where you had an M of one kind plus an M of another kind divided by one of the first M 's looks very much like the virtual mass way of doing things as in ship design work. Is this correct?

Mr. Blake: Yes. It was the sum of the beam mass and added mass divided by the beam mass.

Mr. Mains: I always get a little bit fried at this added mass business. It is so easy to do it as a velocity dependent force. Why do you not do it that way instead of fiddling around with added mass?

Mr. Blake: Do it as an added velocity dependent force?

Mr. Mains: Yes. The force with which you are dealing, that is causing this change in behavior is one that is dependent on velocity. Why do you not put it in the velocity term instead of in the acceleration term?

Mr. Blake: The reason for accounting for the added mass that way was because it depends differently on the width of the beam than the total resistance. I wanted to make a clear cut comparison of resistances by the different mechanisms so I thought it better to base everything on the dry beam mass.

Mr. Mains: A paper about 1963 by F.T. Mavis, and a man named Crum, in either the ASCE Structural or Engineering Mechanics Journal compared the loss of frequency in air and in water for beams, and I think some other shapes too, with quite interesting losses in frequency resulting from submergence in water. You might find it worth looking up.

OPTIMUM DAMPING DISTRIBUTION FOR STRUCTURAL VIBRATION

R. Plunkett
University of Minnesota
Minneapolis, Minnesota

Structural damping using constrained viscoelastic layers, inserts, or material treatment is increasingly being used to control the resonant vibration response of structural systems. Any of these techniques impose a weight and cost penalty. In this study we investigate the optimum distribution and amount of damping treatment for controlling the vibration response of a uniform beam in bending with various end restraints. For reasonable parameters it is found that optimal distribution is highly peaked at the center, but that a uniform distribution of the same weight of damping treatment will increase the response by only a few percent. It is also found that optimum damping for theoretical minimum response is practically unobtainable so that almost any increase in the amount of damping treatment will reduce the vibration level. The question then changes from one of structural optimization regardless of cost to one of cost-effectiveness.

INTRODUCTION

Modern lightweight, high strength, high speed structures are very susceptible to damage by vibration. Deliberately introduced damping treatment is being used more and more to control resonant vibration to reduce noise, improve comfort, or control fatigue failure. Now that it has been established that such treatment is useful for some problems, it becomes a proper engineering task to ask about the cost and weight tradeoffs. The techniques for finding the response of beams in bending for various configurations and end conditions have been reduced to practice and are widely cited in the technical literature, e.g. [1,2]. Studies have been made to find optimal configurations for the cross sections of damped beams of uniform cross section [3]. The techniques for finding the vibration response of complex structures with many degrees of freedom and complex mode shapes are readily available in current texts, e.g. [4].

In previous studies it has been shown that there are optimal locations and strengths for concentrated dampers in distributed systems [5,6]. If the strength of a concentrated damper is either greater than or less than optimal, the vibration

response is increased. Fortunately, for most configurations the response level is not very sensitive to reasonable deviations from optimality; for example a damper of either twice or half optimal strength will increase the response by about 25% [5]. It is pertinent to ask if there is an optimal distribution of distributed linear damping and, if so, what is the sensitivity to deviations from an optimal distribution.

It is certainly possible to investigate this question for specific configurations and the methods of this report can be used for such a purpose. It might be of somewhat wider interest to attempt a more general problem. In this report we have sought the optimal distribution of bending damping, such as that from constrained viscoelastic layers, for a uniform beam. The effect of the impedance of the end supports has been investigated but no attempt was made to determine the effect of different kinds and locations of vibratory loads. Previous work indicates that, except for pathological cases, the optimum answer does not depend markedly on such parameters. The answer one gets for optimum damping does depend

on the criterion used; in one case the value changed by a factor of 4 to 1 depending on which of three reasonable criteria were chosen [7], however, if the middle value were chosen, the response at the extremes was only increased by 25% as expected.

METHOD

The method used in this study was to choose a particular beam and support combination, and then conduct a search in function space for that distribution and amount of bending damping which would minimize the maximum response over the whole frequency range. The search was made with a digital computer using a technique previously developed [5] which consists of changing the minimax problem to one of unconstrained minimization. This is done by finding the maximum response as a function of frequency for each trial configuration and minimizing this auxiliary function with respect to the other parameters of the problem. A number of search techniques can be employed, the particular one used was a second order gradient controlled iteration.

The problem was also changed from a search in Hilbert space for the configuration of a continuous system to one in Euclidean space with a finite number of dimensions by expanding the continuous functions in a set of appropriate functions, using the coefficients of the expansion as the controlling parameters and truncating the series at a point where the answer was essentially independent of the number of terms. The rate of convergence of this technique has not been formally investigated but there should be no difficulty with it if sufficient care is taken in the choice of functions.

SYSTEM PARAMETERS

In this study we chose to examine the specific problem of a uniform beam in bending, supported at the ends by damped linear springs offering no moment constraint, and excited at the center by a concentrated transverse load with sinusoidal time variation. The response criterion was the transverse displacement at the center. As mentioned before, the objective was to find that distribution and amount of bending damping which minimizes the response ratio maximized with respect to frequency. In all of our studies we have found that for any reasonable distribution of damping the maximum response ratio is at that frequency corresponding to the first bending mode.

This means that a relatively small number of generalized coordinates give an adequate description of the deflection shape.

For simplicity, we have confined our study to linear damping; since the active frequency range of interest is narrow, the frequency dependence is relatively unimportant. In this study we have chosen to use structural damping in which the energy dissipation per cycle is proportional to the maximum strain energy regardless of frequency. The use of viscous or other frequency dependent damping would have little influence on the results.

The problem studied is the configuration shown in figure 1. The governing equation is [4]:

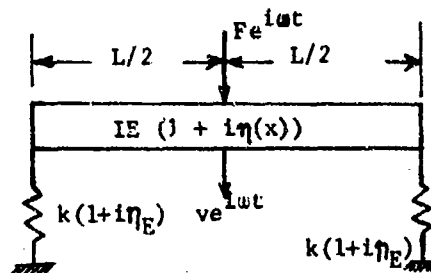


Fig. 1 - Beam Configuration

$$\frac{\partial^2}{\partial x^2} (EI(1+i\eta(x)) \frac{\partial^2 \tilde{v}}{\partial x^2} + \rho A \frac{\partial^2 \tilde{v}}{\partial t^2} = \tilde{q}(x, t). \quad (1A)$$

Making the harmonic substitution so that:

$$\tilde{q}(x, t) = q(x) e^{i\omega t} \text{ etc.}$$

$$\frac{d^2}{dx^2} EI(1+\eta(x)) \frac{d^2 v}{dx^2} - \rho \omega^2 v = q(x) \quad (1B)$$

This equation can be put into discrete algebraic form by taking advantage of its self-adjointness. To do this, we expand v in a set of functions complete over the interval 0 to L , letting:

$$v(x) = \sum_j a_j \varphi_j(x) \quad (2)$$

We substitute this expansion into equation 1B, multiply by $\varphi_k(x)$, integrate over 0 to L (inner product), and interchange summation and integration:

$$\sum_j a_j \int_0^L \varphi_k(x) \frac{d^2}{dx^2} EI(1+i\eta(x)) \frac{d^2 \varphi_j(x)}{dx^2} dx - \sum_j a_j \omega^2 \int_0^L \rho A \varphi_k(x) \varphi_j(x) dx = \int_0^L \varphi_k(x) q(x) dx$$

The first integral may be integrated twice by parts to give:

$$\begin{aligned} & \varphi_k \sum_j a_j (EI(1+i\eta(x)) \varphi_j'')' \Big|_0^L \\ & - \varphi_k' \sum_j a_j EI(1+i\eta(x)) \varphi_j' \Big|_0^L \\ & + \sum_j a_j \int_0^L (EI(1+i\eta(x)) \varphi_k'' \varphi_j'' dx \\ & - \sum_j a_j \omega^2 \int_0^L \rho A \varphi_k \varphi_j dx \\ & = \int_0^L \varphi_k(x) q(x) dx \end{aligned} \quad (3)$$

The first summation is the shear force evaluated at the support points and the second is the bending moment at the same points. Using the boundary conditions, the bending moment is zero (simple support) and the shear force is

$$\begin{aligned} & \sum_j a_j (EI(1+i\eta(x)) \varphi_j'')' \Big|_0^L \\ & = \pm k (1+i\eta_E) \sum_j a_j \varphi_j \Big|_0^L \end{aligned} \quad (4)$$

Now let

$$\begin{aligned} M_{jk} &= \int_0^L \rho A \varphi_j \varphi_k dx \\ S_{jk} &= \int_0^L EI \varphi_j'' \varphi_k'' dx \end{aligned} \quad (5)$$

This same expansion is not convenient for the dissipation term so we let

$$\eta(x) = \sum_i b_i \psi_i(x)$$

and define

$$D_{ijk} = \int_0^L EI \psi_i(x) \varphi_j''(x) \varphi_k''(x) dx \quad (6)$$

Letting

$$Q_k = \int_0^L \varphi_k(x) q(x) dx \quad (7)$$

equation 3 becomes:

$$\begin{aligned} & \sum_j a_j [k(1+i\eta_E) (\varphi_j(0) \varphi_k(0) + \varphi_j(L) \varphi_k(L))] \\ & + \sum_j a_j S_{jk} + i \sum_{ji} a_j b_i D_{ijk} - \omega^2 \sum_j a_j M_{jk} = Q_k \end{aligned} \quad (8)$$

The trick is now to choose the $\varphi_j(x)$ and the $\psi_i(x)$ to form complete sets, to minimize the coupling among the equations and to get the fastest convergence. Since the system and the external excitation are both symmetric, the optimal damping distribution and the response will also be symmetric about the midpoint. With these criteria, the functions used were:

$$\left. \begin{aligned} \varphi_0 &= 1 \\ \varphi_j &= \sin \frac{(2j-1)\pi x}{L} \quad j=1 \dots \infty \\ \psi_0 &= 1 \\ \psi_j &= \cos \frac{2j\pi x}{L} \quad j=1 \dots \infty \end{aligned} \right\} \quad (9)$$

Then

$$\begin{aligned} S_{0j} &= 0 \\ S_{jk} &= 0 \quad j \neq k \\ S_{jj} &= \frac{EIL}{2} \left[\frac{(2j-1)^2 \pi^2}{L^2} \right] = \frac{M_0}{2} \omega_j^2 = \frac{M_0}{2} (2j-1)^2 \omega_1^2 \end{aligned} \quad (10)$$

(Note, ω_1 are the odd frequencies of a simply supported beam in bending.)

$$\left. \begin{aligned} M_{0j} &= 0 \\ M_{jk} &= 0 \\ M_{jj} &= \frac{\rho A L}{2} = \frac{M_0}{2} \end{aligned} \right\} j \neq k \quad (11)$$

$$\left. \begin{aligned} D_{0jk} &= 0 & j \text{ or } k &= 0 \\ &= 0 & j &\neq k \\ &= \frac{EIL}{2} \left[\frac{(2j-1)\pi}{L} \right]^4 & j &= k \\ & & i &\neq 0 \end{aligned} \right\} \quad (12)$$

$$\begin{aligned} D_{ijk} &= \frac{EIL(2j-1)^2(2k-1)^2\pi^4}{4L^4}; i \pm (j-k) = 0 \\ &= \frac{EIL(2j-1)^2(2k-1)^2\pi^4}{4L^4}; i \pm (j+k) = 0 \end{aligned}$$

For a concentrated load, F , at the center

$$Q_k = (-1)^{j+1} F \quad (13)$$

It should also be noted that

$$\varphi_0(0) = \varphi_0(L) = 1 \quad (14)$$

$$\text{and } \varphi_j(0) = \varphi_j(L) = 0 \quad j > 0$$

For optimization purposes we let $F=1$ and take $v(L/2)^2$ as the objective function.

$$v(L/2)^2 = \left| \sum_j (-1)^{j+1} a_j \right|^2 \quad (15)$$

The optimization problem has now been reduced to minimizing the objective function, equation (15), with respect to the parameters b_i and maximizing with respect to ω^2 where the components of the objective function are determined by equation (8). A sufficient number of the a_j must be taken that the result is essentially unchanged by increasing the number. In

our case we found that 8 degrees of freedom was ample for the symmetric problem. The results may be constrained by limiting the number of b_i considered; if only b_0 is used, then the optimal value for uniform damping is found. As many as six b 's were included to define the optimum distribution of damping.

Using the methods outlined previously [5] the distribution of damping required to minimize the maximum value of $v(L/2)$ at any frequency was found for a range of stiffnesses and damping in support springs. The distribution of damping and the relative vibration amplitude depend only on the ratio of spring stiffness to beam stiffness. The dimensionless stiffness is described in terms of that pair of springs which would give the same frequency as the simply supported beam if the beam were a rigid mass:

$$k_0 = \frac{\pi^4 EI}{2L^3}$$

All frequencies are referred to the lowest simply supported bending beam mode

$$\omega_1 = \left[\frac{\pi^4 EI}{\mu L^4} \right]^{1/2}$$

The relative amplitudes are given in terms of:

$$v_0 = x_0 = F/2k_0$$

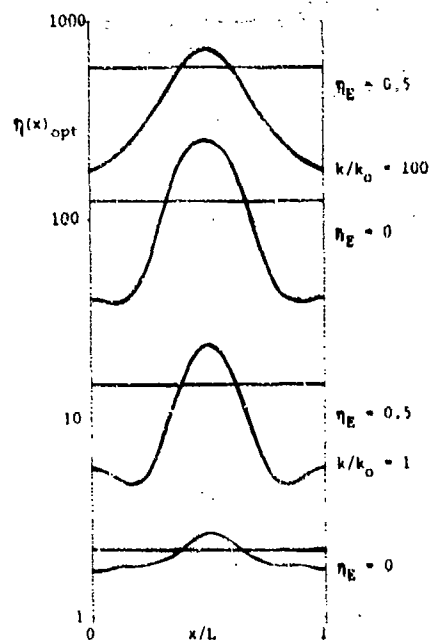


Fig. 2 - Optimum Distributed and Uniform Damping

Figure 2 shows the optimal distribution of damping for very stiff ($k/k_0 = 100$) and medium stiff ($k/k_0 = 1$) supports for two different loss tangents ($\eta_E = 0$ and 0.5). The optimal uniform damping is shown for

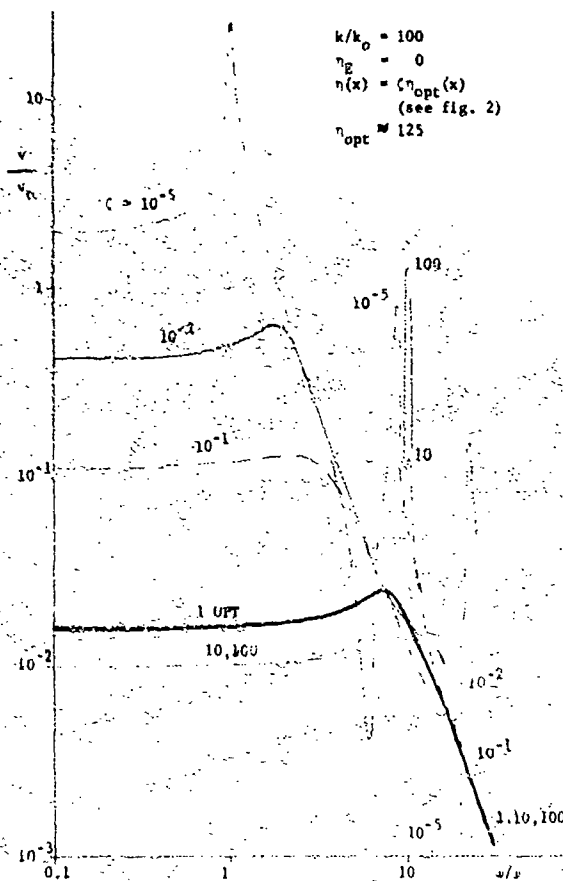


Fig. 3 - Vibration Response at Optimum and Off-Optimum Damping

comparison. Figure 3 shows the frequency response with very stiff undamped supports for non-optimal damping. Figure 4 shows optimal uniform damping versus support stiffness with support damping as a parameter; the amount of optimally distributed damping varies in about the same way.

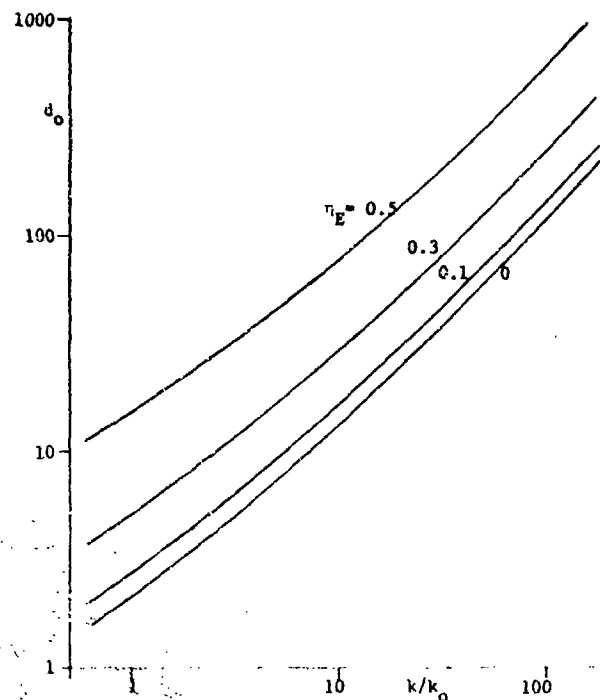


Fig. 4 - Optimum Uniform Damping vs. Support Stiffness

QUALITATIVE RESULTS

We are interested in the effects of the various parameters on the response maximized with respect to frequency. The significant parameters for this problem are

- 1.) Beam damping distribution
- 2.) Amount of beam damping
- 3.) End support stiffness
- 4.) End support damping ratio

The last two terms may be considered as representative of the impedance of the end support with the stiffness corresponding to the reactive portion and the support damping ratio corresponding to the loss tangent. There is little difference in optimal behavior between a mass-like termination and a spring-like termination; the only obvious effect is to make the frequency shift for maximum response positive instead of negative. Therefore only one of these, the spring-like support, was studied.

If the relative impedance is very high, further increases make little difference to a beam with reasonable amounts of damping; the beam behaves like a simply supported beam on a rigid support. As a result,

for values of $\eta(x)$ less than 1, there are resonances at each of the symmetric beam bending frequencies whose amplitudes are controlled by the beam damping (Fig. 3, $\zeta = 10^{-5}$). For values of η greater than 1 ($\sim 10^{-2}$) the beam bending resonances are almost suppressed. From a practical standpoint, values of η much larger than 1 are of little interest because materials do not have such large damping factors; nonetheless it is interesting to note that the optimum damping is essentially that which makes the beam impedance match the support impedance.

For support impedances comparable to the beam impedance, the optimum η is still appreciably larger than 1 so that any practical construction is suboptimal (fig. 4). As the supporting impedance becomes very small, the beam starts acting like a free-free beam and optimization depends on whether the very low frequency behavior is of interest. Since in most practical structures, low support impedance is associated with internal resonances, this implies relatively high frequencies. As a result, regardless of the answer for the simplified analysis of the case of constant support stiffness, a loss tangent for the beam as high as can be obtained will almost always be desirable.

The qualitative behavior of this system is much like that of other multi-degree of freedom systems (fig. 4). For light damping, $\zeta \ll 1$, the beam resonances and anti-resonances succeed themselves in an orderly fashion as the frequency is increased. As the beam damping is increased above 1, the beam bending modes are suppressed and the maximum amplitude continues to decrease in value and increase in frequency until an approximate impedance match is obtained. The optimum damping gives maximum response at a frequency between the lowest beam bending frequency and the frequency corresponding to the beam mass on the support stiffness. Increasing the damping still more makes the beam act like a rigid mass whose response is controlled by the support damping. Damping either greater than or less than optimal increases the maximum response according to [2]:

$$\frac{v_{\max}}{(v_{\max})_{\text{opt}}} = \frac{1}{2} \left[\frac{\eta}{\eta_{\text{opt}}} + \frac{\eta_{\text{opt}}}{\eta} \right]$$

This simple relationship is invalid for beam damping so large that the vibration amplitude is controlled by the support damping. As mentioned before, this is of little practical interest except for very flexible supports.

DAMPING DISTRIBUTION

The major purpose of this study was to find if large gains could be had by properly distributing the damping. Because the surface in parameter space is so flat near optimum damping, major changes in the distribution make little difference in the response if the average value is about right. For flexible supports, optimum distribution is almost uniform (fig. 2). As either the stiffness or the damping of the support is increased, the optimum damping distribution becomes highly peaked in the middle of the beam as might be expected. For a dimensionless spring constant of 1 and $\eta_g = 0.5$, the optimum distribution of $\eta(x)$ varies by a factor of 5 to 1 from center to ends; however, the response only increases by 1% between optimally distributed damping and optimum uniform damping. Similar results are had for other stiffness values. There is a weight penalty for using uniform damping; the total amount of optimum uniform damping is 1.5 times that of optimally distributed damping. However, if this latter were uniformly distributed so as to give 0.67 times the optimum uniform damping, the response would only increase by 8% more. One would expect similar results for any degree of end fixity, linear or angular.

CONCLUSIONS

The maximum vibration response of uniform beams in bending is relatively insensitive to deviations from optimum damping distribution in the direction of uniformity. Obviously the converse cannot hold; if bending damping were concentrated at points along the beam where the bending moment were zero, it would have no net damping effect.

This conclusion is subject to the limitations of the type of system investigated. The one described here is highly symmetrical: the two end supports are the same, it is loaded at the center and the controlled response is at the center. It would undoubtedly be possible to construct a pathological case in which an optimum distribution would reduce a

response manyfold below that of a uniform distribution.

In view of the large variation of the impedance of structural attachment points with frequency, the difficulty of constructing a non-uniform damping distribution and the relatively small return to be had from it for any reasonable choice of parameters, we are forced to conclude that a uniform distribution of damping is best for uniform beams in bending regardless of end fixity. Except for unusual configurations, the larger the damping factor the smaller the maximum response; since we can hardly get values of η greater than 1, optimal amounts and distribution of damping cannot be had for ordinary beams on supports of reasonable stiffness. This conclusion does not hold for amplitude dependent damping devices such as tuned absorbers; in their case the desirable location is critically dependent on the tuning frequency and overdamping is all too easy.

ACKNOWLEDGEMENT

This work was supported by NASA Grant NGR-24-005-095 under the technical guidance of Dr. J.P. Raney. Permission to publish these results is gratefully acknowledged. Several students have contributed to the work at different times, in particular D. Gimmetstad and W. Chen have done most of the programming and data generation.

REFERENCES

1. DiTaranto, R. S., "Theory of Vibrating Bending for Elastic and Viscoelastic Layered Finite-Length Beams," Jour. Appl. Mech., 32, Trans ASME, 87, 1965, pp. 881-886.
2. Plunkett, R. and Lee, C.T., "Optimum Configurations for Damping by Constrained Viscoelastic Layers," Jour. Acoust. Soc. Am., 47, 7, July, 1970 (pt. 2).
3. Derby, T.F., Ruzicka, J.E., "Loss Factor and Resonant Frequency of Viscoelastic Shear Damped Structural Composites," NASA CR-1269, 1969.
4. Tong, K.N., "Theory of Mechanical Vibrations," John Wiley, New York, 1963, p. 255.
5. McMunn, J.C. and Plunkett, R., "Multi-Parameter Optimum in Linear Dynamical Systems," ASME, 69-VIBR-42, April, 1969.
6. Snowden, J.C., "Vibration and Shock in Damped Mechanical Systems," John Wiley, New York, 1968.
7. Mixson, J.S. and Steiner, R., "Optimization of a Simple Dynamic Model of a Railroad Car," Stochastic Processes in Dynamical Problems, J.L. Bogdonoff and A. Piersol, Eds., ASME, 1969.

DISCUSSION

Mr. Peralta (Bell Telephone Laboratories): Did you investigate whether the addition of damping in the supports would lead to a more practical distribution of optimum damping?

Mr. Plunkett: Yes we did investigate that, especially the effects of added damping in the supports. I put values of η of 10 and 100 etc. into the supports and found that it did not make any difference at all.

Mr. Thomas (Naval Ship Research and Development Center): Are you familiar with Nelson's and Hoke's work reported in an ASME publication about a year ago that sort of contradicts your results both analytically and experimentally?

Mr. Plunkett: No.

Mr. Leibowitz (Naval Ship Research and Development Center): It appears to me that your optimum results apply to the modal patterns that are forced by the excitation at the center of the beam, if however there were a special distribution of forces I do not see that that would be the optimum result.

Mr. Plunkett: You are absolutely correct and in good academic tradition. I always open an escape hatch behind the written paper because I can always be misquoted during my presentation. I am certain that a pathological case can be built that will contradict these general conclusions. There might be an excitation that would excite only the tenth mode of the beam and I am certain it is an optimum distribution. There is one that is considerably more unsymmetric than that. You are absolutely correct.

Mr. Leibowitz: I refute your statement that this is the general case.

Mr. Plunkett: I agree, this is not the general case! Various studies indicate that most things of interest are relatively symmetric. The general statement that you cannot find an optimum distribution that will vary much from uniform of course is incorrect. For example for tuned absorbers we know that there are optimum positions for damping out specific modes.

A LAYERED VISCOELASTIC EPOXY RIGID FOAM MATERIAL FOR VIBRATION CONTROL

C. V. Stahle and Dr. A. T. Tweedie
General Electric Company
Space Division
Valley Forge, Pa.

An approach to the control of vibration is presented which uses a combination of a rigid polyurethane foam layer and a viscoelastic epoxy high damping layer. The layered configuration offers the advantages of both stiffness and high damping when applied to sheet metal panels. The rigid foam layer is used to offset the damping layer from the metal surface to be controlled. The effect of the foam is to impose larger strains on the damping layer resulting in a much higher loss factor for the layered configuration than could be obtained using the damping material directly on the metal surface. The viscoelastic epoxy (SMRD 100F50) has a higher loss factor than some of the available viscoelastic materials. Additional advantages are that both the foam and the viscoelastic material are castable, have low outgassing properties, and have a low density compared to other available viscoelastic materials.

Experimental results are presented for cantilever beam element tests used to determine the damping characteristics of selected space compatible materials and evaluate layered and laminated configurations. The use of the layered material for a relay panel installation in the NASA-Goddard Space Flight Center Earth Resources Technology Satellite Power Switching Module is described and vibration test results are presented.

INTRODUCTION

The design of spacecraft electronic components to withstand the launch vibration environment requires packaging methods which provide both stiffness and damping. The required rigidity of the design depends on the vibration environment of the component as reflected in the component vibration specification. In general, packaging methods which provide dynamic magnifications of less than 10 are considered to have adequate damping, although smaller magnifications are sometimes required.

Early vibration development tests of the NASA-Goddard Space Flight Center Earth Resources Technology Satellite (ERTS) Power Switching Module (PSM) indicated that although the packaging design provided adequate stiffness, additional damping was needed to assure the adequacy of the design. The component vibration specification subjected the PSM to sinusoidal vibration

levels in the thrust axis of 10g in the frequency range from 60 to 150 Hertz while the level was reduced to 5g above 150 Hertz. Consequently, the design goal was to provide resonances above 150 Hertz. The PSM is comprised of two major sections: a section containing printed circuit boards and a section containing two relatively large relay panels, Figure 1. Although adequate stiffness could readily be provided for the PC boards, the relay panels weighed approximately 3 pounds each and were designed using .093 inch aluminum sheet supported to the basic box structure on three edges and including an angle stiffener in the center of the panel. The vibration response near the center of the panel, Figure 2, showed that the fundamental resonant frequency was adequate, 160 Hertz, but that the dynamic magnification, 40, was excessive. Studies were subsequently initiated to evaluate relay panel modifications which would provide both the desired stiffness and damping to the design. Because the design

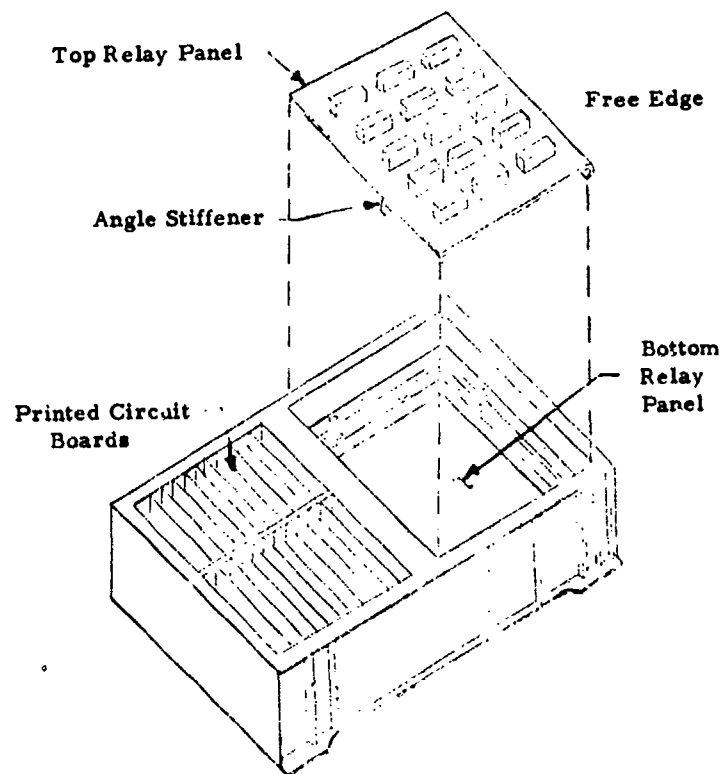


Fig. 1 - ERTS PSM Relay Panel Installation

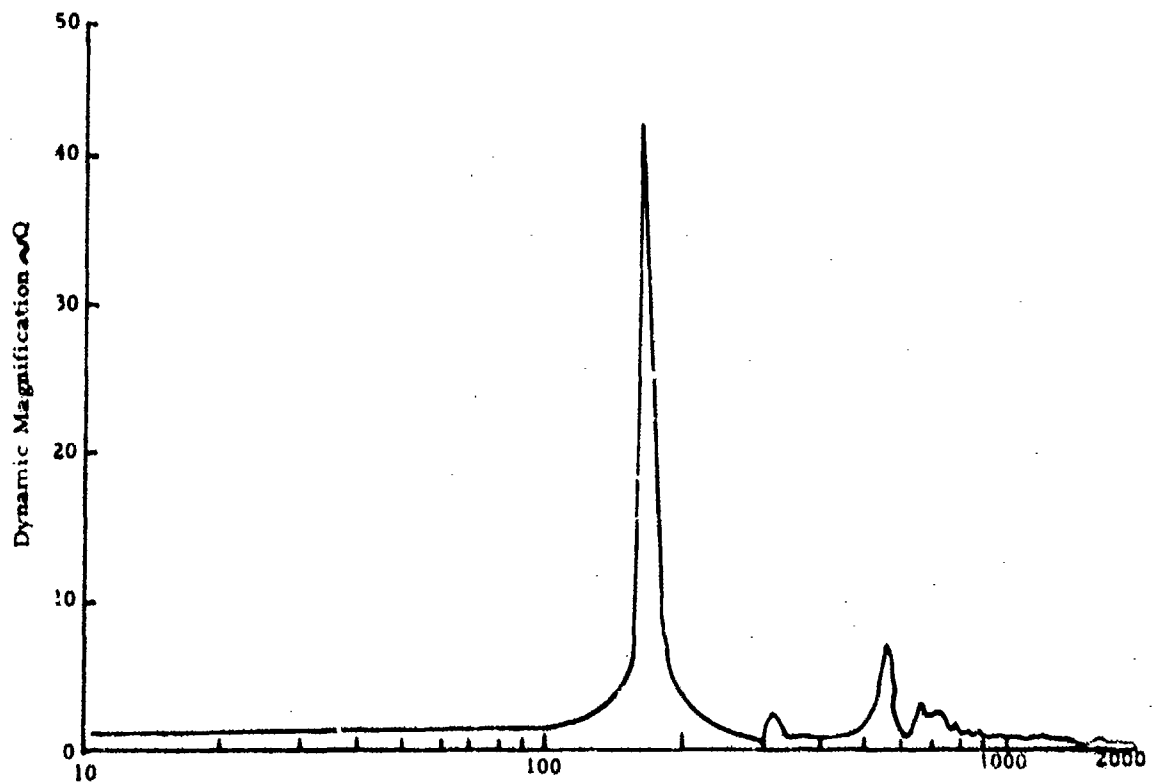


Fig. 2 - Response at Center of ERTS PSM Relay Panel for Original Panel Configuration

is required to be space compatible, the materials used to provide damping were limited to those known to be space compatible and required initial evaluations of their damping characteristics.

The following sections of this paper describe the space compatible materials selected for evaluation, the method and results of the damping tests of these materials, and the modification of the relay panel to provide both stiffness and damping. A unique layered material configuration resulted which appears to have application to many other design problems.

MATERIAL SELECTION

The requirements for a vibration damping material for use on a spacecraft include space compatibility, and low weight, as well as high hysteresis in the frequency range of interest. Space compatibility in the intended application (inside a component) means low outgassing under vacuum. The material was exposed to the space environment directly, resistance to ultraviolet light and ionizing radiation would also be a factor. In addition, of course, the material must meet the usual requirements of having adequate mechanical and physical properties and be capable of being satisfactorily processed.

The materials selected for testing came originally from a list of materials already approved for use on the spacecraft. They all had been tested for outgassing rate and found to be satisfactory. A polyurethane conformal coating and potting compound, Solithane 113-300, Thiokol Chemical Co., was selected for test as a typical space compatible urethane elastomer, although it was felt that it was rather more elastic than wanted. A polyurethane rigid foam that met the outgassing requirements, Eccofam FPH, 12 lb./ft.³, Emerson & Cummings was tested as a stiffening and spacer material. A flexible non-plasticized epoxy resin developed at GE Space Systems as a sterilizable conformal coating and potting compound was chosen for test because it appeared to have good damping characteristics to the touch. This material, designated SMRD 100, with some modifications, proved to have the necessary properties to solve the problem. SMRD 100 is a clear amber viscoelastic material that is used as a conformal coating and potting compound where relief of strains induced by high temperature cycling is wanted. It offers good adhesion to most substrates like any epoxy and will withstand long time exposure to 120°C temperatures. Two other versions of SMRD 100 were also tested. SMRD 101 is a clear slightly softer version and SMRD 100F, which is filled with glass microspheres (Eccospheres, Emerson & Cummings) to reduce weight. SMRD 100F can be made in a wide

range of hardnesses. The SMRD 100F material used for this program has a nominal hardness of 50 using a Shore A durometer. It is therefore designated SMRD 100F50. The nominal properties of the SMRD 101 and SMRD 100F50 are given in Table 1.

The SMRD 100 compounds used for this program were cast in Teflon coated aluminum molds in thicknesses ranging from 1/8" to 3/4" thick. The resulting sheets were either used as cast or, where dimensions were critical, machined to size on a milling machine using a fly cutter. The very soft SMRD 100F50 has sticky surfaces when freshly machined so that without special care and technique, the cuttings adhere to the surface. Use of a spray of fluorocarbon solvent on the material lubricates and cools the material making it stiff allowing normal machining. A hand wash bottle of fluorocarbon solvent has been found satisfactory. Although the fluorocarbon solvent is not toxic, adequate ventilation should be provided to prevent excessive build up of fumes.

Sheets of SMRD 100 and SMRD 100F50 can be bonded to foam, aluminum, or other materials using epoxy adhesives, for example EPON 828 and TETA, Shell Chemical Co. For applications where it is not convenient to use cured sheets of the compounds, they can be cast in place. They require a cure time of 24 hours at 115°C.

CANTILEVER BEAM ELEMENT TESTS

Cantilever beam element tests were used to establish the stiffness and damping characteristics of the various materials and to investigate several material combinations. The basic test arrangement followed that of Nashif (1), but was modified to enable a number of samples to be tested simultaneously. A series of cantilever beam elements were mounted to a shaker and excited using base excitation, Figure 3. Using the basic relations for excitation of uniform cantilever beam modes through base excitation, the damping of the test beam can readily be determined from the dynamic magnification at the tip of the beam. The relation for material loss factor and stiffness can then be determined using the equations presented by Nashif (1).

The cantilever beam specimens that were evaluated are summarized in Table 2. Specimen No. 1, a bare .093" aluminum beam provided a baseline configuration while Specimen Numbers 2, 3, 4 and 5 were used for evaluating material characteristics of conformal coating,

TABLE 1
Physical Properties of SMRD 101 and SMRD 100F50

Property	SMRD 101	SMRD 100F50
Specific Gravity @ 20 - 24°C	1.08	.72
Hardness, Shore	D45	A50
Thermal Conductivity BTU/Hr. /Ft. ² /°F/Ft. ₁		.08
Volume Resistivity Ohm - cm. Min.	1×10^{14}	
Dielectric Constant @ 1 MHz, Max.	4.0	
Compressive Stress at 10% Compression, psi	.03	45

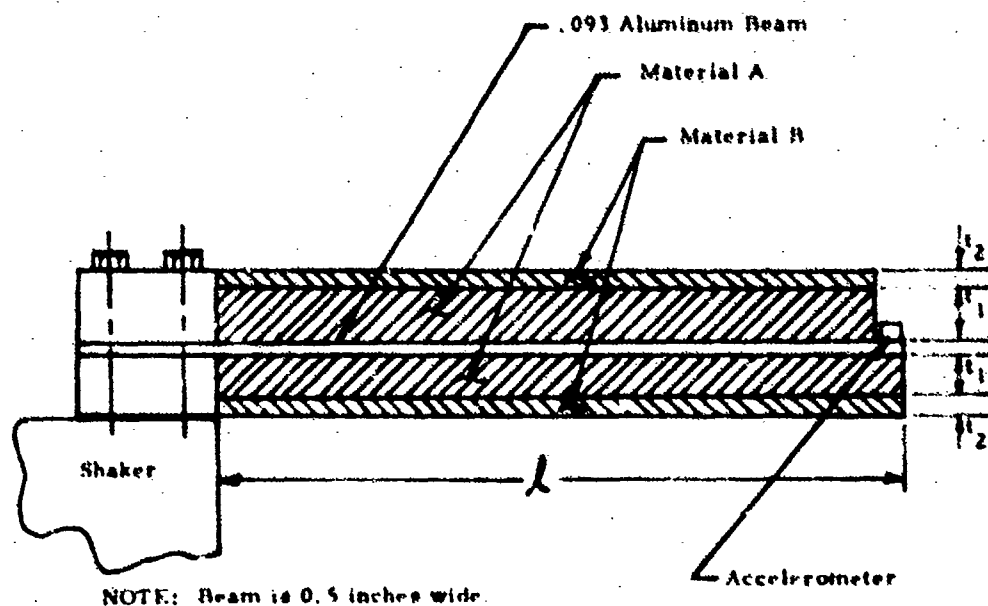


Fig. 1 - Cantilever Beam Specimen

TABLE 2
Cantilever Beam Test Specimen Descriptions

Specimen Number	Description	l (Inches)	Dimensional Data		Materials	
			t_1 (Inches)	t_2 (Inches)	A	B
1	Bare Aluminum Beam	7	N/A	N/A	N/A	N/A
2	Conformal Coating	7	0.25	N/A	Solothane 113-300	N/A
3	Polyurethane Foam	7	0.5	N/A	Eccoloam FPH-12	N/A
4	Viscoelastic Epoxy	7	0.25	N/A	SMRD 101	N/A
5	Viscoelastic Epoxy	7	0.25	N/A	SMRD 100F50	N/A
6	Viscoelastic Epoxy/Polyurethane Foam Layered	7	0.5	0.25	Polyurethane Foam (Eccoloam FPH-12)	SMRD 100F50
7	Viscoelastic Epoxy/Polyurethane (<u>One Side Only</u>)	7	0.5	0.25	Polyurethane Foam FPH-12	SMRD 100F50
8	Viscoelastic Epoxy/Polyurethane Foam Layered	7	0.35	0.25	Polyurethane Foam FPH-12	SMRD 101
9	Viscoelastic Epoxy/Polyurethane Foam Layered	7	0.475	0.125	Polyurethane Foam FPH-12	SMRD 101
10	Viscoelastic Epoxy Laminate (Two 093 Al. Beams)	5.7	0.125	N/A	SMRD 101	N/A

polyurethane foam, SMRD 101 and SMRD 100F50. Specimen Numbers 6 through 10 provided comparative data for layered configurations using Polyurethane foam with SMRD 100F50 and SMRD 101 as well as a laminated configuration using SMRD 101.

The results of these element tests are summarized in Table 3 for various accelerations of the base of the beam. From the results of the material evaluation, Specimen Numbers 2 to 5, it is evident that conformal coating and polyurethane foam have little damping although the polyurethane foam is effective as a stiffening material. Although both SMRD 101 and SMRD 100F50 provide a much higher damping, SMRD 100F50 is the better of the two damping materials. In order to obtain both stiffness and damping, a layered configuration using SMRD 100F50 and SMRD 101 in combination with the polyurethane foam was selected, Specimen Numbers 6, 8 and 9. Comparison of the dynamic magnification factors for these layered specimens indicates that SMRD 100F50 is the most effective from the standpoint of damping while the stiffness is not appreciably affected. In order to arrive at a configuration adaptable to the relay panel modification, the layered Polyurethane Foam/SMRD 100F50 specimen was modified to a one-sided configuration, Specimen No. 7. Although there was a loss in stiffness, the damping was not appreciably affected. The laminated configuration using SMRD 101 (Specimen No. 10) did not appear to provide a significant increase in damping relative to the other layered configuration (No. 4), although it was much stiffer.

The apparent loss in damping of the SMRD 101 layered specimens with an increase in the thickness of the damping layer seems to indicate an optimum thickness of damping material. Comparison of the dynamic magnification factors of Specimens No. 8 and 9, indicates that the dynamic magnification was increased from approximately 7 to approximately 13 when the thickness of the SMRD 101 was increased from 1/8 inch to 1/4 inch. Although this change could be due to frequency dependent damping effects, it seems more likely that the thicker SMRD 101 was sufficient to overpower the foam material so that it was not strained to the same degree as the thinner material. On the other hand, the SMRD 100F50 is soft compared to the SMRD 101 and was effectively strained through the foam layer.

MATERIAL LOSS FACTORS

The material loss factors were determined for the various materials tested to compare with other available damping materials. Using the equation for base excitation of the fundamental

cantilever mode of a beam, ϕ , the composite loss factor can be obtained from the expression

$$\eta = \frac{\phi_{TIP} \int \phi^2 dm}{\int \phi^2 dm} \cdot \frac{1}{\sqrt{Q^2 - 1}} = \frac{1.56}{\sqrt{Q^2 - 1}}$$

where the denominator accounts for the in-phase and quadrature components of the response. Then from Nashif (1), the relative bending stiffness and material loss factor are defined by:

$$\frac{E_2 I_2}{E_1 I_1} = \left(\frac{W_n}{W_{ln}} \right)^2 \left(\frac{\mu}{\mu_1} \right) - 1$$

$$\eta_2 = \eta \left[1 + \left(\frac{E_1 I_1}{E_2 I_2} \right) \right]$$

- where $E_1 I_1$ = bending stiffness of the aluminum beam
- $E_2 I_2$ = bending stiffness of the damping material
- W_n = resonant frequency of the composite beam
- W_{ln} = resonant frequency of the aluminum beam
- η_2 = loss factor of the damping material
- μ_1 = density per unit length of the aluminum beam
- μ = density per unit length of the composite beam

Using these expressions, the loss factors for the materials were calculated as shown in Table 4. An additional value for the SMRD 100F50 was determined using the same expressions but considering the foam-aluminum beam as the basic configuration. Because of the probable frequency dependency of the damping characteristics, the frequency at which the loss factor was determined is also noted. These results indicate that SMRD 100F50 is by far the best of the various materials from the standpoint of damping.

The damping properties of SMRD 100F50 are compared to LD400 (1) in Figure 4. It will be noted that only two damping values are available for SMRD 100F50 to draw the curve. However, the data indicate that the SMRD 100F50 has a loss factor of approximately twice as high as that of the LD-400 viscoelastic material. On the other hand, the SMRD 100F50 is more flexible than the LD-400 material as indicated in Figure 5. Both materials exhibit an increase in stiffness and a reduction in damping with increasing frequency.

TABLE 3

Summary of Cantilever Beam Vibration Tests

Input Level	Bare Aluminum		Conformal Coating		Poly-urethane Foam		SMRD 101		SMRD 100F50	
(G's)	Q	fn (Hz)	Q	fn (Hz)	Q	fn (Hz)	Q	fn (Hz)	Q	fn (Hz)
0.5	64	46	(100)	30.5	35	96	12	65	7.2	35
1.0	39	46	90	32	41	99	13	65	7.2	35
2.0	50	48	82	32	41	99	14	65	7.2	35
5.0	60	48	37	32	36	98	14	65	7.6	34.5
10.0	--	--	--	--	--	--	13	62	--	--

Input Level	Foam/SMRD 100F50		Foam/SMRD 100F50 (one side)		Foam SMRD 101 (1/4" thick)		Foam/SMRD 101 (1/8" thick)		SMRD 101 Laminate	
(G's)	Q	fn (Hz)	Q	fn (Hz)	Q	fn (Hz)	Q	fn (Hz)	Q	fn (Hz)
0.5	4.8	115	4.8	95	12	125	5.4	100	14.6	230
1.0	4.8	115	--	--	14	125	6.6	100	--	--
2.0	4.8	115	5	95	13	127	6.9	101	17	230
5.0	4.8	115	5.2	93	13	128	7.3	100	16	225
10.0	--	--	5.4	90	13	124	7.4	98	16	230

TABLE 4
Material Loss Factors

Material	Loss Factor	Frequency (Hz)
Conformal Coating (Solithane 113-300)	.005 to .14	32
Polyurethane Foam (Eccofoam FPH-12)	.018	98
SMRD 100F50	.89	35
	.58*	115
SMRD 101	.15	65
*Determined using the foam-aluminum beam as a reference.		

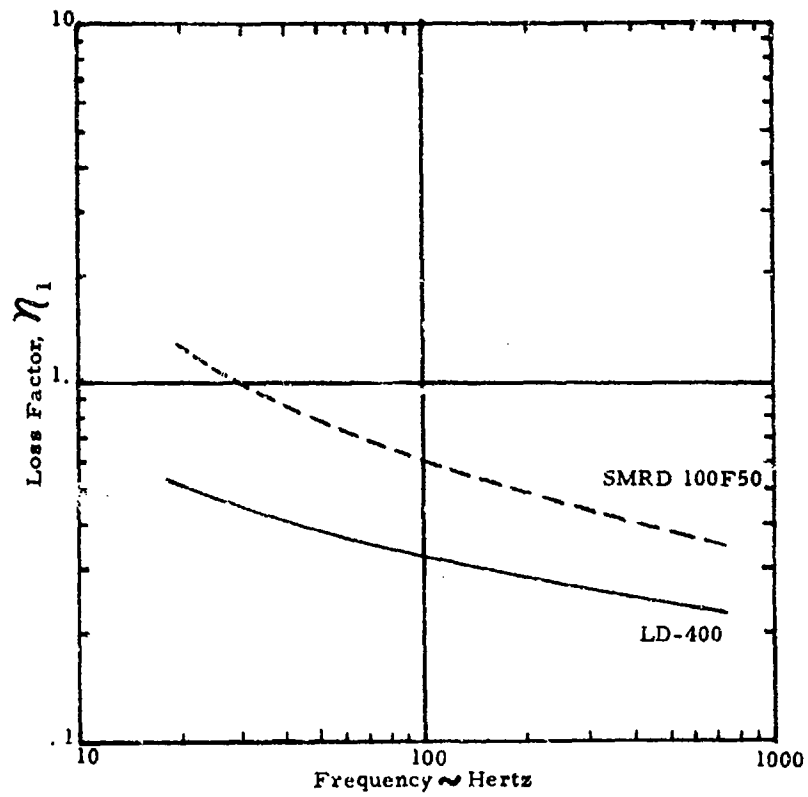


Fig. 4 - Loss Factor Comparison

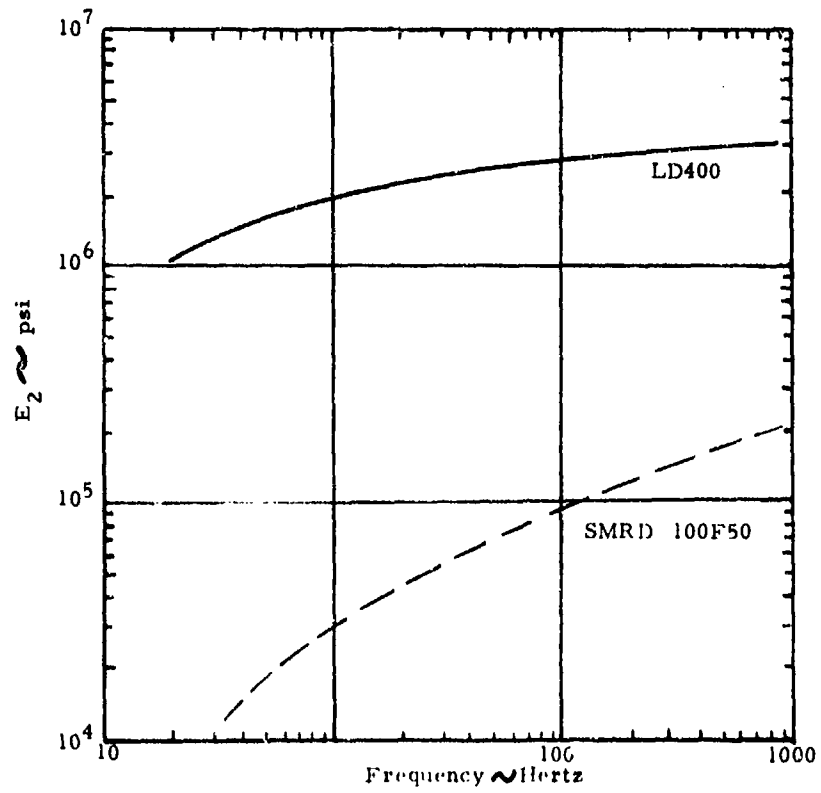


Fig. 5 - Real Part of Young's Modulus Comparison

RELAY PANEL MODIFICATION

The layered Foam/SMRD 100F50 combination stiffening and dampening treatment was applied to the FSM relay panels. The center stiffening angle was removed from the panel. Eccofoam FPH, nominal density 12 lbs/ft³ was cast in place on the inner side of the panels. Polymethylmethacrylate blocks were used as removable inserts to leave spaces in the foam for the relays which protrude through holes in the panels. Aluminum angle was clamped around the edges to make a form. The foam was cast and allowed to rise freely. After curing, the foam was machined to the specified thickness and SMRD 100F50 pads were bonded to the surface. Epoxy adhesive Epon 828 was used. The SMRD pad was then machined to the correct thickness. Machining was necessary because of the limited space available with resulting close tolerances. Cut-outs for the relays were made in the SMRD pads using a scalpal.

Vibration tests of the modified relay panel installed in the PSM showed that the layered damping treatment reduced the dynamic magnification by a factor of approximately 6, Figure 6. The response in the center of the panel was reduced from a dynamic magnification of 40 to less than 7. Similar reductions were also obtained for the high frequency resonance between 500 and 1000 Hertz. The fundamental panel resonance was increased slightly from 160 Hertz to 180 Hertz which was sufficient to remove the resonance from the severe vibration environment below 150 Hertz.

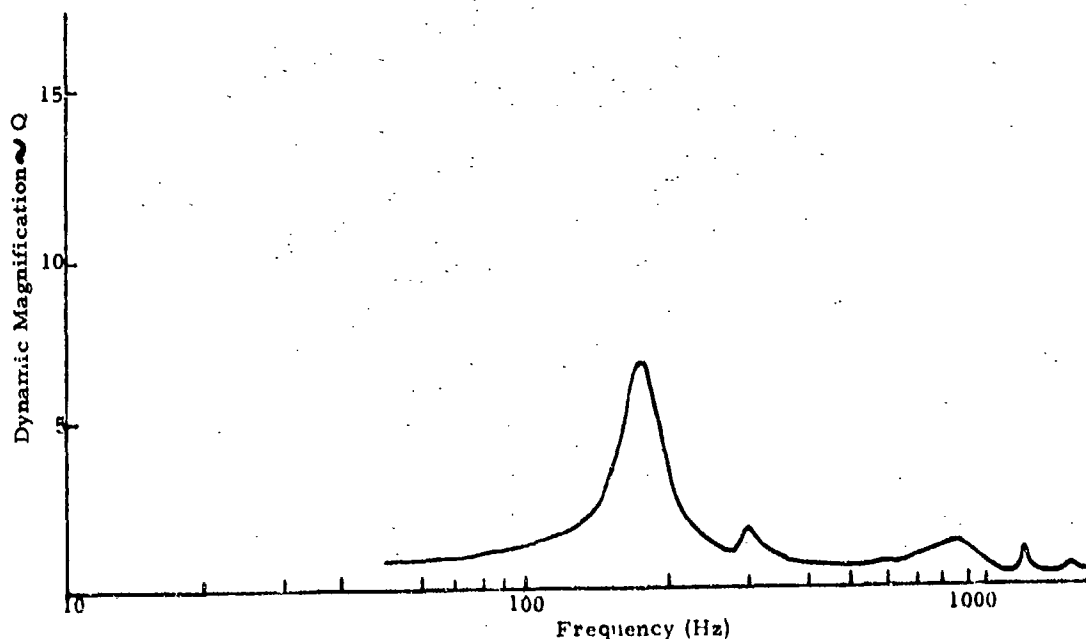


Fig. 6 - Response at Center of ERTS PSM Relay Panel with Foam/SMRD Modification

CONCLUSIONS

On the basis of the results presented in this paper, the following conclusions are made:

1. SMRD 100F50 is an excellent lightweight, castable, space compatible damping material.
2. A layered damping configuration using a rigid foam to offset the damping material from the parent sheet metal is an effective way to provide both stiffness and damping.
3. The layered configuration provided higher damping than could be obtained by applying the damping material directly to the aluminum.
4. The layered material need be applied to only one side of the basic sheet metal.
5. There is an optimum combination of foam and damping material. If the damping material is stiff relative to the foam, a large thickness of damping material may provide less composite damping than a small thickness.
6. The Polyurethane/SMRD 100F50 layered stiffening-damping treatment was effective in reducing the dynamic magnifications of the ERTS PSM relay panel by a factor of approximately 6. Dynamic magnifications were approximately 7 to 1 at the center of the relay panel with the stiffening-damping treatment.

ACKNOWLEDGEMENTS

This paper is the result of work performed on the Earth Resources Technology Satellite program (Contract NAS 5-11320) under the cognizance of G. Branchflower and D. Murray of NASA-Goddard Space Flight Center. The contributions of R. Sipple in performing the test; R. Boileau and A. Panarello in fabricating the test specimens, and T. Gresko for performing the computations and preparing the figures, are gratefully acknowledged.

REFERENCES

1. A. D. Nashif, "A New Method for Determining the Damping Properties of Viscoelastic Materials," Shock and Vibration Bulletin No. 36, Pt. 4, 1967.

DISCUSSION

Mr. Epstein (Endevco Corporation): You mentioned that these tests were done mostly at room temperature. Do you have any indication whether these materials will work at the temperatures encountered in space applications?

Mr. Stahle: This would be a loss environment. I guess you could have extremes but in general I would expect that the material would behave fairly well at the normal range of temperatures that you would expect to see in the sound wave. That is a controlled environment.

Mr. Mixon (Holloman Air Force Base): What was the weight increase of the panel? You said it was originally three pounds.

Mr. Stahle: I do not know. The foam itself is very light and this material has a specific gravity of 0.7 and it also had quarter-inch-thick cut-outs in it. I do not really know exactly what the final increase was. Most of the three pounds was the relays and the wiring and I do not think it was in the damping treatment.

Mr. Volin (Naval Research Laboratory): You mentioned that the Q values of a thinner sample tended to be less than those of a thicker sample. Could you give any reason for this behavior?

Mr. Stahle: I can only give you a feeling for it. If you make the damping layer stiff enough so that you cannot carry the strain through the foam you never strain the damping material. Therefore some matching of the damping layer with the foam is needed, and if you make the damping material too stiff it just is not going to work.

Mr. Ungar (Bolt Beranek and Newman): I think that most of the effects that you have found are entirely predictable. The theory of layered damping media has been around for a long time. If I gather correctly you used some to the theory to get back at your material properties from a system test. Is that right?

Mr. Stahle: Yes.

Mr. Ungar: Did you ever measure material properties by themselves and then use them to predict what the system would do? You only have two data points on your damping material. That is very limited.

Mr. Stahle: Yes, and as it turns out we used two different specimens to get those, that is true. I am not really sure that I see your point.

Mr. Ungar: My whole point is that I think many of the effects that you found by lots of testing could have been predicted.

Mr. Stahle: When we started we did not know what the damping characteristics of the material were so the first thing we had to do was to establish these. The next problem, and I think it is not really that predictable, is that you have to be careful what you are doing when the two materials are put together. I never saw the foam-damping material combination before. Perhaps you have seen it.

Mr. Ungar: There is a theory of so called space damping which is all worked out in great detail.

Mr. Stahle: This involves using metal pieces to offset the damping material.

Mr. Ungar: It does not matter what the offsetting material is if you know the stiffness. You can play the entire prediction game. Let me also point out that it is not only the loss factor in the damping material that counts, but it is the product of the loss factor and the stiffness. I am not selling Lord's material, but if you multiply the loss factor of the damping material by its modulus, the LD 400 still comes out better. Am I wrong?

Mr. Stahle: I think there is one basic problem with the LD 400. I do not think it is space compatible. Of course it is not as easy to use as this material. It can be cast. Incidentally this material comes in a number of different durometers. That is why we put the 50 on the end. I am sure you are right that there is some trade-off which was not really investigated; certainly some other durometer may ultimately provide an increased composite loss factor, if you do not lose a loss factor in making it stiffer.

Mr. Ungar: I am sure its good to have a material that is space compatible but I am sure you also have to do a lot more work before you can use it.

Mr. Stahle: It is being used on the ERTS.

OPTIMIZATION OF A COMBINED RUZICKA AND SNOWDON VIBRATION ISOLATION SYSTEM

Dennis E. Zeidler
Medtronic, Inc.
Minneapolis, Minnesota

and

Darrell A. Frohrib
University of Minnesota
Minneapolis, Minnesota

An isolator combining the advantages of optimized Ruzicka and Snowdon models is presented. This isolator is demonstrated to have superior performance properties as evaluated by a criterion function of the form $I_t = DT_p + \log T_h$.

INTRODUCTION

The quality of a vibration isolation system is usually described by its steady state transmissibility properties. The criteria for selecting the best isolator vary with the application. Often a tradeoff between low transmissibility at resonance and low transmissibility in a high frequency range is involved. This study was motivated by the well known optimizations performed on specific passive isolator types by J. Ruzicka (1)* and J. Snowdon (2,3).

Ruzicka discussed the relaxation isolator shown in Figure 1. He shows that the transmissibility is given by,

$$T = \left[\frac{1 + ((N+1) \frac{2\rho f}{N})^2}{(1-f^2)^2 + [2\rho f(N+1-f^2)/N]^2} \right]^{1/2}$$

Optimality in the Ruzicka sense relates ρ and N to realize a maximum response at the fixed point:

$$\rho_{opt} = \frac{N}{2(N+1)} \sqrt{\frac{N+2}{2}}$$

Snowdon discusses the two inertia system shown in Figure 2. That transmissibility is:

$$T = \left[\frac{P^2 + Q^2}{R^2 + S^2} \right]^{1/2}$$

where,

$$P = Y - 4f^2\rho^2\Delta Z^4,$$

$$Q = 2f\rho Z^2(\Delta + Y),$$

$$R = \alpha f^4 Z^4 - f^2 Z^2(1 + Y + 4\Delta\rho^2 Z^2 + \alpha) + Y,$$

*Bibliography references.

NOMENCLATURE

$D, N, U, V, Y, Z, \alpha, \beta, \gamma, \Delta$ -- dimensionless constants as indicated in the Figures or defined in the text

C -- viscous damping coefficient

f -- frequency ratio, ω/λ

I_t -- transmissibility index

K -- spring constant

M -- mass to be isolated

P, Q, R, S -- transmissibility terms defined in the text

t -- time

T -- transmissibility, $|\bar{X}_t/\bar{X}_B|$

T_h -- transmissibility in the isolation range, above the highest resonance

T_p -- resonant or peak transmissibility

ω -- excitation frequency

\bar{X}_B -- sinusoidal input motion, $X_B e^{i\omega t}$

X_1, X_2, X_3 -- motion coordinates of the form $X e^{i\omega t}$

λ -- natural frequency of undamped system.

ρ -- damping ratio, $C/2M\lambda$

Preceding page blank

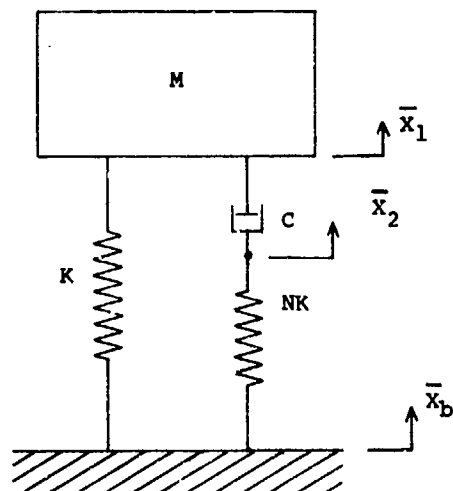


Figure 1; Ruzicka isolator

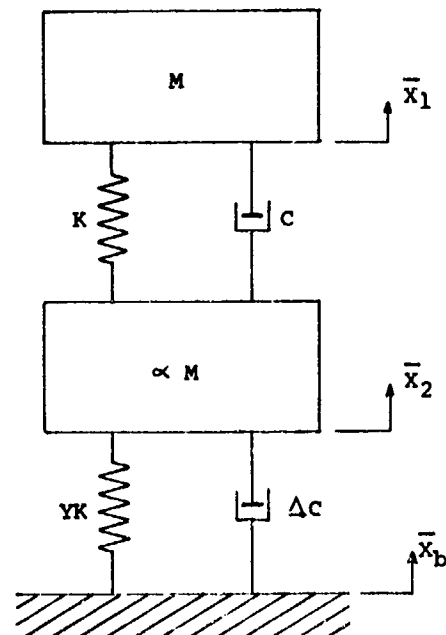


Figure 2; Snowdon Isolator

$$\text{and } S = -2 f^3 \rho Z^4 (1 + \Delta + \alpha) + 2 f \rho Z^2 (\Delta + Y) .$$

The natural frequency of the undamped system is:

$$\lambda = Z \sqrt{K / M} ,$$

where,

$$Z^2 = (1 + Y + \alpha - \sqrt{(1 + Y + \alpha)^2 - 4 Y \alpha}) / 2 \alpha .$$

(Introducing Z in this form normalizes the response curves so that the lower resonant frequency occurs near $f = 1$.) Snowdon optimality determines the ratio of inertias, α , that minimizes the frequency interval between the two resonant frequencies so as to gain as large an isolation range as possible.

There,

$$\alpha_{opt} = Y - 1 .$$

Optimum Ruzicka and optimum Snowdon curves are compared in Figures 3a and 3b. In Figure 3a the two curves have the same T_H values but the Ruzicka curve has a lower T_P . In Figure 3b the two curves have equal T_P values but the Snowdon curve has a lower T_H . Our study combines the two isolator systems to gain the advantages of each at resonance and in the isolation range.

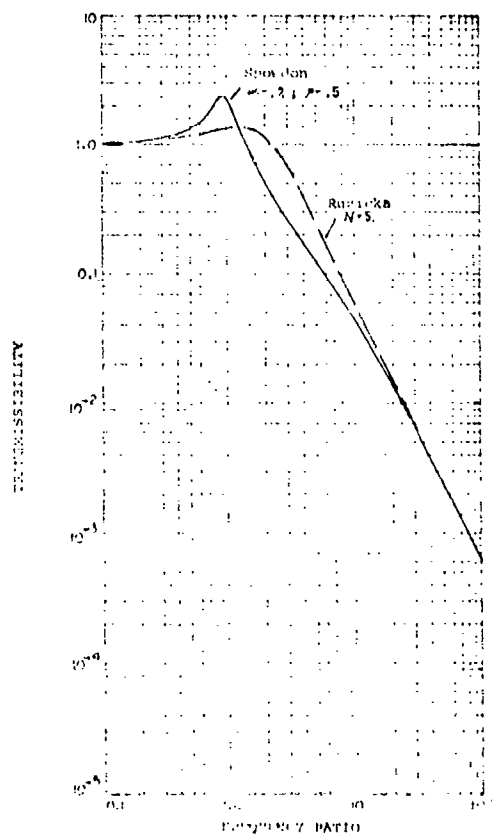


Figure 3; Comparison of Ruzicka and Snowdon response curves

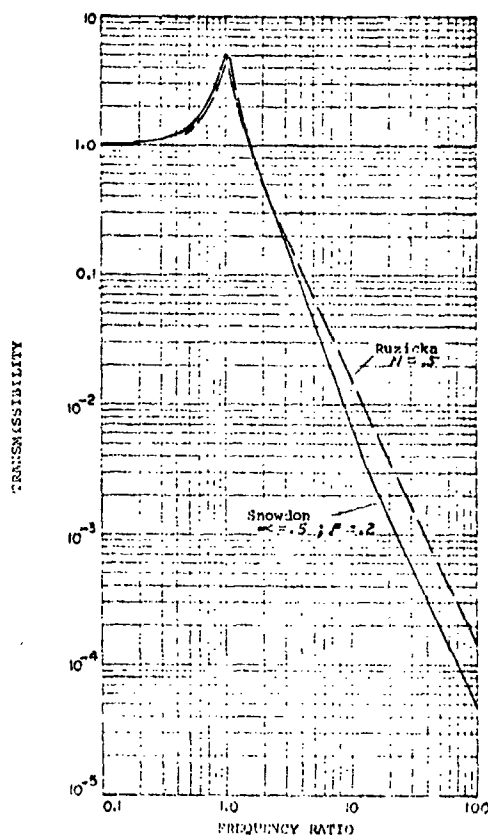


Figure 3b: comparison of Ruzicka and Snowdon responses

ANALYSIS

The isolator model is shown in Figure 4; we are interested in controlling \bar{X}_1/\bar{X}_B .

In the subsequent discussion the following criterion function was employed:

$$I_t = D T_p + \log_{10} T_h,$$

where the objective is to minimize I_t for a given weighting factor D . For example, in the following discussion T_h is assigned the value of transmissibility at frequency ratio 100, i.e.

$$T_h = T \Big|_{f=100}$$

For some applications, minimizing T_p is much more important than minimizing T_h ; we will classify this type of application as a TYPE 1 design criterion. For example, for the classical isolator shown in Figure 5a, the TYPE 1 values of I_t for a value of $D = 5$ are 5.35,

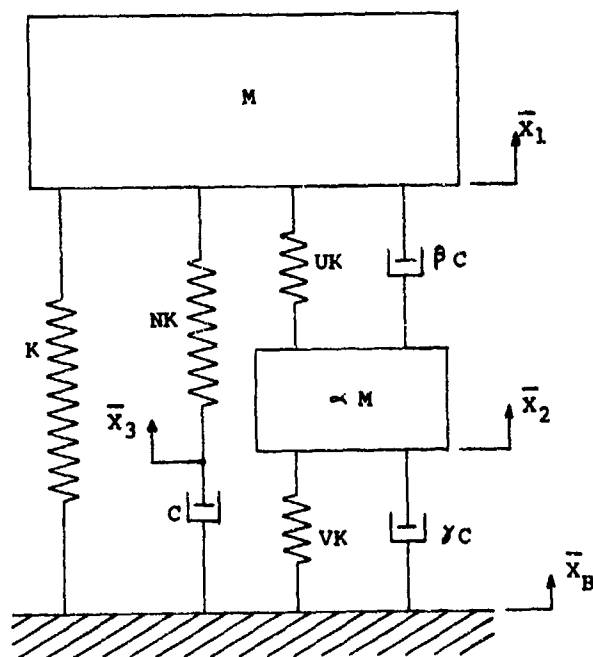


Figure 4: Combined isolator

4.08, and 3.85 corresponding to ρ of 0.5, 1.0, and 2.0. Since $\rho = 2.0$ gives the lowest value of I_t , it is the best TYPE 1 curve.

Conversely, applications for which T_h is more important than T_p will be categorized as TYPE 2. Finally, applications in which T_p and T_h are equally important are referred to as TYPE 3. In Figure 5b, the $\rho = 0.5$ and $\rho = 1.0$ curves are respectively the best TYPE 2 and best TYPE 3 curves. Table 1 summarizes the criteria designations and typical values for the weighting coefficient D .

Table 1

Criteria Designation	Description of Design Criteria	Value of D
TYPE 1	Minimizing T_p , the peak transmissibility is more important	5.0
TYPE 2	Minimizing T_h , the high frequency transmissibility is more important	0.5
TYPE 3	T_p and T_h are equally important	2.0

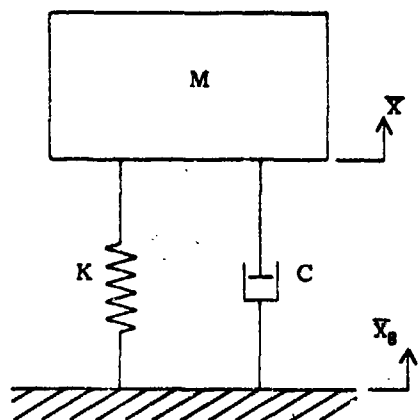


Figure 5a; Classical isolator

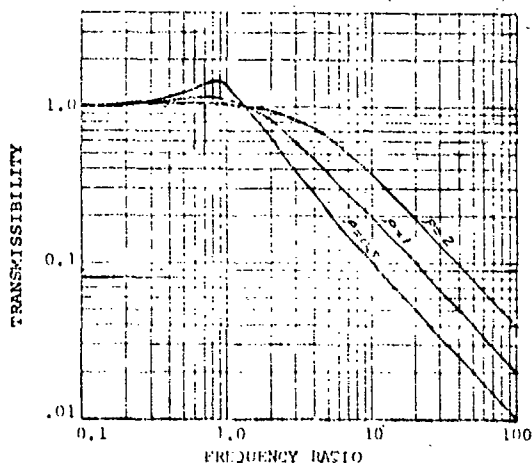


Figure 5b; Response curves of classical isolator

The governing equations for the model in Figure 4 are:

$$\begin{bmatrix} M & 0 & 0 \\ 0 & \alpha M & 0 \\ 0 & 0 & 0 \end{bmatrix} \begin{bmatrix} \ddot{x}_1 \\ \ddot{x}_2 \\ \ddot{x}_3 \end{bmatrix} + \begin{bmatrix} \beta C & -\beta C & 0 \\ -\beta C & (\beta + \gamma)C & 0 \\ 0 & 0 & C \end{bmatrix} \begin{bmatrix} \dot{x}_1 \\ \dot{x}_2 \\ \dot{x}_3 \end{bmatrix} + \begin{bmatrix} (U+N+1)K & -UK & -NK \\ -UK & (U+V)K & 0 \\ -NK & 0 & NK \end{bmatrix} \begin{bmatrix} x_1 \\ x_2 \\ x_3 \end{bmatrix} = \begin{bmatrix} 0 \\ \gamma C \\ -C \end{bmatrix} \begin{bmatrix} x_0 \\ \dot{x}_0 \\ \ddot{x}_0 \end{bmatrix} + \begin{bmatrix} K \\ VK \\ 0 \end{bmatrix} \begin{bmatrix} x_0 \\ \dot{x}_0 \\ \ddot{x}_0 \end{bmatrix}$$

We again define $\lambda = Z \sqrt{K/M}$ where Z is now given by $Z^2 = (U+V+\alpha+\alpha U - \sqrt{(U+V+\alpha+\alpha U)^2 - 4\alpha(U+V+UV)})/2\alpha$.

The transmissibility is:

$$T = \frac{P^2 + Q^2}{R^2 + S^2}$$

where

$$P = -2Z^2f^2 [N\alpha + 4Z^2\rho^2 (N(\beta + \gamma + \beta\gamma) + \beta + \gamma + \beta V + \gamma U)] + N(U+V+UV),$$

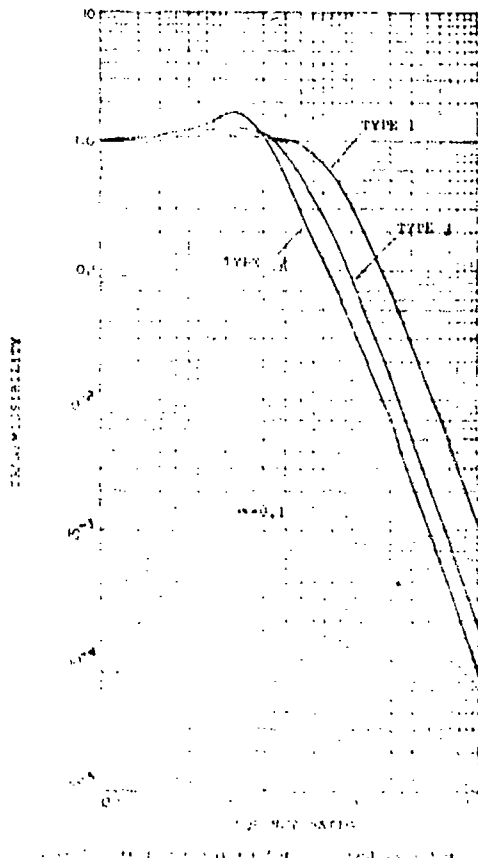
$$Q = -2Z^4f^3\rho (\alpha + N\alpha + 4Z^2\rho^2\beta\gamma) + 2Z^2f\rho [N(\beta + \gamma + U+V + \beta V + \gamma U) + U+V+UV],$$

$$R = Z^4f^4 [N\alpha + 4Z^2\rho^2 (\beta + \gamma + \beta\alpha)] + N(U+V+UV) - Z^2f^2 [N(U+V+\alpha + \alpha U) + 4Z^2\rho^2 (\beta\gamma N + \gamma + \beta N + \gamma N + \gamma U + \beta V + \beta)],$$

and

$$S = 2Z^6f^5\rho\alpha - 2Z^4f^3\rho [N(\beta + \gamma + \beta\alpha + \alpha) + U+V+\alpha + \alpha U + 4Z^2\rho^2\beta\gamma] + 2Z^2f\rho [N(\beta + \gamma + \gamma U + \beta V + U+V) + U+V+UV].$$

Although a formal seven dimensional ($\alpha, N, U, V, \rho, \beta, \gamma$) optimization study was not performed, the transmissibility index I_t was evaluated using a digital computer for a wide range of parameter values. The best curves obtained using 5000 parameter combinations for TYPES 1, 2, and 3 are shown in Figures 6a, 6b, and 6c; parameter values for these curves are given in Table 2.



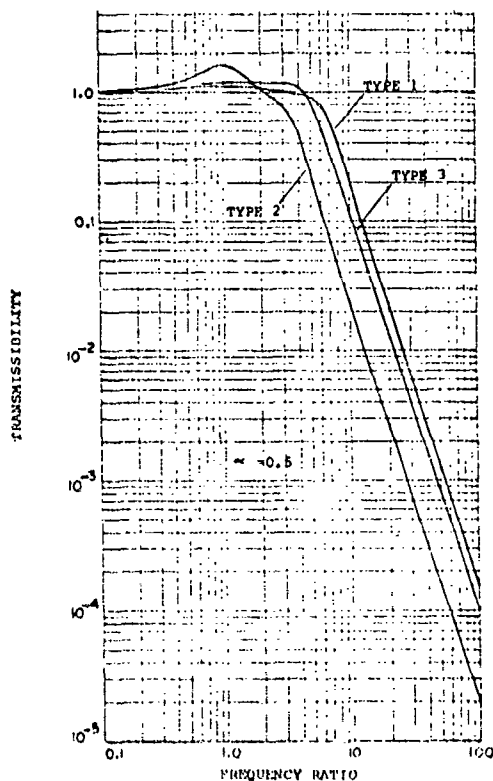


Figure 6b: response curves for combined isolator

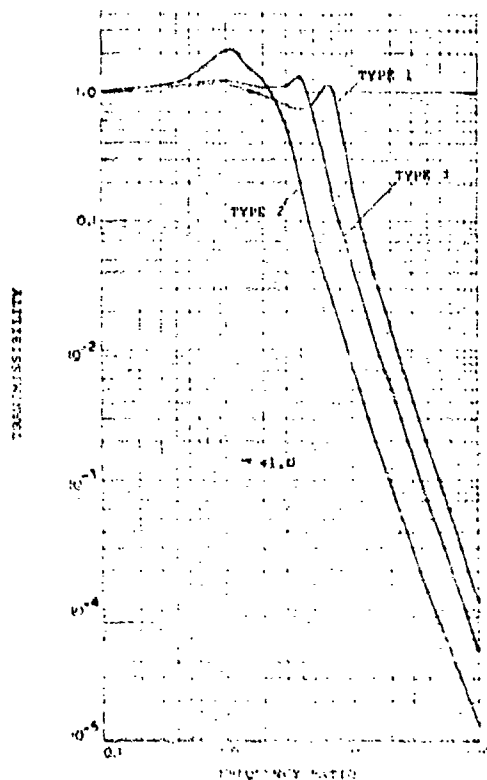


Figure 6c: response curves for combined isolator

Table 2

Fig.	TYPE	α	N	U	V	ρ	β	γ
6a	1	0.1	0	50.0	1.0	1.0	0	2.0
6a	2	0.1	0	30.0	10.0	1.0	0	1.0
6a	3	0.1	0	10.0	0.5	1.0	0	1.0
6b	1	0.5	0	50.0	3.0	1.0	0	2.0
6b	2	0.5	0	90.0	30.0	1.0	0	1.0
6b	3	0.5	0	90.0	10.0	1.0	0	2.0
6c	1	1.0	0	50.0	3.0	1.0	0	2.0
6c	2	1.0	0	30.0	20.0	1.0	0	1.0
6c	3	1.0	0	30.0	5.0	1.0	0	1.8

Note that the best response curves were obtained with $N = \beta = 0$. Thus the best performance was gained from the simplified system of Figure 7.

For this system:

$$Z^2 = \frac{(1/2\alpha) [1 + U + \alpha U + \alpha V - \sqrt{(1+U+\alpha U+\alpha V)^2 - 4\alpha(U+V+UV)}]}{1}$$

$$P = -Z^2 f^2 \alpha V + U + V + UV$$

$$Q = 2Z^2 \rho f (U + V)$$

$$R = Z^4 f^4 \alpha - Z^2 f^2 (1 + U + \alpha U + \alpha V) + U + V + UV$$

$$S = -2Z^4 \rho f^3 + 2Z^2 \rho f (U + V)$$

The best response curves obtained in this study for the simplified isolator are summarized in table 3.

It can be noted from Table 3 that for the best TYPE 2 curves, the stiffness of the left spring in Figure 7 is equal to zero.

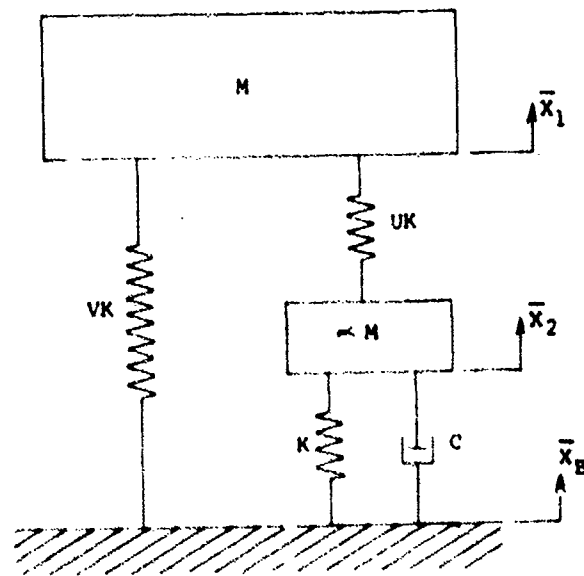


Figure 7: Simplified combined isolator

Table 3

α	U	V	ρ	T_p	T_h	Curve Type	I_t
0.1	50	1.0	2.0	1.08	1.1×10^{-3}	TYPE 1	2.41
0.2	30	0.3	2.0	1.08	5.5×10^{-4}	TYPE 1	2.17
0.5	10	0.1	2.0	1.16	1.2×10^{-4}	TYPE 1	1.84
1.0	10	0	2.0	1.19	8.2×10^{-5}	TYPE 1	1.88
0.1	3	0	1.0	1.64	8.3×10^{-5}	TYPE 2	-3.26
0.2	3	0	1.0	1.63	4.5×10^{-5}	TYPE 2	-3.54
0.5	3	0	1.0	1.64	2.1×10^{-5}	TYPE 2	-3.86
1.0	3	0	1.0	1.75	1.3×10^{-5}	TYPE 2	-4.01
0.1	50	5.0	1.0	1.24	2.2×10^{-4}	TYPE 3	-1.17
0.2	10	0.5	1.0	1.32	9.6×10^{-5}	TYPE 3	-1.37
0.5	9	0.1	2.0	1.17	1.0×10^{-4}	TYPE 3	-1.64
1.0	10	0.1	2.0	1.21	7.7×10^{-5}	TYPE 3	-1.70

Tables 4, 5, and 6 compare the response curves of the classical, the Ruzicka, the Snowdon and the combined isolator for the three types of design criteria. For each of the three types, the combined isolator displays significant improvement over both the optimum Ruzicka and the optimum Snowdon responses.

Table 4; TYPE 1 Curve Comparison

ISOLATOR	T_p	T_h	I_t
Combined ($\alpha = .5$)	1.13	1.6×10^{-4}	1.84
Combined ($\alpha = .2$)	1.08	5.5×10^{-4}	2.17
Ruzicka ($N = 8$.)	1.25	9.0×10^{-4}	3.20
Snowdon ($\alpha = .5$)	1.46	1.2×10^{-3}	4.38
Classical ($\rho = .5$)	1.47	1.0×10^{-2}	5.35

Table 5; TYPE 2 Curve Comparison

ISOLATOR	T_p	T_h	I_t
Combined ($\alpha = .5$)	1.64	2.1×10^{-5}	-3.86
Combined ($\alpha = .2$)	1.64	4.3×10^{-5}	-3.54
Snowdon ($\alpha = .5$)	5.16	4.8×10^{-5}	-1.74
Snowdon ($\alpha = .2$)	5.13	9.6×10^{-5}	-1.46
Ruzicka ($N = .5$)	5.00	1.5×10^{-4}	-1.32
Classical ($\rho = .05$)	10.06	1.0×10^{-3}	2.03

Table 6; TYPE 3 Curve Comparison

ISOLATOR	T_p	T_h	I_t
Combined ($\alpha = .5$)	1.17	1.0×10^{-4}	-1.64
Combined ($\alpha = .2$)	1.31	1.0×10^{-4}	-1.37
Ruzicka ($N = 2$.)	2.00	3.0×10^{-4}	0.48
Snowdon ($\alpha = .5$)	2.28	3.0×10^{-4}	1.04
Classical ($\rho = .25$)	2.28	5.0×10^{-3}	2.26

CONCLUSIONS

This study demonstrates that the combined isolator model (Figure 4) can be synthesized to provide superior performance compared to the optimized Ruzicka or Snowdon models. A search of 5000 parameter combinations indicated that a smaller I_t could be realized by appropriate combinations of the two models. Furthermore, the search revealed that superior performance can be gained from a model only slightly more complex than the Ruzicka or Snowdon models. For example, the isolator in Figure 7 performs better than either of the two standard models and is equally practical for certain isolator applications.

The definition of the transmissibility index, I_t , could be expanded. For some applications it may be more meaningful to modify the definition of I_t to include additional factors such as average transmissibility or the slope of the curve at high frequencies.

LIST OF REFERENCES:

- 1.) Ruzicka, J. E., "Resonance Characteristics of Unidirectional Viscous and Coulomb-Damped Vibration Isolation Systems," Journal of Engineering for Industry, Trans. ASME, November, 1967.
- 2.) Snowdon, J. C. , "Vibration and Shock in Damped Mechanical Systems," Wiley, New York, 1967, Chapters 1 - 3.
- 3.) Snowdon, J. C., "Isolation from Mechanical Shock with One- and Two-stage Mounting Systems," Journal of the Acoustical Society of America, Volume 31, July, 1959.

TRANSIENT RESPONSE OF PASSIVE PNEUMATIC ISOLATORS

Gary L. Fox
Barry Division of Barry Wright Corporation
Burbank, California

and

Edward Steiner
Barry Division of Barry Wright Corporation
Burbank, California

The dynamic characteristics of pneumatic isolators in their nonlinear region of operation has become of recent interest. In the following paper, a system of equations are derived for the general nonlinear case where the volume change is greater than approximately 10%. The effects of orifice flow damping is included, and comparison between experimental and theoretical results are presented.

INTRODUCTION

The system to be analyzed is shown in Figure 1 as a pendulum type pneumatic isolator. A column of compressed gas in the load and damping chambers supports the attached platform. An orifice plate separates the load chamber from the damping chamber. As will be subsequently shown, a force out of phase with the platform displacement is produced, due to gas flow from one chamber to the other. The phase difference results from an increase or decrease of gas in the load chamber due to the flow. The net effect of this force is observed as damping. If the relative volume change in the load chamber is large, nonlinearities introduced by pressure change and fluid flow rate cannot be ignored. A large volume change for the isolator shown would be from 1 to 8 inches relative displacement between the ceiling and platform. This type of excitation could be from an earthquake or nuclear ground shock.

Some qualitative characteristics of the isolator may be deduced from a linear analysis [1]. As the orifice varies in area from 0 to the largest maximum area, i.e., the orifice plate area, the "frequency" of vibration increases monotonically from one value to another. One would also expect a particular orifice to give the maximum damping, this maximum value increasing with the damping volume to load volume ratio. The above expectations are substantiated by theory and test results alike, if the system parameters and excitation time history are both held constant.

* Since the motion is not truly periodic, the term frequency is somewhat incorrect, but proves to be a useful concept.

FIGURE 1
Pendulum Pneumatic Isolator

ANALYSIS

If the pressure in the load chamber is taken as P_L , summing the forces on the mass yields

$$m\ddot{X} = P_L A - mg \quad (1)$$

The value for A is approximately the area of the orifice plate and $X(t)$ describes its position vs. time. Referring to Figure 2, $X(t)$ also describes the motion of the platform.

For an ideal gas, undergoing an isentropic process, the relation between the flow rate, pressure, and volume of a chamber is given by [1]

$$\frac{d}{dt} n = \frac{1}{RT} \left(P \frac{d}{dt} V + V/k \frac{d}{dt} P \right) \quad (2)$$

The volume of the damping chamber is constant. The volume of the load chamber is given by

$$V_L = V_0 + A (U - X) \quad (3)$$

Where $U(t)$ is some prescribed motion of the ceiling and V_0 is the volume of the damping chamber when the system is in equilibrium.

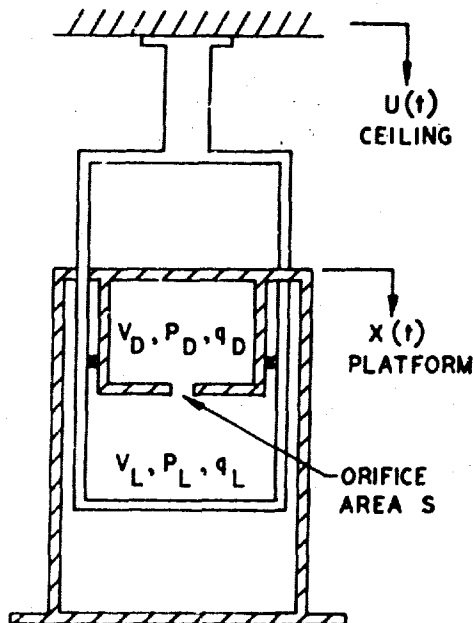


FIGURE 2
Isolator Schematic

Variable Definitions

m	Mass of Platform
g	Acceleration Due to Gravity
A	Load Area
P	Pressure
n	Moles of Gas
V	Volume
$X(t), \dot{X}, \ddot{X}$	Absolute Displacement, Velocity, Acceleration of the Platform
$U(t), \dot{U}$	Absolute Displacement, Velocity of the Ground
k	Specific Heat Ratios of an Ideal Gas
q	Gas Density
S	Orifice Area
R	Universal Gas Constant
T	Temperature, Absolute
N	Damping Volume to Load Volume Ratio

Subscripts

L	Variable Value in Load Chamber
D	Variable Value in Damping Chamber
0	Equilibrium Value of Variable
$1,2$	Variable Value in Either Chamber Where $P_1 > P_2$
$\frac{d}{dt}$	Derivative with Respect to Time

Application of Equation (2) to the damping chamber produces,

$$\frac{d}{dt} n_D = \frac{n_D}{P_D k} \frac{d}{dt} P_D \quad (4)$$

and to the load chamber,

$$\frac{d}{dt} n_L = \frac{n_L A (\dot{U} - \dot{X})}{V_0 + A(U - X)} + \frac{n_L}{k P_L} \frac{d}{dt} P_L \quad (5)$$

Since the orifice is thin, the same amount of gas enters one chamber that leaves the other.

Mathematically,

$$-\frac{dn_D}{dt} = \frac{dn_L}{dt} \quad (6)$$

For the orifice of area S , under consideration, frictionless adiabatic flow appears acceptable. Letting G_m be the mass per mole of the gas, the governing equation for the flow is [2].

$$\frac{dn_L}{dt} = \frac{q_2 S}{G_m} \left[2 P_1 q_1 \left(\frac{k}{k-1} \right) J(P_2/P_1) \right]^{1/2} \quad (7)$$

where

$$J(P_2/P_1) = \left(\frac{P_2}{P_1} \right)^{2/k} - \left(\frac{P_2}{P_1} \right) \frac{k+1}{k} \quad (8)$$

and q_1 and q_2 are the gas densities at P_1 and P_2 such that P_1 is greater than P_2 . Equations (7) and (8) apply provided the pressure ratio is greater than .53*. This condition was met for all test cases.

The direction of mass flow can be written as

$$\frac{P_D - P_L}{|P_D - P_L|} = \pm 1$$

This gives a negative flow from the load chamber if P_L is greater than P_D and positive if P_D is greater than P_L .

At equilibrium, let the total number of moles be n_0 at pressure P_0 and temperature T_0 . From the equation of state

$$n_0 = P_0 (V_0 + V_D) / RT_0 \quad (9)$$

The densities can be calculated in terms of n_L and n_0 to be

$$q_L = \frac{n_L G_m}{V_0 + A(U-X)} \quad (10)$$

$$q_D = \frac{(n_0 - n_L) G_m}{V_D}$$

If we set $Y = \frac{dX}{dt}$ a system of first order differential equations can be written as follows:

$$\frac{dY}{dt} = \frac{P_L A}{m} - g \quad (11a)$$

*For air where $k = 1.4$

$$\frac{dX}{dt} = Y \quad (11b)$$

$$\frac{dP_D}{dt} = - \frac{P_D k}{(n_0 - n_L)} \frac{dn_D}{dt} \quad (11c)$$

$$\frac{dn_L}{dt} = (\pm 1) q_2 S \sqrt{2 P_1 q_1 \left(\frac{k}{k-1} \right) J(P_2/P_1)} \quad (11d)$$

$$\frac{dP_L}{dt} = \frac{P_L k}{n_L} \left(\frac{dn_L}{dt} - \frac{n_L A(\dot{U} - \dot{Y})}{V_0 + A(U-X)} \right) \quad (11e)$$

Solution of the preceding coupled differential equations were obtained by utilizing a Runge-Cutta Fourth Order Integration Scheme. The integration increment was reduced until the solution converged. This is about 1.5 milliseconds in most cases, although for larger orifice sizes, area ratios above .05, required about an 0.1 millisecond interval for convergence. The excitation motion was taken in the downward (positive) direction as illustrated in Figure 3.

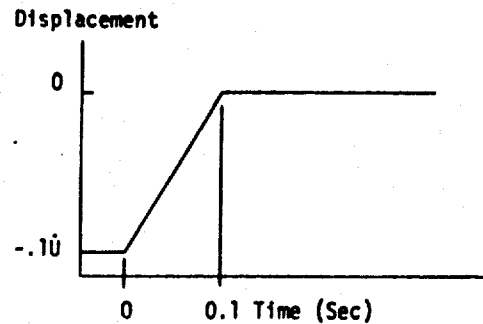


FIGURE 3

Excitation Time History

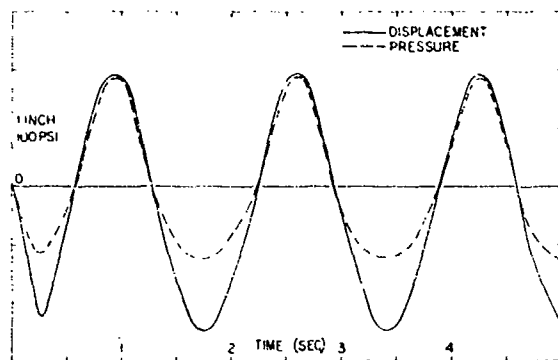
The excitation can be defined mathematically by

$$U(t) = \begin{cases} \dot{U}t & 0 \leq t \leq 0.1 \\ .1\dot{U} & .1 < t \end{cases} \quad (12)$$

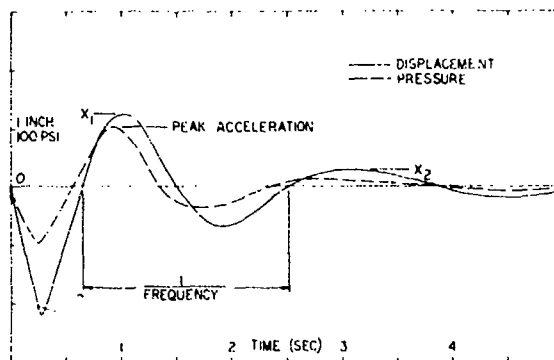
Where \dot{U} is a constant velocity. This closely resembled the test excitation.

Before proceeding to test results, it is possible to discuss further the damping mechanism, using the results of the preceding analysis.

Figure 4a shows pressure and platform displacement vs. time for an undamped system. Since pressure is directly proportional to the applied force, the displacement and force are seen to be in phase. Looking now at Figure 4b, the same system and input is used as in Figure 4a, except that an orifice for maximum damping is used. The effect of the difference in phase



(a)
Undamped



(b)
Damped

FIGURE 4

Comparison of Damped and Undamped Isolators

of the force and displacement is now apparent.

Figure 4b is used also to define some useful terms. Since frequency and damping vary with displacement, a unique position on the time history record must be selected to make the linear terminology meaningful. As the displacement approaches zero, the damping approaches zero and the frequency approaches that associated with a large orifice. This is expected, since for very low flow, the orifice offers relatively little restriction. Figure 4b shows this trend by a smaller phase angle at the lower displacements.

COMPARISON WITH TEST RESULTS

A photograph of the instrumentation is shown in Figure 5. The displacement input is achieved by releasing the pendant, whose mass is approximately one tenth of the supported mass. This results in approximately a 10 G acceleration of the pendant due to the pressure in the load chamber. As the load chamber expands, the pendant is forced downward until its motion is arrested by a deceleration mechanism when the required displacement is achieved.

Tests were conducted using 12 different orifice to load area ratios. For each area ratio there were four volume ratios, $V_D/V_L = N$, tested. The percent volume change of the load chamber for the different N's are shown in Table 1.

Reproduced from
best available copy.



FIGURE 5

Photo of Test Equipment

2.20	34	2 In.
1.64	51	4 In.
1.30	61	6 In.
1.08	67	8 In.
Volume Ratio N	% Volume Change	Displacement Input

TABLE 1

The displacement and acceleration time histories were recorded on an X-Y plotter. The system frequency was low enough that a plot could be in recorded in real time.

A comparison of measured and calculated peak accelerations are presented in Figure 6. Note that the acceleration decreases for larger N. This is due not only to increased damping,

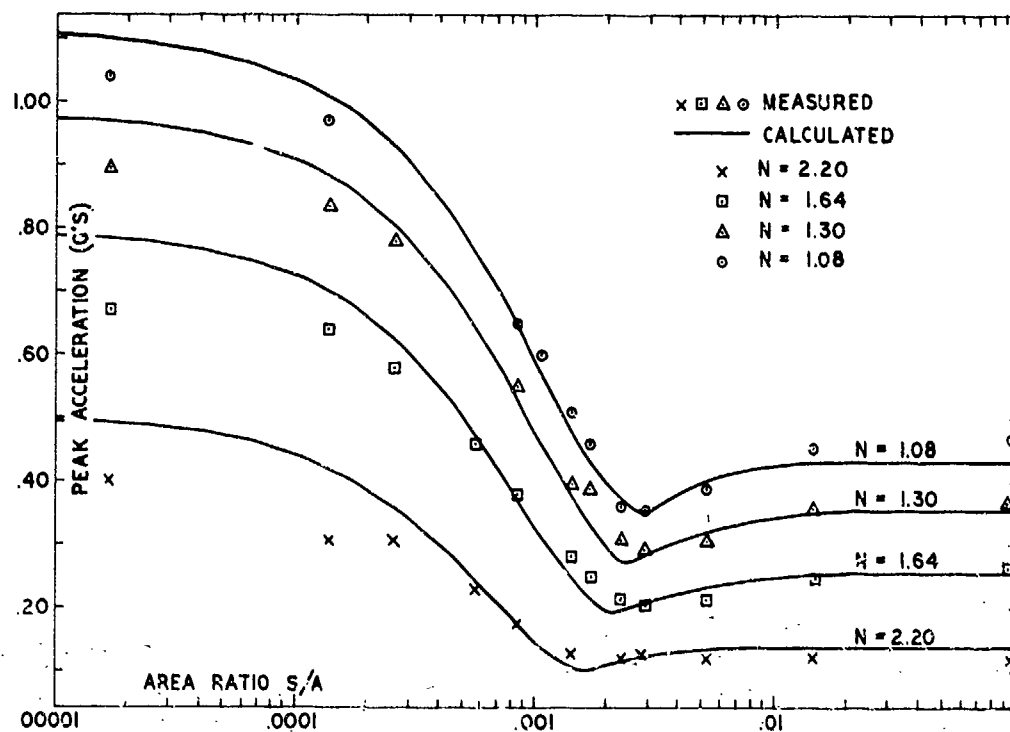


FIGURE 6
Peak Acceleration Vs. Area Ratio

but also to a smaller displacement excitation. Figures 7 and 8 compare the frequency and damping. All three figures use a common abscissa, the orifice area to load area ratio, S/A . A close correlation between test and theory can be noted in these figures, especially 6 and 7. The ordinate of Figure 8 is the damping ratio calculated from the linear system analogy by

$$\xi = \left[1 + \left(\frac{2\pi}{\ln \frac{X_2}{X_1}} \right)^2 \right]^{-1/2} \quad (13)$$

where X_1 and X_2 are as defined in Figure 4b. The authors felt reasonably justified in adding 2% critical damping to the calculations after analyzing the time history response of an undamped isolator. Amplitude ratios of the first four peaks showed that the decay was nearly exponential. If .02 is subtracted from these curves, the values will correspond to an equivalent system with no viscous damping. The addition of this damping force lowered the calculated system frequency by about 1% and the peak G-level by about 5%. Of course, actual friction forces could not be easily calculated or measured, although the effect is apparent as increased damping. Since the maximum damping appears at the expected area ratio, it seems likely the discrepancy between measured and calculated values is due to friction.

A comparison of how peak acceleration, frequency, and damping interact as the area ratio varies, is shown in Figure 9. The initial drop in peak acceleration is due to both the increase in damping and lower system frequency, the frequency effect dominating until it becomes constant. The slight rise in peak acceleration after the frequency levels out, is due to the lowering in damping as the orifice to load area ratio increases.

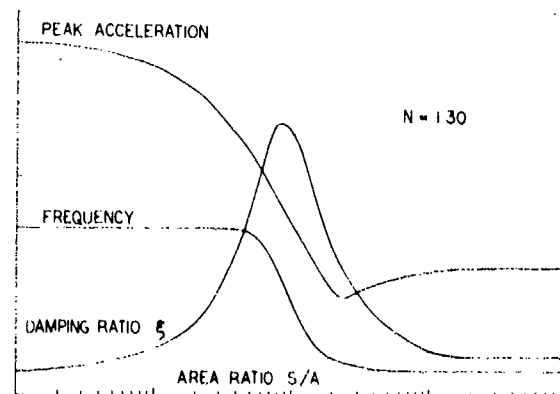


FIGURE 9

Comparison of Response Characteristics

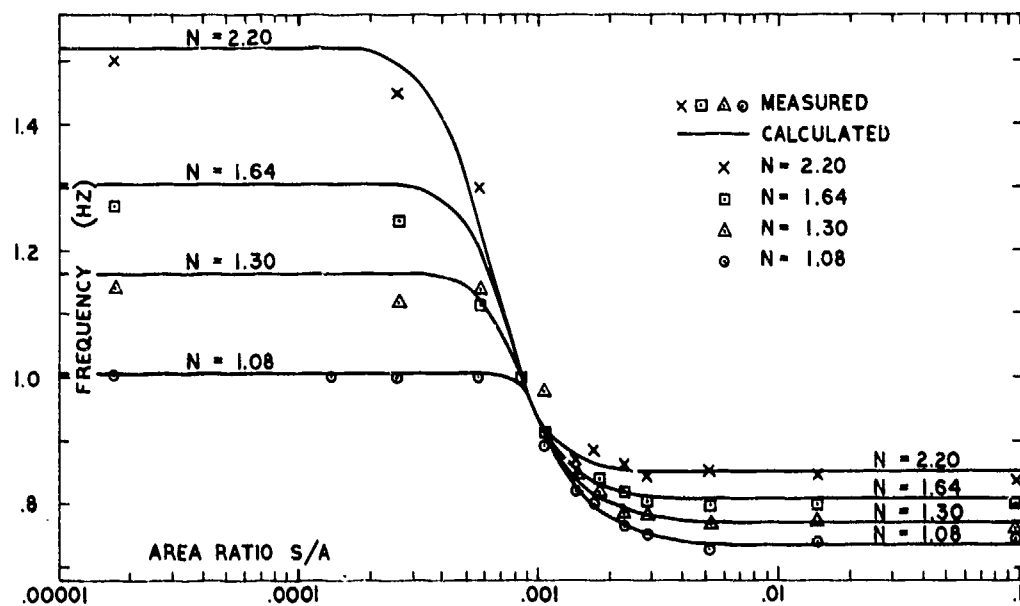


FIGURE 7
Frequency Vs. Area Ratio

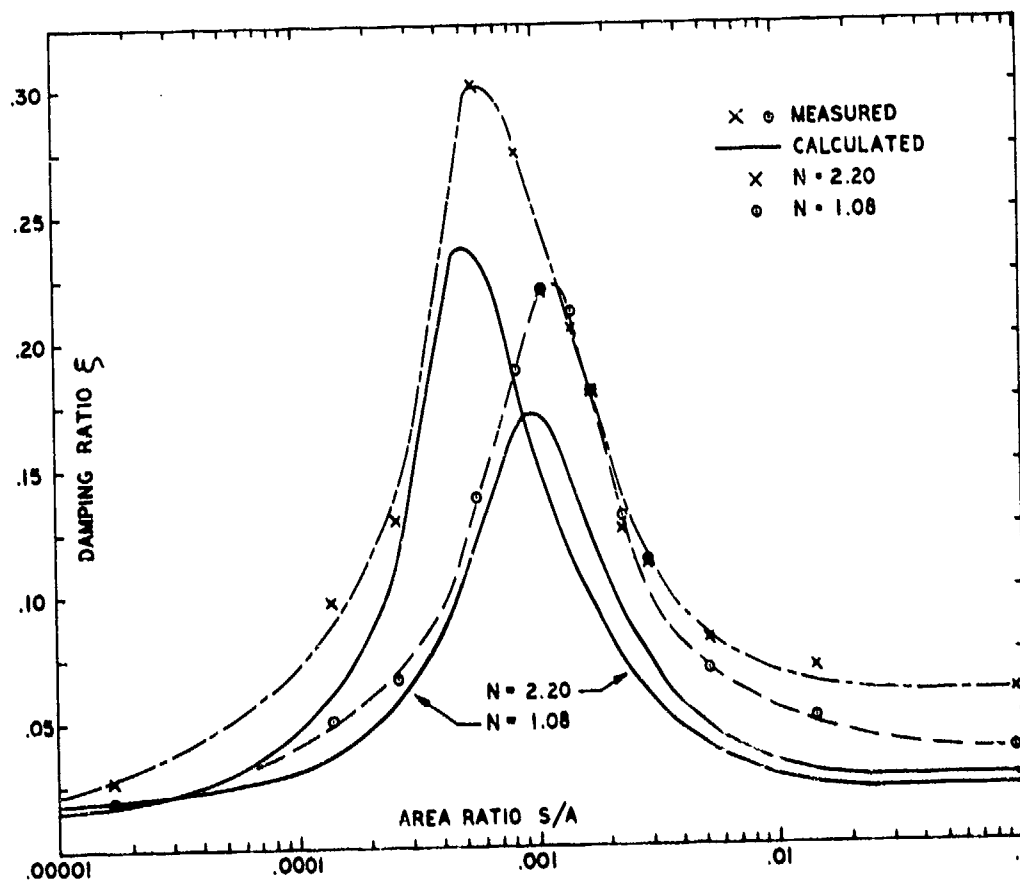


FIGURE 8
Damping Vs. Area Ratio

3,600 Pounds	12 In. ²	1.3	.0014	.204	.84	.40
20,000 Pounds	66.6 In. ²	1.4	.0012	.213	.85	.39
Supported Weight	Load Area	Volume Ratio	Area Ratio S/A	Damping Ratio	System Frequency	Peak G

TABLE II
Comparison of Different Load Areas

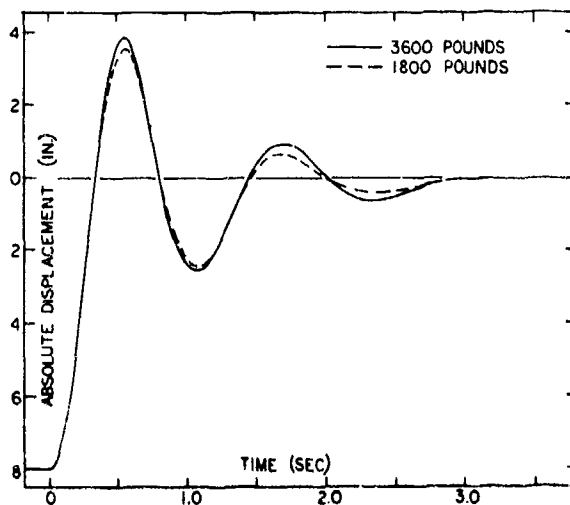


FIGURE 10
Response Comparison for Different Weights

An ideal property that these pneumatic isolators possess is their dynamic equivalence with different supported weights. An indication of this equivalence can be seen in equation (11a). As long as the ratio $P_0 A/m$ remains constant, the system will exhibit identical characteristics. This prediction is borne out by experiment. Figure 10 shows displacement-time histories of the same isolator supporting 3600 and 1800 pounds, corresponding to an equilibrium pressure of 300 and 150 psi respectively.

The slight differences in response is due only to friction effects, the same friction force being more apparent with the lighter weight system. This implies that when a mass is leveled by adjusting the pressures in the various isolators, the system will automatically be decoupled along the isolator axis.

Similar dynamic characteristics may also be obtained with totally different isolators, providing their physical parameters are similar. Comparison of the response of two isolators with different support area can be seen in Table II. The excitation displacement in both cases was 8 inches, resulting in a 60% volume change in the load chamber.

REFERENCES

1. Richard D. Cavanaugh, "Air Suspension and Servo-Controlled Isolation Systems," Chapter 33, Shock and Vibration Handbook, ed. by Harris and Crede. McGraw-Hill, New York, 1961.
2. Bird, Stewart, and Lightfoot, Transport Phenomena, pp. 480-481. John Wiley & Sons, 1960.
3. Ruzicka, J. E., and R. D. Cavanaugh, "Vibration Isolation," Machine Design, Vol. 30, October 16, 1968.
4. Kunica, S., "Servo-Controlled Pneumatic Isolators--An Advanced Concept for Vibration Isolation, Proceedings of Inst. of Environmental Sciences Annual Technical Meeting, 1965.

EXPERIMENTAL DETERMINATION OF STRUCTURAL AND STILL
WATER DAMPING AND VIRTUAL MASS OF CONTROL SURFACES

by
Ralph C. Leibowitz and Arthur Kilcullen

Naval Ship Research and Development Center
Washington, D.C.

An experiment has been designed for determining the damping constants and virtual mass for the control surface systems of USS ALBACORE (AGSS 569) and USS SAMPSON (DDG 10); theoretical methods for determining the virtual inertias (including virtual mass) of these control surfaces are also given. The theoretical foundation for the experimental design and the procedure for analyzing the experimental data to obtain the parameters are described. These damping and inertial parameters are essential to the performance of a hull-control surface vibration and/or flutter analysis.¹⁻⁵

INTRODUCTION

The solution for the vibrations and flutter characteristics of a combined hull-control surface system can be obtained if the physical and hydroelastic parameters in the equations of motion representing the system are evaluated; the theory underlying the derivation of these equations has been shown to have some degree of verification.³ The method of evaluation of physical (mass-elastic) parameters associated with equations of motion of the hull alone is given in Reference 5. The method of evaluation of certain hydroelastic parameters for the control surface (e.g., rudder and/or diving plane) is given in reference 2.

The primary objective of this report is to add to the method of evaluation of the control surface parameters by describing experimentally based methods for computing damping constants and virtual mass for the control surface. In addition, certain equations are presented for calculating the virtual inertias (including virtual mass) by theory alone. The entire procedure is demonstrated for the case of two ships, USS ALBACORE (AGSS 569) and USS SAMPSON (DDG 10).

SUMMARY OF RESULTS

Equations and other identifying material for the experimental determination of control surface* and hull motions, the logarithmic

decrement and damping for these motions, the virtual mass and virtual mass moments of inertia of the control surface about axes through its center of mass are given in Table 1. These motions are due to an impulsive load acting on the control surface. The equations developed are applicable for motion associated with a single frequency; thus, each modal frequency of a complex motion is treated in turn. Extension to several superposed modes is discussed in the text.

DESCRIPTION OF RUDDER-STOCK-HULL SYSTEM

The representation of a rudder-stock-hull system† and its motions is based on the following assumptions:

1. The rudder is considered to be a rigid body attached to a flexible stock, which, in turn, is attached to a flexible hull. The point of attachment of the rudder to the stock will be different for each rudder system. In this report it will be assumed to be located at the top of the rudder. (For the ships tested here, the stocks were welded into the control surfaces such that the portion of the stock within the surface moves rigidly with the surface).

2. Of the six possible motions of the rudder associated with a symmetrical rigid rudder-flexible stock system, only three

* The control surfaces considered here are rudders and stern planes.

† Stern plane-hull systems are similarly treated.

contribute significantly to the total coupled athwartship motion. These are the rotations γ and α about the z- and x-axes and the translation v along the y-axis respectively (see Figure 1).

3. Small vibration theory is applicable, i.e., the system is linear for small angular and translational displacements.

4. The combined still water and structural damping force is proportional to the velocity of the rudder, i.e., viscous damping is assumed.

THEORETICAL ANALYSIS

The analysis underlying the derivation of the equations in Table 1 is described in this section.

Figures 1 and 2 are schematic diagrams of the instrumentation of the rudder-stock-hull system. The d_i 's in these figures represents the displacements of the system at the points indicated when the rudder-stock-hull system is set into free vibration by an impulsive loading on the rudder. Kinematic relationships between the displacements d_i and the corresponding components for rotational and translational motions γ , α , and v about the z- and x-axes respectively and along the y-axis, are derived in Appendix A. The resulting equations (1) through (3b) are summarized in Table 1.

The preceding analysis for the rudder vibration includes the contributions of the hull motion for during a vibration of the entire rudder-hull system, the flexible hull also translates and rotates along the y- and about the x- and z-axes, respectively. Hence, the hull's motional contribution must be subtracted from the recorded rudder motions in order to determine the motions of the rudder relative to the hull; this is equivalent to finding the motions of the rudder system (rudder and effective length of stock) attached to a rigid hull. The hull motions are considered to be applied to the rudder stock at the effective points of attachment of rudder stock to hull. These points of attachment for bending and torsion of the rudder stock which permit us to compute corresponding effective lengths of the stock are determined from the recorded data by extrapolation and interpolation methods as explained in Appendix B.

The effects of motions of the tiller and steering system upon the total recorded motion of the rudder have not been included in this

analysis. In some problems, these effects may be significant enough to require an extended treatment of the analysis presented here. The methods basic to this extension will be similar to those given in the text; the detailed procedure will depend upon the particular application, i.e., the particular hull-rudder system.

Equations (4) - (6b) of Table 1, which are derived in Appendix C, define the logarithmic decrements of the γ , α , and v motions corresponding to the transient displacements of the rudder system including the contributions of the hull motions.* Similarly, Equation (7) is the decrement for the coupled γ , α , v motions.† The corresponding decrements for the motions of the rudder relative to the hull are given by Equations (10) - (12) using Equations (8) and (9) and the procedure given in Appendix B for obtaining γ_h ; see Appendix C. Equation (13), also derived in Appendix C, defines the modal decrement of the rudder motions relative to the hull.

The method for determining the zero speed damping parameters of the rudder and the relationship between these parameters and the logarithmic decrements of the rudder is now treated (see Appendix D).

Page 78 of Reference 1 gives the several damping parameters associated with motions $\dot{\gamma}$ and $\dot{\alpha}$ and \dot{v} of the rudder. Of these several parameters, only the parameters C and c associated with rudder translation athwartship (along y-) and rudder rotation about an axis parallel to the stock (about z-) have been considered as significant and are therefore the only ones included in the equation of motion (62a, b) of Reference 1, which are the basis for determining the damping parameter values here.

Since we are considering the damping of the system in still water, terms containing S (ship speed) in Equations (62a, b) are equated to zero. Also, since damping in the α degree of freedom will be assumed to be negligible, Equation (62c) is omitted from the discussion. Equations (62a, b) may be used directly to obtain (at zero speed) the parameters C and c in terms of the variables γ , α , v , γ_b , α_b , v_b and certain geometrical and physical parameters.

The variables are obtained from the test records and the constants are determined by the methods of Reference 2 and/or from measurements. It may turn out that when variables obtained from one portion of the records are inserted into these equations, the calculated

* The logarithmic decrement corresponds to a single mode of vibration (i.e., decaying sinusoidal oscillation). Consideration for several superposed modes is discussed in the text. To obtain each decrement, we look at the motion in one degree of freedom at a time, ignoring the motions in the other two degrees of freedom.

† Here the logarithmic decrement is for one mode of vibration of the rudder system including the contributions of the motions γ , α , and v in the three degrees of freedom.

values of C and c are different from those corresponding to the variables obtained from another portion of the record. This indicates that $C=C(t)$ and $c=c(t)$. If the variation is small, then C and c may be sensibly considered to be constant for convenience. If the record shows that the modes are discrete at different times, then each mode may in turn be treated as predominant over the pertinent time interval and substitution of the variables will show if C and c vary with the mode (or frequency), i.e., whether $C=C(\omega)$, $c=c(\omega)$. Appendix D gives the derivation of the resulting Equations (14) and (15) which are based upon Equations (62a, b) of Reference 1. In these equations,

$-\frac{\mu}{\omega} = \frac{\delta}{2\pi} = \frac{C}{C_c} = \frac{c}{c_c}$ (see Reference 3) where δ is the logarithmic decrement of the waveform, μ is the real part of λ indicating the degree of damping, and ω is the imaginary part of λ which is the circular frequency of vibration; i.e., $\lambda = \mu + j\omega$; δ , ω (and hence μ) are directly obtainable from the waveform on a given record for a particular mode of vibration. C_c and c_c are critical damping constants for the translational and rotational degrees of freedom, respectively.

If all modes, or two of the three modes, persist simultaneously, then each mode may be filtered in turn from a taped signal and an oscillogram of the filtered mode signal can be obtained. Thus postulating that $v(t)$ may be represented by:

$$v(t) = \sum_{i=1}^3 v_i e^{\lambda_i t}$$

where

$$\lambda_i = \mu_i + j\omega_i \quad i = 1, 2, 3$$

Then if the i^{th} mode predominates for a particular period of time or is filtered out of the taped signal, the equation for $v(t)$ becomes

$$v(t) = v_i e^{\lambda_i t} \quad i = 1, 2, 3$$

for the corresponding signal and similarly for the variables γ , a , v_b , γ_b , a_b (see Appendix N).

Equations (62a, b) of Reference 1 may be solved to obtain C/C_c or $\frac{\delta}{2\pi} = -\frac{\mu}{\omega}$ by the analytic procedures of Reference 3.* This value may be compared with C/C_c or $c/c_c = \frac{\delta}{2\pi}$ obtained from the measurements described above and in Appendix C. Close agreement would indicate that the computation for C/C_c and c/c_c from experimental data as prescribed here is valid. It should be noted that for a particular mode, the decay ratio for translational motion v alone is the same as that for rotational motion

γ alone or a alone and is also the same as that for the total displacement (at any point on the rudder) consisting of contributions of the coupled motions γ , a , and v .

When more than one mode is present simultaneously, each contributes to the v (or a) motion. The motion in each degree of freedom may then be considered to be the sum of sinusoids with frequencies corresponding to the modes present. Note that the phase relationships are also included in the equations.

Thus in general

$$v(t) = \sum_{i=1}^3 e^{\mu_i t} (v_{i,1} \sin \omega_i t + v_{i,2} \cos \omega_i t)$$

$$v_b(t) = \sum_{i=1}^3 e^{\mu_i t} (v_{i,b1} \sin \omega_i t + v_{i,b2} \cos \omega_i t)$$

$$a(t) = \sum_{i=1}^3 e^{\mu_i t} (a_{i,1} \sin \omega_i t + a_{i,2} \cos \omega_i t)$$

with similar expressions for a_b , γ , γ_b . The equations for these variables and their derivatives may then be substituted into Equation (62a, b) and C_i and c_i found in a manner similar to that given above for $i = 1$ or 2 or 3 only. The resulting equations which are more complex will not be given here but can be easily obtained.

The mass and flexibility of the rudder can be calculated using the methods of References 4 or 5. Extension of the damping computation to include certain damping constants omitted in deriving Equation (62) of Reference 1 can be performed using the methods of Reference 6.

TEST PROCEDURE

The computation of the parameters c , C , δ , C/C_c , etc., requires that experimental data be obtained for insertion into the equations of Table 1. This section describes the test procedure for obtaining such data.

Figures 1 and 2 show the schematic diagrams of the rudder, rudder stock, and hull with accelerometers at locations d , which are directed normal to the vertical centerplanes of the rudder-stock and hull. Care must be taken to locate (i.e., compute prior to testing) the exact center of mass of the rudder in order to accurately determine the rotational and translational components of the total measured motion of the rudder.

The rudder-hull system was set into free

* Details of the method of solution of the decay ratio C/C_c and application to actual problems are given in this reference.

† See footnote in Appendix A.

vibration by impulsive excitation of the rudder. The excitation was produced by a snub-nosed ram capable of creating an impulsive load of large magnitude with duration sufficient to excite the lower modes of vibration. Excitations are produced at different locations on the rudder in order to agitate all (lower) modes of interest.

The vibratory responses picked up by the accelerometers are converted into electrical signals which are then amplified and recorded onto magnetic tape or oscillograph charts. Figures 3a and 3b are block diagrams of the recording systems used in ALBACORE and SAMPSON tests, respectively.

In general, such tests are to be performed in air and in water.

RESULTS

The results of analyzing the data obtained from zero speed tests in drydock flooded and unflooded on ALBACORE and SAMPSON are shown in Table 2. The methods of data analysis yielding these results are now discussed.

ALBACORE RESULTS

A typical trace taken from ALBACORE records is shown in Figure 4. Analysis was made for the 20-cps stern plane vibrations (in air), for the 24.5-cps rudder vibration (in air), and for the 13-cps rudder vibration (in water); these are the predominant frequencies. No measurements were made on the submerged stern planes.

Since no hull motions were recorded for which γ_b , a_b , and v_b could be determined, computations for δ_γ , δ_a , and δ_v only were made using Equations (4), (5), (6a), and (6b) of Table 1. Equation (i) was used to compute δ_{modal} for each gage; these values were averaged to give one value of δ_{modal} for the entire system, i.e., one value for the rudder system and one for the stern plane system.

The records were analyzed by fairing a curve through the peak amplitudes of the oscillograms and by measuring peak amplitudes at the same instant of time of all traces obtained from a particular impulsive excitation.* The faired curves represent the envelope of a decaying sinusoidal wave. Values of γ , a , and v for several peak amplitudes of the trace were obtained by substituting the measured values of d_i corresponding to fixed times into Equations (1) - (3b). Ratios of the successive values of γ , a , and v were formed, and the logarithmic decrements for these ratios were computed. Approximately 10 to 15 values for the decrement of γ , a , and v

were averaged to yield δ_γ , δ_a , and δ_v from a single record (i.e., single excitation).

Since the rudder and stern plane stocks were not accessible for instrumentation during the tests, the effective lengths of stock, L and L_T could not be computed. Also, values for the hull motions γ_b , a_b , and v_b , required for the computation of C and c by Equations (14) and (15), were not available. However, since phase angles between corresponding rudder and hull motions (e.g., between v and v_b , etc.) were observed to be immeasurably small, the terms with subscript 2 (e.g., a_2 , a_{b2} , etc.) in the right members of these equations may be ignored, thereby reducing the equations to the simpler forms of Equations (16) and (17). Equation (16) is independent of γ_b , a_b , and v_b as is Equation (17) also if we assume $\gamma_{b1} = 0$ for convenience of calculation. Under these conditions, damping values C and c in air and in water were computed (see Table 2). In computing the damping values C and c , average values of the decrements $\delta_v = (\delta_v)_{\text{ave}}$ and $\delta_\gamma = (\delta_\gamma)_{\text{ave}}$ are used.

Virtual mass and mass moments of inertia were computed for the rudder using Equations (18) - (21) (see Table 1) and are tabulated in Table 2. Similar results were not obtained for the stern plane since they were tested in air only.

SAMPSON RESULTS

Analyses were made on the two most readable records from the SAMPSON trials.⁷ Both of these were for in-water trials. In-air testing of the SAMPSON rudder provided no usable data since the lower modes of vibration were not excited sufficiently. Hence no computations were made for virtual mass or virtual mass moments of inertia using Equation (18) which requires in-air frequency data. The total mass of the rudder in translation was obtained by adding the virtual mass computed by Equation (19) to the structural mass.

Plots were made of the total displacement of each gage from both records and are shown in Figure 5. The figure shows that there is no significant rotation of the SAMPSON rudder because all displacements appear to have the same amplitude. As a result, the total motion measured by each gage was not separated into its γ , a , and v components.

Further, since the hull displacements were nearly equal to the values of the rudder displacements, hull contributions to the total recorded motion were not extracted. The analysis thus consisted of determining the logarithmic decrement from each gage for both runs. This amounts to determining δ_{modal} for

* The peak amplitudes could be measured simultaneously because phase shifts on the rudder were found to be negligible.

each gage. The results of the analysis for the predominant frequency of 2.18-cps are presented in Table 2.

DISCUSSION

Table 2 shows that the procedure developed for computing the logarithmic decrements yields results which do not vary widely. It, therefore, provides reasonable (i.e., order of magnitude) estimates for the decrements and corresponding damping values for the control surfaces useful for ship vibration and flutter analysis. A similar statement may be made for computation of the virtual mass (see Table 2d).

Since the rudder is attached through a flexible stock to a flexible hull, the frequencies in Equation (18) will depend on the mass-elastic properties of the hull as well as on the properties of the rudder-stock system. Apart from hull effects, the frequency data used in Equation (18) correspond to the (measured) coupled x , y , z motions of the rudder whereas strict application of Equation (18) requires that frequency data associated with uncoupled cantilevered motions be used (see Appendix E). Nevertheless, transgression of this rigorous application of Equation (18) incurred only a 10 percent deviation from the average of the results obtained by use of Equations (18) and (19); (see Table 2d).

In general, fluctuations in the results may be largely attributed to difficulty in reading records accurately due to a variety of causes.

For SAMPSON data, an attempt was made to filter the frequencies of interest from the total recorded signal because so many frequencies were excited. Figures 6a, b are typical traces of SAMPSON records. Figure 6a shows the total recorded response of a given gage and Figure 6b shows the filtered response; the center frequency of the filter is 2.18-cps. Note that prior to time t_0 , the point in time when the rudder is impulsively excited, a signal of the same frequency, 2.18-cps, occurs in the trace. This signal apparently persists after impact and is superposed upon the decay curve. The source of this signal is uncertain.

We surmise that the predominant signals with the frequency of 2.18-cps correspond to horizontal bending vibration of the hull for the following reasons. The displacements of the rudder and stock and hull are all approximately equal. The hull gage at Location 5 (Figure 1) which is approximately 91 in. forward of the rudder stock recorded approximately the same response as the rudder stock gages. Moreover, the 2.18-cps frequency is well within the region of lateral vibration of ships, particularly destroyers, whereas the fundamental measured frequencies of some other rudder systems is in the region of 1-8-cps.^{9,10}

It should be noted that the fundamental frequency observed for ALBACORE is considerably higher.

Future simplification of data analysis should take advantage of the fact that any decrement δ_i can be determined: (1) graphically from oscillographic or magnetically taped records of the signals $d_1(t)$, $d_2(t)$, etc., or by (2) devising electrical circuitry to record the values of the decrements directly either as soon as the signals are measured or in the laboratory using tape stored signal data.

CONCLUSIONS

Based on the foregoing analysis and test results, the following conclusions have been reached:

1. It appears likely that reliable results for damping coefficients and inertial parameters for control surfaces can be obtained using the methods presented here.

2. Use of modal analysis equipment (filters) which gives the frequency, logarithmic decrement, and damping for each mode and the relative phase between any two vibratory displacements at different points on a structure, for a particular mode, is vital for the practical application of the present analysis.¹¹⁻¹⁴

3. The test procedure must be improved. Impulsive loading should be controlled so that all significant modal frequencies of the control surfaces are excited (see DISCUSSION). Extraneous noise and vibration effects on the recorded data must be eliminated or minimized by controlling the source of the trouble and/or improving the instrumentation.

RECOMMENDATIONS

1. Further tests on control surfaces of surface ships, submarines, hydrocrafts, etc., should be conducted in accordance with the procedure presented here to obtain realistic damping and inertial parameters for these surfaces.

2. The analysis should be extended to include the mass-elastic effects of tiller connections, links, and other steering gear machinery on the vibrational response of the system.

3. Analysis equipment should be developed or purchased in order to obtain the desired results from the recorded data.

ACKNOWLEDGEMENTS

The authors are grateful to Mr. G. Franz, Mr. E. Noonan and Dr. E. Buchmann for constructive criticism. Dr. Buchmann also helped

in the planning of the tests. The authors wish to express their appreciation to Mr. R. Price for conducting the vibration test on ALBACORE and to Mr. R. M. Murray for conducting the vibration test on SAMPSON. We are also grateful for the assistance of LCDR W. A. Greene, Captain of the ALBACORE, and his crew and of CDR F. W. Isen, Captain of the SAMPSON, and his crew in conducting these tests. Mr. Max Morris reduced the damping data for ALBACORE, and Mr. Ed Hoyt evaluated the damping data for SAMPSON.

APPENDIX A

DEVELOPMENT OF EQUATIONS FOR DETERMINATION OF RUDDER MOTIONS γ , α , v

Figure 1 is a diagram of the gage layout on the rudder. The gages are placed along x-, z-axes whose origin is at the center of mass of the rudder.* Thus, x_1 is the distance between the center of mass and Gage 4 which measures displacement d_4 . It is assumed that no α contribution to the total measured motion of a gage exists on the horizontal axis (x-axis) through the center of mass. Likewise, no γ contribution to the total measured motion of a gage exists on the vertical axis (z-axis) through the center of mass. Only motions in the γ , α , and v degrees of freedom contribute significantly to the total coupled athwartship motion of the rudder. Referring to Figure 1,

$$d_4 = v + x_1 \gamma$$

$$d_8 = v - x_2 \gamma$$

from which

$$\gamma = \frac{1}{x_1 + x_2} (d_4 - d_8) = K_1 (d_4 - d_8) \quad [A-1]$$

where $K_1 = \frac{1}{x_1 + x_2} = \text{constant}$

likewise $d_2 = v - z_1 \alpha$

from which $\alpha = \frac{1}{z_1 + z_2} (d_6 - d_2)$

$$= K_2 (d_6 - d_2) \quad [A-2]$$

where $K_2 = \frac{1}{z_1 + z_2} = \text{constant}$

From the equations leading to [A-1] and [A-2] we have

$$v = K_3 (d_2 + K_4 d_6) \quad [A-3a]$$

or

$$v = K_5 (d_4 + K_6 d_8) \quad [A-3b]$$

where

$$K_3 = \frac{z_2}{z_1 + z_2}$$

$$K_4 = z_1/z_2$$

$$K_5 = \frac{x_2}{x_1 + x_2}$$

$$K_6 = x_1/x_2$$

* Prior to the conduction of the test, the centers of mass of the rudder in air and in water must be computed. The center of mass in water is computed to be the center of mass of the combined rudder-rudder stock system including the virtual mass which is approximated by the volume of water contained in an ellipsoidal cylinder of revolution taken about a rudder axis (see Reference 4, page 12). The virtual mass computed in accordance with the method of this reference (Equation (19), Table 1) may be compared with the experimental value determined from the data by use of Equation (18), Table 1.

APPENDIX B

DETERMINATION OF EFFECTIVE LENGTHS OF CONTROL SURFACE STOCK

Assume a set of cartesian coordinate axes (x', y', z') with the origin O' at the point of attachment of the control surface to the stock (usually at the top of the control surface) such that the z' -axis runs through the center of the control surface stock (see Figure 7); note $z' = z - b$ and $x' = x - h$. For simplicity, we will call our control surface a rudder. All equations and statements apply equally well to stern planes.

Referring to Figure 8, define $(d_{v,a})_{7-11}$ as the displacement of the stock between Gage Positions 7 and 11 due to the a and v motions of the stock. Also, let γ_{7-11} be the γ rotation of the stock between Gage Positions 7 and 11. Then,

$$d_7 = (d_{v,a})_{7-11} + x_7 \gamma_{7-11} \quad [B-1]$$

$$d_{11} = (d_{v,a})_{7-11} - x_{11} \gamma_{7-11} \quad [B-2]$$

From [B-1] and [B-2], noting that $x_7 = x_{11}$, we have

$$\gamma_{7-11} = K_7 (d_7 - d_{11}) \quad [B-3]$$

$$\text{where } K_7 = \frac{1}{2x_7} = \frac{1}{2x_{11}} = \text{constant}$$

$$\text{Similarly } d_{12} = (d_{v,a})_{10-12} + x_{12} \gamma_{10-12} \quad [B-4]$$

$$d_{10} = (d_{v,a})_{10-12} - x_{10} \gamma_{10-12} \quad [B-5]$$

from which (since $x_{10} = x_{12}$),

$$\gamma_{10-12} = K_8 (d_{10} - d_{12}) \quad [B-6]$$

$$K_8 = \frac{1}{2x_{10}} = \frac{1}{2x_{12}} = \text{constant}$$

From Equations [B-1], [B-2], [B-4], and [B-5] we obtain

$$(d_{v,a})_{7-11} = \frac{1}{2} (d_7 + d_{11}) \quad [B-7]$$

$$(d_{v,a})_{10-12} = \frac{1}{2} (d_{10} + d_{12}) \quad [B-8]$$

From Figure 1,

$$d_3 = (d_{v,a})_{1-3} + x_3 \gamma_{1-3} \quad [B-9]$$

$$\text{and } d_1 = (d_{v,a})_{1-3} - x_6 \gamma_{1-3} \quad [B-10]$$

From Equations [B-9], and [B-10] we have

$$\gamma_{1-3} = K_{14} (d_3 - d_1) \quad [B-11]$$

and

$$(d_{v,a})_{1-3} = K_{12} (d_3 + K_{13} d_1) \quad [B-12]$$

$$\text{where } K_{12} = \frac{x_6}{x_5 + x_6} = \text{constant}$$

$$\text{and } K_{13} = \frac{x_5}{x_6} = \text{constant}$$

$$K_{14} = \frac{1}{x_5 + x_6} = \text{constant}$$

Figures 8 and 9 are plots of $(d_{v,a})_{z'}$ and γ versus z' respectively obtained from the values calculated by the above equations. For a rigid control surface, γ has a constant value, i.e., the value of γ obtained by Equation [A-1] should equal that obtained by Equation [B-11]. Both $(d_{v,a})_{1-3}$ and γ_{1-3} are plotted at $z'=0$.

In Figure 8, the curve of $(d_{v,a})$ against z' approaches the straight line whose slope is the tangent of $\frac{a}{b} + a_b$. This line appears as the dotted line in Figure 8. The angle this makes with the vertical (parallel to z') is a_b . The method of measuring a_b and the location of this line in the plane will be discussed later in this appendix. These straight lines (or asymptotes) remain straight for increasing z' since they represent the rigid body motions and torsional motions of the hull. Bending of the hull in the horizontal plane would give rise to additional curvature of the curve in Figure 8 at a value of z' in the vicinity of the hull.

The quantities γ_h , z'_T , and z'_B are measured from the plots of Figures 8 and 9; z'_T and z'_B are the distances from the point of attachment of the rudder stock to rudder (usually, although not always, at the top of

the rudder) to the point of attachment of stock to hull in torsion and bending, respectively. The measured values of γ_b will be used in subsequent calculations.

When γ is plotted against z' , it is expected that a point will be reached at which the curve is vertical. The value of γ at this point will be called γ_b . The quantity L_T is the distance along z' from the point on z' where $\gamma = \gamma_b$ to the center of mass of the rudder. It is computed by measuring z' from $z' = 0$ to z' at $\gamma = \gamma_b$ and adding the quantity b (see Figures 8 and 9) to this result, i.e., $L_T = z'_T + b$.

In the plot of $d_{v,a}$ versus z' , note that the point where the curve $d_{v,a}$ versus z' becomes linear is the point of attachment of the rudder stock to the hull in bending. The value of $d_{v,a}$ at this point, which is obtained by extrapolation (or interpolation), will be called $(d_{v,a})_{R-H}$. The linear portion of the curve makes an angle a_b with the vertical (see Figure 8); a_b will be determined below. The value of L is the distance along z' from the point on z' where $d_{v,a} = (d_{v,a})_{R-H}$ to the center of mass of the rudder. It is computed by measuring z' from $z' = 0$ to z' at $d_{v,a} = (d_{v,a})_{R-H}$ and adding the quantity b (see Figures 7 and 8) to this result, i.e., $L = z'_B + b$.

The hull angle of torsion, represented by a_b , may be determined by the following method (see Figures 2 and 10).

The ship is instrumented with two accelerometers (Gages 13 and 14) to measure the athwartship motions of the section of the hull in line with the rudder stock and two accelerometers (Gages 15 and 16) to measure the vertical motions of the hull in the transverse plane which contains the rudder stock. In Figure 10 let,

L_P = vertical distance between Gage Locations 13 and 14,

L_H = vertical distance between Gage Location 13 and the center of mass of the rudder,

y_P = horizontal distance between Gage Locations 15 and 16, and

$d_{13}, d_{14}, d_{15}, d_{16}$ = displacement of the hull at Gage Locations 13, 14, 15, and 16, respectively.

The solid line in Figure 10 represents the undisturbed position of the ship and the dotted line represents the horizontal torsion-bending motions of the ship after impact on the control surface, assuming the control surface-stock system remains completely rigid with respect to the hull, so that the motion

of the control surface due to the motion of the hull may be determined.

$$\text{Then } a_b = \frac{(d_{13} - d_{14})}{L_P} \quad [B-13]$$

$$\text{and } a_b = \frac{(d_{16} - d_{15})}{y_P} \quad [B-14]$$

This value of a_b determines the slope of the linear part of the curve in Figure 8. Hence, the displacement of the center of mass of the control surface due to the coupled torsion-horizontal-bending motions of the hull is given by (see Figure 10);

$$d_{R-H} = d_{13} + L_H a_b - h\gamma_b \quad [B-15]$$

Substituting Equation [B-13] into the above expression, Equation [B-15] may be written as

$$\begin{aligned} d_{R-H} &= d_{13} + \frac{L_H}{L_P} (d_{13} - d_{14}) - h\gamma_b \\ &= \left(1 + \frac{L_H}{L_P}\right) d_{13} - \frac{L_H}{L_P} d_{14} - h\gamma_b \end{aligned}$$

$$\text{or } d_{R-H} = K_9 d_{13} - K_{10} d_{14} - h\gamma_b \quad [B-16]$$

$$\text{where } K_9 = 1 + \frac{L_H}{L_P} = 1 + K_{10} = \text{constant}$$

$$K_{10} = \frac{L_H}{L_P} = \text{constant}$$

Also, by using Equation [B-14],

$$d_{R-H} = d_{13} + L_H \frac{(d_{16} - d_{15})}{y_P} - h\gamma_b$$

$$\text{or } d_{R-H} = d_{13} + K_{11} (d_{16} - d_{15}) - h\gamma_b \quad [B-17]$$

$$\text{where } K_{11} = \frac{L_H}{y_P} = \text{constant}$$

In determining the motion of the rudder relative to the hull in the y -direction when a flexible stock is considered, the displacement of the hull must be accounted for because the displacement on the hull is included in the

the rudder motions measured by the gages on the rudder. Referring to Figure 10, we may define the motion of rudder relative to the hull at the Mth gage position by

$$d_{M_R} = d_M - (d_{13} + L_M a_b - x_M \gamma_b) \quad [B-18]$$

where d_M is the motion of the Mth gage which includes the contribution of the hull motions as well as the effects of rudder stock flexibility and where L_M is the vertical distance between the Mth gage and Gage 13 and x_M is the horizontal distance between the Mth gage and the rudder stock (x_M is positive when the Mth gage is aft of the stock and negative if forward of the stock).^{*} If the contribution of the term $x_M \gamma_b$ is negligible, the following expression may be used:

$$d_{M_R} = d_M - (d_{13} + L_M a_b) \quad [B-19]$$

^{*} When the Mth gage is at the center of mass, the term in parenthesis in Equation [B-18] reduces the right hand side of Equation [B-15].

APPENDIX C

DETERMINATION OF LOGARITHMIC DECREMENTS

In determining the motion of the center of mass of the rudder relative to the hull in the y-direction, the displacement of the hull must be accounted for (in addition to the displacement of the center of mass associated with the elasticities of the flexible stock) because it is included in the rudder motions measured by the gages on the rudder. Thus, rudder motion relative to the hull motion in the y degree of freedom is

$$v - d_{R-H} = v - (d_{13} + L_H a_b), *$$

This is equivalent to the motion of the center of mass of the rudder attached through a flexible stock to a rigid hull.

The values for γ , a_b , and d_{R-H} must be subtracted from the recorded γ , a , and v motions of the rudder to obtain the true rudder relative to hull motion.

The logarithmic damping decrement for a motion A (t) is

$$\delta_A = \frac{1}{q} \log_e \left[\frac{A_{t_0}}{A_{t_0 + q\tau}} \right] \quad [C-1]$$

where A_{t_0} = the value of A at time $t=t_0$

$A_{t_0 + q\tau}$ = the value of A at time $t=t_0 + q\tau$

where τ is the period of oscillation and q is an integer equal to the total number of periods of oscillation of A between the measured amplitudes (see Figure 11). Similar relationships hold for the motions $\gamma(t)$, $a(t)$, and $v(t)$.

We define the logarithmic decrement of the γ motion of the rudder relative to the hull by

$$\delta_{\gamma_R} = \frac{1}{q} \log_e \frac{[\gamma - \gamma_b]_{t=t_0}}{[\gamma - \gamma_b]_{t=t_0 + q\tau}} \quad [C-2]$$

the logarithmic decrement of the a motion of the rudder relative to the hull by

$$\delta_{a_R} = \frac{1}{q} \log_e \frac{[a - a_b]_{t=t_0}}{[a - a_b]_{t=t_0 + q\tau}} \quad [C-3]$$

and the logarithmic decrement of the v motion of the rudder relative to the hull by

$$\delta_{v_R} = \frac{1}{q} \log_e \frac{[v - d_{R-H}]_{t=t_0}}{[v - d_{R-H}]_{t=t_0 + q\tau}} \quad [C-4]$$

In terms of displacement, these Equations [C-2], [C-3], and [C-4] respectively become Equations [10], [11], and [12] of Table 1.

Similarly, the decrement of the relative motion of the M^{th} location on the rudder is given by (see Equation [13] of Table 1)

$$\delta_{M(modal)_R} = \frac{1}{q} \log_e \left\{ \frac{[d_M - (d_{13} + L_M a_b - x_M \gamma_b)]_{t=t_0}}{[d_M - (d_{13} + L_M a_b - x_M \gamma_b)]_{t=t_0 + q\tau}} \right\} \quad [C-5]$$

In these equations, d_M is the recorded displacement of the rudder at the M^{th} position and L_M is the vertical distance of the M^{th} position to the gage where the displacement d_{13} is measured.

For some applications, the term $x_M \gamma_b$ may be negligible. In the present application to ALBACORE and SAMPSON, the terms $d_{13} + L_M a_b - x_M \gamma_b$ were not considered (see Results) so that Equation [C-5] reduces to Equation [7] of Table 1.

Theoretically $\delta_{v_R} = \delta_{\gamma_R} = \delta_{a_R} = \delta_{modal}$.

The analysis of the record should verify this assertion.

* In Equation [B-18], $d_M = v$, $L_M = L_H$, and the term $x_M \gamma_b$ has been neglected for the present application.

APPENDIX D

DERIVATION OF EQUATIONS FOR PARAMETERS C AND c

Derivation of Equations [14] and [15] of Table 1 are presented in this Appendix.

Consider Equation [62a] of Reference 1. At zero ship speed, this is (see Notation):

$$M_y \ddot{v} = -12k_s [v - v_b + h\gamma - ba - \frac{1}{2}l(a + a_b)] - C\dot{v}$$

$$C = \frac{-M_y \ddot{v} - 12k_s [v - v_b + h\gamma - ba - \frac{1}{2}l(a + a_b)]}{\dot{v}}$$

Suppose the motion in each degree of freedom is a damped sinusoid. Then*

$$v = v_1 e^{\mu t} \sin \omega t$$

$$a = e^{\mu t} (a_1 \sin \omega t + a_2 \cos \omega t)$$

$$\gamma = e^{\mu t} (\gamma_1 \sin \omega t + \gamma_2 \cos \omega t)$$

$$v_b = e^{\mu t} (v_{b1} \sin \omega t + v_{b2} \cos \omega t)$$

$$a_b = e^{\mu t} (a_{b1} \sin \omega t + a_{b2} \cos \omega t)$$

$$\gamma_b = e^{\mu t} (\gamma_{b1} \sin \omega t + \gamma_{b2} \cos \omega t)$$

where $a_1, a_2, \gamma_1, \gamma_2, v_{b1}, v_{b2}, a_{b1}, a_{b2}, \gamma_{b1},$

γ_{b2} are constants,

The exponent μ , the frequency ω , and the constants a_1, a_2 , etc., can all be determined from records. Moreover,

$$\dot{v} = v_1 (\mu \sin \omega t + \cos \omega t) e^{\mu t}$$

$$\ddot{v} = v_1 [(\mu^2 - \omega^2) \sin \omega t + 2\mu\omega \cos \omega t] e^{\mu t}$$

$$\ddot{a} = \{ [a_1(\mu^2 - \omega^2) - 2a_2\mu\omega] \sin \omega t + [a_2(\mu^2 - \omega^2) + 2a_1\mu\omega] \cos \omega t \} e^{\mu t}$$

$$\ddot{\gamma} = \{ [\gamma_1(\mu^2 - \omega^2) - 2\gamma_2\mu\omega] \sin \omega t + [\gamma_2(\mu^2 - \omega^2) + 2\gamma_1\mu\omega] \cos \omega t \} e^{\mu t}$$

$$\dot{\gamma} = [(\gamma_1\mu - \gamma_2\omega) \sin \omega t + (\gamma_1\omega + \gamma_2\mu) \cos \omega t] e^{\mu t}$$

$$\dot{\gamma}_b = [(\gamma_{b1}\mu - \gamma_{b2}\omega) \sin \omega t + (\gamma_{b1}\omega + \gamma_{b2}\mu) \cos \omega t] e^{\mu t}$$

Substituting the appropriate variable $\ddot{v}, \dot{v}, v, v_b, \gamma, a, a_b$ in the equation for C, we find at time

$$t = \frac{2n\pi}{\omega}; n = 0, 1, 2, \dots$$

$$C = -2M_y\mu + \frac{12k_s}{v_1\omega} \left[v_{b2} - h\dot{\gamma}_2 + ba_2 + \frac{l}{2}(a_2 + a_{b2}) \right]$$

* It may be desirable in future calculations or measurements to express these equations in the following alternative forms:

$$v = v_1 e^{\mu t} \sin \omega t$$

$$v = v_1$$

$$\phi_1 = \tan^{-1} \left(\frac{a_2}{a_1} \right)$$

$$a = A e^{\mu t} \sin(\omega t + \phi_1)$$

$$A = \sqrt{a_1^2 + a_2^2}$$

$$\phi_2 = \tan^{-1} \left(\frac{\gamma_2}{\gamma_1} \right)$$

$$\gamma = \Gamma e^{\mu t} \sin(\omega t + \phi_2)$$

$$\Gamma = \sqrt{\gamma_1^2 + \gamma_2^2}$$

$$\phi_3 = \tan^{-1} \left(\frac{v_{b2}}{v_{b1}} \right)$$

$$v_b = v_b e^{\mu t} \sin(\omega t + \phi_3)$$

$$v_b = \sqrt{v_{b1}^2 + v_{b2}^2}$$

etc.

etc.

etc.

Similarly from Equation [62b] of Reference 1
(see Notation)

$$I_z \ddot{\gamma} - I_{xz} \ddot{a} = -12k_s h(v - v_b) + 6k_s h(\ell + 2b)a$$

$$- \left[\frac{GJe}{L_T} + 12k_s h^2 \right] \gamma + 6k_s h a_b + \frac{GJe}{L_T} \gamma_b - c(\dot{\gamma} - \dot{\gamma}_b)$$

or

$$c = \left[\frac{1}{\dot{\gamma} - \dot{\gamma}_b} \right] \left\{ -I_z \ddot{\gamma} + I_{xz} \ddot{a} - 12k_s h(v - v_b) + 6k_s h(\ell + 2b)a \right.$$

$$\left. - \left[\frac{GJe}{L_T} + 12k_s h^2 \right] \gamma + 6k_s h a_b + \frac{GJe}{L_T} \gamma_b \right\}$$

Substituting the appropriate variables $\ddot{\gamma}$,
 \ddot{a} , v , v_b , a , γ , a_b , γ_b in the equation for
 c , we find at time

$$t = \frac{2n\pi}{\omega}; n = 0, 1, 2, \dots$$

$$c = \frac{1}{(\gamma_1 - \gamma_{b1})\omega + (\gamma_2 - \gamma_{b2})\mu} \left\{ -I_z \left[\gamma_2(\mu^2 - \omega^2) + 2\gamma_1\mu\omega \right] \right.$$

$$+ I_{xz} \left[a_2(\mu^2 - \omega^2) + 2a_1\mu\omega \right]$$

$$+ 12k_s h \left[v_{b2} - h\gamma_2 + b a_2 + \frac{\ell}{2}(a_2 + a_{b2}) - \frac{GJe}{L_T}(\gamma_2 - \gamma_{b2}) \right] \left. \right\}$$

$$\text{In these equations, } -\frac{\mu}{\omega} = \frac{\delta}{2\pi} = \frac{C}{C_c} = \frac{c}{c_c}$$

(see Reference 3) where δ is the logarithmic decrement of the waveform, μ is the real part of λ indicating the degree of damping and ω is the imaginary part of λ which is the circular frequency of vibration. Here C_c and c_c are critical damping constants for the translational and rotational degrees of freedom, respectively. It should be clear that δ , ω , (and hence μ) are directly obtainable from the waveforms for a particular mode of vibration as are the constants v_{b2} , γ_2 , a_2 , etc. Thus, C and c are determined from measured and calculated data.

APPENDIX E

DETERMINATION OF VIRTUAL MASS AND MASS MOMENTS OF INERTIA

Methods for determining the virtual mass and virtual mass moments of inertia are given in this Appendix.

In order to obtain "ball park" values for the frequencies of the rudder by means of a simple computation, let us assume first that we are treating a two degree-of-freedom system, consisting of v- and γ -motions, i.e., α -motions are neglected. With this approach, two types of calculations can be made. The simpler type of calculation treats the system as uncoupled, whereas the second type which involves a bit more computation, treats the system as a coupled one.^{9*}

Equations developed for determining the frequencies associated with uncoupled motions in two degrees of freedom, v-translation and γ -rotation, are given in Reference 9, page 321. The frequencies associated with uncoupled motions are inversely proportional to the mass and mass moments of inertia, respectively. The equations for the frequencies associated with uncoupled γ - and γ -motions are

$$f_v = \frac{1}{2\pi} \sqrt{\frac{3EI_p}{2m_y L^3}} \quad \text{and} \quad f_\gamma = \frac{1}{2\pi} \sqrt{\frac{GI_p}{I_z}} \quad [E-1]$$

which may be written as

$$f_v \propto m_y^{-1/2} \quad \text{and} \quad f_\gamma \propto I_z^{-1/2} \quad [E-2]$$

where, in general (i.e., for any medium), f_v is the frequency of the translational motion and f_γ is the frequency of the rotational motion, m_y is the total mass† of the rudder, I_z is the mass moment of inertia of the rudder about the rudder stock axis, and I_p is the polar moment of inertia of the rudder stock.

In air

$$f_{v,a} = \frac{1}{2\pi} \sqrt{\frac{3EI_p}{2m_{y,a} L^3}} \quad , \quad f_{\gamma,a} = \frac{1}{2\pi} \sqrt{\frac{GI_p}{I_{z,a}}} \quad [E-3]$$

or

$$f_{v,a} \propto m_{y,a}^{-1/2} \quad , \quad f_{\gamma,a} \propto (I_{z,a})^{-1/2} \quad [E-4]$$

where $f_{v,a}$ is the frequency associated with translational motion (only) in air and $f_{\gamma,a}$ is the frequency associated with γ rotation (only) in air. Similarly

$$f_{v,w} \propto m_{y,w}^{-1/2} \quad , \quad f_{\gamma,w} \propto (I_{z,w})^{-1/2}$$

$$\frac{f_{v,a}}{f_{v,w}} = \sqrt{\frac{m_{y,w}}{m_{y,a}}}$$

But $m_y = m_a + m_{vir}$ [E-5]

$$\text{Therefore} \quad \frac{f_{v,a}^2}{f_{v,w}^2} = \frac{m_a + m_{vir}}{m_a} = 1 + \frac{m_{vir}}{m_a}$$

Hence

$$m_{vir} = m_a \left[\left(\frac{f_{v,a}}{f_{v,w}} \right)^2 - 1 \right] \quad [E-6]$$

This is Equation [18] of Table 1. An alternative method for computing m_{vir} based on Reference 15 is given by Equation [19] of Table 1. Similarly, since

$$(I_z)_w = (I_z)_a + (I_z)_{vir}$$

assuming that m_{vir} and m_a lie close to the center of mass of the rudder in water (otherwise use the parallel axis theorem to transfer all moments to this latter center of mass; see footnote next page)

* For example, the numerical values for the parameters of the "barn door" type rudder of Reference 9 indicate that the maximum difference in the corresponding frequencies obtained from the use of these two types is not likely to exceed 15 percent for one of the modes and 20 percent for the other mode.

† In a fluid medium, this includes the virtual mass of the fluid as well as the structural mass; similarly for I_z .

then

$$(I_z)_{vir} = (I_z)_a \left[\left(\frac{f_{\gamma,a}}{f_{\gamma,w}} \right)^2 - 1 \right] \quad [E-7]$$

Finally, to treat α -motions, we postulate

$$f_{\alpha,a} \propto (I_x)_a^{-1/2} \quad \text{and} \quad f_{\alpha,w} \propto (I_x)_w^{-1/2}$$

Then, making the same assumption as for $(I_z)_w$,

$$(I_x)_w = (I_x)_a + (I_x)_{vir} \quad [E-8]$$

$$(I_x)_{vir} = (I_x)_a \left[\left(\frac{f_{\alpha,a}}{f_{\alpha,w}} \right)^2 - 1 \right] \quad [E-9]$$

The methods for computing the frequencies of the coupled (v, γ) motions are given on pages 321 and 322 of Reference 9. The coordinates y and γ used here are x and α , respectively, in Reference 9.

Actually, for the ships under consideration, the frequencies that were used in calculating m_{vir} , $(I_z)_{vir}$, and $(I_x)_{vir}$ are the predominant ones associated with measured coupled motions rather than the frequencies corresponding to the uncoupled motions. Thus since we cannot really discriminate between f_y , f_γ , and f_α in these calculations (if measured frequencies are used), Equations [E-6], [E-7], and [E-9] may lead to poor or questionable results. Calculation showed that use of Equation [E-6] for ALBACORE leads to satisfactory results whereas use of Equations [E-7] and [E-9] do not.* Hence, alternative formulations for $(I_z)_{vir}$ and $(I_x)_{vir}$ based on Reference 13 are given by Equations [20] and [21], respectively, of Table 1. In Equations [20] and [21], note that the first terms in the right members are virtual mass moments of inertia of the rudder about a z - and a x -axis, respectively, through the center of mass; i.e., geometrical center of the ellipsoidal volume of water which approximates the volume of the rudder (see Reference 4, pages 11 and 12). The terms $r^2 m_{vir}$ and $s^2 m_{vir}$ transfer these moments to x - and y -axes through the center of mass of the entire rudder-fluid system; r and s are the distances between these x - and y -axes, respectively.

* This follows from comparisons with the results of Equations [19], [20], and [21] of Table 1, respectively. In this case, f_y probably closely corresponds to the predominant frequency whereas f_γ , f_α do not. Hence, while the Equations [E-7] and [E-9] may be sound, the data inserted in them are of doubtful validity. In performing these calculations, all moments were transferred by means of the parallel axis theorem to axes with origin at the center of mass of the entire rudder-fluid system.

REFERENCES

1. Kennard, E. H. and Leibowitz, R. C., "Theory of Rudder-Diving Plane-Ship Vibrations and Flutter, Including Methods of Solution," David Taylor Model Basin Report 1507 (Feb 1962).
2. Leibowitz, R.C. and Belz, D.J., "A Procedure for Computing the Hydroelastic Parameters for a Rudder in a Free Stream," David Taylor Model Basin Rept 1508 (Apr 1962).
3. Leibowitz, R.C. and Belz, D.J., "Comparison of Theory and Experiment for Marine Control-Surface Flutter," David Taylor Model Basin Report 1567 (Aug 1962).
4. Leibowitz, R.C., "USS ALBACORE (AGSS 569) Modes of Rudder Vibration," David Taylor Model Basin Report 1540 (Sep 1961).
5. Leibowitz, R.C. and Kennard, E.H., "Theory of Freely Vibrating Nonuniform Beams Including Methods of Solution and Application to Ships," David Taylor Model Basin Report 1317 (May 1961).
6. Leibowitz, R.C. and Kennard, E.H., "Theoretical and Experimental Determination of Damping Constants of One-to-Three Dimensional Vibrating Systems," David Taylor Model Basin Report 1770 (Jun 1964).
7. Hoyt, Edgar D., "USS SAMPSON (DDG 10) Rudder Vibration Tests," Robert Taggart, Inc. Technical Report prepared under contract NObs 86122 (4 Jan 1963).
8. McGoldrick, R.T., "Ship Vibration," David Taylor Model Basin Rept 1451 (Dec 1960).
9. Bunyon, T.W., "A Study of the Cause of Some Rudder Failures," Northeast Coast Institution of Engineers and Shipbuilders, Vol. 68, Part 7 (May/Jun 1952).
10. Ayling, P.W. and Taylor, K.V., "Measurements of Strain and Vibration on the Rudder and Sternframe of a Single-screw Dry-cargo ship of 13,000 SHP, Part I," The British Shipbuilding Research Association Report 383 (1962).
11. Maset, R., "Some Aspects of Ground and Flight Vibration Tests," AGARD Report 40-T, (Apr 1956).
12. Anderson, J.E. and Comley, W., "Transient Response Data Reduction and a Unique Transient Wave Analyzer," Proceedings of the AIEE Conference, Santa Monica, California (May 23-25, 1960).

13. Wolfe, M. O. W. and Kirkby, W.T., "Several Techniques for Flight Flutter Testing," Part I AGARDograph 56 (Sep 1960).
14. Stringham, R. H., Jr., "A Method for Measuring Vibration Modes of a Transiently Heated Structure," SAE-ASNE National Aeronautical Meeting, Wash., D.C. (8 Apr 1963).
15. Wendel, K., "Hydrodynamic Masses and Hydrodynamic Moments of Inertia," "(Hydrodynamische Massen und Hydrodynamische Massen-tragheitsmomente)," Jahrb. d. STG, Vol. 44 (1950). TMB Translation 260 (Jul 1956).

NOTATION

- A Amplitude of rotational motion α of the rudder about the x-axis
- A_b Amplitude of rotational motion of the hull about the x-axis at the point of attachment of rudder stock to hull (point of attachment here is associated with bending of rudder stock)
- b z-coordinate of effective point of attachment of rudder to rudder stock
- C Damping constant associated with the motion of the rudder in the transverse (y-) direction
- C_c Critical damping constant for translational degree of freedom
- c Damping constant associated with the motion of the rudder about the vertical (z-) axis
- c_c Critical damping constant for rotational degree of freedom
- d_i Displacement of the rudder at the i^{th} location on the rudder or stock
- d_{R-H} Displacement of center of mass of the rudder due to the coupled torsion-horizontal-bending motions of the hull
- $(d_{v,a})_z$ Coupled (v, a) motion of the rudder along the vertical z'-axis through the center of the rudder stock
- E Young's modulus of elasticity
- $(f_v, f_\gamma, f_{v,a}, f_{v,w}, f_{\gamma,a}, f_{\gamma,w}, f_{a,a}, f_{a,w})$ frequencies (defined in Appendix K)
- G Shear modulus of elasticity
- g Acceleration of gravity
- h x-coordinate of effective center of attachment of rudder to rudder stock
- I Area moment of inertia of cross section of rudder stock relative to a diameter through the centroid
- I_p Polar moment of inertia of rudder stock about z'-axis
- I_a Moment of inertia of combined rudder and virtual mass about the z-axis with origin at the effective center of mass of the rudder in water

$(I_x)_a, (I_z)_a$ Moment of inertia of the rudder about the x- and z-axes respectively with origin at the center of mass of the rudder in air

$(I_x)_{vir}, (I_z)_{vir}$ Virtual mass moment of inertia of rudder about x- and z-axes respectively with origin at the center of mass of the rudder in water (see Equations [21] and [20] respectively of Table 1 and Discussion at end of Appendix E).

I_{zx} Product of inertia corresponding to I_x, I_y, I_z

J_e Polar moment of inertia of cross section of rudder stock about a perpendicular axis through the centroid

K_1 Geometrical constants of the rudder (see Appendixes A and B)

k_s Defined as $k_s = \left(\frac{1}{1 + \frac{12EI}{KAGL^2}} \right) \left(\frac{EI}{L^3} \right)$ where

KAG is the shear rigidity of the rudder stock

L_H, L_p Distances between gages on rudder hull system (see Appendix B)

L_H Vertical distance between the H^{th} gage and Gage 13

L, L_T Live length of rudder stock from center of gravity of rudder to the points of attachment of rudder stock to hull in bending and torsion, respectively

m_a Mass of the rudder in translation in air

m_{vir} Virtual mass of the rudder in translation

m_y Total mass of the rudder in translation including virtual mass

q Integer

S Forward speed of ship

t Time

v Amplitude of translational motion (v) of the rudder in y-direction

v_b Amplitude of translational motion of the hull in the y-direction at the point of attachment of rudder stock to hull (point of attachment here is associated with bending of rudder stock)

v	Small translation of effective center of mass of the rudder in the y-direction	λ_i	Complex circular frequency of vibration of i th mode
v_b	Corresponding translation at the point of attachment of rudder stock to hull	μ_i	Real part of λ_i indicating the degree of damping
x, y, z	Right-handed rectangular coordinates with x-axis always parallel to the ship axis; the origin is always at the effective center of mass of the rudder and the z-axis is vertical and positive upward	ρ	Density of seawater
x', y', z'	As above, but with origin at the point of attachment of rudder to rudder stock	τ	Period of oscillation
$\bar{x}, \bar{y}, \bar{z}$	Mean chord, height, and thickness of rudder, respectively	ϕ_i	Phase angles defined in Appendix D
y_p	Horizontal distance (in y-direction) between Gages 15 and 16	ω_i	Imaginary part of λ_i indicating circular frequency of oscillation
z'_B	z' coordinate of point of attachment of stock to hull in bending		
z'_T	z' coordinate of point of attachment of stock to hull in torsion		
α	Small rotation of the rudder about x-axis		
α_b	Small rotation of the hull at the point of attachment of rudder stock to hull about the x-axis (point of attachment here is associated with bending of rudder stock)		
Γ	Amplitude of rotational motion γ of the rudder about the x-axis		
Γ_b	Amplitude of rotational motion of the hull about the x-axis at the point of attachment of rudder stock to hull (point of attachment here is associated with torsion of rudder stock)		
γ	Small rotation of the rudder about x-axis		
γ_b	Small rotation of the hull at the point of attachment of rudder stock to hull about the x-axis (point of attachment here is associated with torsion of rudder stock)		
δ	Measured values of logarithmic decrements		
$\delta_\gamma, \delta_\alpha, \delta_v$	Logarithmic decrements which are defined in Table 1		
$\delta_{\gamma_R}, \delta_{\alpha_R}, \delta_{v_R}$			
$\delta_{\alpha(\text{model})_R}, \delta_{\alpha(\text{model})_M}$			

Table 1

Summary of Equations of Motion and Parameters Associated with Control Surfaces*

NUMBER	EQUATION	ASSOCIATED CONSTANTS	DEFINITION AND REMARKS	SOURCE
1	$\gamma(t) = K_1(d_4 - d_8)^{**}$	$K_1 = \frac{1}{x_1 + x_2}^{***}$	Total rotational motion of the rudder about the x-axis.	Appendix A
2	$\alpha(t) = K_2(d_6 - d_2)$	$K_2 = \frac{1}{x_1 + x_2}$	Total rotational motion of the rudder about the x-axis.	Appendix A
3a	$v(t) = K_3(d_2 + K_4 d_6)$	$K_3 = \frac{x_2}{x_1 + x_2}$ $K_4 = \frac{x_1}{x_2}$	Total translational motion of the rudder along the y-axis.	Appendix A
3b	$v(t) = K_5(d_4 + K_6 d_8)$	$K_5 = \frac{x_2}{x_1 + x_2}$ $K_6 = \frac{x_1}{x_2}$	Total translational motion of the rudder along the y-axis.	Appendix A
4	$\delta_y = \frac{1}{q} \log_e \left[\frac{(d_4 - d_8)_{t=t_0}}{(d_4 - d_8)_{t=t_0+qr}} \right]$	$K_6 = \frac{x_1}{x_2}$ $q = \text{integer}$ $r = \text{period of oscillation.}$	Logarithmic decrement of $\gamma(t)$ motion.	Appendix C
5	$\delta_\alpha = \frac{1}{q} \log_e \left[\frac{(d_6 - d_2)_{t=t_0}}{(d_6 - d_2)_{t=t_0+qr}} \right]$		Logarithmic decrement of $\alpha(t)$ motion.	Appendix C
6a	$\delta_v = \frac{1}{q} \log_e \left[\frac{(d_2 + K_4 d_6)_{t=t_0}}{(d_2 + K_4 d_6)_{t=t_0+qr}} \right]$		Logarithmic decrement of $v(t)$ motion.	Appendix C
6b	$\delta_v = \frac{1}{q} \log_e \left[\frac{(d_4 + K_6 d_8)_{t=t_0}}{(d_4 + K_6 d_8)_{t=t_0+qr}} \right]$		Logarithmic decrement of $v(t)$ motion.	Appendix C
7	$\delta_{(modal)} = \frac{1}{q} \log_e \left[\frac{(d_M)_{t=t_0}}{(d_M)_{t=t_0+qr}} \right]$		Logarithmic decrement of the total recorded motion at the M^{th} position.	Appendix C
8a	$a_b(t) = \frac{d_{13} - d_{14}}{L_p}$	Constants L_p, γ_p defined in Appendix B and Figure 1.	Contribution of the $\alpha(t)$ motion of the hull to the total recorded motion of the control surface.	Appendix B
8b	$a_b(t) = \frac{d_{16} - d_{15}}{\gamma_p}$		Contribution of the $\gamma(t)$ motion of the hull to the total recorded motion of the control surface.	Appendix B
9	$d_{R-H}(t) = d_{13} + K_H a_b$	Constant K_H defined in Appendix B and Figure 1.	Displacement of center of mass of the rudder due to the coupled torsion-horizontal-bending motions of the hull. The contribution of $\gamma(t)$ to $d_{R-H}(t)$ in the present application has been neglected. See Equation (B-19) and footnote in Appendix C. The more general expression is given by Equation (B-15).	Appendix B

Table 1 (Cont'd)

NUMBER	EQUATION	ASSOCIATED CONSTANTS	DEFINITION AND REMARKS	SOURCE
10	$\delta_{y_R} = \frac{1}{q} \log_e \left\{ \frac{[K_1(d_4 - d_8) - \gamma_b]_{t=t_0}}{[K_1(d_4 - d_8) - \gamma_b]_{t=t_0+q\tau}} \right\}$		Logarithmic decrement of the rotational motion of the rudder relative to the hull about the z-axis. γ_b computed in accordance with the procedure of Appendix B.	Appendix C
11	$\delta_{v_R} = \frac{1}{q} \log_e \left\{ \frac{[K_2(d_6 - d_2) - a_b]_{t=t_0}}{[K_2(d_6 - d_2) - a_b]_{t=t_0+q\tau}} \right\}$		Logarithmic decrement of the rotational motion of the rudder relative to the hull about the x-axis. a_b computed in accordance with the procedure of Appendix B.	Appendix C
12a	$\delta_{v_R} = \frac{1}{q} \log_e \left\{ \frac{[K_3(d_2 + K_4 d_6) - d_{R-H}]_{t=t_0}}{[K_3(d_2 + K_4 d_6) - d_{R-H}]_{t=t_0+q\tau}} \right\}$		Logarithmic decrement of the translational motion of the rudder relative to the hull along the y-axis.	Appendix C
12b	$\delta_{v_R} = \frac{1}{q} \log_e \left\{ \frac{[K_5(d_4 + K_6 d_8) - d_{R-H}]_{t=t_0}}{[K_5(d_4 + K_6 d_8) - d_{R-H}]_{t=t_0+q\tau}} \right\}$		Logarithmic decrement of the translational motion of the rudder relative to the hull along the y-axis.	Appendix C
13	$\delta_{M(modal)_R} = \frac{1}{q} \log_e \left\{ \frac{[d_M - (d_{13} + L_M a_b - X_M \gamma_b)]_{t=t_0}}{[d_M - (d_{13} + L_M a_b - X_M \gamma_b)]_{t=t_0+q\tau}} \right\}$	Constants L_M , X_M , defined in Appendixes B and C.	Logarithmic decrement of the relative displacement between rudder and hull at the M^{th} location. Note that the term $X_M \gamma_b$ was considered negligible in the present application.	Appendices B and C
14	$C = -2m_y \mu + \frac{12k}{v_1} [v_{b2} - h\gamma_2 + b a_2 - \frac{t}{2} (a_2 + a_{b2})]$	All constants are defined in Appendix B or in Notation.	Damping constant associated with the motion of the rudder along the y-direction.	Appendix D
15	$c = \frac{1}{(\gamma_1 - \gamma_{b1})\mu + (\gamma_2 - \gamma_{b2})\mu} \left\{ -I_x [\gamma_2 (\mu^2 - \omega^2) + 2\gamma_1 \mu] \right. \\ \left. + I_{xz} [a_2 (\mu^2 - \omega^2) + 2a_1 \mu] \right. \\ \left. + 12k h [v_{b2} - h\gamma_2 + b a_2 + \frac{t}{2} (a_2 + a_{b2}) - \frac{GJ}{L_T} (\gamma_2 - \gamma_{b2})] \right\}$	All constants are defined in Appendix B or in Notation.	Damping constant associated with the motion of the rudder about the z-axis.	Appendix D
16	$C = -2m_y \mu = 2m \frac{f \delta}{v_y}$	$f = \omega/2\pi$ $\mu = \frac{\delta_v}{2\pi}$	Approximated form of Equation [14] where it is assumed that $\gamma_2 = a_2 = \gamma_{b2} = v_{b2} = 0$ (see Discussion).	Appendix D
17	$c = 2 \left(I_{xz} - I_{xx} \frac{a_1}{\gamma_1} \right) f \delta_y$	$\mu = \frac{\delta_y}{2\pi}$	Approximated form of Equation [15] where it is assumed that $\gamma_2 = a_2 = \gamma_{b2} = v_{b2} = 0$ (see Discussion).	Appendix D

Table 1 (Cont'd)

NUMBER	EQUATION	ASSOCIATED CONSTANTS	DEFINITION AND REMARKS	SOURCE
18	$m_{vir} = m_a \left[\left(\frac{t_{v,a}}{t_{v,w}} \right)^2 - 1 \right]$		Virtual mass of rudder in translation. All terms defined in Appendix E.	Appendix E
19	$m_{vir} = \frac{\pi \rho}{g} \left(\frac{z}{2} \right)^2 \ddot{z}$	$g = 32.17 \text{ ft/sec}^2$ $\rho = 64.15 \text{ lb/ft}^3$ \bar{x} = mean chord of rudder \bar{z} = mean vertical height of rudder	Virtual mass of rudder in translation.	Ref. 15, Ref. 4, Ref. 5(43)
20	$(I_{z,vir}) = \frac{\pi \rho}{8} \left[\left(\frac{z}{2} \right)^2 - \left(\frac{y}{2} \right)^2 \right] \ddot{z} + r^2 m_{vir}$	\bar{y} = mean width of rudder in y-direction; r defined in Appendix E.	Virtual mass moment of inertia of rudder about z-axis with origin as the center of mass of the rudder in water.	Ref. 15, Ref. 4 (Table 4), Appendix E
21	$(I_{x,vir}) = \frac{3\pi \rho}{20} \left(\frac{z}{2} \right)^4 \ddot{x} + s^2 m_{vir}$	s defined in Appendix E.	Virtual mass moment of inertia of rudder about x-axis with origin at the center of mass of the rudder in water.	Ref. 15, Ref. 4 (Table 4), Appendix E
<p>* Values for parameters ℓ and ℓ_T, the effective lengths of stock for bending and torsion, respectively, are computed by extrapolation or interpolation methods given in Appendix B.</p> <p>** $d_i = d_i(t)$</p> <p>*** Constants x_i and z_i are defined in Figure 1.</p>				

Table 2

Test Results for ALBACORE and SAMPSON

USS ALBACORE (AGSS 569)

1. RUDDER (a)

MEASURED FREQUENCIES (cps)	
In Air	In Water
20.1	13.0 (predominant)
24.5 (predominant)	45
123	80
	87

(b)

LOGARITHMIC DECREMENTS					
In Air (24.5 cps)				In Water (13.0 cps)	
EQUATION NUMBER*	DECREMENT**	VALUE	PERCENT DEVIATION FROM AVERAGE	VALUE	PERCENT DEVIATION FROM AVERAGE
4	δ_a	0.0524	-23.4	0.0952	-20.8
5	δ_a	0.0671	-2.0	0.0936	-22.3
6a	δ_a	0.0758	+10.8	0.1212	+0.1
7	δ_{modal}	0.0783	+14.5	0.1717	+42.5
AVERAGE		0.0684	+12.1	0.1285	+21.3
*See Table 1 **See Notation					

(c)

DAMPING CONSTANTS				
EQUATION NUMBER*	In Air (24.5 cps)		In Water (13.0 cps)	
16	$C = 0.3241 \text{ ton-sec/ft}$		$C = 1.1424 \text{ ton-sec/ft}$	
17	$c = 0.1655 \text{ ft-ton-sec}$		$c = 1.2346 \text{ ft-ton-sec}$	
	QUANTITY	SOURCE	QUANTITY	SOURCE
	$m_a = 0.0678 \text{ ton-sec}^2/\text{ft}$	Reference 4, Table 4	$m_y = 0.3613 \text{ ton-sec}^2/\text{ft}$	Reference 4, Table 4
	$I_a = 0.3320 \text{ ft-ton-sec}^2$	Ship Plans	$I_y = 0.6446 \text{ ft-ton-sec}^2$	Reference 4, Table 4
	$I_{aa} = -0.1647 \text{ ft-ton-sec}^2$	Ship Plans	$I_{yy} = -0.1514 \text{ ft-ton-sec}^2$	Reference 4, Table 4
DATA**	$\alpha + 2\eta = 24.5 \text{ sec}^{-1}$	Table 2a	$\alpha + 2\eta = 13.0 \text{ sec}^{-1}$	Table 2a
	$\delta_1/\gamma_1 = -1.5877$	Experimental Data	$\delta_1/\gamma_1 = -0.9631$	Experimental Data
	$\delta_y = 0.0758$	Table 2b	$\delta_y = 0.1216$	Table 2b
	$\delta_x = 0.0524$	Table 2b	$\delta_y = 0.0952$	Table 2b
*See Table 1 **See Notation				

Table 2 (Cont'd)

(d)

VIRTUAL INERTIAS			
EQUATION NUMBER*	QUANTITY	AVERAGE	PERCENT DEVIATION FROM AVERAGE
18, 19	$m_{vir} = 0.2240 \text{ ton-sec}^2/\text{ft}; m_{vir} = 0.2735 \text{ ton-sec}^2/\text{ft}$	0.2488	10
20	$(I_z)_{vir} = 0.3085 \text{ ft-ton-sec}^2$		
21	$(I_x)_{vir} = 1.75 \text{ ft-ton-sec}^2$		
QUANTITY		SOURCE	
DATA**	$\bar{x} = 6.2084 \text{ ft} \quad \rho = 64.15 \text{ lb/ft}^3$ $\bar{y} = 1.1250 \text{ ft} \quad g = 32.17 \text{ ft/sec}^2$ $\bar{z} = 10.1667 \text{ ft} \quad r^2_{m_{vir}} = s^2_{m_{vir}} \approx 0$	Reference 4, Table 4	
*See Table 1 **See Notation			

2. STERN PLANES (e)

MEASURED FREQUENCIES (cps) - IN AIR ONLY*
20 (predominant)
77
120

(f)

LOGARITHMIC DECREMENT (20 cps)				
DECREMENT*	FIXED PORTION**		MOVABLE PORTION**	
	VALUE	PERCENT DEVIATION FROM AVERAGE	VALUE	PERCENT DEVIATION FROM AVERAGE
δ_x	0.0933	+1.5	0.1098	+12.7
δ_y	0.0792	-16.4	0.0968	-32.7
δ_z	0.1316	+11.8	0.0971	+4.1
δ_{modal}	0.1161	+20.6
AVERAGE	0.0947	+11.9	0.0933	+20.4
Because of the orientation of the stern planes δ_x , δ_y , δ_z are decrements corresponding to motions \dot{x} , \dot{y} and \dot{z} about the x- and y-axes and along the z-axis, respectively. **Each stern plane consists of a plane rigidly attached to the hull and to a fixed plane				

Table 2 (Cont'd)

USS SAMPSON (DDG-10)

1. RUDDER (g)

MEASURED FREQUENCIES (cps) - IN WATER ONLY
2.18 (predominant)
4.36
7.6
9.0

(h)

LOGARITHMIC DECREMENT (2.18 cps)		
DECREMENT*	VALUE	PERCENT DEVIATION FROM AVERAGE
δ_{modal}	0.02225	-44.8
	0.0562	+44.8
AVERAGE	0.0402	± 44.8
*See Table 1, Equation [7]		

(i)

DAMPING CONSTANT	
EQUATION NUMBER*	IN WATER (2.18 cps)
16	$C = 0.1479 \text{ ton-sec/ft}$
DATA**	$m_y = 0.8420 \text{ ton-sec}^2/\text{ft}$ $\omega = 2\pi \times 2.18 \text{ sec}^{-1}$ $\delta_v = 0.0402$
* See Table 1 ** $m_y = m_A + m_{\text{vir}}$; $m_A = 0.1953$ was calculated from ship plans and m_{vir} calculated from data in Table 2j. Also δ_v is approximated by the value of δ_{modal} .	

(j)

VIRTUAL MASS		
EQUATION NUMBER*	QUANTITY	
19	$m_{\text{vir}} = 0.6467 \text{ ton-sec}^2/\text{ft}$	
	QUANTITY	SOURCE
DATA**	$\bar{x} = 9.9778 \text{ ft}$ $\bar{z} = 9.25 \text{ ft}$ $\rho = 64.15 \text{ lb/ft}^3$ $g = 32.17 \text{ ft/sec}^2$	Ship Plans
* See Table 1 ** See Notation		

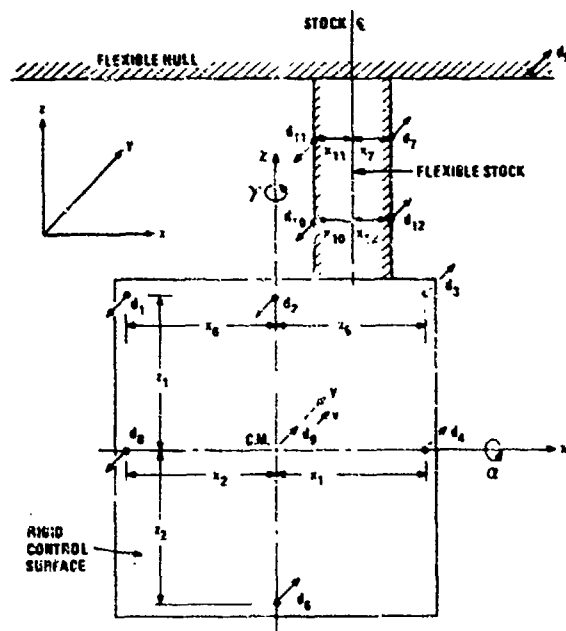


Figure 1. Location of Gages and Identification of Displacements of Rudder-Stock-Hull System.

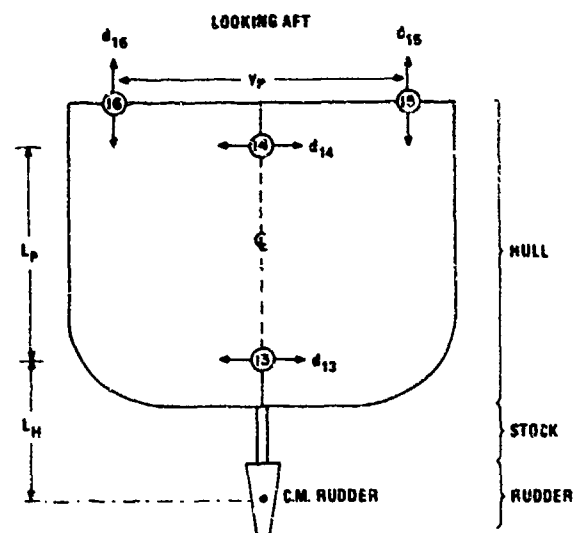


Figure 2. Gage Locations and Orientations for Determining Hull Motions.

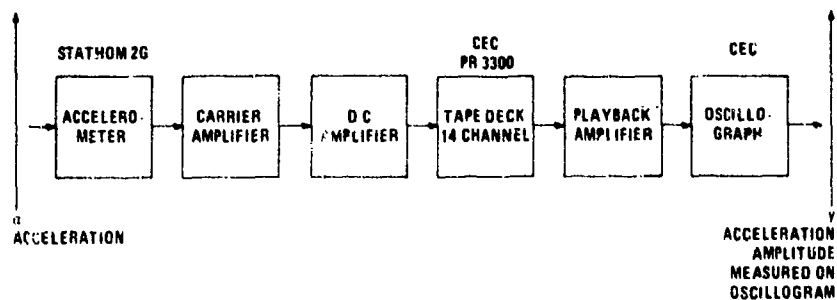
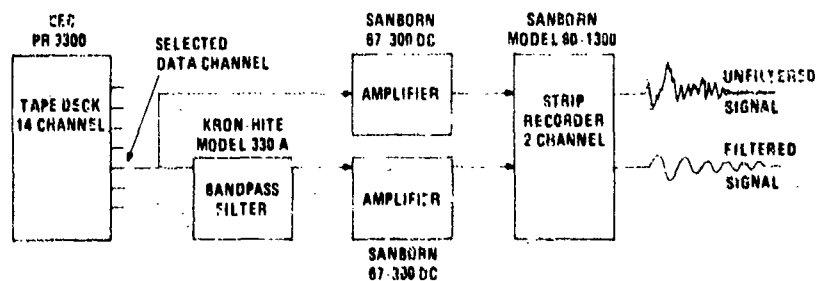


Figure 3a - Recording System for Rudder Vibration Trials of ALBACORE



NOTE: INPUT TO TAPE DECK IS SAME AS THAT FOR ALBACORE

Figure 3b - Data Analysis for Rudder Vibration Trials of SAMPSON

Figure 3. Recording and Analysis Systems.

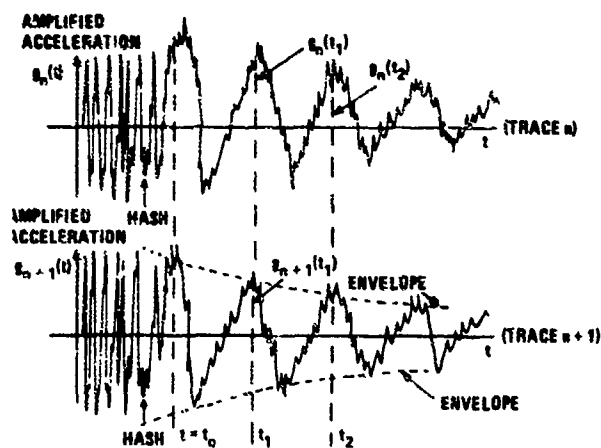


Figure 4. Portion of Oscillogram Record (2 Channels of 12) From ALBACORE Rudder Vibration Tests.

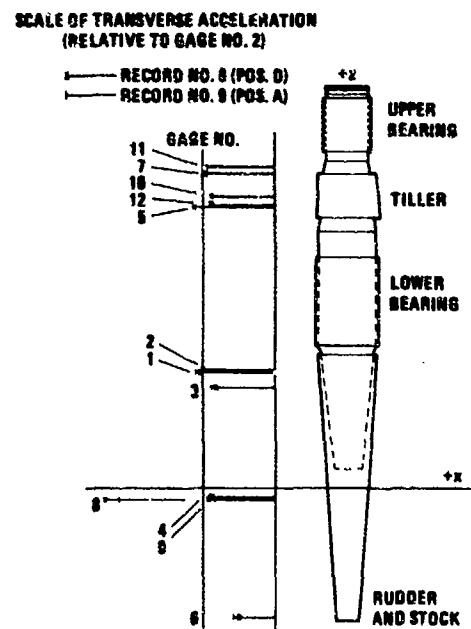


Figure 5. Displacements d_1 Normalized to Gage 2 for 2 Records from SAMPSON Rudder Vibration Tests.

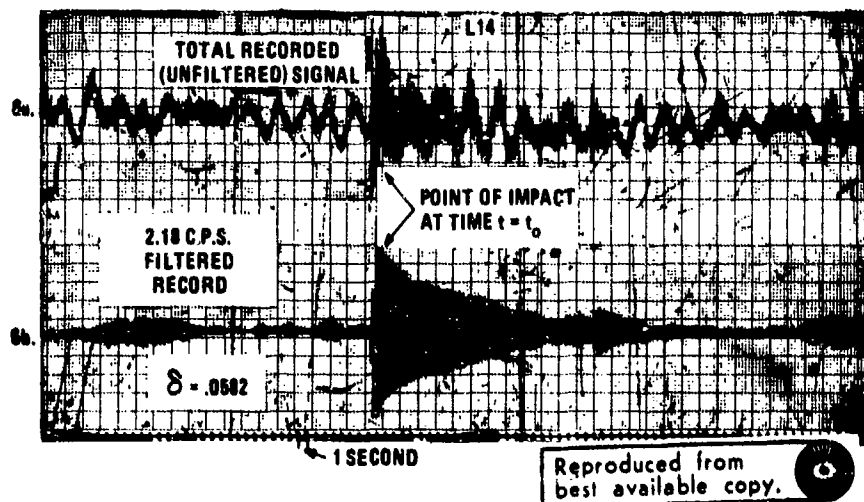


Figure 6a. Total Recorded Signal

Figure 6b. Filtered Signal (2.18-cps)

Figure 6. Sample of Accelerometer Data Obtained From One Channel of SAMPSON Tests.

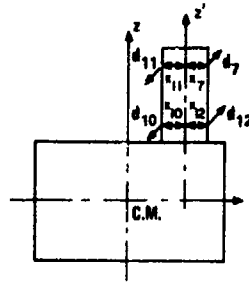


Figure 7a. Location of Gages Used to Record Rudder Stock Motions.

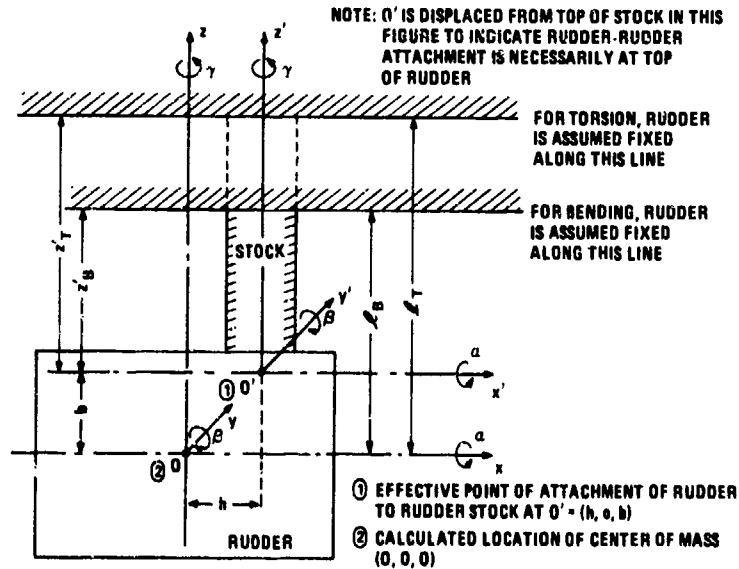


Figure 7b. Rudder Axes

Figure 7. Rudder Coordinates and Locations of Gages.

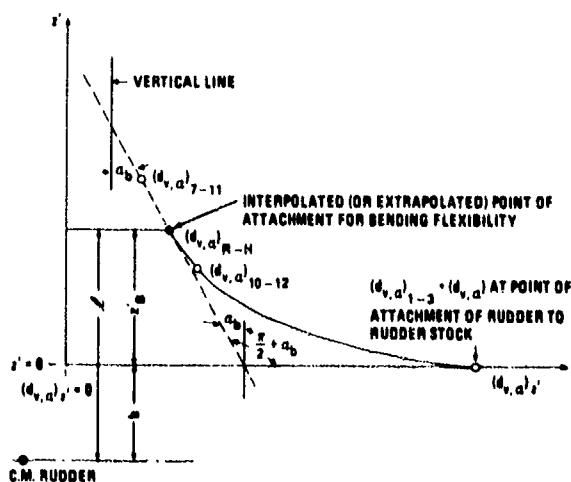


Figure 8. Curve for Determination of Effective Length of Stock for Bending Motion.

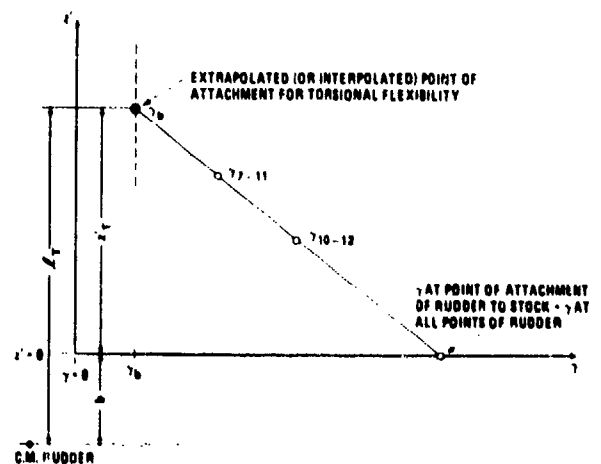


Figure 9. Curve for Determination of Effective Length of Stock for Rotational Motion (Torsion).

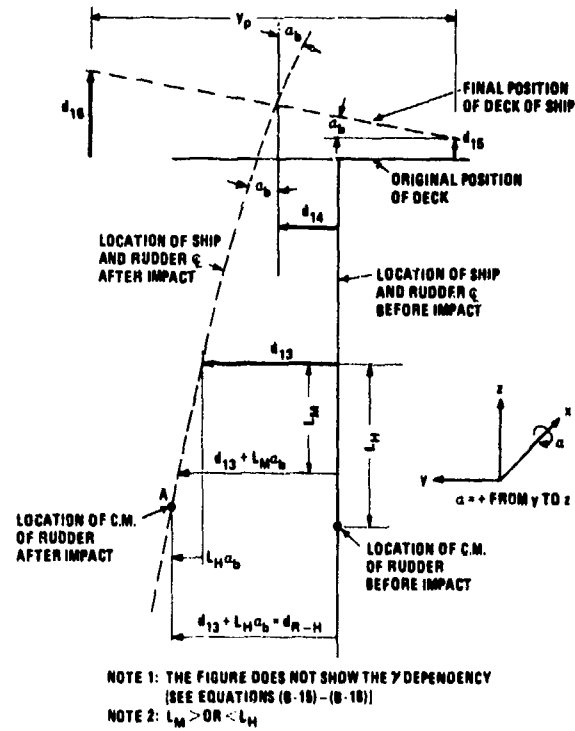


Figure 10. Motion of Hull and Rudder, with No Relative Motion Between Rudder and Hull.

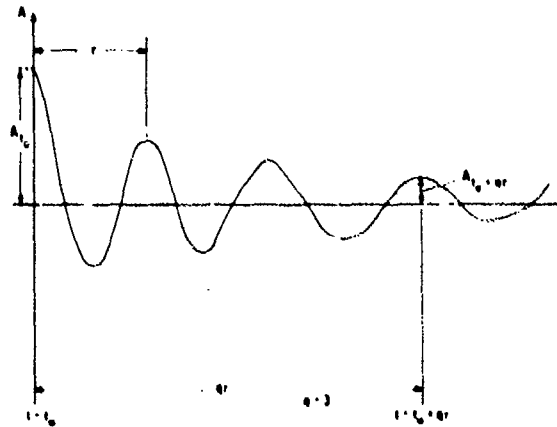


Figure 11. Sinusoidal Wave Form Showing Decay due to Viscous Damping.

DAMPING OF A CIRCULAR RING SEGMENT BY A CONSTRAINED VISCOELASTIC LAYER

Cpt. C. R. Almy
U.S. Army Electronics Command
Ft. Monmouth, New Jersey

and

F. C. Nelson
Department of Mechanical Engineering
Tufts University, Medford, Mass.

An analytical study has been made of the variation of the composite loss factor with opening angle and shear stiffness of the viscoelastic layer for a constrained viscoelastic layer on a circular ring segment. There is evidence that optimum damping of a curved beam requires a stiffer viscoelastic layer than the corresponding straight beam.

Constrained viscoelastic layers are effective in augmenting the damping of beams and plates and many investigators have developed means of predicting the extent of the damping augmentation in these structures. Considerably less work is available on predicting the damping augmentation due to a constrained viscoelastic layer on a curved structure. This paper reports results of an analytical study of the damping induced in a circular ring segment by a constrained viscoelastic layer and how this damping varies with the shear stiffness of the viscoelastic layer and the ring opening angle.

The geometry of interest and the notation used are shown in Figure 1. As indicated in the figure, the ring segment ends are simply supported at the centroid of the main elastic beam and, in addition, restrained against tangential motion at that point.

The in-plane vibration at the fundamental, symmetric natural frequency and its corresponding composite loss factor have been calculated under the following assumptions.

- (1) The system is lightly enough damped to permit the frequency to be computed via the Rayleigh-Ritz procedure and the composite loss factor by

$$\eta = \frac{\beta U_3}{U_1 + U_2 + U_3 + U_4 + U_5} \quad (1)$$

where

- U_1 = peak flexural energy of curved main beam
- U_2 = peak extensional energy of curved main beam
- U_3 = peak shear energy of viscoelastic layer
- U_4 = peak flexural energy of constraining layer
- U_5 = peak extensional energy of constraining layer
- β = shear loss factor of viscoelastic material

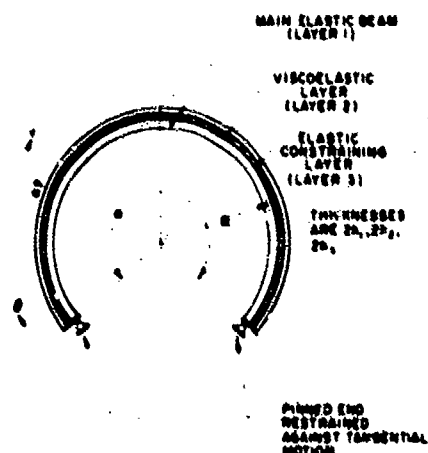


Fig. 1. Geometry of Thin, Uniform Circular Ring Segment with Constrained Viscoelastic Layer

Preceding page blank

In equation (1) it is assumed that all the energy dissipated is dissipated in the viscoelastic layer and, further, that it is dissipated by simple shear. This latter assumption is equivalent to assuming that the viscoelastic material is soft enough to justify ignoring the effects of direct stress. If direct stress effects are ignored, the shear deformation will be uniform through the thickness of the viscoelastic layer.

- (2) Deformation in the radial direction is neglected so that at a given cross section

$$w = w_1 = w_2 = w_3$$

- (3) There is no shear deformation in the elastic layers. Rotary inertia is neglected in all layers. As such, the elastic members behave as curved Bernoulli-Euler beams; however, the extensional bending theory of such beams is used. This point is important because it can be shown by comparison that using the simpler, but more restrictive, inextensional bending theory results in a significant reduction in the shear energy of the viscoelastic layer.
- (4) There is no tangential slip between the layers.

The implications of these assumptions are embodied in Figure 2. From this figure, it is clear that there must be compatibility relations among the v 's and the ϕ 's. Using the figure, we can write these relations as

$$v_2 = v_1 + h_1 \phi_1 + h_2 \phi_2 \quad (2)$$

and

$$v_3 = v_1 + h_1 \phi_1 + 2h_2 \phi_2 + h_3 \phi_3 \quad (3)$$

where from the extensional theory of curved beams

$$\phi_1 = \frac{v_1}{R_1} + \frac{1}{R_1} \frac{dw}{d\theta}$$

$$\phi_2 = \frac{v_2}{R_2} + \frac{1}{R_2} \frac{dw}{d\theta} - \psi$$

$$\phi_3 = \frac{v_3}{R_3} + \frac{1}{R_3} \frac{dw}{d\theta}$$

Equation (3) can be solved for ψ , the shear in

the viscoelastic layer, to give ψ in terms of v_1, v_2, v_3 and w . For the special case of a flat composite beam, i.e., $R_1, R_2, R_3 \rightarrow \infty$, the expression for ψ reduces to the standard one, for example that of reference [1].

The appropriate peak strain energy expressions are

$$U_1 = \frac{E_1 I_1}{2R_1^3} \int_0^\alpha \left[\frac{d^2 w}{d\theta^2} + \frac{dv_1}{d\theta} \right]^2 d\theta \quad (4)$$

$$U_2 = \frac{E_1 A_1}{2R_1} \int_0^\alpha \left[w - \frac{dv_1}{d\theta} \right]^2 d\theta \quad (5)$$

$$U_3 = \frac{G_2 A_2 R_2}{2} \int_0^\alpha \psi^2 d\theta \quad (6)$$

$$U_4 = \frac{E_3 I_3}{2R_3^3} \int_0^\alpha \left[\frac{d^2 w}{d\theta^2} + \frac{dv_3}{d\theta} \right]^2 d\theta \quad (7)$$

$$U_5 = \frac{E_3 A_3}{2R_3} \int_0^\alpha \left[w - \frac{dv_3}{d\theta} \right]^2 d\theta \quad (8)$$

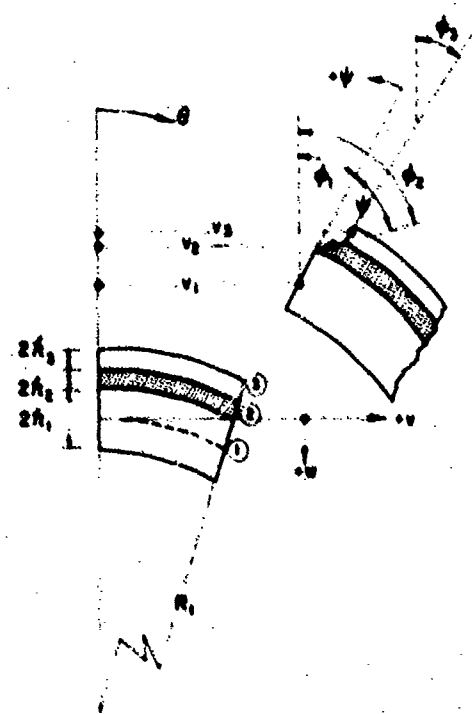


Fig. 2. Before and After Configuration of an Element of the Composite Circular Ring Segment

In these expressions

- E_1 = Young's modulus for layer 1
- G_2 = shear storage modulus for layer 2
- I_1 = area moment of inertia for layer 1
- A_1 = area of layer 1
- R_1 = radius of layer 1

The expressions for reduced kinetic energy are

$$\bar{T}_1 = \frac{R_1 \mu_1}{2} \int_0^a [w^2 + v_1^2] d\theta, i=1,2,3 \quad (9)$$

where

μ_1 = mass per unit arc length of layer 1

Clearly, if we can find expressions for the displacements w, v_1, v_2, v_3 and ψ which satisfy the boundary conditions and the compatibility conditions, equations (1) and (2), we can use them in equations (4) - (8) to evaluate the energies and then compute the composite loss factor from equation (1). In addition, we could substitute these displacement expressions into equation (9) and determine the natural frequencies by Rayleigh's Principle.

The necessary steps to reach these goals

are too lengthy to detail here; we shall only outline the procedure. Limiting ourselves to radial deformations that are symmetric about the midpoint of the ring segment, we choose

$$w = \sum_{n=1,3,5,\dots} a_n \sin \frac{n\pi\theta}{a} \quad (10)$$

$$v_1 = \sum_{n=0,1,3,5,\dots} b_n \cos \frac{n\pi\theta}{a} \quad (11)$$

$$v_3 = \sum_{n=0,1,3,5,\dots} c_n \cos \frac{n\pi\theta}{a} \quad (12)$$

The compatibility conditions can be used to eliminate the variables v_2 and ψ in terms of w, v_1 and v_3 . These expansions can be substituted into the energy expressions to obtain $U_1 = f(a_n, b_n, c_n)$, etc.

The energy expressions can in turn be substituted into the Rayleigh-Ritz energy function

$$\sum_i U_i - \omega^2 \bar{T} \quad (13)$$

Extremalization of this energy function will yield the natural frequencies and the values of the a_n 's, b_n 's and c_n 's corresponding to the natural mode shapes. With these mode shapes, the

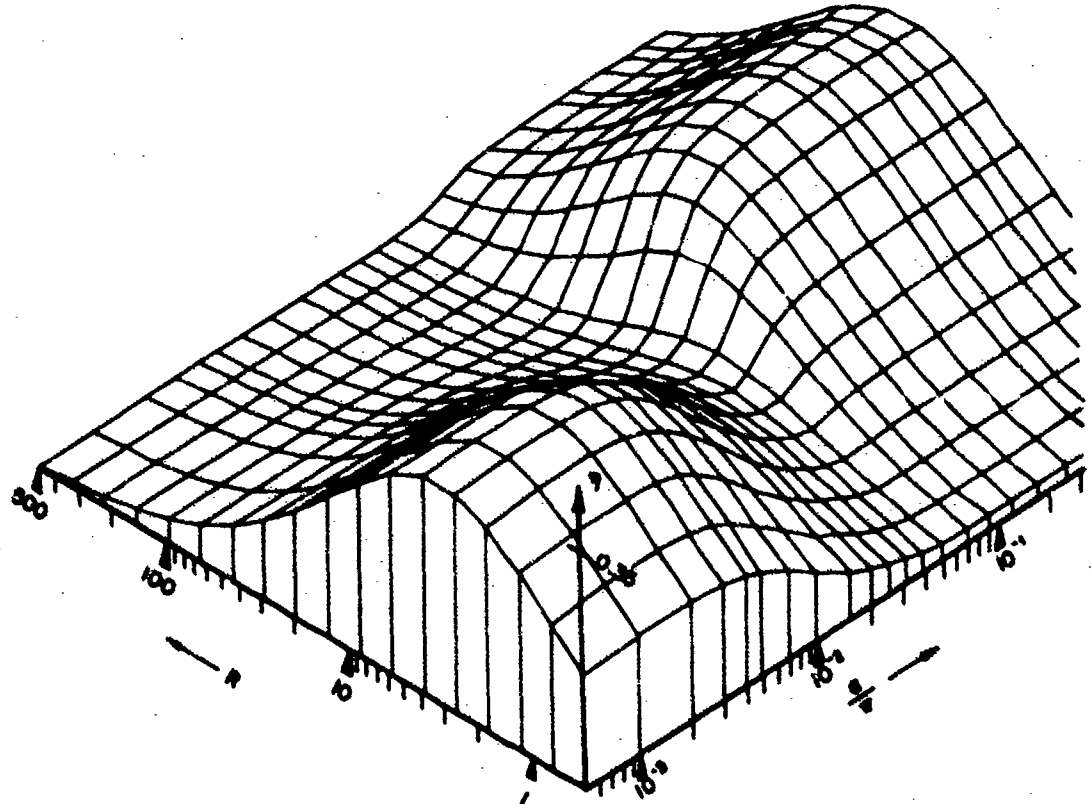


Fig. 3. Variation of Composite Loss Factor (η) with Shear Parameter (β) and Opening Angle (α)

composite loss factor can be determined

One complication should not be glossed over even in a brief outline. The expansions (10), (11) and (12) do not satisfy all the geometric boundary conditions. In order to satisfy $v_1(0) = v_1(a) = 0$, we must have

$$\sum_{n=0,1,3,5,\dots} b_n = 0 \quad (14)$$

Thus (13) must be extremalized subject to the constraint offered by (14). An effective technique to accomplish such constrained extremalization is with a Lagrangian multiplier (the technique for circular ring segments is described in reference [2]). We shall omit completely a discussion of the means for efficient computer manipulation and solution of the natural frequencies, mode shapes and loss factors.

The result of performing all these computations for a specific geometric configuration is given in Figure 3. In this figure, the composite loss factor, η , is plotted against the opening angle of the ring segment, α , and the shear parameter R , where

$$R = \frac{G_2 W L^2}{h_2} \left(\frac{1}{A_1 E_1} + \frac{1}{A_3 E_3} \right)$$

with

W = width (same for all layers)

L = developed length (same for all layers)

The specific geometry is the same as that used by Nokes in reference [3] for a straight beam and is repeated in Table 1.

TABLE 1

	Layer		
	1	2	3
Thickness	0.125"	0.050"	0.631"
Width	1"	1"	1"
Material	Steel	--	Steel
Developed Length	20"	20"	20"

R is varied by allowing G_2 to vary. The material loss factor is assumed constant at $\beta = 1$.

For $\alpha = 0$ (straight beam) the results of Figure 3 agree with those of Nokes when the slightly different boundary conditions are taken into account. As Figure 3 also shows, the straight beam peak in loss factor at $R \approx 4$ disappears quickly with increasing opening angle; in fact, it has disappeared completely when α reaches a value of only 10° . However, it is interesting to note that for $\alpha > 10^\circ$ another peak in damping occurs at a larger value of R ; for the geometry considered, this new peak is at $R \approx 30$. On this basis, one would expect that maximum damping of a deep, curved

structure would require a stiffer viscoelastic material than that for the corresponding straight beam.

The distribution of energy among flexure, extension and shear in the three layers has also been studied. The peaks and valleys in the loss factor surface of figure 3 can be shown to coincide with shifts in the partition of energy in the main beam. The valleys correspond to most of the energy being in extension of the main beam; the peaks correspond to most of the energy being in flexure of the main beam.

This work is continuing and, in particular, it is hoped to verify the analytical prediction with experimental measurements.

REFERENCES

- [1] D. J. Mead, S. Markus, "The Forced Vibration of a Three-Layer, Damped Sandwich Beam with Arbitrary Boundary Conditions," *J. Sound Vib.*, Vol. 10, No. 2, pp. 163-175, 1969
- [2] F. C. Nelson, "In-Plane Vibration of a Simply Supported Circular Ring Segment," *Int. J. Mech. Sci.*, Vol. 4, pp. 517-527, 1962
- [3] D. S. Nokes, F. C. Nelson, "Constrained Layer Damping with Partial Coverage," *S & V Bulletin* 38, Part 3, pp. 5-12, Nov. 1968

DYNAMIC ANALYSIS OF THE RUNAWAY ESCAPEMENT MECHANISM

Gene W. Hemp
Department of Engineering
Science and Mechanics
University of Florida
Gainesville, Florida

A mathematical model is developed for the nonlinear damping of the runaway escapement mechanism. A kinematics study develops expressions for the effective linkage ratios between the driving (starwheel) and driven (pallet assembly) members of the escapement for both entrance and exit engagements. The kinetics of the escapement action accounts for six phases of motion during one complete cycle of the pallet assembly and starwheel encounter. Accounting for the variability of the linkage ratios for the first time in an analytical treatment, an expression for the damping of the escapement is derived. This expression is used to predict the behavior of a centrifugally driven mechanism for which experimental information is available. For steady state operation, the equation of motion for such units is solved in terms of elliptic integrals of the first kind.

INTRODUCTION

Mechanical oscillating mechanisms can provide a reliable, low-cost means of introducing damping into mechanical systems. The runaway escapement mechanism has been used extensively in ordnance applications to provide a safety and arming function. In order to better understand the operation of such units and subsequently provide an analytical means of design, several studies have been made on various types of mechanisms [1-6].

The runaway escapement mechanism consists of two principal units: (1) the starwheel shown in part on the right in Figure 1, and (2) the pallet assembly shown on the left. The starwheel is pinned at its geometrical center and is driven by a torque which is assumed to act counterclockwise. Motion of the starwheel is impeded by a series of impacts between pins extending upward from the pallet and the faces of the starwheel teeth. The pallet assembly is pivoted at such a distance from the starwheel pivot that a pallet pin may strike a face of a starwheel tooth, slide along it and leave that tooth allowing the starwheel to be free to accelerate until it encounters the other pallet pin at another tooth face of the starwheel - usually one or two

removed from the previous tooth in contact. In addition to the energy lost in the impacts, there is the pallet assembly inertia for the driving torque to overcome while the pins are in contact with the starwheel. The result is a reduction in the rate of rotation of the starwheel.

KINEMATICS

Figure 1 shows the general configuration for the upper (entrance) pallet pin in contact with the front face of a starwheel tooth. During this phase of the encounter between the two assemblies, the pallet is accelerated in the counterclockwise direction. The next contact, between the lower (exit) pallet pin and a starwheel face, accelerates the pallet in the clockwise sense.

An important quantity during the engaged motion is the ratio of angular velocities of the pallet and starwheel or the effective linkage ratio. This is the ratio of the moment arms of the normal force between the pallet pin and a starwheel tooth face about the pivots of the starwheel and pallet respectively. The kinematic condition arises from the requirement that the pallet pins slide along a tooth face while in contact.


$$N_{EN} = \frac{f}{\theta} = \frac{df}{d\theta} = \frac{A_{PN}}{A_{PN}(\theta)} = 1 - \frac{D \cos(\theta - \gamma)}{A_{PN}(\theta)} \quad (1)$$
$$A_{PN}(\theta) = [0^2 - (D \sin(\theta - \alpha))^2 - R \sin \gamma - r]^2 \quad (2)$$
$$N_{EX} = - \frac{1}{\theta} = - \frac{d\theta}{d\phi} = \frac{A_{EX}}{A_{PX}} = 1 - \frac{D \cos(\theta - \gamma + NA)}{A_{PX}(\theta)} \quad (1)$$
$$A_{px}(\theta) = [S^2 - (D \sin(\theta - \theta_0) + R)^2 - R^2 \sin^2 \theta]^{1/2} \quad (4)$$
$$\alpha = \alpha - \gamma - \sin^{-1} \left(\frac{D \sin(\alpha - \gamma) - H \sin \gamma}{D} \right) \quad (5)$$

● 一 二 三 四 五 六 七 八 九 十 ●

$$+ \sin^{-1} \left(\frac{D \sin(\theta - \gamma + \alpha) - r - R \sin \gamma}{R} \right) \quad (6)$$

$$W-E = E \sin\left(\frac{\pi}{2}\right) \cos\left(1 + \frac{\pi}{2}\right) = E \cos\left(1 + \frac{\pi}{2}\right) \quad (7)$$

126

From Figure 1 the initial value of A_{WN} is found to be

$$A_{WN}(\theta) = R \cos \gamma - P(W-E) = A_{PN}(\theta) - D \cos(\theta - \gamma) \quad (8)$$

where $A_{PN}(\theta)$ is given by (2). This equation can be solved for θ as a function of the geometrical parameters and the fraction of engagement, P . With $0 \leq P \leq 1$, the solution $\theta = \theta_1$ corresponds to the initial value of θ for engaged motion while $P = 0$ yields the value $\theta = \theta_2$ which corresponds to the final value for engagement. (The assumption that $P = 0$ corresponds to the final engaged position is equivalent to the assumption that the pallet pin leaves the starwheel tooth face with a velocity tangent to the face.)

From a similar analysis of the exit engagement one finds

$$A_{WX}(\theta) = R \cos \gamma - P(W-E) = -A_{PX}(\theta) - D \cos(\theta - \gamma + \pi/2) \quad (9)$$

from which the initial, θ_1 , and final, θ_4 , values of θ may be obtained.

Expressions (1), (2) and (5) are thus valid for $\theta_1 \leq \theta \leq \theta_2$ while (3), (4) and (6) are valid for $\theta_3 \leq \theta \leq \theta_4$.

KINETICS

The mathematical model considered here has six phases of motion (impact, coupled motion, free motion, impact, coupled motion, free motion) during one complete cycle of the pallet assembly, i.e. for contact between the starwheel and both of the pallet pins.

Major assumptions for this model are:

1. Friction forces between pallet pins and starwheel tooth faces are neglected.
2. Impacts between pallet pins and starwheel tooth faces are assumed perfectly inelastic.
3. The angular velocities of the starwheel and pallet are assumed zero at the beginning of coupled motion.

The third assumption greatly simplifies the later mathematics and over estimates the amount of energy lost at each impact. The first and second assumptions neglect energy dissipating mechanisms.

A. Governing Equations and First Integrals

Coupled Motion. - The entrance pallet pin and a starwheel face are engaged.

The equations of motion for the starwheel and pallet assembly are given by

$$\begin{aligned} I_S \ddot{\theta} &= T_S - F_N A_{WN}(\theta) \quad , \quad \theta_1 \leq \theta \leq \theta_2 \\ I_P \ddot{\phi} &= F_N A_{PN}(\theta) - T_P \quad , \quad \theta_1 \leq \theta \leq \theta_2 \end{aligned} \quad (10)$$

where F_N is the normal force between the pin and the starwheel, T_S is the net driving torque applied to the starwheel and T_P is the frictional torque at the pivot of the pallet assembly.

The normal force, F_N , can be eliminated from equations (10). Furthermore, using the kinematical constraint $\dot{\phi} = \dot{\theta} N_{EN}(\theta)$ from (1), the following equation for θ can be obtained:

$$\begin{aligned} (1 + H^2(\theta)) \ddot{\theta} + \dot{\theta} \frac{dH^2(\theta)}{d\theta} &= \frac{T_S}{I_S} - \frac{T_P}{I_S} N_{EN}(\theta) \end{aligned} \quad (11)$$

where

$$H^2(\theta) = \frac{I_P}{I_S} N_{EN}^2(\theta) \quad (12)$$

Recognizing the fact that $\dot{\theta} = \frac{d}{dt} \frac{\theta^2}{2}$ and that $(\frac{d}{dt} H^2(\theta) + 1) = \frac{dH^2(\theta)}{d\theta}$ the following integral can be obtained

$$\dot{\theta}^2 = \frac{2}{I_S (1 + H^2(\theta))} (T_S - T_P N_{EN}(\theta)) d\theta \quad (13)$$

where assumption 1. has been used to eliminate $\dot{\phi}$.

Assuming that the net driving torque, T_S , on the starwheel and the frictional torque, T_P , at the pallet pivot are constant over the interval of integration, this becomes

$$\dot{\theta}^2 = \frac{2T_S}{I_S} \frac{\theta - \theta_1}{1 + H^2(\theta)} - \frac{2T_P}{I_S} \frac{1 - \theta_1}{1 + H^2(\theta)} \quad (14)$$

where use has been made of the relation $d\theta = N_{EN}(\theta) d\phi$ from (1).

The angular velocity of the pallet during this phase of the motion is then given by

$$\dot{\phi}^2 = \frac{2T_S}{I_P} \frac{(\theta - \theta_1)H^2(\theta)}{1+H^2(\theta)} - \frac{2T_P}{I_P} \frac{(\phi - \phi_1)H^2(\theta)}{1+H^2(\theta)} \quad (15)$$

$$\phi_1 < \phi < \phi_2$$

where $\phi = \phi(\theta)$ is defined by (5).

Free Motion. - The starwheel and pallet assembly are disengaged.

After the entrance pallet pin leaves the tooth face, the motions are independent until the exit pallet pin strikes another tooth face.

The equations of motion for the two units during this phase are:

$$I_S \ddot{\theta} = T_S \quad \theta_2 < \theta < \theta_3 \quad (16)$$

$$I_P \ddot{\phi} = -T_P \quad \phi_2 < \phi < \phi_3$$

These are easily integrated assuming T_S and T_P are constants over the range of integration. These first integrals are:

$$\dot{\theta}^2 = \dot{\theta}_2^2 + \frac{2T_S}{I_S} (\theta - \theta_2) \quad \theta_2 < \theta < \theta_3 \quad (17)$$

$$\dot{\phi}^2 = \dot{\phi}_2^2 - \frac{2T_P}{I_P} (\phi - \phi_2) \quad \phi_2 < \phi < \phi_3 \quad (18)$$

During this phase of free motion, the starwheel accelerates due to the drive torque while the pallet decelerates due to friction losses at the pivot. After some finite rotation of each unit, the exit pallet pin strikes the face of another starwheel tooth and the units begin another phase of engaged motion. However, the pallet is now accelerated in the clockwise direction. The value of θ for which this impact occurs corresponds to some fraction of engagement - usually around $P = 0.6$. (The minimum value of P can be calculated by freezing the motion of the pallet at $\theta = \theta_1$ and allowing the starwheel to rotate until the exit pin makes contact. For typical values for the geometrical values this is around $P = 0.5$.) The correct value can be determined only through an iterative process.

Coupled Motion. - The exit pallet pin and a starwheel tooth face are engaged. After the impact, the two units begin another phase of engaged motion. The angular velocities are related by

$$\dot{\phi} = -N_{EX}(\theta) \dot{\theta} \quad (19)$$

and the equations of motion are

$$I_S \ddot{\theta} = T_S - F_{NWX}(\theta) \quad \theta_3 < \theta < \theta_4$$

$$I_P \ddot{\phi} = T_P - F_{NPX}(\theta) \quad \phi_3 < \phi < \phi_4 \quad (20)$$

Proceeding as in the previous phase of engaged motion, the following first integrals are obtained:

$$\dot{\theta}^2 = \frac{2T_S}{I_S} \frac{(\theta - \theta_3)}{1+X^2(\theta)} + \frac{2T_P}{I_S} \frac{(\phi - \phi_3)}{1+X^2(\theta)} \quad (21)$$

$$\theta_3 < \theta < \theta_4$$

and

$$\dot{\phi}^2 = \frac{2T_S}{I_P} \frac{(\theta - \theta_3)X^2(\theta)}{1+X^2(\theta)} + \frac{2T_P}{I_P} \frac{(\phi - \phi_3)X^2(\theta)}{1+X^2(\theta)} \quad (22)$$

$$\theta_3 < \theta < \theta_4$$

where

$$X^2(\theta) = \frac{I_P}{I_S} N_{EX}^2(\theta) \quad (23)$$

and $X = X(\theta)$ is defined by (6). The assumption of zero velocities at the beginning of engaged motion has eliminated $\dot{\theta}_1$.

Free Motion. - The exit pin slides along the starwheel tooth face until the two units become engaged.

The equations of motion for this phase of the motion are

$$I_S \ddot{\theta} = T_S \quad \theta_4 < \theta < \theta_5$$

$$I_P \ddot{\phi} = T_P \quad \phi_4 < \phi < \phi_5 \quad (24)$$

which may be integrated to yield

$$\dot{\theta}^2 = \dot{\theta}_4^2 + \frac{2T_S}{I_S} (\theta - \theta_4) \quad \theta_4 < \theta < \theta_5 \quad (25)$$

$$\dot{\phi}^2 = \dot{\phi}_4^2 + \frac{2T_P}{I_P} (\phi - \phi_4) \quad \phi_4 < \phi < \phi_5 \quad (26)$$

At the end of this phase of motion, the entrance pallet pin impacts with another starwheel tooth. The fraction of engagement P is again unknown.

It is assumed that after some transient period, there will exist a steady state motion that will repeat itself, i.e. $\theta_5 = \theta_1 + \Delta$ and $\phi_5 = \phi_1$. This is verified by experimental evidence.

B. Damping Due to the Escapement Mechanism

The damping torque exerted by the pallet assembly-starwheel combination on any mechanism with which it is used may be determined by solving for T_S , the torque required to drive the system.

In each of the coupled and free motion phases it has been possible to obtain an expression of the form (See (14), (17), (21) and (25))

$$T_S = C(\theta)\dot{\theta}^2 + T_P\theta \quad (27)$$

Use of these equations to express the damping would be unmanageable in practice since there is generally a large number of complete encounters which must be considered in applications.

It is proposed to replace these expressions for the retarding torque by a similar expression with average, constant coefficients C_E and B_E . (Experimental evidence also shows that the average running rate, $\bar{\theta}$, is proportional to $T_S^{1/2}$). Such an expression would be valid for the entire motion:

$$T_S = C_E\dot{\theta}^2 + T_P\theta \quad (28)$$

In order to determine the proper values for C_E and B_E it is necessary to calculate the mean square angular velocity of the starwheel for one complete encounter:

$$\bar{\theta}^2 = \frac{1}{\theta_5 - \theta_1} \int_{\theta_1}^{\theta_5} \dot{\theta}^2(\theta) d\theta \quad (29)$$

where the range of integration is divided into the four intervals corresponding to the engaged and free phases of the motion. The integrands are given for each of the integrals by (14), (17), (21) and (25) respectively.

The integrations for the free motion phases are easily performed. However, the complexity of the integrands given by (14) and (21) require the integrals to be approximated. Since $\theta - \theta_1$, $\theta_1 - \theta_2$ and $\theta - \theta_3$, $\theta_3 - \theta_4$ are small quantities, the integrands can be expanded in Taylor series in $\theta - \theta_1$ and $\theta - \theta_3$ respectively and the series integrated term by term. (Calculations for typical mechanisms indicate that retention of quadratic terms in $\theta - \theta_1$ etc. yields 95% or better accuracy for the integration.)

Performing these operations the expression for $\bar{\theta}^2$ is found to be:

$$\bar{\theta}^2 = \frac{2T_S}{I_S} G_1(\theta_1, \theta_2, \theta_3, \theta_4) - \frac{2T_P}{I_S} G_2(\theta_1, \theta_2, \theta_3, \theta_4) \quad (30)$$

where

$$G_1 = \frac{1}{6} \frac{(\theta_2 - \theta_1)^2}{2(I + H_1^2)} \left(1 - \frac{4H_1 H_1' (\theta_2 - \theta_1)}{3(I + H_1^2)} \right) + \frac{(\theta_2 - \theta_1)(\theta_3 - \theta_2)}{I + H_2^2} + \frac{(\theta_3 - \theta_2)^2}{2} + \frac{(\theta_4 - \theta_3)^2}{2(I + X_3^2)} \left(1 - \frac{4X_3 X_3' (\theta_4 - \theta_3)}{3(I + X_3^2)} \right) + \frac{(\theta_4 - \theta_3)(\theta_5 - \theta_4)}{I + X_4^2} + \frac{(\theta_5 - \theta_4)^2}{2} \quad (31)$$

and

$$G_2 = \frac{1}{6} \frac{(\theta_2 - \theta_1)^2}{2(I + H_1^2)} \sqrt{\frac{I_S}{I_P}} (H_1 + \frac{(\theta_2 - \theta_1) H_1'}{3} \left(1 - \frac{4H_1^2}{I + H_1^2} \right)) + \frac{(\theta_3 - \theta_2)(\theta_2 - \theta_1)}{I + H_2^2} + \frac{(\theta_4 - \theta_3)^2}{2(I + X_3^2)} \sqrt{\frac{I_S}{I_P}} \left(X_3 + \frac{(\theta_4 - \theta_3) X_3'}{3} \left(1 - \frac{4X_3^2}{I + X_3^2} \right) \right) + \frac{(\theta_5 - \theta_4)(\theta_3 - \theta_4)}{I + X_4^2} \quad (32)$$

where primes denote differentiation with respect to θ .

Solving (30) for T_S and comparing this expression with that obtained by integration of (28) with respect to θ over the same range, the following definitions are obtained:

$$C_E = I_S/2G_1 \quad (33)$$

$$B_E = G_2/G_1$$

The amount of retardation exerted by the pallet assembly and starwheel is seen to depend on the fraction of engagement, P , through θ_1 and θ_3 and on the geometrical and inertial properties of the units through $H(\theta)$, $X(\theta)$ and $\zeta(\theta)$.

It should be noted that the quantities $1+H^2(\theta)$ and $1+X^2(\theta)$ as well as the derivative of each with respect to θ are important in the damping. An increase in any of these quantities will cause the damping to increase. These cannot be arbitrarily increased however. Further analysis including the effect of friction forces between the pallet pins and starwheel faces shows that the drive torque may not be large enough to initiate motion if they are too large [6].

The expressions for the damping coefficients and effective linkage ratios have been used to examine the sensitivity of these quantities to variations in the geometrical parameter. The range of variation was limited by manufacturing tolerances for existing mechanisms. All quantities were found to be more sensitive to changes in the pallet pin locations (Q and S) than the other geometrical parameters. The half angle, γ , of the starwheel tooth was the next most sensitive parameter.

Figure 2 shows calculated values for C_E and B_E as a function of the fraction of engaged motion, P , over the entire theoretical range $0 \leq P \leq 1.0$. For a steady state operation of the mechanism, the fraction of engagement is constant. Interest is therefore centered on one value each for C_E and B_E at that value of P . Values shown in Figure 2 are for the runaway escapement mechanism contained in the M125A1 booster safety and arming mechanism (S & A) currently in use in ordnance applications. [5]

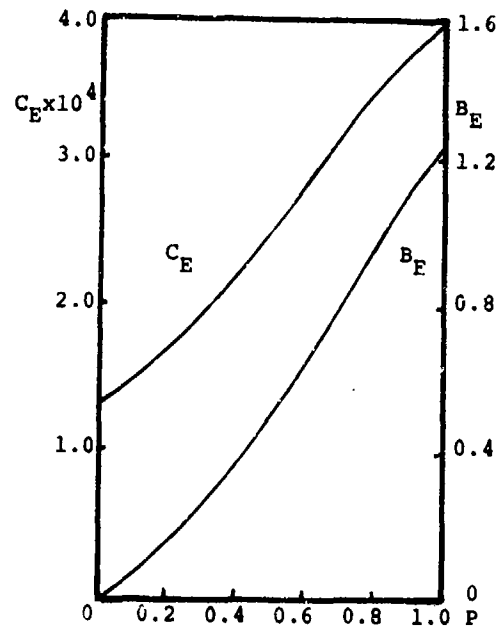


Fig. 2 DAMPING COEFFICIENTS

KINETICS OF A SAFETY AND ARMING MECHANISM

In order to evaluate the proposed mathematical model for the damping action of the runaway escapement it is necessary to predict the operating behavior of a unit containing the escapement, investigate the behavior experimentally, and compare the predicted and measured values defining this behavior. The M125A1 S&A was chosen for this task. The quantities to be compared are the time-to-arm and turns-to-arm where the latter is the product of the former and the spin speed of the entire S&A.

This unit has a spin-driven rotor assembly (the rotor is pivoted about an axis not passing through its center of mass), the motion of which is retarded by a runaway escapement mechanism connected to the rotor through a gear train. The equation of motion for the rotor has been shown to be [5]

$$I_R \ddot{\psi} + R_I + R_F + R_E = M \quad (34)$$

where M is the rotor driving torque, R_I is the inertial resistance of the gear train and starwheel, R_F is the frictional resistance of the gear train, and ψ is the displacement of the rotor. R_E

is the resistance due to the escapement action. It is the previously obtained damping torque multiplied by the net gear ratio for the gear train including an estimate of the efficiency of meshing action of the gears. It can be shown that

$$R_E = C\dot{\psi}^2 \quad (35)$$

where C is proportional to the damping coefficient C_E .

After a short transient phase (compared with the total running time), the angular acceleration of the rotor becomes quite small and may be neglected without substantial error [5]. Equation (34) may be written as

$$C\dot{\psi}^2 = n^2(A \sin \psi - \mu(F+B)) - M_0 \quad (36)$$

where n is the spin speed of the S&A, B is proportional to R_E , F is related to the frictional resistance torque, R_F , M_0 is the torque required to initiate motion of the rotor, μ is the coefficient of friction at the pivots and A is related to the moment arm for the driving torque. (For details of the derivation of these equations and definition of the above constants see [5-6].)

Define

$$\sin \psi = 1 - 2k^2 \sin^2 \beta \quad (37)$$

where

$$k' = \frac{1}{2} \left(1 - \frac{\mu(F+B)n^2 + M_0}{An^2} \right), \quad (38)$$

$$0 < k^2 < 1$$

Using (37) in (36), one can obtain

$$\left(\frac{d\beta}{dt} \right)^2 = 1 - k^2 \sin^2 \beta \quad (39)$$

where

$$\tau = t \sqrt{\frac{n^2 A}{2C}} \quad (40)$$

Equation (39) may be integrated to yield

$$\tau - \tau_0 = K(\beta, k) - K(\beta_0, k) \quad (41)$$

where $K(\beta, k)$ is the Jacobian elliptic integral of the first kind [7].

Using (40) and assuming $\tau_0 = 0$ at $\beta = \beta_0$, one can obtain

$$t = \frac{1}{n} \sqrt{\frac{2C}{A}} (K(\beta, k) - K(\beta_0, k)) \quad (42)$$

where β is related to ψ through (37).

The time for the rotor to complete its motion, i.e. $t = t_F$, $\psi = \psi_F$ is thus given by (42) with $\beta = \beta_F$. The number of turns or rotations of the entire S&A during this motion is simply nt_F .

The angular displacement of the rotor can be obtained as a function of time from (42) using (37) and the identity [7]

$$\text{sn}(K(\beta, k)) = \sin \beta \quad (43)$$

where sn is the Jacobian elliptic sine. The result is given by:

$$\psi = \frac{\pi}{2} - 2 \sin^{-1} \left(k \text{sn} \left(nt \sqrt{\frac{A}{2C}} - K(\beta_0, k) \right) \right) \quad (44)$$

$$0 = t_0 \leq t \leq t_F$$

Figure 3 shows the calculated values for turns-to-arm versus spin rate for 95% efficient gear meshes and for a coefficient of friction at the pivots of 0.15.

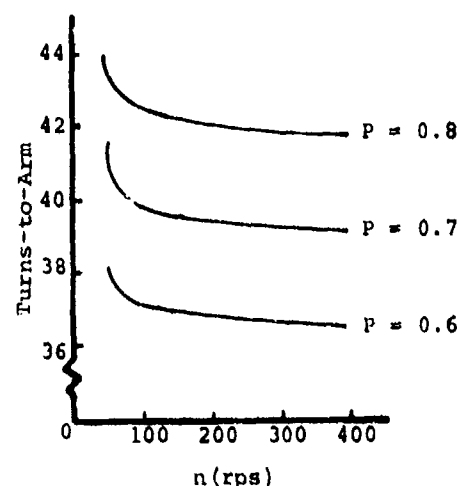


Fig. 3 THEORETICAL TURNS-TO-ARM VERSUS SPIN SPEED

It should be noted that an increase in P of 0.1 yields an increase in the minimum turns-to-arm characteristic of 2 to 3 turns. Similar increases can be effected holding P constant and increasing the coefficient of friction by 0.05 or by decreasing the efficiency of the gear meshes by 1%.

The curves of Figure 3 have P as a constant value. However, it is expected that the fraction of engaged motion depends on the driving torque and hence on n^2 . As the spin speed is increased, the starwheel has a greater acceleration during phases of free motion and catches up with the pallet sooner. Therefore, P is of the form

$$P = P_0 + \delta P n^2, \quad \delta P > 0 \quad (45)$$

Figure 4 shows the effect this relation would have on the turns-to-arm characteristics for $P_0 = 0.5$ and $\delta P = 10^{-5}$. The magnitude of the value for P_0 was obtained from analysis of high-speed movies (10,000 frames per second) taken of laboratory tests of the M125A1 S&A. These movies along with a numerical solution of equations (14), (15), (17), (18), (21), (22), (25) and (26) for the condition that the angular velocities were zero at the beginning of engaged motion provided an estimate of δP . (It should be pointed out that the numerical analysis showed the values of P to be greater than one. This is probably the effect of the assumption that the angular velocities are zero at the beginning of engaged motion.) Also shown in Figure 4 are the results of the laboratory tests.

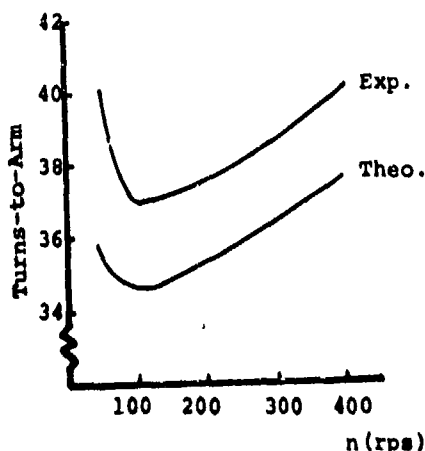


Fig. 4 COMPARISON OF EXPERIMENTAL AND THEORETICAL TURNS-TO-ARM VERSUS SPIN SPEED

DISCUSSION

While Figure 4 shows good agreement between calculated and experimental results it should be recalled that there are several parameters which need to be estimated and these can have a profound effect on the final results. Fortunately, only the value of P is an unknown for the damping calculations. Thus proposed designs for a runaway escapement can be evaluated and compared using the proposed damping model.

In an effort to further validate the damping model, another escapement mechanism, the M125A1E3, which has been built for possible ordnance use was also tested and the results compared with predictions using the proposed model. In this case the model predicted only 40-45% of the turns-to-arm [6]. This result is unacceptably low and indicates further work is necessary in the development of an accurate model for the damping of a wide range runaway escapement mechanism.

ACKNOWLEDGMENTS

The work presented here was performed at the Harry Diamond Laboratories (Branch 420) in Washington, D.C. during the summer months of 1970 and 1971 under the A.R.O.-D. summer consultant program and at the University of Florida. The author wishes to acknowledge invaluable discussions with and encouragement from David Overman, Branch 420, during all phases of this research.

REFERENCES

- [1] "A Study of the Dynamics of an Untuned Clock Mechanism," by VMI Department of Physics, Lexington, Va. under Contract CST-1224 (DAI-49-186-ORD(P)-100 with HDL; September, 1953.
- [2] "A Study of the Effect of Geometrical Factors Upon the Behavior of an Untuned Clock Mechanism," by VMI Department of Physics, Lexington, Va. under Contract CST-1224 (DAI-49-186-ORD(P)-100 with HDL; June, 1954.
- [3] J. N. Shinkle, "A General Study of Verge Escapement Performance," Sandia Laboratories Research Report SC-RR-69-495, October, 1969.

- [4] M. E. Anderson and S. L. Redmond,
"Runaway (Verge) Escapement
Analysis and Guide for Designing
Fuze Escapements," NWCCL TP 860,
December, 1969.
- [5] David Overman, "Theoretical
Analysis of the M125 Booster
Mechanism," HDL TR-1550, June,
1971.
- [6] Gene W. Hemp, "Damping Proper-
ties of the Runaway Escapement
Mechanism," HDL-TR (to appear).
- [7] P. F. Byrd and M. D. Friedman,
"Handbook of Elliptic Integrals
for Engineers and Scientists,"
Springer-Verlag, 1954.

PREDICTION AND EXPERIMENTAL TECHNIQUES

A METHOD FOR PREDICTING BLAST LOADS

DURING THE DIFFRACTION PHASE

W. J. Taylor

Ballistic Research Laboratories
Aberdeen Proving Ground, Maryland

Recent work undertaken by the Ballistic Research Laboratories was directed toward improving the accuracy of the predicted load-time diagram for simple structures so that more precise calculations of structural response could be made. The established prediction schemes do not differentiate between two- and three-dimensional structures so this is the area of primary interest in this paper. The results of this analytical and experimental investigation show substantial differences in loading between two- and three-dimensional cases. A method for determining the load during the diffraction phase is presented and compared to experimental data.

INTRODUCTION

In the early 1950's laboratory and field experiments were conducted to define the blast loading on structures. The work of that era was synthesized by contractors to the Corps of Engineers and published in a Corps of Engineers Manual EM 1110-345-413, "Design of Structures to Resist the Effects of Atomic Weapons." This work received wide distribution and in 1965 it was republished as a Dept. of the Army Technical Manual TMS-856-1. It has served as a very useful document for both the designers of blast hardened structures and for those having responsibility for vulnerability studies. Vulnerability work and present day design requirements indicate a degree of accuracy that is beyond the scope of this document. For such studies one should know the load history at any point on a structure. Complex computational techniques can provide this type of resolution for two-dimensional structures and work is progressing toward solving such problems on three-dimensional structures. The requirement for precise point loading information does not relieve the requirement to provide more precise average load-time histories and this paper is aimed at giving the problem solver a simple, but more accurate method for estimating average blast loads on the front and rear surface of structures.

Figure 1 illustrates the technique outlined in the technical manual for determining average loads on the front and rear surfaces. As one can see, one of the more important calculations made when determining the load-time curve on a structure is that which determines the length of time that some component of reflected pressure persists on the

structure. This time is referred to as clearing time, t_c , and as determined by the technical manual is $3S/a_5$, where S is either the height of the structure or one-half the width, whichever is smaller, and a_5 is the speed of sound in the reflected pressure region on the face of the model. Some design manuals use U , the shock front velocity just prior to shock front impingement on the structure, instead of a_5 . The difference between U and a_5 is small at low pressures so it makes little difference which value is used. At pressures above 20 psi however the differences exceed 15 percent.

On the rear of the structure the average rear surface pressure is determined from the equation

$$P = P_s (.5) (1 + (1-\beta) e^{-\beta})$$

where $\beta = .5P_s/p_0$, p_0 = atmospheric pressure

The time, t_b , required to reach the pressure is given by the equation

$$t_b = .4S/c_0$$

where S is the height of the structure or one-half the width whichever is smaller and c_0 is the speed of sound in air before shock arrival.

If we examine the clearing time equation we see that two targets that are widely different could have the same average load. If the height for instance, was the limiting dimension, then any width greater than two times the height

Preceding page blank

would not change the average load. We know from experiment that this is not the case. Also, on the rear surface the equation which gives the rate of rise to maximum pressure is insensitive to shock overpressure since it assumes pressure disturbances to be propagated at a speed equal to the speed of sound in ambient air.

ANALYSIS AND EXPERIMENT

With these current prediction techniques in mind we performed a simple analysis and conducted a shock tube study which was aimed at observing the differences between average loads on two- and three-dimensional models. The analysis shows that the rarefaction wave activity on the two-dimensional target is less than on the three-dimensional target during a fixed time interval. These waves travel at the local speed of sound and set up the flow from the zone of high pressure to one of lower pressure near the free edges. A structure with either a large or small height to width ratio receives a very different unloading pattern than one with dimensions which are equal, or near equal. This is illustrated in Figure 2, which shows six rarefaction waves crossing in the clearing time T_0 on a structure with a height to width ratio of 1/2 and four on the structure which is very wide.

The experimental program to investigate the difference in loading between two- and three-dimensional structures was conducted in the square test section of the BRL 24" shock tube. A steel model was instrumented with three piezoelectric gages on one face. The gages and their positions on the model remained unchanged during the experiment, but the model was turned 180 degrees for observing back face loading. The three-dimensional model was converted to a two-dimensional model by adding wood blocks to fill the space between the model and shock tube wall. Figure 3 shows the various test configurations. Shock pressures of 5, 10, 15 and 20 psi were applied to these test configurations and the data were recorded on oscilloscopes.

An attempt was made to position the gages on the model so that an average pressure during the diffraction phase would be obtained by combining the records. The front surface of the model was sectioned as shown in Figure 4A and gages were placed at the centroid of the area A, C and D as shown in Figure 4B. Position A was given a weight of 2, and C and D each a weight of 1 in an averaging channel which combined the gage output and displayed them as a single record. Figure 5 shows the records made from a typical shot along with the output of the averaging channel. The averaging channel was considered to describe the average load on the face and was used in the comparison of data throughout the program.

Figure 6 shows separate wave diagrams for the rarefaction waves coming from the top

and sides of the three-dimensional model subjected to a 5 psi shock wave. The rarefaction wave speed used is that of the speed of sound in the reflected gas zone. Gage position A is swept by a rarefaction wave emanating from the tip of the model at 140 useconds and this is reflected from the ground surface and again sweeps the gage position at 400 useconds. Similar signals from the sides are received at 50 and 450 useconds. Arranging these in the order of their occurrence produces a signal at 50, 140, 400 and 450 useconds. The first two are readily identified in Figure 7. Positions C and D receive their first signals at the same time, 140 useconds from different edges and are also readily identified. Each rarefaction wave that passes contributes to the unloading but when the individual gage positions are summed, the passes are as seen in Figure 5, less distinct.

The wave diagram in Figure 6 can be used to identify the shock or compression wave interactions on the rear surface at the 5 psi level where the pressure wave propagation, as determined from the experiments, is nearly the same speed as the rarefaction wave speed. Figure 8 shows records from the rear surface with time beginning when the pressure wave starts down or across that surface. Position A receives a pressure pulse at approximately 50, 140, 400 and 450 useconds, but these waves exhibit a compression rather than a shock rise time so the pressure peak occurs later in time. The arrival times after the first wave are actually somewhat longer or shorter than what the wave diagram shows because of the direction of particle flow. Positions C and D exhibit near identical patterns, as they should and demonstrate that the mirror image barrier is a valid substitute for a ground plane.

The strong interactions at Positions C and D are somewhat balanced by the dip in pressure at Position A on the average pressure plot. Position A, which is close to both the top and side edges, has been influenced by the vortex generated by those edges. In general, the rear surface loading is quite non-uniform and hence more heavily averaged than the front surface loading.

A. Experimental Results-Front Surface

Figures 9 and 10 show the differences in front surface loading between the two- and three-dimensional models for the nominal shock pressures of 5, 10, 15 and 20 psi. The input shock pressures were not precisely the same as the nominal pressure levels, and the difference is indicated by the slight difference in reflection factor and two values of stagnation pressure ratio. These figures show that the three-dimensional model is more swiftly relieved of its reflected pressure than the two-dimensional model. Notice that the pressures go below the stagnation pressure level on the three-dimensional model at 5, 10 and 15 psi level and remain there for about one crossing time before

returning to the stagnation pressure level.

The records from the three-dimensional model show a pressure jump occurring at about 3 or 4 crossing times. This is caused by the reflected wave from the model interacting with the shock tube wall and returning to the model. The records at this point and beyond in time are not considered representative of the free field case. For the two-dimensional model this reflection occurs at a time later than what is plotted and so these records are considered valid for the times plotted.

These records of front face loading show that clearing time, or time for the reflected pressure to decay to stagnation pressure, is something other than $3S/a_5$. The three-dimensional model clears faster than the two-dimensional model and the stronger shocks require more crossing time than weak shocks. In fact, the two-dimensional model does not reach stagnation pressure during the recording time at the higher shock pressure levels. Figure 11 shows a plot of percent of stagnation pressure remaining after a time $3S/a_5$ and points up the error that is introduced in a loading calculation if that criteria is used.

In an attempt to relate the rarefaction wave activity with the amount of unloading, the records shown in Figures 9 and 10 were replotted with the time base changed to number of rarefaction wave crossings. This, in effect, expands the time axis for the three-dimensional model by a factor of 2. This replotting, shown in Figures 12 and 13, shows the correspondence between pressure change and number of rarefaction wave passes, and the agreement is rather good for the first four crossings. The fifth crossing on the two-dimensional model occurs at about the time limit of the records, but from Figures 9 and 10 one can see that the pressure level is approaching the stagnation pressure. On the three-dimensional model interactions of the two wave systems on all but the 20 psi shot cause the pressure to temporarily be reduced to a value below the stagnation level at about the fifth crossing. The pressure is eventually returned to stagnation pressure by a compression wave which the depression creates or a reflection from the shock tube wall if that occurs sooner.

The curves in Figures 12 and 13 suggest that a load-time history can be established by counting the rarefaction waves. An average curve was then drawn for each pressure level and a plot was made (Figure 14) which shows the percent of reflected pressure remaining after each rarefaction wave pass. The tendency for the two-dimensional and three-dimensional data to separate at the fifth rarefaction wave crossing is not then exhibited and both sets of data show the pressure approaching stagnation pressure at the time of the fifth rarefaction. This is a compromise which dilutes accuracy but greatly simplifies making a load time estimate.

B. Experimental Results-Rear Surface

Figures 15 and 16 show the difference in rear surface loading between two and three-dimensional models for the four pressure levels. The time unit is that taken from TM 5-856-1, and according to that publication, four such time units are required before the maximum average rear surface pressure is achieved. These data show that the maximum pressure is achieved in about 2-1/2 time units and that the three-dimensional model achieves a higher pressure than does the two-dimensional model. This is not surprising since the wave diagrams show the three-dimensional model has more compressional wave interactions. Figure 17 is a plot of the average rear pressure ratio at 2-1/2 time units on both models as a function of input pressure.

CONCLUSIONS

This investigation showed that target shape has a significant influence on the load time history. A very high or wide building has:

a. Pressure in excess of the stagnation pressure at the time $3S/a_5$.

b. Maximum pressure that is achieved on the rear surface occurs in about 1/2 the time predicted from TM 5-856-1.

On the structure that has a height to width ratio near 1/2:

a. Stagnation pressure is achieved on the front prior to the time $3S/a_5$.

b. Pressure on the rear is somewhat higher than predicted and achieves its level in about 1/2 the predicted time.

If the results of this study are applied to a structure without thickness, the net force curves shown in Figure 18 are obtained. The solid lines are the constructed curves and the dashed lines are those obtained from the procedure outlined in the technical manual. For the case shown, a 5 psi shock, the impulse delivered during the time $3S/a_5$ is 38 percent less than what would be predicted by current procedure, on the three-dimensional model and 20% less on the two-dimensional model.

ACKNOWLEDGEMENT

The author would like to express his appreciation to Rodney Abrahams and Warren Baily for their valuable assistance.

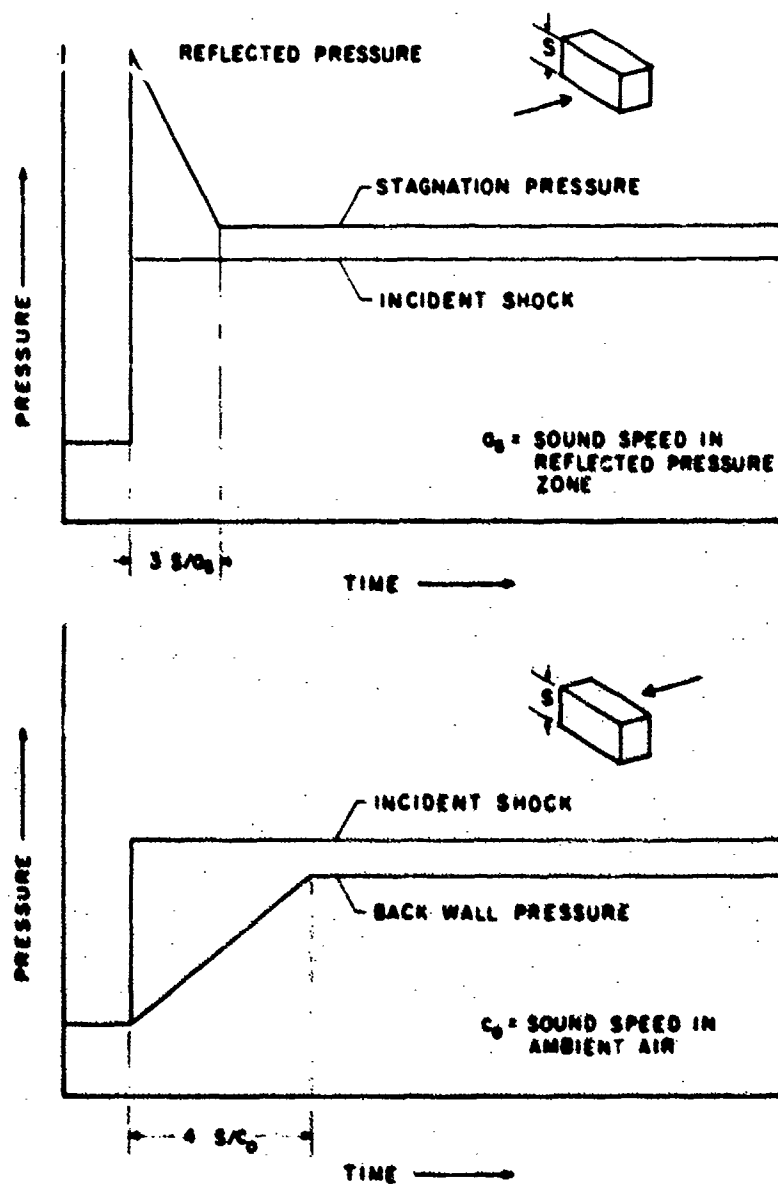


Figure 1. Development of Load Histories for Front and Rear Surfaces

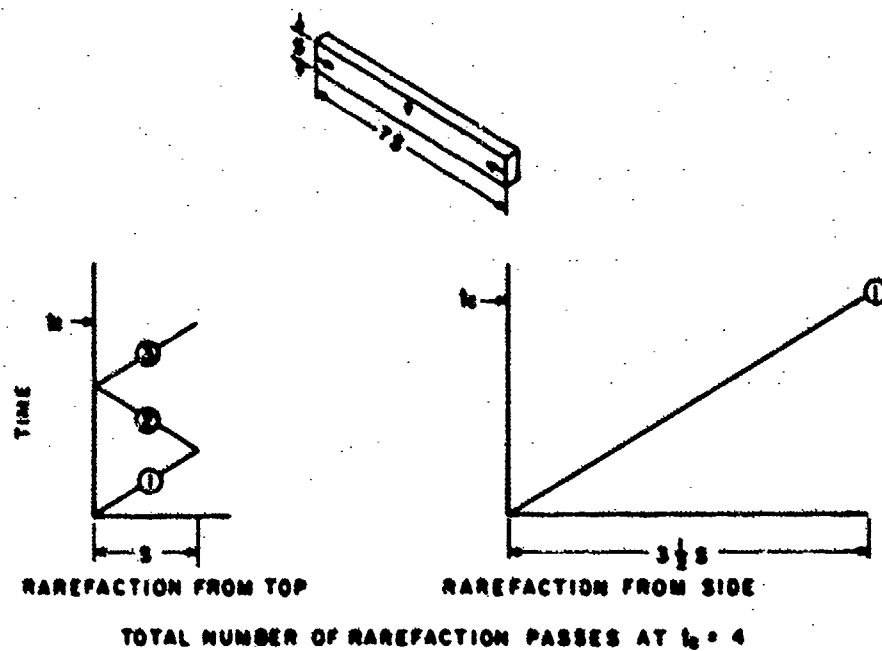
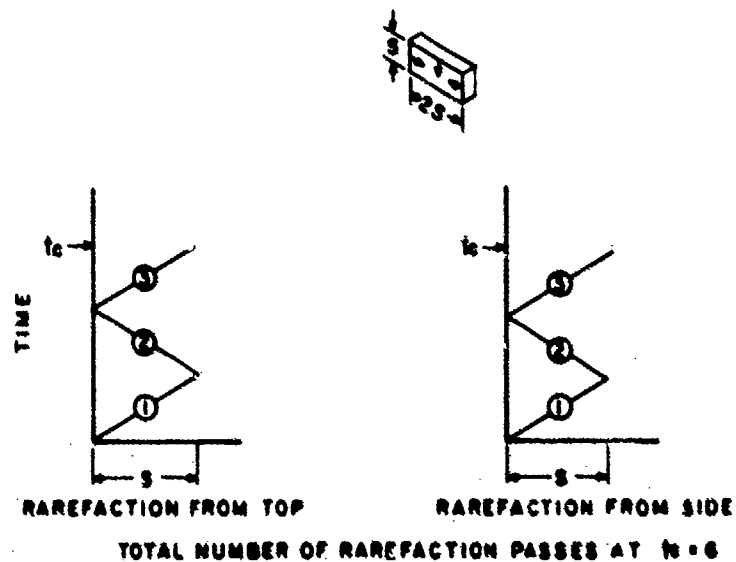


Figure 2. Rarefaction Wave Action on 2 and 3-D Targets

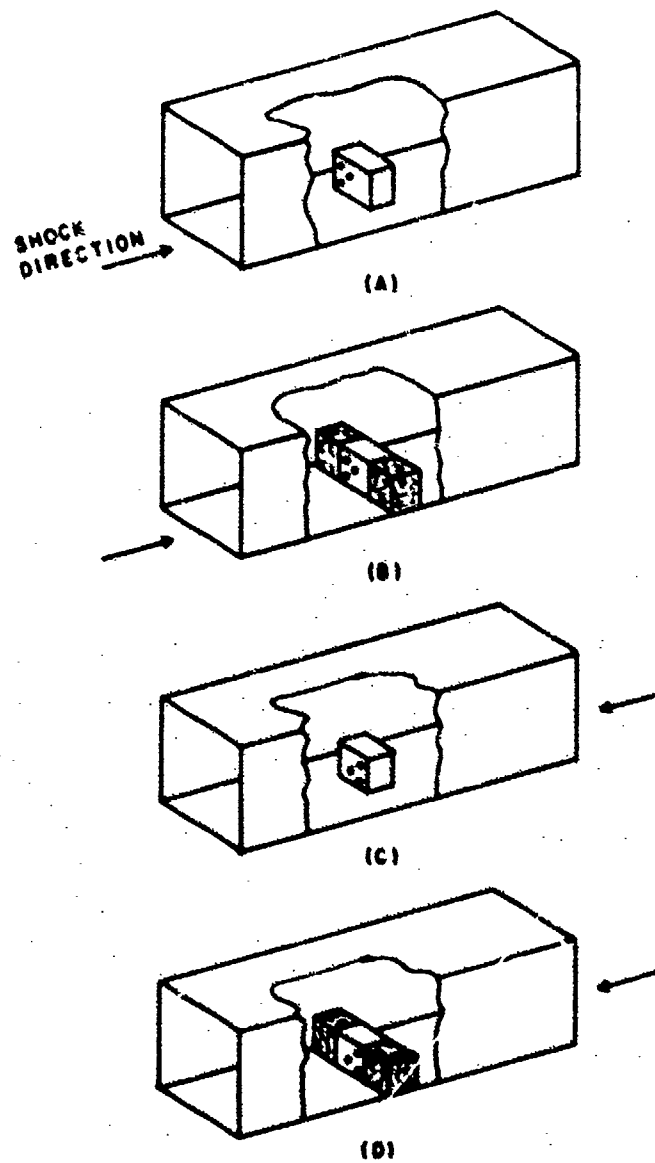
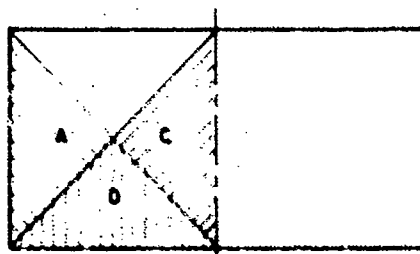
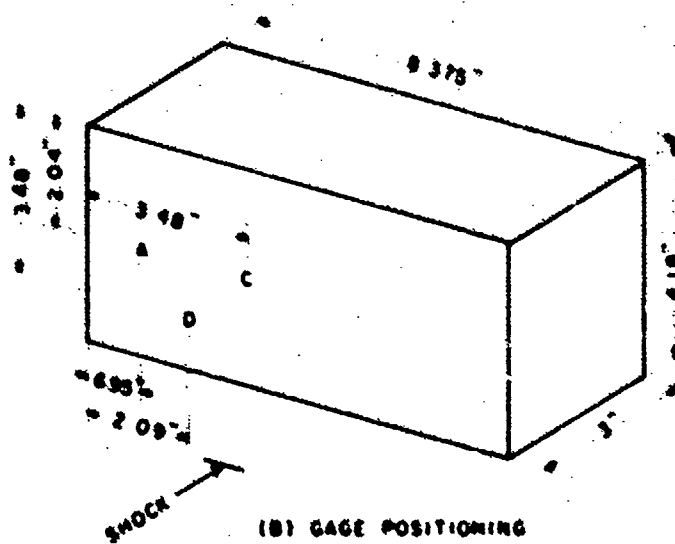


Figure 3. Test Configurations



(A) SURFACE ZONING



(B) GAGE POSITIONING

Figure 4. Gage Positioning

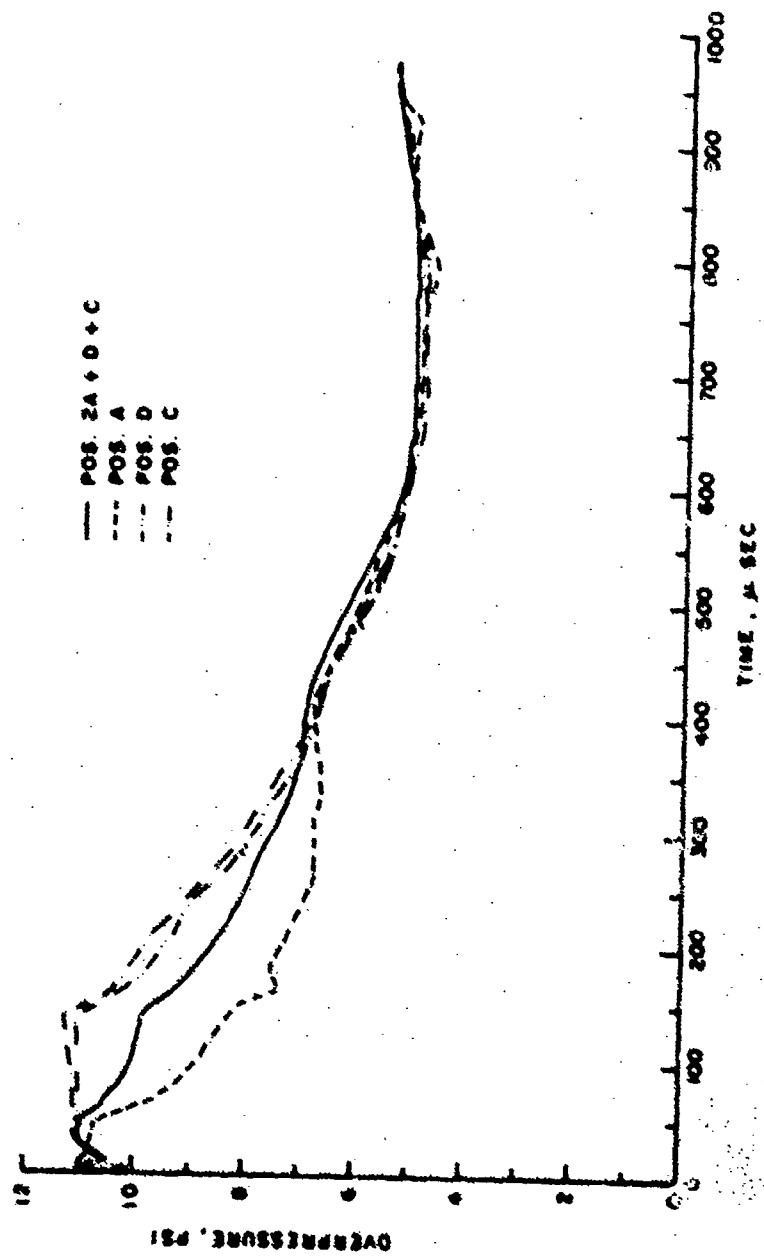


Figure 5. Typical Front Surface Records

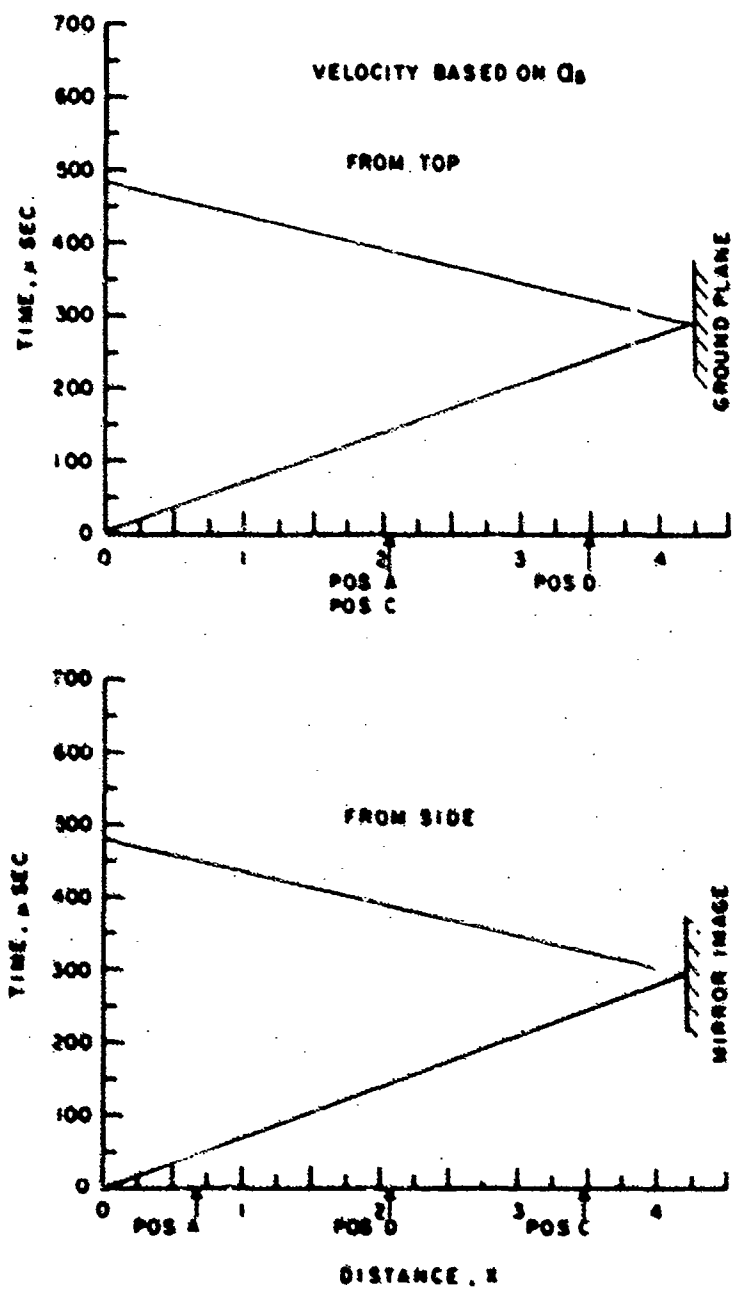


Figure 6. Wave Diagram for X-Pol Check on J-F Model

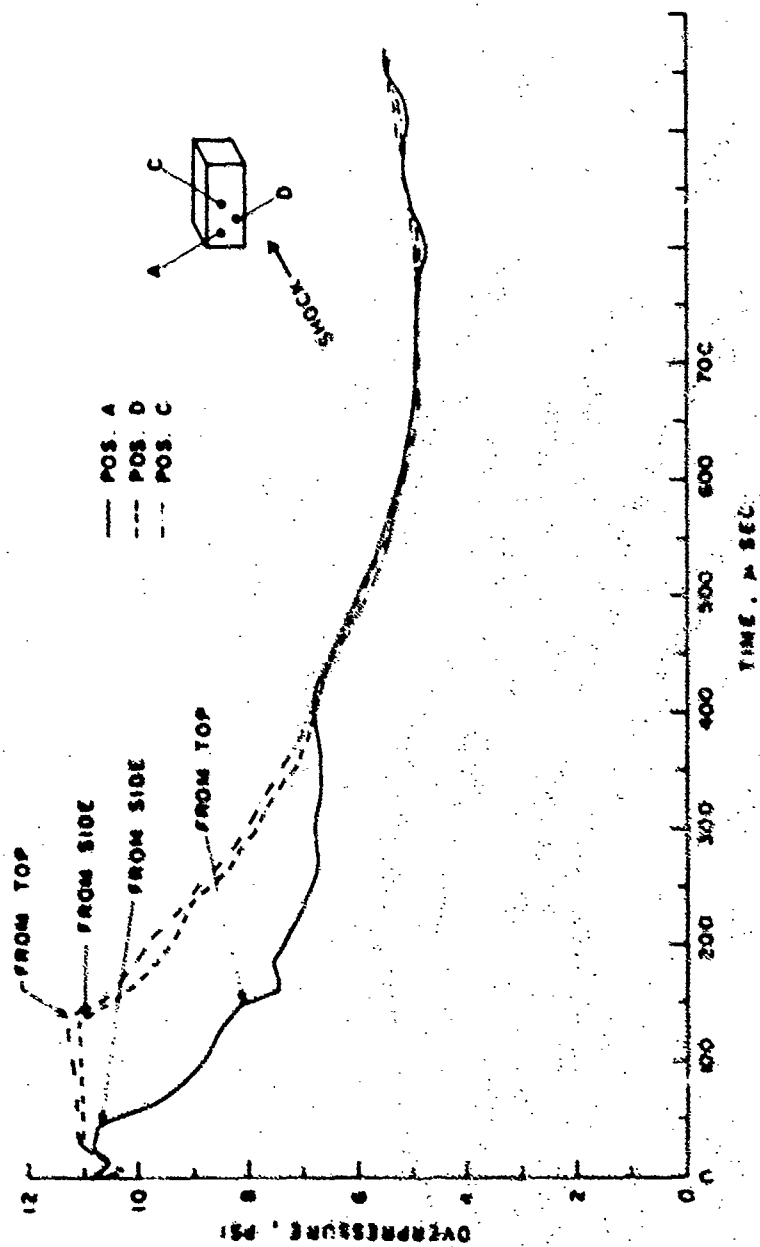


Figure 7. Rarefaction wave identification on front surface

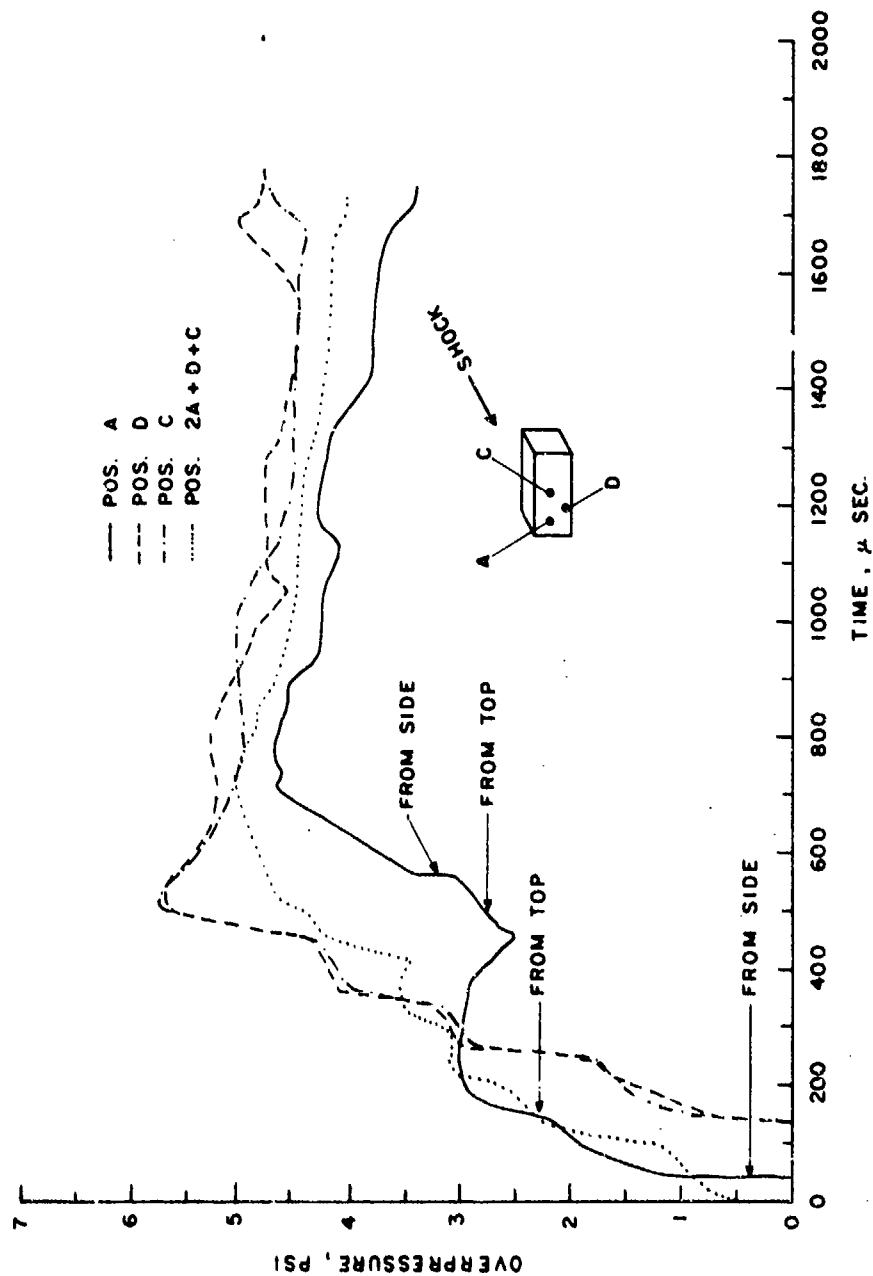


Figure 8. Rear Surface Loading

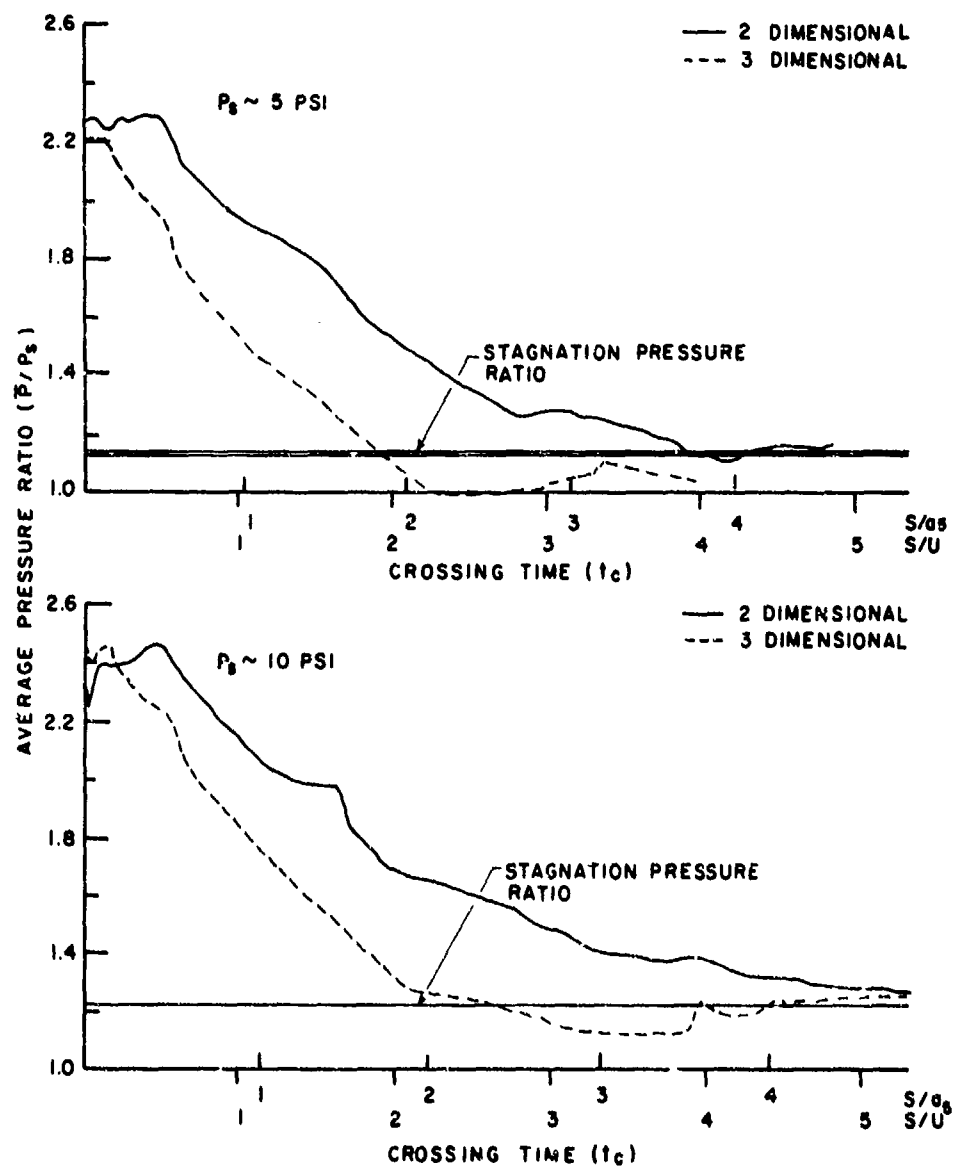


Figure 9. Average Loadings on Front Surface at 5 & 10 Psi Shocks

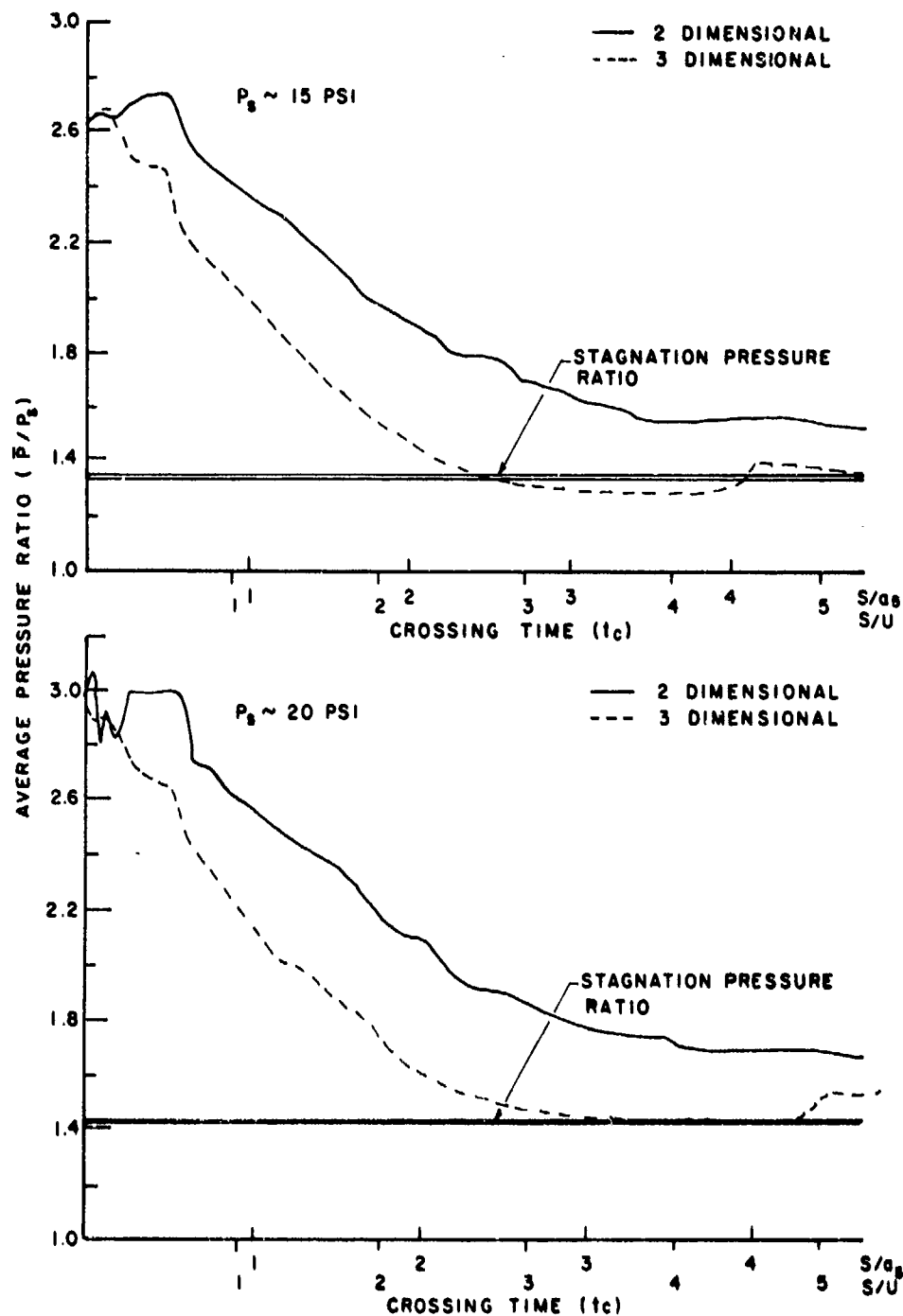


Figure 10. Average Loading on Front Surface at 15 and 20 Psi Shocks

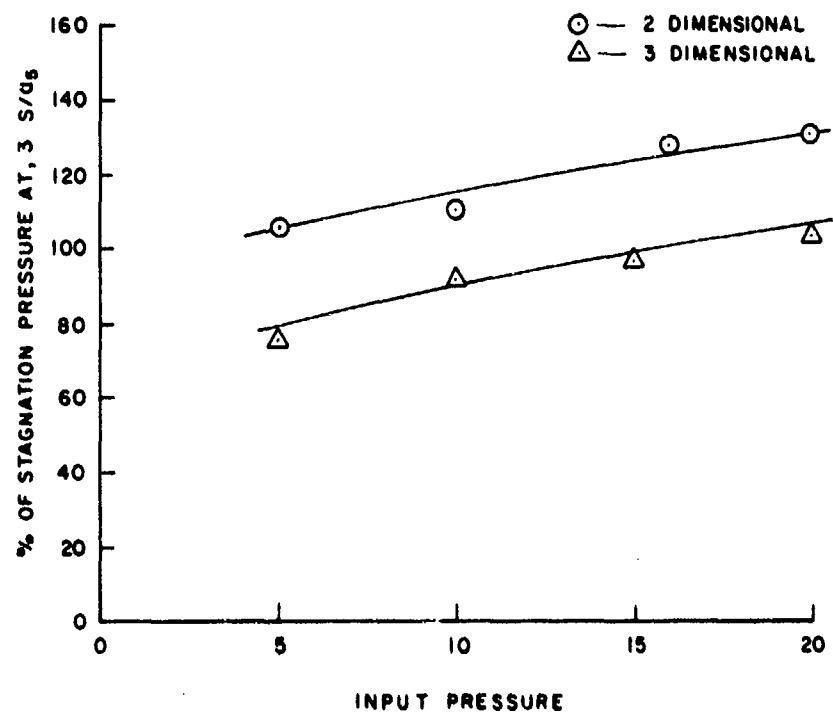


Figure 11. % of Stagnation Pressure After 3 Crossing Times

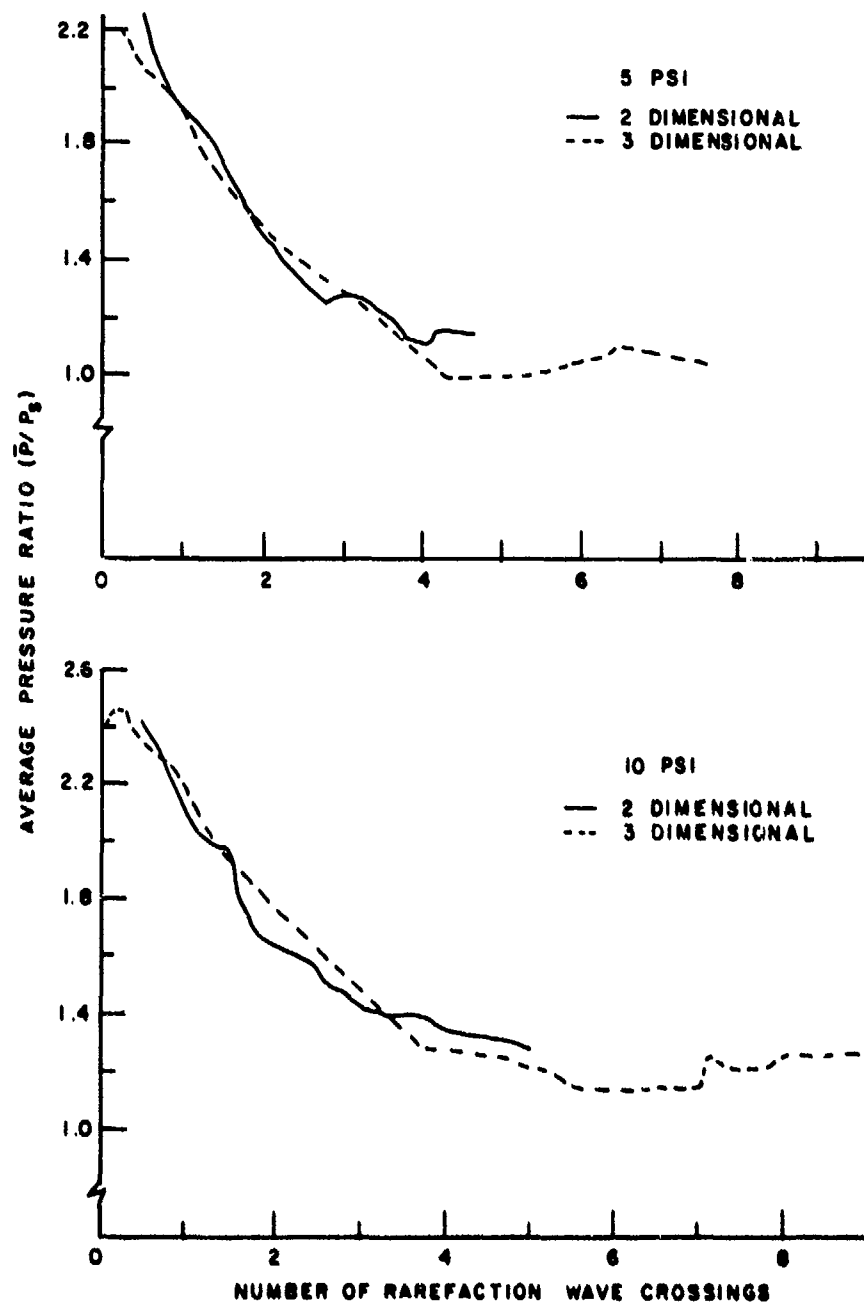


Figure 12. Average Pressure As A Function of Rarefaction Wave Action for 5 and 10 Psi Shocks

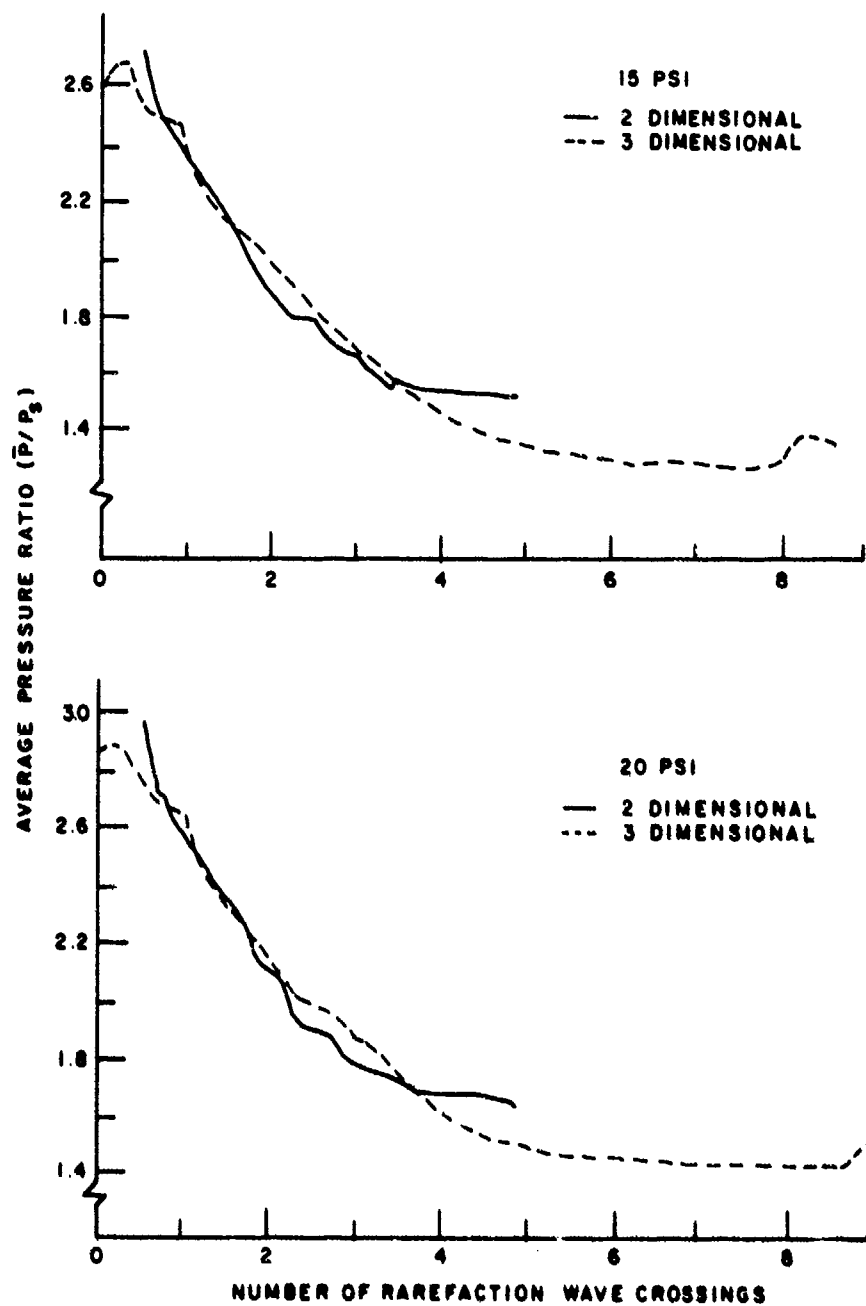


Figure 13. Average Pressure as a Function of Rarefaction Wave Action for 15 and 20 Psi Shocks

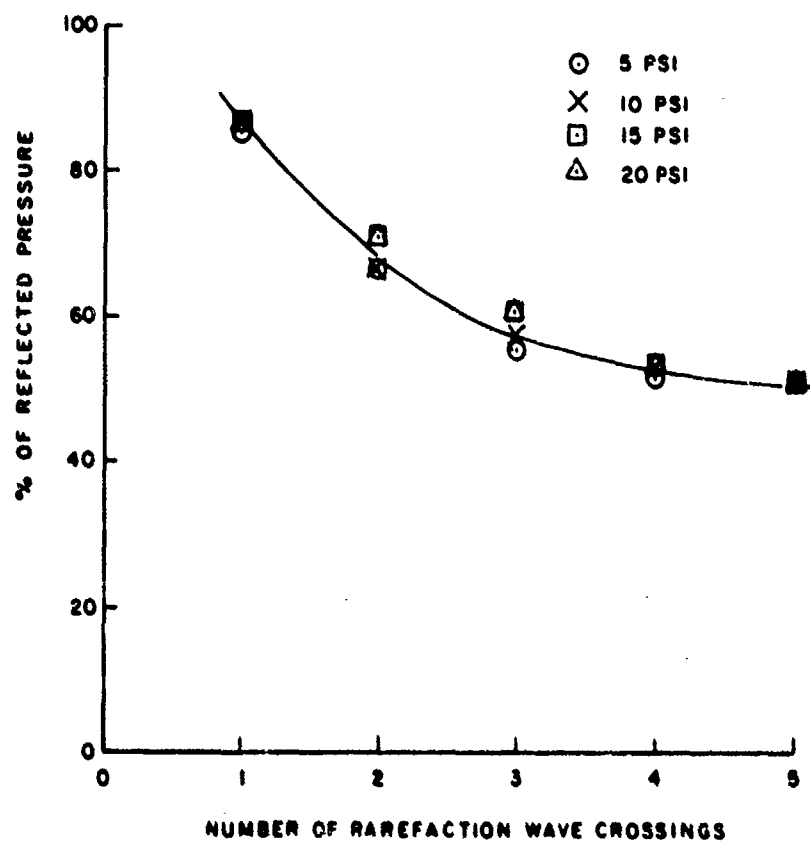


Figure 14. % of Reflected Pressure as a Function of Rarefaction Wave Crossing

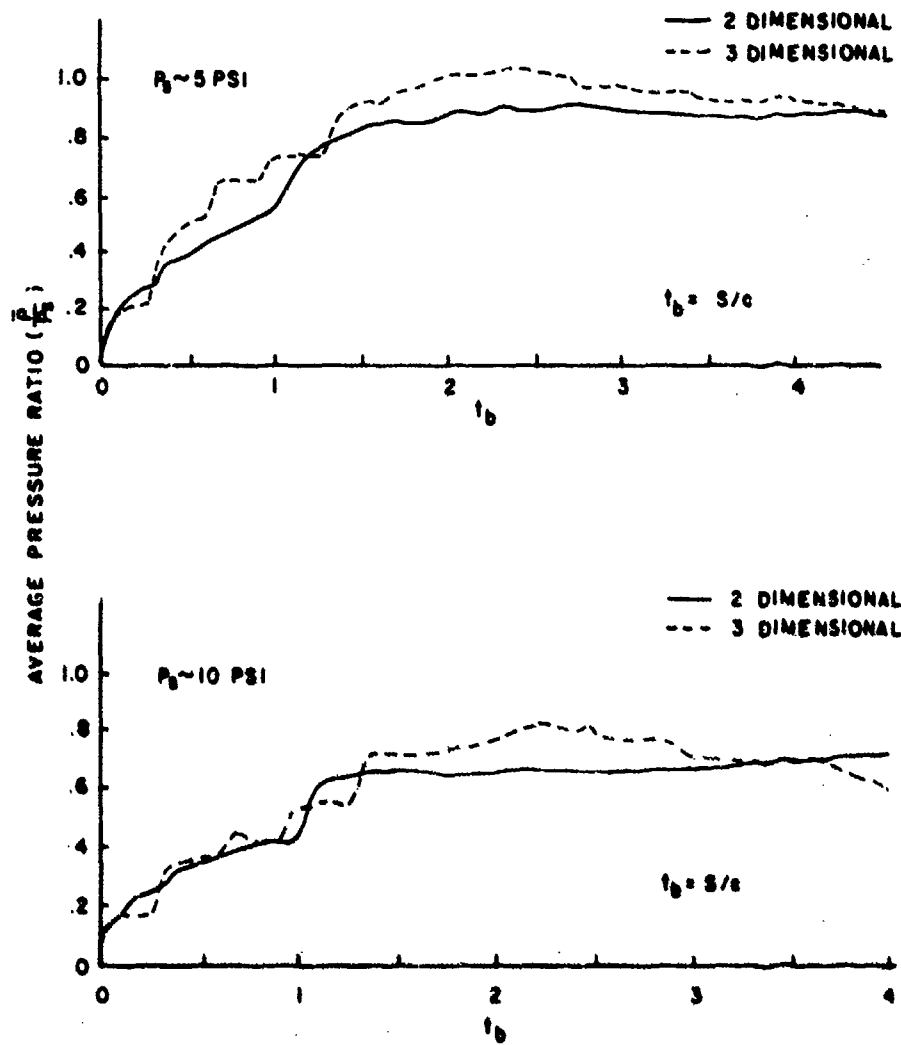


Figure 15. Average Loading on Rear Surface at 5 and 10 Psi Shocks

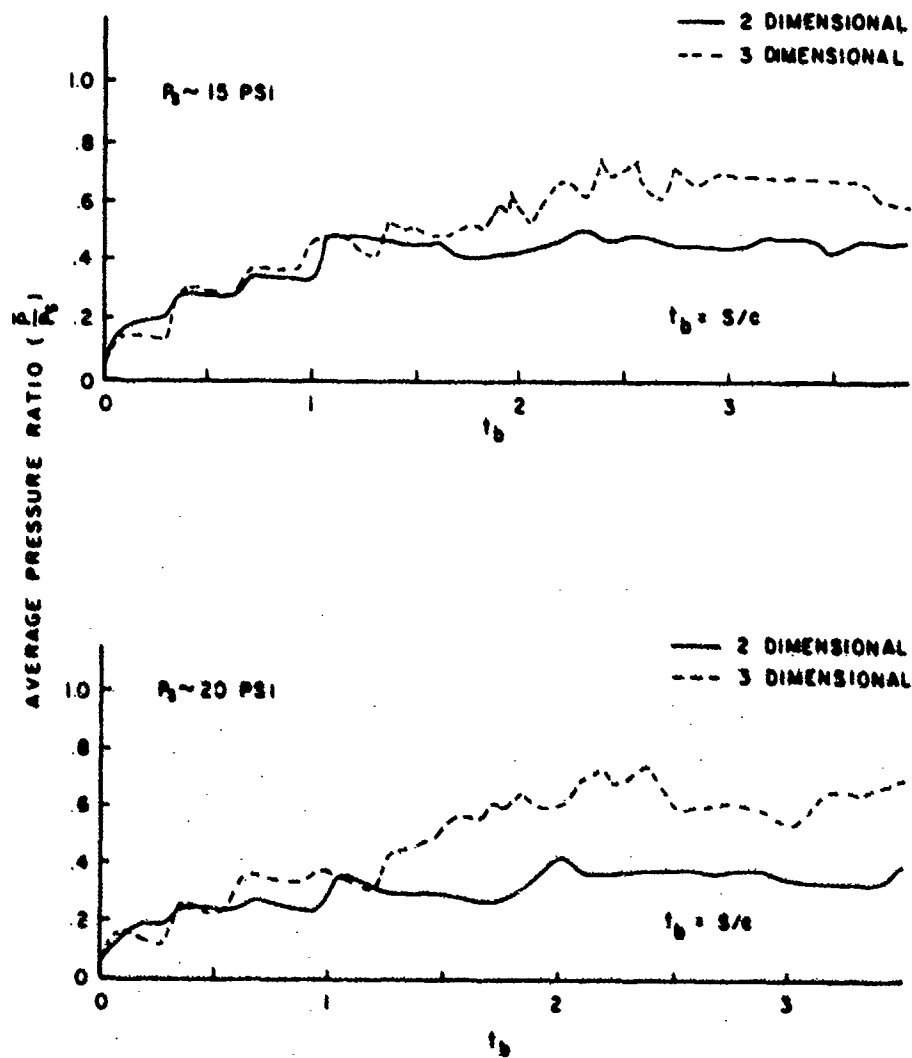


Figure 1b. Average Loading on Rear Surface at 15 and 20 Psi Shocks

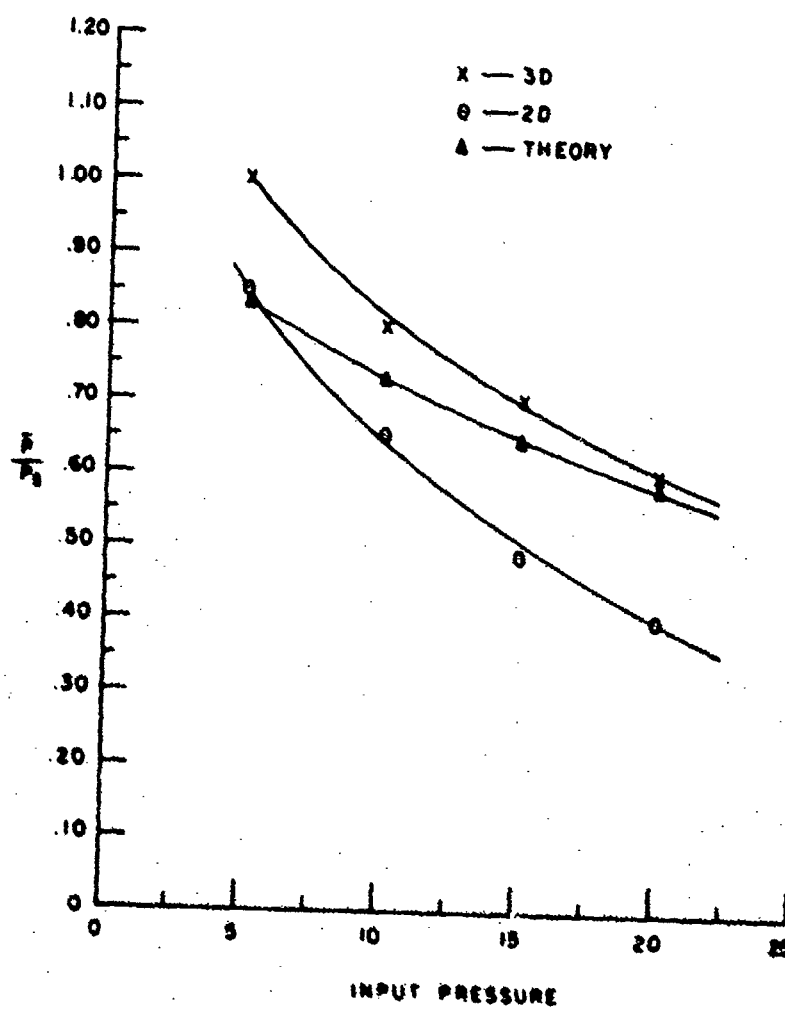


Figure 17. Average Rear Pressure at 2-1/2 Time Units

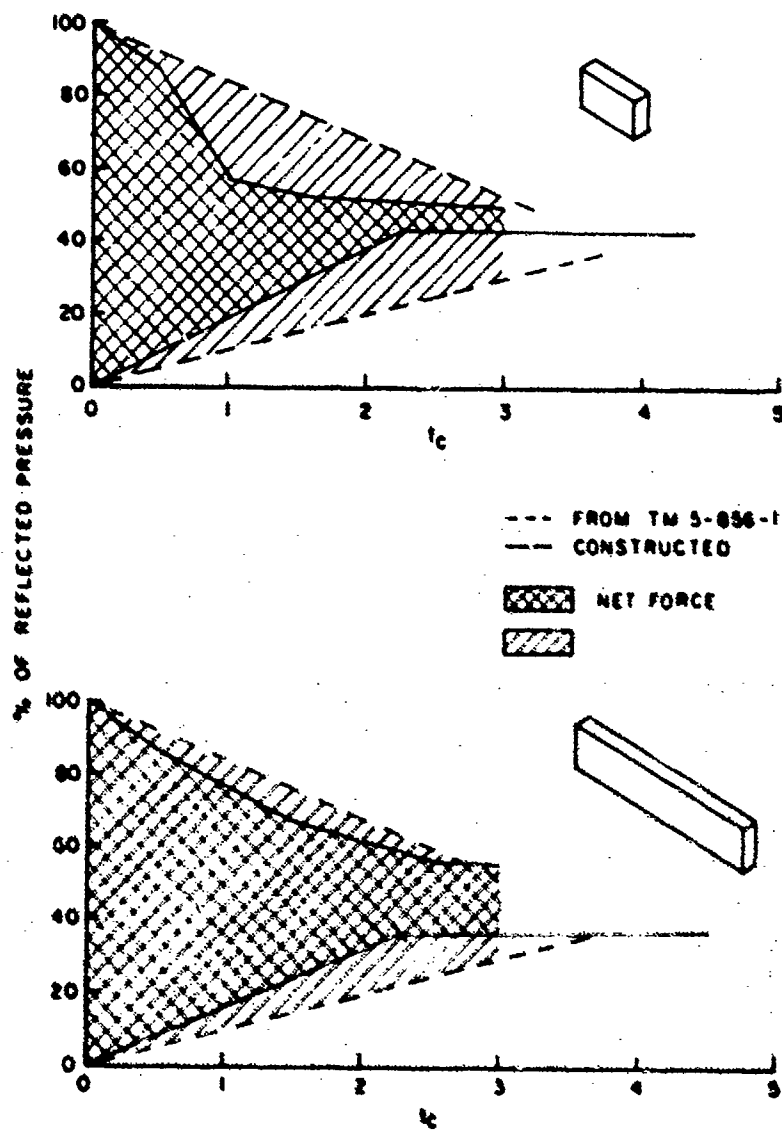


Figure 14. Net Force on 2-D and 3-D Targets

DISCUSSION

Mr. Sallet (University of Maryland): Have you compared your shock to experiments with large scale tests? By putting the model in the shock tube you partially constrict the flow. Consider the two extremes. In a closed shock tube a shock will be reflected as a shock; in an open end tube the shock will be reflected as an expansion. Now in a partially restricted tube it may go either way. Can you comment?

Mr. Taylor: Yes. A great amount of care went into this program and the model size selected is such that the signals from the wall do not return until just about the end of the load-time curve. At about 900 milliseconds, the signal at the end is from the side walls and on the two dimensional data it does not get back at all, in our testing time. We were quite careful to make sure that the experiment was not contaminated by side wall effects. Now, how does it compare with large scale field data? Unfortunately the nuclear data are poor; most of it was obtained when instrumentation was something less than the best. The durations of the 500 ton explosive tests that have been run in Canada are too short for the size of the structures that are used so that it is not so discernible. We really need another big nuclear field test to be able to make a valid comparison.

Mr. Sallet: Have you changed the size of the model?

Mr. Taylor: We have done that but not on this particular experiment. We suspect there is possibly a model size effect, but it occurs on that gauge which is very close to the edge of the model. The very sudden dip on the back side we feel was under the influence of a vortex. The averaging procedure here would tend to mitigate or to relieve that somewhat.

Mr. Habib (Naval Ship Research and Development Center): In 1965 during Operation

Sailorhat, a 500 ton charge was exploded on the beach, and NSRDC had mounted two full size deck houses on the deck of a cruiser. We put numerous pressure gauges on both deck houses and we tried to correlate the loading with the response of the structure. One of our problems has been to obtain a correlation between the measured stresses and the shear stresses in the transverse bulkheads of the deck house by using the standard loading formula, and we have gone to quite a complex analysis of the structure. We developed a computer program which would handle about 1000 degrees of freedom and we have a consistent discrepancy between our predicted stresses, pure stresses, and the measured ones. It is in the right direction; the measured stresses were about 50% lower than the predicted stresses, and if it turns out that as Mr. Taylor has indicated we have about 38% less load, this accounts for a major amount of our errors.

Mr. Witt (Bell Telephone Laboratories): We have some shock tube and full scale test data which are not from exactly the same type of test that Mr. Taylor ran, but they may indicate that shock tube tests are quite valid. In a Canadian blast test we had an air shaft which was 10 feet on the side and about 30 feet deep and we obtained pressure records on this air shaft. We produced a scale model of this, 4 inches on the side, and inserted it adjoining our shock tube, which is smaller than the one Mr. Taylor used. We were able to duplicate the pressure records almost exactly. We had the same sidewall effect in the shock tube because in the field there is an infinite expanse to act as a reservoir for the pressure wave. We had a relatively small reservoir in the shock tube and in this case we were unable to make the model small enough to eliminate all sidewall effects. However, the results were almost identical.

DRAG MEASUREMENTS ON CYLINDERS IN EVENT DIAL PACK

Stanley B. Mellisen
Defence Research Establishment Suffield
Ralston, Alberta, Canada

The free flight method was used to obtain drag measurements on circular cylinders in the blast wave from a 500 ton TNT burst. Cylinders 3-1/2 to 12 inches in diameter were tested at peak incident overpressures of 5.9 to 20.5 psi.

Drag pressure, drag pressure impulses and drag coefficient were evaluated and tabulated. Transition through critical Reynolds and Mach number regimes were both observed and described.

NOTATION

x	horizontal displacement of cylinder	C_D	coefficient of drag
t	time after shock front hit cylinder	p_D	drag pressure
D	drag force acting on cylinder in blast wave	I	drag pressure impulse
m	mass of cylinder	$p_{D\text{ave}}$	average drag pressure evaluated from drag pressure impulse
a	acceleration of cylinder	q	dynamic pressure at time t
v	velocity of cylinder	q_0	dynamic pressure at time $t=0$
u	fluid particle velocity in the blast wave at time t	M	flow Mach number in blast wave
u_0	fluid particle velocity directly behind the blast front ($t=0$)	C_2	speed of sound in the blast wave at time t
p	peak incident shock overpressure	T_1	atmospheric temperature ahead of shock front
p_1	atmospheric pressure	R	gas constant
C_1	speed of sound in the air ahead of the blast front	γ	specific heat ratio
F	Friedlander pressure decay	T_2	temperature in the blast wave at time t
t_+	positive duration of blast wave	T_{20}	temperature behind the blast front at $t=0$
a_p	fluid particle acceleration in the blast wave	p_{20}	absolute pressure behind shock front at $t=0$
		p_{2t}	absolute pressure in blast wave at time t

Re	Reynolds number
d	cylinder diameter
ν	kinematic viscosity at time t
a_c	acceleration coefficient
a_t	acceleration of fluid relative to cylinder

INTRODUCTION

In Operation PRAIRIE FLAT [1], a project was initiated to measure the aerodynamic drag on circular cylinders by the free flight method [2]. The project was based on the necessity of providing knowledge of blast loading for structural analysis of the lattice type masts, also tested in the trial [3] and for gaining knowledge of aerodynamic drag in the little explored unsteady flow regime behind a spherical blast wave. In Event DIAL PACK held at DRES on July 23, 1970, the free flight method was again used to measure the aerodynamic drag on cylinders using seven cylinders as compared to two as in Operation PRAIRIE FLAT. In addition to following the motions of the cylinders by means of high speed cameras, transducers were also used on all the cylinders to measure their velocity directly. This essentially gave the total load impulse as a function of time. In this way only one differentiation was necessary for obtaining the acceleration and hence the drag force applied to the cylinders as compared to the two necessary for the camera displacement. The lattice type masts which had been tested in Operation PRAIRIE FLAT were tested again in Event DIAL PACK but at higher overpressures and six of the drag cylinder setups were placed near them so that the measurements made could be used directly in the structural analysis. In addition, basic information about drag in unsteady flow at these higher overpressures was derived. The seventh cylinder was placed at a much lower overpressure adjacent to the GRP (Glass Reinforced Plastic) topmast [4] to provide loading information for that structure.

Finally, then, the purpose of the experiments reported herein was to obtain information about aerodynamic drag on seven circular cylinders covering the overpressure range of from about 6 to 25 psi.

APPARATUS AND PROCEDURE

(a) Test Cylinders and Mounts

Each of the seven test cylinder setups consisted essentially of a circular cylinder resting parallel to the ground on the ledge of a base anchored solidly in the ground (Fig. 1). The location, size and weight of each cylinder is given in Table 1. Also given are the positions for which camera coverage was used and the

adjacent structure for which loading data were provided.

The large cylinder at the 5.9 psi location was constructed of sheet steel, spot welded to circular steel end plates and internal stiffeners. The support shafts were 1/2 inch diameter steel rods along the axis of each end of the cylinder. These were welded to the end plates and the first internal stiffener which acted as a hub. The remaining internal stiffeners consisted of circular steel rings placed at 30 inch intervals. Their thickness was such that they counter-balanced the masses of the end pieces for the purpose of preventing possible beam vibrations. The cylinders at the 11.0 and 14.3 psi locations consisted of schedule 80 A1 pipe with 1/4 inch thick aluminum end plates. Each support shaft was a 1/2 inch diameter aluminum rod passed through the end plate along the axis of the cylinder and welded at its inner end to a disk pressed into the cylinder. An aluminum disk 1-1/2 inches wide was pressed into the middle of each of these two cylinders to balance the end masses. The four cylinders at 17.0 and 20.5 psi were solid aluminum rods with 1/2 inch diameter steel support shafts pressed into holes drilled in each end of the cylinders. All the support shafts were machined with a small flat on which the cylinder rested to keep it from rolling. Each cylinder to be used with camera coverage had alternate quadrants of one end painted black and white for fiducial marks for film reading. The surfaces of the cylinders were smoothed so that there were no rough spots to disturb the flow pattern around them. The steel cylinder was painted to prevent it from rusting before the trial took place.

Each mount base consisted of two parallel vertical steel plates 1/4 inch thick bolted to a steel footing placed in concrete in the ground (Fig. 1). The plates were 36 inches long, 30 inches high and were spaced apart a distance equal to the length of the test cylinder. A scale consisting of alternate black and white stripes two inches wide was painted along the top edge of the base plate facing the camera to provide a distance scale in the film record.

Two extension plates were bolted to the top of the base plates at the ends nearest the oncoming blast wave. These plates had gimbals welded to them in which velocity transducers were clamped. The velocity transducers themselves are described in the following section. The extension plates also contained the ledges on which the cylinders rested by their mount shafts. The gimbals and ledges were lubricated with silicon grease so that the friction forces were reduced to negligible quantities in comparison to the drag forces. To prevent disturbances of the oncoming shock wave from interfering with the flow the front edges of the areas of the mount facing the shock wave were tapered so that the shock wave could pass smoothly between the plates which themselves provided high rigidity and low frontal area.

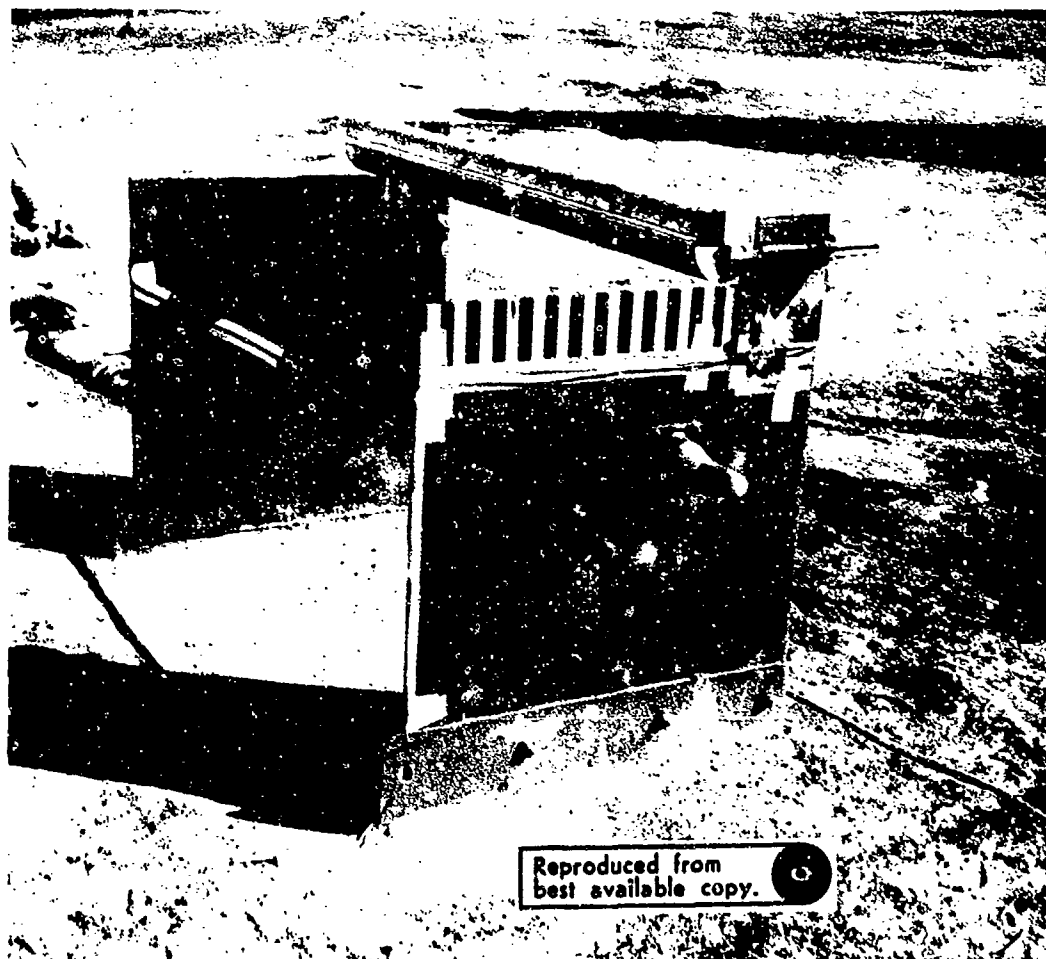


Fig. 1 - Free Flight Drag Cylinder and Mount.

TABLE 1
Size, Weight and Location of Test Cylinders

Location Number	Cylinder			Peak Incident Overpressure psi	Height of Axis Above Ground in.	Camera Used	Adjacent Structure
	Diameter in.	Length in.	Weight lb.				
1	12.00	120.13	107.60	5.9	45	Yes	GRP Top Mast
2	3.49	60.00	19.11	11.0	34	Yes	15 ft Lattice Mast
3	3.49	60.00	19.07	14.3	34	No	None
4	3.49	60.00	57.09	17.0	34	Yes*	30 ft Lattice Mast
5	4.88	60.00	111.31	17.0	34	No	30 ft Lattice Mast
6	3.49	60.00	56.82	20.5	34	No	30 ft Lattice Mast
7	5.73	60.02	157.90	20.5	34	No	30 ft Lattice Mast

* camera failed to operate

INSTRUMENTATION

The velocity transducers for measuring directly the velocity of each cylinder as a function of time were based on the principle that a permanent magnet travelling through a coil produces a voltage which is directly proportional to the velocity of the magnet within the coil. A pair of transducers connected in parallel was used on each cylinder so that the voltage output was proportional to the average velocity of the two ends of the cylinder. The transducers used at all locations other than that at the lowest pressure level were Hewlett Packard Model LV (syn) 6LV4 with a 4-inch nominal working range. The cylinder at 5.9 psi had Model 6LV2 transducers installed which used only a 2-inch nominal stroke. The magnetic rod in each transducer coil was extended by a brass rod fastened to an aluminum eyelet which passed over the shaft on each end of the cylinder.

The output of the transducers was sufficiently high that no amplification was necessary. The output of each transducer pair was simply fed through a potential divider consisting of two resistors mounted on the outside of the base plate into a strain gauge cable passing underground to the recording bunker. The strain gauge cable was connected to a magnetic tape recorder and the voltage-time output recorded.

The transducers were calibrated by two different methods. Before the trial they were calibrated by an electro-mechanical means which consisted basically of shaking the velocity unit and comparing the output voltage to the velocity measured by a standard accelerometer. The second method consisted of integrating voltage-time data obtained during the trial and comparing this to known displacement-time characteristics of the transducers. The details of both methods are described elsewhere [5]. Three of the cylinder setups were equipped with cameras to follow cylinder motion. Fastair cameras with a nominal operating speed of about 600 frames per second, were used at Locations No. 2 and No. 4 (Table 1). A Photosonics camera, with a nominal speed of 1000 frames per second, was used at Location No. 1. Each camera was mounted at the height of the cylinder on a wooden post anchored solidly in the ground. The axis of the camera was oriented perpendicularly to the blast direction. The cameras were placed so that their fields of coverage would allow about two feet of cylinder motion to be followed. This corresponded to roughly half the positive duration of the pressure wave, the interval of greatest interest. This provided for maximum displacement resolution in the film data for studying the motion of the cylinder during this time interval. The drag forces beyond this time would be very small and also the dynamic response of the structures under test was most greatly influenced by the early part of the wave. The speed of each camera was monitored by means of electronic timing marks placed on the film at 100 μ sec intervals.

DATA ANALYSIS

The voltage-time data obtained from the velocity transducers and recorded on magnetic tape during the field trial were converted from analog to digital form after the trial. Most of the high frequency noise was then smoothed out and the curves were fitted to the filtered data using a program in the IBM Statistical System entitled Least Squares Fitting to Orthogonal Polynomials. The fitted curves and the data to which they were fitted are shown by the smooth and wavy lines respectively in Fig. 2. The gap in the data curve is due to a characteristic of the transducers. This is described in detail along with a description of all the data analysis elsewhere [5].

Curves were also fitted to the camera displacement-time data using the same procedure. The fitted curve and the data to which it was fitted (each point shown by an "x") along with the velocity and acceleration obtained by differentiating the fitted curve is shown in Fig. 3 for Location 1 and Fig. 4 for Location 2.

RESULTS

(a) Calculations Used and Detailed Tables of Results

An investigation was made into the possibility of evaluating the various flow parameters in the fluid flow behind the spherically expanding blast front using the fundamental laws of fluid mechanics and thermodynamics along with the measured parameters. A simple, accurate method was not found. Therefore, methods were used involving the empirical Friedlander decay, similar to the methods used previously [2].

The drag force D was obtained by

$$D = ma \quad (\text{Eq. 1})$$

where m is the mass of the cylinder and $a = \frac{d^2x}{dt^2}$ was the cylinder acceleration evaluated using the polynomial curves fitted to the data. The drag pressure p_D on each cylinder was found by dividing the drag force, D , by the frontal area, A , of the cylinder. Thus,

$$p_D = \frac{D}{A} \quad (\text{Eq. 2})$$

The drag pressures evaluated for the 12 inch diameter cylinder using camera data are shown in Table 2 and for the four 3-1/2 inch diameter cylinders using transducer data, they are shown in Table 3. Similar tables for the remaining data are not included but can be found elsewhere [5]. Also shown in these tables, for each cylinder, is the drag coefficient, C_D , drag pressure impulse I , in psi seconds, average drag pressure $p_{D\text{ave}}$, in psi defined in the sequel, displacement x , velocity v , and acceleration a , of each cylinder along with various flow parameters.

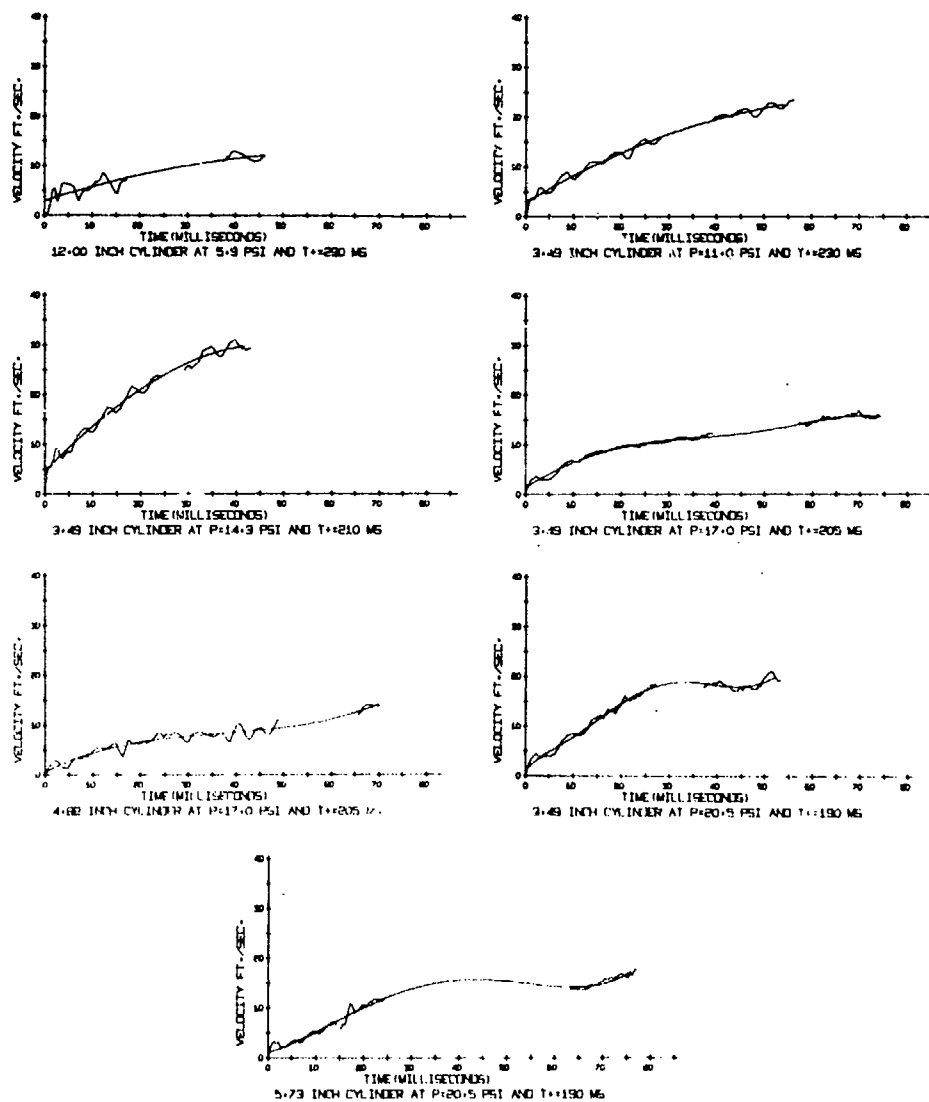


Fig. 2 - Velocity-Time Plots of Transducer Data and Fitted Smooth Curves

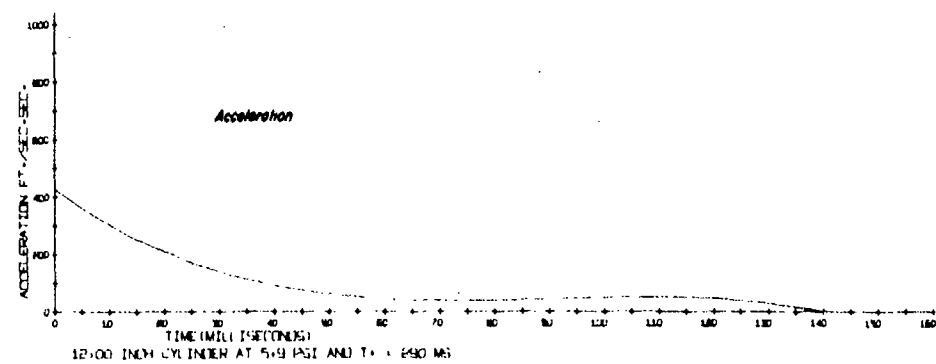
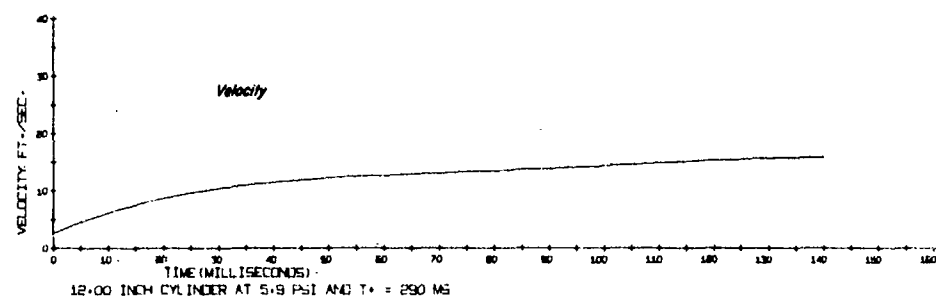
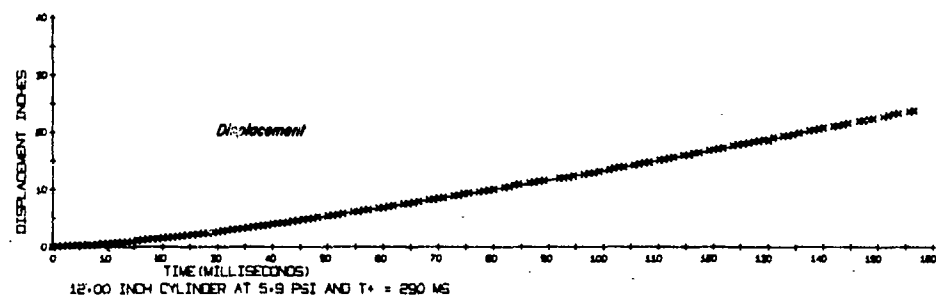


Fig. 3 - Motion of Cylinder for Location 1
From Camera Data

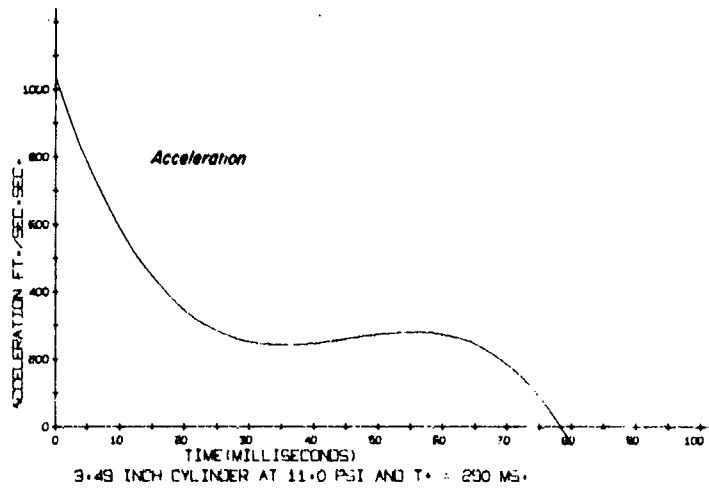
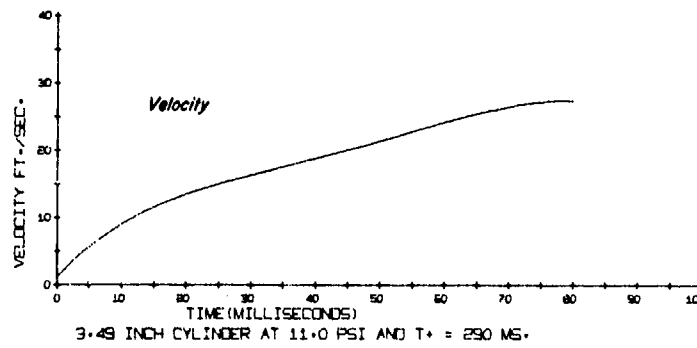
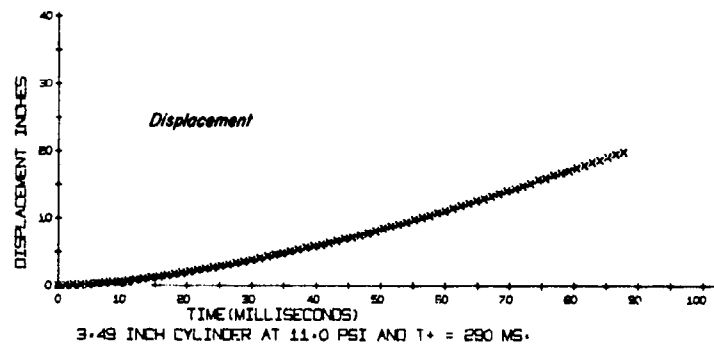


Fig. 4 - Motion of Cylinder for Location 2
From Camera Data

Results for Location 1 Using Cylinder Motion Measured by High Speed Cameras

[illegible]

TABLE 3a
Results for Location 2 Using Cylinder Motion
Measured by Velocity Transducers

5.44 INCH CYLINDER AT P=11.0 PSI AND T=230 MS

TIME AFTER BLAST FRONT T. MSEC.	DISPLACEMENT X INCHES	VELOCITY V FT./SEC.	ACCELERATION A FT./SEC./SEC.	FLUID VFL. U FT./SEC.	FLUID AC. AP FT./SEC./SEC.	OVERPRESSURE P2 - P1 PSI	DRAG IMPULSE I PSI SEC.
0.0	0.000	2.87	577.6	515.23	-4906.9	11.3	0.0081
2.0	0.082	4.01	561.9	505.49	-4837.3	11.0	0.0113
4.0	0.182	5.12	546.2	495.88	-4768.5	10.8	0.0145
6.0	0.328	6.20	530.4	486.41	-4700.6	10.6	0.0179
8.0	0.489	7.24	514.7	477.05	-4633.6	10.4	0.0209
10.0	0.675	8.25	499.0	467.88	-4567.4	10.2	0.0234
12.0	0.886	9.24	483.2	458.81	-4502.0	10.0	0.0261
14.0	1.119	10.19	467.5	449.87	-4437.5	9.8	0.0288
16.0	1.375	11.11	451.8	441.06	-4373.7	9.6	0.0316
18.0	1.652	12.00	436.0	432.27	-4310.8	9.4	0.0340
20.0	1.950	12.85	420.3	423.81	-4248.7	9.2	0.0364
22.0	2.269	13.68	404.6	415.38	-4187.4	9.1	0.0387
24.0	2.607	14.47	388.9	407.06	-4126.9	8.9	0.0410
26.0	2.963	15.23	373.1	398.87	-4067.1	8.7	0.0431
28.0	3.338	15.96	357.4	390.79	-4008.1	8.5	0.0452
30.0	3.730	16.66	341.7	382.83	-3949.9	8.3	0.0472
32.0	4.138	17.33	325.9	374.98	-3892.4	8.2	0.0491
34.0	4.561	17.97	310.2	367.26	-3835.6	8.0	0.0509
36.0	5.000	18.57	294.5	359.65	-3779.6	7.8	0.0526
38.0	5.453	19.14	278.7	352.14	-3724.2	7.7	0.0542
40.0	5.919	19.69	263.0	344.75	-3669.6	7.5	0.0558
42.0	6.398	20.20	247.3	337.47	-3615.7	7.4	0.0572
44.0	6.888	20.68	231.5	330.28	-3562.5	7.2	0.0586
46.0	7.390	21.12	215.8	323.22	-3509.9	7.0	0.0598
48.0	7.902	21.54	200.1	316.25	-3458.1	6.9	0.0610
50.0	8.424	21.92	184.3	309.38	-3406.9	6.7	0.0621
52.0	8.955	22.28	168.6	302.62	-3356.4	6.6	0.0631
54.0	9.493	22.60	152.9	295.96	-3306.5	6.4	0.0640

TIME AFTER BLAST FRONT T. MSEC.	DRAG PRESS. PD PSI	COEFFICIENT OF DRAG CD	FLOW MACH NO. V	REYNOLDS NO. R 1/10000	ACCELERATION COEFFICIENT AC.	DYNAMIC PRESSURE Q PSI	AVG. DRAG PRESS. PS - AVG. PSI
0.0	1.637	0.951	0.417	9.2	0.008	2.88	0.007
2.0	1.682	0.959	0.408	8.0	0.008	2.89	0.009
4.0	1.747	0.968	0.400	6.8	0.008	2.72	0.010
6.0	1.803	0.976	0.392	5.6	0.008	2.60	0.012
8.0	1.858	0.984	0.384	4.4	0.008	2.48	0.014
10.0	1.914	0.991	0.376	3.2	0.008	2.38	0.016
12.0	1.969	0.998	0.368	2.0	0.007	2.28	0.018
14.0	2.025	0.999	0.361	1.8	0.007	2.18	0.020
16.0	2.080	0.993	0.353	1.6	0.007	2.09	0.022
18.0	2.135	0.988	0.346	1.4	0.007	1.99	0.024
20.0	2.191	0.983	0.339	1.2	0.008	1.91	0.026
22.0	2.246	0.978	0.331	1.0	0.008	1.82	0.028
24.0	2.302	0.974	0.324	0.8	0.008	1.74	0.030
26.0	2.357	0.969	0.317	0.6	0.009	1.66	0.032
28.0	2.412	0.965	0.310	0.4	0.009	1.59	0.034
30.0	2.468	0.960	0.303	0.3	0.009	1.51	0.036
32.0	2.523	0.956	0.297	0.2	0.009	1.44	0.038
34.0	2.579	0.953	0.290	0.1	0.009	1.38	0.040
36.0	2.634	0.949	0.283	0.0	0.010	1.31	0.042
38.0	2.689	0.945	0.277	0.0	0.010	1.24	0.044
40.0	2.744	0.942	0.271	0.0	0.011	1.19	0.046
42.0	2.800	0.940	0.264	0.0	0.011	1.13	0.048
44.0	2.856	0.938	0.258	0.0	0.011	1.08	0.050
46.0	2.911	0.937	0.252	0.0	0.012	1.03	0.052
48.0	2.967	0.937	0.246	0.0	0.012	0.98	0.054
50.0	3.022	0.937	0.241	0.0	0.012	0.93	0.056
52.0	3.077	0.937	0.235	0.0	0.013	0.88	0.058
54.0	3.132	0.937	0.229	0.0	0.013	0.84	0.060

MEAN CD 0.680

TABLE 3b
Results for Location 3 Using Cylinder Motion
Measured by Velocity Transducers

5.25 INCH CYLINDER AT $P_1 = 14.5$ PSI AND $T_0 = 21.0$ MS

TIME AFTER BLAST FRONT T. MSEC.	DISPLACEMENT X INCHES	VELOCITY V FT./SEC.	ACCELERATION A FT./SEC./SEC.	FLUID VEL. U FT./SEC.	FLUID AC. AP FT./SEC./SEC.	OVERPRESSURE P2 - P1 PSI	DNAG IMPULSE I PSI SEC.
0.0	0.000	0.00	0.00	0.00	0.00	0.00	0.00
2.0	0.135	6.53	946.5	618.71	-7365.6	14.3	0.0135
4.0	0.317	8.19	917.8	586.85	-7076.3	15.6	0.0277
6.0	0.536	10.20	887.8	575.82	-6935.6	15.3	0.0420
8.0	0.802	11.94	856.6	562.08	-6797.5	12.9	0.0557
10.0	1.109	13.62	826.0	546.62	-6661.9	12.3	0.0685
12.0	1.456	15.24	790.1	534.63	-6528.7	12.3	0.0811
14.0	1.840	16.78	755.0	522.51	-6396.1	12.0	0.0934
16.0	2.261	18.26	718.6	509.84	-6264.8	11.7	0.1056
18.0	2.716	19.66	680.8	497.49	-6133.8	11.4	0.1176
20.0	3.204	20.98	641.8	485.26	-6002.2	11.2	0.1293
22.0	3.723	22.22	601.5	473.34	-5878.6	10.9	0.1408
24.0	4.271	23.39	559.9	461.67	-5759.7	10.6	0.1521
26.0	4.845	24.46	517.0	450.27	-5642.8	10.4	0.1631
28.0	5.444	25.45	472.8	439.01	-5528.7	10.1	0.1739
30.0	6.066	26.35	427.3	427.03	-5415.3	9.8	0.1845
32.0	6.709	27.16	380.5	415.27	-5304.7	9.6	0.1948
34.0	7.369	27.88	332.4	403.73	-5196.2	9.4	0.2048
36.0	8.046	28.49	283.0	392.40	-5089.7	9.1	0.2145
38.0	8.736	29.01	232.4	381.29	-4985.1	8.9	0.2239
40.0	9.448	29.42	180.4	370.38	-4882.5	8.6	0.2332
42.0	10.180	29.73	127.1	359.68	-4781.9	8.4	0.2424

TIME AFTER BLAST FRONT T. MSEC.	DNAG PRESS. P1 PSI	CORRECTION COEFFICIENT	FLUID VELOCITY U FT./SEC.	FLUID ACCELERATION AP FT./SEC./SEC.	OVERPRESSURE P2 - P1 PSI	DNAG IMPULSE I PSI SEC.
0.0	2.154	0.687	0.00	0.00	0.00	0.00
2.0	2.676	0.683	618.71	-7365.6	14.3	0.0135
4.0	2.893	0.679	586.85	-7076.3	15.6	0.0277
6.0	2.917	0.675	575.82	-6935.6	15.3	0.0420
8.0	2.822	0.671	562.08	-6797.5	12.9	0.0557
10.0	2.630	0.666	546.62	-6661.9	12.3	0.0685
12.0	2.294	0.660	534.63	-6528.7	12.3	0.0811
14.0	1.815	0.653	522.51	-6396.1	12.0	0.0934
16.0	1.212	0.645	509.84	-6264.8	11.7	0.1056
18.0	0.575	0.636	497.49	-6133.8	11.4	0.1176
20.0	0.000	0.626	485.26	-6002.2	11.2	0.1293
22.0	1.813	0.616	473.34	-5878.6	10.9	0.1408
24.0	1.453	0.606	461.67	-5759.7	10.6	0.1521
26.0	1.043	0.595	450.27	-5642.8	10.4	0.1631
28.0	0.583	0.584	439.01	-5528.7	10.1	0.1739
30.0	0.073	0.572	427.03	-5415.3	9.8	0.1845
32.0	0.000	0.560	415.27	-5304.7	9.6	0.1948
34.0	1.214	0.548	403.73	-5196.2	9.4	0.2048
36.0	1.453	0.536	392.40	-5089.7	9.1	0.2145
38.0	1.693	0.524	381.29	-4985.1	8.9	0.2239
40.0	1.933	0.512	370.38	-4882.5	8.6	0.2332
42.0	2.173	0.500	359.68	-4781.9	8.4	0.2424

REF: C-10, P-106

TABLE 3c
Results for Location 4 Using Cylinder Motion
Measured by Velocity Transducers

3.49 INCH CYLINDER AT 0.17 IN PSI AND 7.40 IN PSI

TIME AFTER BLAST FRONT + MSEC.	DISPLACEMENT X INCHES	VELOCITY V FT./SEC.	ACCELERATION A FT./SEC./SEC.	FLUID VEL. U FT./SEC.	FLUID AC. AP FT./SEC./SEC.	OVERPRESSURE P2 - P1 PSI	DRAIN IMPULSE 1 PSI SEC.
0.0	0.000	1.45	565.4	704.64	-10311.8	17.0	0.0122
2.0	0.008	2.56	555.6	684.28	-10046.7	16.9	0.0216
4.0	0.022	3.62	518.2	664.44	-9798.1	16.0	0.0307
6.0	0.027	4.63	489.4	644.12	-9555.7	15.9	0.0392
8.0	0.044	5.56	448.7	624.30	-9289.4	15.1	0.0471
10.0	0.068	6.42	409.3	604.96	-9049.1	14.6	0.0544
12.0	0.092	7.25	388.6	585.10	-8814.6	14.2	0.0609
14.0	0.093	7.99	357.4	572.70	-8585.7	13.8	0.0668
16.0	0.090	8.41	287.5	554.75	-8362.4	13.4	0.0716
18.0	1.241	9.09	249.2	539.26	-8144.6	13.0	0.0766
20.0	1.664	9.41	213.4	523.17	-7937.0	12.4	0.0825
22.0	1.687	9.40	187.8	507.51	-7734.6	12.2	0.0896
24.0	1.739	10.79	151.9	492.27	-7532.3	11.9	0.0980
26.0	2.184	12.41	121.3	477.42	-7324.9	11.4	0.0910
28.0	2.664	12.76	107.2	462.86	-7132.3	11.1	0.0910
30.0	2.764	12.46	91.7	448.89	-6944.5	10.8	0.0927
32.0	2.864	11.12	81.1	435.18	-6761.2	10.4	0.0941
34.0	2.934	11.27	76.1	421.86	-6582.4	10.1	0.0964
36.0	3.234	11.42	72.7	408.89	-6408.0	9.8	0.0987
38.0	3.512	11.45	72.5	396.27	-6237.9	9.4	0.0990
40.0	3.746	11.78	68.6	383.89	-6072.4	9.2	0.0993
42.0	4.034	12.76	64.4	371.71	-5912.1	8.9	0.1000
44.0	4.334	12.11	58.2	359.25	-5752.2	8.6	0.1025
46.0	4.634	12.73	52.3	346.40	-5598.3	8.4	0.1044
48.0	4.934	12.59	46.4	333.69	-5449.1	8.1	0.1068
50.0	5.234	12.68	42.1	321.11	-5304.6	7.8	0.1091
52.0	5.534	12.77	38.6	308.67	-5164.7	7.5	0.1114
54.0	5.834	12.41	35.7	296.45	-5029.3	7.2	0.1137
56.0	6.134	12.76	32.7	284.33	-4898.1	6.9	0.1159
58.0	6.434	12.76	29.7	272.34	-4772.3	6.6	0.1182
60.0	6.734	12.76	26.7	260.44	-4651.2	6.3	0.1205
62.0	7.034	12.76	23.7	248.57	-4534.7	6.0	0.1228
64.0	7.334	12.76	20.7	236.71	-4422.9	5.7	0.1251
66.0	7.634	12.76	17.7	224.86	-4315.7	5.4	0.1274
68.0	7.934	12.76	14.7	213.01	-4213.0	5.1	0.1297
70.0	8.234	12.76	11.7	201.16	-4114.7	4.8	0.1320
72.0	8.534	12.76	8.7	189.31	-4020.7	4.5	0.1343
74.0	8.834	12.76	5.7	177.46	-3931.0	4.2	0.1366
76.0	9.134	12.76	2.7	165.61	-3846.7	3.9	0.1389
78.0	9.434	12.76	-0.3	153.76	-3767.0	3.6	0.1412
80.0	9.734	12.76	-3.3	141.91	-3692.3	3.3	0.1435
82.0	10.034	12.76	-6.3	130.06	-3622.6	3.0	0.1458
84.0	10.334	12.76	-9.3	118.21	-3557.9	2.7	0.1481
86.0	10.634	12.76	-12.3	106.36	-3498.2	2.4	0.1504
88.0	10.934	12.76	-15.3	94.51	-3443.5	2.1	0.1527
90.0	11.234	12.76	-18.3	82.66	-3393.8	1.8	0.1550
92.0	11.534	12.76	-21.3	70.81	-3349.1	1.5	0.1573
94.0	11.834	12.76	-24.3	58.96	-3309.4	1.2	0.1596
96.0	12.134	12.76	-27.3	47.11	-3274.7	0.9	0.1619
98.0	12.434	12.76	-30.3	35.26	-3245.0	0.6	0.1642
100.0	12.734	12.76	-33.3	23.41	-3220.3	0.3	0.1665

Reproduced from
best available copy.

74	75	76	77	78	79	80	81	82	83	84	85	86	87	88	89	90	91	92	93	94	95	96	97	98	99	100
1.45	2.56	3.62	4.63	5.56	6.42	7.25	7.99	8.41	9.09	9.41	9.40	10.79	12.41	12.76	12.46	12.76	12.46	12.76	12.76	12.76	12.76	12.76	12.76	12.76	12.76	12.76
565.4	555.6	518.2	489.4	448.7	409.3	388.6	357.4	287.5	249.2	213.4	187.8	151.9	121.3	107.2	91.7	81.1	76.1	72.7	72.5	68.6	64.4	62.1	58.2	52.3	46.4	42.1
704.64	684.28	664.44	644.12	624.30	604.96	585.10	572.70	554.75	539.26	523.17	507.51	492.27	477.42	462.86	448.89	435.18	421.86	408.89	396.27	383.89	371.71	359.25	346.40	333.69	321.11	308.67
-10311.8	-10046.7	-9798.1	-9555.7	-9289.4	-9049.1	-8814.6	-8585.7	-8362.4	-8144.6	-7937.0	-7734.6	-7532.3	-7324.9	-7132.3	-6944.5	-6761.2	-6582.4	-6408.0	-6237.9	-6072.4	-5912.1	-5752.2	-5598.3	-5449.1	-5304.6	-5164.7
17.0	16.9	16.0	15.9	15.1	14.6	14.2	13.8	13.4	13.0	12.4	12.2	11.9	11.4	11.1	10.8	10.4	10.1	9.8	9.4	9.2	8.9	8.6	8.4	8.1	7.8	7.5
0.0122	0.0216	0.0307	0.0392	0.0471	0.0544	0.0609	0.0668	0.0716	0.0766	0.0825	0.0896	0.0980	0.0910	0.0910	0.0927	0.0941	0.0964	0.0987	0.0990	0.0993	0.1000	0.1025	0.1044	0.1068	0.1091	0.1114

MEAN CD = 0.940

TABLE 3d
Results for Location 6 Using Cylinder Motion
Measured by Velocity Transducers

3.48 INCH CYLINDER AT P=20.4 PSI AND T=190 MS

TIME AFTER BLAST FRONT V. WFC.	DISPLACEMENT IN INCHES	VELOCITY V. FT./SEC.	ACCELERATION A. FT./SEC./SEC.	FLUID VEL. U. FT./SEC.	FLUID AC. AP. FT./SEC./SEC.	OVERPRESSURE P2 - P1 PSI	DRAIN PULSE 1 PSI SEC.
0.0	0.000	1.28	937.0	907.76	-12755.9	20.4	0.0106
2.0	0.050	2.03	729.1	787.59	-12400.9	19.8	0.0247
4.0	0.138	4.25	819.8	759.13	-12058.4	19.2	0.0398
6.0	0.253	6.66	581.8	736.36	-11721.2	18.6	0.0559
8.0	0.389	8.61	586.6	711.24	-11384.7	18.0	0.0717
10.0	0.532	7.86	629.3	684.77	-11048.8	17.4	0.0880
12.0	0.776	9.13	666.9	666.99	-10712.2	16.8	0.1049
14.0	1.011	10.49	693.1	646.70	-10375.6	16.2	0.1224
16.0	1.280	11.89	699.1	625.06	-10039.0	15.6	0.1402
18.0	1.592	13.27	679.9	604.01	-9702.4	15.0	0.1581
20.0	1.917	14.59	636.1	583.91	-9365.8	14.4	0.1762
22.0	2.262	15.78	583.6	564.97	-9029.2	13.8	0.1944
24.0	2.627	16.85	529.0	546.18	-8692.6	13.2	0.2127
26.0	3.008	17.87	386.9	527.48	-8356.0	12.6	0.2311
28.0	3.421	18.79	282.8	517.80	-8019.4	12.0	0.2496
30.0	3.866	19.68	162.8	498.21	-7682.8	11.4	0.2681
32.0	4.346	19.84	74.7	479.61	-7346.2	10.8	0.2867
34.0	4.860	19.85	-44.4	461.07	-7009.6	10.2	0.3053
36.0	5.420	18.70	-106.0	442.59	-6673.0	9.6	0.3240
38.0	6.026	18.68	-171.3	424.13	-6336.4	9.0	0.3427
40.0	6.678	18.27	-219.0	405.68	-6000.0	8.4	0.3614
42.0	7.376	17.39	-277.7	387.29	-5663.4	7.8	0.3801
44.0	8.121	16.01	2.0	377.27	-5326.8	7.2	0.3988
46.0	8.912	14.72	119.3	367.23	-4990.2	6.6	0.4175
48.0	9.748	14.54	269.7	357.23	-4653.6	6.0	0.4362
50.0	10.629	14.01	387.8	347.27	-4317.0	5.4	0.4549
52.0	11.555	13.05	497.6	337.37	-3980.4	4.8	0.4736

TIME AFTER BLAST FRONT V. WFC.	DRAG FORCE P2 - P1 PSI	ACCELERATION A. FT./SEC./SEC.	FLUID VEL. U. FT./SEC.	FLUID AC. AP. FT./SEC./SEC.	OVERPRESSURE P2 - P1 PSI	DRAIN PULSE 1 PSI SEC.
0.0	0.000	937.0	907.76	-12755.9	20.4	0.0106
2.0	0.050	729.1	787.59	-12400.9	19.8	0.0247
4.0	0.138	819.8	759.13	-12058.4	19.2	0.0398
6.0	0.253	581.8	736.36	-11721.2	18.6	0.0559
8.0	0.389	586.6	711.24	-11384.7	18.0	0.0717
10.0	0.532	629.3	684.77	-11048.8	17.4	0.0880
12.0	0.776	666.9	666.99	-10712.2	16.8	0.1049
14.0	1.011	693.1	646.70	-10375.6	16.2	0.1224
16.0	1.280	699.1	625.06	-10039.0	15.6	0.1402
18.0	1.592	679.9	604.01	-9702.4	15.0	0.1581
20.0	1.917	636.1	583.91	-9365.8	14.4	0.1762
22.0	2.262	583.6	564.97	-9029.2	13.8	0.1944
24.0	2.627	529.0	546.18	-8692.6	13.2	0.2127
26.0	3.008	386.9	527.48	-8356.0	12.6	0.2311
28.0	3.421	282.8	517.80	-8019.4	12.0	0.2496
30.0	3.866	162.8	498.21	-7682.8	11.4	0.2681
32.0	4.346	74.7	479.61	-7346.2	10.8	0.2867
34.0	4.860	-44.4	461.07	-7009.6	10.2	0.3053
36.0	5.420	-106.0	442.59	-6673.0	9.6	0.3240
38.0	6.026	-171.3	424.13	-6336.4	9.0	0.3427
40.0	6.678	-219.0	405.68	-6000.0	8.4	0.3614
42.0	7.376	-277.7	387.29	-5663.4	7.8	0.3801
44.0	8.121	2.0	377.27	-5326.8	7.2	0.3988
46.0	8.912	119.3	367.23	-4990.2	6.6	0.4175
48.0	9.748	269.7	357.23	-4653.6	6.0	0.4362
50.0	10.629	387.8	347.27	-4317.0	5.4	0.4549
52.0	11.555	497.6	337.37	-3980.4	4.8	0.4736

MEAN CD = 0.976

The drag force impulse was derived from Newton's Second Law, thus,

$$D = \frac{d(mv)}{dt}$$

Integration gives

$$\int_0^t D dt = \int_0^t d(mv).$$

Since the mass was constant and the initial velocity was zero, this equation becomes

$$\int_0^t D dt = mv. \quad (\text{Eq. 3})$$

The drag pressure impulse, I , was found by dividing the drag force impulse, given by Eq. 3, by the frontal area of the cylinder, thus

$$I = \frac{mv}{A}. \quad (\text{Eq. 4})$$

That is, the drag pressure impulse was directly proportional to the cylinder velocity. The average drag pressure $p_{D\text{ave}}$, up to any specified time, t , was given by

$$p_{D\text{ave}} = \frac{I}{t}. \quad (\text{Eq. 5})$$

The displacement x , and velocities v , of the cylinders were evaluated from the polynomial curves fitted to the camera displacement-time data and to the transducer velocity-time data. The displacement was obtained from the latter curves by means of numerical integration using Simpson's rule for an odd number of points and the trapezoidal rule for evaluating the contribution to the integral by the last increment when the number of points was even.

The fluid velocity directly behind the blast front (time $t=0$), was obtained from the equation

$$u = u_0 F \quad (\text{Eq. 6})$$

where u_0 , the fluid velocity directly behind the blast front (time $t=0$), was obtained from the Rankine-Hugoniot relations

$$u_0 = \frac{5p}{\rho_1} \frac{C_1}{\left(1 + \frac{6p}{\rho_1}\right)^{1/2}} \quad (\text{Eq. 7})$$

where p was the peak shock overpressure, ρ_1 was the atmospheric pressure, C_1 was the speed of sound in the air ahead of the blast front,

$$f = \left(1 - \frac{t}{t_s}\right) e^{-\frac{kt}{t_s}}, \text{ the Friedlander pressure decay rate, giving } p(t) = pf,$$

where t was the time elapsed after the blast front had passed the cylinder, t_s was the positive duration of the wave.

The value of p_1 was 13.57 psi [6]. The value of k used was 1.0 at Locations 1 and 2 and 2.0 at Locations 4, 5, 6 and 7. The value of k was determined from pressure-time records obtained at the pressure levels of these locations [7]. The value of k at Location 3, which was about half-way in peak incident overpressure between Location 2 and Locations 4 and 5, was assumed to be 1.5.

The fluid particle acceleration a_p was found by differentiating Eq. 6 thus

$$a_p = \frac{du}{dt} = -\frac{u_0}{t_s} \left(kF + e^{-\frac{kt}{t_s}} \right). \quad (\text{Eq. 8})$$

The drag coefficient was found by

$$C_D = \frac{p_D}{q} \quad (\text{Eq. 9})$$

where

$$q = q_0 \left(1 - \frac{v}{u}\right)^2 F^2 \quad (\text{Eq. 10})$$

where q_0 , the dynamic pressure at $t=0$, obtained from the Rankine-Hugoniot equation was given by

$$q_0 = \frac{5}{2} \frac{p^2}{\rho_1 + p} \quad (\text{Eq. 11})$$

The Mach number M of the flow behind the shock front was given by

$$M = \frac{u - v}{C_2} \quad (\text{Eq. 12})$$

where C_2 was the speed of sound behind the shock front obtained from

$$C_2 = C_1 \sqrt{\frac{T_2}{T_1}} \quad (\text{Eq. 13})$$

where $C_1 = \sqrt{\gamma R T_1}$ was the speed of sound in the atmosphere ahead of the shock front, T_1 was the atmospheric temperature ahead of the shock front the measured value of which was 535.19°R [6], R was the gas constant, γ was the specific heat ratio, T_2 was the temperature of the flow behind the shock front approximated by the isentropic relationship

$$T_2 = T_{20} \left(\frac{p_2}{p_{20}} \right)^{\frac{\gamma-1}{\gamma}} \quad (\text{Eq. 14})$$

where T_{20} was the temperature directly behind the shock front obtained from the Rankine-Hugoniot relations and given as follows:

$$T_{20} = T_1 \left(\frac{7 + \frac{P_{20}}{P_1}}{7 + \frac{P_1}{P_{20}}} \right) \quad (\text{Eq. 15})$$

$$\text{where } P_{20} = P + P_1 \quad (\text{Eq. 16})$$

$$P_2 = P_1 + PF \quad (\text{Eq. 17})$$

The Reynolds number was given by

$$Re = \frac{(u - v)d}{\nu} \quad (\text{Eq. 18})$$

where d was the cylinder diameter
 ν was the kinematic viscosity given by

$$\nu \times 10^6 = \left[\frac{14.7}{P_1} \left(\frac{6 + \frac{P_{20}}{P_1}}{1 + 6 \frac{P_{20}}{P_1}} \right) \left(\frac{P_{20}}{P_2} \right)^{0.714} \right] \sum_{n=0}^k b_n T^n \quad (\text{Eq. 19})$$

where the b_n are coefficients [2] obtained by fitting a polynomial to values of ν for air at specific temperatures. The acceleration coefficient, an indication of the effect on drag of relative acceleration between fluid and cylinder was given by

$$a_c = \frac{da_t}{(u - v)^2} \quad (\text{Eq. 20})$$

where a_t is total acceleration defined by

$$a_t = a - a_p \quad (\text{Eq. 21})$$

(b) Summarized Results

The average drag coefficient obtained for each of the test cylinders is given for various time intervals in Table 4. These were obtained from the values given at two millisecond intervals as shown in Tables 2 and 3 and averaging these values over the specified time range given in Table 4.

A log-log plot of the drag pressure impulse at the various peak incident overpressures for which results were obtained on 3.49 inch diameter cylinders is given in Fig. 5.

DISCUSSION

The values of C_D shown as functions of time in Table 2 for Location 1 and in Table 3 for Location 4 indicate clearly that the flow around the cylinder had passed from turbulent flow to laminar flow Reynolds number regimes. This is shown by comparison of the drag coefficients and Reynolds numbers obtained for flow in the blast wave to known values for transition in steady incompressible flow. A minimum value of the drag coefficient, C_D , between 0.290 and 0.480 was reached between Reynolds number 5.7×10^5 and 10.1×10^5 , passing to a maximum value of slightly greater than 1 between Reynolds number of 4.2×10^5 and 5.6×10^5 in the same varying flow of the passing blast wave for locations 1, 4 and 5. For steady flow, on the other hand, the main part of the transition regime occurs approximately between Reynolds number 5×10^5 and 1×10^6 , where the drag coefficient changes from a minimum value of approximately 0.3 to a value of approximately 1.0 [8]. The effect of compressibility is such that the drag coefficient and Reynolds number of the transition regime both increase with Mach

TABLE 4
Average Drag Coefficients Over Various Time Ranges

Location	Peak Incident Overpressure p psi	Cylinder Diameter d inches	Average Drag Coefficient							
			For First 24 Milliseconds		For First 40 Milliseconds		For Full Test Range			
							$C_{D_{ave}}$		Milliseconds	
1	5.9	12.00	0.84	0.94*	0.79	0.81*	0.76	0.72*	16	140*
2	11.0	3.49	0.60	0.71*	0.61	0.63*	0.60	0.75*	54	70*
3	14.3	3.49	0.56		0.61		0.59		42	
4	17.0	3.49	0.66		0.53		0.80		68	
5	17.0	4.88	0.68		0.54		0.62		50	
6	20.5	3.49	0.93		--		0.92		26	
7	20.5	5.73	1.07		--		1.07		24	

* from camera data

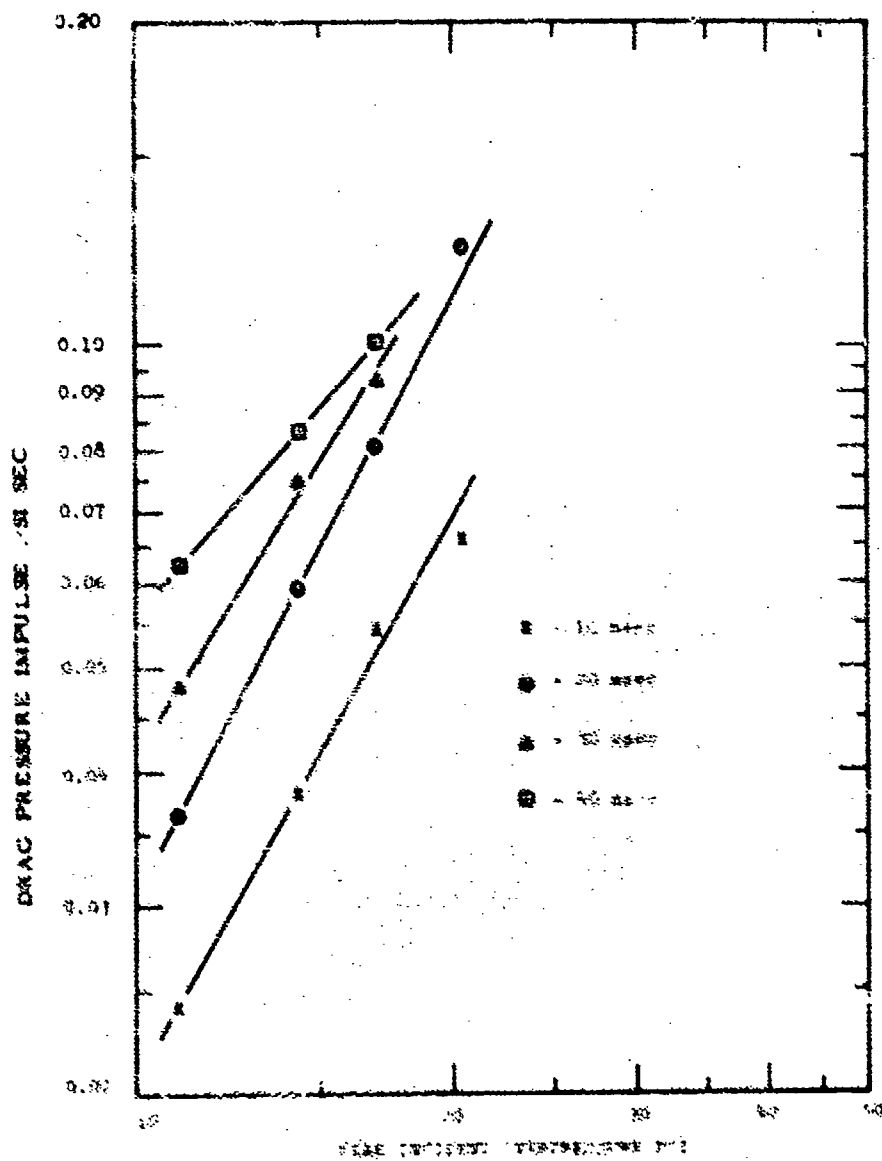


Fig. 5 - Drag Pressure Impulse for Various Elapsed Times for 3.49 inch Diameter Cylinder

number which explains why the values found were slightly above those known for steady incompressible flow.

It is interesting to note that the drag coefficient increased, during a time in the transition regime, at a higher rate than the dynamic pressure decreased in the blast wave, producing a net increase in drag pressure here.

The average value of drag coefficient over the supercritical Reynolds number regime was found generally to increase with the peak overpressure of the location. This is in agreement with the well-known steady flow result that drag coefficient increases with flow Mach number.

In Tables 2 and 3 the average drag pressure was always found to be higher than that which would be obtained by averaging the numbers shown in the drag pressure column for each position. This is because the average drag pressure was evaluated from the drag impulse, which was the time integral of all the forces acting on the cylinder including the initial diffraction phase; while the drag pressure was determined by the derivatives of smooth curves fitted to the displacement and velocity data. Due to rapidly changing initial loads, these curves produced inaccurate derivatives and hence inaccurate drag load resulted over about the first five milliseconds of time. Generally, the effect of smoothing by the fitted curves was such that the curves yielded velocities greater than zero at time $t=0$, and lower acceleration in the first few milliseconds than actually occurred.

The velocity of the two cylinders at Locations 6 and 7, both of which were at the same and higher overpressure location were found to decrease with time in part of the time range of measured velocity. This behavior is shown in Fig. 2. There are no apparent flow conditions which can be used to explain this behavior because it implies a force in the opposite direction to the blast wave over several milliseconds, which does not seem possible. The cylinders and stands were carefully checked immediately after the field trial and no indication of the cylinders striking the stands so as to slow the cylinders down was found. The drag pressure, drag coefficient, drag impulse, and average drag pressure for Location 6 is shown in Table 3 only for the time interval of the first linear output range of the transducers [5]. Beyond these times the fitted curves were considered unreliable for determining quantitative results. The fitted curves do, however, indicate qualitatively that a very sudden decrease in the drag coefficient occurred. There is a possible explanation for this sudden decrease. The supersonic expansion phenomenon causes a very sudden change in drag coefficient in the vicinity of Mach 0.5 at supercritical Reynolds numbers. The drag coefficient drops by a factor of about 4 as the flow Mach number decreases through the critical regime [9]. For Locations 6 and 7 the high mean drag coefficient before the sudden decrease in cylinder acceleration indicates that the cylinder was in the

supercritical Mach number regime and the very sudden drop in acceleration indicates that the transition regime was traversed. The drag pressures and drag coefficients are not shown in Table 2 for the final few milliseconds of the camera data because the instability of the time derivatives of the displacement curve from which they were obtained caused unreliability of the data here.

Oscillations, the frequency of which was about 200 Hz, are clearly shown for Locations 2 and 3 in Fig. 2. These were probably caused by free lateral beam vibrations since this type of vibration had a frequency of about 200 Hz for both test cylinders, which were hollow and practically identical in weight and construction at these two positions. Smaller amplitude vibrations with less clearly defined frequencies are shown in Fig. 2 for the solid test cylinders at Locations 4, 5, 6 and 7. These are probably also mainly due to free lateral beam vibrations. The velocity transducer data for Location 1 (Fig. 2) contained large amplitude oscillations which were probably principally due to oscillations in the large thin walled cylinder used here.

The camera data indicated dust free radial flow at Location 1, with the cylinder travelling so straight that both magnets could be seen leaving the coils on the same film frame. Also, nearly zero rotation about the cylinder axis occurred. The same conditions were observed in the film from Location 2 with the exception that a small amount of dust was visible.

The largest probable error in the results was due to the error in measurement of overpressure. The error in peak incident overpressure was estimated to be about ± 5 percent. This is less than the error estimated for Operation PRAIRIE FLAT [2] due to the near proximity and time of arrival detectors from which the pressures were taken in Event DIAL PACK [7]. The value of k , which determined the rate of decay of the pressure wave was subject to error due to oscillations appearing in the pressure-records [7] from which they were evaluated. However, the total error in the overpressures used in the analysis are estimated to be lower than 10 percent at all times after the blast front. Good agreement is shown in Tables 2 and 3 between camera and transducer results at the two positions where both methods were used, which indicated the reliability of both. Also the results at Location 2 agree with the results obtained by the camera method in Operation PRAIRIE FLAT at the 12.0 psi location [2]. Good agreement between both methods of transducer calibration was found for all positions except Location 6 where a discrepancy of about 25 percent occurred. The calibration by direct method, used in calibration of the results at Location 6, is reliable because it was done after the trial and carefully checked for errors after the disagreement was found.

The slope of the straight lines in the log-log plot of drag pressure impulse versus incident overpressure (Fig. 5) shows that the drag pressure

impulse after 10 to 20 milliseconds varied approximately as the square of the overpressure (the slope of the 20 ms line yields an exponent of 1.9). The results of strain measurement on the lattice masts indicated that the strain in the masts varied as the square of the overpressure also, and that the quarter periods of the fundamental modes of the large masts were about 12-1/2 milliseconds [10]. This indicated that the load imparted to the mast by the blast wave was directly proportional to the drag pressure impulse for the quarter period of the fundamental mode. Consequently, strains in the mast members in the elastic regime can be estimated in the pressure range tested, at least, when the drag pressure impulse is known.

The acceleration coefficient for each cylinder was never greater than 0.650 in the time range tested. This indicated that fluid acceleration is unimportant because the work of Keim [11] and Selberg and Nicholas [12] has shown that the effect of fluid acceleration on the drag coefficient is substantial only when the acceleration coefficient is greater than 0.20.

CONCLUSIONS

The high speed camera method and velocity transducer method were both found to be reliable for measuring aerodynamic loading of the circular cylinders tested in a large spherically expanding blast wave. Drag pressure, drag pressure impulse and drag coefficients obtained by these methods are listed in Tables 2 and 3 for cylinders tested at peak incident overpressure locations of 5.9 to 20.5 psi. Also a summary of the drag coefficients obtained is given in Table 4.

The velocity transducer method could be used at higher overpressures. In future trials new drag information could be obtained at these little explored pressures.

REFERENCES

1. G.H.S. Jones, "Final Operation Manual of Canadian Projects - Operation PRAIRIE FLAT", Suffield Memorandum No. 42/68, Unclassified, 1968
2. S.B. Mellisen, "Drag on Free Flight Cylinders in a Blast Wave", The Shock and Vibration Bulletin, Bulletin 40, Part 2, December 1969
3. R. Geminder, R.W. Hicks and S.Y. Wong, "Analytical and Empirical Study of Shipboard Antenna Masts Subjected to Blast Environment", Mechanics Research Inc., 9841 Airport Boulevard, Los Angeles, California, 1969
4. C.G. Coffey, "Blast Response of the G.R.P. Topmast", Suffield Memorandum No. 10/71, 1971
5. S.R. Mellisen, "Drag Measurements on Cylinders by the Free Flight Method - Event DIAL PACK" (U), Suffield Technical Paper No. 382, Unclassified, 1971
6. R.C.M. Wyld and G.P. Smart, "Canadian Participation in Event DIAL PACK", Suffield Memorandum No. 57/70, Unclassified, 1970
7. J.H.B. Anderson and W.J. Fenrick, "Canadian Overpressure Measurements Carried Out on Event DIAL PACK", Suffield Technical Note No. 296, Unclassified, 1971
8. H. Schlichting, "Boundary Layer Theory", McGraw-Hill Book Company, Toronto, 1960
9. S.F. Hoerner, "Fluid Dynamic Drag", S.F. Hoerner, 2 King Lane, Greenbriar Birch Town, N.J. 08723, 1965
10. D.S. Walkinshaw, "Study of Shipboard Antenna Masts Under Blast Loading", Suffield Memorandum No. 25/71, Unclassified, 1971
11. S.R. Keim, "Fluid Resistance to Cylinders in Accelerated Motion", Procs. of the Amer. Soc. of Civ. Engs, J. of Hydraulics Div, Vol. 82, HY6, PAPER 1113, 1956
12. B.P. Selberg and J.A. Nicholas, "Drag Coefficient of Small Spherical Particles", AIAA Journal, Vol. 6, No. 3, March 1968

DIAL PACK BLAST DIRECTING EXPERIMENT

L.E. Fugelso, S.F. Fields, W.J. Byrne
General American Research Division
Niles, Illinois

A two-ton TNT blast directing experiment was undertaken to extend the capabilities of the blast directing technique and to verify the accuracy of code predictions and predictions based on scaling considerations. This experiment was conducted at the Defense Research Establishment (Suffield, Alberta) of the Canadian Department of National Defense as a part of Operation DIAL PACK. Several individual TNT charges weighing 66 pounds each were distributed over a semi-circular disk 37.5-feet in radius and detonated, causing an air blast which was measured by total and side-on pressure gages placed in the one-dimensional flow region and beyond. On the blast axis, ground motion induced by the air blast was also measured.

The experimental data have been correlated with smaller yield blast directing data and theoretical predictions, and compared with data from larger yield HE hemispheres. These results show that the two-ton TNT blast directing experiment simulated the air blast, over a limited area, from a larger yield HE detonation.

INTRODUCTION

The basic concept of the blast directing technique is that the detonation of explosives distributed in a planar array can be used to generate an air blast whose time history at a given peak overpressure will simulate the blast wave generated by the detonation of a TNT hemisphere of larger yield. It is well known that for equal weights of explosive charge, the pressure decay associated with a one-dimensional blast wave is much less than that accompanying a spherical blast wave. Blast characteristics in the first case are similar to those occurring in a shock tube while in the second case they are similar to those produced by an unconfined explosion. For this reason, the blast directing technique can produce blast effects which appear to have been produced by a much larger explosive charge than what has actually been used. This technique therefore makes it possible to study various air blast effects with substantially less explosive than would normally be required.

Previous experiments at the General American Research Division's Ballistic Test Station with 100 pounds of TNT distributed over half

discs indicated that this type of planar array could generate a blast wave with enhanced duration, over a limited area. The current experiment was undertaken to extend the capabilities of the technique and to verify the accuracy of code predictions and predictions based on scaling considerations.

The experiment was conducted on August 6, 1970, at the Defense Research Establishment (Suffield, Alberta) as a part of Operation DIAL PACK.

Figure 1 shows the plan view of the experiment. There is a triangular region in which the blast wave generated by the system is planar. The region is gradually eroded by a rarefaction wave emanating from the edge of the array. From strong shock theory the extent of the plane wave region can be calculated. The maximum extent along the blast axis is $\sqrt{6} R$, where R is the radius of the TNT array. In addition, that part of the plane wave region with duration longer than the decay time to half-peak pressure has a maximum extent of $1.24R$ along the blast axis. It is in this region close to the array that the optimum zone for duration enhancement of the blast wave

Preceding page blank

occurs. However, the plane wave region does not start at the array. Closer in, the shock waves caused by the individual charge detonations will be discernable.

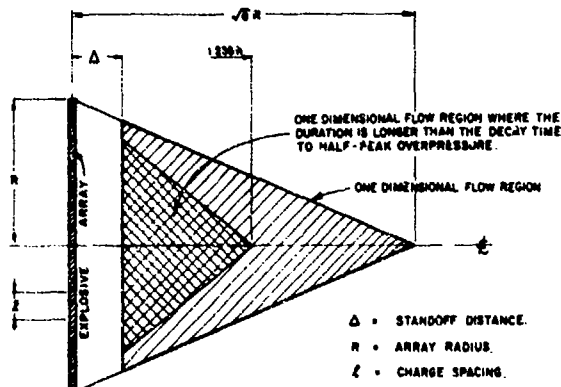


Fig. 1 - Plan View of Blast Directing Experiment

The blast directing concept was originated by Balcerzak, Johnson and Kurz [1]. They made numerical computations of the pressure-time histories in the one-dimensional flow region behind the blast front for discs of TNT, PETN and CH_4/O_2 . In the one-dimensional flow region, longer duration from the arrival of the planar shock to, say, the time to half-peak overpressure is attained than for a hemispherical explosive charge of the same weight. Lindberg [2] in a study of blast wave simulation techniques, came to a similar conclusion using the theoretical similarity solution pressure-time histories for one-dimensional and spherical blast waves (the similarity solutions are due to Sedov [3] and Korobeinikov [4]). Lucole and Balcerzak [5] experimentally verified the concept for 100-pound charges of TNT, Primacord and CH_4/O_2 (in a disc-shaped balloon). Lindberg [2] conducted similar experiments using Primacord and sheet explosives.

EXPERIMENTAL PROCEDURE

Two tons of TNT were distributed in a planar array over a half circle of 37.5-foot radius. The charges in the array were composed of a number of 33-pound cast TNT blocks, each block measuring 12 by 12 by 4 inches. The blocks were suspended from a charge support system constructed of telephone poles, wood beams and steel cables. A drawing of the array showing the details of the charge assembly is presented in Figure 2. There were 62 charge locations; at 60 of these were two 33-pound blocks, while single blocks were at the remaining two locations. The total weight of TNT was nominally 4026 pounds. The actual weight of each block was 32.6 pounds, so that the total charge weight was 3977 pounds. The vertical spacing between

the center of mass of each charge was 6'-0", and the horizontal spacing was 6'-3"; these dimensions were chosen to attain a uniform charge density per unit area. The area density of the array was 1.80 lbs TNT/ft².

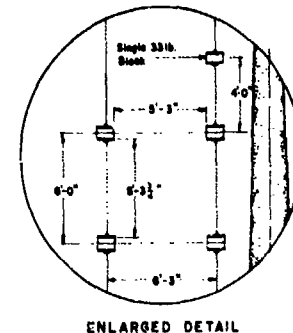
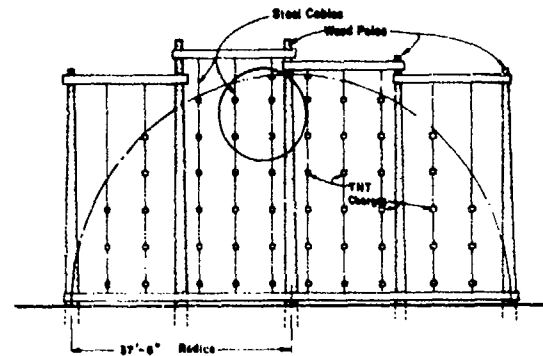


Fig. 2 - Two-Ton Blast Directing Experiment Charge Array

Each 66-pound tandem block was mounted in the array in the following manner. Two strands of 400-grain per foot Primacord, each strand consisting of four strands of 100-grain per foot Primacord in parallel, were placed between each pair of 33-pound blocks; the blocks were mounted between two 1/4-inch thick sheets of plywood; and this whole rig was suspended on steel cable from the charge support structure. A hole was provided through the center of the TNT blocks for the steel cable. The Primacord was used to detonate the TNT. Photographic records from previous experimental tests of individual 66-pound tandem blocks indicated that detonation ultimately occurred with this configuration. A detonation cord assembly was constructed to ensure simultaneous detonation of the array. Equal lengths, 86.7 feet, of speed tested Primacord ran from the detonator to each TNT block. The detonation velocity of the Primacord was 22500 ± 400 feet per second. Dual 7-grain PETN detonators (Type X - 128 High Energy Seismocaps)* were used to ignite the Primacord.

* TM Canadian Industries, Ltd.

The detonation and air blast were monitored by pressure gages. Both total pressure and side-on pressure were measured. BRL had the responsibility for emplacement of these gages, as well as recording and reducing the data. Figure 3 shows the locations of the pressure gages. In addition to the gages shown, two gages were installed on the blast axis 530 and 850 feet from the array. The total pressure gages were approximately 1.5 feet above the surface, while the side-on pressure gages were flush-mounted in concrete pedestals. Photographic coverage of the event was provided by several Fastax and Millikin cameras.

Ground motion gages were placed along the blast axis at 1.5-foot and 5-foot depths. Either accelerometers or velocity gages were used. Figure 4 shows the location and type of each gage. WES had the responsibility for installation of these gages and the recording and reduction of the ground motion data.

EXPERIMENTAL RESULTS

Figure 5 shows the sequence of the detonation from the front of the array. The framing rate for this sequence is 5465 frames per second. Figure 6 shows a close-up of the ignition of the Primacord system. Ignition of the TNT blocks was very nearly simultaneous;

less than 0.1 millisecond separated the individual detonations. Figure 7 shows the fireball after the individual fireballs have coalesced. Post-shot inspection of the blast debris about the test site indicated that the detonation was symmetric about the blast axis.

Typical experimental overpressure-time records taken at ranges of 10, 50 and 105 feet along the blast axis are shown in Figure 8. The gage at 10 feet shows several peaks which are attributable to the signals from individual charges. The first shock that passes the gage at 50 feet is planar; the decay of the pressure behind the shock is that of a plane shock until a rarefaction wave from the edge of the explosive array arrives. When this rarefaction wave arrives, as indicated by the small arrow on the graph, there is a sharp break in the pressure decay curve. This change in slope occurs at smaller time intervals after the shock arrival as the range from the array increases. The decay rate before the arrival of the rarefaction wave is roughly half the rate thereafter. The overpressure-time profiles at the 105-foot gage locations shows a smooth decay after shock arrival.

Typical ground motion records are shown in Figure 9. The vertical and horizontal accelerations, velocities, and displacements, which were integrated from the acceleration record, are shown for the 50-foot range, 1.5-foot depth.

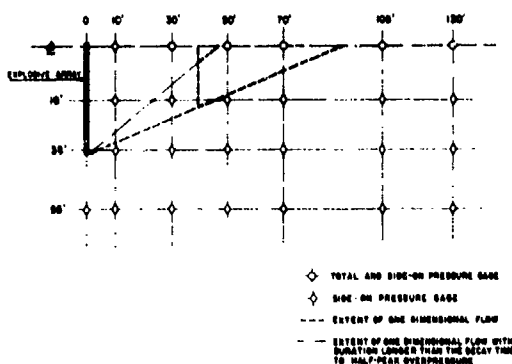


Fig. 3 - Blast Directing Experiment Gage Locations

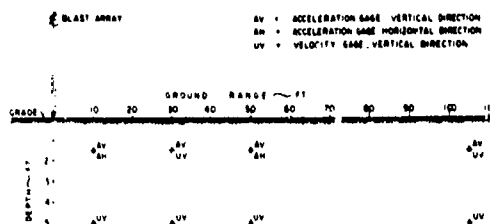


Fig. 4 - Location of Ground Motion Gages on Blast Axis

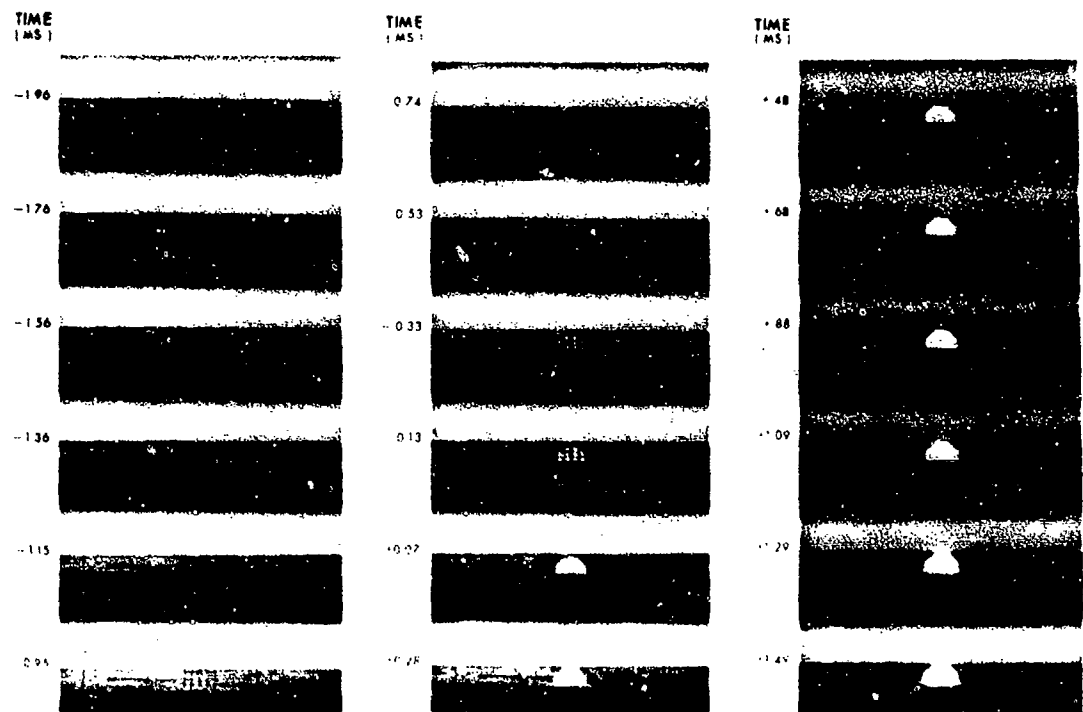
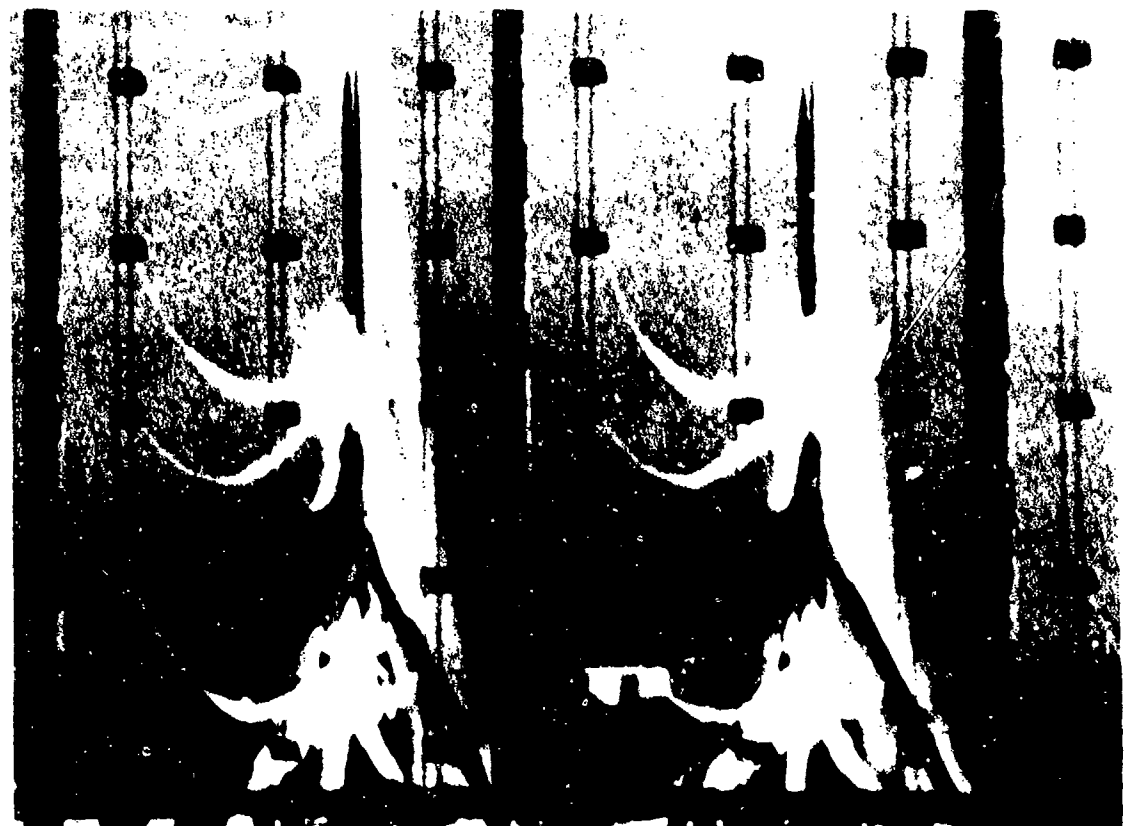


Fig. 5 - Framing Camera Sequence of Detonation (Front View)



Reproduced from
best available copy.

Fig. 6 - Ignition of Detonation Cord Assembly

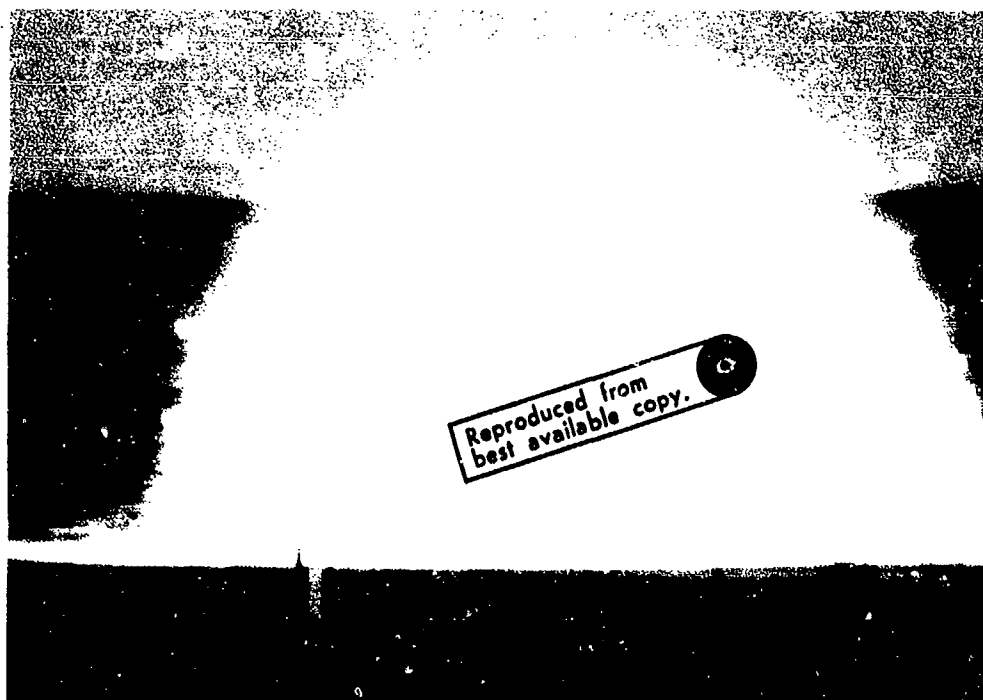


Fig. 7 - Fully Developed Fireball (Front View)

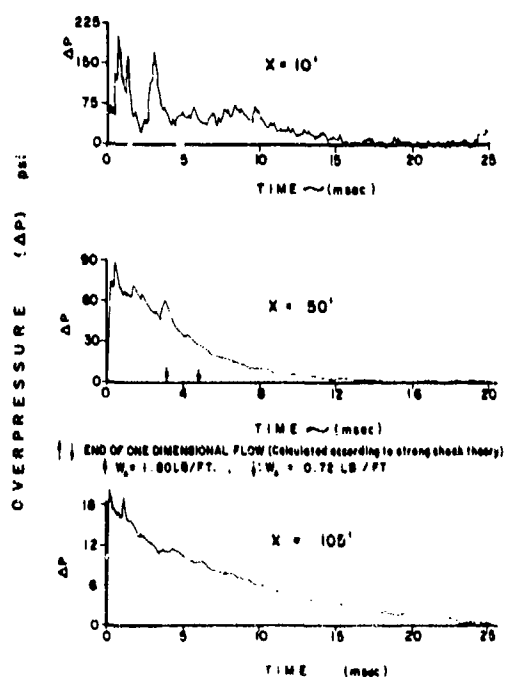


Fig. 8 - Typical Overpressure Vs. Time Records on the Blast Axis

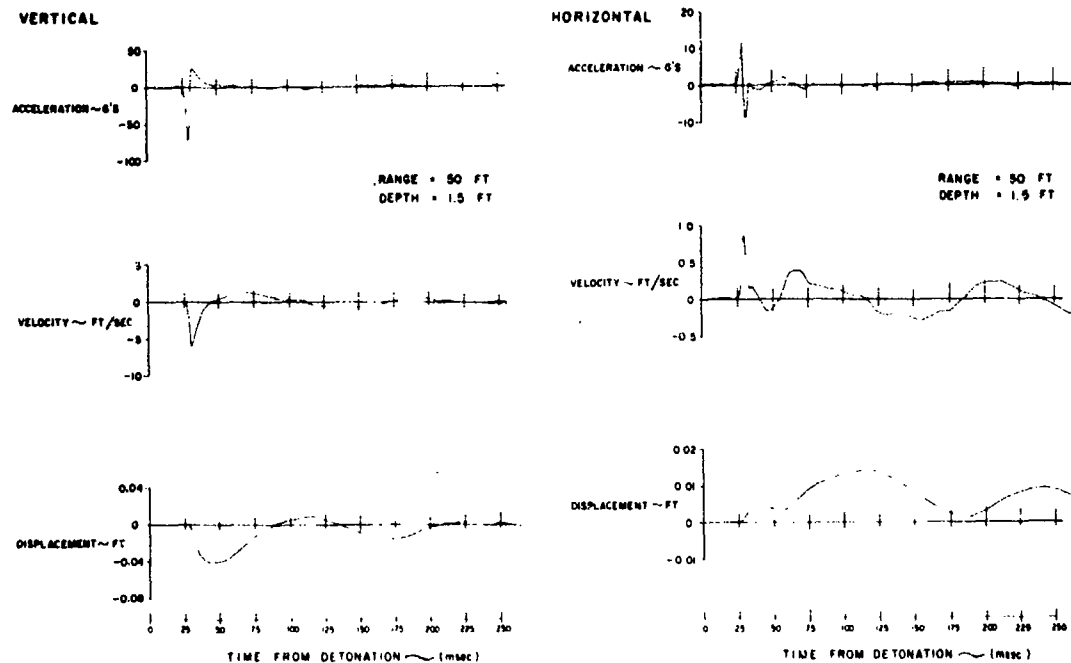


Fig. 9 - Typical Ground Motion Records at $r = 50$ Ft. $z = 1.5$ Ft.

DISCUSSION OF EXPERIMENTAL RESULTS

According to strong shock theory, the maximum extent of the plane wave region along the blast axis is $\sqrt{6} R$, where R is the radius of the array. Dimensional analysis indicates that for a given peak overpressure, the distance from the array scales inversely with the charge weight per unit area within this plane wave region and inversely with the cube root of the total charge weight for the region beyond. Close to the array, the shock waves caused by individual charge detonations will be discernible. In this region, another parameter, namely, charge spacing over the cube root of the individual charge weight, must also be considered. Insufficient data were taken in this region for comparative purposes. However, the peak overpressure versus scaled range data together with the results of the AFWL two-dimensional axisymmetric code calculations shown in Figures 10 and 11 indicate that this region extends for at least 5 charge spacings from the array. This conclusion is in general agreement with the results of additional AFWL code calculations for peak overpressure versus range for an infinite line charge distribution and an infinite line of spherical charges.

Figure 10 shows the peak overpressure versus scaled range data in the plane wave region. In this figure, x is the range measured perpendicular to the plane of the array. The similarity solution for an infinite sheet explosive due to Korobeinikov [4] is also

plotted on the graph, together with the AFWL two-dimensional axisymmetric code predictions. The AFWL code predictions start with the TNT charge distributed in unequal tori. Also shown are the points from the 100-pound TNT blast directing experiments. [5] Figure 11 shows the peak overpressure versus scaled range data for the gages beyond the plane wave region.

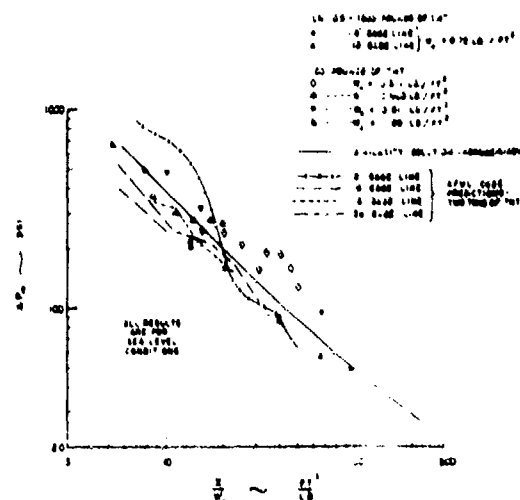


Fig. 10 - Peak Overpressure vs. Range - One Dimensional Flow Region

In this figure, r is the slant range measured from the center of the array. The AFWL code predictions, the 100-pound data and experimental data for the detonation of a TNT hemisphere [6] are also shown on the graph. In both figures, the two-ton blast directing data have been scaled using a total effective charge weight of 1600 pounds. By scaling the data in this manner, a concurrence of theory, scaled predictions and two-ton blast directing data is obtained.

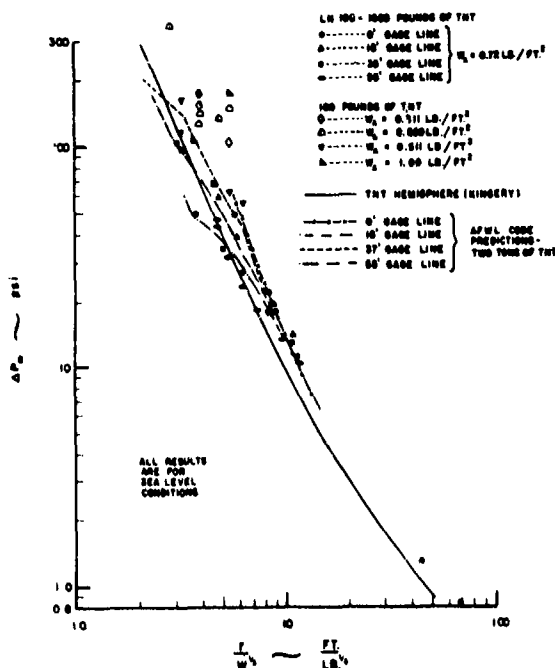


Fig. 11 - Peak Overpressure Vs. Range - Beyond One Dimensional Flow Region

The low effective total charge weight is attributed to the finite induction distance necessary for sympathetic detonation of the TNT as cast. The shock induced in the TNT by the detonation of the Primacord must propagate a certain distance before a self-sustaining detonation is generated. There is some experimental evidence that this induction distance is about 4 inches for the 12 by 12 by 4-inch cast TNT blocks at Suffield. [7,8] The conclusion in this case is that in each block the TNT contained in 6-inch diameter cylinders surrounding the two Primacord strands deflagrated rather than detonated. That is, 60 percent of the TNT deflagrated. Thus the effective total charge weight for the shock front overpressures is about 1600 pounds.

Scaled positive phase overpressure impulse data is plotted versus scaled range in Figure 12 together with the curve for a TNT hemisphere and AFWL code predictions for both one and two tons of TNT. The blast directing data has been

scaled using total charge weights of 1600 pounds and 3977 pounds. Once again, reasonable agreement is obtained between the AFWL code predictions and the blast directing data using the lower effective total charge weight. The positive phase overpressure impulse data is substantially enhanced in comparison with the curve for a TNT hemisphere in this case, particularly in the range corresponding to the region near the fireball.

Essentially the same positive phase overpressure impulse data presented in Figure 12 is plotted versus peak overpressure in Figure 13.

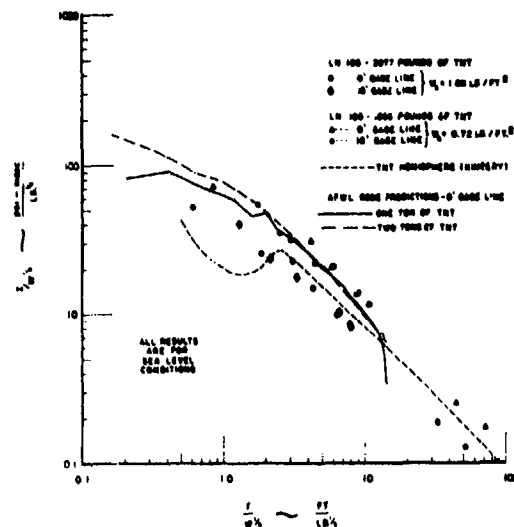


Fig. 12 - Positive Phase Overpressure Impulse Vs. Range

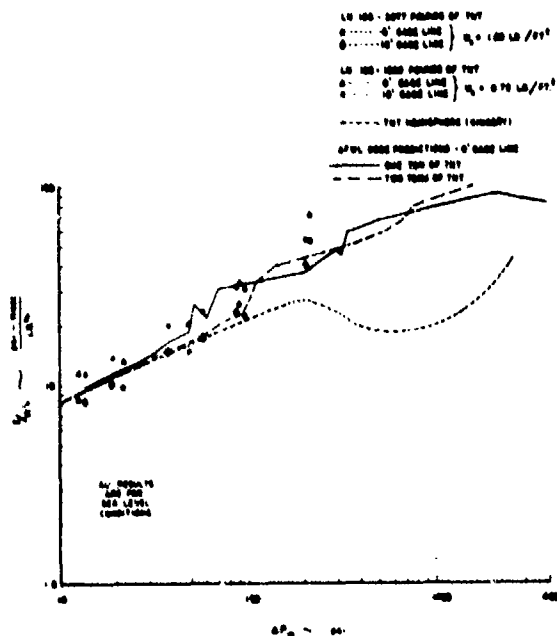


Fig. 13 - Positive Phase Overpressure Impulse Vs. Peak Overpressure

This particular plot is not very informative as to the effective total charge weight for the blast directing experiment. This is due primarily to both the positive phase overpressure impulse data and the peak overpressure data being lower than expected. Nevertheless, enhancement of the positive phase overpressure impulse data over the curve for a TNT hemisphere is again evident, particularly at high peak overpressures.

Cube root scaling has been used in both Figures 12 and 13. This is not strictly correct for data obtained at points close to the blast directing array due to one-dimensional flow effects. The curves based on the AFWL code predictions give an indication of this. The most interesting one-dimensional flow effect can be seen in Figure 13 where the region of significant enhancement extends to lower peak overpressures for the lower charge weight (1 ton). Finally, while the blast directing data has been scaled using total charge weights of 1600 and 3977 pounds for these two figures, an intermediate total charge weight might also be appropriate, since the impulse data undoubtedly was affected by the TNT that deflagrated as well as the TNT that detonated.

Vertical ground motions induced by air blast loading may be correlated on the basis of ground motion-to-air blast ratios. The ratio of peak vertical acceleration-to-peak overpressure versus peak overpressure and the ratio of peak vertical velocity-to-peak overpressure versus peak overpressure are shown in Figures 14 and 15. On each graph, the same parameters are plotted for the ground motion of the blast directing experiment as for several spherical and hemispherical TNT detonations in the same soil. Included are the Distant Plain Events 6, 1A and 3 and the Flat Top II and III events [9]. The overpressures used in the calculation of these ratios were not corrected for initial pressure in order that the comparison with the other HE data, also not corrected, but at the same initial pressure, might be shown.

The blast directing ground motion points fall within the scatter of the other HE experiments. The general trend in both graphs is toward lower values of these ratios with increasing peak overpressure.

The magnitudes of the peak vertical velocity attenuate with depth, averaging 32% less at the 5-foot depth than at the 1.5-foot depth. For comparison, the Distant Plain 6 attenuation was about 40% in the same overpressure range. This difference may be attributed to the much smaller net yield in this experiment or the associated shorter positive phase duration.

The ground shock profile is plotted in Figure 16, using the time of arrival for air shock and ground shock measured from the detonator initiation. The soil structure in the general area consists of a 200-foot thick layer

of clay overlying bed rock. Above the water table, at a depth of 25 feet, there is a dry clay with a P wave velocity of about 1050 feet per second. At the water table, the P wave velocity jumps to 5100-5500 feet per second. [10] The observed wavefront patterns are P waves attached to the air shock which is supersonic with respect to the upper, dry-clay layer. Later portions of the motion profiles indicate either reflected waves or refracted waves from the top of the water-saturated layer or from bedrock; or directly transmitted waves from the explosive array.

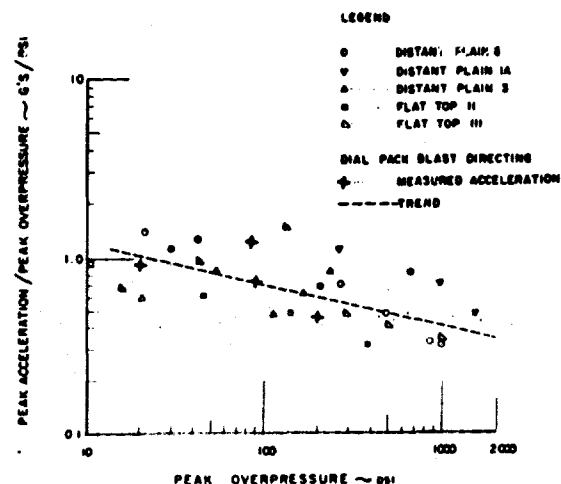


Fig. 14 - Ground Motion Correlation, Peak Acceleration to Peak Overpressure Ratio Versus Peak Overpressure

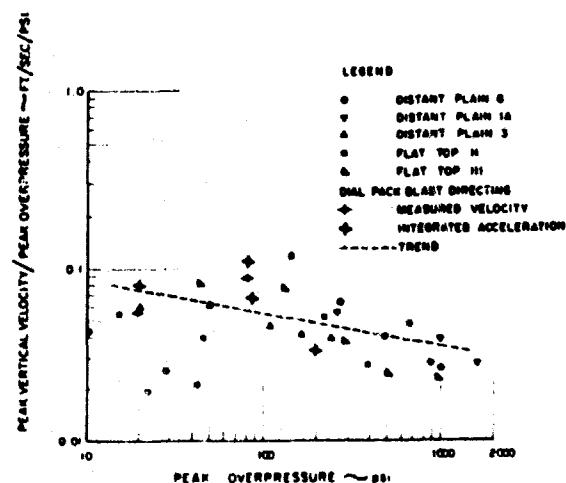


Fig. 15 - Ground Motion Correlation, Peak Vertical Velocity to Peak Overpressure Ratio Versus Peak Overpressure

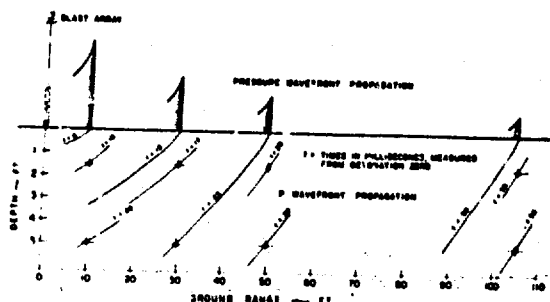


Fig. 16 - Approximate Location of P Wavefront Due to Blast Directing Array

CONCLUSIONS AND RECOMMENDATIONS

The blast directing array generates a pressure wave which, in a limited area extent, simulates the blast wave generated by the detonation of a larger yield hemispherical charge. This effect is most pronounced in the high overpressure region. Sufficiently close to the array, the radius of curvature of the blast front is larger and the time of decay to half-peak overpressure, for example, is extended compared to a hemispherical burst of the same weight.

At the conclusion of this test, five blast directing experiments with TNT have been performed, four at 100 pounds and one at two tons.

The experimental results of these tests verify the blast directing concept. The data taken in the two-ton test was somewhat anomalous. While the results are explainable, the use of this corrected data should not be used to extrapolate to much higher yields. Another blast directing experiment of similar or slightly larger yield should be conducted to (1) eliminate the anomalous lower yield factor and (2) to obtain a statistically significant basis for extrapolation to higher yields.

The array as designed allowed the development of a one-dimensional flow region only at ranges where the peak overpressure was less than 100 psi. Smaller individual charges and smaller charge spacings are recommended to give a larger effective test region with higher peak overpressures.

The detonation efficiency of the recast TNT, with regard to the peak overpressure and positive phase overpressure impulse data was somewhat less than 50%. Better preparation of the TNT is necessary and/or a better ignition system should be devised to ensure more complete detonation of the TNT. This recommendation includes further investigation of the ignition and detonation of cast TNT. As an alternative, a different, more sensitive explosive such as Pentolite could be used.

This work was conducted for the Defense Atomic Support Agency under Contract DASA 01-70-C-0107.

REFERENCES

- Balcerzak, M. J., Johnson, M. R. and Kurz, F. R. (1966), "Nuclear Blast Simulation, Part II, Blast Focusing Technique", DASA-1792-II.
- Lindberg, H. E. (1967), "Simulation of Transient Surface Loads Using Plane, Cylindrical and Spherical Blast Waves", Poulter Laboratories Technical Report 002-67.
- Sedov, L. I. (1959), Similarity and Dimensional Methods in Mechanics, Academic Press, N. Y.
- Korobeinikov, V. P. (1956), "Approximate Formulas for the Calculation of a Shock Wave Front in the Case of a Point Explosion in Gas", Doklady Akad. Nauk SSR, 111, 557-559.
- Lucile, S. W. and Balcerzak, M. J. (1968), "Blast and Shock Simulation, Blast Directing Technique", DASA 2150.
- Kingery, C. N. (1966), "Air Blast Parameters Versus Distance for Hemispherical TNT Surface Blasts", BRL R 1344.
- Holsgrove, B. J. (1968), "Detonation of Stacked TNT Blocks, A Review of the Attenuating Effects of Air Gaps", Suffield Memorandum No. 7/68.
- Technical Cooperative Panel (1970), "Fireball and Shock Wave Anomalies", DASIAC Special Report 105.
- Murrell, D. W. (1970), "Distant Plain Events 6 and 1A, Project 3.02 A, Earth Motion and Stress Measurements", WES TR N-70-14.
- Hendron, A. J., Jr. (1965), "Correlation of Operation Snowball Ground Motion with Dynamic Properties of Test Site Soils", WES Report No. 1-745.

DISCUSSION

Mr. Hughes (Naval Weapons Evaluation Facility): Could you give me the name of the AFWL code and an individual contact at the Air Force Weapons Laboratory?

Mr. Fields: The individual was Charles Needham, I believe, and I do not remember the name of the code. I should add that the Air Force Weapons Laboratory not only did the exact or copredictions for this experiment per se, but they also studied line charge distribution, fully linear line charge distributions, and one consisting of spherical charges on a line. The copredictions here were not for an array exactly as shown. In reality the copredictions were for torria of charges that were unequal in size, sort of a geometrical layout to approx-

imate the array. This was a two dimensional axisymmetric code.

Mr. Baker (Southwest Research Institute): Some years ago I think the people at Stanford used small arrays of primacord or strips of deta sheet to do something similar to this, that is close-in to give a more nearly plane rather than a spherically diverging shock. Do you know about this?

Mr. Fields: Yes, as a matter of fact one of the references for some other similarity solution work that we do was by Lindberg and his experiments on a much smaller scale. I believe he was interested more studying reflected pressures but the ideas are quite similar.

BLAST FIELDS ABOUT ROCKETS AND RECOILLESS RIFLES

W. E. Baker, P. S. Westine, and R. L. Bessey
Southwest Research Institute
San Antonio, Texas

This paper summarizes the results of an extensive series of measurements that were made on the blast fields generated by recoilless rifles and six different types of solid-propellant rocket motors. Peak overpressures and positive impulses are reported for blast waves in free air as well as waves reflected from plane surfaces located near the weapons. Test techniques are also described. Model laws are given for scaling pressures and impulses in the blast fields about recoilless rifles, and these laws are corroborated by comparison with experimental results from these and previous tests. Attempts made to generate scaling laws for prediction of blast parameters about rockets proved unsuccessful. Significant differences were observed in the characteristics of pressure fields generated by different rockets, and these differences are discussed in this paper.

INTRODUCTION

A gun, fired in the vicinity of an aircraft, boat, armored carrier, or personnel, emits a severe blast pressure wave from the muzzle (and breech if it is not closed-breech), which can cause serious damage. In 1968, experimentally verified scaling laws were developed which permit the prediction of muzzle blast pressures and impulses in the free field around muzzles of closed-breech weapons, and imparted to panels underneath them [1,1a]. Open-breech weapons, such as rocket motors and recoilless rifles, also emit severe blast pressure waves. The primary purpose of this study is to develop scaling laws for predicting the blast pressure and impulse fields around these types of weapons. This paper summarizes a much larger report [2] which should be obtained by those wishing greater detail.

To date, fewer blast pressure measurements have been made about open-breech (recoilless rifles) than closed-breech weapons. Peak free-field overpressures have been measured and reported in some tests [3 through 10]; however, until now, insufficient free-field impulse data [3, 8, and 9] existed to create a scaling law for any blast property other than peak free-field overpressure about recoilless

rifles. Also, until now, absolutely no recoilless rifle reflected pressure or reflected impulse data existed; hence it has not been possible to estimate the transient loads imparted to a panel by a recoilless rifle breech or muzzle blast.

Even less blast pressure or impulse data near rockets have existed to date. Three data points [11] for blast pressures from rockets (imparted to the tail boom of a UH-1B helicopter) were known to the authors by 1968 [1]. Since then, some peak pressure measurements were reported by Groetzinger [12, 13] for several modifications of the Light Antitank Weapon (LAW). Unreported data on LAW and 2.75-in. rockets were also available from personnel in the Human Engineering Laboratory at Aberdeen Proving Ground [14]. Unfortunately, the rocket blast data from these sources were recorded at only two locations (one at 2 meters from the breech of the weapon, the other at the gunners' head position).

Although these more recent data are useful, they are too limited to define blast pressure or impulse fields. Absolutely no reflected pressure or reflected impulse data presently are available other than the three data points referred to in Ref. [5].

In order to conduct a similitude analysis and to empirically generate some procedures for predicting peak pressures and positive impulses from rockets and recoilless rifle blasts in the free field and incident upon plane surfaces, it was necessary to take our own data about recoilless rifles and rockets. In this paper, we summarize a blast pressure and impulse measurement program to obtain data in the free field as well as upon reflection from a plane surface. We will also describe a procedure developed for predicting pressures and impulses around recoilless rifles and the difficulties encountered when attempting to generate a similar procedure for predicting blast characteristics of rockets.

DESCRIPTION OF EXPERIMENTS

The 138 experiments in this project were conducted at an outdoor testing range located on the Southwest Research Institute grounds. The primary test area consists of a reinforced concrete pad, with a support and thrust stand located at its center. The thrust stand is oriented so that weapons mounted on it are aimed at an impact area built into the side of a hill, about 150 feet away. Instrumentation is housed in a semitrailer.

The same basic instrumentation system was used throughout the test program. Blast pressures generated by the weapon upon firing were sensed by piezoelectric transducers and the signals from the transducers amplified by multi-channel amplifiers. The amplified signals were transmitted to the input electronics of a multi-channel magnetic tape recorder located in the instrument trailer. The taped records were played back through galvanometer-driver amplifiers and recorded as analog signals on a multi-channel galvanometer oscillograph. The tape recorder has FM input and playback electronics, with a frequency response flat from 0 to 400 kHz. To utilize this frequency response and to expand the short-duration blast records so that they could be manually reduced, data were recorded at 120 ips, and played back at 1-7/8 ips. The galvanometer oscillograph was run at 32 ips for analog recording of all records. The upper limit on frequency response for the system as described above is dictated by the frequency response of the galvanometers, which was 32 kHz.

The actual testing procedure was essentially the same for all experiments. First, the pressure transducers, either free-field or reflected, were mounted and their locations determined relative to the weapon by using a

surveyor's transit and measuring tape. The free-field transducers were mounted at the ends of 4-ft tubes which were in turn attached to vertical pipes on tripod mounts (the gage array for 57-mm recoilless rifle tests is shown in Fig. 1). The flush-mounted transducers were fitted into silicon rubber shock mounts in reflecting surfaces consisting of large plywood tables covered with 1/8-in. aluminum sheets. Additional 4- x 8-ft area tables with no aluminum sheet covering were abutted to the tables containing the transducers, to present an effectively infinite plane for blast wave shock reflection.

After emplacement of the pressure transducers, the weapon being tested was mounted on the thrust stand and fired. For each weapon and configuration of pressure transducers, several tests were conducted. Usually, the first test of a series was played back immediately and the oscillograph records developed to check amplifier settings. Adjustments were then made and two or three additional tests conducted. This process was repeated, changing gage locations, until the blast field was surveyed as completely as possible.

Blast fields were measured about the following weapons during this program:

- (1) 57-mm recoilless rifle, M18A1 (the type of shell fired from this rifle was a training and practice round with a small spotting explosive charge, with designation M306A1).
- (2) 2.75-in. rocket motor, Mark 40 Mod 3, with propellant grain Mark 43 Mod 1
- (3) 2.75-in. rocket motor, Mark 1 Mod 3, with grain Mark 31 Mod 1
- (4) 5.0-in. rocket motor Mark 10 Mod 7
- (5) 4.5-in. rocket T46
- (6) 4.5-in. rocket T161E5
- (7) 66-mm rocket M72A1 (LAW).

All of the rockets were provided with inert-loaded warheads. Only the 66-mm LAW rocket had a burning time sufficiently short to allow flight during test. Both free-field and reflected blast wave measurements were made for weapons (1) through (3) while only free-field measurements were made for weapons (4) through (7).

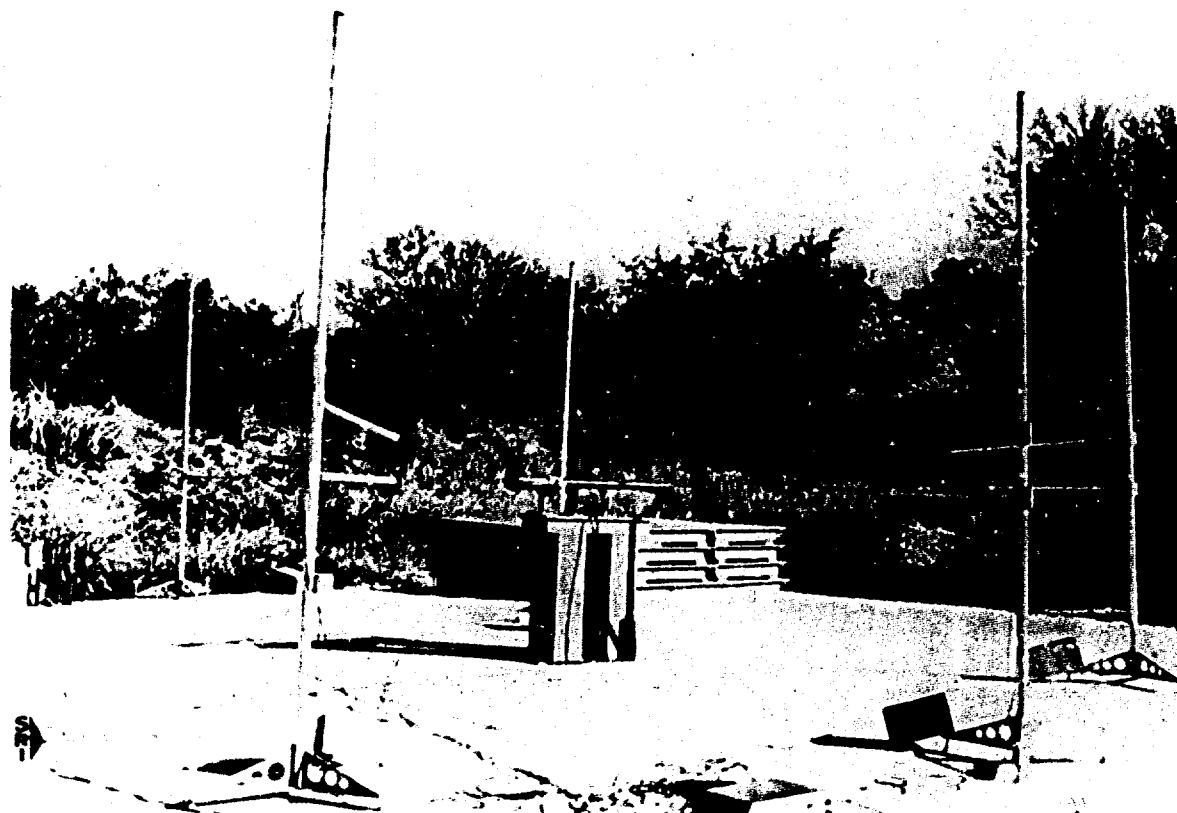


Fig. 1. Field Setup for Free-Field Blast Measurements Around 57-mm Recoilless Rifle

The three parameters measured for each recorded pressure-time history were: (1) peak overpressure, (2) impulse, and (3) overpressure duration. Also, time of arrival data were measured in many cases, although some difficulty was experienced due to the lack of definition of time zero. Peak overpressures were obtained by measuring the peak of the shock trace directly from the records with a rule graduated in 0.01-in. increments, and multiplying by the appropriate transducer and system calibration factor. The time duration was obtained by measuring the shock trace duration from the records and multiplying by the reciprocal of the recording oscillograph speed divided by the tape recorder speed reduction of 64. The impulse was obtained by measuring the area under the shock traces with a planimeter and multiplying by both of the previously-mentioned multiplicative factors.

All data were sorted, and the final results were calculated by computer. In the event

that several shock traces were present on a given channel, the blast parameters were calculated for the most prominent. Complete numerical data are given in Appendices to the Final Report [2].

RESULTS

There are a number of characteristics of the weapons we tested which can conceivably be correlated with the blast field generated when the weapons are fired. Some of these characteristics are available in technical manuals and ordnance publications describing the weapons. These references do not list all of the characteristics which may correlate with the blast field. We have, therefore, supplemented information from these manuals with measurements which we have made on disassembled or burned-out rocket motors and with data available from other sources. The characteristics of the various weapons are summarized in Table 1. The first four columns describe the geometry of the rocket

TABLE 1

Weapons' Characteristics

Weapon	Motor or Bore Vol., (in. ³)	Motor or Bore L. D., (in.)	Nozzle Throat Area (in. ²)	Nozzle Exit Area (in. ²)	Total Prop. Wt. (lb.)	Burning Time (sec.)	Average Chamber Pressure (psia)	Round (Wt., lb.)	Launcher or Muzzle Vel., (fps)	Remarks
57-mm Recoilless Rifle, M13A1	315	2.25	3.04	6.48	0.671	7×10^{-3}	6500	2.78	1200	Fine-grained propellant contained in plastic sack in shell casing.
44-mm LAW Rocket M72A1	8.45	1.284	0.607	3.46	0.14	5.9×10^{-3}	4500	1.32	850	19 hollow cylindrical propellant grains.
2.75-in. Rocket Motor MK40 Mod 3, Prop. Grain MK43 Mod 1	135.3	2.60	0.384	1.36	5.90	1.69	1050**	12.06 (burnt)	2300	Single propellant grain with star-shaped central hole.
5.0-in. Rocket Motor MN10 Mod 7, Prop. Grain Mh18 Mod 0	719	4.63	$\frac{2.65}{3.44}$	$\frac{9.82}{12.96}$	21.0	0.8-1.4 (1.15 nominal)	910**	134	1350	Single cruciform propellant grain.
4.5-in. Rocket, T46	216	4.20	2.60	4.71	4.75	0.10-0.36	920**	40.0	865	10 hollow cylindrical grains of double-base propellant.
4.5-in. Rocket, T161RS	210	4.20	1.171	3.98	7.78	0.35-0.95	1220**	42.0	5250	7 hollow cylindrical grains of double-base propellant.

* This rocket has a central blowout disc surrounded by eight small nozzles. The upper number gives the combined area of the eight small nozzles; the lower number gives the total area for all nozzles plus central blowout area.

** Computed assuming a discharge coefficient C_D of 0.67×10^{-3} lb./lb. sec.

motor casing or the chamber of the recoilless rifle. The next three columns present data relating to the propellant. Total weight of propellant in the round is given for each weapon, followed by a burning time and an average chamber pressure within the rocket motor or rifle bore.* The next two columns present data for the projectile which can allow calculation of its maximum kinetic energy. Some remarks concerning the propellants used in each weapon are given in the last column.

From Table 1, it can be seen that there is a wide range of characteristics in the weapons which we tested. Some contain small amounts of propellant and have very short burning times, some contain intermediate quantities of propellants and have much longer burning times, while the weapon with the largest amount of propellant has an intermediate burning time. This variation is, of course, caused

somewhat by design rather than by accident, because we wished to study scaling of the blast fields from rockets and recoilless rifles and needed to have as large a variation in various characteristics as possible. The 57-mm recoilless rifle is in a different class from all of the rocket weapons because a considerable quantity of free-field data for recoilless rifles exists and also because it is fundamentally a different type of weapon, with multiple rather than single blast sources.

Blast Parameters for 57-mm Recoilless Rifle

A typical set of free-field blast records for this weapon is shown in Fig. 2. This figure shows the analog playback, with one channel repeated on both playback records for time correlation. To an experimenter accustomed to measuring air blast waves from comparatively "clean" sources, such as spherical explosive charges, these records may seem to be quite complex. On many of the traces, multiple shocks are evident, and relatively slowly rising pressures are apparent for some of the gage traces. These are simply the characteristics of the pressure-time histories that can be expected from a complex pair of blast sources, such as the breech and muzzle of the recoilless rifle. Enough free-field measurements were taken to survey the blast field about both the breech and muzzle of the

* The chamber pressure indicated by a double asterisk in the table were computed from the formula $P_C = \dot{m}/C_D A_t$, where \dot{m} is mass burning rate, C_D is a discharge coefficient, and A_t is throat area. The term C_D was computed from this formula for the LAW rocket (P_C known), and assumed constant for all other rockets.

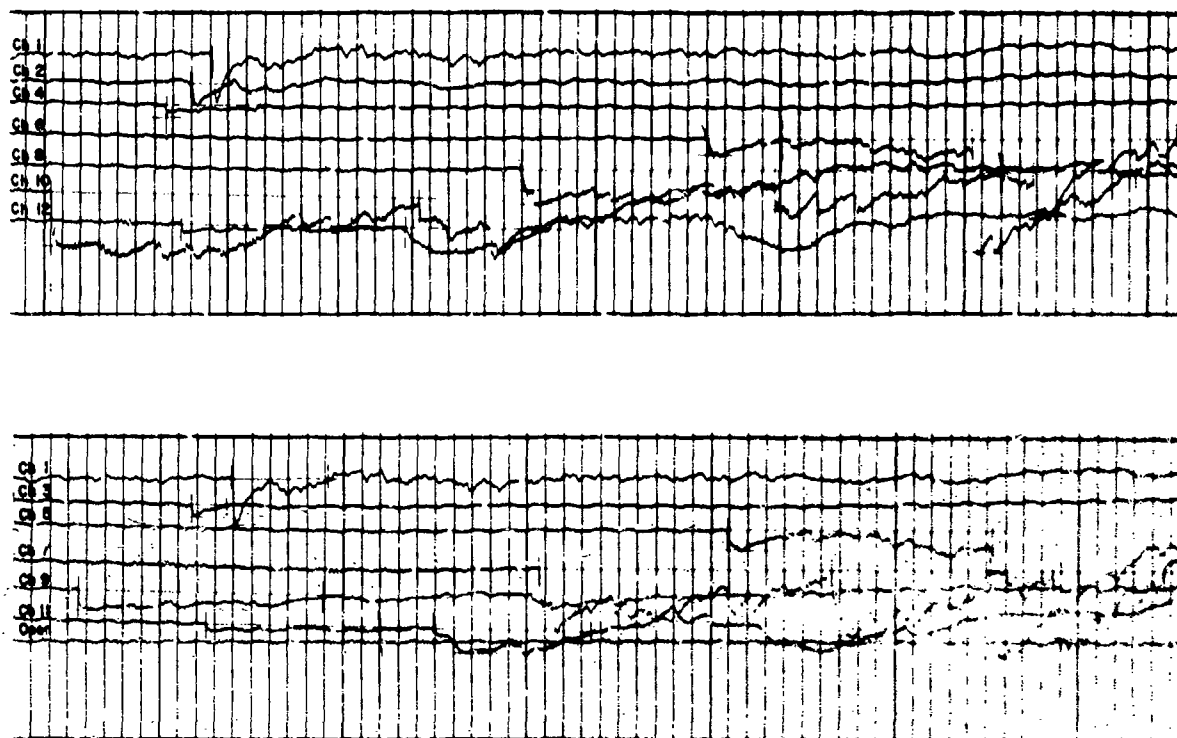


Fig. 2. Typical Record of Blast from 57-mm Recoilless Rifle

weapon rather completely. For the reflected measurements, however, we found early in the test program that the breech blast was so intense that the plywood tables used as reflecting surfaces were severely damaged on each test conducted aft of the weapon and close to the line of fire. Therefore, although we had intended to completely survey the reflected pressure field for four standoff distances from the axis of the weapons, we were forced to eliminate many of the planned experiments at the smaller standoff distances. Near the muzzle of the weapon, the blast field was weak enough that a more complete survey could be made. Typical data for each round included peak overpressures for one or more shocks on each record, positive impulse starting from the time of the first shock arrival, and the positive duration of the first shock. Some of these data will be summarized in scaled plots later in this paper.

Blast Parameters for 2.75-inch Rockets

This rocket generates a pressure field which is totally different from that generated by a closed-breech weapon or by a recoilless rifle. A typical set of free-field pressure-time histories for this weapon is shown in Fig. 3. The pressure-time histories are

characterized by relatively small and irregular initial pressure pulses (whether these pulses can be called shocks or not is open to question). Following these initial pressure pulses, much larger amplitude and irregular pressure fluctuations can be seen. Because of the necessity for holding this weapon captive during firing, the latter portions of these traces are probably not at all representative of the pressures which would be felt by an observer located near a freely-fired weapon. Whereas the character of the blast field generated by the recoilless rifle was relatively repeatable from round to round, the initial portions of the pressure traces generated by the 2.75-in. rocket were quite variable. Occasionally, single peaks and definite shock waves would be recorded; however, the types of records shown in Fig. 3 were much more common. The initial portions of these records would exhibit two, three or even four peaks at times, and the times between these peaks would differ decidedly from round to round. Because of the statistical nature of the data generated during these experiments, large scatter can be seen in Figs. 4 and 5 where the initial overpressure and impulse are plotted, respectively, as functions of distance along a line radiating from the breech of the rocket (at 135° to the line of fire). For the relatively few rounds where single

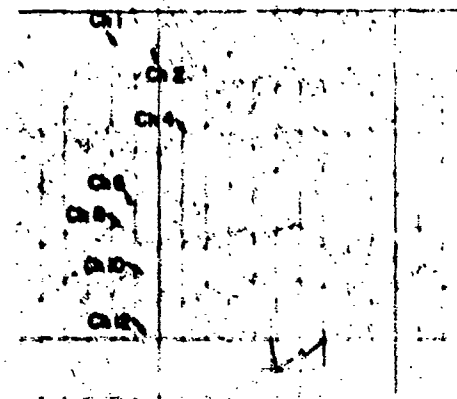
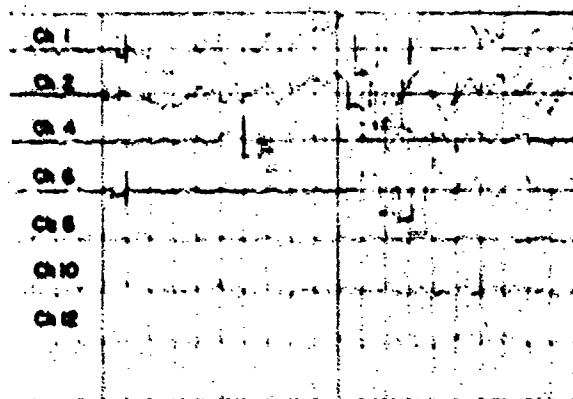
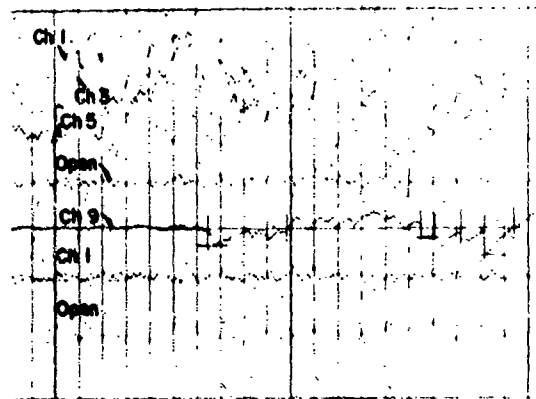
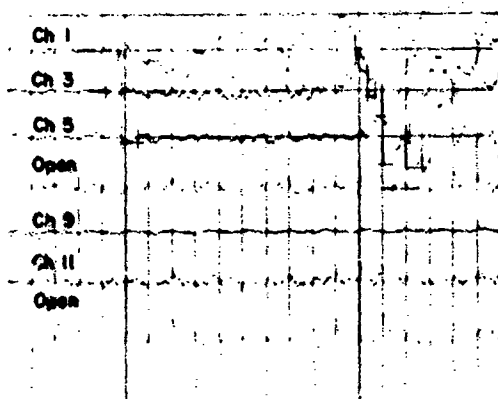


Fig. 3. Typical Record of Pressures Generated by 2.75-in. Rocket

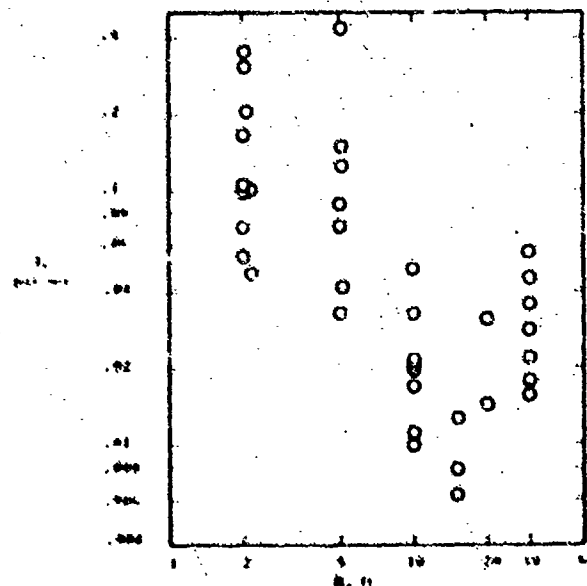
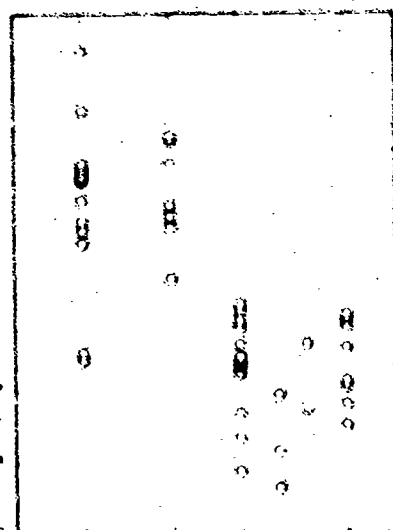


Fig. 4. Free-Field Overpressures Versus Distance - 2.75-in. Rocket, $\theta = 135^\circ$

Fig. 5. Free-Field Impulse Versus Distance, 2.75-in. Rocket, $\theta = 135^\circ$

"starting" shocks were observed, the pressure and impulse amplitudes were much greater than for the majority of the rounds. We thought that the wide variation in pressure signal was perhaps due to failures of disc closures in the four rocket nozzles at different times. Tests with two or more of these discs removed before firing, however, showed no systematic change in the pressure field.

Blast Parameters for 66-mm LAW Rocket

Only free-field data were obtained for this weapon. Pressure-time histories were similar to those produced by the 57-mm recoilless rifle. Distinct shock waves were generated, and there was no later spectrum of noise. Data were also found to be relatively repeatable from round to round. Typical graphs of overpressure versus distance and impulse versus distance along a line perpendicular to the breech are shown in Figs. 6 and 7.

Blast Parameters for 5.0-in. Rocket

There were only enough rounds available for this weapon to survey the free-field blast parameters. At locations close to the rocket nozzle, the multiple shocks merged into a single strong shock. There was much less

evidence of noise following the initial "starting shock" than for the 2.75-in. rocket. Why this rocket should produce so different a pressure signal than the 2.75-in. rocket is not clear. Both have multiple exhaust nozzles with closures which must blow out on rocket ignition, both have relatively long burning times, and both were held captive during the experiments.

Blast Parameters for 4.5-in. Rocket

The 4.5-in. rockets were by far the oldest of the weapons tested, made in 1944. Of the ten rockets, eight were fin-stabilized and had a single rocket nozzle. The remaining two weapons were spin-stabilized, having multiple canted nozzles. Although somewhat newer than the first type, they were still made many years ago. The pressure fields from these weapons varied quite widely from round to round, often showing gradual rises to maximum pressure rather than starting shocks. A typical set of free-field records is shown in Fig. 8. Because of the wide variability in data for these old rockets, we have made no plots of overpressure or impulse versus distance. As for the 2.75-in. rocket, the pressure fields from these weapons showed large noise signatures following the starting shock.

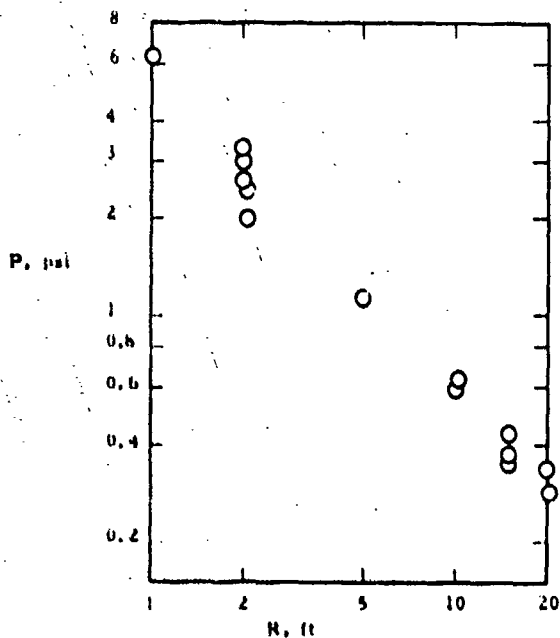


Fig. 6. Free-Field Overpressures Versus Distance - LAW Rocket, $\theta = 90^\circ$

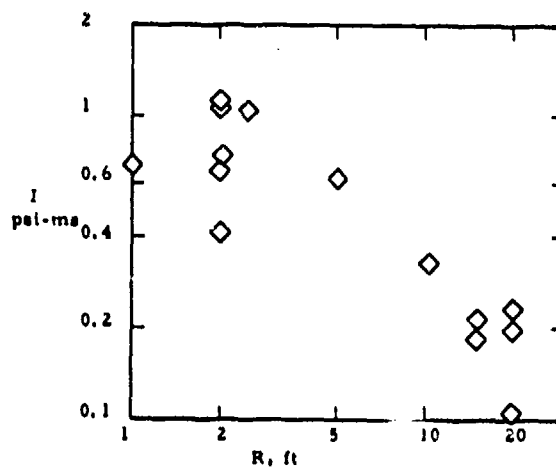


Fig. 7. Free-Field Impulse Versus Distance, LAW Rocket, $\theta = 90^\circ$

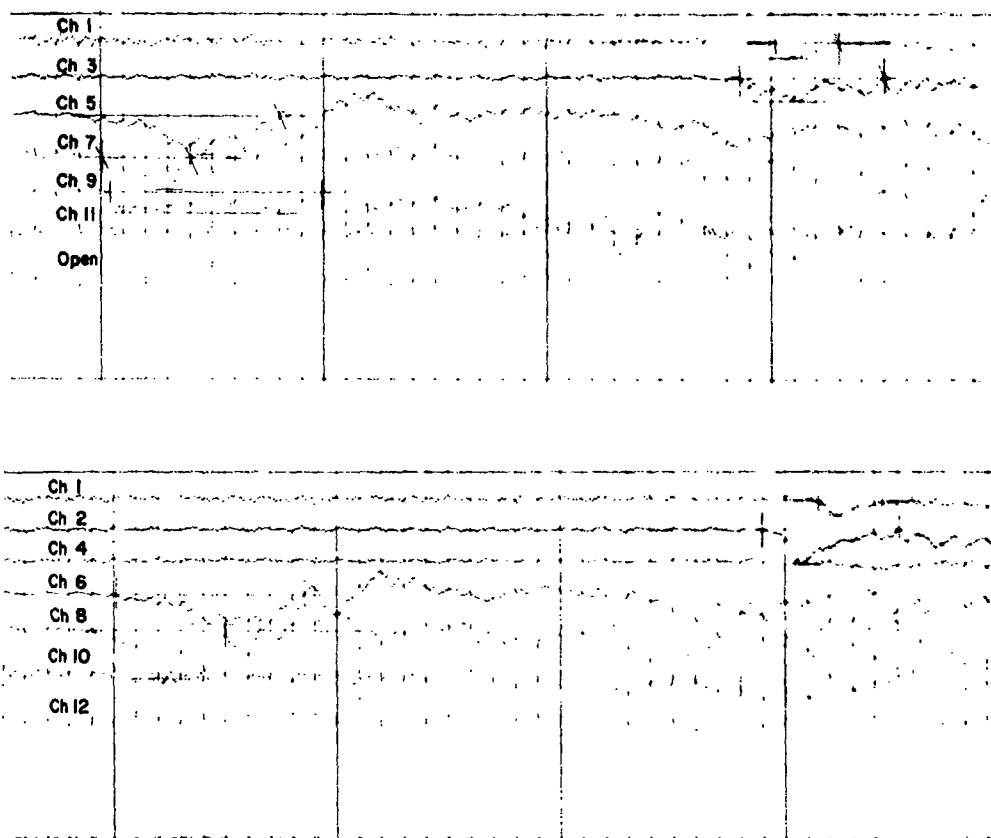


Fig. 8. Typical Pressure Records for 4.5-in. Rocket

MODELING THE BLAST FIELDS AROUND RECOILLESS RIFLES

Scaling Peak Pressure

An earlier report [1] showed that the blast pressure field around recoilless rifles might be defined by

$$\frac{Pc^3}{W} = f\left(\frac{L_{11}}{c}, \frac{L_{\perp}}{c}\right) \quad (1)$$

where

P = peak overpressure

L_{11} = standoff position parallel to line of fire

L_{\perp} = standoff position perpendicular to line of fire

c = caliber of weapon

W = energy in the propellant minus the kinetic energy of the projectile.

A similar equation was known to apply for closed-breech weapons. We will show that an equation similar to Equation (1) is applicable to recoilless rifles, but with additional restrictions which make another choice of parameters superior. Equation (1) requires geometric similarity, i. e., similarity in length of gun and in geometry of nozzle. Many recoilless rifles are approximately the same scaled length, i. e., 30 calibers; however, a number of different nozzles can be attached to the same basic gun (changes in nozzle geometry modify the chamber pressures and the rates of energy release from the breeches). The total energy release may be only an approximate parameter for normalizing breech blast pressures around recoilless rifles.

In Table 2, a summary is presented of test data taken at Picatinny Arsenal near the breech of a 105-mm recoilless rifle [3]. All the data points in this table are for peak pressure measured 17.5 ft ($L/c = 50.3$) directly behind the breech of the rifle. Although there were small changes in propellant weight (energy) in these tests, the principle changes

made were in propellant types and in nozzle geometry. If Equation (1) were to apply, the numbers in the last column of Table 2 should be nearly identical. Instead, they indicate that Equation (1) furnishes reliable predictions of scaled peak overpressure to only the nearest order of magnitude. More accurate predictions are desired for most engineering applications.

Equation (1) can be rewritten as

$$\frac{P}{P_C} = f \left(\frac{L_{11}}{c}, \frac{L_1}{c} \right) \quad (2)$$

where

P_C = peak chamber pressure in the recoilless rifle. [All other parameters are as defined by Equation (1)].

Table 3 presents the data from Table 2 with the resulting peak pressures scaled according to Equation (2). This table demonstrates that Equation (2) is a more appropriate relationship than Equation (1) for normalizing the blast field about recoilless rifles.

TABLE 2

Blast Pressures 17.5-Ft Aft of Breech of
105-mm Recoilless Rifle as a Function of
Propelling Charge Weight

Picatinny Test No.	Propelling Charge, W (lb)	Peak Over- pressure, P (psi)	Peak Overpres- sure Divided by Propelling Charge Weight, (P/W) (psi/lb _m)
22	2.20	5.71	2.60
25	2.20	3.87	1.76
47	2.70	9.11	3.38
49	2.70	7.08	2.62
62	2.50	1.24	0.497
63	2.50	1.12	0.448
68	2.50	1.25	0.500
69	2.50	1.14	0.457
70	2.50	0.92	0.368

TABLE 3

Blast Pressures 17.5-Ft Aft of Breech of
105-mm Recoilless Rifle as a Function of
Chamber Pressure

Picatinny Test No.	Chamber Pressure, P_C (psi)	Peak Pressure, P (psi)	Peak Overpres- sure Divided by Peak Chamber, (P/ P_C) Pressure
22	5919	5.71	0.966×10^{-3}
25	Not measured	3.87	Not measured
47	8040	9.11	1.13×10^{-3}
49	7411	7.08	0.955×10^{-3}
62	1266	1.24	0.980×10^{-3}
63	1027	1.12	1.09×10^{-3}
68	904	1.25	1.39×10^{-3}
69	740	1.14	1.54×10^{-3}
70	717	0.92	1.28×10^{-3}
			$\mu = 1.66 \times 10^{-3}$
			$\sigma = 0.217 \times 10^{-3}$
			$\sigma = 18.6\%$

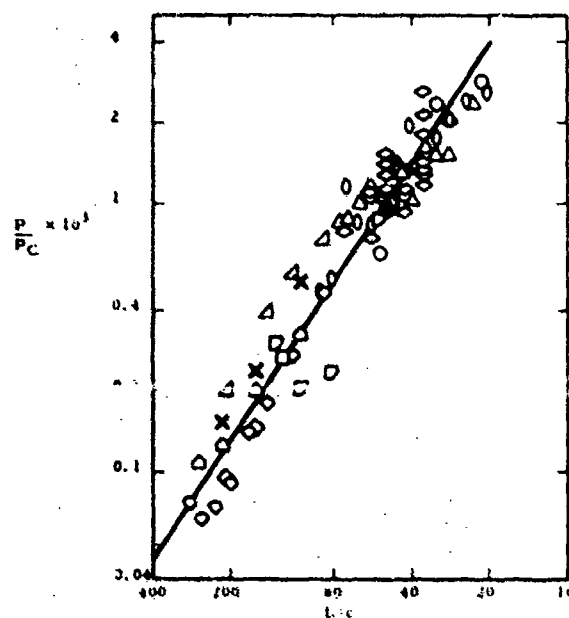
Equation (2) for recoilless rifles is consistent with Equation (3), from Ref. [1], for the blast field around closed-breech weapons

$$\frac{Pc^2l}{W} = f\left(\frac{L_{11}}{c}, \frac{L_{\perp}}{c}\right) \quad (3)$$

where l is barrel length. This is because the quantity W/c^2l in Equation (3) has dimensions of pressure and can be thought of as chamber pressure, or as energy per unit volume, in a gun tube. Westine [15] discussed the equivalence of Equations (2) and (3) in great detail for closed-breech weapons.

Chamber pressure is perhaps the most appropriate measure of energy entering the air blast. Chamber pressure is affected by nozzle geometry, and thus may indirectly account for the effects of nozzle geometry on the rate of energy release.

In the Final Report [2], which we are summarizing in this paper, we present a number of plots of scaled overpressure, P/P_C , versus scaled standoff position relative to either the breech or the muzzle of recoilless rifles. One of these plots is reproduced here in Fig. 9. Experimental test data from nine different sources were used to develop such plots. Included among these data are the blast pressures measured in the free space around the 57-mm recoilless rifle in this test program. Other data come from Refs. [3] through [10]. The Picatinny experimental test data referred to in Table 4 have also been included in these figures. The variety of weapons being considered is extensive, ranging from experimental test guns (T series) to field weapons (M series) and including a range of calibers from 57- to 106-mm. Many of the weapons are experimental models with some unreported gun characteristics such as amounts of propellant or chamber pressures. To use test data from Refs. [4] through [8] and Ref. [10], the writers were forced to assume chamber pressures. Chamber pressures for any of the M series guns are well-known and are known for most of the Picatinny tests in Ref. [3] because chamber pressure was measured for that series of firings. Table 4 summarizes the chamber pressures that were used for the recoilless rifles. Handbook values of chamber pressure are all obtained either from the Final Report giving the experimental results or from Ref. [16]. Some of the assumed values for chamber pressure appear to be too great and others too little. Nevertheless, a single assumed value of chamber pressure makes the normalized pressures for all T series weapons scale well.



Sym.	Ref.	Weapon
X	SwRI	57-mm M18A1
U	5	90-mm T219 (PAT)
◇	10	75-mm T21
△	8	105-mm T19
○	7	75-mm T21
○	6	57-mm T66E6
○	4	106-mm T170E1
□	9	106-mm M40A1
△	7	105-mm M27
○	7	57-mm M18
◇	1	105-mm M127 (modified)

Fig. 9. Overpressures for Recoilless Rifles, 0° to Breech

The scaled plots, only one of which is shown here, indicate that all test data for pressures in the free space around recoilless rifles can be normalized into a single function. Some scatter exists, but this is understandable when one realizes that a single standard deviation at some arbitrary location experiencing repeat firings will range from 9% to 20% for a single weapon system. The scatter that can be expected from repeated experiments to measure muzzle blast around closed-breech guns is discussed in Ref. [15]. The scatter of the recoilless rifle data is somewhat greater; but, pressures shown in these figures were obtained from various sources, with most of the experimenters totally unconcerned that any attempt might be made to scale their experimental data. Neither the height of gun barrels above the reflecting

TABLE 4
Assumed and Actual Values of Peak Chamber Pressure
for Various Recoilless Rifles

Gun	Reference	Maximum Chamber Pressure P_C (psi)	Comment
57-mm-M18A1	2	6,500	Handbook Value
105-mm-modified	3 (Picatinny)	Various	Measured
106-mm-T170E1	4	30,000	Assumed
90-mm-T219 (PAT)	5	3,000	Assumed
57-mm-T66E6	6	12,000	Assumed
57-mm-M18 (nozzle adapter)	7	4,800	Handbook Value
75-mm-T21	7	18,000	Assumed
105-mm-M27	7	10,000	Handbook Value
105-mm-T19	8	11,000	Assumed
90-mm-M67	9	6,400	Handbook Value
106-mm-M40A1	9	9,700	Handbook Value
57-mm-M18A1	9	6,500	Handbook Value
75-mm-T21	10	18,000	Assumed

surface or ground nor the height of pressure transducers above the ground has been simulated in obtaining these experimental results. In addition, much of the data are very old and could be subject to some systematic errors because the experimenters could not use today's more modern instrumentation.

Equation (2) to predict side-on or free-field overpressures can be extended or rewritten as Equation (4) for the prediction of peak reflected pressures imparted to a panel. Equation (4) defines a three-dimensional space

$$\frac{P}{P_C} = f\left(\frac{L_{11}}{c}, \frac{X}{c}, \frac{h}{c}\right) \quad (4)$$

where

- h = height of gun above the plane of the panel
- X = distance in the plane from point of interest to line of fire.

It takes advantage of the symmetry which exists in the free field about the line of fire. Placing a panel in the vicinity of the weapon destroys this symmetry; thus, an additional geometric parameter is required as in

Equation (4) to define the peak pressures that are imparted to a panel. Insufficient data exist to demonstrate that Equation (4) is appropriate for recoilless rifles. Unfortunately, the relationship between Equations (4) and (2) is directly analogous to a similar relationship for reflected and side-on pressures around closed-breech weapons (see Ref. [1]). To predict the blast pressures imparted to a panel by firing recoilless rifles, we will assume that Equation (4) is applicable because Equation (2) is appropriate and because it has been demonstrated that a similar equation works for closed-breech weapons.

Scaling Impulse

Maximum positive impulse in the free field around a recoilless rifle appears to scale according to

$$\frac{Ic}{P_C^{1/3} W^{2/3}} = f\left(\frac{L_{11}}{c}, \frac{L_1}{c}\right) \quad (5)$$

where I is positive specific impulse. This particular combination of the parameters, I , c , P_C , and W was chosen because: (1) it defines a nondimensional group, and (2) it works, as is demonstrated by using experi-

mental data. Very little experimental free-field impulse data have been taken around the muzzles and breeches of recoilless rifles; nevertheless, an adequate quantity is available from Refs. [3, 8, 9], and the SwRI 57-mm tests to demonstrate that Equation (5) is applicable. Figure 10 shows one plot of scaled impulse as a function of scaled position, L/c . Although the variety of weapons is not as complete as was used to demonstrate these scaling laws for peak pressure, sufficient data do exist to strongly indicate that Equation (5) is appropriate for normalizing the impulse field around the breech and muzzles of recoilless weapons.

The reflected impulse counterpart to Equation (5) for free-field impulse is

$$\frac{I_c}{P_C} = \frac{L}{c} \cdot \frac{h}{c} \quad (6)$$

The addition of a reflecting surface under the muzzle or breech of a recoilless rifle destroys the symmetry which exists about the line of fire in a free field. To account for the additional geometric coordinate, an extra geometric parameter must be added to Equation (5). This action is similar to the development of Equation (4) from Equation (2) for peak reflected pressures.

Predicting Free-Field Pressure or Impulse

Figure 11 shows a recoilless rifle and two groups of two equations for predicting peak pressure and/or impulse in the free field either forward of the muzzle or aft of the breech of a recoilless rifle. These equations are Equations (2) and (5) expressed in polar coordinates rather than rectangular ones, and with a functional format selected to curve-fit experimental data. The solid lines drawn on Figs. 9 and 10 and others in Ref. [2] indicate that these equations fit experimental test results exceptionally well.

Observe in Fig. 11 that peak free-field pressure and impulse are independent of the angle θ forward of the gun muzzle. The shock emitted from the muzzle of a recoilless rifle is essentially spherically symmetric about the muzzle of the gun. It is also much weaker than the shock emitted from the breech.

Sym.	Ref.	Weapon
X	SwRI	57-mm M18A1
△	8	105-mm T19
○	9	57-mm M18A1
□	9	90-mm M67

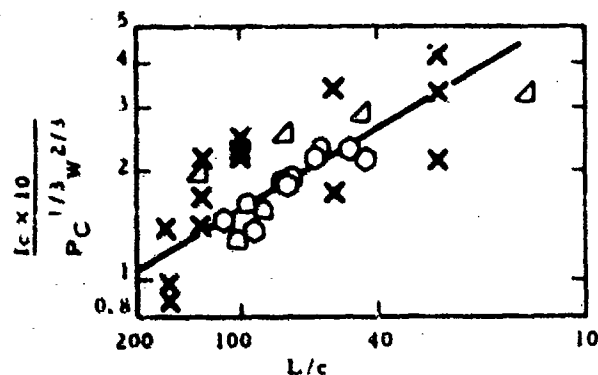


Fig. 10. Scaled Impulse for Recoilless Rifles, 90° to Breech

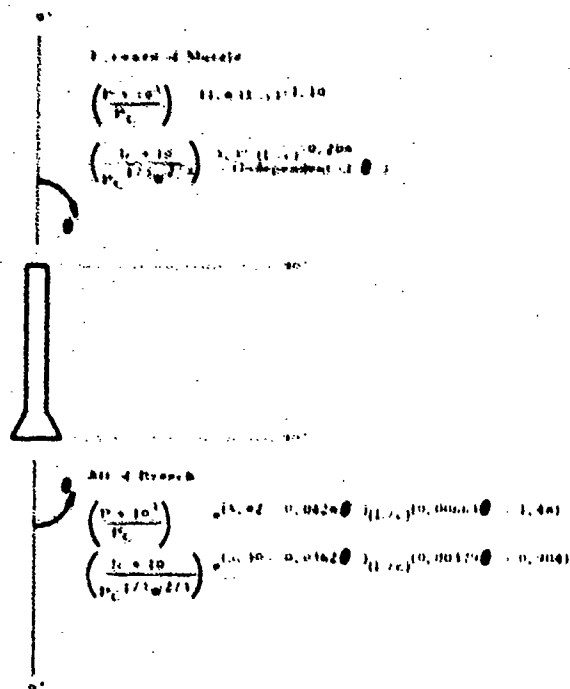


Fig. 11. Peak Free-Field Overpressures Around the Muzzles and Breeches of Recoilless Rifles

Predicting Reflected Pressures and Impulses

Figure 12 is a plot of peak reflected pressure as a function of L/c and x/c for a constant normalized height, h/c , of 18.0 for the weapon over the firing table. The isobars in Fig. 12 are constant normalized pressures, P/P_C , which have been sketched from data for SwRI, 57-mm recoilless rifle tests. Figure 12 is a graphical presentation of Equation (4) for normalized reflected peak pressure. Inadequate test data exist to develop additional figures for other distances between the table and rifle, i. e., other ratios of h/c .

In a similar fashion, Fig. 13 is a plot of Equation (6) for normalized reflected specific impulse when h/c equals 18.0. The isoclines in Fig. 13 are for constant values of $I_c/(W^{2/3}P_C^{1/3})$. Additional figures of scaled reflected impulse for other heights have not been developed because there are even less

impulse data than there are pressure data available. Units employed for physical quantities in the scaled impulse parameter are $I = \text{psi-ms}$, $c = \text{in.}$, $P_C = \text{psi}$, and $W = \text{lb}_m$ of propellant.

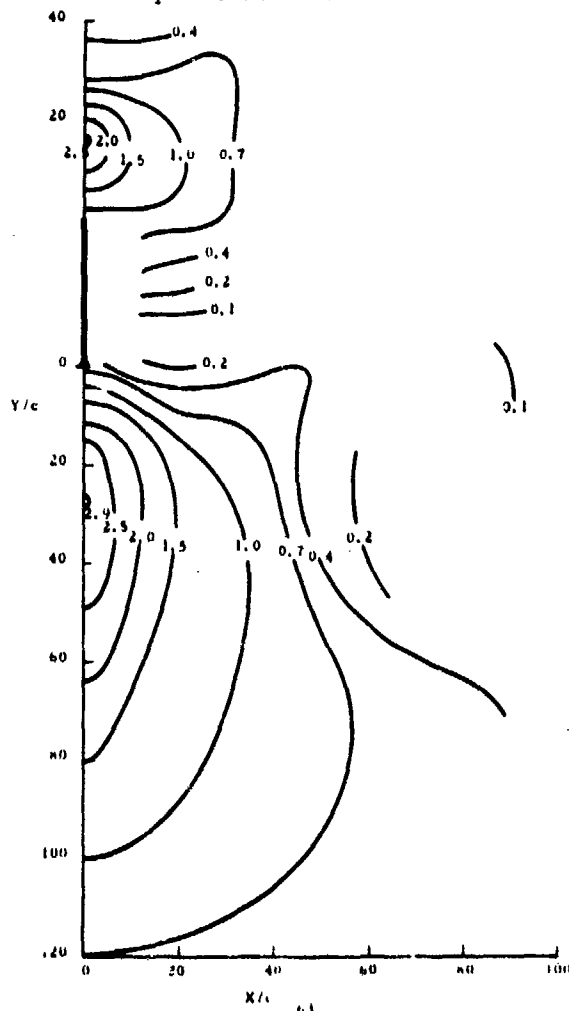


Fig. 12. Normalized Peak Reflected Pressure, $(P/P_C) \times 10^3$, for $(h/c) = 18.0$

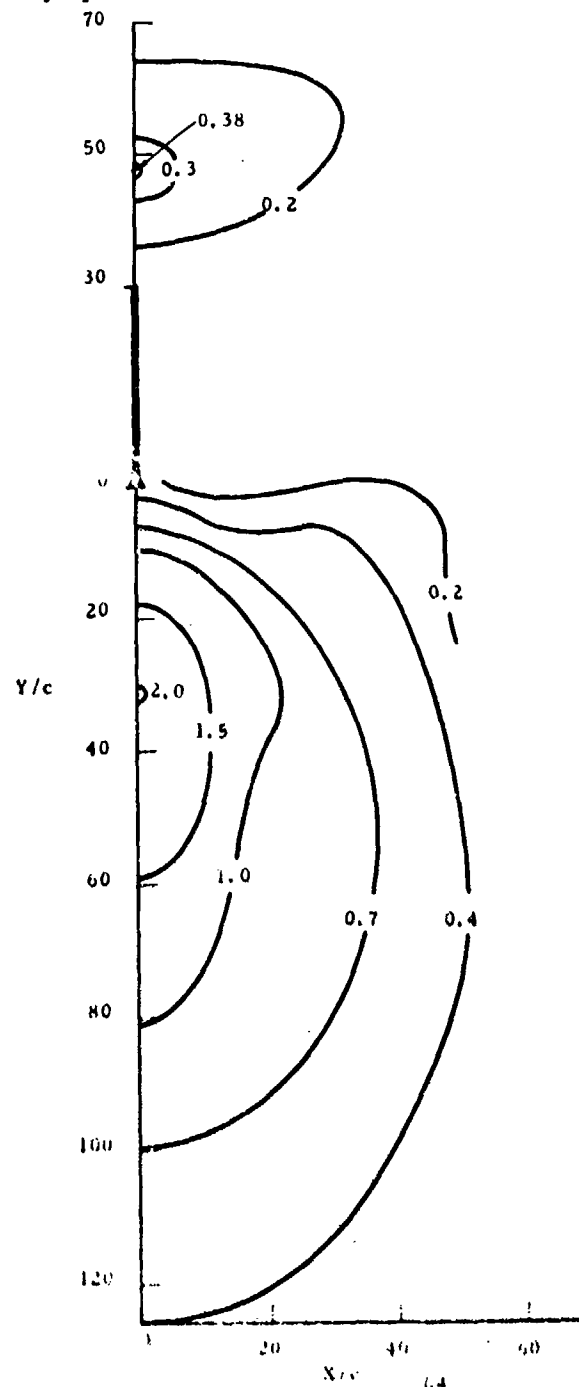


Fig. 13. Normalized Reflected Impulse,

$$\frac{I_c}{P_C^{1/3} W^{2/3}}$$

for $(h/c) = 18.0$

MODELING THE BLAST FIELDS AROUND ROCKETS

We noted in the previous section that there were significant differences in the blast waves generated by the different types of rockets tested during this program. The LAW rocket and the 5.0-in. rocket both generated distinct and reasonably repeatable blast waves, while the 2.75-in. and 4.5-in. rockets produced variable, relatively small amplitude initial pressure waves followed by larger amplitude "noise" fields. We have come to refer to the two types of pressure waves as "bang" or "no bang". Differences were sought between various scaled combinations of rocket parameters in Table 1 and with other parameters which could be computed from the data, e. g., mass rate of flow, pressure at nozzle exit, etc. No grouping of parameters could be found which placed the LAW and 5.0-in. rockets in one class, and the 2.75-in. and 4.5-in. rockets in another class. Furthermore, no combination of rocket parameters could be found which would scale the blast fields generated by the two "bang" rockets. Many different combinations were tried, but none proved satisfactory. We, therefore, have a body of blast data for small rockets which did not exist before, and which can be useful in estimating the blast loading of helicopter structures for four specific rockets of fairly widely varying characteristics, but we do not have a method of prediction for other rockets for which no measurements have been made. There are suggestions in Refs. [12] and [13] that blast scaling correlates with mass flow rate and/or rate of pressure rise or initiation of burning. We had no way of measuring the latter parameter, but can show no correlation with the former.

DISCUSSION

In the experimental program reported here, a large body of data has been generated for the blast fields about recoilless rifles and solid-propellant rockets. All but a few of the 138 tests yielded useful data, which are presented round-by-round in Ref. [2]. The primary data reported are peak overpressures and positive impulses, for free-field blast waves and for waves reflected from plane surfaces parallel to the line of fire of the weapon. The free-field data obtained on a 47-mm recoilless rifle supplement existing measurements for the same weapon and other calibers of recoilless rifles. Reflected wave data obtained for this weapon constitute the first such measurements. Few reliable previous blast measurements exist for rockets, and there-

fore the results reported in Ref. [2] constitute the first significant group of measurements of the blast fields generated by solid-propellant rockets.

A primary aim of this program was to generate or corroborate laws for scaling of blast parameters generated by recoilless rifles and rockets. We were successful in generating such laws for recoilless rifles, but could not do so for rocket blast.

A significant feature of the test results for rockets was that different types of these weapons generated distinctly different pressure waves, with sharp shocks being formed for some and not for others, and with some rockets generating large-amplitude noise after the initial shocks. The rockets which did not produce sharp initial shocks ("no-bang" rockets) also exhibited great round-to-round variability in pressure wave characteristics, while the "bang" rockets showed smaller data scatter. Pressure fields measured for all but one of the rockets (66-mm LAW) undoubtedly represent upper bounds on the actual pressure fields because these weapons were held captive during testing rather than being allowed to fly as they would be in actual use.

We feel that the test results obtained in this study, and the scaling law for prediction of blast from recoilless rifles, significantly enhance the ability to predict transient pressure loads imparted to helicopters, airplanes, ships, and other objects. This is a necessary first step in estimating the effects of such blast on structures and personnel.

ACKNOWLEDGMENTS

The work reported in this study was supported by the U. S. Army Ballistic Research Laboratories, Aberdeen Research and Development Center, under Contract No. DAAD05-70-C-0170 with Southwest Research Institute. Throughout the program, we received continual aid from our technical monitor, Mr. O. T. Johnson, and from Mr. William Noonan of the BRL Staff. Mr. Johnson provided expert guidance and advice throughout this program, and Mr. Noonan was instrumental in locating and shipping the required ammunition, weapons, and spare parts. Thanks are also due to Mr. George S. Murray of Aberdeen Proving Grounds for instructing our staff members and technicians in techniques for disassembly of the rounds and weapons, and in their safe handling.

Many staff members at Southwest Research Institute contributed to the success of this program in addition to the authors of this report. The field test firings were conducted ably and efficiently by Messrs. Ernest Garcia, Marvin Rumbaugh, Ernest Spacek, Jr., and Robert Marin. All data reduction was performed by Messrs. Andrew Coindreau and Eugene Persyn. Figures in the report were prepared by Mr. Victoriano Hernandez.

REFERENCES

1. P. S. Westine, "Structural Response of Helicopters to Muzzle and Breech Blast, Vol. I of Final Technical Report, Blast Field About Weapons", Southwest Research Institute, November 1968. AD 844 287L
- 1a. P. S. Westine, "The Blast Field About the Muzzle of Guns," Bulletin 39, Part 6, The Shock and Vibration Bulletin, March 1969, pp. 139-149.
2. W. E. Baker, P. S. Westine, R. L. Bessey, "Blast Fields About Rockets and Recoilless Rifles," Southwest Research Institute Final Report on Contract No. DAAD05-70-C-0170 with Ballistic Research Laboratories, May 1971.
3. J. R. Zimmerman and R. A. Vecchio, "Back Blast Determination of a 105-mm Recoilless Rifle for an Aerial Artillery Weapon System," Picatinny Arsenal Tech. Report 1420, August 1966.
4. "Peak Pressures for Breech and Muzzle Blast Measurements, 106-mm Rifle, T170E1 Mount, 106 mm, T149E1," Analytical Section, A&A Division, D. & P. S., August 14, 1953 (no report number).
5. "Ballistic Analysis of Blast Results for 70-mm Recoilless Rifle, T219 (PAT)," Analytical Laboratory Report 54-B-120, October 18, 1956.
6. Ballistic Analysis of Blast Pressure Results for 57-mm Recoilless Rifle T66E1," Analytical Laboratory Report 55-B-67, January 10, 1956.
7. "Investigation of the Effect of Blast from Recoilless Rifles," Armour Research Foundation, Contract No. DA-11-022-ORD-1227, for Frankford Arsenal, June 10, 1954.
8. Firing Record No. M-46345, Project No. 6001 (428-M5-245), Ordnance Research and Development Center, Aberdeen Proving Ground, Maryland, August 10, 1945.
9. "Engineer Design Test of Sound Pressure Level Measurement of Rockets and Recoilless Rifles," Firing Record No. P-74650, USATECOM Project No. 8-7-2320-02, Aberdeen Proving Ground, Maryland, August 1967.
10. Firing Record No. M-40455, Project No. 3845 (202-M10-214), Aberdeen Proving Ground, Maryland, February 2, 1945.
11. R. Randall, "Guided Missile Firing Test Report, TOW-H59," Hughes Aircraft Co., Culver City, California, Contract No. DA-04-495-AMC-877(a), with U. S. Army Missile Command, June 1968.
12. W. H. Grootzinger, III, "In-Tube-Burning Rockets for Advanced Light Assault Weapons (U)," Technical Report S-208, Rohm & Haas Co., Redstone Research Laboratories, Huntsville, Alabama, April 1969. AD 501 103L.
13. W. H. Grootzinger, III, "Evaluation of In-Tube-Burning Rockets for Advanced LAW," Tech. Report S-244, Rohm & Haas Co., Redstone Research Laboratories, Huntsville, Alabama, December 1969. AD 506 419L.
14. G. Garinther and D. Lince, Unpublished Data, Human Engineering Laboratory, Aberdeen Proving Ground, Md.
15. P. S. Westine, "Modeling the Blast Field Around Naval Guns and Conceptual Design of a Model Gun Blast Facility," Final Report, Southwest Research Institute, Contract No. NOD-178-69-C-0118 with U. S. Naval Weapons Laboratory, September 1970.
16. H. B. Anderson, "Master Standard Propellant Calibration Chart for Artillery Ammunition," D. & P. S. Report No. 1375, Tenth Revision, November 1966.

DISCUSSION

Mr. Sallet (University of Maryland): From your last data can you construct the induced flow field of the ambient air and the combustion gases?

Mr. Baker: No, I would say we could not. We have the over pressure time-histories and what data one can abstract from them, so I would say it would be very very difficult to try to get from this to the induced flow field.

TRANSONIC ROCKET-SLED STUDY OF FLUCTUATING
SURFACE-PRESSURES AND PANEL RESPONSES

Eric E. Ungar

Bolt Beranek and Newman Inc.
Cambridge, Massachusetts 02138

and

Harry J. Sandgren, Jr. and Robert Erwin
National Aeronautics and Space Administration
George C. Marshall Space Flight Center
Huntsville, Alabama 35812

Some results are presented of a continuing investigation of the fluctuating pressures on aerospace vehicle surfaces and of the corresponding panel responses. Techniques for predicting fluctuating pressure spectra associated with transonic shock/boundary-layer interaction and for estimating correlations and coherences of boundary layer pressures are reviewed and compared with data obtained on a 1/10-scale model of Saturn V mounted on a rocket-propelled test sled. The agreement is found to be acceptable in general, although the test results exhibit considerable scatter and suffer from some signal/noise-ratio problems. At Mach numbers above about 0.6, sound from the propulsion rockets is shown to have no appreciable effect on the fluctuating pressure data obtained on the rocket-sled model. Predicted panel responses to the observed fluctuating pressures are found to be in reasonable agreement with corresponding rocket-sled data.

INTRODUCTION

Predictions of the vibrations of aerospace vehicle structures induced by aero-acoustic excitation are generally needed in the early design stages, primarily for the purpose of establishing preliminary design and test criteria. One may obtain such predictions most logically by first determining the excitations and then calculating the corresponding responses, but whereas techniques for calculating the responses of fully specified structures to given excitations are reasonably well in hand, general methods for predicting aero-acoustic excitations and the associated responses of structures that are not defined in detail still remain to be developed and validated.

The complexity of the total problem of predicting the fluctuating-pressure environment of an aerospace vehicle under given flight conditions may be reduced by determining what flow regimes occur at various locations on the

vehicle, and then establishing the fluctuating-pressure characteristics associated with each flow regime. A compilation of techniques for predicting these fluctuating-pressure characteristics was presented in [1]^{*}, but lack of suitable experimental data so far has prevented evaluation of the general validity of these techniques. In order to take some steps toward this validation, and also in order to study related response-prediction methods, a program of investigations has been undertaken, based on a 1/10-scale model of the forward half of the Saturn V vehicle, propelled along the Holloman Air Force Base rocket-sled test track.

As discussed in [2], use of such a model avoids the expenses associated with full-scale tests, overcomes a number of difficulties associated with testing of small wind tunnel models

^{*}Numbers in square brackets refer to the appended list of references.

(i.e., tunnel-blockage and shock losses, and the need for extremely small transducers with very high frequency capabilities) and permits one to reach reasonably realistic Reynolds numbers. Descriptions of the test model and system, instrumentation, data reduction and analysis, and test and operational procedures appear in [2], and therefore are not repeated here.

Reference [2] also summarizes techniques for predicting the fluctuating pressure spectra associated with attached turbulent boundary layers and with subsonic flow separation aft of flares, and it compares rocket-sled data with predictions obtained by means of these techniques. It is the purpose of this paper in essence to serve as a continuation of [2], to explore further the utility of rocket-sled models for aero-acoustic excitation and response measurements, to deal with additional flow regimes and fluctuating pressure characteristics, and to investigate the utility of a simple response prediction technique. Accordingly, the first of the following sections addresses itself to the possible contamination of boundary-layer data by rocket noise, the second section deals with transonic-shock/boundary-layer interaction, the third discusses boundary-layer pressure correlations and cross-spectra, and the fourth deals with the responses of panels to random pressure fluctuations. Conclusions, recommendations, and plans for further studies are discussed in the final section.

EVALUATION OF CONTAMINATION OF FLUCTUATING-PRESSURE DATA BY ROCKET NOISE

In using a rocket sled to obtain data on the aero-acoustic environment and responses of a test model, one must naturally consider whether the effects one attempts to observe are obscured by those due to noise from the propulsion rockets. Therefore, a number of calculations were carried out to estimate the rocket-noise environment at the sensor locations on the test vehicle, and to compare these estimates with data obtained from these sensors.

Table I, below, summarizes the thrust-histories and propulsion systems associated with the various test runs during which significant data were collected. Table II lists the salient characteristics of the propulsion systems.

TABLE I
Thrusts and Propulsion Systems Used
In Rocket Sled Tests

Test Designation	Time Interval (sec)	Thrust (1000 lb)	Propulsion
SN-A4	0.1- 5.7 6.0- 7.5	195 70	3 Bomarc "A"'s
SN-B1	0.1- 5.1 6.2- 9.1 9.6-12.5 14.3-17.2	107 108-147 85-98 36-46	2 Mk3 Terriers 3 Nikes 2 Nikes 1 Nike
SN-B2 and SN-B3	0.1- 5.1 6.2- 9.2 9.6-12.5	107 108-147 72-98	2 Mk3 Terriers 3 Nikes 2 Nikes

TABLE II
Propulsion System Parameters

System	Nike	Mk3 Terrier	Bomarc "A"
Nozzle Throat Diam. (in.)	6.15	6.15	8.63
Expansion Ratio	7.15	6.8	4.0
Exit cone half-angle (degr.)	15.0	15.0	17.5

Calculations to estimate the rocket noise environment were carried out, using the "source-location method" as described in [3] and an estimated exhaust velocity of 8500 ft/sec, which is believed to be typical of high-performance rockets [4]. These calculations took into account the effects of motion of the vehicle relative to the effective sound sources by adding to the predicted sound pressure levels the correction term $20 \log (1-M)$, where M represents the vehicle's Mach number. (Of course, this correction is valid only for $M < 1$. For $M \geq 1$, the rocket noise never reaches forward on the vehicle.) The prediction calculations also included a 3 dB increase to ac-

*Pressure-doubling occurs essentially only if the acoustic wavelength is greater than the vehicle circumference, - i.e., for frequencies $f(\text{Hz}) > c/\pi D$, where c represents the speed of sound and D the vehicle diameter [3].

count for the effect of (random) reflection from the irregular ground surface, plus a 6 dB increase at frequencies above 200 Hz to account for pressure-doubling at the sensors.

Figure 1 shows the locations of the various flush-mounted microphones on the test model. Figures 2 and 3 show one-third octave band sound pressure levels sensed by four different microphones (flush-mounted on the top surface, near the front of the S-IVB portion of the test model), together with predictions (estimates) of the rocket noise to which these sensors are exposed and approximate predictions of the fluctuating pressures due to boundary layer turbulence experienced by these sensors. Figure 2 pertains to a vehicle Mach number of 0.6, and Fig. 3 to a Mach number of 0.8. Figures 4 and 5 are similar to Figs. 2 and 3, but pertain to a different test run and to Mach numbers 0.4 and 0.6 respectively.

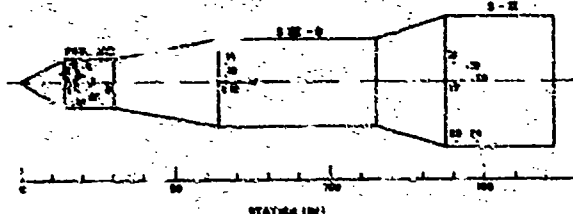


Figure 1

Positions of Flush-Mounted Microphones on 1/10-Scale Saturn V Model

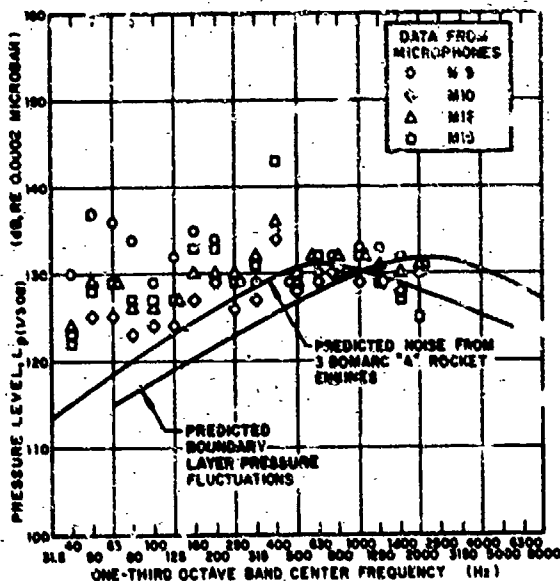


Figure 2

Comparison of Rocket Sled Test Data with Predictions of Engine Noise and of Boundary Layer Turbulence (Test 5NA-4, Mach 0.6, Accelerating)

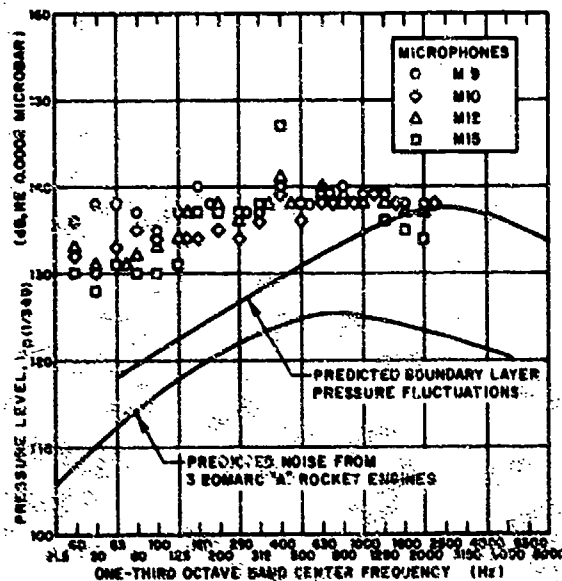


Figure 3

Comparison of Rocket Sled Test Data with Predictions of Engine Noise and of Boundary Layer Turbulence (Test 5NA-4, Mach 0.8, Accelerating)

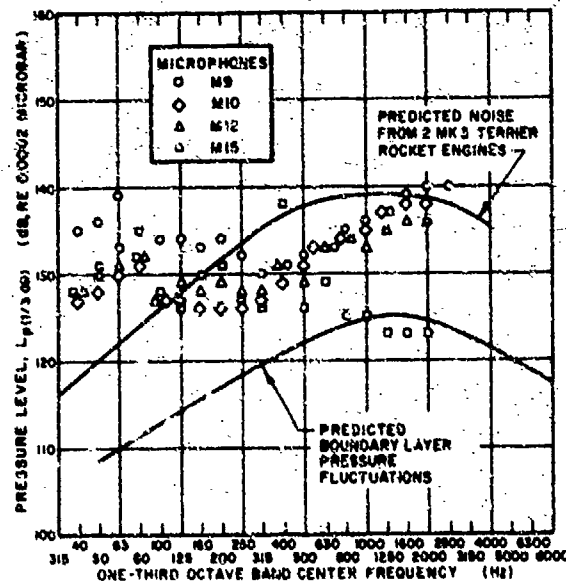


Figure 4

Comparison of Rocket Sled Test Data with Predictions of Engine Noise and of Boundary Layer Turbulence (Test 5N-B1, Mach 0.4, Accelerating)

One may observe that up to Mach 0.6, rocket noise is likely to be dominant, whereas at Mach 0.8, the boundary-layer turbulence pressures far exceed those associated with rocket noise. Thus, data obtained from this test run at Mach numbers below 0.6 must not be ascribed to the boundary layer (except, of course, for the decelerating portion of the run, where the rockets were not firing), whereas data obtained for the most interesting transonic region above Mach 0.8 may be expected to be relatively uncontaminated by rocket noise.

TRANSONIC-SHOCK/BOUNDARY-LAYER INTERACTION

At Mach numbers slightly below 1.0, regions of local supersonic flow appear on vehicles aft of flares, where the flow turns and expands. These supersonic regions are terminated by shocks that cause the boundary-layer to separate, producing an unsteady interaction between the shock and the boundary layer (see Fig. 7). The complete flow pattern of shocks, separation, reverse flow and boundary layer reattachment, then oscillates in the stream-wise direction at relatively low frequencies [1].

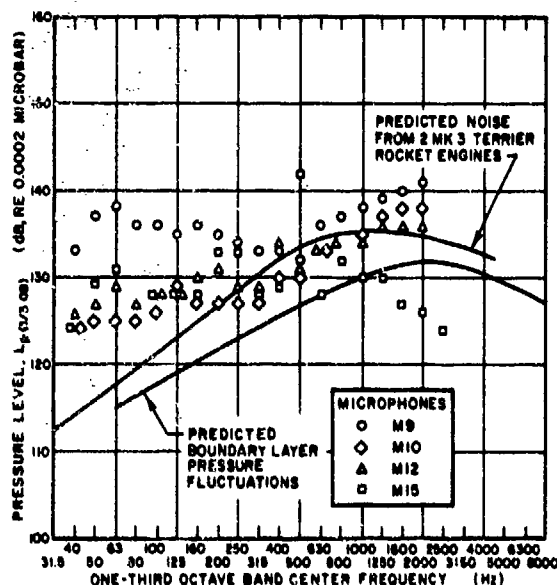


Figure 5

Comparison of Rocket Sled Test Data with Predictions of Engine Noise and of Boundary Layer Turbulence (Test 5N-B1, Mach 0.6, Accelerating)

Prediction Method

Figures 6 and 7 are suggested prediction charts for the maximum (overall) fluctuating pressure due to this transonic shock/boundary-layer interaction and for the Mach number at which this maximum occurs. These figures have been extracted from [1] and are based on the work of Wiley and Seidl [5], who have carried out a comprehensive summary and correlation of wind tunnel data on this interaction phenomenon.

Reference [1] suggests that the "shock oscillation frequency", i.e., the frequency f_{osc} at which the flow pattern oscillates in the stream-wise direction, may be predicted by

$$f_{osc} = 0.045 U/x_F \quad (1)$$

where U represents the free-stream velocity and x_F the distance from the edge of the flare to the observation point. This frequency corresponds to the peak in the associated non-dimensionalized fluctuating-pressure spectrum of Fig. 8, which is also based on [1]. Figures 6 - 8 thus provide one with a technique for predicting the pressures associated with transonic shock/boundary-layer interaction.

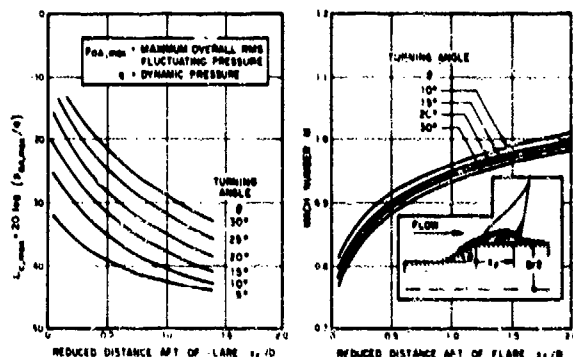


Figure 6 (left)

Maximum Overall Fluctuating Pressure Aft of Flares in Transonic Flow

Figure 7 (right)

Mach Number at Which Maximum Overall Fluctuating Pressure (Fig. 6) is Obtained

Rocket-Sled Model Data

Plots of the overall pressure level $L_p(OA)$ versus time are available for various flush-mounted microphones from the digitally reduced telemetered rocket sled test data. Two examples of such plots for one test run are shown in the upper part of Fig. 9. In the lower part of this figure is shown the Mach number/time profile for the same test run, obtained from test range data. On the basis of such a profile, one may calculate how the dynamic pressure q varies with time in a given test, and one may then compute the value of the "dynamic pressure level" $L_q = 20 \log (q/p_{ref})$ for each instant. (See Fig. 8 for definitions of symbols.) The variation of L_q with time for the test run under consideration is shown in the upper part of Fig. 9; however, $L_p = 40$ has been plotted there instead of just L_q , in order to make this curve fall closer to those for the microphone data.

In view of the definitions of the pressure levels, one may note that

$$L_p(OA) - L_q = 20 \log (p_{OA}/q) \equiv L_c. \quad (2)$$

Thus, L_c corresponds directly to the difference between the microphone data curves and the L_q curve of Fig. 9; where this difference is greatest, one obtains

$L_{c,max}$, the parameter whose value is predicted by Fig. 6. By noting the Mach number at which $L_{c,max}$ occurs, one may also determine the value that corresponds to the prediction indicated by Fig. 7.

Figure 10 shows the results of analysis of applicable rocket-sled model data in the previously described manner, together with the corresponding prediction curves taken from Figs. 6 and 7. Because of the limited number of microphone positions used in the test runs, data are available for only a very few x_p/D values. The quite considerable spread in the indicated data comes about from the differences in the pressures sensed by a given microphone in different test runs, and also from differences in the signals obtained from different (but similarly located) microphones in the same test run. The agreement between the data and the predictions may be seen to be quite reasonable in general, except at $x_p/D = 1.7$. All of the data corresponding to this reduced distance value was obtained from one microphone, which was located about 45 in. aft of a 9° flare, but also only 6 in. ahead of a 17° flare; the prediction was based on the flow disturbance due to the 9° flare, but it seems possible that the disturbance due to the 17° flare may have had a more pronounced effect.

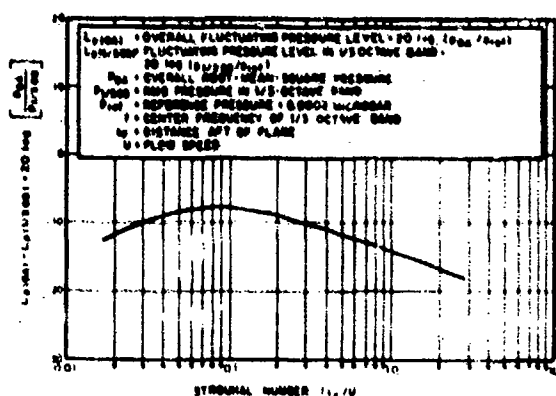


Figure 8

Nondimensional Third-Octave Band Spectrum of Pressure Fluctuations Under Transonic Oscillating Shock Aft of Flare

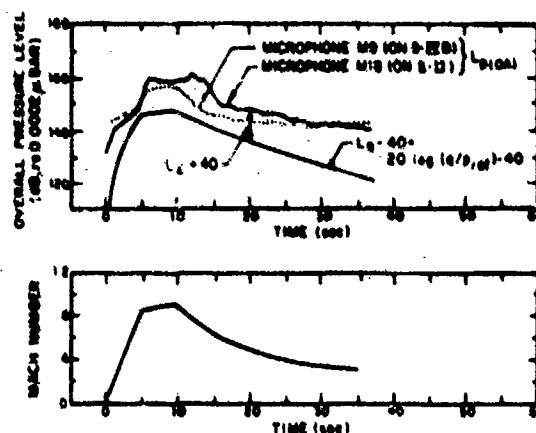


Figure 9

Overall Fluctuating Pressure Records Obtained from Two Microphones in Test 5N-A4, as Compared to Dynamic Pressure History

Figure 10 indicates how well one can predict the overall fluctuating pressure associated with transonic shock/boundary-layer interaction, and Fig. 11 provides similar information concerning the corresponding 1/3-octave band spectra. In addition to the prediction curve taken from Fig. 8, Fig. 11 shows some typical data from six different microphones and two test runs, all plotted in the same nondimensional form as the prediction curve. The scatter may be seen to be quite considerable, but on the whole within +5 dB and -10 dB of the prediction for Strouhal numbers below 0.2, and within +7 dB and -5 dB for higher Strouhal numbers. The data points cluster somewhat better about the "average of data" curve; clearly, this curve may be expected to yield better predictions (at least for the model under investigation) than the previously suggested prediction curve.

PRESSURE CORRELATIONS AND CROSS-SPECTRA UNDER TURBULENT BOUNDARY LAYERS

Correlations

In order to calculate the responses of a structure to a random pressure field, one requires some information concerning the spatial distribution of the pressures, in addition to the pressure spectra observed at various locations on the structure. Information concerning spatial distributions of ran-

dom pressures is most often expressed in terms of cross-correlations functions defined as

$$R(x_1, z_1, t; x_2, z_2, t+\tau)$$

$$= \langle p(x_1, z_1, t) p(x_2, z_2, t+\tau) \rangle \quad (3)$$

where x_1, z_1 and x_2, z_2 denote the coordinates of two observation points on the structural surface under consideration, t denotes time, and τ a time delay. The brackets $\langle \dots \rangle$ indicate averaging with respect to time. (In other words, the cross-correlation function is obtained by multiplying together two surface pressure measurements, and time-averaging the resulting product; one measurement is taken at the point x_1, z_1 at time t , the other is taken at x_2, z_2 at time $t+\tau$.)

It is usually assumed that surface-pressure fields associated with turbulent flow are spatially and temporally homogeneous - that is, that the correlation functions depend only on the spatial separations

$$\xi = x_2 - x_1, \quad \eta = z_2 - z_1 \quad (4)$$

between the two measurement locations and on the time separation τ , and not on the measurement coordinates and observation time as such. For homogeneous pressure fields, one may thus write

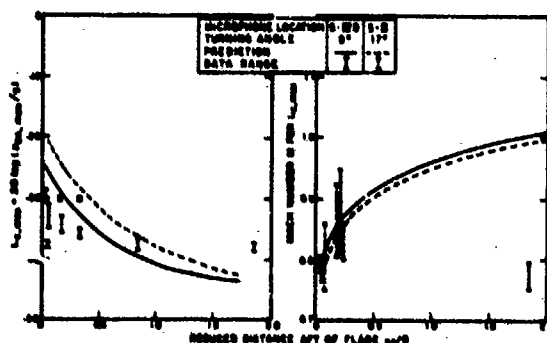


Figure 10

Comparison of Rocket Sled Data (from Various Microphones, Four Different Test Runs) with Predictions: Mach Numbers and Maximum Overall Fluctuating Pressure for Transonic Shock/Boundary-Layer Interaction

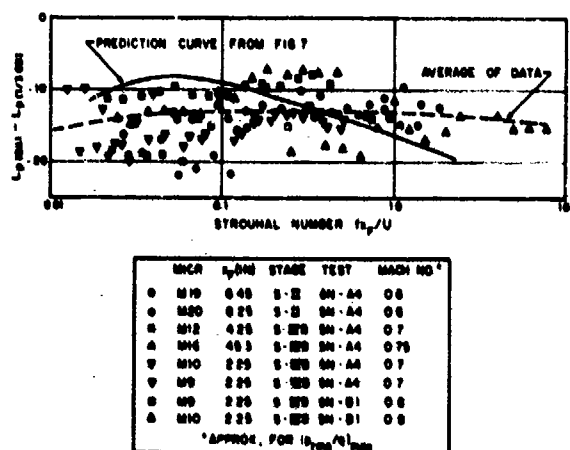


Figure 11

Comparison of Rocket Sled Data with Predictions: Nondimensional Spectrum of Pressure Fluctuations due to Transonic Shock/Boundary-Layer Interaction

$$R(\xi, \eta, \tau) = \langle p(x_1, z_1, t) \cdot$$

$$p(x_1 + \xi, z_1 + \eta, t + \tau) \rangle \quad (5)$$

The curves shown in Figs. 12 and 13 were taken from [6] and summarize data on $R(\xi, 0, 0)$ and $R(0, \eta, 0)$ obtained by several authors. Both of these functions pertain to zero time-delay τ ; the first indicates the effect of only stream-wise separation ξ of the measurement locations, and the second indicates the effect of separation η transverse to the flow-direction by itself. Note that the data in Figs. 12 and 13 are presented in terms of separation distances normalized with respect to the boundary layer displacement thickness δ^* .

Also shown in Figs. 12 and 13 are data obtained from the one rocket-sled run for which extensive cross-correlation computations were undertaken. Values of the cross-correlation functions were obtained directly from computer print-outs of $R(\xi, 0, \tau)$ or $R(0, \eta, \tau)$ for various microphone pairs. From the microphone locations on the test vehicle, the separation distances ξ and η were known to be 2.0, 6.0, and 10.5 in. The boundary layer displacement thickness was calculated for each individual microphone from [6,2]

$$\delta^* = 0.16U/f_p \quad (6)$$

where U represents the free-stream velocity (i.e., here the speed of the

rocket-sled). The frequency f_p at which there occurs the peak in the "hay-stack" third-octave band spectrum of pressure sensed by the microphone under consideration was determined simply by inspection of the appropriate third-octave band spectrum plot. Because the two microphones of a cross-correlated pair generally do not yield the same value of f_p , one usually obtains two values of ξ/δ^* or η/δ^* for each value of R . Thus, each value plotted in Figs. 12 and 13 is shown not as a single point, but as two points connected by a horizontal (constant R) line.

The rocket sled data may be seen to agree generally with the prior data. However, the rocket-sled data points exhibit considerable scatter, and a large number of these points for normalized separation distances below about 3.0 correspond to $|R| < 0.1$. There appears to be no physical reason for such behavior; it is possible that these small correlation values result from relatively large signal/noise ratios in the system. (The occurrence of such signal/noise ratios may be suspected from the very irregular character of the various computed correlation and coherence functions.)

Convection Velocity

The convection velocity U_c of a correlation is often taken as a typical measure of its time-separation dependence. This velocity is usually found by dividing the stream-wise separation distance ξ for a given microphone pair

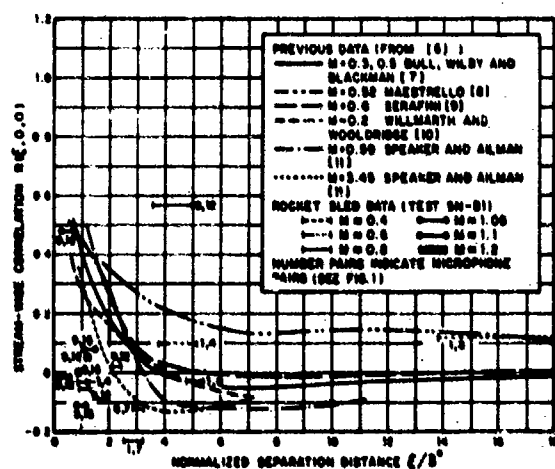


Figure 12

Space-Correlation of Boundary Layer Pressure Fluctuations in the Flow Direction

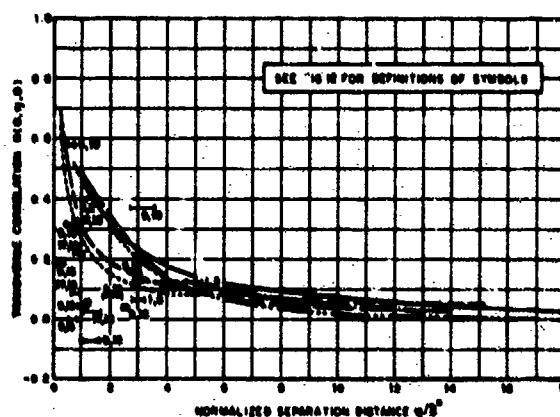


Figure 13

Space Correlation of Boundary Layer Pressure Fluctuations in Direction Transverse to Flow

by the delay time τ for which the correlation $R(\xi, 0, \tau)$ is a maximum. Figure 14 presents some such results of previous investigators, as taken from [6].

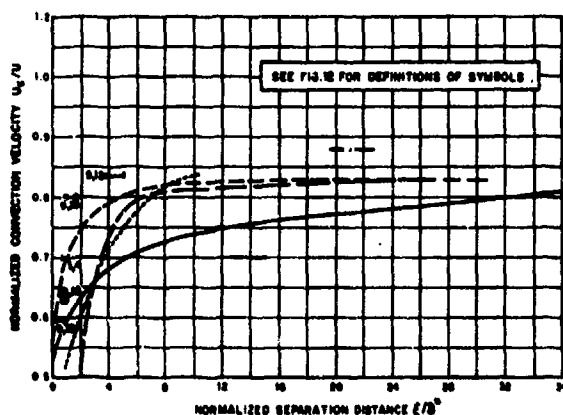


Figure 14

Spatial-Separation Dependence of Broad-Band Convection Velocity U_c , Normalized with Respect to Free-Stream Velocity U

The correlation functions computed for the rocket sled data were too irregular (probably because of the previously mentioned signal/noise problems) to permit one to select appropriate correlation function peaks for comparable calculations. However, since one expects the phase ϕ to vary as

$$\phi = \omega t = \omega \xi / U_c \quad (7)$$

where $\omega = 2\pi f$ represents the radian frequency, one may estimate U_c from values of ϕ/ω obtained from computer-generated plots of ϕ versus frequency f . Corresponding rocket-sled data, for those limited number of cases where definite values of ϕ/f could be read from the plots, are also indicated in Fig. 14. The rocket-sled data may be seen to agree reasonably well with the prior data.

Coherence

The frequency-behavior of an homogeneous cross-correlation function is usually specified in terms of its Fourier transform, which is called the cross-spectral density,

$$\Gamma(\omega, \xi, \eta) = \frac{1}{2\pi} \int_{-\infty}^{\infty} R(\xi, \eta, \tau) e^{-i\omega\tau} d\tau \quad (8)$$

For zero spatial separation, the cross-spectral density reduces to the ordinary power spectral density $\Phi(\omega)$;

$$\Gamma(\omega, 0, 0) \equiv \Phi(\omega)$$

$$= \frac{1}{2\pi} \int_{-\infty}^{\infty} R(0, 0, \tau) e^{-i\omega\tau} d\tau \quad (9)$$

where $R(0, 0, \tau)$ represents the auto-correlation function (which is independent of location for homogeneous systems). One often also normalizes the cross-spectral density with respect to the spectrum; the result is called the coherence*;

$$C(\omega, \xi, \eta) = \frac{|\Gamma(\omega, \xi, \eta)|}{\Phi(\omega)} \quad (10)$$

In [12] it is suggested that for turbulent boundary layers one may expect the coherence to obey

$$C(\omega, \xi, \eta) = A(\omega \xi / U_c) \cdot$$

$$B(\omega \eta / U_c) e^{-\omega \xi / U_c} \quad (11)$$

where A and B are two experimentally determined functions, as shown in Fig. 15.

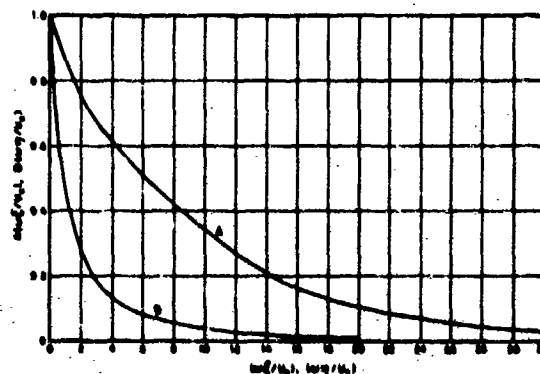


Figure 15

Amplitudes of One-Dimensional Longitudinal and Lateral Cross-Spectral Densities for Turbulent Boundary Layer (After Corcos, Ref. 12)

Corresponding plots of the streamwise and transverse coherences, $C(\omega, \xi, 0)$ and $C(\omega, 0, \eta)$, are shown in Figs. 16a and 16b, respectively, together with data points obtained from rocket-sled test run 5N-51 (the only run where sufficient data reduction for extraction of coherence data was accomplished). These points correspond to several microphone pairs, but only to frequencies

*This definition assumes that the power spectral density is the same for the two locations being cross-correlated.

of 250, 500, and 1000 Hz. Points corresponding to these arbitrarily chosen frequencies* were read from smoothed coherence-vs-frequency plots for the various microphone pairs. Although many of the data points cluster reasonably well about the predicted curves, many data points for $\omega r/U_c$ greater than about 1.5 lie considerably above the curves. This discrepancy may again be attributed to signal/noise problems, which are evident from the very irregular character of the experimental coherence-vs-frequency plots (many of which appear not to decrease with increasing frequency).

PANEL RESPONSE

Prediction Approach

The "statistical energy analysis" approach has proven useful for many response prediction applications where the excitations and the responding structures are only incompletely known [13]. This approach gives only "broad-brush"

*Reference [12] shows that finite transducer diameters lead to errors in the measured spectra, and that for microphones with radius r this error is less than 10% if $\omega r/U_c$ is less than 0.15. For $r = 3/8$ in. and $U_c = 0.8U$ (see Fig. 14), one finds that here the error is less than 10% if $f(\text{Hz}) < 1600 M$. Thus, for $M = 0.6$, the data is essentially valid up to about 1000 Hz.

estimates, but has two significant advantages; it is relatively easy to use, and it requires a minimum of input information.

Dyer [14] has delineated how this approach may be used to predict the responses of lightly damped (and also ribbed) cylindrical shells, cylindrically curved panels, and flat panels (typical of aerospace structures) to randomly fluctuating pressures. One may rewrite his results conveniently as

$$\frac{a_{\text{rms}}}{p_{\text{rms}}} = \left[\frac{\pi \beta}{2 \gamma m^2} \right]^{1/2} \quad (12)$$

where

$$\beta = \begin{cases} \frac{3}{\pi} \sqrt{\frac{\omega \beta}{c_L}} & \text{for } \frac{\omega \beta}{c_L} < 1 \\ 1 & \text{for } \frac{\omega \beta}{c_L} > 1 \end{cases} \quad (13)$$

and p_{rms} = root-mean-square pressure in a given frequency band

a_{rms} = resulting root-mean-square acceleration in same frequency band

m = mass of panel (or shell) per unit area

$\omega = 2\pi f$ = radian frequency

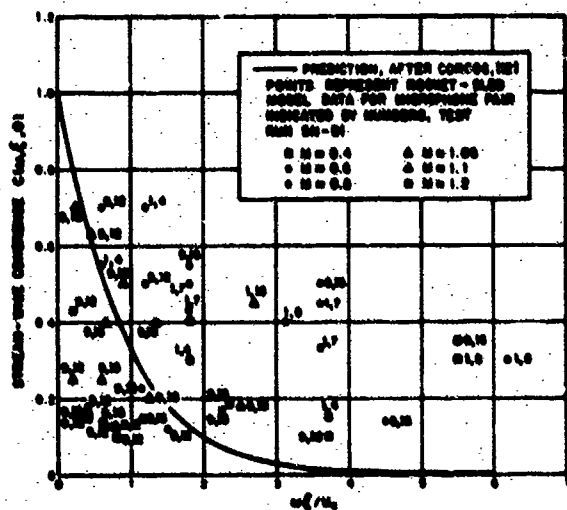


Figure 16a

Coherence of Boundary Layer Pressure Fluctuations in the Flow Direction

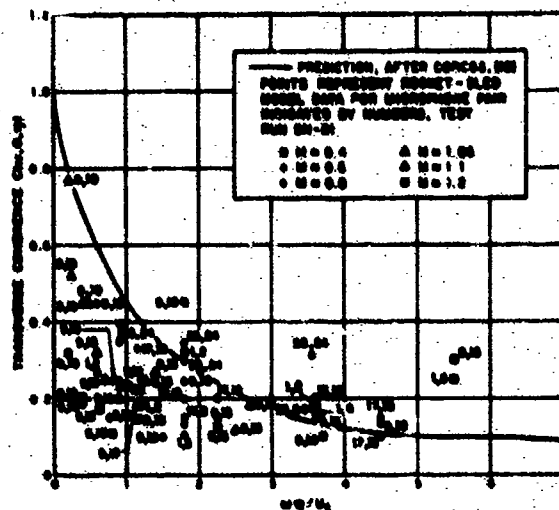


Figure 16b

Coherence of Boundary Layer Pressure Fluctuations in Direction Transverse to Flow

- a = panel or shell radius
 c_L = longitudinal wavespeed in panel or shell material
 $\approx 2 \times 10^5$ in./sec for steel or aluminum
 γ = panel edge absorption coefficient.

All of the parameters required for the evaluation of Eqs. (12) and (13) may be determined very easily, with the exception of the absorption coefficient γ . This coefficient, which characterizes the damping of the structure, may be determined from damping measurements [15] or may be estimated by use of appropriate generalized prediction charts [16]. For typical riveted, spot-welded, or bolted panels, γ varies between about 0.05 and 0.3 and increases with increasing frequency.

Comparison With Test Data

In order to study panel responses, some of the "boiler plate" panels on the top of the rocket sled model were

replaced by thinner panels in the later test runs. In these runs, the vibrations of these panels were monitored by means of several light-weight accelerometers attached to each panel, and the fluctuating pressures were measured simultaneously by means of flush-mounted microphones that protruded through the panels (but did not touch them).

Figure 17 illustrates some third-octave band pressure and acceleration data for a panel in the payload section (see Fig. 1) of the model; Fig. 17a corresponds to rather rough turbulent flow, whereas Fig. 17b corresponds to much smoother reattached flow.

Figure 18 shows average values of arms/prms calculated from Fig. 17 and from similar data obtained from a panel mounted in the S-II section of the test model. Although the two panels were of considerably different appearance (see Table III), the points in Fig. 18 cluster remarkably well - attesting to the fact that only a very few parameters affect the response ratio arms/prms .

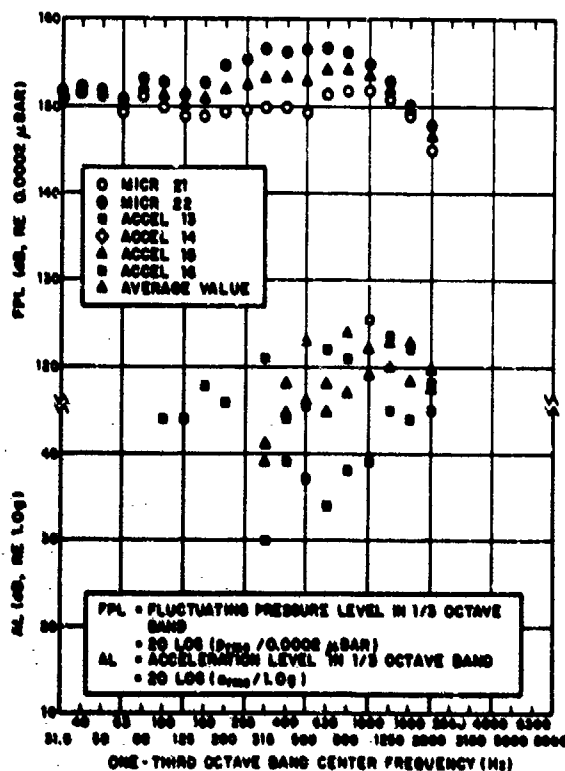


Figure 17a
Pressures and Accelerations Measured on Payload Panel in Turbulent Flow (Test 5N-R2, Mach 1.0)

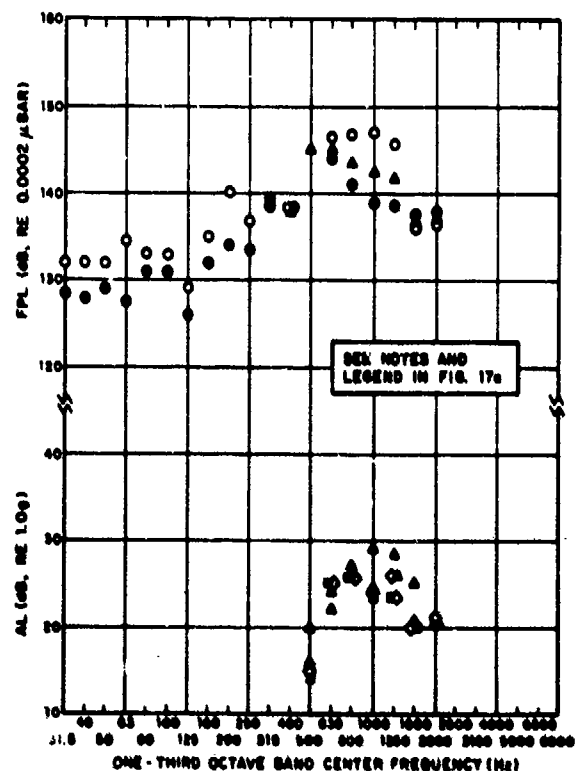


Figure 17b
Pressures and Accelerations Measured on Payload Panel in Reattached Flow (Test 5N-R2, Mach 1.25)

significantly, and that these parameters are not very different for the two panels.

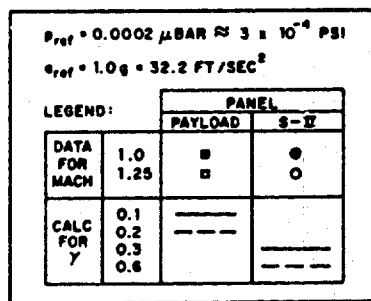
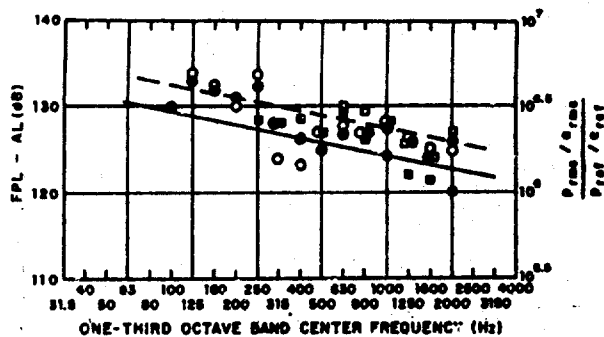


Figure 18

Comparison of Measured and Calculated Panel Responses

TABLE III
Test Panel Parameters

Panel Location	Payload	S-II
Skin (Aluminum)	0.12"	0.16"
Radius (in.)	7.57	19.67
Axial length (in.)	15.5	34.8
Subtended Angle	180°	180°
Ribs	None	10 axial, plus 1 circumferential
Approx. mass per unit area (lb/in. ²)	0.012	0.009

Also shown in Fig. 18 are two lines representing values calculated for various reasonable constant values of γ . Since for $\omega a/c_L < 1$ Eqs. (12) and (13) indicate that the ratio ρ_{rms}^2/a_{rms}^2 is

proportional to $\gamma m^2/\sqrt{a}$, a theoretical line that corresponds to a certain value of γ for the payload panel corresponds to a higher value of γ for the lighter, larger-radius, S-II panel. The agreement between the measured data and the values calculated for reasonable assumed values of γ is seen to be quite satisfactory. Unfortunately, direct measurement of the γ 's at the test panels has not yet been accomplished.

CONCLUSIONS AND RECOMMENDATIONS

It has been shown that rocket-sled tests can be extremely useful for the study and simulation of the fluctuating pressures that act on aerospace vehicles, particularly at transonic and high subsonic speeds, and of the associated responses of surface structures. However, during the initial (low subsonic) portions of the acceleration phase, noise from the propulsion rockets tends to predominate and to make it practically impossible to obtain useful fluctuating-pressure data from this phase.

Rocket-sled model data on the levels and spectra associated with transonic-shock/boundary layer interaction and on the Mach numbers corresponding to these "oscillating shocks" were found on the average to agree reasonably well with predictions based on previously developed methods. Values of stream-wise and transverse correlations, convection velocities, and coherences calculated from the rocket-sled data were also found to be in reasonable agreement with similar values obtained from earlier investigations.

The data obtained from the rocket-sled tests exhibit a great deal of scatter. In order to determine how much of this scatter is inherent in the actual signals, and to verify the performance of the data acquisition systems, it would be instructive to carry out some comparison tests under less severe environmental conditions, e.g., in a wind tunnel.

Panel response data obtained from measurements taken during rocket-sled runs were found to be in reasonable agreement with corresponding values calculated from a simple expression that was derived on the basis of statistical energy analysis. These calculations were based on reasonable estimated values of the panel edge absorption coefficient; experiments to measure this coefficient directly would be useful in order to determine how well the estimated values used in the calculations represent the actual values.

It would be of considerable general interest to apply the rocket-sled test system also to investigate the excitations and responses associated with base-pressure fluctuations and with flows aft of protuberances and in wakes. In addition, it would be extremely useful to study the Reynolds-number dependences of the various fluctuating-pressure phenomena by comparing the 1/10-scale model data obtained in the present program with similar smaller-scale wind-tunnel model data and with full-scale vehicle flight data. In addition, a more thorough study of the structural response - to account, for example, for the effect of matching of the flexural wavespeed with the convection speed, and for the nonuniform modal densities known to occur with uniformly spaced ribs - should prove to be most rewarding.

ACKNOWLEDGEMENT

The authors are greatly indebted to Messrs. David M. Green and Ken Crane of Teledyne Brown Engineering, who have been most helpful in providing information on data acquisition and reduction systems. Data concerning the test-sled propulsion rockets was supplied by Mr. Berle E. Engle of the Track Operations Office, Holloman Air Force Base. Mr. Robert Abilock of Bolt Beranek and Newman Inc. assisted in some of the data analysis and interpretation.

REFERENCES

1. K.L. Chandiramani, S.E. Widnall, R.H. Lyon, and P.A. Franken, "Structural Response to Inflight Acoustic and Aerodynamic Environments", Bolt Beranek and Newman Inc. Report No. 1417 (prepared for NASA Marshall Space Flight Center) (July 1966).
2. E.E. Ungar, R.E. Jewell, H.J. Bandgren, "Rocket-Sled Model Study of Prediction Techniques for Fluctuating Pressures and Panel Response", Shock and Vibration Bulletin No. 41, Part 7, pp. 1-7 (Dec. 1970).
3. P.A. Franken, et al., "Methods of Space Vehicle Noise Prediction", WADC Technical Report 58-343 (Sept. 1960).
4. F.M. Wiener, "Acoustical Considerations in the Planning and Operation of Launching and Static Test Facilities for Large Space Vehicles - Phase I", Bolt Beranek and Newman Inc. Report No. 884 (prepared for NASA Marshall Space Flight Center) (Dec. 1961).
5. D.R. Wiley and M.G. Seidl, "Aerodynamic Noise Tests on X-20 Scale Models", U.S. Air Force AFFDL-TR-65-192 (1965).
6. D.A. Bies, "A Review of Flight and Wind Tunnel Measurements of Boundary Layer Pressure Fluctuations and Induced Structural Response", NASA CR-626 (Oct. 1966).
7. M.K. Bull, J.F. Wilby, and D.R. Blackman, "Wall Pressure Fluctuations in Boundary Layer Flow and Response of Simple Structures to Random Pressure Fields", University of Southampton, Department of Aeronautics and Astronautics Report No. 243 (July 1963).
8. L. Maestrello, "Measurement and Analysis of the Response Field of Turbulent Boundary Layer Excited Panels", J. of Sound and Vibration 2, No. 3, p. 270 (July 1965).
9. J.S. Serafini, "Wall-Pressure Fluctuations and Pressure Velocity Correlations in a Turbulent Boundary Layer", NASA TR R-165 (Dec. 1963).
10. W.W. Willmarth and C.E. Wooldridge, "Measurements of the Fluctuating Pressure at the Wall Beneath a Thick Boundary Layer", University of Michigan, Department of Aeronautical Engineering Technical Report No. 02920-1-T (April 1962).
11. W.V. Speaker and C.M. Ailman, "Spectra and Space-Time Correlations of the Fluctuating Pressures at a Wall Beneath a Supersonic Turbulent Boundary Layer Perturbed by Steps and Shock Waves", Douglas Report SM-498C5 (Nov. 1965).
12. G.M. Corcos, "Resolution of Pressure in Turbulence", J. Acoust. Soc. Amer., 35, 192 (1963).
13. E.E. Ungar and J.E. Manning, "Analysis of Vibratory Energy Distributions in Composite Structures", Dynamics of Structured Solids, G. Herrmann, ed., Amer. Soc. Mech. Engrs., New York, 1968, p. 62.
14. I. Dyer, "Response of Space Vehicle Structures to Rocket Engine Noise", Chap. 7 of Random Vibration, Vol. 2, S.H. Crandall, ed., The M.I.T. Press, Cambridge, 1963.
15. E.E. Ungar and J.R. Carbonell, "On Panel Vibration Damping Due to Structural Joints", AIAA Journal, 4, No. 8, 1385 (Aug. 1966).
16. E.E. Ungar, "Damping of Panels", Chap. 14 of Noise and Vibration Control, L.L. Beranek, ed., McGraw-Hill Book Co., New York, 1971.

DISCUSSION

Mr. Sutphin (Martin Marietta Corporation): I understand that the vibration environment on rocket sleds is pretty tough and it frequently makes hash out of pressure measurements. Did you make any pressure measurements on panels protected from the flow as a check?

Mr. Ungar: No we did not do that, but we were very careful about the microphones. They were not isolated but were vibration compensated as far as possible. We knew the acceleration sensitivity of each microphone and we knew the acceleration level at each microphone, therefore we knew what data were good and what data were bad. And we got mostly good data, surprisingly enough, although, as you say, the vibration environment on the rocket sled is pretty rough.

Mr. Sallet (University of Maryland): In your experiments on the oblique shock running into what looked like a normal shock, you had a shock bifurcation, a laminar shock. Did you measure the shock angles, and if so, have you tried to compare your results with theory?

Mr. Ungar: No, we had a hard enough time measuring surface pressures, and the shock pressures are completely obscured by the surface pressures. We tried very hard to extract the pressure discontinuity but we could not resolve whether or when the shock straddled the microphones or passed over the microphones.

Mr. Leibowitz (Naval Ship Research and Development Center): Many investigators have sought to obtain a universal curve by plotting the correlation function against u_r/u_c . I took the data of J. A. Serafini; Henry Bakerwell; and W. S. Willmarth and S. W. Roos, and others, and used a similarity variable $(u_r/u_c) \sqrt{s/\delta^*}$ and found that the universal curve is much improved.*

Mr. Ungar: We did not try to do the same thing that you suggested. We had a hard enough time with the calculations as far as they have gone. One of the problems, as you well know, is that it is easy to turn on the computer and let it do the thing and produce miles and miles of printout. The next question is what do you do with it? Usually one cannot take those same computer printouts and feed them back into the computer and have it do all the dirty work; this amounts to people doing a lot of dirty work, thus the amount of slide rule processing must be very limited.

Mr. Leibowitz: You are also aware that programs are available for computing the cross correlation of the response data.

Mr. Ungar: We have lots of cross correlations to response data but I would like to find a simple way of predicting the cross correlations or response. It is no trick at all to turn on the computer and compute anything. You can go mad, but what does it mean? What does it mean on the next try? It is usually a job to find out what happened in the past but I am usually more interested in finding out what is going to happen on the next one because I do not usually care about the past one except to develop some general understanding. The real purpose of this paper, and the previous paper, is to validate prediction methods. What is going to happen next, how good are the various empirical and theoretical models that we have? That is one of the things we have tried to accomplish.

Mr. Van Ert (Aerospace Corporation): Since this was a scale model did you make any comparisons with the full scale measurements that were made as part of the Saturn Program?

Mr. Ungar: No we did not try to match any of the flight profiles because this was not really the purpose. I would very much like to have the opportunity to collect 1/100 scale data from the wind tunnel, 1/10 scale data from the rocket sled, full scale data from the vehicle, and then study the effect of Reynolds number. I think that needs to be done and it has not been done yet to my knowledge. One of the big questions that we have run into is: what is the effect of Reynolds number? Space shuttle is having their problems now that people are making predictions from model studies which are on the order of 1/2 size models, and these Reynolds numbers are off. In some simple flows we can predict what happens, but what happens to complicated flows when the shuttle comes down flat side first? There are no predictions. How does one do that and how does one get a realistic Reynolds number test? As far as I know there is only one wind tunnel in the world that can come close to getting the right Reynolds number and that happens to be a single shock facility in Brussels that uses high density gas to jack up the Reynolds number. But you still have a small model and a short duration flow in the tunnel so that the problem of deciding whether you really have fully developed flow and so on still exists.

*Computer Programming for Correction of Boundary Layer Pressure Fluctuations for Hydrophone Size and Boundary Layer Thickness Effects—Option 1," by Ralph C. Leibowitz and Delores R. Wallace. NSRDC Report 29764, Sept. 1970.

SUPPRESSION OF FLOW-INDUCED VIBRATIONS
BY MEANS OF BODY SURFACE MODIFICATIONS

D. W. Sallet*
Naval Ordnance Laboratory
Silver Spring, Maryland

and

J. Berezow
Naval Ordnance Laboratory
Silver Spring, Maryland

The flow-induced vibrations of an elastically supported cylinder which is exposed to crossflow can be reduced by two methods: one method is to change the parameters of the vibrational system in such a fashion that the approach velocity never equals or exceeds the critical velocity, i.e., the velocity at which large amplitudes start to occur; and the second method is to reduce the flow-induced vibrations by changing the flow around the cylinder, i.e., to change the surface of the cylinder. This report discusses at length the effects of surface modifications on the flow-induced vibrations. It is seen that surface modifications can reduce the amplitudes of the flutter motions.

INTRODUCTION

The flutter phenomenon which occurs when an elastically supported circular cylinder is brought into steady fluid flow has been extensively discussed by several researchers in the past 6 years [1]. In this investigation, the elastically supported cylinder is a submerged moored buoy, 21 inches in diameter and 106 inches long. This cylinder has positive buoyancy and is restrained from rising to the surface or being swept downstream by a mooring cable which is attached to the lower face of the cylinder. The resulting vibrational system resembles a double pendulum. Detrimental flutter motions occur when the moored system is subjected to currents which exceed a certain critical velocity.

METHODS OF FLUTTER PREVENTION

The problem of preventing these self-excited vibrations, or at least reducing the amplitudes to a tolerable level, can be approached in two

fundamentally different ways: one, from the vibration dynamics point of view, is to change the elastic support in such a fashion that the excitation forces will not cause detrimental case motions; two, from the fluid dynamics point of view, is to influence the mechanism by which energy is transferred from the flowing medium to the vibrating system in such a fashion as to inhibit an asymmetrical pressure distribution which alternates periodically.

The first approach, i.e., changing the elastic support parameters, is of only limited interest. As is easily visualized, these parameters consist in the present system of the mooring cable length, the positive buoyancy (the displacement volume is fixed) and the separation distance of the centers of gravity and buoyancy. However, due to the desired flexibility in employment of the buoy system and due to the inherent design features of the system, the mooring cable length must stay variable over large limits and the remaining two parameters cannot be altered significantly. The onset of flow-induced motion cannot, therefore, be appreciably delayed. A rather simplistic parametric study suffices to

*Assoc. Professor, Department of Mechanical Engineering, University of Maryland, College Park, Maryland

clarify and justify this conclusion. The parametric study is given in the next section.

The second approach, namely, to arrest or at least sufficiently influence the fluid dynamic mechanism by which energy is transferred from the ocean currents to the oscillating cylinder, is of more practical interest. Upon closer examination of the flow around a blunt body such as a circular cylinder, the following physical phenomena are observed. Vorticity is continuously created on the upstream face of the cylinder (see Figure 1). The axes of these small line vortices are parallel to the cylinder axis. Since the length-to-diameter ratio is five, a two-dimensional flow consideration is sufficient. The vorticity is convected to the rear of the cylinder, where it will cause two large vortices of opposite rotation to form. As long as the Reynolds number (based on the undisturbed approach velocity, and the cylinder diameter) remains below 50, the vortices will remain attached and symmetrical as shown in Figure 1. Once the Reynolds number exceeds a value of approximately 50, the vortices will shed from the cylinder. The vortex shedding occurs periodically. The relation between the frequency of vortex shedding, the fluid velocity relative to the cylinder, and the diameter, was originally determined by V. Strouhal [2]:

$$f = S \frac{U}{D} \quad (1)$$

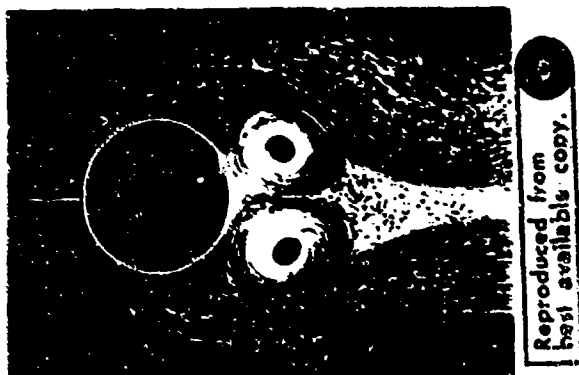


Fig. 1 - Stationary Vortices

The constant of proportionality S , the so called Strouhal number, is a function of the Reynolds number. This function has been experimentally determined for various body shapes over a wide Reynolds number range. For circular cylinders the following values were found:

$Re < 50$: no vortex shedding is observed [3]
$50 < Re < 150$: $S = 0.212 (1 - 21.2/Re)$ [3]
$300 < Re < 2000$: $S = 0.212 (1 - 12.7/Re)$ [3]
$2 \times 10^3 < Re < 1 \times 10^5$: S lies between 0.18 and 0.21 [4, 5]
$Re \approx 2 \times 10^5$: S lies between 0.25 and 0.33 [5]
$Re > 3.5 \times 10^6$: $S = 0.27$ [6]

The vortices do not shed simultaneously but individually in alternating fashion. Consequently, an asymmetrical flow field is established around the cylinder. The integral of the resulting pressure distribution over the upper (first and second quadrant) and the lower (third and fourth quadrant) side will now yield the magnitude of the oscillating lift force. The maxima of these lift forces (the so called Kármán forces) are of the same order of magnitude as the total steady drag force acting on the cylinder [5]. In all of the above investigations, which determined the Strouhal numbers at various Reynolds numbers and which correlated the pressure distribution with the wake and the forces acting on the cylinder, the cylinder was held rigidly in place; i.e., no motion of the cylinder took place. The resulting near-wake structure is the well-known Kármán vortex street [7].

From the fundamental observations described in the above paragraph, it is seen that there are, in turn, three different approaches which will sufficiently impair the mechanism by which energy is transferred from the fluid flow to the vibrating body:

1. preventing the shedding of the vortices,
2. preventing the formation of strong vortices behind the cylinder, and
3. preventing the vortex shedding to occur suddenly along the total length of the cylinder.

The first approach, i.e., to prevent flutter by stabilizing the vortices, led to a complete success [8, 9]. It was found that the two vortices behind the cylinder can only

be at rest with respect to the cylinder if they lie on symmetrical positions on the Föppl path (see Figure 2) which is given by the equations

$$\pm 2 y_1 = r_1 - \frac{1}{r_1} \quad i = 1, 2 \quad (2)$$

The condition of zero translational velocity of the vortices with respect to the cylinder also requires the strength of each vortex to depend upon its position on the Föppl path and the approach velocity; the required vortex strength is given by the relation

$$\kappa = 2Uy_1 \left(1 - \frac{1}{r_1^4}\right) \quad i = 1, 2 \quad (3)$$

Suppose that due to a disturbance in the flow field the vortices are displaced from their position at which they are at rest with respect to the cylinder. The vortices will return to their position on the Föppl path, if the displacement of the vortices from this path is symmetrical with respect to the x-axis (see Figure 2). An asymmetrical displacement of the vortices from their equilibrium position will result in instability, i.e., the vortices will shed.

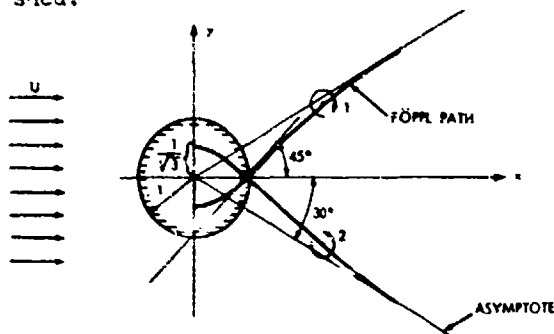


Fig. 2 - Equilibrium Positions of Vortices

A method of stabilizing the vortices now becomes apparent. If a thin plate is placed along the x-axis and perpendicular to the plane of the paper, the x-axis must then be treated as a solid wall. Due to the image effect, any displacement of a vortex is symmetrical with respect to the x-axis and stability is therefore guaranteed. The technical realization of this principle, a splitter plate, is shown in Figure 3.

The second approach, namely, to prevent the formation of strong vortices behind the cylinder, has led only to a partial success. It was attempted to create many small vortices having vortex vectors which are at right angles with respect to the cylinder axis. In this way, it may be possible to prevent the formation of a strong vortex

with a vortex vector parallel to the cylinder axis. No analytical solution has been attempted. However, an extensive experimental program was carried out. The vortices at right angles to the cylinder axis were generated by a matrix of small circular cylinders mounted on the surface of the large test cylinder. These little studs were made of lexan or rubber. Figure 4 shows a typical array of such studs. The lexan studs were bonded to a thin rubber sheet, which was then wrapped around the cylinder. Figure 5 shows the large cylindrical rods (1 inch in diameter and 6 inches long) attached to the test cylinder. Further details as to size and spacing of these surface modifications are described later in the report.

The third approach, which can sufficiently impair the mechanism by which energy is transferred from the fluid flow to the vibrating system, is to prevent the vortex shedding from occurring suddenly along the total length of the cylinder. The method of finding solutions for this approach was again implemented by means of a large-scale experimental test program. Different surface modifications, such as spirals or irregular protrusions, were fixed to the test cylinder (see Figure 6). While such modifications solve a similar flutter problem when the flowing medium is air, extensive tests of many variations of these surface modifications showed only limited diminishing of the self-excited vibrations in water.

CRITICAL FLOW VELOCITIES

The free-stream velocity at which flutter starts is called the critical flow velocity U_{crit} . The flutter motions of the system will start as the vortex shedding frequency approaches the natural frequency of the system. From Equation (1) we may therefore estimate the critical flow velocity as

$$U_{crit} = \frac{D}{S} f_{nat} \quad (4)$$

It is seen that for a system having several degrees of freedom, several critical flow velocities may occur. However, since the flutter motions occur over a large range of approach velocities, so that very often the system may still be in a flutter state due to its lowest natural frequency when flutter due to its higher natural frequencies starts, the lowest critical flow velocity will be of prime importance.

A simplified analysis suffices to predict the critical flow velocities of the submerged moored cylinder.



Fig. 3 - Cylinder with Splitter Plate

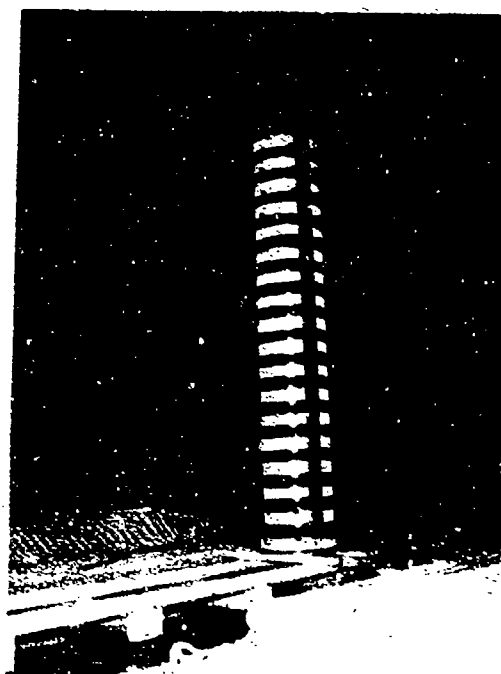


Fig. 5 - Array of Large Cylindrical Protrusions

Reproduced from
best available copy.



Fig. 4 - Typical Array of Lexan Studs

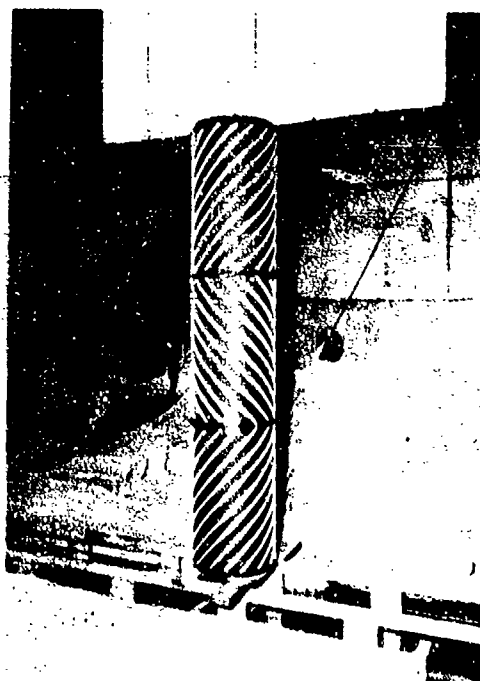


Fig. 6 - Typical Herringbone Pattern
(5/8-inch nylon rope)

Assuming an initial simple excitation in a vertical plane, the equations of motion of the cylinder in a stagnant fluid (no forcing function is acting on the cylinder) are:

$$\ddot{\theta} + \ddot{\phi} \frac{l}{L} \cos(\psi - \theta) - \dot{\psi}^2 \frac{l}{L} \sin(\psi - \theta) + \frac{W}{mL} \sin \theta + \frac{B}{mL} K_1 = 0 \quad (5)$$

and

$$\ddot{\phi} + \ddot{\theta} \frac{Lm}{mL^2 + I} \cos(\psi - \theta) + \dot{\theta}^2 \frac{Lm}{mL^2 + I} \sin(\psi - \theta) + \frac{Wl}{mL^2 + I} \sin \psi + \frac{B}{mL^2 + I} K_2 = 0 \quad (6)$$

where $W = B - w$. The nomenclature is shown in Figure 7.

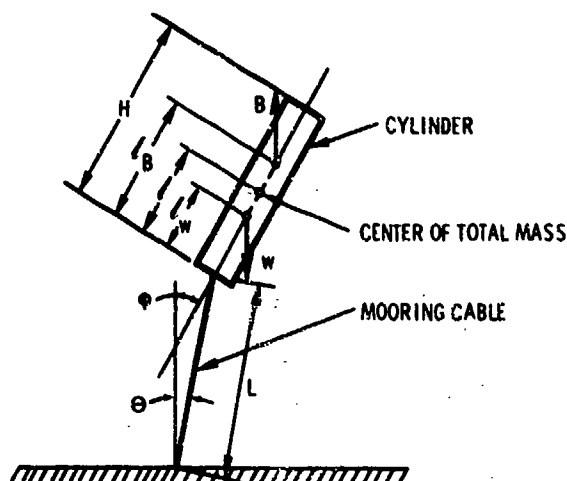


Fig. 7 - Nomenclature of Vibrating System

In deriving Equations (5) and (6), it was assumed that the center of mass of the cylinder, the center of added mass, and the center of buoyancy coincide:

$$l_w = l_B = l \quad (7)$$

The damping which occurs over the complete cylinder was considered lumped at the top and the bottom of the cylinder. In this way, all of the occurring motions are damped. For "velocity proportional" damping K_1 and K_2 , assume the values:

$$K_1 = 2L\dot{\theta} + H\dot{\phi} \cos(\psi - \theta) \quad (8)$$

$$K_2 = H[H\dot{\theta} + L\dot{\phi} \cos(\psi - \theta)] \quad (9)$$

For "velocity squared proportional" damping K_1 and K_2 , assume the values

$$K_1 = 3/2 \left\{ L^2 \dot{\theta}^2 + [L^2 \dot{\theta}^2 + H^2 \dot{\phi}^2 + 2LH\dot{\theta}\dot{\phi} \cos(\psi - \theta)]^{1/2} \cdot [L\dot{\theta} + H\dot{\phi} \cos(\psi - \theta)] \right\}$$

and

$$K_2 = 3/2 [L^2 \dot{\theta}^2 + H^2 \dot{\phi}^2 + 2LH\dot{\theta}\dot{\phi} \cos(\psi - \theta)]^{1/2} [H^2 \dot{\phi} + LH\dot{\theta}^2 \cos(\psi - \theta)] \quad (10)$$

For the vibrational system here considered, U_{crit} may be estimated by employing the undamped natural frequency of the linearized system. Equations (5) and (6) are linearized by limiting the motion to small angles, so that $\sin \theta \approx \theta$ and $\sin \psi \approx \psi$. These conditions were met for the initial cylinder motions experienced within the experimental part of this investigation as long as the approach velocity of the fluid did not exceed the critical value. For the simplified configuration for which Equation (7) is valid, the circular frequencies are:

$$\omega_{1,2}^2 = W \frac{\left\{ \left(\frac{l}{mL^2 + I} + \frac{1}{mL} \right) \right\} \pm \sqrt{R_1}}{2 \left(1 - \frac{l^2 m}{mL^2 + I} \right)} \quad (12)$$

where

$$R_1 = \left(\frac{l}{mL^2 + I} + \frac{1}{mL} \right)^2 - 4 \left(1 - \frac{l^2 m}{mL^2 + I} \right) \cdot \left(\frac{l}{mL(mL^2 + I)} \right) \quad (13)$$

For the case in which the center of mass of the cylinder, the center of added mass, and the center of buoyancy do not coincide, Equation (12) becomes:

$$\omega_{1,2}^2 = \frac{\left\{ \frac{l_B - l_w}{mL^2 + I} + \frac{W}{mL} \right\} \pm \sqrt{R_2}}{2 \left(1 - \frac{m l^2}{mL^2 + I} \right)} \quad (14)$$

where

$$R_2 = \left(\frac{L_B B - L_W W}{mL^2 + I} + \frac{W}{mL} \right)^2 - 4 \left(1 - \frac{mL^2}{mL^2 + I} \right) \quad (15)$$

$$\frac{W(L_B B - L_W W)}{mL(mL^2 + I)}$$

The critical velocities near which excessive amplitudes will start to occur, therefore, are:

$$U_{1,2}(\text{crit}) = \frac{(w_{1,2})D}{2\pi s} \quad (16)$$

where the circular frequencies $w_{1,2}$ are given by Equation (14) for the more general case and by Equation (12) for the physical configuration for which Equation (7) is valid.

For the sake of clarity, it is best to present Equation (16), which contains the rather complex term (12), or term (14), graphically. The cylinder in this parametric study also has a diameter of 21 inches and a length of 108 inches.

Figures 8 to 13 give the frequencies and critical velocities as a function of the cable length. While for Figures 8 to 11 the separation "s" is held constant and the parameter "w" is varied, Figures 11 to 13 show the influence of the separation "s" on the critical velocity with the positive buoyancy "w" held constant. Figures 9, 11, and 13 show the critical velocities when the moment of inertia I is 20 percent lower than the theoretically calculated value. When deriving this value, the added mass was assumed to be equal to the mass of the displaced fluid. This rather customary assumption (for long circular cylinders) proved to be quite accurate when predicted natural frequencies were compared with the frequencies obtained in pendulum tests in water, as long as the motion of the cylinder was basically a translatory motion. When the higher natural frequency is excited, the cylinder will undergo a rotary motion around an axis which is perpendicular to the plane in which the translatory motion occurred. For this type of motion, the added mass is smaller than the mass of the displaced fluid. Experiments suggested the shown lower value for the moment of inertia. The dotted line in Figures 8 to 13 is valid for the cylinder which was tested in the full-scale towing tests (see Figures 15 to 18) and to which also surface modifications were applied. The parameters for this cylinder were:

$W = 319$ lbs, $w = 999$ lbs, $s = 12.0$ inches, and $I = 542.36$ slug-ft².

TEST PROCEDURE

A 20-foot flexible steel cable moored the cylinder to a sled which moved on tracks along the bottom of the tank (Figure 14). Quartz-iodide lamps (650 watts) were used in the tank for frontlighting. A six-lamp light bank was placed slightly above camera level on the south wall of the tank. Another six-lamp light bank was placed on the east wall at the beginning of the effective range, and about 22 feet above the bottom of the tank. A nine-lamp light bank was also placed on the east wall about 25 feet downrange from the second light bank and about 22 feet above the bottom of the tank. The camera was placed at the south end of the tank about 32 feet above the bottom of the tank and behind the center viewing port.

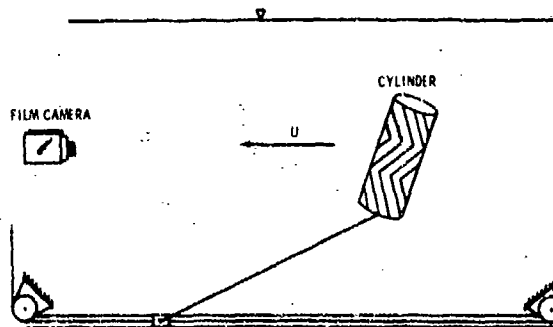


Fig. 14 - Test Arrangement

The driving D.C. motor moved the towing cable which was attached to both ends of the sled.

For tests A-II inclusive, a Mitchell 35mm camera with type no. 2479 film was used, operating at about 24 frames per second. For the remaining tests, a Flight Research 35mm camera with a 25mm lens was used with type no. 2479 film, running at about 10 frames per second.

In a typical test, the sled towed the cylinder, starting from a position at rest at the south end of the test tank. When the front end of the sled was observed to reach the starting point of the test run, the camera and an electric timer were started. When the front end of the sled was observed to reach the end point, the camera and timer were stopped. Time of travel and motion observations were recorded. The approach distance to the start of the run was 40 feet. The length of the test run was 43 feet long.

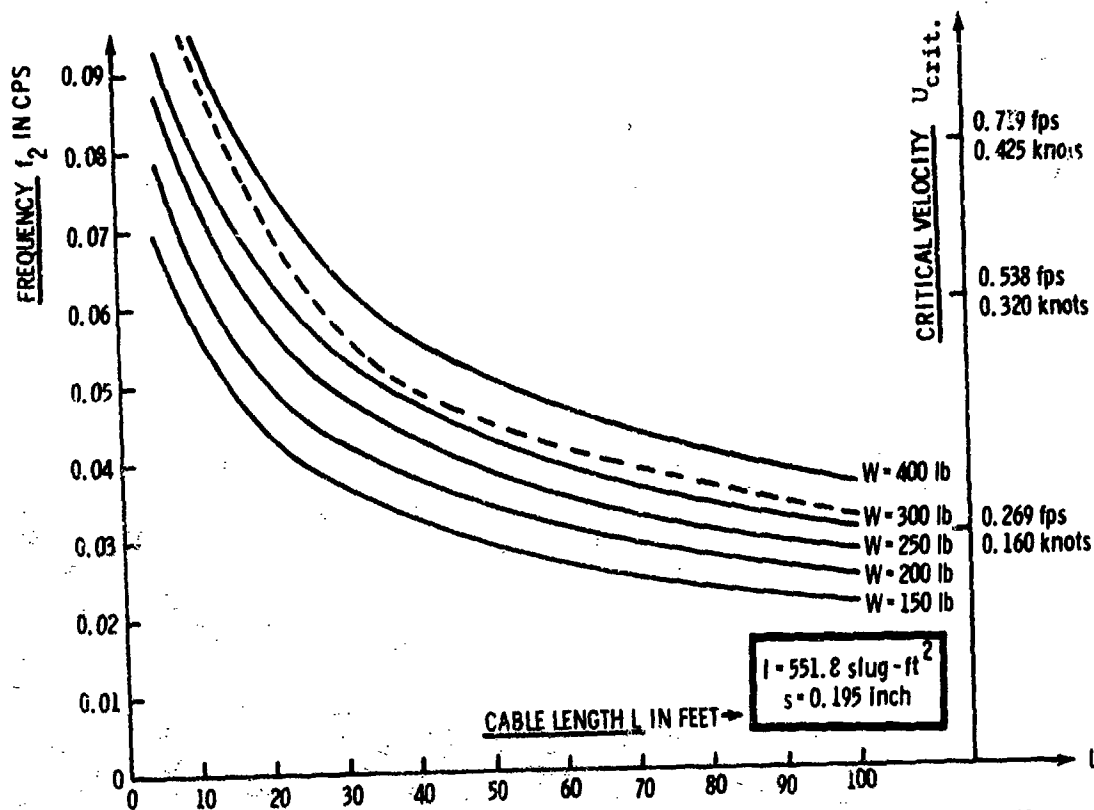


Fig. 8 - Lower Critical Velocity vs Cable Length with Positive Buoyancy W as a Parameter, Moment of Inertia $I = 551.8 \text{ slug-ft}^2$

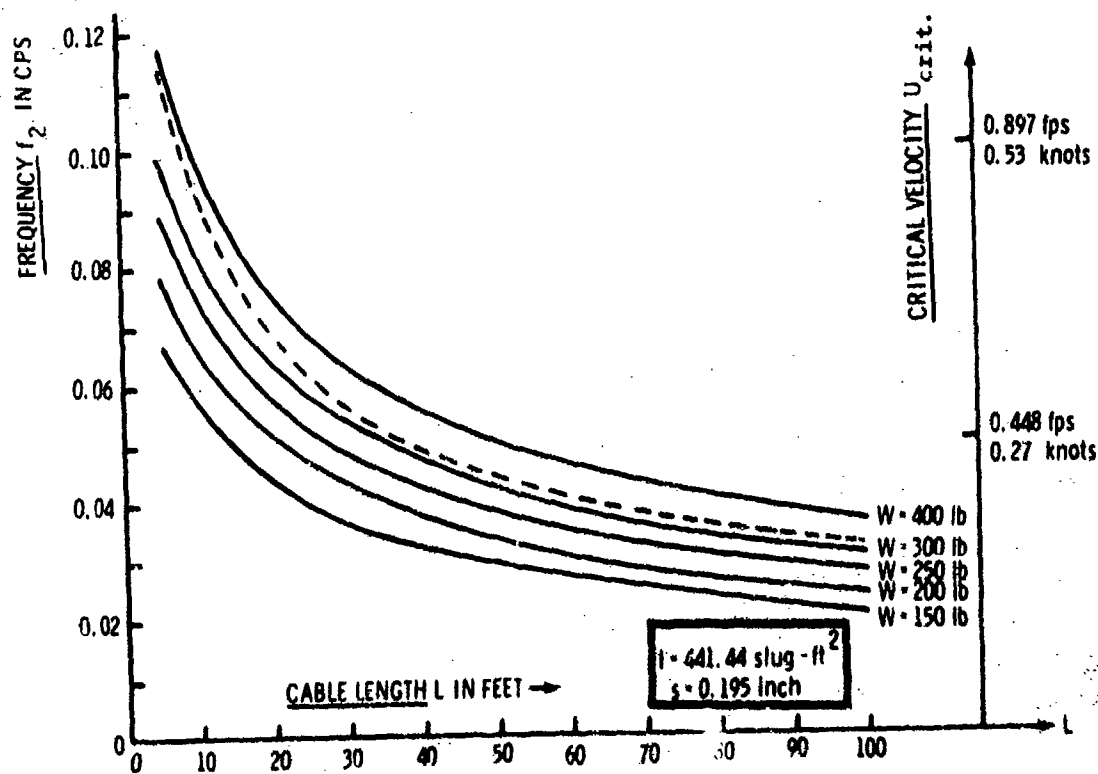


Fig. 9 - Lower Critical Velocity vs Cable Length with Positive Buoyancy W as a Parameter, Moment of Inertia $I = 441.44 \text{ slug-ft}^2$

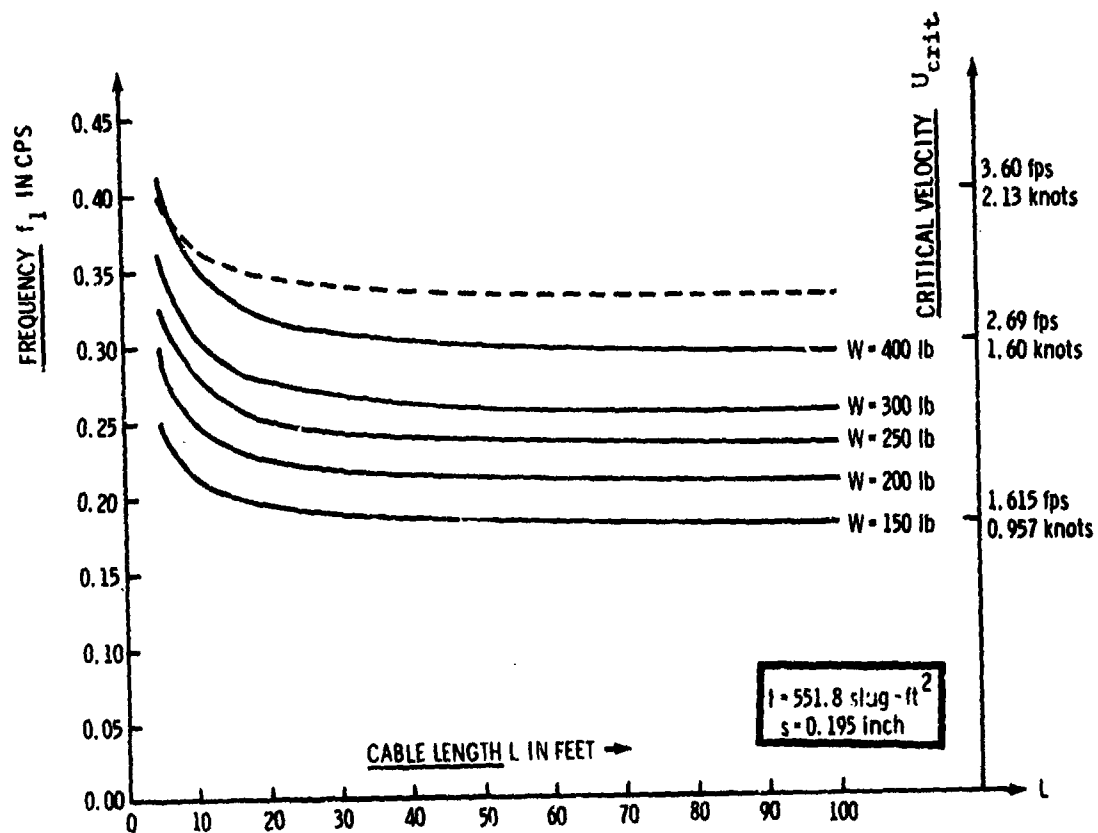


Fig. 10 - Higher Critical Velocity vs Cable Length with Positive Buoyancy W as a Parameter, Moment of Inertia $I = 551.8 \text{ slug-ft}^2$

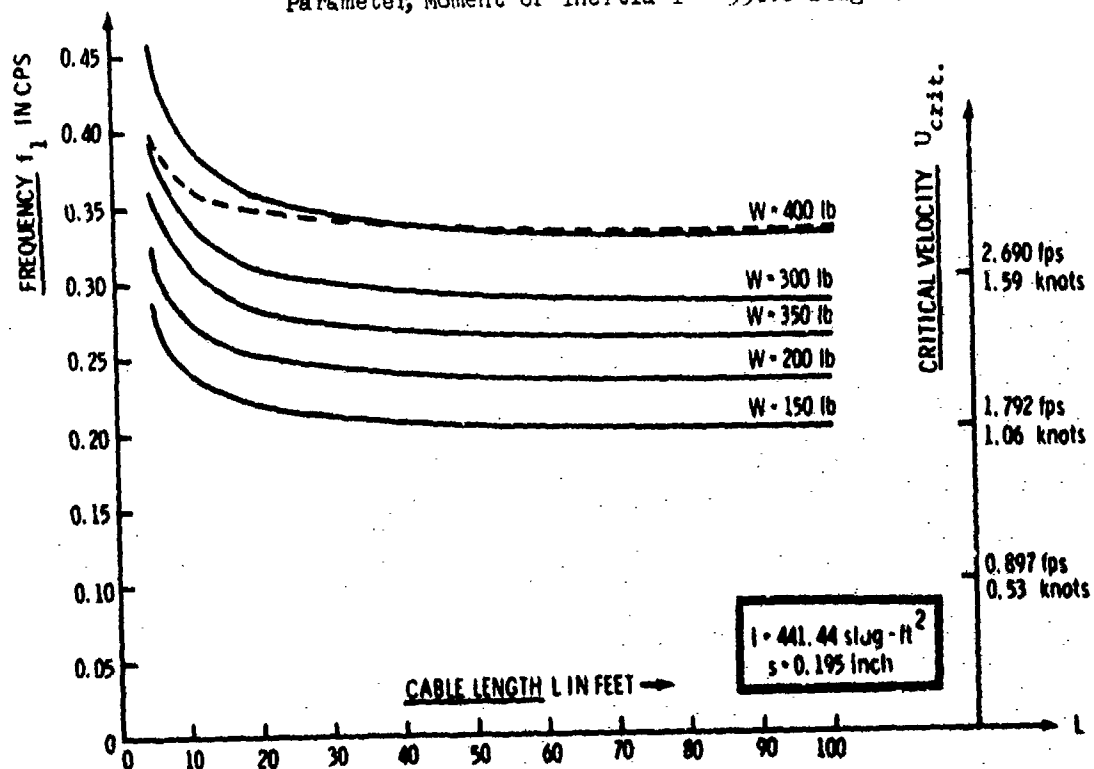


Fig. 11 - Higher Critical Velocity vs Cable Length with Positive Buoyancy W as a Parameter, Moment of Inertia $I = 441.44 \text{ slug-ft}^2$

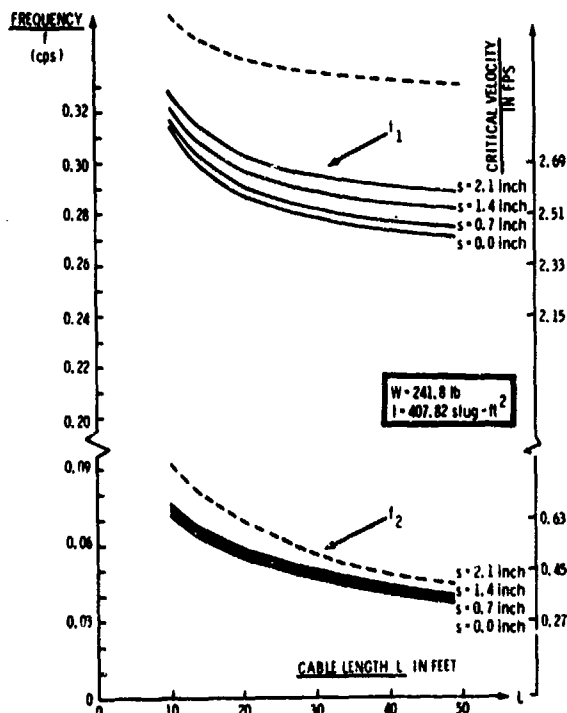


Fig. 12 - Lower and Higher Critical Velocity vs Cable Length with Center of Gravity - Center of Buoyancy Separation "S" as a Parameter. Moment of Inertia $I = 407.82 \text{ slug-ft}^2$

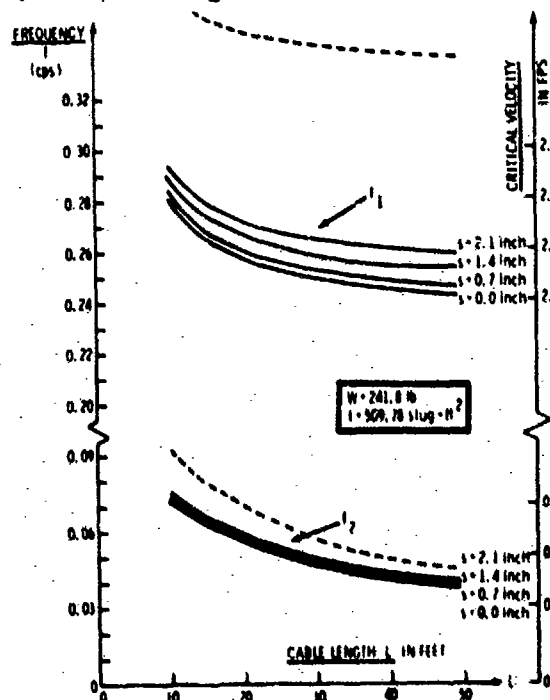


Fig. 13 - Lower and Higher Critical Velocity vs Cable Length with Center of Gravity - Center of Buoyancy Separation "S" as a Parameter. Moment of Inertia $I = 509.78 \text{ slug-ft}^2$

SURFACE MODIFICATIONS

Most surface modifications were fabricated onto three sheets of 1/16-inch-thick Neoprene (Shore Durometer 80+5) which were then taped onto the cylinder. The description of the various modifications is as follows:

A. No surface modification.

D. 1/2 inch in diameter, 1/2-inch-long lexan rods spaced 6 inches in a row, and 3 inches in a column; rows and columns were staggered. (Columns run parallel to the cylinder axis.)

E. Same as D, but 1/4 inch in diameter.

H. 5/8-inch nylon rope, herring-bone pattern, 45° , rope separated 6 inches on centers.

I. Same as D but 2 inches long.

J. Same as E but 2 inches long.

K. Same as D but spaced 3 inches in a row.

L. Same as E but spaced 3 inches in a row.

N. Same as H but 60° pattern.

P. Same as H but 30° pattern, separated 3 inches on centers.

Q. Same as P but rope is separated 6 inches on centers.

R. Rubber rods 1 inch in diameter and 6 inches long, separated 5-1/2 inches and bonded on 2-inch-wide rubber strips. The strips are separated so that the rubber rods are 6 inches apart on centers. Rods line up, one behind the other.

S. Same as P except that the separation between the strips is such that rods are 3 inches apart on centers. This modification reduced the positive buoyancy of the cylinder by 15 pounds.

Y. Inverted "T" rubber spiral, 6 turns around the case.

Z. Irregularly spaced 1/4-inch-by-1-inch-by-1-inch rubber protrusions.

AA. 2-inch-long triangular rubber pieces spaced 3 inches in a row, 5 inches in a column, flat sides facing each other in pairs. (Columns run parallel with the cylinder axis.)

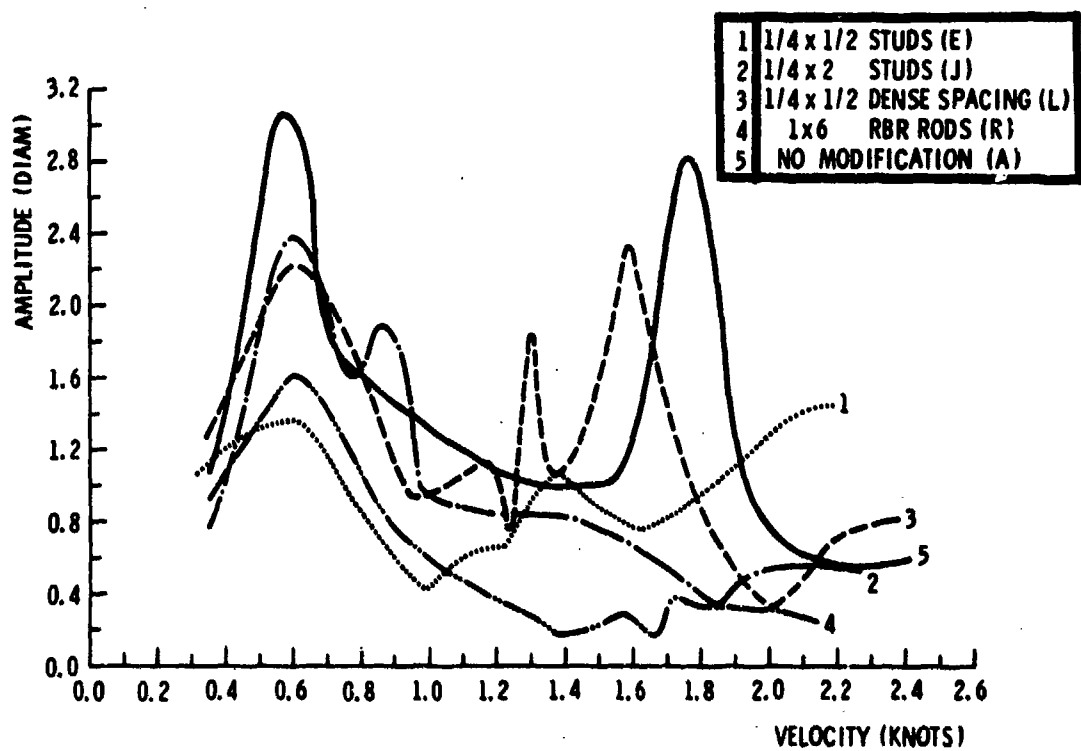


Fig. 15 - Effect of Surface Modifications on Flutter Amplitude

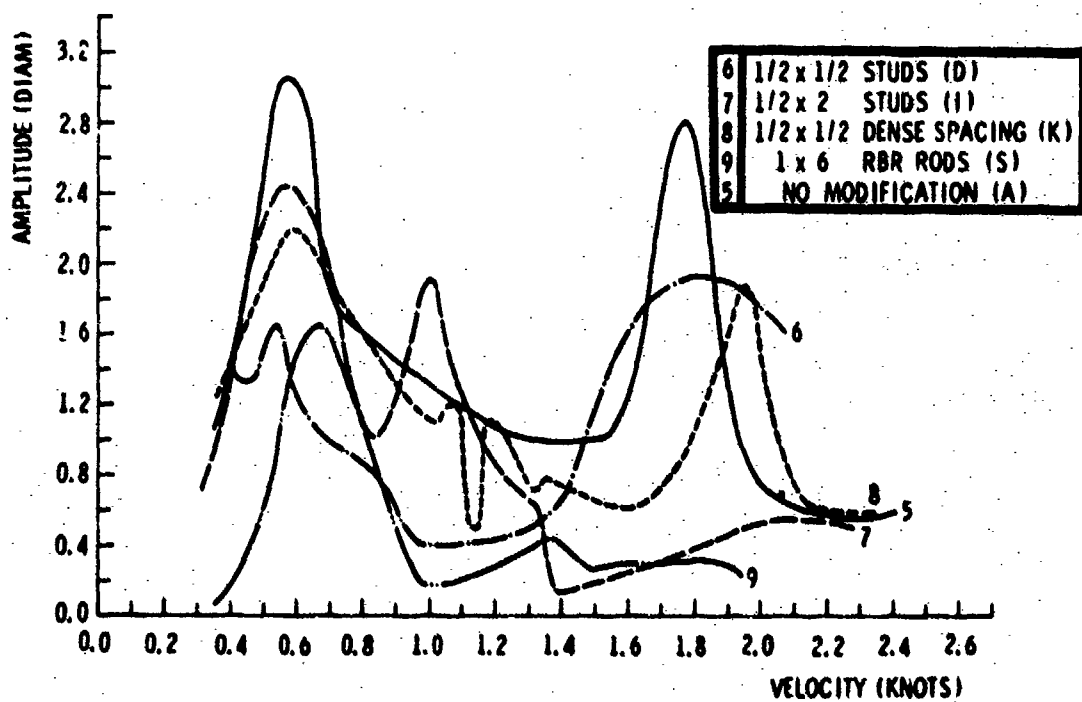


Fig. 16 - Effect of Surface Modifications on Flutter Amplitude

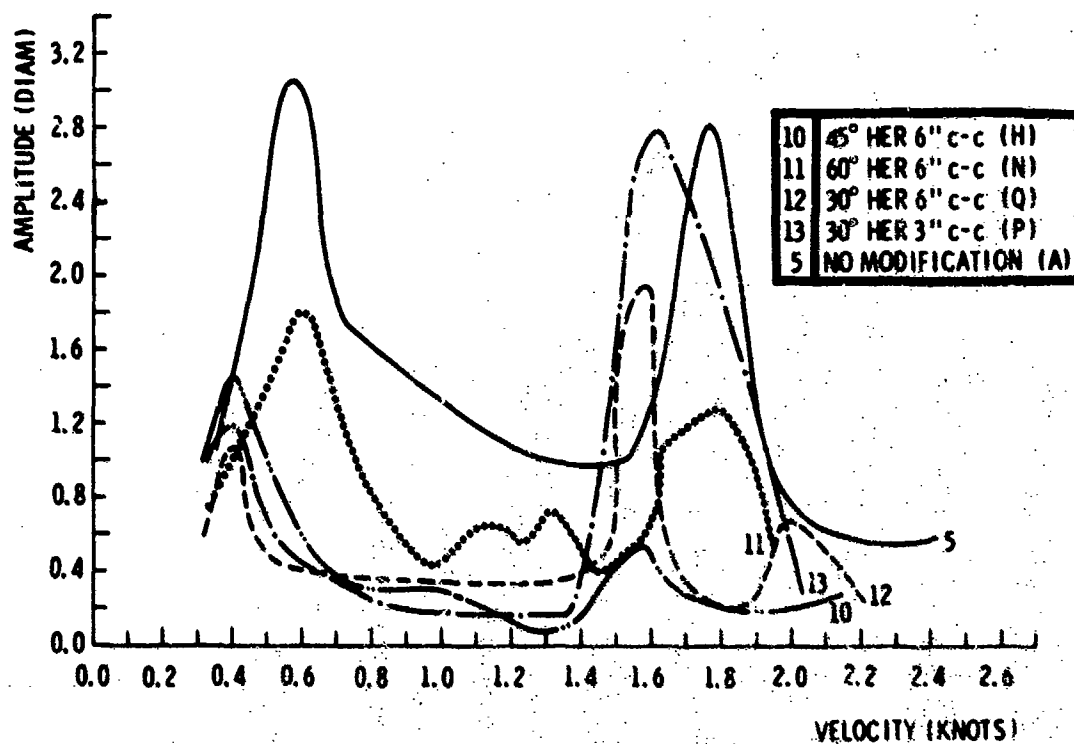


Fig. 17 - Effect of Surface Modifications on Flutter Amplitude

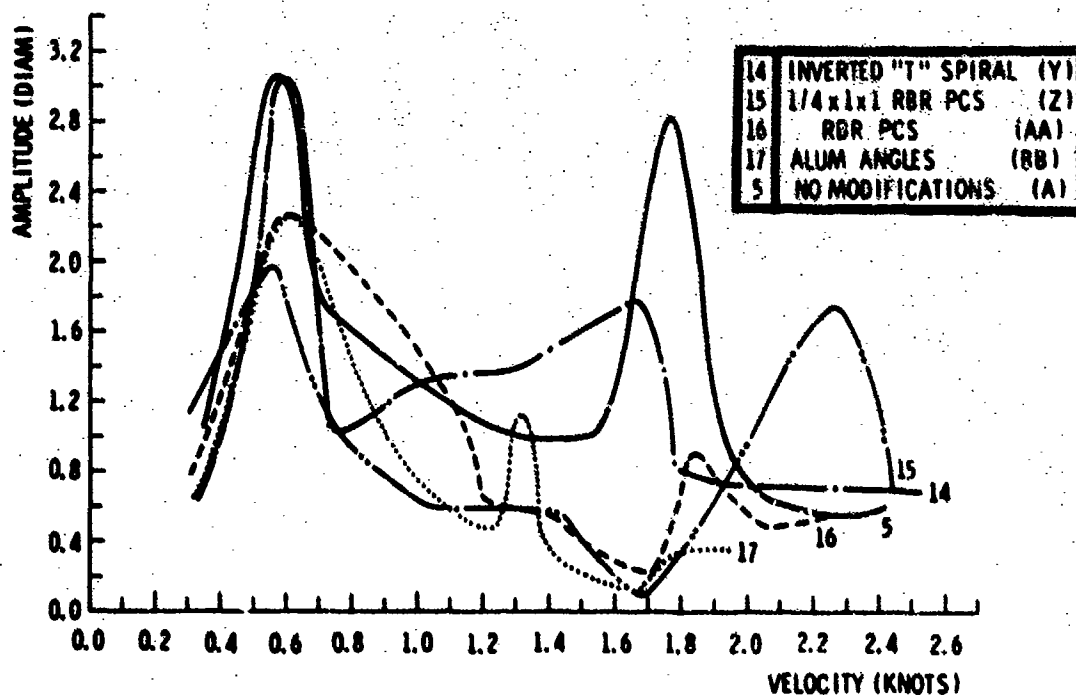


Fig. 18 - Effect of Surface Modifications on Flutter Amplitude

BB. 0.032-inch aluminum angle 3/4 inch by 1/2 inch by 3 inches long, separated 3 inches in a row, 4 inches in a column. (Columns run parallel to the cylinder axis.)

TEST RESULTS

The films of the cylinder motion were reduced on a Vanguard Motion Analyzer. The coordinates of the four corner points of the cylinder when the cylinder was in the extreme left or extreme right position were recorded. The deviation of the geometric center of the case from its equilibrium position was calculated utilizing a BASIC computer program to perform the necessary averaging procedures.

Figures 15 to 18 show the amplitudes in cylinder diameters of the geometric center of the cylinder as a function of the towing velocity. The full line, which is repeated for all four figures, shows the motion of the basic case. The parameters of this cylinder are given at the end of the section on critical flow velocities. By the method shown in this section, the lower critical velocity for this cylinder is predicted to be 0.37 knot, and the higher critical velocity is predicted to be 1.80 knots. It is seen from Figure 15 that the first "resonance" starts at the predicted value. Since the critical velocity is based upon the velocity of the fluid relative to the cylinder, and since at higher velocities the cylinder motion is not only due to towing but also due to cylinder flutter in its primary mode, the predicted value of the higher critical velocity is roughly verified. (An exact determination of the fluid velocity with respect to the cylinder was not undertaken, but just estimated.)

Figures 15 and 16 show the amplitude as a function of the towing velocity for surface modifications which were intended to prevent the formation of strong vortices. Figures 17 and 18 show the amplitude as a function of the towing velocity for surface modifications intended to prevent the vortex shedding from occurring suddenly along the total length of the cylinder.

The problem of fluctuating lift forces due to unsymmetrical flow around blunt bodies has been repeatedly investigated during the past 35 years. The bulk of these investigations was undertaken to find a remedy to a specific flutter problem. Usually a "try-this and try-that" type philosophy governed the experiments. The

authors of the present report were led by some, mostly intuitive, reasoning in their choice of surface modifications. However, only the response of the system and not the flow around the cylinder, was observed and recorded.

It is of utmost importance to relate the flow field characteristics with the response of the system if any results of more unilateral validity are to be obtained. Further experiments, therefore, should include flow visualization.

ACKNOWLEDGEMENT

This work was sponsored by the Naval Ordnance Systems Command, Code 035. The authors would like to acknowledge Mr. C. Seidman for his suggestions for case modifications to reduce case motion.

SYMBOLS

B	= buoyancy of cylinder
D	= diameter of the cylinder
f_{nat}	= natural frequency of the suspended cylinder in the fluid
H	= length of the cylinder
I	= total moment of inertia (including the added moment of the cylinder around the center of total mass)
z	= distance from bottom surface of cylinder to center of total mass (including the added mass)
z_B	= distance from bottom surface of cylinder to center of buoyancy
z^*	= distance from bottom surface of cylinder to center of mass of cylinder
L	= length of mooring cable
m	= total mass of cylinder (including added mass)
r_1	= distance of 1 st vortex from origin
z	= distance between center of mass and center of buoyancy
S	= Strouhal number
U	= velocity of approaching flow
U_{crit}	= critical velocity
w	= weight of cylinder
W	= B - w
y_1	= ordinate of vortex 1
x_1	= abscissa of vortex 1
θ	= angle between cylinder axis and vertical
$\dot{\theta}, \ddot{\theta}$	= first and second time derivative of θ
κ	= vortex strength
θ	= angle between mooring cable and vertical
$\dot{\theta}, \ddot{\theta}$	= first and second time derivative of θ
ω	= circular frequency

REFERENCES

1. D. W. Sallet, "On the Self-Excited Vibrations of a Circular Cylinder in Uniform Flow," The Shock and Vibration Bulletin, Bulletin 40, Part 3, Dec 1969, pp. 303-309.
2. V. Strouhal, "Über eine besondere Art der Tonerregung," Analen der Physik, Vol. 5, 1878, pp. 216-251.
3. A. Roshko, "On the Development of Turbulent Wakes from Vortex Streets," NACA Rpt 1191, 1954.
4. E. F. Relf, "The Frequency of the Eddies Generated by the Motion of Circular Cylinders through a Fluid," Tech. Rep. of the A.R.C. 1924-25, Vol. 2, London, 1926, pp. 658-660.
5. H. Drescher, "Messung der auf querangeströmte Zylinder ausgeübten zeitlich verändernden Drücke," Z. f. Flugwissenschaften, Vol. 4, 1956, pp. 17-21.
6. A. Roshko, "Experiments on the Flow past a Circular Cylinder at Very High Reynolds Number," J. Fluid Mech. 10, 1961, pp. 345-356.
7. Th. von Karman and H. Rubach, "Über den Mechanismus des Flüssigkeits und Luftwiderstandes," Physik. Zeitschrift, Vol. 13, 1912, pp. 49-59.
8. D. W. Sallet, "A Method of Stabilizing Cylinders in Fluid Flow," Journal of Hydronautics, Vol. 4, No. 1, Jan 1970, pp. 40-45.
9. D. W. Sallet, "On the Reduction and Prevention of the Fluid-Induced Vibrations of Circular Cylinders of Finite Length," The Shock and Vibration Bulletin, Bulletin 41, Part 6, Dec 1970, pp. 31-37.

DISCUSSION

Mr. Ungar (Bolt Beranek and Newman): Have you tried to correlate the effect of correlation length along the cylinder with the amplitude response, or have you studied the effect of turbulent fluid?

Mr. Sallet: Yes, the facility always has water pumps running continuously to keep the water clean. In order to see the effect of what might be called a rather large scale turbulence I ran tests with the pumps running and then ran tests with completely still water, allowing two or three days time for the water to settle. I saw no appreciable difference between the responses of the system when the pumps were running and when the pumps were not running.

Mr. Ungar: I guess those turbulences are very large compared with your test systems. In buildings I think it has been found that the response to turbulent winds is much less than the response to clean flow. I am almost inclined to suggest you might see the same sort of thing and that you might get some relation between your response and the correlation along the surface. It would be too hard to measure pressure correlations on the surface.

Mr. Sallet: No, if you are thinking of obtaining turbulent boundary layers we are within that range. We will have turbulent boundary layers and even at low speeds I have tripped the boundary layer on purpose.

Mr. Ungar: One reason that the spiral idea works is that the vortices are not shed along the entire length.

Mr. Sallet: Yes, that was the idea behind them. But again one has to be very careful when applying wind tunnel data to a water tunnel. I find that time and time again methods which do reduce this type of vibration in air do not most of the time reduce the vibration in water.

Mr. Martin (NASA Langley Research Center): Are you familiar with the study of oscil-

lations in tethered spherical balloons in high winds that was performed for the military at the Langley Research Center? These balloons were used for antennas or distress signals. I believe Tracy Redd performed a study similar to yours in shaping the balloons.

Mr. Sallet: Yes, I am familiar with that report.

Mr. Martin: You called this type of instability flutter or self-excited oscillation. I would not consider that to be a flutter or self induced oscillation. I consider a forced oscillation as one in which the force exists on the body whether the body is moving or not, then if the body responds to that force it is a forced oscillation. If a body has no force when there is no motion, and if a force starts as a result of motion, and if the phase of that force is such that it reinforces that motion, then that is a self excited oscillation or flutter. I would consider your study as strictly on forced oscillations. If the body stops vibrating the force exists, it does not start as a result of the oscillation.

Mr. Sallet: No, even by your definition it is flutter because the forces increase if the body moves.

Mr. Martin: The forces may increase but they are there if the body does not move. The initial force is there.

Mr. Sallet: That is correct.

Mr. Martin: That is a forced oscillation. In a self excited oscillation, or flutter if the motion is stopped there is no force.

Mr. Sallet: The forces are there. If you examine the spectrum the forces may not be large enough to cause the body to move so there may be forces present with no response. But once the body moves the forces may gain sufficient magnitude to obtain a response so I still prefer to call this flutter.

AN EXPERIMENTAL TECHNIQUE FOR DETERMINING VIBRATION MODES OF STRUCTURES

WITH A QUASI-STATIONARY RANDOM FORCING FUNCTION

Robert G. Christiansen and Wallace W. Parmenter
Naval Weapons Center
China Lake, California

A slender beam is subjected to random vibration. The modes of response of the beam are determined using spectral analysis techniques made available by the NWC spectral analysis computer program.

INTRODUCTION

The response of structures to random loading has been treated theoretically by many investigators (Ref. 1 through 4). However, the experimental corroboration of these theoretical modes has not met with much success. Those experimental investigators venturing into the field (Ref. 5) before the advent of the Fast Fourier Transform (FFT) were doomed to tedious numerical Fourier transformation techniques. The calculation of cross-spectral density functions and transfer functions required that the cross-correlation function be computed via analog computer techniques, followed by numerical computation of the Fourier transform of this function. This process was time consuming and provided inaccuracies.

The incorporation of the FFT into time series analysis programs (Ref. 6) allowed the conversion of time series data directly into the frequency domain (without first squaring the time series). Several investigators used this type of analysis technique to examine the response of simple structures (Ref. 7 and 8).

But even these investigators encountered numerous problems, ranging from limited computer and analysis capabilities to insufficient equipment and laboratory techniques. Their approach was to attach a small (a few pounds force) exciter on the structure. Then a force power spectral density (PSD) function was controlled at a point on the structure that was usually uncontrollable in terms of the response of the structure and dynamic range of the exciter. In retrospect, these investigators attempted an approach that led to insurmountable problems.

In the process of developing a positive empirical method of calibration and evaluation for the NWC spectral analysis computer program (Ref. 9), the response to random acceleration of the boundary of a fixed-free beam was measured (Ref. 10). The relationship between several points, each to the other, was analyzed in the cross-correlation portion of the program. By careful inspection of textbook examples of beam

modes shape, in conjunction with prior knowledge of the positioning of the response accelerometers, certain relationships in the cross-functions could be corroborated and proper program operation could be verified.

The corollary this suggested was obvious: through a known random input at the boundary or properly chosen structural point, the modes and modal frequencies could be determined. Furthermore, if the spectrum shape of the excitation is free of large peaks and valleys, it is very easy to determine the mode shapes from only response accelerometer data. As is well known, the frequency response functions for lightly damped structures (Ref. 11) can be determined from response data alone, hence, with a knowledge of the input spectrum (smooth), the complete structural response of the structure can be determined. This time savings over traditional experimental methods of determining modal vibration is of an order of magnitude.

THEORY

The classical Bernoulli-Euler beam has been dealt with in many texts (Ref. 12 and 13) and only the results are shown here. The equation of motion in a plane of the beam is given by

$$EI \frac{\partial^4 y}{\partial x^4} + \mu \frac{\partial^2 y}{\partial t^2} = F(x, t) \quad (1)$$

where $y = y(x, t)$, x is the position of a point on the beam, E is the modulus of elasticity, I is the area moment of inertia, μ is the mass per unit length, and $F(x, t)$ is the forcing function.

In the homogeneous case $F(x, t) = 0$, variables are separable in Eq. 1 with

$$y(x, t) = \lambda(x) T(t) \quad (2)$$

to give solutions to Eq. 1 in the form

$$X(x) = A_1 \exp(ax) + A_2 \exp(-ax) + A_3 \sin(ax) + A_4 \cos(ax) \quad (3)$$

$$a = \left(\frac{16\omega^2}{EI} \right)^{1/4} \quad (4)$$

where ω = frequency in radians/sec.

Using the boundary constraints

$$\text{Simple Support: } y = 0; \quad \frac{\partial^2 y}{\partial x^2} = 0$$

$$\text{Free Support: } \frac{\partial^2 y}{\partial x^2} = 0; \quad \frac{\partial^3 y}{\partial x^3} = 0$$

$$\text{Fixed Support: } y = 0; \quad \frac{\partial y}{\partial x} = 0$$

and evaluating at $x=0$ and $x=l$, the following frequency equations are obtained

$$\text{Fixed-Simple: } \tan(al) - \tanh(al) = 0 \quad (5)$$

$$\text{Fixed-Free: } \cos(al) \cosh(al) = -1 \quad (6)$$

$$\text{Fixed-Fixed: } \cos(al) \cosh(al) = 1 \quad (7)$$

$$\text{Free-Free: } \cos(al) \cosh(al) = 1 \quad (8)$$

Solving for consecutive zeros in Eq. 5-8 yields the modal resonant frequencies. (The first 20 roots to Eq. 5-8 are given in Appendix A.)

The values of "a" listed in Appendix A and the corresponding frequencies predicted by Eq. 4 are somewhat in error for the higher modes due to the omission of shear effects and rotary inertia. These effects (Timoshenko beam) are accounted for in the computer program* used to calculate the modal shapes and frequencies. The effects of the mass of the accelerometer and accelerometer cables were omitted in this calculation.

The spectral functions and theory used in the analysis of the beam motion are well known (a good overall presentation is given in Ref. 11). The functions used in this analysis and the relationships between these functions will be outlined in the following paragraphs. Several

excellent texts develop these relationships and their engineering applications (Ref. 14 and 15). For a rigorous mathematical treatment of these stochastic processes, Ref. 16 and 17 are recommended.

In the computation of frequency domain functions, a discrete Fourier transformation of the time series data at response points is performed as follows:

$$A_k = \frac{1}{N} \sum_{\alpha=0}^{N-1} X_{\alpha} e^{-i \frac{2\pi \alpha k}{N}} \quad (9)$$

where

$$k = 0 \dots N-1$$

N = number of data points in time slice

X_{α} and A_k are discrete Fourier transform pairs and X_{α} is given by

$$X_{\alpha} = \sum_{k=0}^{N-1} A_k e^{i \frac{2\pi \alpha k}{N}} \quad \alpha = 0 \dots N \quad (10)$$

Here X_{α} is the value of the time series at the point $\alpha \Delta t$ in the time slice, Δt is the interval between digital samples, $N \Delta t$ is the period of the slice, $1/N \Delta t = \Delta F$ is the fundamental frequency of the transform, $k \Delta F$ is the upper cutoff frequency, ΔF is the lower cutoff frequency, $M \Delta F$ is the bandwidth, and M is an integer.

When two or more time series are to be examined, the time slice is such that the fundamental frequency (ΔF) is the same. In addition, when complex response functions are used to examine two or more points for cross correlation, the time slices examined are such that each record is examined during the same period of time. This is a simple fact to state, but often overlooked when digitizing pairs of data signals.

All of the functions are discrete in nature so that these functions are only approximations of the rigorously developed continuous functions as shown in Ref. 11.

The following functions are used in the analysis of the beam:

*Naval Weapons Center. Beam, A Computer Program for Calculating the Natural Vibration Modes of a Non-Uniform Beam, by E. Jeter. China Lake, Calif., NWC, June 1970. (NWC TN 4062-49.)

$G_{xx}(f)$ = Power-Spectral Density function (PSD) or auto PSD of a response point at x on the beam. In this report the PSD will be the square

of the Fourier coefficients obtained when the time slice of interest is transformed into the frequency domain. These coefficients are then divided by a constant (the filter bandwidth).

$G_{xy}(f)$ = Cross-Spectral Density Function (cross PSD) between the response at point x and the response at point y. In this report the cross PSD will be the complex product of the Fourier transform coefficients of a time slice out of the time series $x(t)$ and $y(t)$. The resulting product is then divided by a constant (the filter bandwidth). The cross PSD is a complex vector which can be written as

$$G_{xy}(f) = |G_{xy}(f)| e^{-i\phi_{xy}}$$

$$= C_{xy}(f) - iQ_{xy}(f)$$

where

$C_{xy}(f)$ = Co-spectral density function (Co)

$Q_{xy}(f)$ = Quadrature-spectral density function (Quad)

$\phi_{xy}(f) = \tan^{-1} \frac{Q_{xy}}{C_{xy}} = \text{phase angle} = \text{argument of the complex vector}$

The following point-to-point relationships which utilize the cross PSD are used in the analysis of the beam motion.

The transfer function $H_{xy}(f)$ (a complex vector) is defined as

$$G_{xy}(f) = H_{xy}(f) G_{xx}(f), \text{ or } H_{xy}(f) = \frac{G_{xy}(f)}{G_{xx}(f)} = |H_{xy}(f)| e^{-i\phi_{xy}(f)}$$

also for a third point (z) on the beam

$$G_{xz}(f) = H_{xy}(f) \cdot H_{yz}(f) G_{xx}(f)$$

$$\text{or } H_{xz}(f) = H_{xy}(f) \cdot H_{yz}(f) \dots$$

$$\text{or } |H_{xz}(f)| = |H_{xy}(f)| \cdot |H_{yz}(f)| \dots$$

= gain factor or modulus of the complex vector (this assumes no feedback)

and

$$\phi_{xz}(f) = \phi_{xy}(f) + \phi_{yz}(f)$$

The transfer function is determined by the physical characteristics of the structural system between the response points. Hence, if a suitable math model containing structural system parameters does exist, empirical determination of the transfer function implies empirical determination of the system parameters.

The ordinary coherence function is

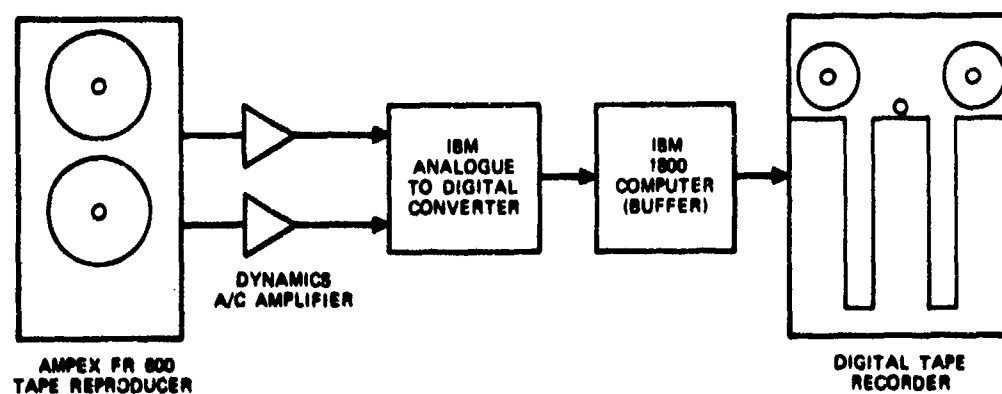
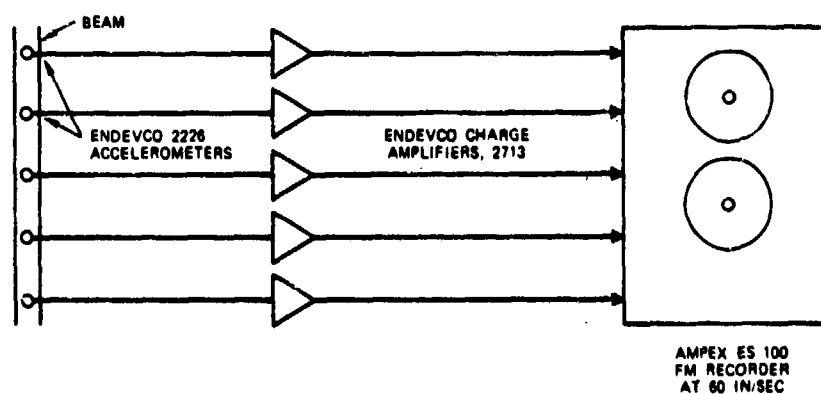
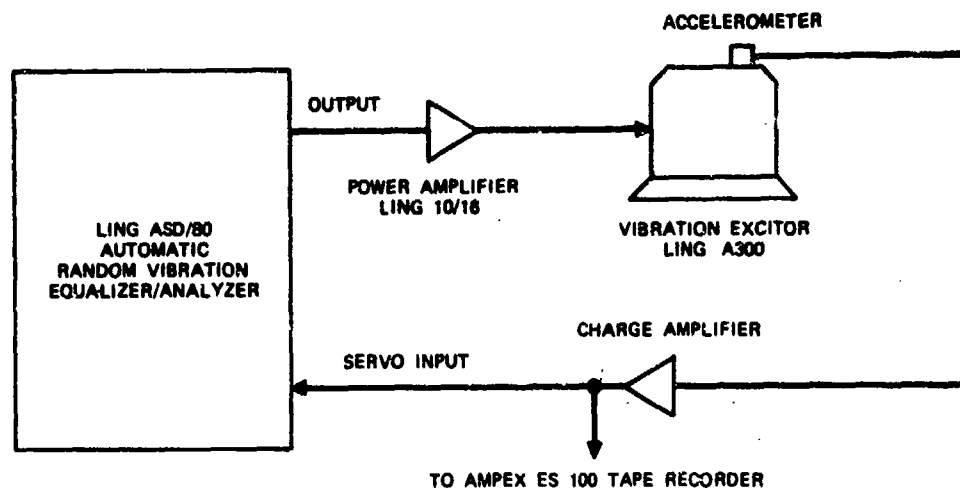
$$\gamma^2(f) = \frac{|G_{xy}(f)|^2}{G_{xx}(f) G_{yy}(f)} \leq 1$$

It is a measure of the amount of coherence between the response at points x and y as a function of frequency. When $\gamma^2=0$, the responses are incoherent; i.e., this is not a vibration transmission path between x and y on the beam at a given frequency.

EXPERIMENTAL DESCRIPTION AND TECHNIQUES

When the beam was mechanically excited, the auto-spectrum of the boundary motion was shaped and controlled using a Ling ASD/80 Equalizer/Analyzer (Fig. 1). This equalizer/analyzer is common to many environmental test laboratories and is capable of 25 Hz bandwidth control from 100 to 2,000 Hz with finer bandwidth control below 100 Hz. The electrodynamic exciter and power amplifier were Ling Models A300 and 10/16, respectively. The input boundary motion control accelerometer was an Endevco Model 2270 used in conjunction with an Endevco Model 2713 charge amplifier. During the experiment the calibration sensitivity for each amplifier was selected such that the maximum sensitivity would be three times the anticipated overall rms test level. This is important for signal clipping considerations and maximum signal to noise ratio. Endevco Model 2226 response accelerometers were used in all cases. The charge amplifiers used were, again, Endevco Model 2713 (Fig. 2). The overall level of the input and the response accelerometers was monitored using a Ballantine true rms voltmeter, while a Tektronics oscilloscope was used to monitor the inputs and responses for waveform and possible clipping.

The inputs and responses were recorded on magnetic tape using an Ampex ES100 tape recorder. The record speed was 60 in/sec (FM record, 108 kHz center frequency), 1402 deviation which allowed maximum signal-to-noise ratio while providing digitizing flexibility for playback at slower tape speeds. The analog/digital conversion process included an Ampex FR 600 tape recorder, used during playback mode, and an A/C amplifier used as an amplifier/impedance matching device (Fig. 3). The tape output signals were



fed into the A/D converters. The IBM 1800 acted as a buffer (1,028 16-byte words) which would transfer each buffer load onto a digital tape. The A/D system was limited to 8,000 samples/second/track, hence only two channels of data were digitized at a rate of 4,000 samples/

second. Due to phase considerations (Appendix B), two methods of sampling were used during the digitizing process--linear and sample and hold. The data were properly digitized and put into format, then processed by the NWC spectral analysis computer program (Ref. 9) as shown in Fig. 4.

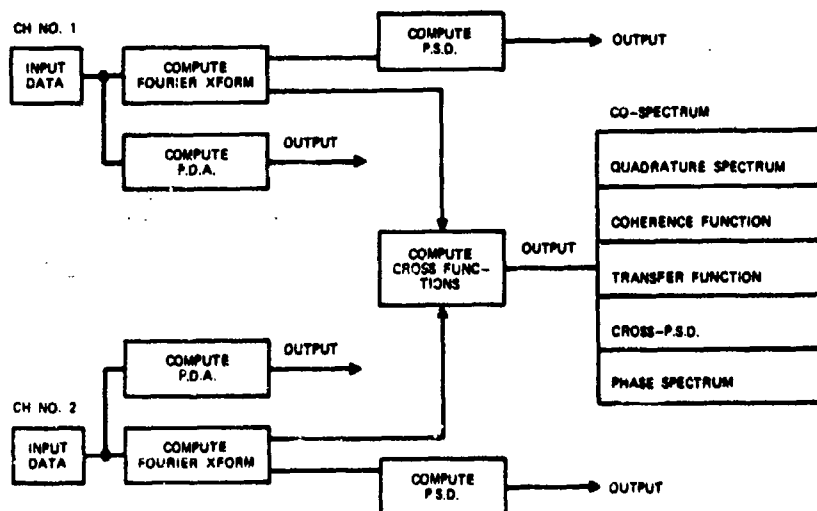


FIG. 4. Computer Scheme.

To achieve fixed (stationary) boundary conditions, a 1 in²-cross-section solid beam was attached at the fixed end as shown in Fig. 5. The slot that held the beam was machined to provide a height clearance of 0.005 inch and a width clearance of 0.011 inch. The slack was compensated for by using brass shim stock. The simple end condition was hardest to achieve. The technique used was to mount the beam between a knife edge and circular bar. When clamping the knife edge and bar to the beam, rubber washers were used to allow some give in the fixture and preclude support of bending moments. Figure 6 shows the fixture used to achieve the simple boundary condition. When fixed-fixed, fixed-simple, and simple-fixed boundary conditions were required, one end of the beam was rigidly attached to a concrete wall, 2 by 10 by 30 feet, while the other end was attached to the electrodynamic vibration exciter as shown in Fig. 7. The response accelerometers were mounted at nine places, symmetric about the center of the beam for the 100- and 102-inch-long beam and in six places for the cantilever condition (Fig. 8).

The following configurations of end conditions and excitation points were examined for the 1 in²-cross-section solid beam:

- a. Fixed-fixed Excitation from one fixed end (100 inches long)
- b. Fixed-free Excitation from the fixed end (52 inches long)
- c. Fixed-simple Excitation from fixed end (and the reverse case) (102 inches long)

d. Free-free

Acoustic excitation only (108 inches long)

The locations of accelerometers on the beam were dictated by the anticipated mode shapes. They were placed so that their position on the beam coincided with the maximum number of antinodes within the desired spectrum. Each accelerometer on the beam was equidistant from the adjacent accelerometer.

The proper operation of the spectral analysis computer program was verified by measuring the auto-spectral density plots on both the Ling ASD/80 Equalizer/Analyzer and on a Time/Data 100 analyzer.

The beam used in this experiment was measured for cross-section area, length, mass, and mass density variation as shown in Table 1. The values for Young's modulus and density were taken as ASM 2024 aluminum alloy with the weight/length measurement used as a cross check on density. The density uniformity was verified by an ultrasonic scan which detected no variations in density greater than those dictated by volume variations.

The beam was manufactured via the continuous extrusion method which involves large temperature gradients during the cooling process. Due to these temperature gradients, a slight skew and bend were noted in the beam. This skew and gravity bias would affect the mode shape (eigenvectors) but not the modal frequencies (eigenvalues).



FIG. 5. Fixed Boundary Fixture.

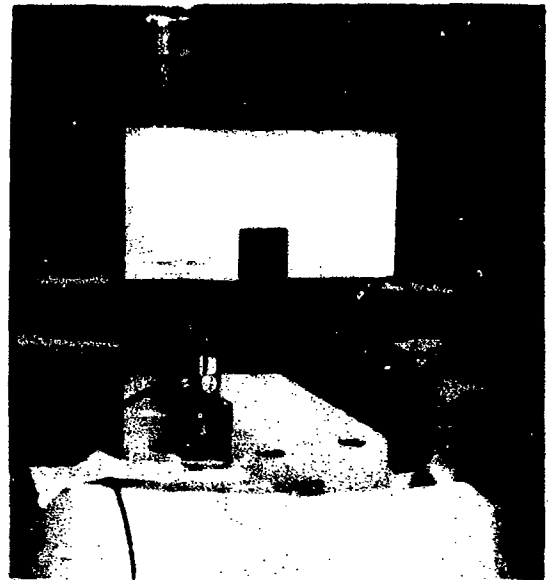


FIG. 6. Simple Boundary Fixture.

Reproduced from
best available copy.

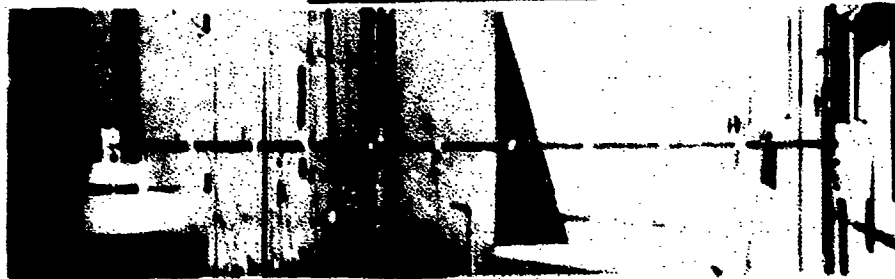


FIG. 7. Overall View of Fixed-Simple Boundary Conditions. One end is connected to the shaper while the other is connected to a concrete wall.

TABLE 1. Experimental Beam Physical Characteristics.

Parameter	Value	Variation
Young's Modulus, E	10.6×10^6 lb/in	10.5×10^6 compression 10.7×10^6 tension
Length, L (overall)	108.32 inches	± 0.005
Area, A	0.998 in^2	± 0.002
Weight, W	10.860 pounds	± 0.001
Weight/unit length, w	0.100 lb/in	± 0.003

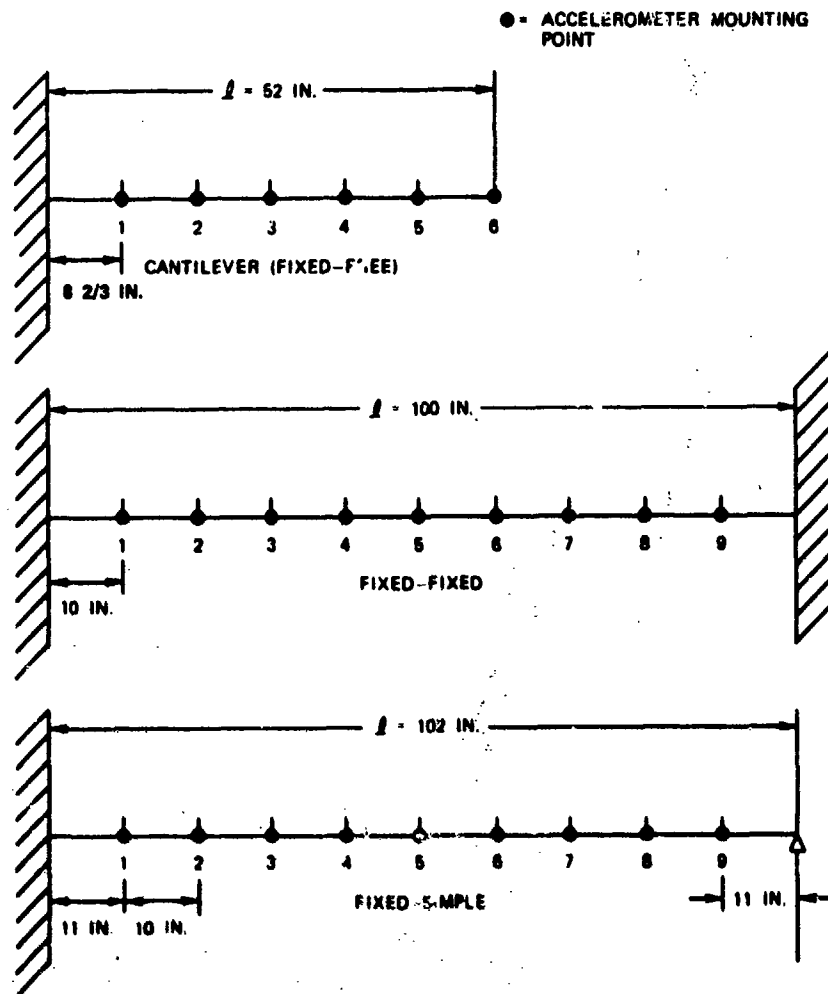


FIG. 8. Accelerometer Placement and Dimensions.

RESULTS AND DISCUSSION

Analysis

The method of analysis involves the examination of an auto function for relevant modal frequency information, then progresses to the cross functions to observe and retrieve phase information. The auto functions yield frequency information and amplitude information; the cross functions also yield frequency information and phase information. The combination of the analyses can be used to construct the various mode shapes. Their resolution is dependent upon the number of points being measured on the beam.

Table 2 shows the calculated modal frequencies and the corresponding experimental values for the 100-inch fixed-fixed beam, the 102-inch fixed-simple beam (excitation from either end), the 52-inch fixed-free beam, and the 100-inch free-free beam. Figure 8 shows the accelerometer placements on the beams. The beam with the

physical properties shown in Table 1 was used throughout the program. Figures 9a, 10a, 11a, 12a, and 13a are typical of the acceleration response spectra for each of the different configurations. Figures 9b, 10b, 11b, and 12b show the corresponding boundary input acceleration spectra; Fig. 13b is the acoustic spectrum at the mid-point of the free-free beam. The acoustic spectrum was uncontrollable, hence the deviations in the input spectrum of more than four decades. This made identification extremely difficult for all but the first and second modes. Notice that each input spectra (except for acoustics) is relatively flat (within a decade), while the response spectra show large peaks associated with a modal frequency.

A graphic demonstration that both modal frequency information and mode shape information are present in auto spectra is shown in Fig. 14a and 14b. Figure 14a shows the response PSD of an accelerometer at the center of a fixed-fixed beam, while Fig. 14b shows the response PSD for

TABLE 2. Modal Frequencies by Mode Number.

Mode No.	Bernoulli-Euler	Timoshenko	Experimental
Fixed-Fixed			
1	20.8	20.77	20.5
2	57.3	57.14	57.0
3	112.4	111.68	110.0
4	185.9	183.89	180.0
5	277.6	273.0	268.0
6	387.8	379.73	370.0
7	516.3	502.41	490.0
8	663.2	640.91	625.0
9	828.3	794.73	790.0
10	1011.9	963.38	970.0
Fixed-Simple			
1	13.73	13.76	14.0
2	44.51	44.52	45.0
3	92.87	92.64	94.0
4	158.80	157.86	161.0
5	242.36	239.83	242.0
6	343.48	338.13	340.0
7	462.18	452.33	455.0
8	538.67	521.93	590.0
9	752.36	726.48	730.0
10	924.35	885.30	900.0
11	1112.88
Free-Free			
1	17.7	17.67	17.5
2	48.8	48.59	48.5
3	95.7	94.96	95.0
4	158.1	156.35	150.0
5	225.0	232.46	225.0
6	330.0	322.95	330.0
7	420.0	427.0	420.0
8	520.0	545.0	520.0
Fixed-Free			
1	12.0	12.07	12.0
2	75.5	75.2	75.0
3	211.5	208.9	202.0
4	414.4	404.5	400.0
5	685.1	658.7	662.0
6	1023.4	966.8	975.0

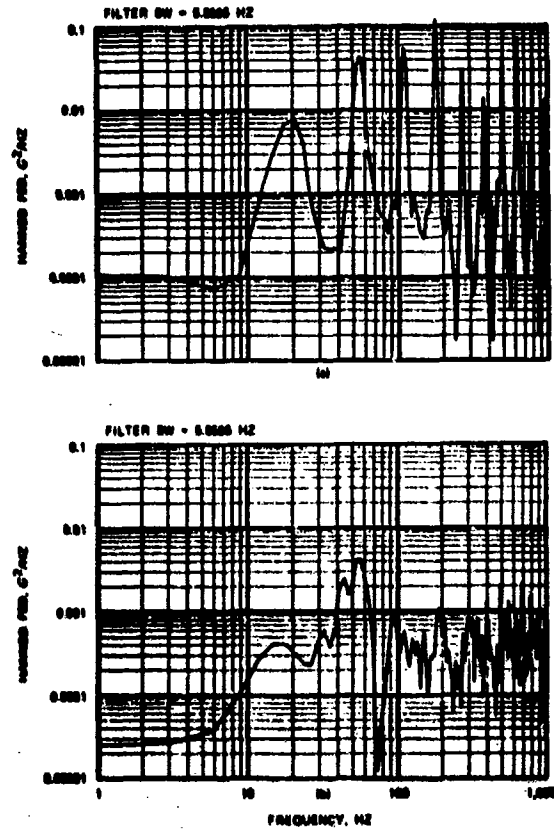


FIG. 9. Response at Point 2 (a) on the Fixed-Fixed Beam to the Input (b) at the Fixed Boundary.

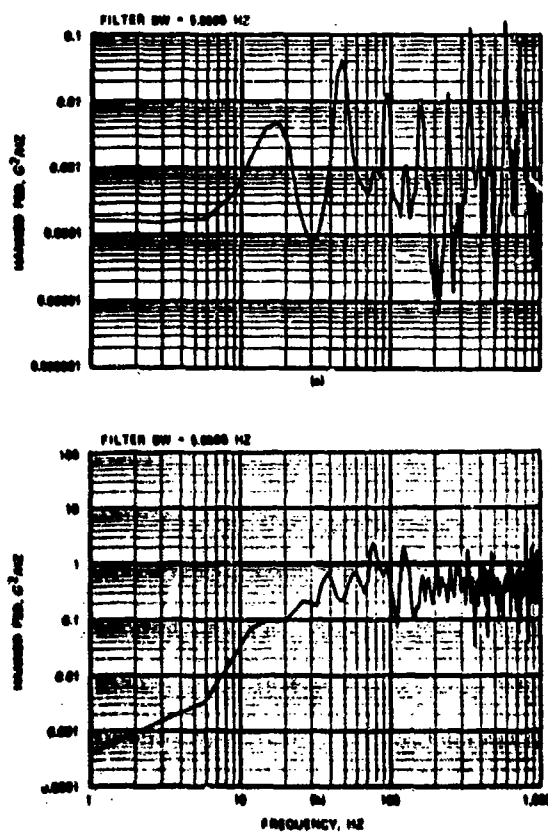


FIG. 10. Response at Point 6 (a) on the Fixed-Simple Beam to the Input (b) at the Fixed Boundary.

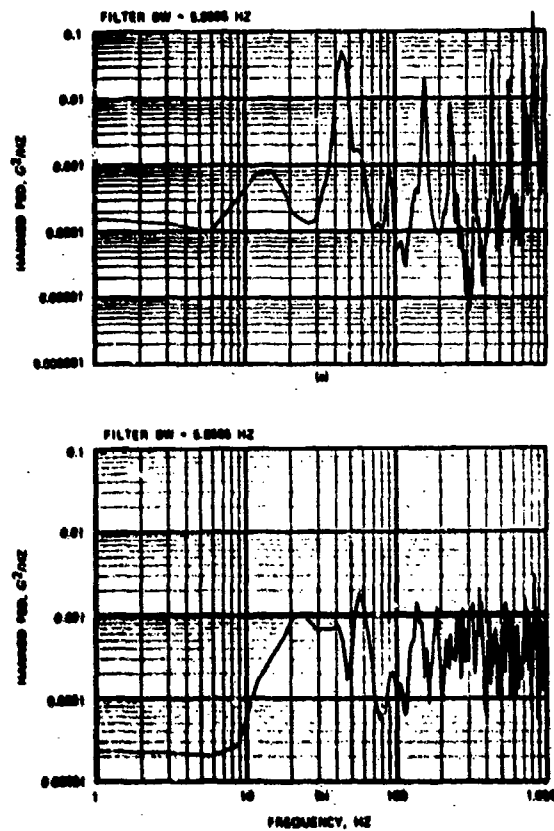


FIG. 11. Response at Point 3 (a) on the Fixed-Simple Beam to the Input (b) at the Simple Boundary.

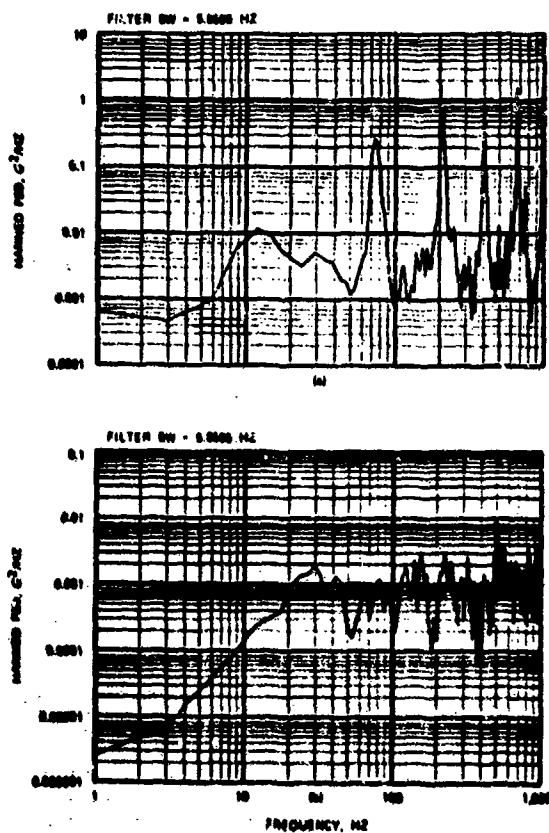


FIG. 12. Response at Point 6 (a) on the Fixed-Free Beam to the Input (b) at the Fixed Boundary.

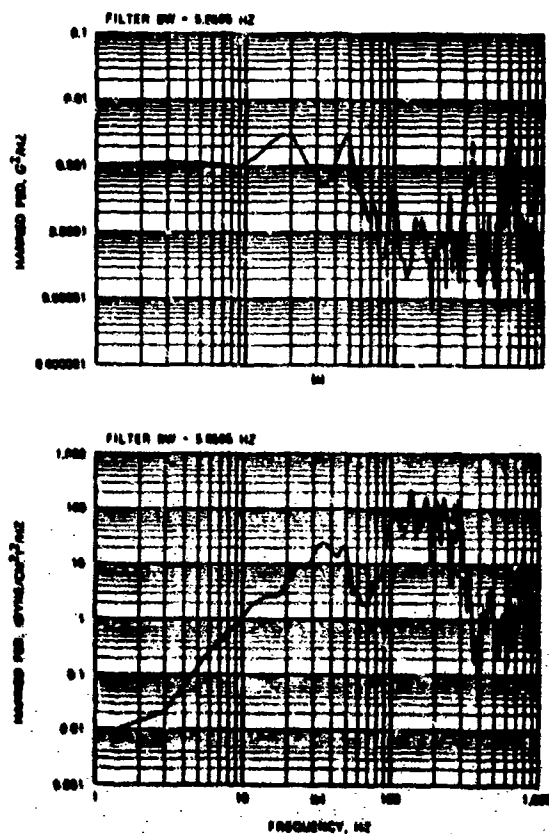


FIG. 13. Response of a Point (a) at the End of the Free-Free Beam and the Acoustic Spectrum at the Center (b). The spectrum was quasi-free field with direction normal to the axis of the beam.

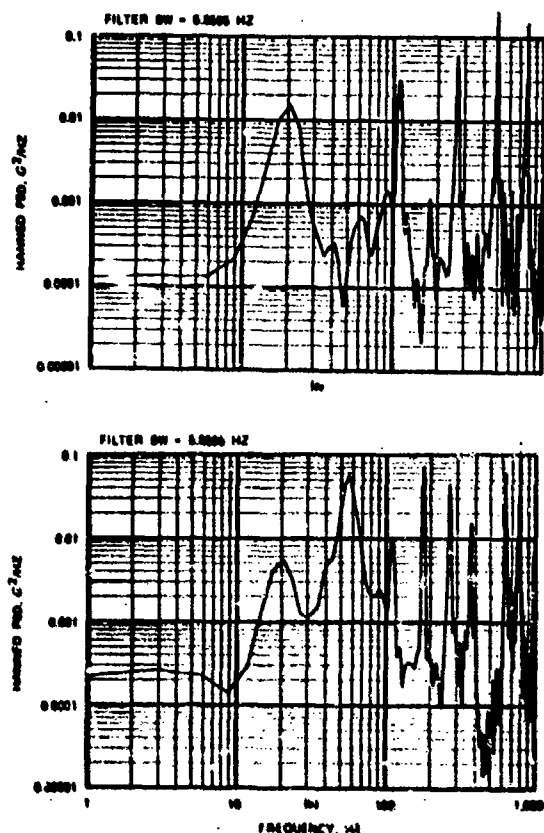


FIG. 14. Responses at Points 5 (a) and 7 (b) on the Fixed-Fixed Beam.

an adjacent accelerometer. Notice the suppression of even numbered modes in 14a compared to 14b. This phenomena is readily explainable on examination of theoretically computed mode shapes given in Fig. 15. (The black circle indicates the location of the two accelerometers being discussed.) The center position turns out to be a nodal point for those modes.

A rough quantitative determination of mode shapes would use the amplitudes in the auto spectra plots. Table 3 shows normalized amplitudes for each of six response accelerometers on a beam in the fixed-free configuration. The values of g^2/Hz versus frequency were converted to rms acceleration versus frequency, then multiplied by the bandwidth and divided by a constant

to produce a unitless normalized amplitude component. The phase relationships between the various response accelerometers can be deduced by careful examination of the co-spectral density plot and the phase plot. Consider the co-spectrum plot of accelerometers located at response points 4 and 6 (Fig. 16). It was determined that 75 Hz is a modal frequency by examination of the auto spectra and comparison with theoretical results. The negative value on the co-spectrum plot can be thought of as oppositely directed motion, or when response 4 is moving in a positive direction relative to the center line of the beam, response 6 is moving in the negative direction. Next consider Fig. 17, the co-spectrum between response 3 and response 6. Again there is a negative value, which can be interpreted as oppositely directed motion of the two response points. Figure 18 shows the same relationship between response 2 and response 6. Applying positive direction to responses 2, 3, and 4, and negative direction to response 6, in conjunction with the amplitude in Table 3, yields a mode shape indicated by Fig. 19. Figure 19 also shows the theoretical mode shape.

Alternate methods of determining the modal frequencies can be developed using the co-spectral density plots of response accelerometers and the transfer function plots of the input accelerometer and any output accelerometer. Figure 20 shows the co-spectrum of response points 6 and 9 on a fixed-simple beam. Notice the definition of each modal frequency. The frequency values compare exactly with those observed for auto-functions. The relative direction of amplitudes between each point is graphically demonstrated for each frequency.

TABLE 3. Normalized Experimental Amplitudes.

	Fixed-free 75 Hz	Fixed-fixed 20 Hz
Response 1	0.28	0.20
Response 2	0.51	0.40
Response 3	0.80	0.74
Response 4	0.45	0.90
Response 5	0.30	1.0
Response 6	1.0	0.98
Response 7	0.63
Response 8
Response 9	0.28

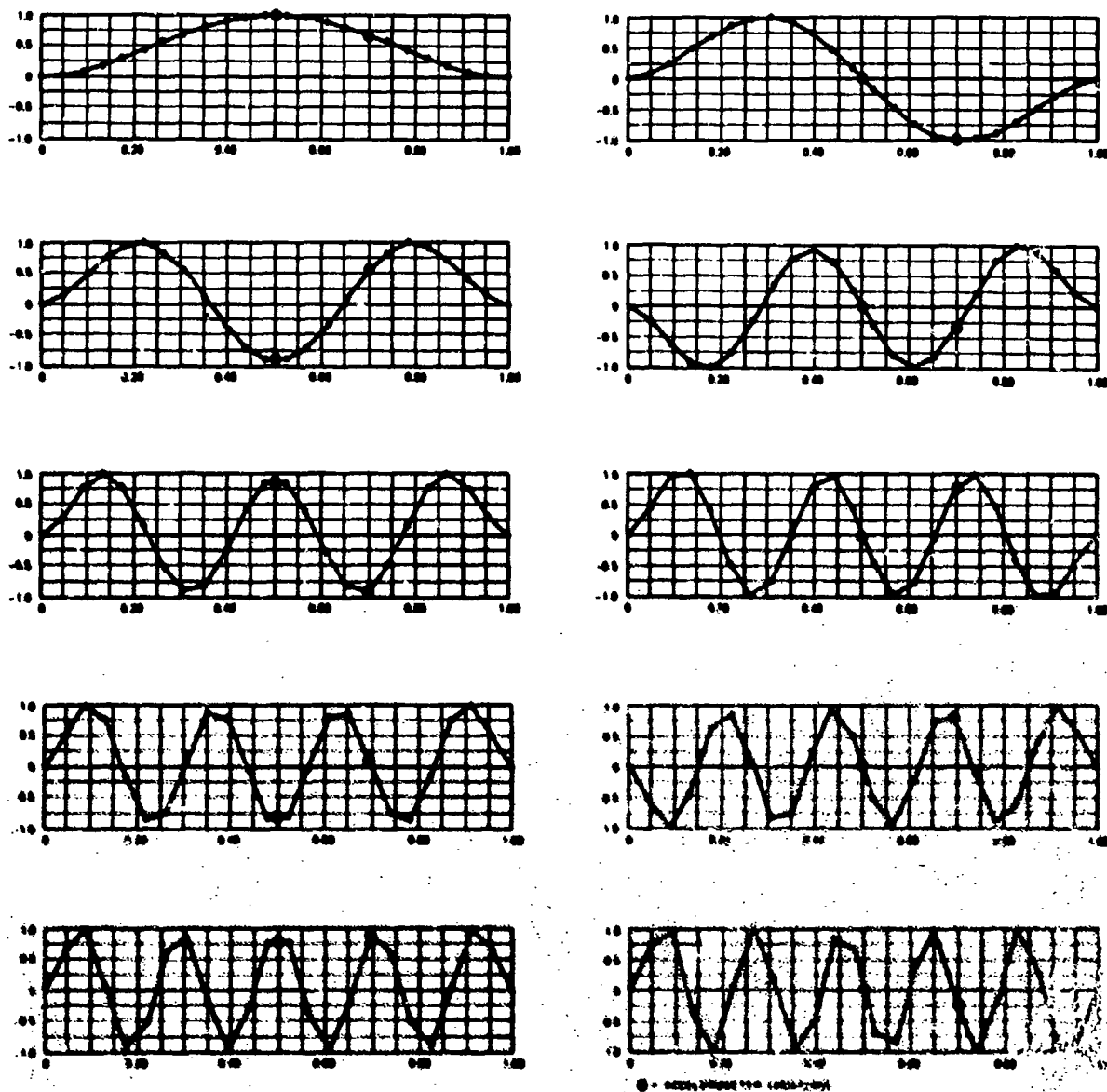


FIG. 15. Theoretical Mode Shapes for the First Ten Modes of the Fixed-Fixed Beam.

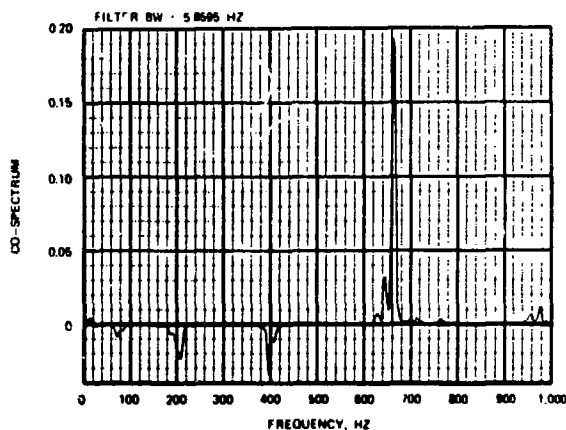


FIG. 16. Co-Spectrum of Responses at Points 4 and 6 on the Fixed-Free Beam.

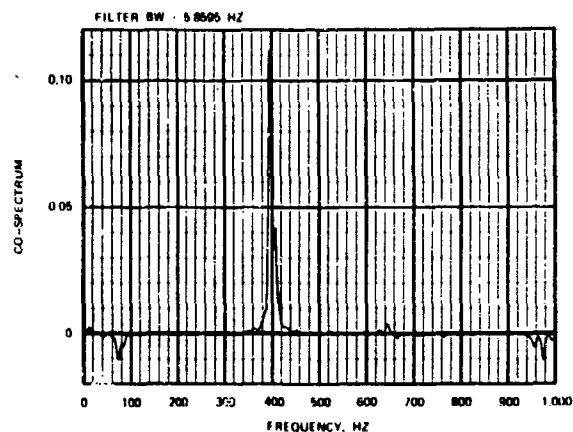


FIG. 17. Co-Spectrum of Responses at Points 3 and 6 on the Fixed-Free Beam.

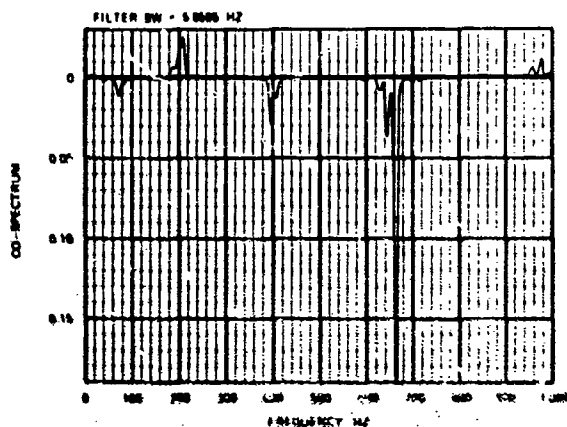


FIG. 18. Co-Spectrum of Responses at Points 2 and 6 on the Fixed-Free Beam.

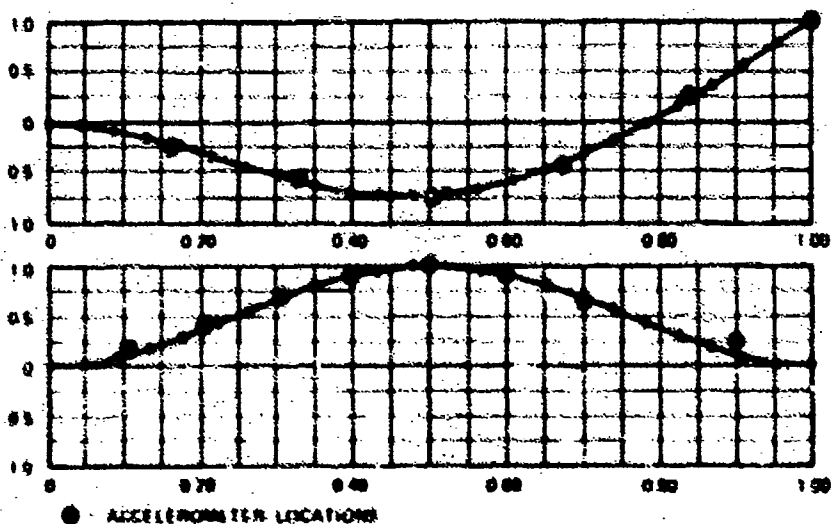


FIG. 19. Theoretical and Experimental Mode Shapes for the Fixed-Free Beam 75 Hz Mode (Top) and the Fixed-Fixed Beam 20 Hz Mode (Bottom).

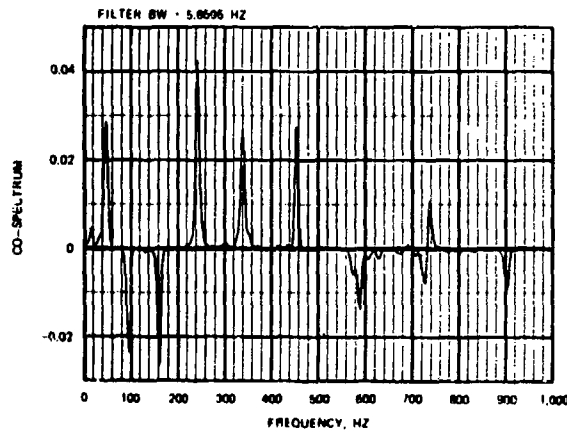


FIG. 20. Co-Spectrum of Responses at Points 6 and 9 on the Fixed-Simple Beam.

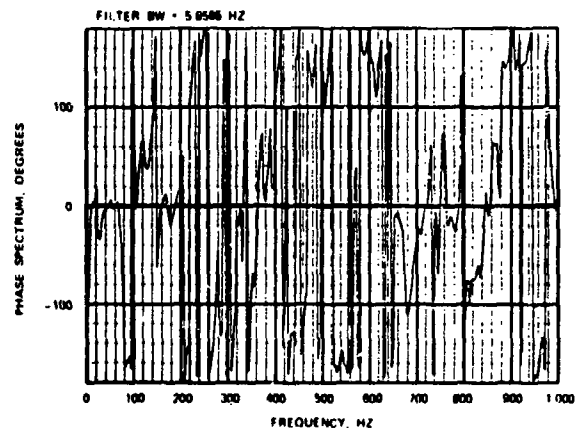


FIG. 22. Phase Spectrum Associated With Transfer Function in Fig. 18.

Figures 21 and 22 show the modulus of the transfer function and the phase spectrum for the input and response point 2 on a fixed-free beam. Each modal frequency stands out on the transfer function plot. Verification of a modal frequency is helped by observing that the phase angle has a transition through zero at the modal frequency. It should be noted that at higher frequencies the phase spectrum plot is unreliable for the computation scheme used here. When the distance between two response points becomes greater than the distance between two nodes of the mode shape, the phase plot breaks down because of the inherent limitations of the \tan^{-1} . The principle values of the \tan^{-1} are between $-\pi$ and π ; after this region is left there is no way to distinguish how the phase vector was arrived at, and only the principle value of the phase is computed.

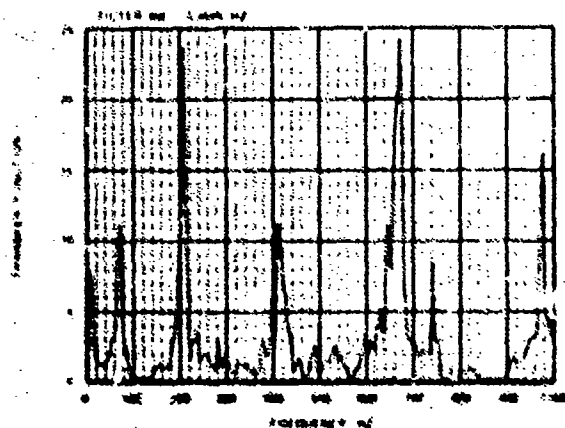


FIG. 21. Transfer Function of the Boundary and the Response at Point 2 on the Fixed-Free Beam.

Figure 23 shows the co-spectrum of points on a fixed-simple beam and is a graphic demonstration of one of the "do's" of response accelerometer placement--use symmetry whenever possible. The logic is: since the cross functions are just a measure of what the two points on a structure have in common (in the frequency domain), the use of symmetry will make common modes more prominent in that the amplitudes will be the same at modal frequencies.

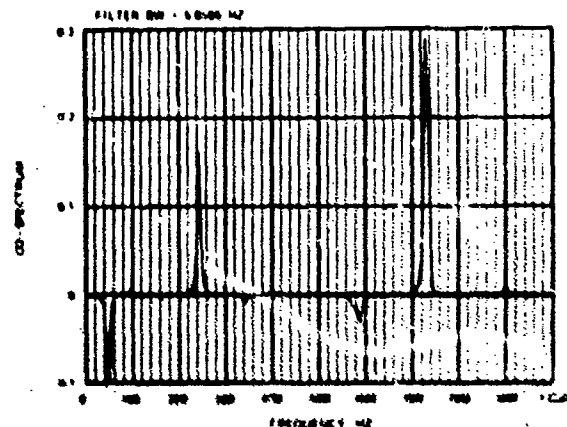


FIG. 23. Co-Spectrum of Responses at Points 1 and 7 on Fixed-Simple Beam.

Other methods of confirming the existence of modes is by computation of acceleration transfer functions between response points. Because of reflections (feedback) and out-of-plane mode coupling, the transfer functions calculated in this manner are dependent on input and statistical consideration. However, due to large response values at modal frequencies, the transfer functions between points are relatively independent of input at those frequencies.

An additional method of corroborating the existence of modal frequencies is by examination of coherence function plots. In general, if response accelerometer placement is such that the accelerometer is not at a nodal point or a point where the output is low, the coherence function will be close to 1. This value typifies a completely correlated response. If the response signal is near to the noise floor or nodal point, the coherence function will be somewhat less than 1 at that frequency. Figures 24 and 25, plots of points on the cantilever beam, show this behavior. Notice that at 12, 75, 200, 400, 660, and 990 Hz, the value is near 1. Figure 26 shows the coherence function of a response accelerometer placed near a node point for both the 660 and 200 Hz modes. This graphically demonstrates one of the pitfalls in using the coherence function.

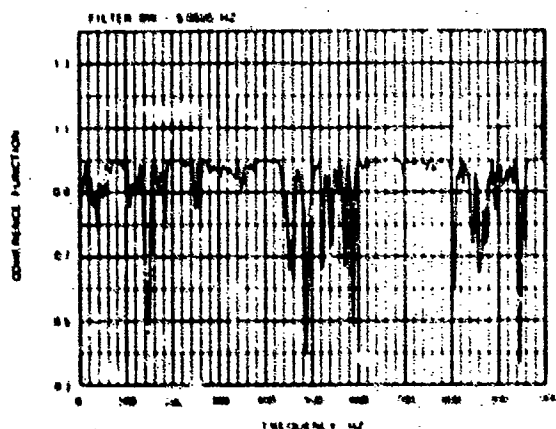


FIG. 24. Coherence Function of Responses at Points 4 and 6 on the Fixed-Free Beam.

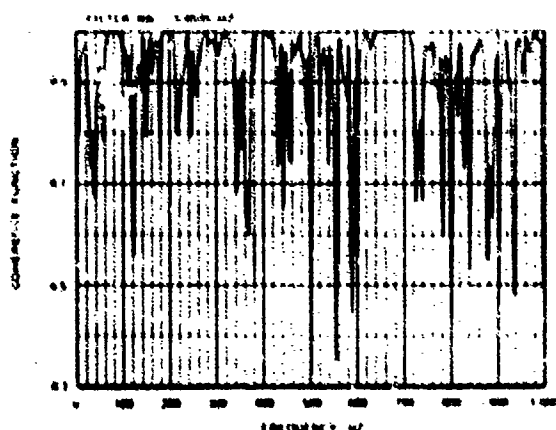


FIG. 25. Coherence Function of Responses at Points 2 and 6 on the Fixed-Free Beam.

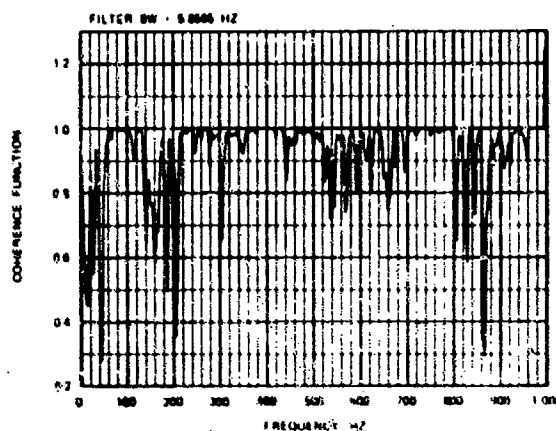


FIG. 26. Coherence Function of Responses at Points 3 and 6 on the Fixed-Free Beam.

Figures 27 through 31 show the modulus of the transfer functions between points on a fixed-fixed beam, digitized to circumvent phase problems (see Appendix B). The relationship

$$|H_{16}(f)| = |H_{13}(f)| + |H_{34}(f)|$$

$$+ |H_{45}(f)| + |H_{56}(f)|$$

is verified at least to the accuracy of our ability to read the plots.

Figures 32 through 36 show the phase spectrum for the points shown in Fig. 27 through 31. In the region where they are valid, i.e., where the points are less than a node apart, the relationship

$$\phi_{16} = \phi_{13} + \phi_{34} + \phi_{45} + \phi_{56}$$

is verified.

COMPARISON OF TECHNIQUE WITH OTHER METHODS

To compare the results of the modal analysis techniques developed in this paper with other, classical methods, the beam used as a test item in this experiment was subjected to a more traditional modal survey*. The beam was tested in what approximated a free-free configuration by hanging the beam by cotton twine from the nodes

* Naval Weapons Center. Beam Vibration Experiment, by E. Jeter. China Lake, Calif., NWC, 7 June 1971. (Reg. 4062-079-71.)

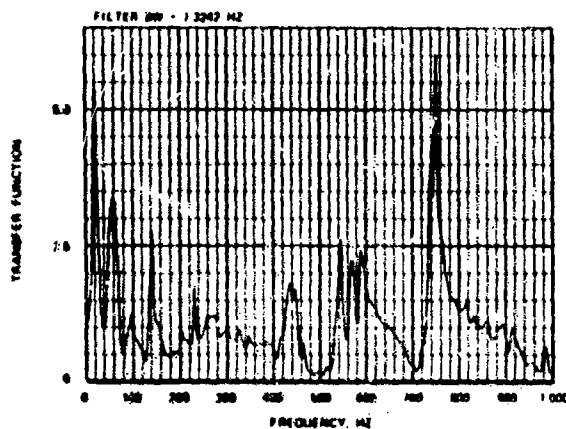


FIG. 27. Transfer Function of Input and Response at Point 3 on the Fixed-Fixed Beam.

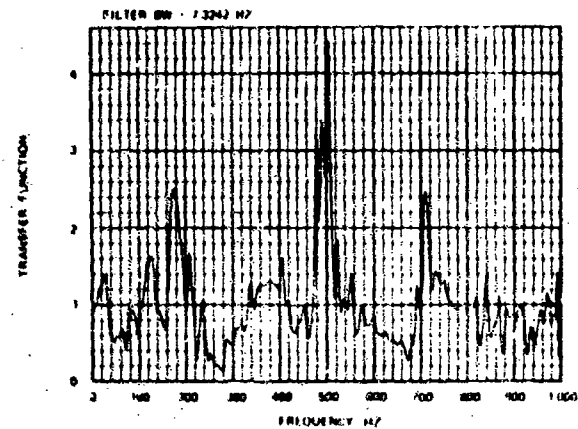


FIG. 28. Transfer Function of Responses at Points 3 and 4 on the Fixed-Fixed Beam.

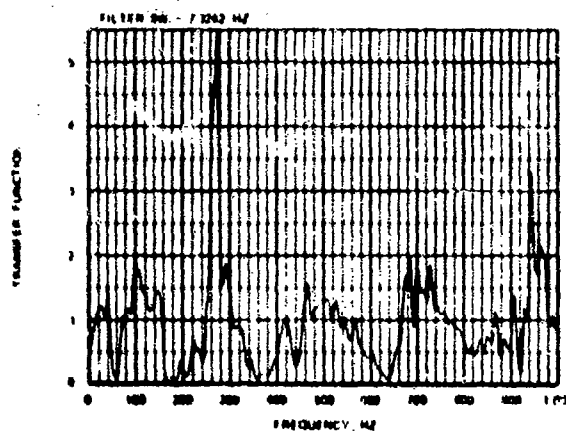


FIG. 29. Transfer Function of Responses at Points 4 and 5 on the Fixed-Fixed Beam.

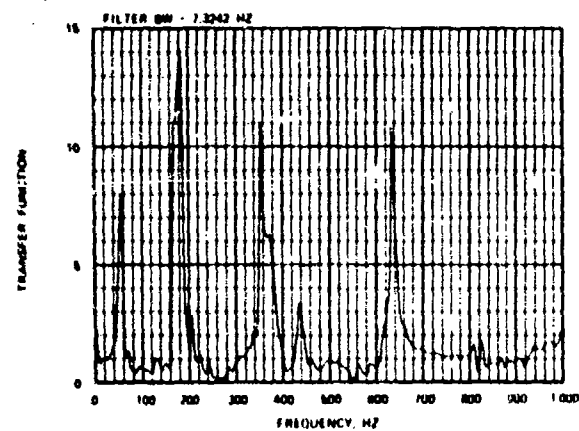


FIG. 30. Transfer Function of Responses at Points 5 and 6 on the Fixed-Fixed Beam.

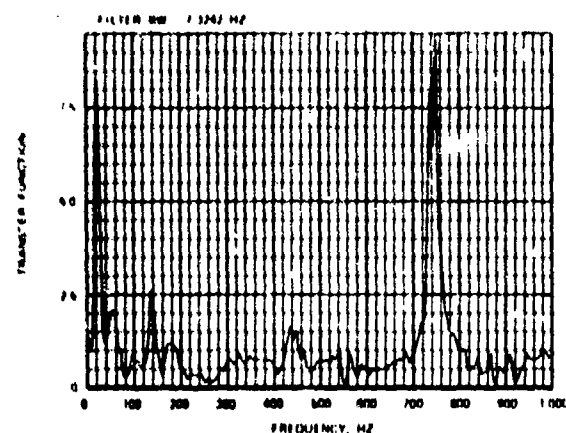


FIG. 31. Transfer Function of Input and Response at Point 6 on the Fixed-Fixed Beam.

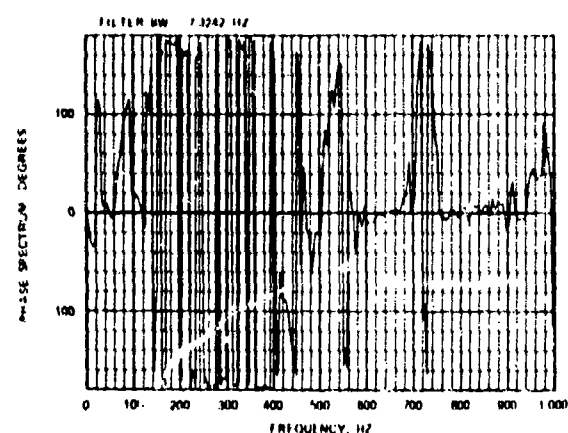


FIG. 32. Phase Spectrum of Input and Response at Point 3 on the Fixed-Fixed Beam.

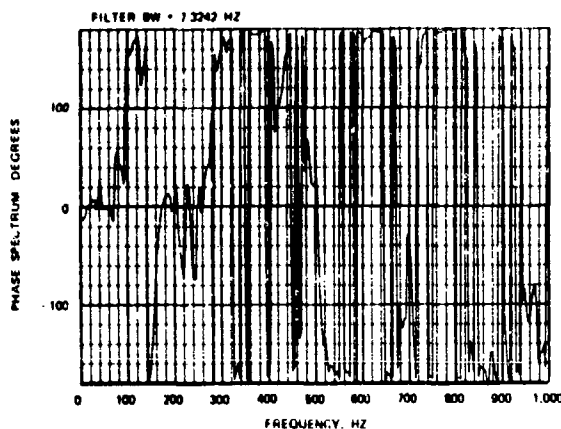


FIG. 33. Phase Spectrum of Responses at Points 3 and 4 on the Fixed-Fixed Beam.

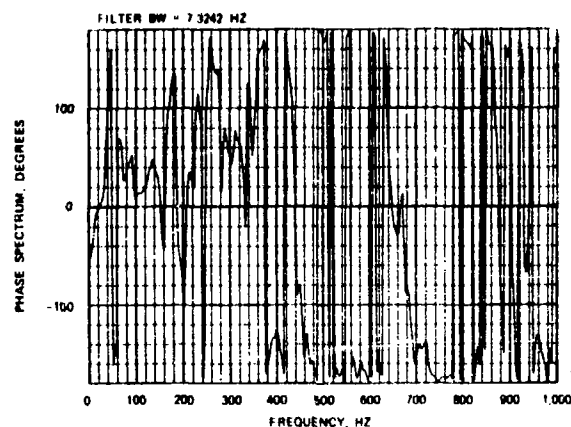


FIG. 34. Phase Spectrum of Responses at Points 4 and 5 on the Fixed-Fixed Beam.

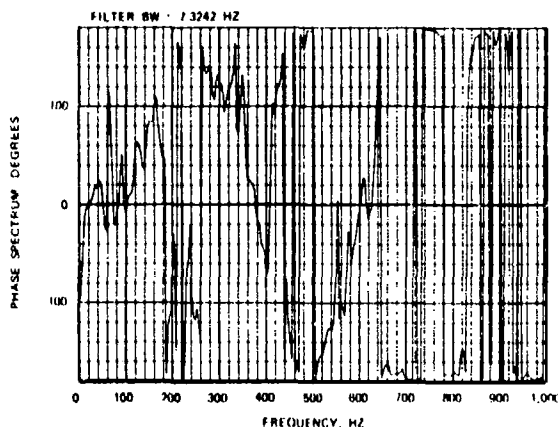


FIG. 35. Phase Spectrum of Responses at Points 5 and 6 on the Fixed-Fixed Beam.

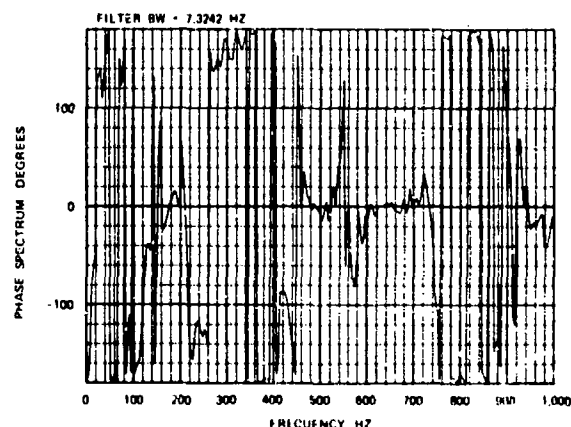


FIG. 36. Phase Spectrum of Input and Response at Point 6 on the Fixed-Fixed Beam.

of the first bending mode. An impedance head and force exciter were attached to one end of the beam and response accelerometer measurements were made at the center and opposite end of the beam. Figure 37 shows a mobility plot, the force input at one end divided into the velocity of the response at the other end.

To develop auto-spectrum, co-spectrum, and quadrature spectrum plots of the beam response to a constant-force sine-wave input, a Spectral Dynamics SD-log Co-Quad Analyser was used. Figure 38 shows the auto-spectrum of the response accelerometer at the end of the beam. Figure 39 shows the co-spectrum of the response at the middle of the beam and a point at the end of the beam. When test plots are examined using the logic and techniques developed for the analysis of random data, the same motion/modal information is developed.

CONCLUSIONS AND RECOMMENDATIONS

Using proper techniques, modal information can be retrieved from random data. Given certain minimum constraints on the spectrum of the forcing function, the sharp peaks in the response spectrum can be attributed to the response at a mode of the structure. Examination of the response plots shows that range between the maximum and minimum values of the input spectrum should be less than an order of magnitude. When acoustic excitation was used in this experiment the input spectrum at the center of the beam varied at least five orders of magnitude, making the modal information difficult to retrieve.

The precision with which the modal frequency can be identified is dependent on the investigator. In this report, the goal was not precise measurement of the modal frequency, but a general demonstration of some of the techniques which can be

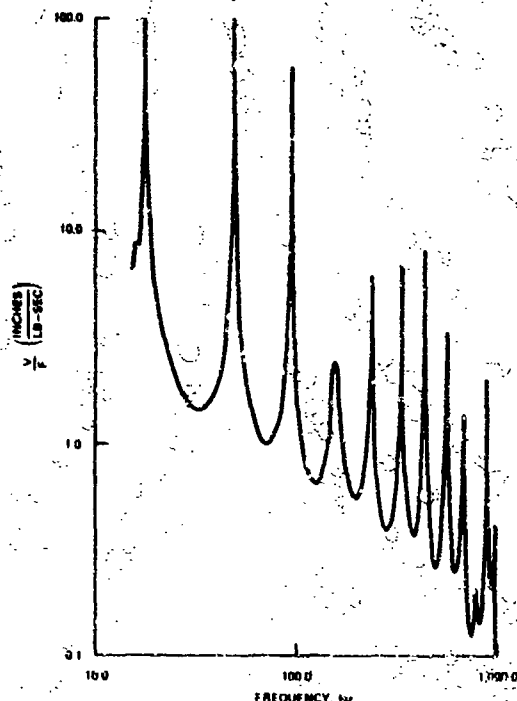


FIG. 37. Mobility Plot of a Constant Force input at One End and Response at the Opposite End on the Free-Free Beam.

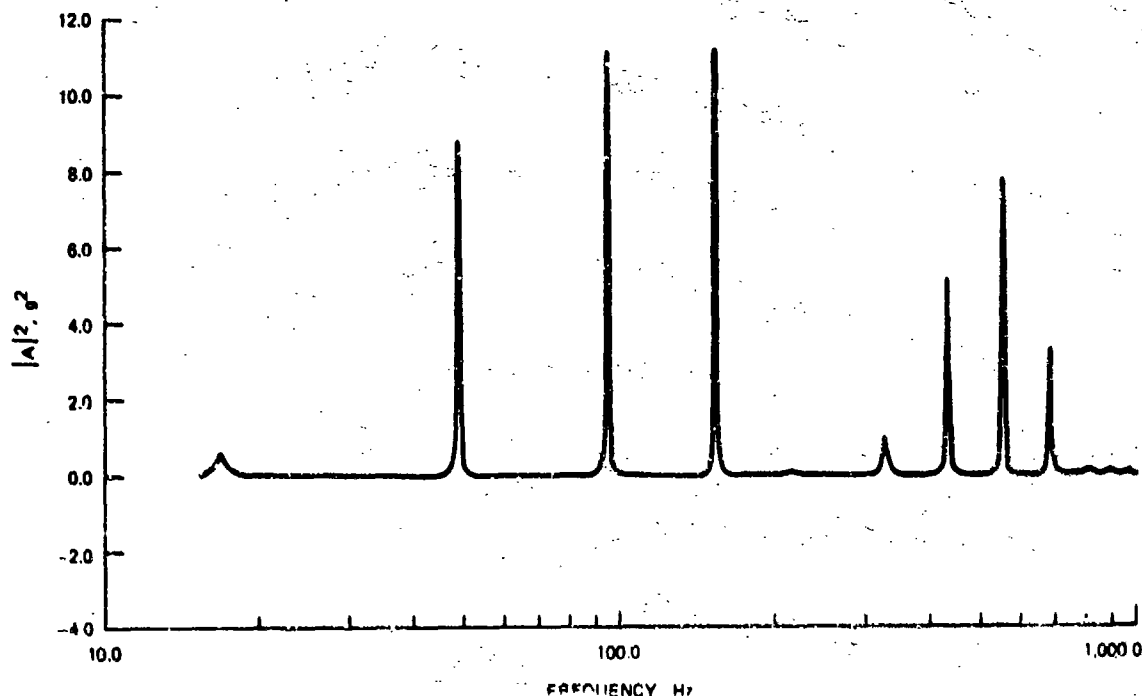


FIG. 38. Auto Spectrum of a Point on the End of the Free-Free Beam.

used to extract the information from the random data. If precise frequency information is required, long time slices should be used with tabular printouts instead of plots. If T is the time slice or data window,

$$\frac{1}{T} = \text{fundamental discrete Fourier transform frequency}$$

$$= \Delta f$$

Δf will be the limit of resolution in the frequency domain.

Non-linear effects, such as boundary reflections (feedback), out-of-plane mode coupling, etc., make the use of response transfer functions less reliable. However, the responses at modes of the structure are so large in comparison with response at non-modal frequencies, that the relationships pointed out in the text of this report are applicable.

The computer program, used in conjunction with a UNIVAC 1108 digital computer, had the capability of computing the various complex functions exhibited. When dealing with a complex structure whose modes are not widely separated or easily defined, all of the functions shown would need to be used. When the structure is simple with widely spaced modes which are easily modeled and compared to theory, the auto-spectrum and the co-spectrum would provide all the information needed to totally describe the mode.

This technique should be examined with a view toward retrieving structural coefficients, i.e., damping, effective mass, stiffness.

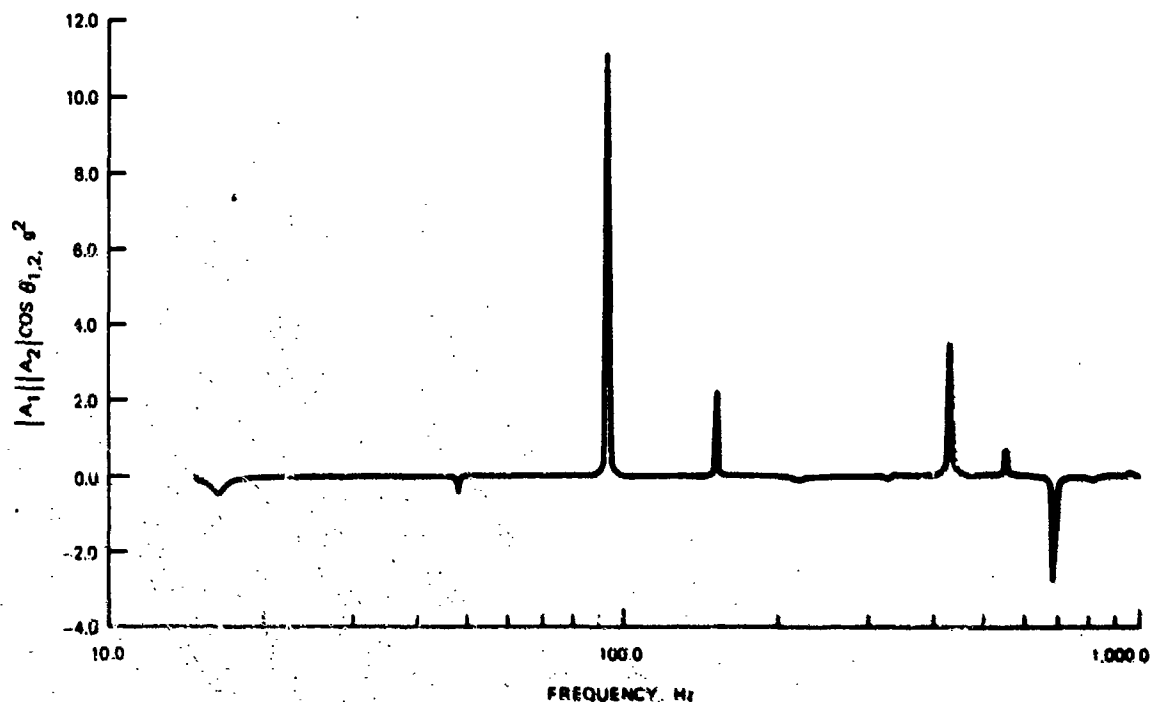


FIG. 39. Co-Spectrum of a Point at the Center and a Point at the End of the Free-Free Beam.

Appendix J

FIRST 20 ROOTS TO THE FREQUENCY EQUATIONS

The first 20 roots are given for the following frequency equations.

Fixed-simple: $\cos(at) - \cosh(at) = 0$

Fixed-free: $\cos(at) \cosh(at) = -1$

Fixed-fixed: $\cos(at) \cosh(at) = 1$

Free-free: $\cos(at) \cosh(at) = 1$

4.	10.9955407	14.	42.4115008
5.	14.1371683	15.	45.5530934
6.	17.2787595	16.	48.6944861
7.	20.4203522	17.	51.8362787
8.	23.5619449	18.	54.9778714
9.	26.7035375	19.	58.119464
19.	29.8451302	20.	61.2610567

Fixed-Fixed and Free-Free

Fixed-Simple

1.	1.92668231	11.	35.3429173
2.	7.06858274	12.	38.48451
3.	10.2101763	13.	41.6261026
4.	13.3517487	14.	44.7676953
5.	16.4933614	15.	47.9092879
6.	19.634954	16.	51.0508806
7.	22.7765467	17.	54.1924732
8.	25.9181393	18.	57.3340659
9.	29.059732	19.	60.4756585
10.	32.2013247	20.	63.6172512

Fixed-Free

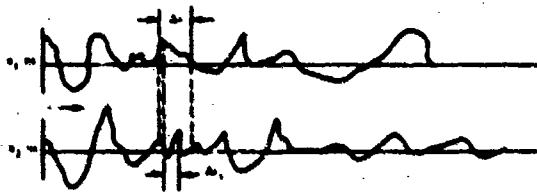
1.	1.87510406	11.	32.9867228
2.	4.69409113	12.	36.1283155
3.	7.85475743	13.	39.2699081

1.	1.13061228	11.	32.9867228
2.	4.73004074	12.	36.1283155
3.	7.85320362	13.	39.2699081
4.	10.9956078	14.	42.4115008
5.	14.1371654	15.	45.5530934
6.	17.2787596	16.	48.6944861
7.	20.4203522	17.	51.8362787
8.	23.5619449	18.	54.9778714
9.	26.7035375	19.	58.119464
10.	29.8451302	20.	61.2610567

Appendix B

PHASE CONSIDERATIONS

Phase problems are present due to the signal conditioning procedures. One digitizing method used results in a phase lag of one channel of data relative to the other when two channels are sampled. For instance, let $X_1(t)$ and $X_2(t)$ be two time series under consideration:



Looking at time records X_1 , X_2 , the fundamental sampling interval for both records is Δt , but the interval or lag in sampling first record X_1 then record X_2 during the fundamental interval Δt , is Δt_1 . Looking at the Fourier transforms of X_1 , X_2 , the fundamental frequency of the transform is $\Delta F = \frac{1}{N\Delta t}$, and any discrete frequency is given by $k\Delta F = \frac{k}{N\Delta t}$; the point sampled in record X_1 is given by $n\Delta t$, the point in X_2 by $(n\Delta t + \Delta t_1)$, write

$$A_k = \frac{1}{N} \sum_{n=0}^{N-1} X_{n1} e^{-i2\pi \frac{nk}{N}} \quad k = 0 \dots N$$

$$B_k = \frac{1}{N} \sum_{n=0}^{N-1} X_{n2} e^{-i2\pi \frac{nk}{N} + \theta} \quad k = 0 \dots N$$

θ is the relative phase between X_1 and X_2 when both are sampled in the same interval Δt .

$$\theta = 2\pi \frac{\Delta t_1}{N \Delta t} k$$

Seen in this light, θ becomes a function of k (frequency). The higher k , the more pronounced the effect of the phase on the relative

phase between A_k and B_k . For instance, in the system used there was a built-in system lag of $\Delta t_1 = 0.055$ msec between channels, while the sampling rate was 4,000 words/sec/track or a Δt of 0.250 msec, then $\Delta t_1/\Delta t \approx 1/5$. Thus, when higher frequencies are to be examined or when precise phase information is desired, different digitizing techniques are dictated. Two of the records examined for the above phase problem were also examined using a series of sample and hold amplifiers where the time uncertainty in digitizing electronics for adjacent channels is on the order of 0.1 msec. Thus, uncertainties in phase information for the second technique are reduced to the limitations of the tape recorder response and variations in system electronics. However, these are not considered in this report.

Other problems in interpreting the phase at higher modes arise due to mode shape and accelerometer placement. The phase plots (shown in the body of the report) were arrived at by calculating $\tan^{-1} \frac{\text{Quad}}{\text{Co}}$, of which the principal values are $-\pi$ to π . The problem can best be understood by looking at the first six bending modes of a fixed-free beam (Fig. 40). Points A and B in Fig. 40 are for reference. Notice that in the first mode the points are somewhat out of phase; the phase lag for the second through sixth mode are as follows:

Second mode $\approx \pi$

Third mode $\approx \frac{3\pi}{2}$

Fourth mode $\approx 2\pi$

Fifth mode $\approx \frac{5\pi}{2}$

Sixth mode $\approx 3\pi$

The problem in computing phases of greater than 2π is how to assign a sign to the phase angle, or how was the angle arrived at or in which direction does the vector rotate in a phasor diagram. For structural work where only the lower modes are of interest, this is a minor problem.

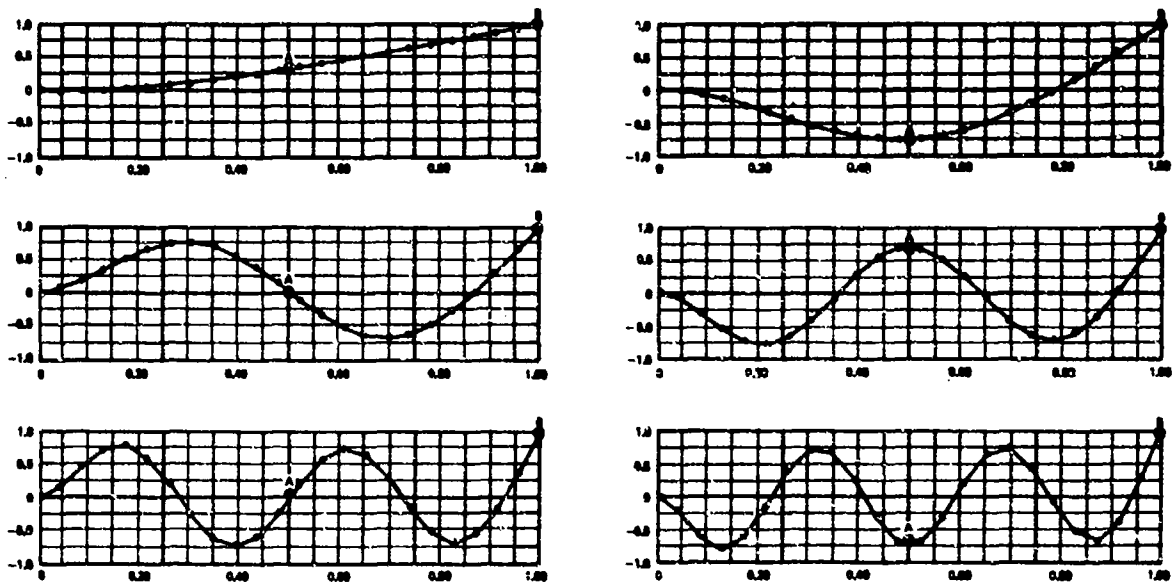


FIG. 40. The First Six Bending Modes of a Fixed-Free Beam.

REFERENCES

1. Eringen, A. C. "Response of Beams and Plates to Random Loads," *Tans. ASME Ser. E*, Vol. 24, No. 46, pp 46. 1957.
2. Jullien, Y. G. "On the Response of Continuous Structures to Random Excitation," *Proc. of Fourth U.S. Nat. Cong. of App. Mechanics*, Berkeley, Calif. 1962.
3. Stanisic, M. M. "Response of Plates to Random Load," *J. Acous. Soc. Am.*, Vol. 43, No. 6, pp. 1351. 1968.
4. Thompson, W. T. "Continuous Structures Excited by Correlated Random Forces," *Int. J. Mech. Sci.*, Vol. 4, pp. 109. 1962.
5. Trubert, M. R. P. "Response of Elastic Structures to Statistically Correlated Multiple Random Excitations," *J. Acous. Soc. Am.*, Vol. 35, No. 7, pp. 1009. 1963.
6. Cooley, J. W., P. A. W. Lewis, and P. D. Welch. "The Fast Fourier Transform and Its Applications," *IBM Research Paper*, RC 1743. 1967.
7. University of California, Davis. *Random Vibration of Cantilever Plates in Air*, by A. L. Jones, Ph.D. Dissertation. 1967.
8. University of Houston. *Simulation With Minimum Equipment of Random Vibration Induced by Complex Equipment*, by O. E. Crenwelge, Master D. Tech. Report No. 22. August 1970.
9. Lockheed Electronics Co. *MSC Statistical and Wave Analysis Program (VIBAN3)*, by J. McBryde. Program Documentation, Program No. Q467, Project No. 4587. 1969.
10. Naval Air Systems Command. *Environmental Criteria Determination Techniques*. Task No. A34520/216/71F17532401, Semi-Annual Progress Report. December 1970.
11. Bendat, J. S. and A. G. Piersol. *Measurement and Analysis of Random Data*. New York, John Wiley & Sons, Inc. 1966.
12. Chen Y. *Vibration: Theoretical Methods*. Addison-Wesley, Reading, Mass. 1966.
13. Timoshenko, S. *Vibration Problems in Engineering*. New York, D. Van Nostrand Co., Inc. 1937.
14. Crandall, S. H. *Random Vibration*, Vol. 2. M.I.T. Press, Cambridge, Mass. 1963.
15. Harris, B. *Spectral Analysis of Time Series*. New York, John Wiley. 1967.
16. Papoulis, A. *Probability, Random Variables and Stochastic Processes*. New York, McGraw-Hill. 1965.
17. Parzen, E. *Modern Probability Theory and Its Applications*. New York, John Wiley. 1960.

ACKNOWLEDGMENTS

The authors extend their thanks to Mr. E. L. Jeter, who conducted modal analysis using mechanical impedance techniques, Mr. T. Hayes for the beam studies utilizing the computer program "Beam", and Mrs. R. Kleeper for converting the MSC wave analysis program, VIBAN 3 to the MSC spectral analysis program and for programing assistance.

DISCUSSION

Mr. Smith (Lockheed Missiles and Space Co.): In regard to the results that were obtained at the lower end of the frequency spectrum, Clarkson and Mercer several years ago showed that the filter bandwidth must be considerably narrower than the bandwidth of the specimen. In this case your lower frequency modes did not meet that condition. Therefore one underestimates the amplitude of the peak and overestimates the width of the band and the damping.

Mr. Christiansen: We did not make an attempt to retrieve damping information but we felt we had a choice. If one has to trade-off one will see good amplitudes at high frequencies and poor amplitudes at low frequencies if one uses g^2 spectra. But to address myself to your point, I do not think that holds in the computing scheme that we used because we actually have a filter bandwidth and a Fourier transform bandwidth, which is another thing, and in this case it was about 1/4 of the bandwidth you showed.

RESPONSE OF AIR FILTERS TO BLAST

E. F. Witt, C. J. Arroyo, and W. N. Butler
Bell Laboratories
Whippany, N. J.

Overpressure pulses can enter underground nuclear-blast resistant buildings if blast valves fail to close, or transmitted into the building if such valves be closed directly by the blast itself. Tests simulating these conditions were conducted at the Bell Laboratories Chester facility to determine the degree of damage sustained by commercial air filters and dampers installed close to blast valves, and to determine the magnitude and duration of overpressure pulses which caused no damage or only initial damage. Test results indicated that air filters would be undamaged by long-duration pulses with overpressure of about 1.3 psi, and would tolerate higher pressures of shorter duration. No damage should be expected for pulses of 2 to 3 millisecond length with peak pressure of 7 psi.

Much of the long distance communication network of the Bell System is constructed to resist the effects of nuclear bomb explosions. Included are the buried coaxial cables with associated underground buildings. These buildings require large amounts of air for cooling and in the operation of emergency electrical generators. Blast valves are used on intake and exhaust ports to prevent interior blast damage.

It is possible for air blasts to pass through the valves. Free-field overpressures of less than about 1 psi will not trigger the valves; thus a long duration, low overpressure blast could be transmitted into the building. The blast valves used in Bell System buildings are closed before blast arrival by an electrical control system. These valves, however, have a blast-closing backup feature. The valve is slammed shut directly by blast forces on the moving elements of the valve. If this should happen, a short duration, high overpressure pulse would be transmitted into the building. It is also possible to use valves that blast-close only. These would always allow some

pressure to be transmitted through. Valves of this type are not now used by the Bell System, but may be considered for future use because of their low cost.

Filters and dampers are very vulnerable elements in a blast-resistant building because they are located near the blast valves and are inherently weak structures normally designed for low air pressures. The blast resistance of sheet metal ducts has also been investigated (Reference 1).

The tests described in this paper were conducted to demonstrate the resistance of filters and dampers to the above described blast pulses. The air blast was produced using the shock tube at the Bell Laboratories facility at Chester, N. J. Blast valves were put upstream of the filters to produce the short blast pulses. Longer pulses were produced with the valves removed. The effects of a very long duration pulse were simulated by passing a steady high-velocity flow through the filters. The filters and dampers tested were typical of those used in Bell System underground buildings. Tested

TABLE I
Apparatus Tested

Name	Manufacturer	Size	Model
Rigid Aerosolve Filter	Cambridge Air Filter Co.	24" x 24" x 24"	43D-45
Hi-Flo Filter	Cambridge Air Filter Co.	24" x 24" x 29"	43X-45
Hi-Cap Filter	Cambridge Air Filter Co.	24" x 24" x 15"	45HC-2500
Flo Filter (roll-type)	Cambridge Air Filter Co.	30" x 46"	VH RF-3-50
Damper	Arrow Lower and Damper Corp.	34" x 46"	(Made to Order)

were three models of 2-foot square filter modules, a roll-type filter, and a damper with extruded aluminum blades. Model information is presented in Table I.

BLAST TESTING OF 2-FOOT SQUARE FILTER MODULES

The shock tube used in these tests is driven with compressed air released by a fast-acting valve designed and built by the Defence Research Establishment, Suffield, Alberta, Canada. The expansion section of the shock tube, a 14-inch diameter pipe, is joined into the test area, as shown in Figure 1.

The first expansion is into a 16-inch square test area. The blast valves, when used, are located either within this 16-inch square area or at the junction where this area expands

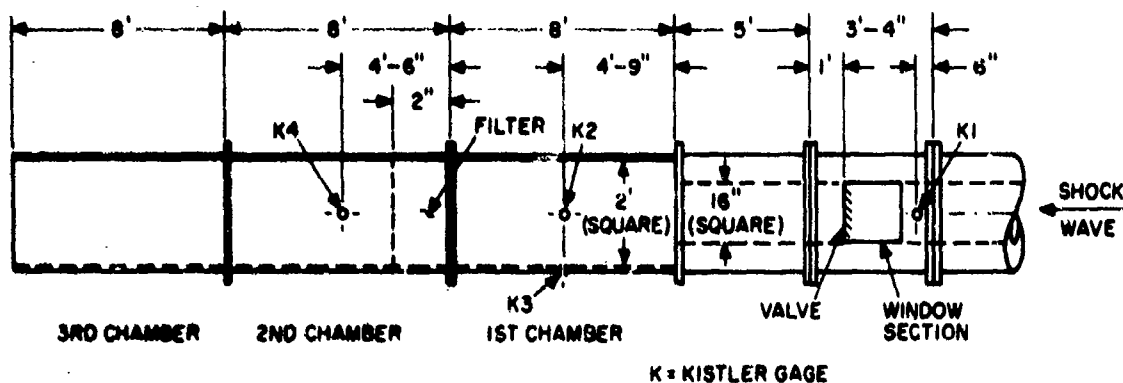
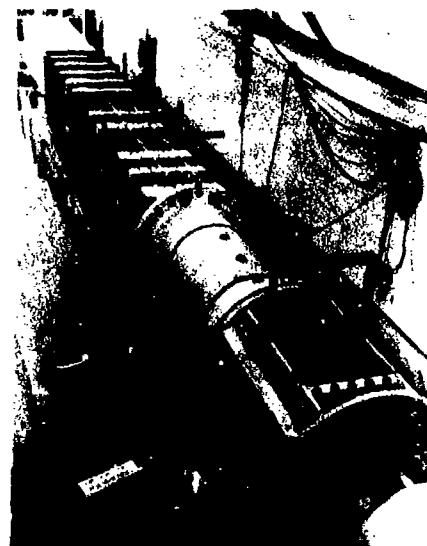


Figure 1. Shock Tube Set-up

to a 24-inch square section. The first 24-inch square section, which is 8 feet long, allows the shock to reform in the larger area. Filters were mounted in the front of the second 24-inch square section. A third section was used in most tests to delay the formation of the rarefaction wave at the filter. These three sections were made of plywood, reinforced with steel angles.

Two blast valves were used in these tests to produce blast pulses. A quarter-scale model of the louver valve (shown in Figure 2) was used to produce intermediate pulse lengths. The louver blast valve is now being made for use in Bell System buildings. Tests on this model are described in Reference 2. The model was mechanically tripped so that it started to close when the blast arrived. Shorter duration pulses were produced by a reed blast valve. This is a fast-closing, blast-actuated valve with seven fiberglass reinforced epoxy blades 1-1/4" wide, 12" long, and 1/16" thick.

Pressures upstream of the blast valve and upstream and downstream of the filters were measured. Transducer locations are



Figure 2. Louver Valve Model in Shock Tube

shown in Figure 1. The Kistler 701A transducers were isolated from the test chamber by an air gap to eliminate unwanted acceleration-produced signals.

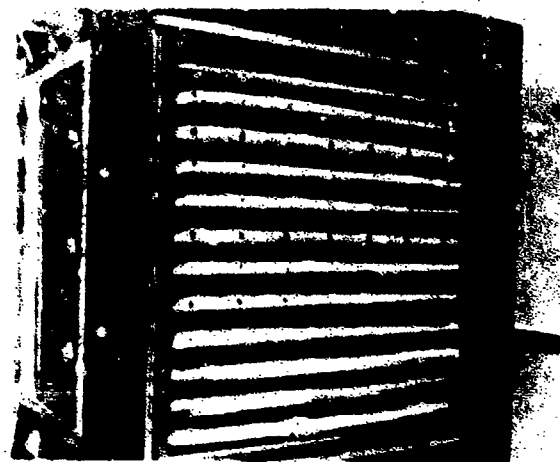
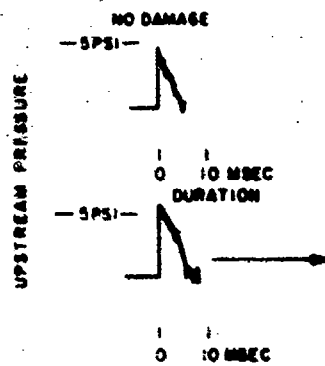
RESULTS FOR 2-FOOT SQUARE FILTER MODULES

Figure 3 shows the three types of filter modules tested. Overpressure time waveforms upstream of the filter at gage location 2 (Figure 1) are reproduced for the highest overpressure blast pulse which produced no damage and the lowest overpressure pulse which produced the damage illustrated in the photographs. Each filter was subjected to increasingly higher pressure pulses until damage occurred, and was then discarded.

The Aerosolve filter had the filtering material punctured, as a result of a 5-psi overpressure pulse. The Hi-Flo filter had the supporting ribs bent and torn from the frame by a pulse with a peak overpressure of about 7 psi. The filtering material in the Hi-Cap filter was torn by a pulse with a peak overpressure of about 8 psi.

The pulses producing the above described filter damage were generated by passing the blasts through the quarter-scale louver blast valve. In order to produce longer durations, the shock tube was operated without any blast valves. Similar filter damages were produced, but with lower overpressures. Intermediate pulse durations were obtained with the last 2-foot square section removed. This allowed a faster return of the rarefaction wave, which tended to blow out the filtering material. Since it was not possible to separate positive from negative pulse damage, these test results are not used here.

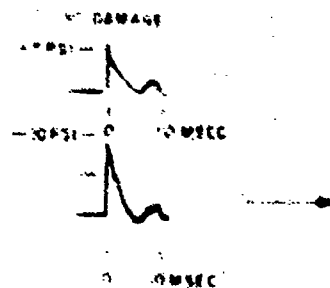
The peak pressure and duration of the highest pressure blast pulse which did not cause damage, and the lowest pressure pulse which did, are plotted in Figure 4. The shaded area lies between certain damage and no damage for the three filters. In addition to the



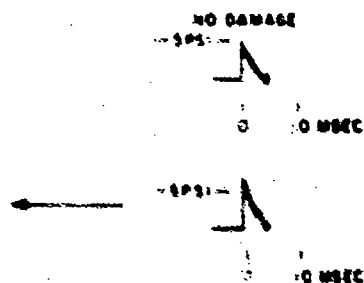
Damaged Aerosolve Filter



Damaged HI-Flo Filter



Reproduced from
best available copy.



Damaged HI-Cap Filter

Figure 3. Damaged Filters and Corresponding Pressure Pulses

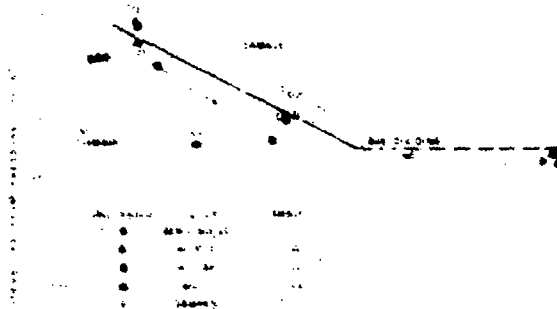


Figure 4. Filter Damage as a Function of Upstream Pressure and Duration

data described above, the shorter duration pulses produced by the reed valve are represented by the three points on the left-hand side of the figure. These caused no damage because the peak pressures were too low. It was not possible to operate this valve with higher incident pressures to produce higher pressures on the filters.

The response of the filters to pressure loading is better portrayed in Figure 5, a plot of the pressure differential ($P_2 - P_4$) across the filter versus pulse duration. The shaded area in Figure 5 corresponds to that in Figure 4. A curve representing the constant product of the peak pressure and the duration has about the same slope as the test data. Filter damage occurred at approximately a constant impulse. This is only an approximation since this type of response applies to a very low frequency linear oscillator.

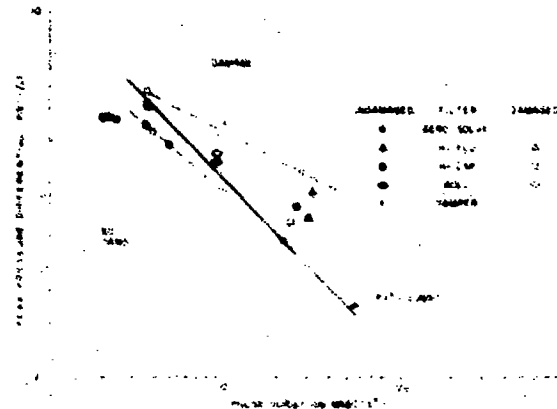


Figure 5. Filter Damage as a Function of Differential Pressure and Duration

STEADY FLOW THROUGH 2-FOOT SQUARE FILTER MODULES

The shock tube tests simulated relatively short duration blasts compared to those produced by large yield nuclear explosions. An infinite duration blast was simulated using a steady high-velocity flow through the filters using the test apparatus shown in Figure 6. It was not possible to create filter-damaging velocities with this apparatus. Tests were run with the blower at maximum capacity. Velocities at the filter face were measured at a number of points and the average values are given in Table II. The table also lists the overpressures of blast waves which have the same air velocities as measured. These are between 1.2 and 1.4 psi. These tests did not simulate the initial shock in the blast wave, but this did not affect test results. The filters withstood higher pressure shocks in the blast pulse tests.

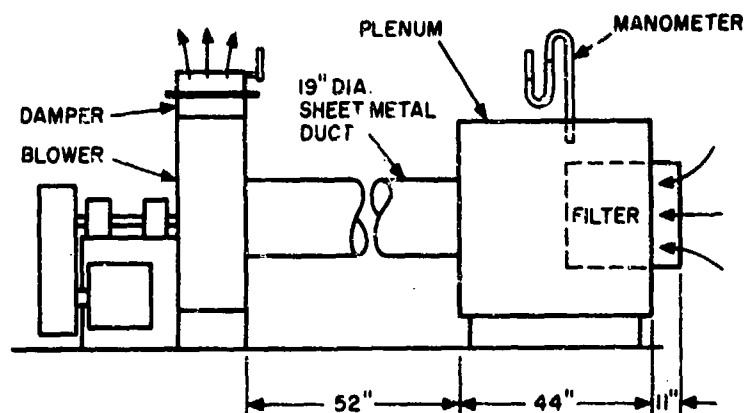
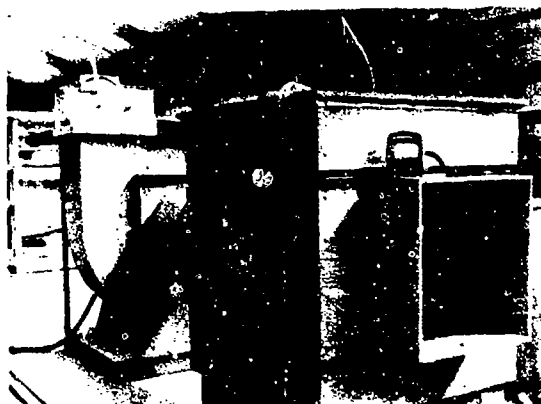


Figure 6. Steady Flow Test Apparatus

TABLE II
Results of Steady Flow Tests

Filter	Maximum Average Velocity FT/SEC	Corresponding Shock Overpressure PSI
Aerosolve	64	1.2
Hi-Flo	74	1.3
Hi-Cap	73	1.3

TESTS ON ROLL-TYPE FILTER AND A DAMPER

These large pieces of equipment required the use of a large test section (Figure 7). The shock was expanded by means of a conical section tapering in diameter from 14 inches to approximately 4 feet, at which end a rectangular duct was attached. The roll-type filter shown

in Figure 8 was placed adjacent to the opening in the duct and the damper was placed inside.

The damage to the roll-type filter (Figure 9) occurred with a peak overpressure of 1.7 psi at a duration of 8 milliseconds. The filtering material was blown out of its track and the vertical rods were bent and forced out

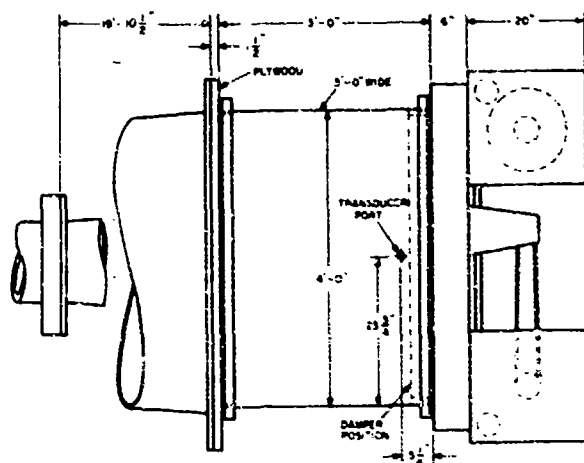


Figure 7. Apparatus for Testing Roll-Type Filter and Damper

Figure 8. Roll-Type Filter in Test Position

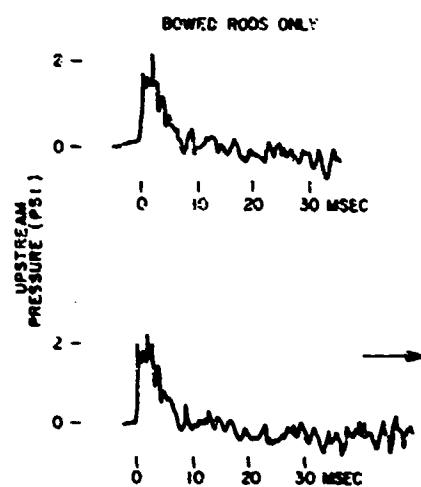
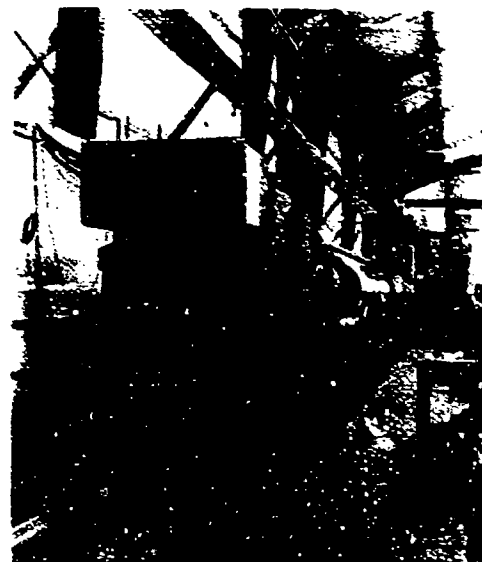


Figure 9. Roll-Type Filter Damage and Corresponding Pressure Pulse

of their anchors. Lower pressure blast pulses just bend the vertical rods.

The damper (Figure 10) was only slightly deformed by a pulse with a peak overpressure of 5 psi in a duration of 10 milliseconds. This occurred with the damper closed, its most vulnerable position. In this case, the peak pressure was a reflected pressure, produced by an incident pressure of 2.5 psi. The damper operated freely after the test.



Figure 10. Damper Being Checked for Deformation by Blast Pulse

DISCUSSION OF RESULTS

The results of the blast pulse and steady flow tests of the 2-foot square filters and the roll-type filter are superimposed in Figure 4. There is an average dividing line shown in the figure between damage and no damage to the 2-foot square modules. The constant pressure portion of the line on the right side is estimated from the steady flow data, where filter damage was not obtained. Results for the roll-type

filter fall considerably below the spread of data for the 2-foot square filters. This is due at least partially to the rapid reduction in pressure downstream of the roll-type filter because the blast pulse exhausted into a large room. This allows a rarefaction wave rapidly to reduce the downstream pressure. The 2-foot square filter modules were tested in a constant cross-section duct, and the downstream pressure on the filter was maintained when the filter was loaded by an upstream pressure. If the downstream pressure on the roll-type filter is assumed to be ambient, the pressure differential on this filter is upstream pressure. The data points for a roll-type filter then fit neatly within the spread of data for the other filters, as shown in Figure 5. This suggests that the roll-type filter in the size tested is of similar blast resistance to the other filters with the same type of downstream conditions. This discussion suggests an extended interpretation for Figures 4 and 5: The former is for filters with about the same plenum areas upstream and downstream; the latter is for filters with a very large downstream plenum.

The damper tested survived a peak overpressure of almost 5 psi which was the reflection of a 2-1/2 psi incident pressure. This incident pressure with a duration of about 10 milliseconds places the resistance of the damper at the lower bound of the shaded area in Figure 4. This indicates that this particular damper is about as resistance to blasts as the filters tested. Downstream conditions would have no effect on a closed damper.

CONCLUSIONS

Application of these test results to actual conditions will not be considered. The 2-foot square filters were found to withstand a long-duration blast of over 1-psi overpressure. The free-field overpressure could be larger because of attenuation in the passages leading into the building. Filters were also found to be undamaged by rarefaction waves of about 1-psi

negative pressure. A rarefaction of this magnitude is associated with the positive peak overpressure of about 5 psi. It is unlikely that the filters would suffer primary damage from negative pressure loading.

Short duration pulses, which are transmitted through closing blast valves, have a damaging potential which is a function of both peak overpressure and duration. For very short pulses about 2 to 3 milliseconds long, the filters should not be damaged by peak pressures of about 7 psi. It was not possible to damage the filters in these tests with pulses from the very fast closing reed valve.

The damage criterion used in this report was the first sign of visible damage. The slight damage observed in these tests might not prevent satisfactory filter performance, so the criteria discussed here should be conservative.

However, the supporting structures for filters and dampers have not been investigated. This might very well be the weak link in a commercially installed system. The effective pressures acting on the filters, summarized in Figure 5, can be used to obtain the loading and response of the supporting structure.

References

1. Witt, E. F., "Pressures Downstream of Blast Closing Valves, Project LN116," DIAL PACK Symposium, Ottawa, March, 1971 (to be published).
2. McCoy, R. G., Nevrincean, G., and Witt, E. F., "Prediction of Blast Valve Response Using Models," The Shock and Vibration Bulletin, No. 40, Part 2, December, 1969.